coatings

Special Issue Reprint

Research Progress of Metals and Alloys by Thermal Layering and Deposition

Edited by
Ashish Kumar Srivastava and Amit Rai Dixit

www.mdpi.com/journal/coatings

MDPI

Research Progress of Metals and Alloys by Thermal Layering and Deposition

Research Progress of Metals and Alloys by Thermal Layering and Deposition

Editors

Ashish Kumar Srivastava
Amit Rai Dixit

MDPI

Basel • Beijing • Wuhan • Barcelona • Belgrade • Novi Sad • Cluj • Manchester

Editors

Ashish Kumar Srivastava
G.L.Bajaj Institute of
Technology and Management
India

Amit Rai Dixit
Indian Institute of Technology
(Indian School of Mines)
Dhanbad
India

Editorial Office
MDPI
St. Alban-Anlage 66
4052 Basel, Switzerland

This is a reprint of articles from the Special Issue published online in the open access journal *Coatings* (ISSN 2079-6412) (available at: https://www.mdpi.com/journal/coatings/special_issues/Thermal_Layering_Deposition).

For citation purposes, cite each article independently as indicated on the article page online and as indicated below:

Lastname, A.A.; Lastname, B.B. Article Title. *Journal Name* **Year**, *Volume Number*, Page Range.

ISBN 978-3-0365-7844-6 (Hbk)
ISBN 978-3-0365-7845-3 (PDF)
doi.org/10.3390/books978-3-0365-7845-3

Contents

About the Editors

Ashish Kumar Srivastava

Dr. Ashish Kumar Srivastava received B.Tech from the (Govt. college) Institute of Engineering and Technology, VBS Purvanchal University, Jaunpur and M.Tech from Uttar Pradesh Technical University, Lucknow. He completed his Ph.D. at the Indian Institute of Technology (ISM) Dhanbad, India in 2018 in Materials and Manufacturing Specialization. He possesses experience of more than 17 years in the field of teaching, research and administration. He is presently working as a Professor in the Department of Mechanical Engineering, G.L. Bajaj Institute of Technology & Management, Greater Noida, India. Dr. Srivastava has published more than 100 research papers in SCI, Scopus and peer-reviewed journals and conference papers at national and international levels. Prof Srivastava was named in the top 2% of scientists in the world in the list prepared by Stanford University and Elsevier BV in the year 2022. He has successfully completed 2 government-funded projects and is currently working on a project grant of Rs 10.19 Lacs received from the Council of Science and Technology (CST) UP. Recently, he has published 7 patents under the Government of India. Presently, he is guiding 4 Ph.D. scholars and has guided 8 PG and 45 UG projects.

Amit Rai Dixit

Dr. Amit Rai Dixit completed his postgraduate and doctoral degree in Mechanical Engineering at MNNIT, Allahabad, India. He is currently working as Associate Professor at the Indian Institute of Technology (Indian School of Mines), Dhanbad, Jharkhand, India. He has been Head of the Mechanical Engineering Department since 2020. Dr. Dixit has 21 years of teaching and research experience. Dr. Dixit has published more than 150 research papers in different international journals and conferences. He has guided 11 PhDs and 32 postgraduate theses. Prof Dixit was named in the top 2% scientists in the world in the list prepared by Stanford University and Elsevier BV in the years 2021 and 2022. He has also visited many renowned universities abroad for research and teaching assignments. He was awarded international teaching mobility under the European-Union-sponsored Erasmus+ in 2018. Prof Dixit has established state-of-the-art labs on additive manufacturing, non-traditional manufacturing, tribology, and flexible manufacturing at the institute. He is currently undertaking research in the area of additive manufacturing, non-conventional manufacturing processes, the machining of exotic materials, etc. Prof Dixit has successfully completed five externally funded research projects and is currently handling two high-value funded projects. He is an executive member of different professional bodies.

Preface

It is well known that research focused on the creation of specific materials that can withstand high temperatures, high wear, and high corrosion is essential for the industrial sector. Many issues in manufacturing are related to the wear and corrosion of parts, which serves as the primary cause of the failure of the entire product. According to their engineering use, the local characteristics of materials are altered during the design process. One effective method for extending a component's life is coating. Additional techniques include functionally graded materials, friction stir layer deposition, additive layer coatings, and friction stir coating. These methods can be used to solve problems related to the high wear and corrosion of an automobile's mating parts as well as enhance their mechanical and microstructural qualities. Techniques for plastic deformation, such as severe plastic deformation (SPD) and friction stir processing (FSP), are important factors to improve surface characteristics and a material's overall performance.

As a result, several advanced methods for depositing nano- and microstructured coatings by thermal layer deposition, microwave-assisted coatings, cold-spray and electroless coatings, along with well-known characterization approaches, have been presented here.

Other similar techniques not exactly related to the type of coating, but that still improve microstructural and mechanical surface properties in a similar way, are included in this volume. The readers of this volume can explore various experimental results that provide a wide range of processing and characterization methods. For example, friction stirring was used to create the surface composite Al359/Si3N4/Eggshell, and the influence of this surface composite on microstructural and tribological characteristics was examined. The management of dynamic and static parameters was examined in order to enhance the welding strength achieved using friction stir spot welding (FSSW), with an innovative control system based on fuzzy logic to optimise the process. Due to their inadequate tribological properties, titanium and titanium alloys are insufficient in friction and wear conditions. Because of their homogeneous thickness, better hardness, and superior corrosion resistance, electroless coatings have been discovered to be efficient as surface treatment techniques. The investigation of the tribological features of microwave-assisted g-C3N4/MoS2 nanocomposite coatings indicated a number of potential research directions. The results revealed that the addition of g-C3N4 in nanocomposites can reduce friction and improve wear life, producing superior results to those obtained with MoS2 alone. Biowaste, such as CBP (chicken bone powder), an example of a biowaste material produced in a poultry farm, contains particles that can be utilized to enhance the overall properties of a material. Surface composites may be an appropriate alternative material for structural and automobile components. Various applied loads, sliding speeds, and weight percents of additive graphitic carbon nitride in a molybdenum disulphide nanocomposite coating on a steel substrate were employed in tests to enhance the settings for Pin-on-Disc wear apparatus. A high-performance base oil additive compound called Liquid Crystals (LCs) was created to handle a variety of operating circumstances. Investigations were carried out into how the mesogenic phase temperatures range of LCs affected tribological features. These are some of the interesting findings that are discussed in this volume.

Ashish Kumar Srivastava and Amit Rai Dixit
Editors

coatings

MDPI

Editorial

Research Progress in Metals and Alloys by Thermal Layering and Deposition

Ashish Kumar Srivastava [1,*] and Amit Rai Dixit [2,*]

[1] Department of Mechanical Engineering, G.L. Bajaj Institute of Technology and Management, Greater Noida 201306, India
[2] Department of Mechanical Engineering, Indian Institute of Technology (ISM), Dhanbad 826004, India
* Correspondence: ashish7185@gmail.com (A.K.S.); amitraidixit@iitism.ac.in (A.R.D.)

Over the last 20 years, because of their superior hardness, chemical stability, and outstanding oxidation barrier, many coating systems have now been extensively researched using various deposition processes and employed for wear-resistant protection [1]. These surface coatings have been explored across a variety of technological disciplines, including aeronautics and transportation, tools and die, chemicals and petrochemicals, nuclear research, electronics, and healthcare. Coating technology applies single or several layers of an appropriate substance to a material surface without changing the bulk material's composition, allowing it to function in different environments and overcome challenges caused by abrasion, temperature, fatigue, corrosion, erosion, and friction [2]. Consistent research on innovative coatings has significantly contributed to worldwide economic advances over the past few decades. Depending on the exact use, different coating materials (such as ceramics, metals, composites, or polymers) and coating methods are used [3].

In the production of conventional devices, top-down procedures, such as etching and photolithography, are often used for patterning at the nano scale. However, bottom up procedures are increasingly being looked at as potential substitutes owing to physical restrictions on downscaling those processes. A vapor-phase process called atomic layers deposition is used to deposit thin films on different substrates through a series of self-contained surface reactions [4,5]. Molecular layering (ML) and atomic layers epitaxy (ALE), two techniques that were initially presented in 1970s, form the foundations of ALD [6]. Graphite, graphene, and amorphous state carbon are examples of carbon-based inhibitors that are often deposited via solution methods, such as ion implantation, or chemical vapor deposition (CVD). However, it is challenging to use these techniques on substrates with high aspect ratios [7]. Similar to ALD, a molecular layers deposition (MLD) technique can produce conformal thin films of materials on three-dimensional objects [8]. Substantial thermal stresses occur between the coating and the metallic bond due to the latter's poor fracture toughness and comparatively low coefficient of thermal expansion. Consequently, the thermal cycle life of the single layer covering is often limited [9]. The multilayer concept is an efficient technique used to overcome such drawbacks and enhance shock life due to thermal loading [10]. Additionally, as an outer layer, the multilayer consists of an erosion-resistant layer, thermal barrier layer, corrosion- and oxidation-resistant layer, a layer controlling thermal stress, and a layer resisting diffusion [11].

A total of 13 papers were published in this Special Issue. From these 13 papers, a total of 8 papers focused on surface modification, surface treatment, microstructural examinations and mechanical properties. The published papers form comprehensive and sufficient learning materials that are sure to attract the attention of scholars in the manufacturing field. Authors also made significant efforts to produce qualitative research. For example, Kumar et al. [12] investigated the mechanical properties of nano-composites with a lower concentration of reinforcing nano particles, such as graphene, and ceramics in the matrix epoxy to assess the stability and damping properties of hybridized epoxy,

Citation: Srivastava, A.K.; Dixit, A.R. Research Progress in Metals and Alloys by Thermal Layering and Deposition. *Coatings* **2023**, *13*, 366. https://doi.org/10.3390/coatings13020366

Received: 31 December 2022
Revised: 1 February 2023
Accepted: 3 February 2023
Published: 6 February 2023

employing vibration methods to obtain precise findings. Mechanical testing, such as three-point bending, validates the efficiency of the impact hammer vibration method as a function of the Young's modulus of a nanocomposite. The nanocomposite of graphene contains 1% of epoxy, whereas the nanocomposite of ceramic contains 3% of epoxy. The frequency reduction in the heated environment was found to be much lower hybrid nanocomposites, but the decrease in pure epoxy was high; therefore, advancements in thermal and mechanical stability were found.

Srivastava et al. [13] investigated the surface tribological performance of Al359/Si_3N_4/Eggshell by friction stir processing (FSP). In the past, researchers explored techniques that will help to develop lightweight materials with dimensional accuracy, a smooth surface finish, and less production cost. With all these abilities, it will become eco-friendly. An aluminum matrix composite is an advanced engineering material in this field of research. The impression of the microstructural properties is to develop a defect-free surface that will help with grain refinement and enhance the mechanical properties of the top surface of the base alloys. Si_3N_4 is used in defense applications due to its ballistic and mechanical properties. Si_3N_4 is evaluated as a standard reinforced material that has a low density, high melting point, high thermal stability, and good chemical stability. Eggshell is a valuable material used as a new, reinforced engineering material as it contains around 95% calcium carbonate ($CaCO_3$), 3% phosphorus, and some other materials, such as zinc, potassium, sodium copper, magnesium, and iron. Many studies have been conducted to improve the mechanical and modified microstructures of matrix materials that have several disadvantages, such as porosity, solute redistribution, and solidification cracking. FSP is a popular technique that is used for versatile, solid-state processing, and green-energy-efficient techniques. It has negligible residual stresses and a refined microstructure, densification, and structural homogeneity. Generally, composites have a high coefficient of friction. Surface composites are made using a vertical milling machine. Al-6% Si_3N_4/Eggshell composites are undertaken to investigate frictional properties with the help of tribological tests. Light microscopy and FE-SEM equipped with EDS mapping are used in microstructural research. SiC, Al_2O_3, and B_4C are reinforced in the metal matrix, improving their tensile strength, yield strength, and hardness but reducing ductility. Liquid- and solid-phase fabrication methods have been successfully conducted to form the desired composite.

Lashin et al. [14] investigated the regulation of dynamic and static factors in order to maximize the welding strength achieved via friction stir spot welding (FSSW). As a novel technique, a control system based on fuzzy logic was applied to improve the process. Static and dynamic conditions influenced the tensile strength of stir spot welding. The collected findings demonstrate that the fuzzy logic system was a simple and low-cost technology that could be applied in the prediction and optimization of FSSW strength [14]. Gunduz et al. [15] discovered that titanium and its alloys had insufficient friction and wear settings due to their poor tribological characteristics. Electroless coatings were discovered to be effective as surface enhancement treatments due to their homogenous thickening, higher hardness, and superior resistance to corrosion. The auto-catalytic reduction in coating processes significantly improved surface quality. To improve weak tribological properties, an electroless coating of Nickel-P-Gr was applied to a Ti6Al4V alloy, and samples were put to abrasion in a linear-type reciprocating ball on plate configuration to examine tribological characteristics. Its hardness increased by approximately 34% with a graphene-reinforced Nickel-P coating in the electroless coatings procedure, whereas it increased by about 73% with applied thermal treatments. Moreover, the substrate's wear rate was nearly 98% greater than the heat-treated nanocomposite coatings. The heat-treated nano composite coatings had the maximum wear resistance.

Saxena et al. [16] investigated the tribological properties of microwave-assisted g-C_3N_4/MoS_2 nanocomposite coatings. The calcination approach was used to produce the g-C_3N_4 nanosheet, and the microwave-assisted method was used to developed nanocomposite with MoS_2. A pin on disc setup was used to investigate tribological qualities. A morphological examination indicated that elements coexisted, and the layered structure of

MoS_2 was evenly distributed over gC_3N_4. The presence of MoS_2 nano particles reduced the pore volume and surface area of the composite, confirming that the pores of calcinated gc_3n_4 were filled by MoS_2. The tribological properties of the nanocomposite were studied under various conditions, such as applied load, sliding speeds, and material compositions. The findings suggest that the inclusion of g-C_3N_4 in nano composites can minimize friction and enhance wear life. These results were superior to those obtained with MoS_2 alone.

Kumar N et al. [17] used three waste materials as a reinforcement to develop surface composites of aluminum alloys using FSP. Currently composites are being used as substitutes for many alloys due to their high strength-to-weight ratio, hardness, and tensile strength. Surface composites can be suitable alternative material to structure and automotive components. Hybrid composites consist of two or more reinforcements, whereas a non-hybrid has only one reinforcement. Biowaste materials also have particles that can strengthen certain materials [18]. Chicken bone powder (CBP) is an example of biowaste material, which is produced in poultry farm. The use of waste in products and its disposal, are great challenges since they form unwanted and harmful. CBP is strengthened by its sufficient amounts of carbon and calcium. Walnut shell powder (WSP) is a green waste formed during the manufacturing of walnuts products, containing cellulose and lignin. It is able to enhance the bonding strength of existing material. Rice husk powder (RHP) is agricultural waste produced by farming. The storage of this waste remains a major issue; many farmers burn this waste, which causes significant pollution. These three biowastes are utilized in the matrix alloy of aluminum and processed with FSP to take advantage of grain refinement and surface treatment. As a result, tensile modulus, yield and ultimate strength, percentage elongation and elastic coefficient are improved by 20%–30% [19].

Saxena et al. [20] attempted to improve the settings for the Pin-on-Disc wear apparatus. Various applied loads, sliding speeds, and the wt. of additive graphitic carbon nitride in a molybdenum disulfide nanocomposite coating on a steel substrate were used in the studies. ANOVA was performed to evaluate the effect of the interactions between different criteria. The maximum influences of applied loads on friction coefficient and wear were found to be approximately 59.6% and 41.4%, respectively, with sliding speed coming in second. The optimum conditions for the lowest coefficient of friction and wear depth in the nanocomposites were established to be at 15 N applied load, 750 mm/s sliding speed, and 9 wt.% of CN. Even at a 95% level of confidence, applied loads were determined to have the greatest impact on COF then sliding speed, whereas material composition had the greatest impact on wear. Taguchi technique and RSM results correlate well with experimental tests.

Wu et al. [21] created liquid crystal compounds (LCs) as a high-performance additive for a base oil that can fulfil a range of operating conditions. The influence of the mesogenic phase temperatures range of LC on tribological characteristics was investigated. Compared to the basic oil, the addition of LCs caused a significant decrease in the fictional coefficient (21.57%) and width of wear (31.82%). Furthermore, LCs exhibited improved tribological properties under temperature conditions of the mesogenic phase.

The above literature constitutes a summary of previously published research. However, some additional papers are still under extensive review to help them fit the scope of this Special Issue.

Author Contributions: Conceptualization, writing and editing, A.K.S.; Supervision, review and editing, A.R.D. All authors have read and agreed to the published version of the manuscript.

Conflicts of Interest: The authors declare no conflict of interest.

References

1. Deng, Y.; Chen, W.; Li, B.; Wang, C.; Kuang, T.; Li, Y. Physical vapor deposition technology for coated cutting tools: A review. *Ceram. Int.* **2020**, *46*, 18373–18390. [CrossRef]
2. Makhlouf, A. Current and advanced coating technologies for industrial applications. In *Nanocoatings and Ultra-Thin Films*; Woodhead Publishing: Shaxton, UK, 2011; pp. 3–23.
3. Upadhyay, R.K.; Kumar, A. Micro-Indentation Studies of Polymers. *Polymers* **2021**, *2*, 928–937.

4. Mackus, A.J.; Merkx, M.J.; Kessels, W.M. From the Bottom Up: Toward Area-Selective Atomic Layer Deposition with High Selectivity. *Chem. Mater.* **2019**, *31*, 2–12. [CrossRef] [PubMed]
5. Ritala, M.; Leskelä, M. Chapter 2—Atomic layer deposition. In *Handbook of Thin Films*; Singh Nalwa, H.B.T.-H., Ed.; Academic Press: Burlington, VT, USA, 2002; pp. 103–159.
6. Puurunen, R.L. A short history of atomic layer deposition: Tuomo Suntola's atomic layer epitaxy. *Chem. Vap. Depos.* **2014**, *20*, 332–344. [CrossRef]
7. Stevens, E.; Tomczak, Y.; Chan, B.; Altamirano Sanchez, E.; Parsons, G.N.; Delabie, A. Area-Selective Atomic Layer Deposition of TiN, TiO_2, and HfO_2 on Silicon Nitride with Inhibition on Amorphous Carbon. *Chem. Mater.* **2018**, *30*, 3223–3232. [CrossRef]
8. Lee, B.H.; Yoon, B.; Abdulagatov, A.I.; Hall, R.A.; George, S.M. Growth and Properties of Hybrid Organic-Inorganic Metalcone Films Using Molecular Layer Deposition Techniques. *Adv. Funct. Mater.* **2013**, *23*, 532–546. [CrossRef]
9. Cao, X.Q.; Vassen, R.; Jungen, W.; Schwartz, S.; Tietz, F.; Stöver, D. Thermal stability of lanthanum zirconate plasma-sprayed coating. *J. Am. Ceram. Soc.* **2001**, *84*, 2086–2090. [CrossRef]
10. Tamura, M.; Takahashi, M.; Ishii, J.; Suzuki, K.; Sato, M.; Shimomura, K. Multilayered thermal barrier coating for land-based gas turbines. *J. Therm. Spray Technol.* **1999**, *8*, 68–72. [CrossRef]
11. Cao, X.Q.; Vassen, R.; Tietz, F.; Stoever, D. New double-ceramic-layer thermal barrier coatings based on zirconia–rare earth composite oxides. *J. Eur. Ceram. Soc.* **2006**, *26*, 247–251. [CrossRef]
12. Kumar, N.; Babu, A.; Das, A.K.; Srivastava, A.K. Effective Evaluation of Elastic Properties of a Graphene and Ceramics Reinforced Epoxy Composite under a Thermal Environment Using the Impact Hammer Vibration Technique. *Coatings* **2022**, *12*, 1325. [CrossRef]
13. Srivastava, A.K.; Dwivedi, S.; Saxena, A.; Kumar, D.; Dixit, A.R.; Singh, G.K.; Bhutto, J.K.; Verma, R. Tribological Characteristics of Al359/Si_3N_4/Eggshell Surface Composite Produced by Friction Stir Processing. *Coatings* **2022**, *12*, 1362. [CrossRef]
14. Lashin, M.M.A.; Al Samhan, A.M.; Badwelan, A.; Khan, M.I. Control of Static and Dynamic Parameters by Fuzzy Controller to Optimize Friction Stir Spot Welding Strength. *Coatings* **2022**, *12*, 1442. [CrossRef]
15. Gunduz, H.; Karslioglu, R.; Ozturk, F. Microstructural Evaluation of Graphene-Reinforced Nickel Matrix Ni-P-Gr Coating on Ti-6Al-4V Alloy by the Electroless Coating Method. *Coatings* **2022**, *12*, 1827. [CrossRef]
16. Saxena, M.; Sharma, A.K.; Srivastava, A.K.; Singh, R.K.; Dixit, A.R.; Nag, A.; Hloch, S. Microwave-Assisted Synthesis, Characterization and Tribological Properties of a g-C_3N_4/MoS_2 Nanocomposite for Low Friction Coatings. *Coatings* **2022**, *12*, 1840. [CrossRef]
17. Kumar, N.; Singh, R.K.; Srivastava, A.K.; Nag, A.; Petru, J.; Hloch, S. Surface Modification and Parametric Optimization of Tensile Strength of Al6082/SiC/Waste Material Surface Composite Produced by Friction Stir Processing. *Coatings* **2022**, *12*, 1909. [CrossRef]
18. Srivastava, A.K.; Saxena, A.; Dixit, A.R. Investigation on the thermal behaviour of AZ31B/waste eggshell surface composites produced by friction stir processing. *Compos. Commun.* **2021**, *28*, 100912. [CrossRef]
19. Srivastava, A.K.; Kumar, N.; Saxena, A.; Tiwari, S. Effect of friction stir processing on microstructural and mechanical properties of lightweight composites and cast metal alloys—A review. *Int. J. Cast Met. Res.* **2021**, *34*, 169–195. [CrossRef]
20. Saxena, M.; Sharma, A.K.; Srivastava, A.K.; Singh, N.; Dixit, A.R. An Investigation for Minimizing the Wear Loss of Microwave Assisted Synthesized g-C_3N_4/MoS_2 Nanocomposite Coated Substrate Pin on Disc Tribometer. *Coatings* **2022**, *12*, 118.
21. Wu, H.; Jiang, Y.; Hu, W.; Feng, S.; Li, J. Effect of Mesogenic Phase and Structure of Liquid Crystals on Tribological Properties as Lubricant Additives. *Coatings* **2023**, *13*, 168. [CrossRef]

coatings

MDPI

Review

Cold Spray Coatings of Complex Concentrated Alloys: Critical Assessment of Milestones, Challenges, and Opportunities

Desmond Klenam [1,2], Tabiri Asumadu [3], Michael Bodunrin [2], Mobin Vandadi [4], Trevor Bond [5], Josias van der Merwe [2], Nima Rahbar [4,5] and Wole Soboyejo [5,*]

[1] Academic Development Unit, Faculty of Engineering and the Built Environment, University of the Witwatersrand, 1 Jan Smuts Avenue, Johannesburg 2001, South Africa
[2] School of Chemical and Metallurgical Engineering, University of the Witwatersrand, 1 Jan Smuts Avenue, Johannesburg 2001, South Africa
[3] Department of Materials Engineering, Sunyani Technical University, Sunyani P.O. Box 206, Ghana
[4] Department of Civil Engineering, Worcester Polytechnic Institute, 100 Institute Road, Worcester, MA 01609, USA
[5] Department of Mechanical Engineering, Worcester Polytechnic Institute, 100 Institute Road, Worcester, MA 01609, USA
* Correspondence: wsoboyejo@wpi.edu; Tel.: +1-508-831-4694

Abstract: Complex concentrated alloys (CCAs) are structural and functional materials of the future with excellent mechanical, physical, and chemical properties. Due to the equiatomic compositions of these alloys, cost can hinder scalability. Thus, the development of CCA-based coatings is critical for low-cost applications. The application of cold spray technology to CCAs is in its infancy with emphasis on transition elements of the periodic table. Current CCA-based cold spray coating systems showed better adhesion, cohesion, and mechanical properties than conventional one-principal element-based alloys. Comprehensive mechanical behavior, microstructural evolution, deformation, and cracking of cold spray CC-based coatings on the same and different substrates are reviewed. Techniques such as analytical models, finite element analysis, and molecular dynamic simulations are reviewed. The implications of the core effects (high configurational entropy and enthalpy of mixing, sluggish diffusion, severe lattice distortion, and cocktail behavior) and interfacial nanoscale oxides on the structural integrity of cold spray CCA-based coatings are discussed. The mechanisms of adiabatic heating, jetting, and mechanical interlocking, characteristics of cold spray, and areas for future research are highlighted.

Keywords: complex concentrated alloys; cold spray; adiabatic heating; solid-state coating; metallurgical bonding; mechanical interlocking; severe lattice distortion; Johnson–Cook model; finite element method; sluggish diffusion; microstructural evolution

Citation: Klenam, D.; Asumadu, T.; Bodunrin, M.; Vandadi, M.; Bond, T.; van der Merwe, J.; Rahbar, N.; Soboyejo, W. Cold Spray Coatings of Complex Concentrated Alloys: Critical Assessment of Milestones, Challenges, and Opportunities. *Coatings* **2023**, *13*, 538. https://doi.org/10.3390/coatings13030538

Academic Editors: Ashish Kumar Srivastava and Amit Rai Dixit

Received: 30 January 2023
Revised: 21 February 2023
Accepted: 24 February 2023
Published: 1 March 2023

1. Introduction

Complex concentrated alloys (CCAs) are the new frontier for the design of bulk materials and coatings for structural and functional applications [1–5]. This approach by design has disrupted ~5000 years of conventional and serendipitous material discovery processes. The CCA design approach is based on mixing elements in equal amounts without any distinct solvent and solute atoms [5]. This is counterintuitive to the well-established physical metallurgy of using one or two base elements, while systematically adding minute secondary alloying elements to induce the designed and desired properties. These properties could be mechanical, corrosional, thermal, magnetic, electrical, and physical. The approach deviates from exploring compositions at the corners of typical ternary and higher order phase diagrams. This new approach shows promise and is being touted as the future of materials, providing superior structural and functional properties to most conventional alloys [1].

Cold spray is classified as a thermal spray coating technique and an additive manufacturing process [3,6–16]. The technique has been used to deposit coatings [7,9,17,18], to repair materials [6,8,19], and for design of bulk materials for various structural and functional applications [14–16]. The main advantages are: (i) easily applicable to a wide variety of ductile, dissimilar, and thermally sensitive materials, (ii) able to retain initial properties of the feedstock powder material, (iii) high flexibility and precise near-net shape manufacturing, (iv) deposits possess cold-worked microstructural features contributing to high hardness and relatively low porosity, and (v) superior deposition efficiency and rates compared to other types of conventional coating process. Lastly, the method has the unique characteristic of being operated under relatively low temperature (below the melting temperature) of the coating material. The layer-by-layer deposition satisfies the principles of additive manufacturing.

The inherent design principles of bulk materials from CCAs make them expensive compared to most conventional structural and functional alloys [1,2,20]. This hinders scalability and stiff competition from commercially available conventional alloys is inevitable [2,20]. To reduce overall costs, coatings using various techniques are being explored.

Cold spray technology is gaining traction and has been commercialized for various functional and structural applications as coatings and for bulk alloy design. It is instrumental for material repair. As one of the hotspot research areas, there has been increased and timely experimental and published literature on the subject. Since its discovery over 40 years ago in Russia, there have been thematic reviews, book chapters, and books on various aspects of cold spray technology [3,6,9,10,17,21–26]. These ranged from fundamental principles and applications to material perspectives [9,21–25]. Some of the reviews focused on various bonding mechanisms [6,17,27]. The latest review on the bonding mechanism focused on single-particle impact approaches [17]. Similarly, there have been lab-scale experimental approaches augmented with numerical simulations to understand the process better.

Bulk CCAs are expensive with stiff competition from dilute conventional alloys. The design of CCA-based coatings is one of the solutions to reduce the cost. Various types of CCA-based coatings have been developed and reviewed. The cold spray approach, since its proof of concept on CrCoFeMnNi alloy in 2019, is still in its infancy. Apart from a mini review of structural integrity and material aspects of CCA-based cold spray coating published by the authors [3], there is yet to be published a general overview, which critically assesses the current stage of knowledge in the area. This is ideal in highlighting areas for future research direction. By combining the advantages of CCA-based coating and the cold spray technique, robust and next generation multifunctional coatings can be developed and applied in various industries.

2. Thermal Spray Technology—Brief Overview

Thermal spray coating is a coating process that sprays the surface of any substrate with melted or heated particulate matter [28,29]. The thermal energy that heats or even melts the feedstock (precursor coating material) is generated via electrical or chemical means. The molten or heated (semi-molten) particulate matter possesses kinetic energy which helps in accelerating the particles onto the substrate. Adhesion and cohesion are induced by the high temperature and high velocity of the particle which in effect leads to severe plastic deformation. The deformed coating material produces a splat on the substrate, which is a pancake-like impacted particle. The bonding mechanisms are: (i) mechanically induced bonding of the coating particles' splatter on substrate with an interlocking effect, (ii) localized diffusion of the coating and the substrate material, and (iii) bonding is achieved from the interactions of the van der Waals forces of attraction. The main benefits are the ability to repair and strengthen damaged surfaces and high applicability to metals and ceramics. It also requires less heating for effective bonding at the coating and substrate interface. A schematic diagram showing the process is given in Figure 1.

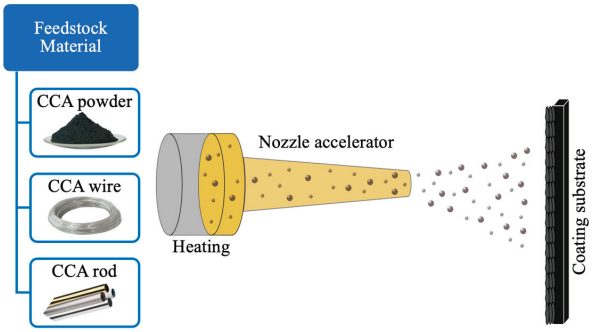

Figure 1. Schematic diagram showing the thermal spray process.

Thermal spray coatings are in three categories based on application of combustion heat sources (flame, detonation gun, and high-velocity oxygen fuel spray), electrical energy sources (plasma or an arc) and thermal energy sources (kinetic, cold, and hypersonic spray) from gas expansion. The classification of thermal spray based on the interdependence of multiplicity of input variables is represented by a process map (Figure 2) [29]. These input variables include the particle temperature at optimized stand-off distance, the particle velocity, and feedstock particle size distribution with its associated physical and mechanical properties [29]. The process map provides a guide for the classes of materials and the suitability of the coating method and their effects on porosity and cohesion strength. The relatively high operation temperatures of conventional thermal spray coatings have some drawbacks. These include high tensile residual stresses, high oxidation rates, defects nucleated in the form of cracks, and phase transformation. These features affect the mechanical, chemical, and physical properties of the coating, hence some of these coatings cannot be used in temperature-sensitive operations. The development of cold spray coatings is one of the ways to minimize the challenges posed by other thermal spray processes.

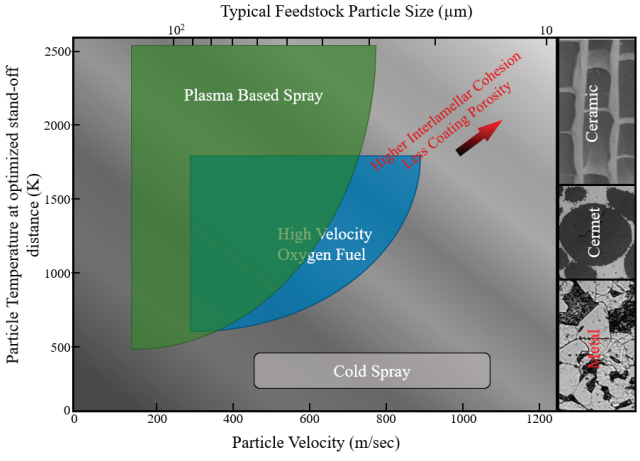

Figure 2. Classification of thermal spray coating methods based on processing parameters such as particle velocity, feedstock particle size distribution, and particle temperature at optimized stand-off distance.

3. Cold Spray Technology: An Overview

3.1. Introduction and General Concepts

The cold spray process of thermal spray coating was discovered and operationalized in 1980s. It is based on the principle that when a particle-laden supersonic gas jet impinges

onto a solid substrate above a critical minimum particle velocity, there is a transition of the metallic particles from a state of abrasion to adhesion, which through plastic deformation are deposited on the substrate. These minute unmelted particles are typically in a size distribution range of approximately 1–50 μm. The system was fully commercialized after the Russian and United States patents were granted. The technological and innovation timeline of cold spray is given in Figure 3 with a project plateau of productivity by 2030.

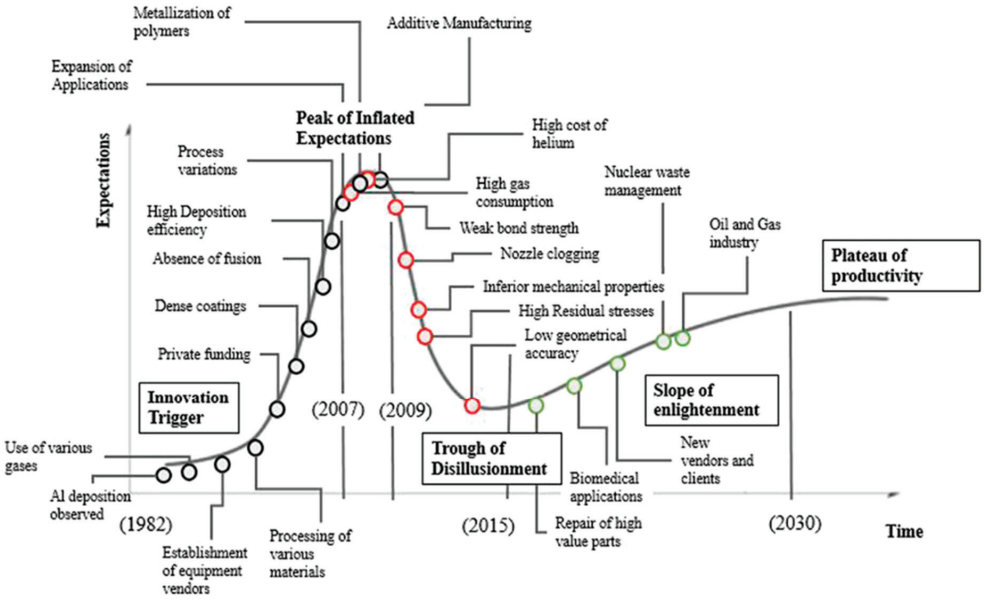

Figure 3. Technology and innovation maturation timeline and projection for cold spray technology [9].

The operational principle is as follows with the schematic diagram shown in Figure 4. The whole architecture of the system is built on high pressure (Figure 4a) [15]. However, recent modification led to the low-pressure system as shown in Figure 4b. Based on Figure 4a, high-pressure gas, which is typically, air, nitrogen, or helium, enters the system and then splits into 5 and 95%. The 5% of the gas goes to the particle feeder adding particles to the flow, whereas the 95% goes to the gas heater. The gas is heated to ~500 to 1000 °C and the two streams recombine at the converging–diverging nozzle (the same as that used in rocket engines, which is called a de Laval nozzle) entrance, then accelerated through the nozzle. The velocity at the nozzle entrance is generally low which increases to as much as ~1000 m/s depending on the gas used. In the case of He, the velocity is very low as He is relatively lighter than nitrogen. The stream then impinges on the substrate while the gas turns away, whereas the particles crash on the surface of the substrate due to the high momentum they possess. The longer the flow is kept, the thicker the deposit. The working principle of cold spray is based on the conservation of energy. The impacting feedstock material possesses kinetic energy, which is converted to heat and deformation energies, causing localized severe plastic deformation upon impact. The heat energy is then transferred to the surface of the substrate, resulting in some adiabatic heating but not high enough to induce phase transformation.

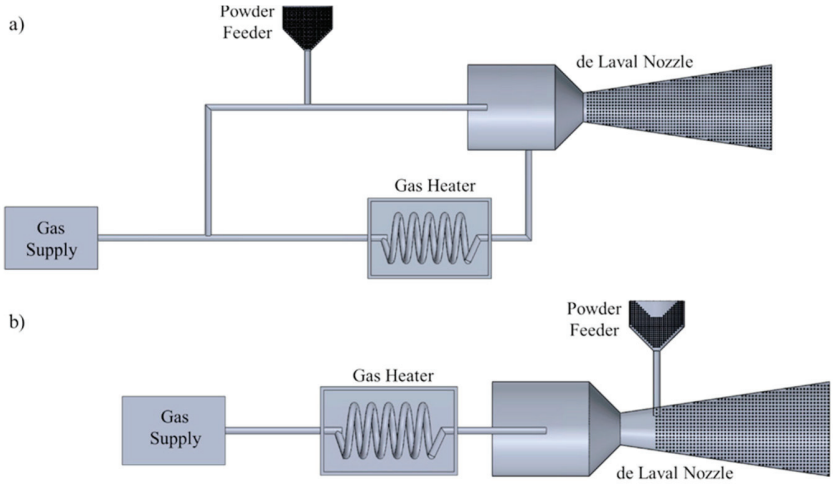

Figure 4. Schematic diagram showing typical cold spray system showing (**a**) high-pressure and (**b**) low-pressure systems. Reprinted with permission from Ref. [3]. Copyright 2022, Elsevier.

The gas is heated to take advantage of the supersonic nozzle design. The nozzle converts the high thermal energy of the gas to kinetic energy at the exit of the nozzle. Thus, the process starts with a hot but slow mixture of gases and feedstock particles at the entrance of the nozzle and ends with a cold fast mixture at the exit. Generally, temperatures as high as 500 °C can be observed at the entrance of the nozzle but they reduce drastically to ~100 °C at the exit of the nozzle, resulting in no melting of the feedstock particles. Therefore, it is a solid-state process of surface coating where deposition of coating can occur from 0 to 800 °C, which is lower than the melting point of the feedstock.

3.2. Processing Parameters of Cold Spray Coatings

Typical cold spray processes have been used to manufacture various bulk mechanical components [10–16]. Among these components are flanges, cylindrical walls, tubes, heat exchanger array fins, and metal labels. The flexibility of the coating process and no detrimental effect on the substrate make it applicable for repair of worn parts of any mechanical component. As a form of additive manufacturing process, comparative analyses of the techniques with three methods of fusion-based additive manufacturing are given in Table 1. The comparison was also made using as-fabricated (AF) and heat treatment (HT) specimens.

Table 1. Comparison of cold spray technology with three methods under powder-based additive manufacturing process.

Property and Parameter	Cold Spray	SLM	EBM	LMD
Powder feed mode	Direct deposition	Powder bed	Powder bed	Direct deposition
Feedstock drawback	Difficult to process high-strength materials	Difficult to process poorly flowable and highly reflective metals	Not suitable for low-melting and non-conducive metals	Difficult to process for highly reflective metals
Powder melting	Not applicable	Applicable	Applicable	Applicable
Product size	Large	Limited	Limited	Large
Dimensional accuracy	Low	High	High	Medium
As-fabricated mechanical properties	Low	High	High	High

Table 1. *Cont.*

Property and Parameter	Cold Spray	SLM	EBM	LMD
Heat treated mechanical properties	High	High	High	High
Production time	Short	Long	Long	Long
Flexibility of equipment	High	Low	Low	Low
Possibility of material repair	Applicable	Not applicable	Not applicable	Applicable

SLM—Selective Laser Melting, EBM—Electron Beam Melting, and LMD—Liquid Metal Deposition.

Gas propulsion parameters are required to accelerate the particles of the powder required to bombard the substrate to induce bonding. The parameters are the nature, type, temperature, and pressure of the gas system. For instance, the pressure of the gas is used to classify cold spray technology as either a high- or low-pressure cold spray system. The high-pressure cold spray system has pressures exceeding 1 MPa. The effects of processing parameters of cold spray coating are summarized in Table 2.

Table 2. Effects of the processing parameters on defects, adhesion, and deposition efficiency of cold spray coatings.

Parameter	Porosity	Residual Stress	Adhesion	Deposit Strength and Efficiency
Pressure of gas	↓	↑	↑	↑
Gas temperature	↓	↑	↑	↑
Gas molecular weight	↑	↓	↓	↓
Particle velocity	↓	Inconclusive	↑	↑
Powder feed rate	↑	↑	↓	↓
Spray angle	↑	↑	↑	↑
Stand-off distance	Effect is inconclusive and indiscernible			

Note: ↑ shows an increase whereas ↓ shows a decrease in most observed experiments.

The effect of particle velocity on residual stresses in the cold spray method is inconclusive for most systems studied [30–38]. The three main residual stress states are peening, thermal, and quenching stresses [31,32,38]. The high-impact velocity of the impinging particles contributes to the peening effects [30]. The mechanism is likened to shot peening for increased fatigue strength in most structural components [38–44]. The quenching stresses are attributed to the compaction of impacted particles often impeded or restricted by the underlying coatings or substrate materials. Thermal stresses are due to differences in the coefficient of thermal expansion (CTE) of the substrate and coating materials. Based on the magnitude of the CTE mismatch of the coating and substrate, tensile or compressive residual stresses can be induced [38,45]. Typical compressive residual stresses are observed in the coatings and tensile stresses in the substrate when $CTE_{substrate} > CTE_{coating}$ [29]. Due to the low deposition temperature of the cold spray coating technique, the cumulative effects of thermal and quench stresses are negligible [29]. However, these effects are pronounced when the temperature of the substrate is above 400 °C and, vice versa, below 400 °C [29].

There is no clear and discernible relationship between residual stresses and impact velocity from both experiments and simulations [33–38,46]. In most instances, residual stresses increase with increasing particle velocity [33,34,36,37], but that is largely dependent on substrate-to-coating pairs and microstructural characteristics. However, this opens opportunities for further research to optimize the process parameters to obtain properties within acceptable limits. A typical example is Cu coatings on Cu substrate, where the difference in CTE is negligible [35]. The residual stresses increased with increasing impact velocity from 300 to 500 m/s. However, when particle velocities increased from 500 to

700 m/s, no discernible relationship was observed. For a Cu/Al substrate–coating pair, residual stresses increased for particle velocities between 300 and 500 m/s. The compressive residual stresses were increased for particle velocities between 500 and 700 m/s [35]. A similar trend of increasing residual stresses with increasing particle velocities has been reported for Ti6Al4V on Ti6Al4V [46]. The residual stress profiles for particle velocities from 700 to 800 m/s were comparable.

Particle size, distribution, and morphology: This is a useful parameter which affects the deposition behavior and quality of cold spray coatings [47]. It is characterized by the particle size, distribution, and morphology. The acceleration of large particles is poor due to the lower velocity of the particles compared to small particles. However, the larger the particle size, the easier it is to reach high temperatures, which contributes to reduced critical velocities [47]. A schematic diagram showing the effect of particle size on the particle impact velocity is given in Figure 5 [48]. There is always an optimum particle size range that impacts the substrate above the critical velocity and below erosion velocities. The optimized particle size range, which is specific to the coating material, leads to good adhesive, cohesive, and quality coatings.

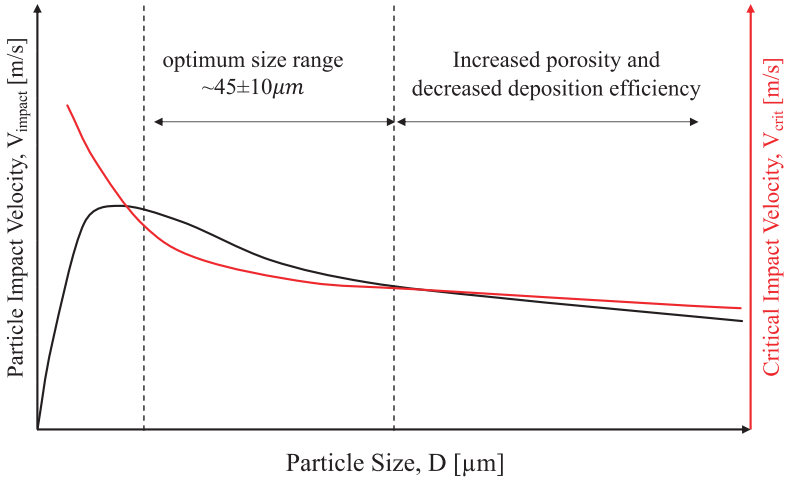

Figure 5. Effect of particle size distribution on the particle impact velocity during a cold spray deposition [49].

3.3. Bonding Mechanisms of Cold Spray of Metallic Materials

The bonding mechanism of cold spray technology shows how the coating and substrate achieve adhesion and cohesion [17,27,47]. While it is known to be a solid–solid bond interaction, the overarching bonding mechanisms are still a bone of contention. However, the core mechanism is based on the ballistic impingement theory where particles are consolidated into coatings on substrate by ballistic impingement [50]. Two main conditions for the theory are the need for particles of certain sizes (below 5 mm) to be accelerated to certain critical velocities (50–3000 ms^{-1}) to induce impact [50,51]. The high kinetic energy impingement of the particle on the substrate results in increased plastic strain and strain rates. Upon impact, the kinetic energy is converted to heat and sound which induce adiabatic heating leading to thermal softening and dynamic hardening effects. There are few reviews on the subject focusing on particle–substrate and particle–particle interactions and bonding mechanisms [52–57]. Metallurgical bonding has been observed using various microstructural characterization techniques [17,27,47,52,53,55–57]. These include scanning and transmission electron microscopy [55,58,59] and various empirical models [48,56,57] have been developed to explain the mechanism.

The schematic representation of the bonding mechanism of a typical cold spray process (tantalum particle on 4340 steel substrate) is given in Figure 6. The process commences with high kinetic energy of the impinging particles from the high velocities and high pressures, generating extreme plastic deformation at the surface of the contact region. This process disrupts any thin surface oxides and exposes clean surfaces of the substrate, aiding the metallurgical bonding process (Figure 6). As the impact progresses, the plastic flow of the materials at the interface extrudes much of the crushed pieces of oxide films to the periphery of the contact interface, enabling an intimate contact of newly exposed clean metal between the particle and substrate (Figure 6). Some of the oxides are removed from the interface altogether through "jetting" observed for particle impacts above the critical velocity. This is shown experimentally in a wide range of engineering materials. For a strong bond to be achieved in non-ductile materials, the systems require the addition of ductile matrix to induce metallurgical bonding and mechanical interlocking, which are critical for adhesion strength [53,54,57].

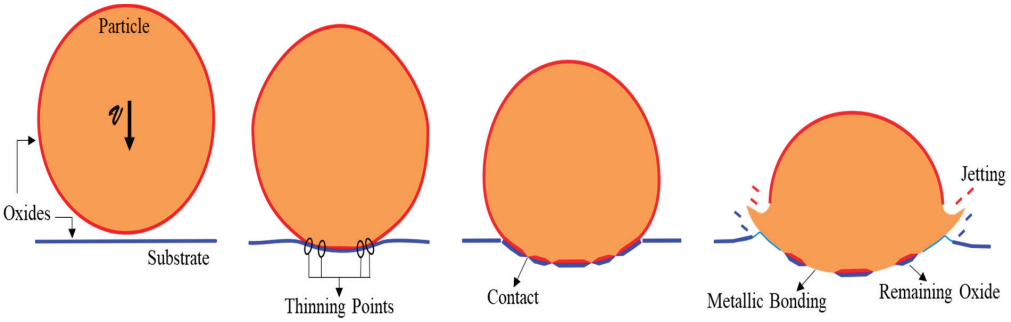

Figure 6. Schematic showing the bonding mechanism of a typical cold spray process.

The presence of oxide-free surfaces due to the initial particle–substrate is the precursor for metallurgical bonding. Surface preparation methods are used to create the oxide-free surfaces. Jetting contributes to removal of interfacial oxides. For many materials, the bulk plastic deformation of particle and substrate results in mechanical interlocking, a characteristic bonding mechanism. Typical bonding strength of cold spray coatings ranges from 10–60 MPa [57]. For the bonding mechanism to be effective, the following conditions should be met [47,52,55,57]:

- The velocity of the particles should be higher than a critical nominal velocity (critical velocity) to induce sufficient kinetic energy, a characteristic of velocity for enough plastic deformation to initiate the interaction between the particle and oxide films on substrate. There are instances where there are no oxide layers, but the particle critical velocity is crucial for cold spray.
- The kinetic energy of the particle upon impact should be lower than the required energy needed to melt the coating particle. Thus, there should not be any melting for the solid-state deposition mechanism [17,27,48,55,56].

The cold spray process is a solid-state process without any element of melting. However, there is localized heating when the particle impinges on the substrate. This is known as adiabatic shear instability (ASI). This is a critical contribution factor to the overall bonding mechanism and strength of the coating. The high strain rates at which the particles are accelerated onto the surface of the substrate result in the localized adiabatic heating.

4. Computational and Numerical Simulation Models—An Overview

Three main types of models are used to simulate the cold spray processes. These include the finite element-based models, constitutive equations, and models for describing

the bonding at the particle–substrate and particle–particle interfaces [39,58]. A summary of the models and their applications to cold spray processes are highlighted.

4.1. Modeling Approaches Using Numerical Simulations

The numerical approaches used for simulating the cold spray processes focus on impact and deformation associated with particle–substrate and particle–particle interaction [17,27,60–73]. The main numerical methods are the Lagrangian [74,75], Eulerian [17,27,60,61,63,64], coupled Eulerian–Lagrangian [57,61,62,76,77], smooth-particle hydrodynamics [65–73], and molecular dynamics [17–19,38].

4.1.1. Lagrangian Approach

The Lagrangian finite element-based approach applies mesh which deforms with the material under applied loads [59]. Tracking particle–substrate and particle–particle interaction is easy during impact even if complex boundary conditions are imposed [74,75]. It is also a good approach to trace any history-dependent variables, hence it is one of the pioneering approaches for simulating solid-state bonding processes. It is widely used due to reduction in computational time as the impact process is assumed as symmetric and quarter (axisymmetric) models are representative and cost effective [38].

The Lagrangian model is great for showing material jetting, which is characteristic for most impact-induced bonding. Although the jets are sharp and sharps are unphysical, they result in severe mesh distortions. This severe distortion of the meshes could compromise the simulation, resulting in premature termination and reducing computational accuracy significantly [60,75,78], sometimes at 19 ns [60]. Severe mesh distortion can be attributed to large strains imposed on the structure, resulting in failure, attributed to near-zero or negative element Jacobians. Localized strains could be as high as 450% in the jetting region, which could lead to overestimation of the bond modeling.

Ways to mitigate the mesh distortion have been explored [57,61,62]. One approach is the use of the arbitrary Lagrangian–Eulerian (ALE) which combines the Lagrangian and Eulerian analyses [59]. The ALE allows for the redefinition of the mesh in a continuous fashion arbitrarily while moving the mesh away from the material. The major challenges associated with the ALE technique are high computational cost [17,27,57,59], unrealistic deformation of particles at high impact velocities [61,62], inaccurate prediction of the particle–particle interactions, and overall reduction in equivalent plastic strains [17,27,60,63]. For the ALE method, the inherent interpolation errors are due to high strain gradients at the particle–substrate interface and adaptive remeshing [60]. In a nutshell, the pure Lagrangian approach is not the ideal technique for a high-strain cold spray modeling process.

4.1.2. Eulerian Approach

The Eulerian approach to modeling cold spray processes improves on the inefficiencies of the pure Lagrangian formulation [27,61,64], thus solving the severe mess distortions and large deformations induced by high strains. The Eulerian approach allows the flow of material mass through stationary points where deformation is independent of the material [64]. This process assumes two overlapping meshes where one is fixed as the background and the other, mesh for the material which allows flows through it easily. The model is flexible, allowing for assigning different parameters to the different parts of the model. Due to the ease of flowability of the material in the mesh, it is easy to model the severe plastic deformation associated with the cold spray process. The error associated with the Eulerian approach is negligible compared to experimental data [64]. For instance, the predicted critical velocity of Cu was compared to the experimental value. It is the right method for modeling the material jetting process of the particle and the substrate. Generally, the demerits associated with this method are long simulation and computational times due to the fine mesh and severe plastic deformation, the difficulty with modifying boundary conditions, and the inability to modify contact properties such as the coefficient of

friction [64]. The inability to track the history-dependent variables in the Eulerian method and numerical dissipation are also possible shortcomings.

4.1.3. Combined (Coupled) Eulerian–Lagrangian Approach

This approach uses the Eulerian and Lagrangian approaches simultaneously to model aspects of the cold spray process [59,64,76,77]. This allows for the merits associated with each technique to be applied in a robust fashion, thus, solving the false positives or impractical results associated with particle–substrate deformation and mesh distortions associated with the Lagrangian method, while being able to track the particle–substrate interface, which is difficult under the Eulerian method. For the Eulerian part, the volume of fluid method is applied [77].

4.1.4. Particle-Based Approach

The particle-based approach is ideal for modeling severe plastic deformation associated with the cold spray process [65–67]. Results from this technique are comparable to experiments that do not underestimate, or overestimate, as observed for most mesh-based techniques [65,66,69]. The approach possesses merits that are not observed for the conventional mesh-based FEM Lagrangian and Eulerian methods [66,67]. A typical example is the smoothed particle hydrodynamics (SPH), a meshless discretization process that deviates from finite 3D meshed elements to discretized particles, the carrier of the information [65–68]. The particles are assigned state variables which describe material based on weight, velocity, and stress states. An authoritative review of the mathematical underpinnings of the SPH [66–70] and key advantages are as follows:

- The SPH, being a particle-based method, allows for the handling of large deformations. This is because connections between the particles are generated as part of the computations and changes with time, especially for the high-velocity impact phenomenon which underpins cold spray technology.
- The SPH method has been successfully applied to conceptualized problems with deformable boundaries with extremely large deformations, free surface, and moving interfaces.
- The SPH is a particle approach of the Lagrangian kind with the Galilean invariant algorithm. It can easily estimate time history of the particles of the material, which are relevant for determining the transport and advection of the system.
- The SPH method, being one of the oldest mesh-free particle methods, has approached maturation and been successfully integrated into commercial software packages for practical applications.
- The SPH is ideal for free surface and interfacial flow modeling characteristics with the cold spray process. The specific location of the particles prior to the commencement of any analysis is critical. This leads to accurate and easily traceable material interfaces and free surfaces by the SPH simulation irrespective of the complexity of the particle movement and interaction, which may be challenging for mesh-based methods.
- The SPH approach is extensively used in applications ranging from the microscale to macroscale and even astronomical scale, and in discrete to continuum systems. It is easy to combine with other methods such as classical molecular dynamics and dissipative particle dynamic methods for various applications.
- Numerical simulations associated with SPH have the objects not under continuum, which is vital for bio- and nanoengineering across the nano- to the microscale.
- The SPH method is comparatively easy to implement and to use to develop 3D numerical models than the mesh-based approaches. It has also gained an acceptable level of accuracy for practical engineering applications.

Considering that SPH is a mesh-free technique, an important factor is the interpolation theory. This is the process where continuum fluid dynamics laws of conservation are converted to integral equations with an interpolation function. While the application of the shape functions is difficult to implement, a weighting SPH kernel function according

to Equation (1) is applied [19,71–73]. Thus, kernel approximation of the function $f(r')$ at specific positions is obtainable by using smooth kernels, W, which are integrated over a certain computational domain. Other governing equations and detailed assumptions are documented elsewhere [66,69,72].

$$f(r) = \int f(r)' W(r - r', h) dr' \quad (1)$$

where: W = weighting function, h = support scale satisfying the normalization process when $\int W(r - r', h) dr' = 1$, the delta function property achieved when smoothing length tends to zero is given as $\lim_{h \to 0} W(r - r', h) = \delta(r - r')$.

Some of the different interpolation kernels used in SPH modeling are given in Table 3 [66,79–81]. These kernel expressions cater for 2D domains only. Typical factors to consider in deciding the type to use are the desirable mathematical behavior and the lack of complexity to adequately describe the properties of the particle. Detailed derivation and the mathematical underpinnings of the kernel function have been summarized elsewhere [66]. The material parameters used for the SPH simulations include material properties (density, Young's modulus, and Poisson ratio), strength parameters (yield strength, hardening coefficient, strain rate constant, softening exponent, strain hardening exponent, heat capacity, thermal conductivity, melting and reference temperatures, reference strain rate) and equation of state (EOS) parameters (speed of sound, gradient of shock velocity, and Gruneisen coefficient).

Table 3. Typical interpolation kernels used for SPH modeling.

Kernel Name	Mathematical Expression [W(r, h)(m^{-2})]
Cubic spline kernel [66]	$\frac{15}{7\pi h^2}\begin{cases}\left[\frac{2}{3} - \left(\frac{\lvert r-r_b\rvert}{h}\right)^2 + \frac{1}{2}\left(\frac{\lvert r-r_b\rvert}{h}\right)^3\right], & 0 \le \lvert r - r_b\rvert \le h \\ \left[\frac{1}{6}\left(2 - \frac{1}{2}\left(\frac{\lvert r-r_b\rvert}{h}\right)^3\right)\right], & h \le \lvert r - r_b\rvert \le 2h\end{cases}$
Quartic kernel [81]	$\frac{5}{\pi h^2}\left\{1 + 3\left[\left(\frac{\lvert r-r_b\rvert}{h}\right)\right]\left[1 - \left(\frac{\lvert r-r_b\rvert}{h}\right)\right]^3, 0 \le \lvert r - r_b\rvert \le h\right.$
Quartic kernel [80]	$\frac{15}{7\pi h^2}\left\{\frac{2}{3} + \frac{9}{8}\left(\frac{\lvert r-r_b\rvert}{h}\right)^2 + \frac{19}{24}\left(\frac{\lvert r-r_b\rvert}{h}\right)^3 - \frac{5}{32}\left(\frac{\lvert r-r_b\rvert}{h}\right)^3,\right.$ $0 \le \lvert r - r_b\rvert \le h$
Quintic spline [79]	$\frac{7}{478\pi h^2}\begin{cases}\left[3 - \left(\frac{\lvert r-r_b\rvert}{h}\right)\right]^5 - 6\left[2 - \left(\frac{\lvert r-r_b\rvert}{h}\right)\right]^5 + 15\left[1 - \left(\frac{\lvert r-r_b\rvert}{h}\right)\right]^5, \\ 0 \le \lvert r - r_b\rvert \le h \\ \left[3 - \left(\frac{\lvert r-r_b\rvert}{h}\right)\right]^5 - 6\left[2 - \left(\frac{\lvert r-r_b\rvert}{h}\right)\right]^5, \\ 0 \le \lvert r - r_b\rvert \le 3h \\ \left[3 - \left(\frac{\lvert r-r_b\rvert}{h}\right)\right]^5, \quad 2h \le \lvert r - r_b\rvert \le 3h\end{cases}$

Some examples of SPH models for cold spray include SPH simulation of cold spray oblique impacting Cu particles which showed well-fitted results to the experimental data [72]. The issues of mesh distortions were completely avoided when the SPH method was applied [72]. There was reduced dependency on the particle weight in the case of the SPH technique compared to the mesh based Lagrangian methods [73]. The effect of interfacial oxide layers on the impact processes during the cold spray was investigated using the particle based SPH technique [65]. Excessive deformation, complex time evolution associated with free surfaces, and large thermal transport processes associated with the mesh based Lagrangian FE model were overcome using the SPH approach [65,66,69,70].

Ceramic particles were deposited using cold spray at room temperature and studied using the SPH [82]. The contact surfaces were free, which was vital in predicting critical velocities and their effects on deposition efficiency. Two main mechanisms were observed through simulation and experiment, which are fragmentation from the submicron- to the

nanoscale and the bombardment of the submicron particles, providing enough bonding energy as pressure and thermal energy for the fragmented particles through the shock waves [82–84]. Although the deformation behavior was adequately simulated, the method was not appropriate for determining the critical and maximum velocities. The technique provided the basis for understanding the deposition behavior numerically.

An SPH and experimental study on cold spray between similar and dissimilar substrates was carried out [84,85]. The ratio of the deposition and rebound energy was used for the cold spray coating evaluation based on porosity rate, hardness, and bonding strength. The quality of the coating on similar metals was better than those of similar metals, as predicted based on high deposition energy and low rebound energy. The effect of interfacial oxides has also been studied using the SPH approach and the results correlated well with experiments [65]. Thus, the application of SPH to cold spraying has been successfully implemented in optimizing process parameters. However, the issues of computational cost and tensile instability are still a strategic research direction.

4.2. Finite Element-Based Numerical Models for Cold Spray Processes

Six main computational models have been used to explain and simulate cold spray particle impacts. These models are used for high strain rate plasticity of various feedstock metallic powders and the overall deposition properties. The models include the Johnson–Cook (JC) plasticity model [85,86], Zerilli–Armstrong (ZA) model, Voyiadjis–Abed (VA) model, Preston–Tonk–Wallace (PTW) model [87], Khan–Huang–Liang (KHL) model, and the Gao–Zhang (GZ) model. The shortcomings of the models led to modified models where initial assumptions are improved to fit predicted data to the experiment ones. The common and widely used model is the JC model which is built into the ABAQUS/Explicit finite element analysis platform.

4.2.1. Johnson–Cook Model

This model was designed by Johnson and Cook and relates the flow stress to the strain rate, plastic strain, and temperature [38,86]. It is simple to use and successful in estimating flow stress more accurately for various engineering applications. The model has three parts focusing on strain hardening, strain rate hardening, and thermal softening as shown in Equation (2) [86]. The model is not suitable for predicting relatively high flow stresses at very high strain rate. In the case of Cu, the JC model fails when the strain rate exceeds 10^{-5} s^{-1} [86]. There is a linear relation between the work hardening and the strain rate on a logarithmic scale. This is indicative of the shortcoming of the JC model as it underestimates the material and mechanical behavior at very high strain rates.

$$\sigma = \left(A + B\varepsilon_p^n\right)\left[1 + C\ln\dot{\varepsilon}_p^*\right]\left[1 - (T^*)^m\right] \quad (2)$$

The homologous temperature in the JC model, which is T^*, is given and defined in Equation (3), where the absolute, transition or reference, and melting temperatures are T, T_r, and T_m, respectively.

$$T^* = \begin{cases} 0, & T \prec T_r \\ \frac{T - T_r}{T_m - T_r}, & T_r \prec T \prec T_m \\ 1, & T \succ T_m \end{cases} \quad (3)$$

where: the parameters A, B, n, C, and m are material-dependent constants, ε_p is an equivalent plastic strain, $\dot{\varepsilon}_p^*$ is an equivalent plastic strain (ratio of the plastic strain rate and reference strain rate).

The JC model is the most successful constitutive model for simulating cold spray behavior of various metallic alloys [38,48,85,86,88–92]. Typical applications of the JC model for Cu, Ni, and 316 steels with the respective JC parameters are given in Table 4. Similar studies have been carried out using refractory Ta powders on 4340 steel substrates [93] and

the effect of nanoscale interfacial oxides on the deformation and cracking phenomena on cold spray Al 6061 powders [94]. These studies used experimental and computational approaches. An overview of some of the ferrous and non-ferrous cold spray coating phenomena, deformation mechanisms, material jetting, and the effects of various microstructural features has been presented [3,95–97].

Table 4. Typical JC model and general parameters used for numerical simulation of cold spray for Cu, Ni, and 316SS extracted from published literature [48,86,95–97].

Parameters	Material		
	Cu	**Ni**	**316**
Johnson–Cook parameters			
A (MPa)	90	163	388
B (MPa)	292	648	1728
C	0.025	0.006	0.02494
m	1.09	1.44	0.6567
n	0.31	0.33	0.8722
Strain (1/s)	1	1	0.00001
Thermal and general properties			
Density (g/cm^3)	8.96	8.90	8.03
Conductivity (W/Km^2)	386	90.6	16
Specific heat (J/kgK)	383	435–446	457
Melting point (K)	1356	~1728	1643
Poisson ratio	0.34	0.31	0.3
Elastic modulus (GPa)	124	200	193

To make up for the lapses in the original JC model, a modified JC model is proposed for relatively high strain rates [96–101]. This is given in Equations (4) and (5) [102,103]. The JC and modified JC models have fewer material constants compared to the typical Preston–Tonk–Wallace (PTW) model. These JC models are extensively used for various materials with their constants are easily accessible in the literature [102–105].

$$\sigma = \left(A + B\varepsilon_p^n\right)\left[1 + C\ln\frac{\dot{\varepsilon}_P}{\dot{\varepsilon}_0}\left(\frac{\dot{\varepsilon}_P}{\dot{\varepsilon}_c}\right)^D\right]\left[1 - \left(\frac{T - T_r}{T_m - T_r}\right)^m\right] \quad (4)$$

$$D = \begin{cases} x, \dot{\varepsilon}_p \geq \dot{\varepsilon}_c \\ 0, \dot{\varepsilon}_p \leq \dot{\varepsilon}_c \\ \dot{\varepsilon}_c = ys^{-1} \end{cases} \quad (5)$$

where: D is a non-zero (x) parameter when $\dot{\varepsilon}_p$ (plastic strain rate) is within a certain critical strain rate ($\dot{\varepsilon}_c$) value and $\dot{\varepsilon}_0$ is the reference strain rate.

A typical bilinear JC model, which is an improvement on the previous JC models with the capacity for two-stage rate sensitivity, has been used for many systems [94,106,107]. The bilinear model incorporates a second constant to improve the approximation of high strain rate sensitivity [107]. A typical bilinear JC model has been implemented in ABAQUS–Explicit for the study of interfacial oxide effects on cold spray of Al [94].

4.2.2. Preston–Tonk–Wallace (PTW) Model

The PTW model was designed for estimating the material behavior of relatively high strain rates as shown in Equations (6) and (7) [87]. This is to correct the challenges associated with the JC model which breaks down at strain rates above $10^4/s$ [17,108].

This is a constitutive parametric model designed based on the dislocation movement and mechanisms during plastic deformation [108]. Typical PTW models have been used for wide strain rate ranges (10^{-3}–10^{13}/s) [17,108].

$$\sigma = 2\left[\tau_s + \alpha \ln\left[1 - \varphi \exp\left(-\beta - \frac{\theta \varepsilon_p}{\alpha \varphi}\right)\right]\right]\mu(p, T) \quad (6)$$

$$\alpha = \frac{S_0 - \tau_y}{d}, \beta = \frac{\tau_s - \tau_y}{\alpha}, \varphi = \exp(\beta) - 1 \quad (7)$$

where: τ_s= normalized work hardening saturation stress, s_0 = saturation stress at 0 K, τ_y= normalized yield stress, θ = strain hardening rate, ε = equivalent plastic strain, d = dimensionless material constant. The "μ" is the shear modulus, which is a function of the temperature and easily estimated using the mechanical threshold stress (MTS) shear modulus model given in Equation (8) [109]. The τ_s and τ_y are given in Table 5.

$$\mu(T) = \mu_0 - \frac{D}{\exp\left(\frac{T_0}{T}\right) - 1} \quad (8)$$

where: μ_0 = shear modulus at 0 K, D and T_0 = material constants, and T = temperature of the material [109]. The standard parameters for the PTW model are the strain rate dependence constant, strain hardening rate, strain hardening constant, yield stress constant at 0 K, yield stress constant at melting, medium strain rate constant, high strain rate constant, high strain rate exponent, saturation stress at 0 K, saturation strength at melting, temperature dependence constant, atomic mass, shear modulus, material constant (D), and temperature material constant [110].

Table 5. Parameters for normalized work hardening and normalized yield stress.

Parameters	Expression
Normalized work hardening saturation stress	$\tau_s = \max\left\{S_0 - (S_0 - S_\infty)\mathrm{erf}\left[k\hat{T}\ln\left(\frac{\gamma\dot{\zeta}}{\dot{\varepsilon}_p}\right)\right], S_0\left(\frac{\dot{\varepsilon}_p}{\gamma\dot{\zeta}}\right)\right\}$
Normalized yield stress	$\tau_y = \max\left\{y_0 - (y_0 - y_\infty)\mathrm{erf}\left[k\hat{T}\ln\left(\frac{\gamma\dot{\zeta}}{\dot{\varepsilon}_p}\right)\right], \min\left\{y_1\left(\frac{\dot{\varepsilon}_p}{\gamma\dot{\zeta}}\right), S_0\left(\frac{\dot{\varepsilon}_p}{\gamma\dot{\zeta}}\right)\right\}\right\}$
Where $\zeta = \frac{1}{2}\left(\sqrt[3]{\left(\frac{4\pi\rho}{3M}\right)}\right)\left(\sqrt{\frac{\mu(\rho,T)}{\rho}}\right)$	

The PTW model is more complicated than the typical Johnson–Cook model, but there is more control of the material parameters. Recent investigations on dilute or conventional metallic materials such Cu and WC-Co and cold spray coating applications have been reported [104,108,111]. Plastic deformation during cold spray processes has been modeled using the PTW model for strain rates up to 10^7/s with comparable results to experiments [87,109]. The PTW has also been applied within the ALE framework due to the good fit at very high strain rates [102].

4.2.3. The Zerilli–Armstrong (ZA) Model

The ZA model is for estimating plastic deformation behavior of materials, focusing on flow stress at relatively high temperatures [103,105,112]. The flow stress is given by the relation shown in Equation (9). The ZA model is a physical model and applies to a range of materials with varying crystal structures sensitive to temperature and strain rate. The exponential term in Equation (9) describes the thermal stress component which is derived experimentally. As the temperature tends to infinity, the thermal stress components become zero.

$$\sigma = (C_1 + C_2\varepsilon^n)\exp\left\{-\left((C_3 + C_4T^*)T^* + (C_5 + C_6T^*)\ln\dot{\varepsilon}^*\right)\right\} \quad (9)$$

where: $T^* = T - T_r$, C_1, C_2, C_3, C_4, C_5, C_6, and n = material constants, ε = equivalent plastic strain, $\dot{\varepsilon}^*$ = normalized equivalent plastic strain, T = absolute temperature, and T_r = reference temperature.

The modification of the ZA model is carried out to improve the temperature-dependent terms of the original model. The modified ZA model gives better results for temperatures above 300 K, and the work hardening is independent of strain rate and temperature, which is an assumption that drives the original model. The flow stress based on the modified ZA model is given in Equation (10).

$$\sigma = B\varepsilon_p^{0.5}\left(1 - \sqrt{x} - x + \sqrt{x^3}\right) + C_6 \tag{10}$$

4.2.4. The Voyiadjis–Abed (VA) Model

The Voyiadjis–Abed model was designed as an improvement on the ZA model [113]. The prediction is more efficient for higher strain rates and higher temperatures than the ZA model. The model is summarized in Equation (11).

$$\sigma = B\varepsilon_p^n\left(1 - \left(\beta_1 T - \beta_2 T \ln \dot{\varepsilon_p}\right)^{1/q}\right)^{1/p} + Y_a \tag{11}$$

where: ε_p = equivalent plastic strain, $\dot{\varepsilon_p}$ = plastic strain rate, T = temperature, and B, Y_a, β_1, β_2, p, q, and n = material constants.

4.2.5. The Other Types of Models

There are other types of models that have been used for estimating the mechanisms of cold spray methods [89]. These include the modified Zerilli–Armstrong [113,114], modified Khan–Huang–Liang (MKHL) [115,116], and the Gao–Zhang models [117]. The details of these models are summarized elsewhere [89].

The current state of the art, looking at numerical and experimental approaches for the design of cold spray coatings are discussed. Emphasis is on concentrated amorphous and crystalline coatings. The amorphous alloy coatings are mainly bulk metallic glasses (BMGs), whereas the crystalline materials are complex concentrated alloys (CCAs).

5. Bulk Metallic Glass Cold Spray Coatings

Bulk metallic glasses (BMGs) have gained traction since the 1990s [118–120]. These are mainly amorphous or partially crystallized materials with medium- to long-range disorder devoid of typical lattice defects such as dislocations and grain boundaries [120–126]. They undergo strain softening, localized shear instability, and easily rupture under applied loads. Most BMGs possess high elastic modulus and high strength [120]. There is a trade-off between strength and ductility, resulting in poor plasticity. Challenges associated with BMGs as structural materials include: (i) size limitation due to limited glass-forming abilities (GFAs) and very high cooling rates (>10^5 K/s) [123]. These alloys can be produced to about few centimeter sizes and are mainly wires, ribbons, and powders, restricting large scale and industrial applications [120–122]; and (ii) poor ambient temperature plasticity and deformation is constrained to concentrated shear zones [125,126]. Thus, they are not the right candidate for load-bearing structural applications [124,125].

Some of the main BMG coating systems include Al, Cu, Fe, Ni, and Zr. Characteristic features and suggested applications of these coatings are given in Table 6. Advantages of BMG cold spray coatings over traditional BMG coatings are:

- High hardness, high strength, and wear resistance: BMG coatings exhibit high hardness and wear resistance, making them suitable for use in harsh environments where traditional coatings may fail.
- Corrosion resistance: BMG coatings have excellent corrosion resistance, making them perfect for use in marine, aerospace, and other corrosive environments.

- Low porosity: BMG coatings have a low porosity, lowering the chance of corrosion and enhancing substrate adhesion.
- High bonding strength: BMG coatings have a strong bond to their substrate, reducing the chance of delamination or cracking.
- Low thermal conductivity: BMG coatings have a low thermal conductivity, making them suitable for use in high-temperature environments where thermal insulation is needed.
- Tailored properties: BMG coatings possess specific properties such as electrical conductivity, magnetic properties, or optical properties, making them useful in a variety of applications.
- Cost effectiveness: As a cost-effective substitute for conventional coating techniques, BMG cold spray coatings can be applied using a relatively inexpensive procedure.

Table 6. Thermal spray coating of various types of metallic glasses.

System	Features	Suggested Applications	Ref
Al based	Very dense structure Excellent corrosion resistance Great strength-to-weight ratio	Automobile and aircraft Sacrificial anode Environmental protection	[127–129]
Cu based	Great mechanical properties Excellent nanosize properties	Microelectromechanical systems Turbine applications	[130]
Fe based	Improved strength Improved wear resistance Excellent corrosion resistance Strong glass formability Low-cost material	Marine and coastal areas Power plants Hydraulic machinery	[131–135]
Ni based	Very high strength High thermal stability Expensive process cost Excellent corrosion resistance	Petrochemical applications Glass industries Nuclear applications	[136,137]
Zr based	Excellent fracture toughness Excellent ductility Excellent corrosion resistance High hardness	Biomedical applications Nuclear applications Bearings	[138,139]

Overall, the distinctive combination of qualities provided by BMG cold spray coatings makes them a desirable option for a variety of applications, including those in the aerospace, automotive, energy, and biomedical industries.

Bulk metallic cold spray coatings are desirable due to the low temperature and solid-state deposition mechanism [54,140–143]. These contribute to effective reduction in porosity and retard recrystallization during cyclic thermal stresses. The low temperature leads to restraining of distortions which could arise from thermal stresses and oxidation phenomena. The process does induce compressive residual stresses in BMG cold spray coatings, while improving metallurgical bonding at the coating–substrate interface and between the various layers of the coatings [140–143]. These alloys have been investigated using numerical and experimental approaches, showing excellent functional and structural properties. The BMG coatings produced from cold spray with processing parameters are given in Table 7.

Table 7. Bulk metallic glass cold spray coatings on various substrates with processing parameters.

BMG Coating	Substrate	Gas	Temperature (°C)	Pressure (MPa)	Ref.
$Al_{88}Ni_6Y_{4.5}Co_1La_{0.5}$	Al 7075	N_2	300–400	3.0–4.0	[144]
$Al_{90.05}Ni_{4.3}Y_{4.4}Co_{0.9}Sc_{0.35}$	Al 6061			3.8	[145]
$Cu_{50}Zr_{50}$	Stainless steel		500–800	~4.0	[146]
$Cu_{54}Ni_6Ti_{18}Zr_{22}$	Cu	He	~550	1.5–3	[147]
FeCrMoWCMnSiZrB	Al 6061		~300	1	[148]
$Fe_{68.8}C_7Si_{3.5}B_5P_{9.6}Cr_{2.1}Mo_2Al_2$	Mild steel		~550	2.1–2.9	[149]
$Fe_{44}Co_6Cr_{15}Mo_{14}C_{15}B_6$	Al/Cu/Ti	N_2	900–950	~4.0	[150]
$Fe_{73}Cr_2Si_{11}B_{11}C_3$	Carbon steel		900–1000	4–5	[142]
$Ni_{57}Ti_{19}Zr_{20}Si_3Sn_2$	Mild steel	He	~600	~3	[151,152]
ZrCuAlNiTi	Cu		~500	2.4	[153]

5.1. Aluminum-Based BMG Cold Spray Coatings

Aluminum bulk metallic glass alloys have low density, high specific strength (1000–1500 MPa) [154,155], great corrosion resistance, and high modulus. They are difficult to deform due to the disordered arrangement of atoms with the low critical resolved shear stresses of Al [120]. A few Al-based BMG coatings have been designed and studied [120,144,145] and their compositions are based on the ternary system (Al–TM–RE), where TM stands for transition metal (Ni, Co, or Fe) and RE stands for rare earth (La, Ce, Gd, or Y) [103]. The transition metals are used to accelerate the atomic packing process, whereas the rare earth elements induce glass formation [103,129,145,156–158]. Some of the main cold spray coating systems are Al-Co-Ce [129,156], Al-Ni-Ce [103], Al-Y-Ni-Co-Sc [145], and Al-Ni-Y-Co-La [144].

The wear and mechanical behavior of Al-based BMG cold spray coatings on Al substrate has been studied. The coating had high hardness due to the glass-forming properties and superior wear resistance was observed compared to the substrate. For corrosion resistance, the coatings were over five times better than the substrate when tested in NaCl solution. The coating has two main factors contributing to the high corrosion resistance. Due to the amorphous nature of the coatings and the chemical homogeneity, it prevents the onset of the formation of galvanic cells [154]. Furthermore, the corrosion resistance improves due to the presence of nanocrystals which accelerate the formation of protective passive films resulting from rapid diffusion of passive element to the interface between the substrate and coatings as well as the surface. This has also been confirmed experimentally [155,157,158]. These nanocrystals were confirmed with high-resolution transmission electron microscopy. Similar results were obtained for AlNiYCoLa on Al 7075 substrate [144]. The combined effect of the amorphous phase and the Al_2O_3 passive oxide layer was the contributing factor to the superior corrosion resistance.

Wear behavior is dependent on the volume fraction of the amorphous phase of the Al-based BMG coatings. The amorphous phase proportion, thickness, strength, porosity, and hardness are dependent on the processing parameters (stand-off distance, gas pressure, and temperature). Excellent wear resistance was observed for Al-based coating with ~81% amorphous phase. The coefficient of friction was also reduced by more than 30%. The wear mechanism of the coating was abrasive grooving with minute surface splat delamination.

5.2. Copper-Based BMG Cold Spray Coatings

Copper-based BMG alloys have structural and functional properties for various engineering applications [159–162]. These properties include corrosion resistance and high strength and hardness which are applicable in biomedical, aerospace, electronics, and sport equipment. The binary systems which are the base for Cu-based BMG are Cu-Ti, Cu-Ni, and Cu-Zr [159–162]. For the 54Cu–22Zr–18Ti–6Ni BMG coating on Al 6061 substrate, a

porosity below 5% was observed with coating thickness ranging from 300–400 μm [161]. The hardness of the coating was 412.8 HV, whereas the wear resistance was three times better than that of the pure Cu coatings. The adhesion strength of the BMG coatings was better than that of the pure Cu coatings due to the synergistic effects of the alloy elements controlling the deformation mechanisms of the substrate. Poor corrosion resistance of the BMG coatings was observed, which is attributed to the high porosity in the amorphous coating layer [161].

Binary 50Cu–50Zr [146] and ternary Cu–Ti–Ni BMG cold spray coating systems have been studied for biomedical applications [163]. In the case of the equiatomic binary Cu–Zr coatings, the gas temperature was critical for the deposition efficiency. The main zones were no bonding, weak bonding, great bonding, and viscous flow. Due to the poor adhesion behavior associated with no bonding and weak bonding, there was no coating on the substrate. The deposition was carried out at 600 °C and 800 °C with the highest hardness and cohesive strength at 800 °C.

The BMG coatings of 50Cu–50—x(Ti)–xNi were produced from low-energy ball milling (mechanical alloying) and cold spray [163]. The milling process reduced the particle sizes and offered some mixing, whereas the cold spray was used to deposit the coatings on austenite stainless steel substrate. The 50Cu–20Ti–30Ni and 51Cu–17Ti–13Ni coatings had the best wear resistance and relatively low coefficient of friction (0.32–0.45), with ~50% reduction in friction coefficient on 304 steel substrate (Figure 7) [163]. The coating sufficiently inhibited the formation of biofilm, thus being a promising coating for biomedical applications. This was mainly due to enhancement of antimicrobial effects of Ni by the relatively high amounts of Ti and Cu.

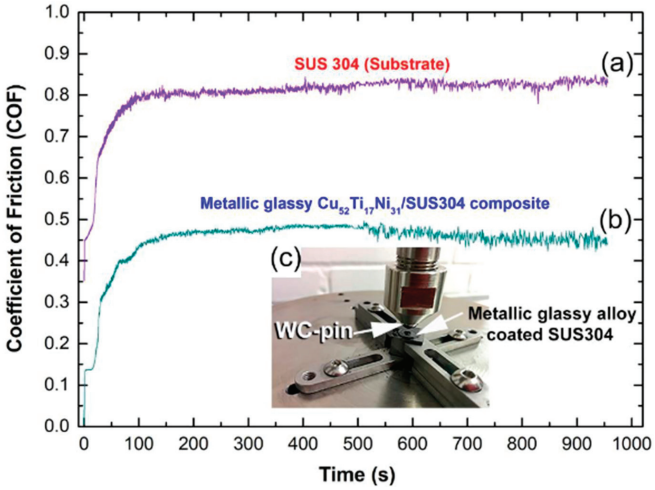

Figure 7. Comparison of the coefficient of friction of CuTiNi BMG cold spray coating with 304 steel substrate where (a) is the untreated 304 substrate, (b) the 304 substrate with Cu-based metallic glass coatings and (c) the experimental set-up for the wear testing [163].

Numerical and experimental approaches have been used to study the nanocrystallization of CuNiTiZr BMG coatings [147]. The numerical and experimental results showed that the kinetic energy of the impacting particles has a significant impact on the activation energy for nucleation and the fraction of crystallinity in BMG coatings [147]. The high-velocity impact resulted in a reduction in the free energy barrier and an increase in the driving force for the phase transition from amorphous to crystalline due to the kinetic energy of the particles. When the CuNiTiZr BMG was subjected to the cold spray technique, the microstructural characterization showed that the nanocrystallization of the substance was related to the strain energy produced by rapid plastic deformation.

5.3. Iron-Based BMG Cold Spray Coatings

These alloys have unique structural properties such as wear resistance and great strength behavior [120,134,164] and functional properties such as superior glass-forming ability, corrosion resistance [165–167], and soft magnetic properties. Initial works include production of cold spray coatings of Fe-Cr-W-Mo-Mn-C-Si-B-Zr on Al substrate showing ultralow porosity along the nominal microcracks [148,165]. Microhardness of the BMG cold spray coating is ~639 $HV_{0.3}$, which is about ten times higher than that of the Al substrate [148]. The degree of amorphization was poor as most of the particles were not fully amorphous. The drawback of the coating on the substrate is the small thickness of ~0.2 mm, which is not durable for long-term and aggressive corrosion or oxidation environments. The bonding mechanism is attributed to adiabatic shear instability which leads to metallurgical bonding at the BMG particles and Al substrate [143,148]. Localized deformation was observed at the particle–particle boundary and softening resulted from adiabatic deformation within the feedstock particles during the formation of the splat [88,168–170]. For typical BMG coatings, the deposition efficiency (DE) is one of the main parameters that ensure structural integrity and the quality of the coating [141,150,166,171]. The DE is also influenced by processing parameters such as gas temperature, stand-off distance, substrate temperature, and process gas pressure (Table 2) [150,166,171].

The tribological behavior of BMG coatings produced from cold spray on various metallic substrates has been studied [120,143,149]. For FeCSiBPCrAlMo coatings, a lower coefficient of friction was observed compared to bearing steel [149]. Similarly, the wear behavior of cold spray coatings of FeCrMoCBY is better than that of BMG coatings produced using other thermal spray methods [143]. The superior tribological behavior of cold spray coatings of BMG compared to high-velocity air fuel (HVAF) was due to excellent adhesion at the particle–particle and particle–substrate interface [18,172,173] and lack of oxidation due to the low heat input. The CS coating also had ~2% porosity and high hardness due to grain refinement resulting from the peening effect associated with cold spray [173–175].

5.4. Nickel-Based BMG Cold Spray Coatings

Typical Ni-based BMG coatings have high strength, high thermal stability, and great corrosion resistance [120,176,177]. The Ni-based BMG systems are from the ternary compositions of Ni–Ti–Zr, Ni–Zr–Al, and Ni–Nb–Ti with slight modification of the microstructure with minute addition of metalloids (Si or B) [120,176,177]. Some of the major compositions which have been studied extensively include 57Ni–18Ti–20Zr–3Si–2Sn [176–178], 59Ni–20Zr–16Ti–2Si–3Sn [151,178], and 53Ni–20Nb–10Ti–8Zr–6Co–3Cu [177], where the compositions are according to weight percent.

The main properties of interest for Ni-based BMG cold spray coatings on different substrates are wear and corrosion resistance [120,145,151,152,179,180]. Cold spray coatings showed better wear and corrosion resistance than other thermal spray techniques such as vacuum plasma and high-velocity oxy-fuel spraying. This is mainly due to negligible phase transformation of the BMG produced by cold spray [151]. The propelling gas plays a critical role in the deposition efficiency of the BMG on mild steel [103]. By switching from nitrogen to helium, there was significant improvement in deposition efficiency [151,152]. The high drag force of helium and the high heating rate of feedstock led to increased splat to crater ratio, enhancing mechanical properties and bond strength [120]. This has been observed in NiTiZrSiSn BMG coating [145,151,152,179,180].

5.5. Zirconium-Based BMG Cold Spray Coatings

Zirconium-based bulk metallic glass (BMG) cold coatings are protective coatings applied to a variety of substrates [118,120,121,123,181]. These amorphous metallic coatings have a unique combination of properties, including high strength, high corrosion resistance, excellent wear resistance, and excellent biocompatibility for biomedical applications [103,120,153,182,183]. These amorphous alloys have a wide supercooled region with excellent glass-forming abilities. The common compositions are based on the quaternary

and quinary systems of Zr–Cu–Al–Ni and Zr–Cu–Al–Ni–Ti [118,120,181]. There have been some additions of Be and Fe for excellent mechanical properties, corrosion and wear resistance [120,181].

The mechanical properties such as hardness and strength are functions of operating temperature and the volume fraction of the amorphous phase. For a typical ZrCuAlNiTi/Cu metallic glass coating, the hardness increased from 500 HV at 400 °C to 620 HV with a 50°C increase in temperature.

6. Complex Concentrated Alloys—Brief Overview

Complex concentrated alloys are a broad class of structural and functional materials which are defined by their design strategy [5,184]. These encompass the medium-entropy alloys, high-entropy alloys (HEAs), and multiple principal element-based alloys (Figure 8). These alloys, by composition, occupy the central region of a typical phase or composition diagram as shown in Figure 9. The high-entropy alloys have multiple principal alloying elements with at least five components. They are in near-equiatomic ratios ranging from 5–35 at% [184]. The design philosophy of HEAs is premised on the assumption that forming solid solutions by constituent elements leads to high configurational entropy or entropy of mixing.

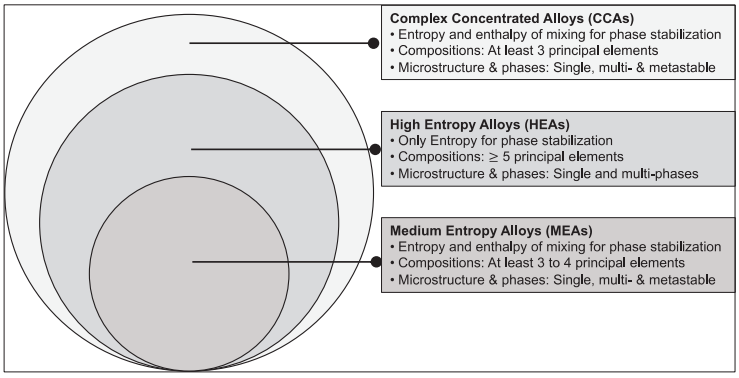

Figure 8. Complex concentrated alloys and their derivatives.

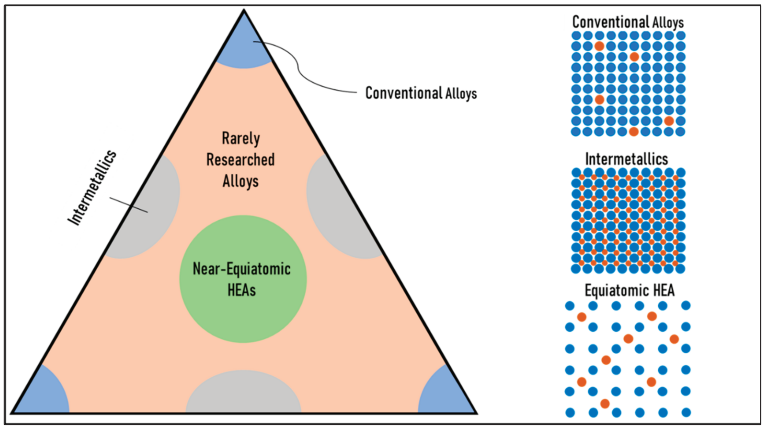

Figure 9. Typical illustration of dilute (compositions at the corners) and complex concentrated (compositions at and near the center) alloys.

These alloys extend the frontiers for alloy design beyond the conventional dilute alloying concentrations with potentially different properties for structural and functional applications [1–3,20,185]. The excellent structural and functional properties are attributed to four core effects.

6.1. Core Effects of Complex Concentrated Alloys

There are four main core effects associated with CCAs/HEAs, which are high configurational entropy of stabilization, sluggish diffusion, severe lattice distortions, and cocktail effects. The core effects and the relationship between the science and the physical metallurgy of CCAs are schematically shown in Figure 10. The entropy effect focuses on the thermodynamics; sluggish diffusion drives the kinetic phenomenon; severe lattice distortions focus on deformation theory, solid-state physics, and the strengthening mechanisms. The cocktail effects relate to how the structural and functional properties are impacted. The three core effects of high configurational entropy of stabilization, sluggish diffusions, and severe lattice distortions have been a bone of contention and require further investigation. They are not overarching and there is limited evidence that the "core effects" play significant roles in determining the unusual properties of CCAs. A brief description of the core effects is summarized.

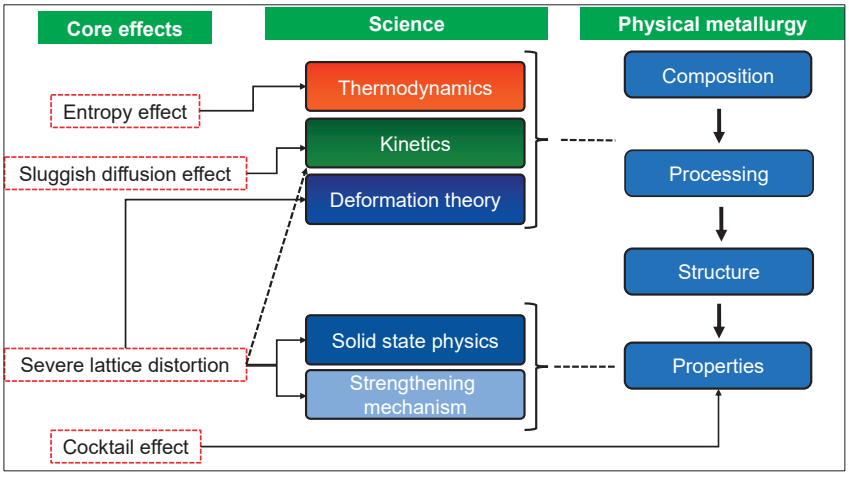

Figure 10. The interrelationship between core effects, the science, and physical metallurgy of CCAs.

High configurational entropy and enthalpy of mixing: The high entropy and enthalpy of mixing effects deviate from the Gibbs phase rule stabilizing phase proportions. This contributes to the observed properties, which are not common to most conventional one- or two-principal element-based materials. Increasing the constituent elements lowers the Gibbs free energy of the system, which outweighs the driving force for detrimental intermetallic phases and restricts their formation. Thus, most CCAs/HEAs should have simple and stabilized solid-solution phases. Configurational entropy and the enthalpy of mixing are related by Boltzmann's relation (Equation (12)).

$$\Delta S_{conf} = k \ln w \quad (12)$$

where: k = Boltzmann's constant, w = possible ways of mixing available energy.

Initial families of CCAs/HEAs supported the assumption of high configurational entropy of mixing. Recent families of HEAs deviate from the possibility of forming stabilized solid solutions across the full range of temperatures. For example, the Cantor alloy (CrCoFeMnNi) is observed to be stable as a face centered cubic solid solution at high temperatures. However, precipitates of tetragonal sigma phases can be observed at inter-

mediate temperatures. A few five-component CCAs are stable to intermetallic formation, hence the high configurational entropy stabilized is not an overarching effect and not quite strong enough for the observed properties in typical CCAs/HEAs. Common additions leading to the decomposition of the solid-solution phases are Ti, V, Cr, Cu, Al, and Mo due to their size difference and entropy. The concept of Hume-Rothery rules still applies to the dominance of enthalpy of formation. Thus, more investigation is required to establish the underlying factors and physical metallurgy principles.

Sluggish diffusion: Based on the atomic environment, there is slow diffusion due to variation in the potential energy of the lattices. This results in low kinetic transformation leading to sluggish diffusion effects. Slow diffusion of the mixing atoms results in variation of lattice potential energy due to differences in the atomic environment. Due to many constituent elements, some of the atoms are easily trapped, contributing to the sluggish diffusion phenomenon. This increases recrystallization temperature, reduces particle coarsening rate, and then leads to nanocrystalline structure.

Severe lattice distortion: This phenomenon is attributed to differences in size, bond energy, and crystal structures, resulting in mismatch [186–189]. It promotes the overall reaction rate [186,188]. Thus, localized and severely distorted lattices are observed but do not have the same effects of broadening X-ray diffraction peaks as in the case of dislocation defects [186,188]. The severe lattice distortions result in more incoherent scattering with reduced intensity of the XRD peaks [190,191]. The best way to measure the severe lattice distortions and quantify them is by a pair distribution function from the total scattering data, an extension of XRD, and neutron diffraction measurements [190–192]. In Figure 11, the weighted average distance to the nearest neighbors (interatomic distance) is shown and the width of the peaks estimates how much distortion occurs within the structure. Neutron diffraction has been used to estimate the lattice distortions in the Cantor alloy which is given in Figure 12 [186,188,189,193].

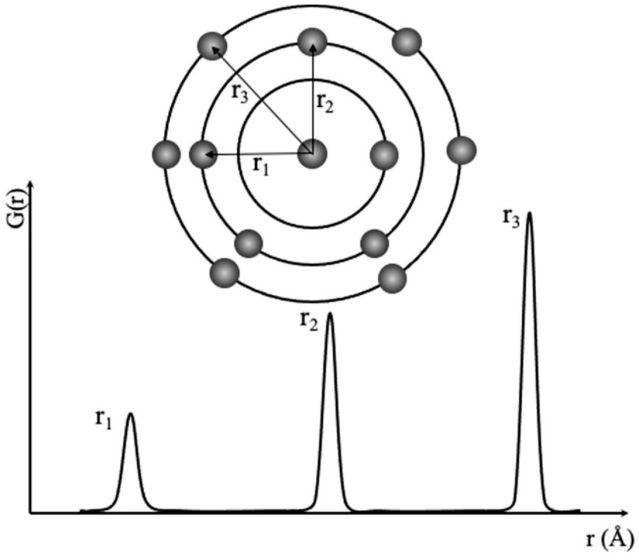

Figure 11. Schematics showing pair-wise distribution function for estimating the severe lattice distortions in CCAs.

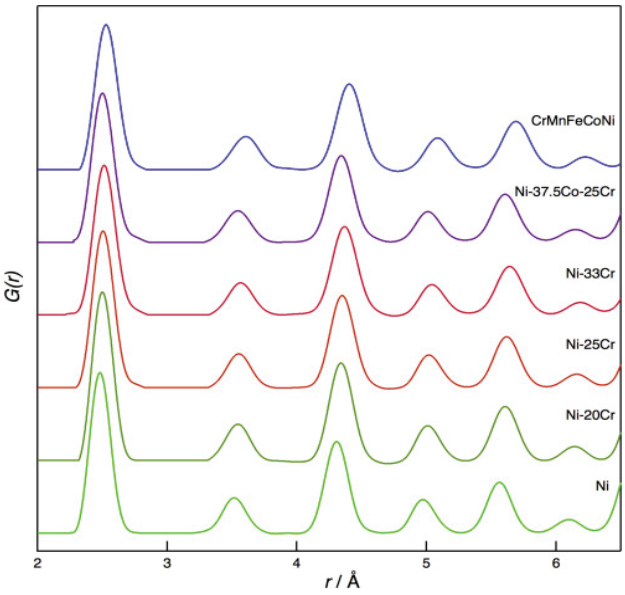

Figure 12. Normalized pair distribution function 3 for typical Ni-based alloys compared with the CrMnFeCoNi alloy based on the first six coordination shells [189].

Based on the pair distribution function, any severe distortions are easily quantified. Each peak in Figure 12 corresponds to a coordination shell around the atom at radius r and the area depends on the interaction of the atomic species and the respective coordination number [189]. In the case of severely distorted lattices, there is an increment in the width of individual peaks due to the noticeable displacement of the atoms from the original lattices or ideal positions. Once these displacements are significant within the coordination numbers with low "r" shells, the cumulative effect at a larger "r" causes more broadening of the peaks, resulting in poorly discernible features as opposed to that which is observed for the alloys in Figure 12. In Figure 12, no significant differences are observed for most of the peaks for the alloys studied, thus well-defined lattices are observed with no severe lattice distortions.

Cocktail effect: This is the overall effect from composition–processing–microstructure of the alloy. This effect is different from traditional or conventional alloys. Although this effect is not clear, it violates the rule-of-mixtures considering solute and solvent atoms are not easily discernible. There are unusual physical, mechanical, and chemical properties of the resulting CCAs, which are better than the average constituent elements. This is mainly attributed to the interaction between constituent elements and the indirect impact of these elements.

6.2. Complex Concentrated Alloy Coatings

Bulk CCAs are expensive due to the high amounts of constituent elements. This is a factor that could hinder massive application and scalability of bulk CCAs for structural and functional applications [1,2,20]. This has necessitated the need for the design of CCA-based coatings to solve the overall cost problem [22]. The superior functional properties of CCAs/HEAs such as wear, irradiation, thermal stability, corrosion, and oxidation resistance are linked to the associated mechanisms and how they differ from different classes of non-conventional coatings. The various approaches to depositing CCAs on various substrates have been reviewed [22]. The fabrication processes are mainly plasma/laser deposition, vapor deposition, and thermal spraying as shown in Figure 13 [22]. These coatings induce surface properties required to improve mechanical, physical, and chemical properties of

engineering components. Reviews focusing on laser and vapor depositions of CCAs/HEA-based alloys are available elsewhere [10,28]. Most of the CCA-based coatings that have been explored using the various techniques on different metallic substrates are given in Table 8.

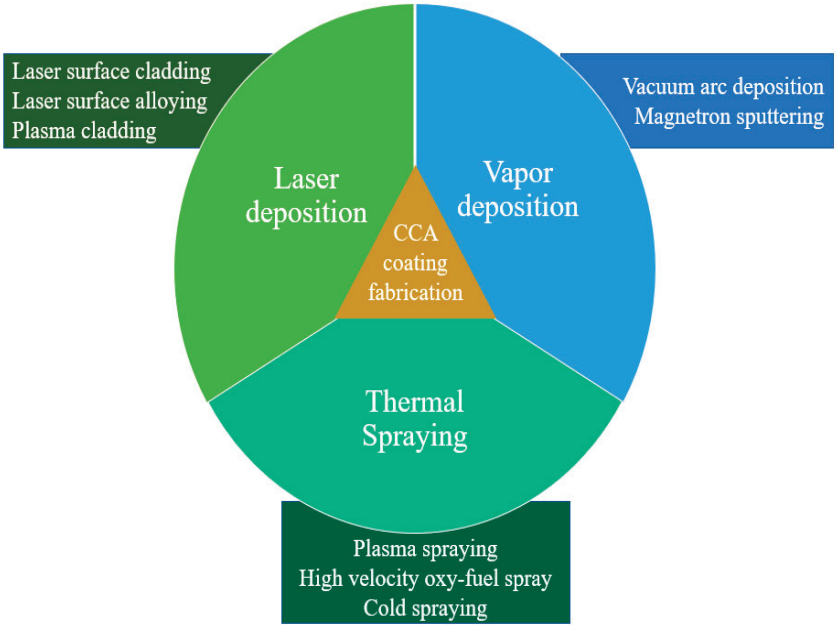

Figure 13. Typical fabrication methods of CCA/HEA coatings [194].

6.2.1. Complex Concentrated Alloy Cold Spray Coatings—An Outlook

Cold spray coatings have been used to deposit CCAs/HEAs on various substrate materials. These cold sprayed CCA/HEA-based coatings have shown excellent particle-to-substrate bonding, particle-to-particle bonding, adhesion strength, cohesive strength, relatively low porosity, and thickness of a few millimeters. These properties are essential in enhancing the physical, mechanical, and corrosion properties of these coatings in ways that induce structural integrity.

Trend analyses of publications with the keyword "cold spray + high entropy alloy" on Scopus and Web of Science were merged. A total of 37 peer-reviewed papers were found between 2019 and 2022, and their respective citations are shown in Figure 14. The first paper on cold spray of CrCoFeNiMn on an Al substrate was published in 2019. There is an increase in publications with an astronomical increase in citations since the pioneering works in March and June of 2019. In January 2023, two papers were published on the subject with 10 citations recorded based on the merged data from Scopus and Web of Science. The main papers are given in Table 9. The general theme is on the microstructural characterization of CCA-based cold spray coatings with a few focusing on the deposition of alloyed CCA-based powders on different metallic substrates. This has been successful as cold spray is a great way of depositing metals and intermetallics on various metallic substrates with ease.

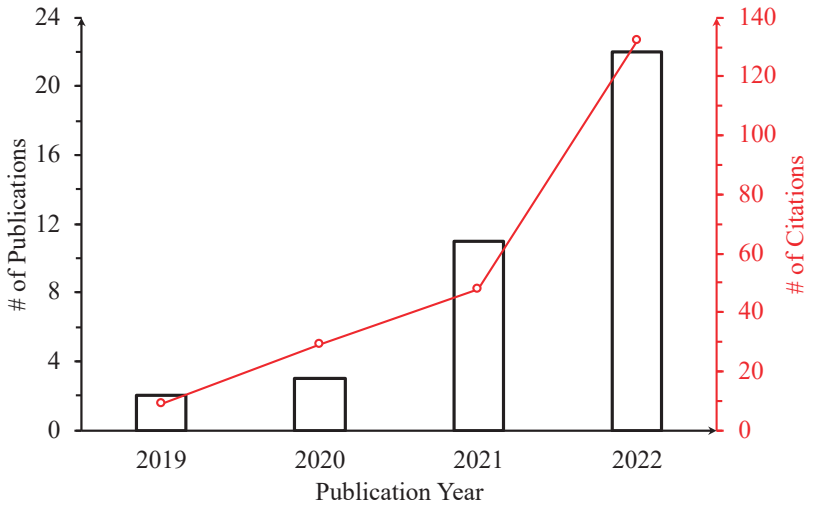

Figure 14. Yearly distribution of published journal articles indexed in Scopus and Web of Science with the corresponding citations from 2019 to 2022.

6.2.2. Mechanical Properties of Cold Sprayed CCAs on Different Metallic Substrates

Hardening mechanisms resulting from work hardening and grain refinements are associated with cold spray coatings in most conventional and complex concentrated alloys [9,27,55,56,88,89,195,196]. Deformation of the coating particles is due to high energy densities resulting in localized adiabatic shear [88,169,170]. The deformations are functions of particle distribution, morphology, size, and mechanical behavior of particles and processing parameters. The general behavior is also assisted by a peening effect of the coating particles, contributing to the enhanced mechanical properties. When the strain energy release rate is higher than the adhesive energy, propagating defects such as cracks interact with the interface layer, resulting in debonding of the coating. This ultimately leads to delamination, a process of the coating separating from the substrate, which is also due to poor wettability.

Strength and hardness properties: Strength and hardness of coatings are functions of composition of the substrate and coating material [27,105,112,197,198], the coating technique with optimized process parameters [91,199–201], quality, and microstructural features of the coating [28,202–206]. The bombardment of particle feedstock on the substrate induces severe plastic deformation [9,27,55,56,88,89,195,196]. This increases the strength and hardness of the cold sprayed coatings and the predominant strengthening mechanisms are mainly work hardening and grain refinement [88,168–170] as reported for CrMnFeCoNi [200] and CrFeNiMn [207] feedstock pre-alloyed through atomization. The porosity of the CrMnFeCoNi was observed to be ~0.47%, whereas that of CrFeNiMn was ~3.3%. The relatively low porosity in most CCA-based cold spray particles compared to other thermal spray processes shows the effect of the process on strengthening mechanisms.

Table 8. Different types of coating systems on different substrates and the resulting crystal structures and thickness.

Method	Substrate	CCA/HEA Coating	Structure	Thickness (μm)	References
Laser deposition techniques					
Plasma transferred arc cladding	Q 235	CoCrCuFeNiNb	FCC + Laves	~2000	[208]
		TiC–TiB2/CoCrCuFeNi	FCC + BCC + TiC + TiB_2		[209]
		CoNiCuFeCr	FCC		[210]
Plasma cladding		$CrCuFe_xNiTi$	FCC + BCC + Fe_2Ti	~2500	[211]
	AISI 1045 steel	FeCoNiAlCu	FCC + BCC	~1000	[212]
	Pure Ti	FeCoCrNiNbx		~1500	[213]
		CoCrFeNiNb	BCC + Cr_2Ti+ Cr_2Nb	~500–600	[214]
Laser cladding	Ti6Al4V	AlTiVMoNb	BCC		[215]
		$CoCrFeNi_2V_{0.5}Ti_{0.75}$	BCC + (Co, Ni)Ti_2 + Ti rich	~800	[216]
	Stainless steel	$Al_2CrFeNiMox$	BCC	-	[217]
	Q 235 steel	6FeNiCoSiCrAlTi		1200	[218]
		$MgMoNbFeTi_2Y_x$	FCC + BCC	~1300	[219]
		$Al_2CrFeNiCoCuTi_x$		~600	[220]
		AlCoCrFeNi/NbC	FCC + BCC + NbC	1200	[221]
		$Al_2CoCrCuFeNiTi_x$	-	500	[222]
		FeCoNiCrCu(SiMnMo)	FCC	~2000	[223]
	Al 5083	$Al_{0.5}FeCu_{0.7}NiCoCr$	FCC + BCC	~600	[224]
	H13 steel	$Co_{34}Cr_{29}B_{14}Fe_8Ni_8Si_7$	Amorphous + $FeNi_3$	~450	[225,226]
	45# steel	AlCoCrxFeNi	FCC + $FeAl_3$	-	[227]
	AZ31 Mg	$AlCoCrCuFeNiSi_{0.5}/Y_2O_3$	FCC + BCC	1500	[228]
	904L SS	$CoCr_2FeNiTi_x$/TiNi	FCC + TiN	1500	[229]
	M2 steel	MoFeCrTiWAlNb	BCC + (Nb, Ti)C + Fe_2Nb	1400	[230]
	253MA steel	$Al_xCoCrFeNi$	FCC + BCC	~900	[231]
	45 # steel	$FeCrCoNiAlMo_x$	BCC	~640	[232]
	H13 steel	FeCoCrBNiSi	Amorphous + FCC	~200	[233]

Table 8. *Cont.*

Method	Substrate	CCA/HEA Coating	Structure	Thickness (μm)	References
Laser alloying	Ti6Al4V	CrCoNiTiVAl	BCC + (Ni, Co)Ti_2		[234]
			BCC + (Ni, Co)Ti_2 + HCP		[235]
	304 SS	FeCoCrAlNi	BCC	~600	[236]
	Q235	FeCoCrAlCu		800	[237]
	A36 steel	CrMnFeCoNi	FCC	2000	[238]
	Ni201	FeCoCrAlCuV_xNi	FCC + BCC	400	[239]
	Pure Cu	FeCoCrAlCuNi$_x$		500	[240]
Vapor deposition techniques					
Vacuum arc deposition	Stainless steel	(TiZrNbAlYCr)N	FCC + BCC	~7	[241]
	C35 steel	(TiZrHfVNbTa)N	Amorphous + FCC + BCC	-	[242]
	C45 steel	(TiZrHfVNb)N	FCC	~4.78	[243]
Magnetron sputtering	304	FeCoCrNiMo$_{0.1}$	FCC	~0.85	[199]
		CrNbTiMoZr	Amorphous	~1.2	[244]
		CuMoTaWV	FCC + BCC	~0.9	[245]
	201	FeAlCuCrCoMn	FCC	~1.8	[246]
	M2 steel	CoCrNi/Ti	FCC + BCC + $CoTi_2$	3.5	[247]
		(TiZrNbHfTa)C	FCC	2.0	[248]
	C45 steel	(TiZrNbHfTa)N	FCC	2.0	
	N36 Zr	AlCoMoNbZr	Amorphous + BCC	3.0	[249]
	Mild steel	(TiAlCrSiV)$_x$N$_y$	Amorphous + FCC	1.7	[250]
	Si (100) wafer	(AlCrNbSiTiV)N		1.0	[251]
		(AlCrMnMoNiZr)N$_x$	FCC	1.5	[252]
		(AlCrMoTaTi)Si$_x$N		1.0	[253]
	Si (100); SiO_2; Al_2O_3	(HfNbTiVr)N		1.2	[254]
	Ti6Al4V	TiTaHfNbZr	Amorphous	~0.8	[255]
		Ag doped TiZrTaNbW		~1.1	[256]

Table 8. *Cont.*

Method	Substrate	CCA/HEA Coating	Structure	Thickness (μm)	References
Thermal spray techniques					
High-velocity oxygen-fuel spraying	ASTM A572	Al0.6TiCrFeCoNi	BCC	~300	[257]
	304/316	$AlCoCrFeNiTi_{0.5}$		~500	[258]
	304L	TiNbMoMnFe		-	[259]
	Incoloy 800H	$Ni_{0.2}Co_{0.6}Fe_{0.2}CrSi_{0.2}AlTi_{0.2}$	BCC + Cr_3Si	~1500	[260]
Plasma spray	316	AlCoCrFeNiTi/TiNi60	FCC + BCC		[261]
	Q235 steel	$(CoCrFeNi)_{95}Nb_5$	FCC + Laves	500	[262]
	Mild steel	CoCrMnFeNi	FCC + BCC + Fe_3O_4	-	[263]
		AlCoCrFeNi	FCC + BCC + $Al_2(Cr, Fe)O_4$	-	
	304	FeCoNiCrMn	FCC	~195	[264]
		$FeCoNiCrSiAl_x$	BCC + FCC	~160	[265]
	Mild steel	AlCoCrFeNi	BCC + FCC		[266]
	Q 235	$(CoCrFeNi)_{95}Nb_5$	BCC	~500	[262]
Atmospheric plasma spraying	304 SS	$NiCo_{0.6}Fe_{0.2}Cr_{1.5}SiAlTi_{0.2}$	FCC + BCC + Cr_3Si	-	[204]
		$Ni_xCo_{0.6}Fe_{0.2}Cr_ySi_2AlTi_{0.2}$	BCC + Cr_3Si	-	[267]
	316 SS	AlCoCrFeNiTi	BCC + FCC	240	[268]

Table 9. Summary of cold spray CCA-based coatings published from 2019 to 2023 from Web of Science and Scopus.

Database	Year	Title of the Published Paper	Refs
Web of Science	2019	Deposition of FeCoNiCrMn high entropy alloy (HEA) coating via cold spraying	[200]
		First report on cold-sprayed AlCoCrFeNi high-entropy alloy and its isothermal oxidation	[269]
	2020	Cold Gas Spraying of a High-Entropy CrFeNiMn Equiatomic Alloy	[207]
		Nanostructured AlNiCoFeCrTi high-entropy coating performed by cold spray	[270]

Table 9. *Cont.*

Database	Year	Title of the Published Paper	Refs
Web of Science	2021	Cold Spray Additive Manufacturing: Microstructure Evolution and Bonding Features	[271]
		Cold spray deposition characteristic and bonding of CrMnCoFeNi high entropy alloy	[272]
		Microstructure and properties of CuFeCrAlNiTi high entropy alloy coating prepared by cold spray assisted in-situ synthesis	
		Nanostructural AlNiCoFeCrTi High-Entropy Coatings Performed by Cold Spraying	[270]
		Solid-state cold spraying of FeCoCrNiMn high-entropy alloy: an insight into microstructure evolution and oxidation behavior at 700–900 °C	[273]
		Synthesis of High-Entropy AlNiCoFeCrTi Coating by Cold Spraying	[274]
		Tuning the Microstructure and Mechanical Properties of Cold Sprayed Equiatomic CoCrFeMnNi High-Entropy Alloy Coating Layer	[275]
	2022	An inclusive numerical framework to assess the role of feedstock features on the quality of cold spray deposits	[276]
		Cold Spray Additive Manufacturing of CoCrFeNiMn High-Entropy Alloy: Process Development, Microstructure, and Mechanical Properties	[206]
		Cold Spray and Laser-Assisted Cold Spray of CrMnCoFeNi High Entropy Alloy Using Nitrogen as the Propelling Gas	[277]
		Cold Spray: Over 30 Years of Development Toward a Hot Future	[9]
		Deposition of High-Entropy Alloy Coating by Cold Spray Combined with Laser Melting: Feasibility Tests	[278]
		Effect of Microstructure on Wear and Corrosion Performance of Thermally Sprayed AlCoCrFeMo High-Entropy Alloy Coatings	[202]
		Fatigue Bending of V-Notched Cold-Sprayed FeCoCrNiMn Coatings	[201]
		Friction Stir Processing of Cold-Sprayed High-Entropy Alloy Particles Reinforced Aluminum Matrix Composites: Corrosion and Wear Properties	[279]
Scopus		Mechanical and microstructural properties of a CoCrFe0.75NiMo0.3Nb0.125 high-entropy alloy additively manufactured via cold-spray	[169]
Web of Science		Microstructural, Mechanical and Wear Behavior of HVOF and Cold-Sprayed High-Entropy Alloys (HEAs) Coatings	[280]
		Microstructure and Mechanical Properties of the Plasma-Sprayed and Cold-Sprayed Al0.5CoCrFeNi2Ti0.5 High-Entropy Alloy Coatings	[197]
		Microstructure and Properties of Cold Spraying AlCoCrCuFeNix HEA Coatings Synthesized by Induction Remelting	[281]

Table 9. *Cont.*

Database	Year	Title of the Published Paper	Refs
Web of Science	2022	Microstructure and tribological properties of Al2O3 reinforced FeCoNiCrMn high entropy alloy composite coatings by cold spray	[282]
Scopus		Microstructure evolution and composition redistribution of FeCoNiCrMn high entropy alloy under extreme plastic deformation	[283]
Web of Science		Microstructures, wear resistance and corrosion resistance of CoCrFeNi high entropy alloys coating on AZ91 Mg alloy prepared by cold spray	[284]
		Modification of cold-sprayed high-entropy alloy particles reinforced aluminum matrix composites via friction stir processing	[170]
Scopus		Numerical and Experimental Analysis of the Deformation Behavior of CoCrFeNiMn High Entropy Alloy Particles onto Various Substrates During Cold Spraying	[285]
Web of Science		Numerical Simulation of Cold Spray Bonding for CrFeNi Medium-Entropy Alloy	[286]
		Structure Evolution and Corrosion Performance of CoCrFeMnNi High Entropy Alloy Coatings Produced Via Plasma Spray and Cold Spray	[287]
Scopus	2023	Cyclic behavior of FeCoCrNiMn high entropy alloy coatings produced through cold spray	[18]
		Sliding wear behavior of high entropy alloy coatings deposited through cold spraying and flame spraying: A comparative assessment	[288]

The core effects of CCAs, such as high configuration entropy of stabilization and enthalpy of mixing, sluggish diffusion, severe lattice distortion, and the cocktail effect due to interaction between atoms, could be contributing effects to the overall behavior of CCA-based coatings. The comparison of hardness of CCA-based coatings based on various thermal spray approaches is given in Figure 15 [28]. There are discernible trends for the approaches with the HVOF and APS having the highest hardness trends. Factors contributing the high hardness can be attributed to the approach used in producing the feedstock. For most of the HVOF and APS approaches, the feedstock was produced using mechanical alloying and high-pressure mechanical blending coupled with tubular mixing. This resulted in reducing the overall grain sizes to ~10–40 μm. The strengthening mechanisms for these processes were a combination of solid solution strengthening, interstitial strengthening, precipitation hardening, cohesive strengthening, and dispersion strengthening. This observation is further strengthened by the mixed phases associated with methods used in producing the feedstock.

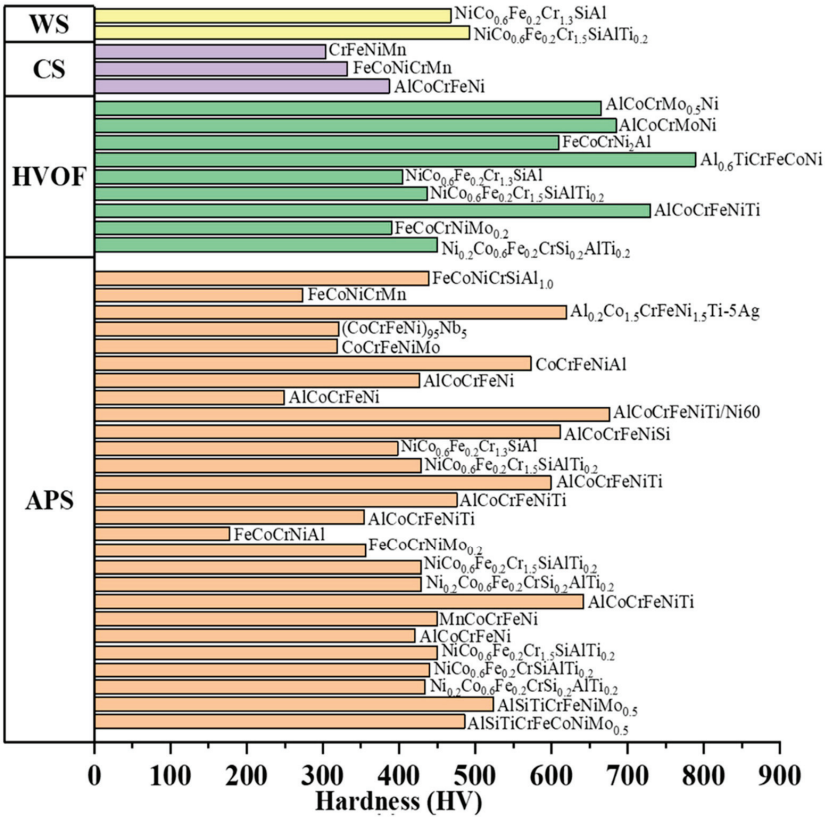

Figure 15. Variation of hardness of various CCA-based coatings through various thermal spray approaches [28].

Most of the coating phases for warm spraying, HVOF, and APS processes were mixtures of FCC, BCC, B_2, and carbides and oxides of constituent elements. For instance, there is hardness variation between cold sprayed and atmospheric plasma spray coatings. The additional hardness of APS was attributed to additional effects from mixed phases of FCC and BCC, and how these phases interact with one-, two-, and three-dimensional defects across various microstructural length scales. The presence of oxide phases induced by the high-temperature APS is also a contributing factor to the higher hardness

than with the cold spray with predominantly a single phase with no formation of oxides or other precipitates. The comparison of the deposition of Cantor alloy (CrCoFeMnNi) using APS and cold spray showed an interesting trend. The cold sprayed coating had relatively high hardness of ~333 HV compared to the APS technique, which had a hardness of ~273 HV. This is due to dynamic recrystallization at highly deformed regions resulting from the plastic deformation, increased dislocation density coupled with numerous grain boundaries [19,51,84,86,163,187], and their interactions with various microstructural features and defects (Figure 16). The effect of the overarching mechanisms for adhesion and cohesion, which is metallurgical interlocking, was a contributing factor (Figure 17).

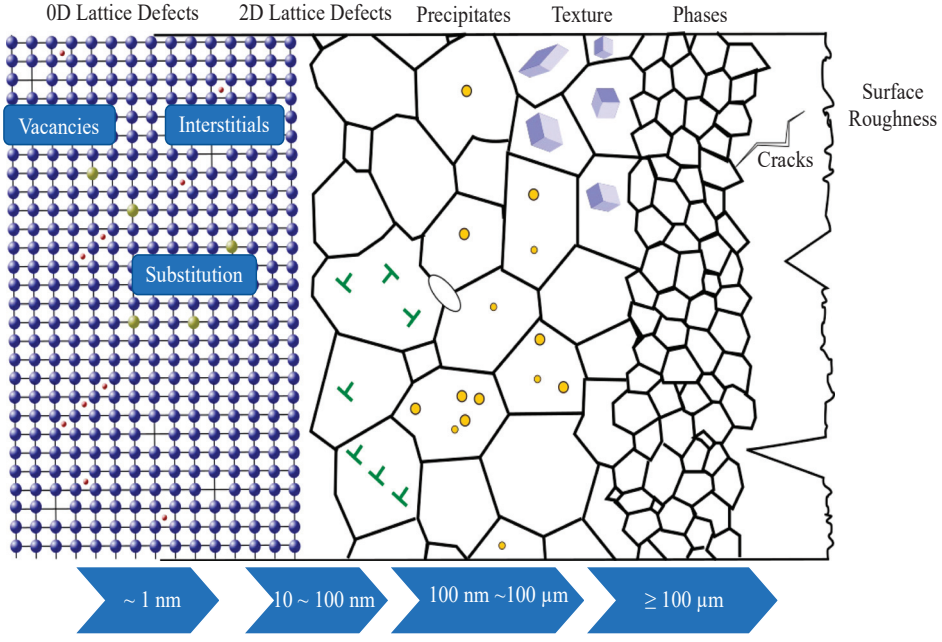

Figure 16. Schematic representation of different types of microstructural defects.

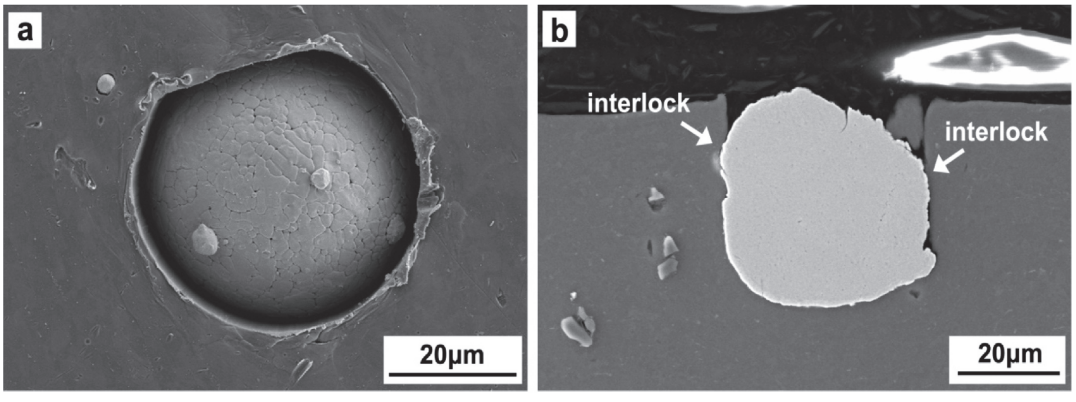

Figure 17. Microstructural characterization of Cantor alloy deposited on Al 6082 substrate showing (**a**) surface morphology and (**b**) cross-sectional view with the mechanical interlocking phenomena. Reprinted/adapted with permission from Ref. [200]. Copyright 2019, Elsevier.

The 6061Al and CrCoFeNi composites designed by using cold spray have showed enhanced strength and hardness after friction stir processing [279]. The replacement of conventional ceramic materials with CCAs is due to poor interface wettability between Al matrix composites reinforced with ceramics [289]. The cold spray process induced geometrically necessary dislocations (GNDs) of 17×10^{15} m^{-2} with an average grain size of 24 μm. The GNDs were further reduced to 9.8×10^{15} m^{-2} with average grain size of ~4 μm, resulting in great hardness and strength properties [279]. Although the strength and hardness behavior of CCA-based cold spray coatings are promising, these properties can be enhanced further by optimizing the process parameters of feedstock, cold spray processing parameters, and post-treatment processes.

Cold sprayed CrMnFeNi has been applied by varying the process parameters (feeding rate and gas pressure) with high hardness of ~304 $HV_{0.3}$ [27]. This value was achieved at gas pressure of 60 bar and feed fate of 1 rpm. The hardness was attributed to work hardening from the severe plastic deformation from the high-impact process of the cold spray technique [19,54,174]. In the case of CrCoFeNi cold spray coatings on AZ91 Mg alloys [284], the hardness was ~315 HV, exceeding conventional Al- and Zn-based cold spray coatings on Mg alloys. The enhanced hardness is due to grain refinement and the high hardness behavior of the CrCoFeNi compared to the Zr and Al alloys [290–297]. Apart from the peening effect resulting in grain refinement of the Mg surfaces, the alpha phase of AZ91 alloy also undergoes dynamic recrystallization contributing to the grain refinement [284].

Fatigue behavior and residual stresses: Fatigue performance of cold spray coatings is enhanced by properties of particles, processing parameters, and metallurgical factors [18]. Excellent fatigue and adhesion strengths were observed for FeCoCrNiMn alloy sprayed on metallic substrate. This was due to dense FeCoCrNiMn coating with optimized process parameters resulting in pancake-like appearance and high flattening ratio and severe grain refinement from the high-energy accelerated particles [18]. The peening effect resulting from the bombardment of the particles on the metallic surface induced high compressive residual stresses [173–175], which led to the high fatigue resistance and the observed adhesion strength [18,172,173]. From the XRD measurement, the maximum compressive residual stress was 200 MPa, about 100 μm from the coating–substrate interface.

Cracks were nucleated at the surface defects [18,172,174]. The first stages of deformation were along the trans-particle paths which were then followed with interparticle and mixed trans-particle fracture mechanisms. The differences in fracture mechanisms are dependent on microstructural features at the coating–substrate and particle–particle interfaces [18,172,174], due to the likelihood of geometric and continuous dynamic recrystallization at these interfaces [170].

The fracture behavior was mainly mixed mode with brittle characteristics during crack propagation and localized fatigue striation characteristics and localized ductile microvoid coalescence resulting from multiple crack initiation sites. The undeformed splat particles and microvoids were stress concentration points accelerating crack propagation rates [172,174].

Corrosion properties: The corrosion and electrochemical behavior of CCA cold spray coatings on various metallic substrates are comparable to their laser cladded or electric arc cladded CCA counterparts. In the case of CrCoFeNi cold spray coatings on AZ91 Mg alloys, an E_{corr} of ~−290 mV_{SCE} was recorded [284]. The presence of mixed and multilayer oxides and passive films of FeO, Cr_2O_3, and NiO retarded the rate of dissolution. This reduced the overall corrosion rate, thus improving the corrosion resistance. After 28 days of immersion, about 1% weight loss was recorded and a localized corrosion mechanism was observed with micropits of ~1 μm on average [284]. The highly uniform and dense microstructure coupled with stable passive oxide films provide the shielding effect needed and contributed to significant improvement in corrosion resistance.

For most coatings derived from Cantor alloys and their derivatives with relatively high Cr, Mo, and Ni contents, the corrosion resistance is comparable and, in some instances,

better than conventional ferritic and austenitic stainless steels. There is still substantial work required and investigations to be carried out in this area.

6.2.3. Microstructural Characterization of Cold Sprayed CCAs

The microstructural defects associated with cold spray deposits, as for any other thermal spray coatings, include porosity, voids, delamination, spalling, interface contamination, cracks (transverse and interlamellar), pull-outs, oxide clusters, and metallic inclusions. Details of these defects and brief definitions are given in Table 10. Generally, oxides are associated with metallic-based coating systems. By understanding the nature, types, and geometries of the defects in cold spray coatings, a critical mechanical property, fracture toughness, can be assessed and quantified. Fracture toughness is used to estimate the stresses required to propagate or accelerate pre-existing defects or flaws. Generally, the main mechanism of the propagation of cracks or defects highlighted in Table 10 is by intersplat decohesion or intersplat cracking [28,29,297]. This can be further exacerbated by cracks or pores interlinking, pore compaction, and the sliding of splat. There can also be issues of bifurcation of cracks and secondary crack formation contributing to increased fracture surface area [28,29].

Table 10. Typical defects and characteristic features associated with thermal spray processes. Reprinted/adapted with permission from Ref. [29]. Copyright 2023, Taylor and Francis.

Defect Types	Characteristic Features and Definitions
Voids	Characteristic microstructural volume defects which are mainly cracks and porosity
Porosity	Volume defects which are mainly pores or holes within the coating—a characteristic microstructural feature with no particulate matter
Spalling	Defects are a result of flaking, detachment, or peeling of surface particles or coating layers
Delamination	This is associated with separation or cracking of a coating, which could be due to poor adhesion between the coating material and the substrate. This defect can be caused by residual stresses during the spray process. Coatings can delaminate without any applied load
Transverse cracks	These are perpendicular cracks resulting from the coating on the substrate
Interlamellar pores	Defects due to non-homogenous filling along intersplat boundaries attributable to relaxation of vertical stresses and incomplete splat stacking
Interlamellar cracks	These are cracks perpendicular to the substrate and in the vertical direction within the splat microstructure
Oxide stringer	Linear oxide striations that are continuous in nature and run parallel to the coating–substrate interface.
Cluster of oxides	Artifacts or oxide defects grouped together
Pull-outs	Porosity that is artificially induced from unsatisfactory and unwanted metallographic preparation
Metallic inclusions	Brittle metallic particles or compounds within the coating which could be stress concentration points or crack initiation sites

7. Areas for Future Research Direction and Implications

The areas for future research directions should focus on materials, methods, and mechanisms for CCA-based cold spray coating. They are schematically shown in Figure 18. For the materials, focus should be on the 3D transition metal based CCAs and the refractory CCAs. For the methods, the two main cold spray techniques: high-pressure and low-

pressure cold spray techniques, should be explored for depositing CCA-based particles on similar and dissimilar metallic materials. The mechanisms of cold spray coatings for structural integrity and failure modes still require some amount of work. Strategic research directions in each thematic area are discussed in the following.

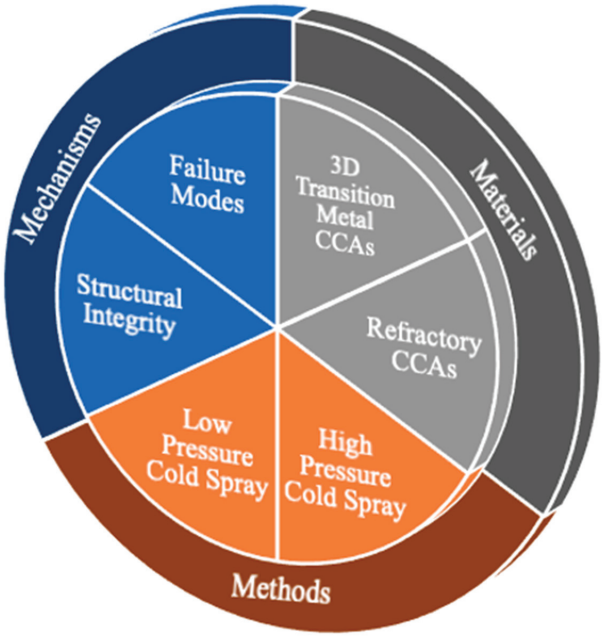

Figure 18. Future perspectives for cold sprayed CCA-based coatings for structural and functional applications.

7.1. Materials

The application of cold spray on dilute metallic alloys as feedstock and substrate has been well studied, although there is still room for improvement. Generally, the process parameters have also been optimized for some systems, especially Cu, Al and Al-based alloys, Ti and Ti-based alloys, Ta and Ta-based alloys, and ferrous alloys. Concerted efforts in simulation-driven cold spray processes have also been carried out, which are thoroughly reviewed in Section 4.

The field of CCAs is less than 30 years old and most of the alloy families show better structural and functional properties than dilute or conventional alloy systems [185,298–300]. As coating material, the classes of CCAs fall under the broad category of 3D transition and refractory metals. When properly developed, these classes of CCAs can be used across the temperature spectrum—from ambient to intermediate to high and ultrahigh temperatures. This will be critical for applications in the thermal barrier coatings (TBCs) for power generation and propulsion [28,29,205,301]. Thus, the CCA-based coatings are best suited for a combination of ambient and high-temperature properties such as strength, oxidation, ductility, thermal stability, and wear resistance. A proof of concept has been carried out using NiCoCrAlSi CCAs through the high-velocity oxy-fuel and air plasma spray (APS) processes as a metallic bond coating for TBCs [205].

Extensive research in the literature showed the elements that are frequently being used for various types of thermal spray applications. They are given in Figure 19 with Cu, Co, Ni, Al, and Fe being the most frequently used elements. Although most of the elements are 3D transition metals, two of the refractory base metals were also used, which could be attributed to the high-temperature oxidation behavior. Figure 19 shows less than

a tenth of the stable metallic elements on the periodic table that could easily be explored for next generation coating materials. This is one of the identified gaps which requires urgent attention and could contribute significantly to understanding the emerging fields of low-cost CCA-based coatings, where the concept of scrap and nature-mixing pre-alloy design concepts can be used.

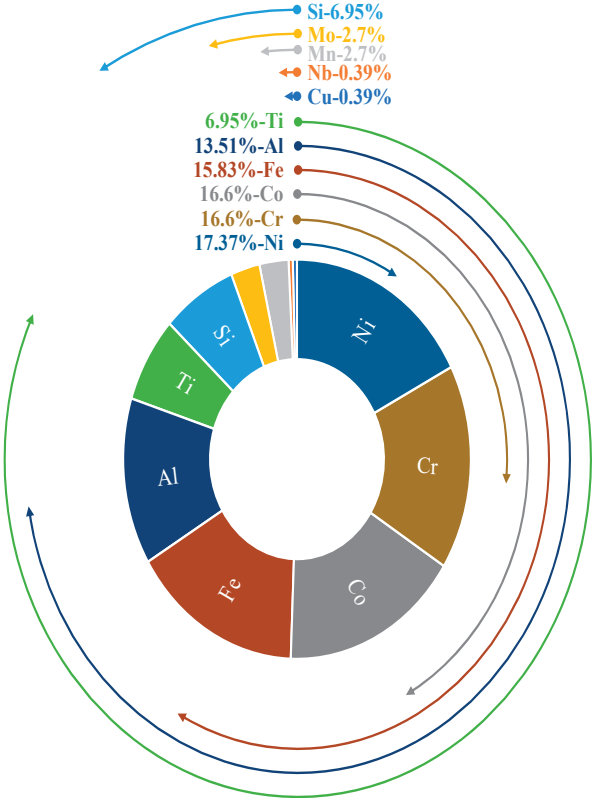

Figure 19. Frequency of use of elements on the periodic table for CCA-based thermal spray coatings as of 2020 [28].

The design and development of new BMG alloys and cold spray coatings with tailored properties are needed for various structural and functional properties. These properties, such as improved mechanical strength, corrosion resistance, and biocompatibility, are critical to produce robust and next generation bulk metallic glass coatings in a cost-effective manner.

7.2. Methods

The two types for cold spray coating are given in Figure 4. These methods need further investigation for depositing pre-alloyed cold spray coating feedstock on various similar and dissimilar substrates of CCAs. Currently, the high-pressure technique is mostly used for most of the coating processes with varying process parameters. Although the results for some classes of CCAs are impressive, the application of cold spray to CCAs is still in its infancy since the first process on CrCoFeMnNi was carried out in 2019 [200]. The search suggests less than 35 research-based articles have been published from 2019 to January 2023. The majority used the high-pressure cold spray approach to deposit the coatings.

Pre-processing of pre-alloyed CCA powders is one area requiring immediate attention. The current powder metallurgy routes such as gas and water atomization and mechanical alloying coupled with spheroidization lead to challenges with oxidation. Approaches such as the ultrasonic atomization process are being explored but could be quite expensive and not easily scalable. Other factors hindering scalability have been highlighted [2,20,185].

Full-scale and detailed mechanical and microstructural characterizations of the particle–substrate and particle–particle interactions need to be ascertained. This will contribute to understanding the mechanism associated with the bond strength. For mechanical characterization, little has been carried out. Therefore, techniques such as tensile adhesion, stud-pull, pin and ring, shear load, peel, laser shock adhesion, scratch, and interfacial indentation tests at the nano- and microscale will be necessary. By conducting thorough mechanical and microstructural assessments, deeper understanding of the physical metallurgy and the mechanisms of these cold spray coatings and how to use them in industrial applications can be implemented effectively.

Porosity is one of the main defects associated with thermal spray coating processes. There is the need to understand the effect of porosity on structural integrity of CCA-based cold spray coatings. Thus, various porosity measurement techniques such as mercury intrusion porosimetry (MIP), gas (He) pycnometry, water absorption or Archimedes (immersion) method, X-ray computed microtomography (CMT), ultrasmall-angle X-ray scattering (USAXS), and electrochemical tests need to be established for the coatings. The working principles of these techniques are reviewed elsewhere [29]. Similarly, measurement of residual stresses using conventional non-destructive methods such as X-ray, synchrotron, laser excitation, and neutron diffraction techniques should also be explored. The implications of these results will contribute to explaining the role of defects in overall structural integrity and overarching mechanisms.

Computational and numerical modeling approaches to studying various aspects of CCA-based cold spray coatings require further attention. Most of these approaches have been adequately discussed for conventional alloys and the highlightes are summarized in Section 4. These simulations and physic-based systems can be adapted for CCAs by revisiting the underlying assumptions. By using these computational approaches synergistically with experiments, the concept of rational development of coatings is more guided leveraging from the merits of both approaches. This builds into the material innovation infrastructure where computations, data science and experimental tools are harnessed to design alloys and coatings within acceptable timelines reducing the material lifecycle (concepts to scalable material or coating) significantly.

7.3. Mechanisms

The main underlying mechanisms of cold spray from microstructural perspectives have been metallurgical interlocking and adiabatic heating. This has been shown for most of the dilute or conventional principal element-based alloys. Similar results have been observed for some CCAs, especially the Cantor alloys and their derivatives. This was expected as the compositions are close to highly alloyed stainless steels, Ni-based superalloys, and Ti-based alloys. However, there is the need to investigate the mechanism of bonding and failure modes as these mechanisms, especially solid-state deformation of particles and bonding to the substrate and each other, are yet to be fully understood. The effects and contributions of various microstructural defects are listed in Figure 14 and Table 9.

The interaction between the cocktail of constituent elements and defects such as stacking faults and dislocations and the effects on bonding mechanisms needs further attention. This will necessitate and drive the next frontiers of cold spray coatings to tailor the coating and substrate microstructures.

There is the need to focus research on process optimization for these classes of coatings. This will require understanding of the process parameters such as spray distance, gas pressure, and powder feed rate. The optimized process parameters can lead to improve-

ments in coating properties, such as density, thickness, and adhesion strength. The coating properties can be studied using advanced mechanical and microstructural characterization techniques to establish the relevant nano- and micromechanisms for better understanding of the performance of BMG and CCA cold spray coatings.

Large-scale applications of these coatings are also areas for further research. Issues that could hinder scalability should be investigated and studied for applications in biomedical, aerospace, and automotive industries. Scaling up is relevant to exploring factors that could have been missed during miniature-sized coating fabrications. Translating laboratory-scale curiosity and science to large-scale industrial applications is critical for BMG and CCA cold spray coatings. This will ensure that issues around standardization of coating systems and mechanisms are investigated. This will allow for consistency and uniformity while providing new insights for further research.

8. Summary and Concluding Remarks

A comprehensive overview of cold spray technology as applied to the emerging fields of complex concentrated alloys is presented. Based on the literature and discussions, the summary and concluding remarks are as follows:

- Cold spray involves feedstock produced from CCAs with relatively low particle size distribution. This is true for CCAs with single, metastable, and multiple phases, a critical parameter which enhances the overall mechanical properties at the coating–substrate interface.
- There is a correlation between processing parameters (e.g., critical velocity, spray angle, stand-off distance, gas pressure, and temperature), bonding mechanism, deposition efficiency, adhesion, and cohesion strength of the coating.
- Although the bonding mechanism has been a bone of contention regarding the particle–substrate and particle–particle interaction, metallurgical bonding is the main mechanism. For the CCA-based feedstock on ductile substrate, mechanical interlocking was observed.
- The computational and numerical simulations employed for cold spray processes are reviewed. The challenges associated with the mesh-based and mesh-free finite element methods are highlighted. Although the Johnson–Cook plasticity model is widely used, its inefficiency at relatively high strains was highlighted. Modifications to the JC model as well as others were discussed considering current research applications. Emphasis was on PTW, VA, and ZA models and how they have been applied to dilute alloy designs.
- The fundamental concepts of bulk and coating based on complex concentrated alloys are highlighted. The influence of the core effects of the CCAs and their contributing factors to enhancing the mechanical and microstructural characterization are discussed. The mechanical, chemical, and physical properties are comparable to those of the conventional bulk and coating materials. According to the technology and innovation maturation timeline of CCA-based coatings, the estimated plateau of productivity is expected by 2030.
- Trend analyses of the CCA-based cold spray coatings on various metallic substrates showed less than 40 publications between 2019 and 2023. The major themes in these publications focused on alloy systems for efficient deposition and tuning of microstructural features to induce desirable mechanical properties. Some have looked at wear resistance, post-processing treatments coupled with other manufacturing routes such as friction stir welding, and other forms of additive manufacturing. The main elements which are constantly being explored for cold spray and other thermal spray coatings are C, Cr, Co, Mn, Fe, Ni, Mo, Nb, Si, and Ti. These elements are the base for Cantor alloys and derivatives, and refractory CCAs.
- The strengthening and hardening mechanisms of the CCA-based cold spray coatings are due to work hardening, grain refinement, and dispersion strengthening. This is because of the severe plastic deformation associated with the high-impact velocity

resulting from the bombardment of the feedstock particles onto the substrate. These mechanisms are different from the precipitation hardening, solid solution strengthening, dislocation strengthening, and oxide formation associated with other forms of thermal spray coating techniques. The deformation mechanisms, which are dependent on the energy density, result in localized adiabatic shear as a function of properties of the particles and the process parameters.

- Microstructural defects across different length scales associated with cold spray mechanisms are highlighted. These defects include intergranular cracks, voids, porosities, delamination, transverse cracks, pull-outs, and metallic inclusions. The effects of these defects on structural and functional properties have been discussed.
- The need for rational alloy and coating design approaches is highlighted. The application of computational, numerical, simulation, and experimental approaches for the design of next generation CCA and BMG coatings is required. By using simulations, the processing parameters can be optimized to ensure the designed and desired mechanical properties, while inducing the required microstructural features.
- This overview provides the theoretical framework for new frontiers in developing and accelerating the next generation of CCA-based cold spray coatings. Furthermore, it highlights challenges and open-ended questions that require future research efforts focusing on materials systems (3D transition and refractory metals), cold spray methods (low- and high-pressure cold spray approaches), and mechanisms underlying structural integrity.

Author Contributions: Conceptualization, D.K., M.B., J.v.d.M., N.R. and W.S., methodology, D.K., T.A., T.B., M.V. and M.B.; formal analysis, D.K., T.A., M.V. and M.B.; investigation, D.K., T.A., M.V. and M.B.; resources, M.B., J.v.d.M., N.R. and W.S.; writing—original draft preparation, D.K., T.A., T.B., M.B. and M.V.; writing—review and editing, D.K., M.B., J.v.d.M., N.R. and W.S.; visualization, D.K., T.A., T.B. and M.V.; supervision, J.v.d.M., N.R. and W.S.; project administration, N.R. and W.S.; funding acquisition, N.R. and W.S. All authors have read and agreed to the published version of the manuscript.

Funding: This research was supported by the Army Research Laboratory (ARL) Grant No. W911NF–19–2–0108. The contributions from the Worcester Polytechnic Institute Global fellowship is also acknowledged.

Institutional Review Board Statement: Not applicable.

Informed Consent Statement: Not applicable.

Data Availability Statement: Not applicable.

Conflicts of Interest: The authors declare no conflict of interest.

References

1. Klenam, D.; Rahbar, N.; Soboyejo, W. Mechanical Properties of Complex Concentrated Alloys: Implications for Structural Integrity. In *Reference Module in Materials Science and Materials Engineering*; Elsevier: Amsterdam, The Netherlands, 2022. [CrossRef]
2. Klenam, D.; Rahbar, N.; Soboyejo, W. Critical Review of Limitations of Equiatomic Composition Alloying Strategy of Complex Concentrated Alloys. In *Reference Module in Materials Science and Materials Engineering*; Elsevier: Amsterdam, The Netherlands, 2022. [CrossRef]
3. Vandadi, M.; Klenam, D.; Rahbar, N.; Soboyejo, W. Advances in the Structural Integrity of Cold Sprayed Alloys—A Critical Review of Process Models and Mechanical Properties. In *Reference Module in Materials Science and Materials Engineering*; Elsevier: Amsterdam, The Netherlands, 2022. [CrossRef]
4. Cantor, B. Multicomponent high-entropy Cantor alloys. *Prog. Mater. Sci.* **2021**, *120*, 100754. [CrossRef]
5. Cantor, B.; Chang, I.T.H.; Knight, P.; Vincent, A.J.B. Microstructural development in equiatomic multicomponent alloys. *Mater. Sci. Eng. A* **2004**, *375–377*, 213–218. [CrossRef]
6. Yin, S.; Cavaliere, P.; Aldwell, B.; Jenkins, R.; Liao, H.; Li, W.; Lupoi, R. Cold spray additive manufacturing and repair: Fundamentals and applications. *Addit. Manuf.* **2018**, *21*, 628–650. [CrossRef]
7. Luo, X.-T.; Li, C.-X.; Shang, F.-L.; Yang, G.-J.; Wang, Y.-Y.; Li, C.-J. High velocity impact induced microstructure evolution during deposition of cold spray coatings: A review. *Surf. Coat. Technol.* **2014**, *254*, 11–20. [CrossRef]
8. Cavaliere, P.; Silvello, A. Crack Repair in Aerospace Aluminum Alloy Panels by Cold Spray. *J. Therm. Spray Technol.* **2017**, *26*, 661–670. [CrossRef]

9. Guo, D.; Kazasidis, M.; Hawkins, A.; Fan, N.; Leclerc, Z.; MacDonald, D.; Nastic, A.; Nikbakht, R.; Ortiz-Fernandez, R.; Rahmati, S.; et al. Cold Spray: Over 30 Years of Development Toward a Hot Future. *J. Therm. Spray Technol.* **2022**, *31*, 866–907. [CrossRef]
10. Vaz, R.F.; Garfias, A.; Albaladejo, V.; Sanchez, J.; Cano, I.G. A Review of Advances in Cold Spray Additive Manufacturing. *Coatings* **2023**, *13*, 267. [CrossRef]
11. Kumar, A.; Goyal, D.K.; Kant, R.; Singh, H. Enhancing Corrosion Performance of Cold-Sprayed Titanium/Baghdadite (Ti/BAG) Bio-Composite Coatings via Laser Treatment. *Coatings* **2022**, *12*, 1010. [CrossRef]
12. Dzhurinskiy, D.; Babu, A.; Dautov, S.; Lama, A.; Mangrulkar, M. Modification of Cold-Sprayed Cu-Al-Ni-Al_2O_3 Composite Coatings by Friction Stir Technique to Enhance Wear Resistance Performance. *Coatings* **2022**, *12*, 1113. [CrossRef]
13. Chen, X.; Li, C.; Gao, Q.; Duan, X.; Liu, H. Comparison of Microstructure, Microhardness, Fracture Toughness, and Abrasive Wear of WC-17Co Coatings Formed in Various Spraying Ways. *Coatings* **2022**, *12*, 814. [CrossRef]
14. Cinca, N.; Lavigne, O.; Peres, R.N.; Conze, S.; Hoehn, S.; Dosta, S.; Koivuluoto, H.; Kim, C.; da Silva, F.S.; Matikainen, V.; et al. Electrochemical Corrosion Characterization of Submicron WC-12Co Coatings Produced by CGS and HVAF Compared with Sintered Bulks. *Coatings* **2022**, *12*, 620. [CrossRef]
15. Manap, A.; Afandi, N.; Mahalingam, S.; Yusof, S.N.A.; Rosli, Z.M. Mechanical and Tribological Study on Aluminum Coatings with High-Pressure and Low-Pressure Cold-Spray Processes. *Coatings* **2022**, *12*, 1792. [CrossRef]
16. Maev, R.G.; Tjong, J.; Leshchinsky, E.; Pantea, M.; Leshchynsky, V. Cold-Sprayed Multilayer Thermal Barrier–Catalytic Coatings for Engine Pistons: Coatings Design and Properties. *Coatings* **2022**, *12*, 1332. [CrossRef]
17. Adaan-Nyiak, M.A.; Tiamiyu, A.A. Recent advances on bonding mechanism in cold spray process: A review of single-particle impact methods. *J. Mater. Res.* **2022**, *38*, 69–95. [CrossRef] [PubMed]
18. Cavaliere, P.; Perrone, A.; Silvello, A.; Laska, A.; Blasi, G.; Cano, I.; Sadeghi, B.; Nagy, S. Cyclic behavior of FeCoCrNiMn high entropy alloy coatings produced through cold spray. *J. Alloys Compd.* **2023**, *931*, 167550. [CrossRef]
19. Champagne, V.; Helfritch, D. Critical Assessment 11: Structural repairs by cold spray. *Mater. Sci. Technol.* **2015**, *31*, 627–634. [CrossRef]
20. Klenam, D.; Rahbar, N.; Soboyejo, W. Critical Review of Factors Hindering Scalability of Complex Concentrated Alloys. In *Reference Module in Materials Science and Materials Engineering*; Elsevier: Amsterdam, The Netherlands, 2022. [CrossRef]
21. Lu, K.; Zhu, J.; Guo, D.; Yang, M.; Sun, H.; Wang, Z.; Hui, X.; Wu, Y. Microstructures, Corrosion Resistance and Wear Resistance of High-Entropy Alloys Coatings with Various Compositions Prepared by Laser Cladding: A Review. *Coatings* **2022**, *12*, 1023. [CrossRef]
22. Li, J.; Huang, Y.; Meng, X.; Xie, Y. A Review on High Entropy Alloys Coatings: Fabrication Processes and Property Assessment. *Adv. Eng. Mater.* **2019**, *21*, 1900343. [CrossRef]
23. Bagherifard, S.; Guagliano, M. Fatigue performance of cold spray deposits: Coating, repair and additive manufacturing cases. *Int. J. Fatigue* **2020**, *139*, 105744. [CrossRef]
24. Raoelison, R.N.; Verdy, C.; Liao, H. Cold gas dynamic spray additive manufacturing today: Deposit possibilities, technological solutions and viable applications. *Mater. Des.* **2017**, *133*, 266–287. [CrossRef]
25. Blose, R.; Walker, B.; Walker, R.; Froes, S. New opportunities to use cold spray process for applying additive features to titanium alloys. *Met. Powder Rep.* **2006**, *61*, 30–37. [CrossRef]
26. Srikanth, A.; Basha, G.M.T.; Venkateshwarlu, B. A Brief Review on Cold Spray Coating Process. *Mater. Today Proc.* **2020**, *22*, 1390–1397. [CrossRef]
27. Assadi, H.; Gärtner, F.; Stoltenhoff, T.; Kreye, H. Bonding mechanism in cold gas spraying. *Acta Mater.* **2003**, *51*, 4379–4394. [CrossRef]
28. Meghwal, A.; Anupam, A.; Murty, B.S.; Berndt, C.C.; Kottada, R.S.; Ang, A.S.M. Thermal spray high-entropy alloy coatings: A review. *J. Therm. Spray Technol.* **2020**, *29*, 857–893. [CrossRef]
29. Ang, A.S.; Berndt, C. A review of testing methods for thermal spray coatings. *Int. Mater. Rev.* **2014**, *59*, 179–223. [CrossRef]
30. Ahmed, R.; Yu, H.; Stoica, V.; Edwards, L.; Santisteban, J. Neutron diffraction residual strain measurements in post-treated thermal spray cermet coatings. *Mater. Sci. Eng. A* **2008**, *498*, 191–202. [CrossRef]
31. Suhonen, T.; Varis, T.; Dosta, S.; Torrell, M.; Guilemany, J.M. Residual stress development in cold sprayed Al, Cu and Ti coatings. *Acta Mater.* **2013**, *61*, 6329–6337. [CrossRef]
32. Valarezo, A.; Sampath, S. An Integrated Assessment of Process-Microstructure-Property Relationships for Thermal-Sprayed NiCr Coatings. *J. Therm. Spray Technol.* **2011**, *20*, 1244–1258. [CrossRef]
33. Yildirim, B.; Muftu, S.; Gouldstone, A. Modeling of high velocity impact of spherical particles. *Wear* **2011**, *270*, 703–713. [CrossRef]
34. Shayegan, G.; Mahmoudi, H.; Ghelichi, R.; Villafuerte, J.; Wang, J.; Guagliano, M.; Jahed, H. Residual stress induced by cold spray coating of magnesium AZ31B extrusion. *Mater. Des.* **2014**, *60*, 72–84. [CrossRef]
35. Li, W.; Yang, K.; Zhang, D.; Zhou, X. Residual Stress Analysis of Cold-Sprayed Copper Coatings by Numerical Simulation. *J. Therm. Spray Technol.* **2016**, *25*, 131–142. [CrossRef]
36. Lin, E.; Chen, Q.; Ozdemir, O.C.; Champagne, V.K.; Müftü, S. Effects of Interface Bonding on the Residual Stresses in Cold-Sprayed Al-6061: A Numerical Investigation. *J. Therm. Spray Technol.* **2019**, *28*, 472–483. [CrossRef]
37. Oviedo, F.; Valarezo, A. Residual Stress in High-Velocity Impact Coatings: Parametric Finite Element Analysis Approach. *J. Therm. Spray Technol.* **2020**, *29*, 1268–1288. [CrossRef]
38. Fardan, A.; Berndt, C.C.; Ahmed, R. Numerical modelling of particle impact and residual stresses in cold sprayed coatings: A review. *Surf. Coat. Technol.* **2021**, *409*, 126835. [CrossRef]

39. Zhang, K.; Song, Y.; Cai, S.; Wang, Z.; Chen, W.; Xie, L. Multiscale Simulation of Shot-Peening-Assisted Low-Pressure Cold Spraying Based on Al-Zn-Al_2O_3 Coatings. *Coatings* **2022**, *12*, 1490. [CrossRef]
40. Wang, S.; Li, Y.; Yao, M.; Wang, R. Compressive residual stress introduced by shot peening. *J. Mater. Process. Technol.* **1998**, *73*, 64–73. [CrossRef]
41. Wei, Y.-K.; Luo, X.-T.; Li, C.-X.; Li, C.-J. Optimization of In-Situ Shot-Peening-Assisted Cold Spraying Parameters for Full Corrosion Protection of Mg Alloy by Fully Dense Al-Based Alloy Coating. *J. Therm. Spray Technol.* **2017**, *26*, 173–183. [CrossRef]
42. Kobayashi, M.; Matsui, T.; Murakami, Y. Mechanism of creation of compressive residual stress by shot peening. *Int. J. Fatigue* **1998**, *20*, 351–357. [CrossRef]
43. Hammersley, G.; Hackel, L.A.; Harris, F. Surface prestressing to improve fatigue strength of components by laser shot peening. *Opt. Lasers Eng.* **2000**, *34*, 327–337. [CrossRef]
44. Torres, M.A.S.; Voorwald, H.J.C. An evaluation of shot peening, residual stress and stress relaxation on the fatigue life of AISI 4340 steel. *Int. J. Fatigue* **2002**, *24*, 877–886. [CrossRef]
45. Kendall, O.; Paradowska, A.; Abrahams, R.; Reid, M.; Qiu, C.; Mutton, P.; Yan, W. Residual Stress Measurement Techniques for Metal Joints, Metallic Coatings and Components in the Railway Industry: A Review. *Materials* **2023**, *16*, 232. [CrossRef] [PubMed]
46. Song, X.; Everaerts, J.; Zhai, W.; Zheng, H.; Tan, A.W.Y.; Sun, W.; Li, F.; Marinescu, I.; Liu, E.; Korsunsky, A.M. Residual stresses in single particle splat of metal cold spray process—Numerical simulation and direct measurement. *Mater. Lett.* **2018**, *230*, 152–156. [CrossRef]
47. Li, W.; Cao, C.; Yin, S. Solid-state cold spraying of Ti and its alloys: A literature review. *Prog. Mater. Sci.* **2020**, *110*, 100633. [CrossRef]
48. Schmidt, T.; Gärtner, F.; Assadi, H.; Kreye, H. Development of a generalized parameter window for cold spray deposition. *Acta Mater.* **2006**, *54*, 729–742. [CrossRef]
49. Schmidt, T.; Assadi, H.; Gärtner, F.; Richter, H.; Stoltenhoff, T.; Kreye, H.; Klassen, T. From Particle Acceleration to Impact and Bonding in Cold Spraying. *J. Therm. Spray Technol.* **2009**, *18*, 794–808. [CrossRef]
50. Klinkov, S.V.; Kosarev, V.F.; Rein, M. Cold spray deposition: Significance of particle impact phenomena. *Aerosp. Sci. Technol.* **2005**, *9*, 582–591. [CrossRef]
51. Champagne, V.; Nardi, A.; Cote, D. Materials characterization of advanced cold-spray aluminum alloys. *Int. J. Powder Metall.* **2015**, *51*, 37–47.
52. Walker, M. Microstructure and bonding mechanisms in cold spray coatings. *Mater. Sci. Technol.* **2018**, *34*, 2057–2077. [CrossRef]
53. Viscusi, A.; Astarita, A.; Della Gatta, R.; Rubino, F. A perspective review on the bonding mechanisms in cold gas dynamic spray. *Surf. Eng.* **2019**, *35*, 743–771. [CrossRef]
54. Champagne, V.; Helfritch, D. The unique abilities of cold spray deposition. *Int. Mater. Rev.* **2016**, *61*, 437–455. [CrossRef]
55. Hussain, T.; McCartney, D.G.; Shipway, P.H.; Zhang, D. Bonding Mechanisms in Cold Spraying: The Contributions of Metallurgical and Mechanical Components. *J. Therm. Spray Technol.* **2009**, *18*, 364–379. [CrossRef]
56. Grujicic, M.; Saylor, J.; Beasley, D.; DeRosset, W.; Helfritch, D. Computational analysis of the interfacial bonding between feed-powder particles and the substrate in the cold-gas dynamic-spray process. *Appl. Surf. Sci.* **2003**, *219*, 211–227. [CrossRef]
57. Li, W.-Y.; Gao, W. Some aspects on 3D numerical modeling of high velocity impact of particles in cold spraying by explicit finite element analysis. *Appl. Surf. Sci.* **2009**, *255*, 7878–7892. [CrossRef]
58. Aleksieieva, O.; Dereviankina, L.; Breuninger, P.; Bozoglu, M.; Tretiakov, P.; Toporov, A.; Antonyuk, S. Simulation of Particle Interaction with Surface Microdefects during Cold Gas-Dynamic Spraying. *Coatings* **2022**, *12*, 1297. [CrossRef]
59. Nélias, D.; Xie, J.; Walter-Le Berre, H.; Ichikawa, Y.; Ogawa, K. Simulation of the Cold Spray Deposition Process for Aluminum and Copper using Lagrangian, ALE and CEL Methods. In *Thermomechanical Industrial Processes: Modeling and Numerical Simulation*; Bergheau, J.-M., Ed.; John Wiley & Sons, Inc.: Hoboken, NJ, USA, 2014; pp. 321–358.
60. Xie, J.; Nelias, D.; Berre, H.W.-L.; Ogawa, K.; Ichikawa, Y. Simulation of the Cold Spray Particle Deposition Process. *J. Tribol.* **2015**, *137*, 041101. [CrossRef]
61. Li, W.-Y.; Liao, H.; Li, C.-J.; Li, G.; Coddet, C.; Wang, X. On high velocity impact of micro-sized metallic particles in cold spraying. *Appl. Surf. Sci.* **2006**, *253*, 2852–2862. [CrossRef]
62. Li, W.-Y.; Zhang, C.; Li, C.-J.; Liao, H. Modeling Aspects of High Velocity Impact of Particles in Cold Spraying by Explicit Finite Element Analysis. *J. Therm. Spray Technol.* **2009**, *18*, 921–933. [CrossRef]
63. Panfilov, P.; Gornostyrev, Y.N.; Kuznetsov, A.R. Breakdown of relationship between chemical bonding and deformation behavior of crystalline materials. *TMS Annu. Meet.* **2010**, *2*, 13–24.
64. Li, W.Y.; Yang, K.; Yin, S.; Guo, X.P. Numerical Analysis of Cold Spray Particles Impacting Behavior by the Eulerian Method: A Review. *J. Therm. Spray Technol.* **2016**, *25*, 1441–1460. [CrossRef]
65. Hemeda, A.; Zhang, C.; Hu, X.; Fukuda, D.; Cote, D.; Nault, I.; Nardi, A.; Champagne, V.; Ma, Y.; Palko, J. Particle-based simulation of cold spray: Influence of oxide layer on impact process. *Addit. Manuf.* **2021**, *37*, 101517. [CrossRef]
66. Liu, M.B.; Liu, G.R. Smoothed Particle Hydrodynamics (SPH): An Overview and Recent Developments. *Arch. Comput. Methods Eng.* **2010**, *17*, 25–76. [CrossRef]
67. Hoover, W.; Hoover, C.; Kum, O.; Castillo, V. Smooth particle applied mechanics. *Comput. Methods Sci. Technol.* **1996**, *2*, 65–72. [CrossRef]
68. Liu, G.R.; Liu, M.B. *Smoothed Particle Hydrodynamics—A Meshfree Particle Method*; World Scientific Publishing Company: Singapore, 2003.

69. Shadloo, M.; Oger, G.; Le Touzé, D. Smoothed particle hydrodynamics method for fluid flows, towards industrial applications: Motivations, current state, and challenges. *Comput. Fluids* **2016**, *136*, 11–34. [CrossRef]
70. Lemiale, V.; King, P.; Rudman, M.; Prakash, M.; Cleary, P.; Jahedi, M.; Gulizia, S. Temperature and strain rate effects in cold spray investigated by smoothed particle hydrodynamics. *Surf. Coat. Technol.* **2014**, *254*, 121–130. [CrossRef]
71. Gnanasekaran, B.; Liu, G.-R.; Fu, Y.; Wang, G.; Niu, W.; Lin, T. A Smoothed Particle Hydrodynamics (SPH) procedure for simulating cold spray process—A study using particles. *Surf. Coat. Technol.* **2019**, *377*, 124812. [CrossRef]
72. Li, W.-Y.; Yin, S.; Wang, X.-F. Numerical investigations of the effect of oblique impact on particle deformation in cold spraying by the SPH method. *Appl. Surf. Sci.* **2010**, *256*, 3725–3734. [CrossRef]
73. Yin, S.; Wang, X.-F.; Xu, B.-P.; Li, W.-Y. Examination on the Calculation Method for Modeling the Multi-Particle Impact Process in Cold Spraying. *J. Therm. Spray Technol.* **2010**, *19*, 1032–1041. [CrossRef]
74. King, P.C.; Bae, G.; Zahiri, S.H.; Jahedi, M.; Lee, C. An Experimental and Finite Element Study of Cold Spray Copper Impact onto Two Aluminum Substrates. *J. Therm. Spray Technol.* **2010**, *19*, 620–634. [CrossRef]
75. Yin, S.; Wang, X.-F.; Li, W.-Y.; Xu, B.-P. Numerical Investigation on Effects of Interactions Between Particles on Coating Formation in Cold Spraying. *J. Therm. Spray Technol.* **2009**, *18*, 686–693. [CrossRef]
76. Bolelli, G.; Dosta, S.; Lusvarghi, L.; Manfredini, T.; Guilemany, J.; Cano, I. Building up WC-Co coatings by cold spray: A finite element simulation. *Surf. Coat. Technol.* **2019**, *374*, 674–689. [CrossRef]
77. Song, X.; Ng, K.L.; Chea, J.M.-K.; Sun, W.; Tan, A.W.-Y.; Zhai, W.; Li, F.; Marinescu, I.; Liu, E. Coupled Eulerian-Lagrangian (CEL) simulation of multiple particle impact during Metal Cold Spray process for coating porosity prediction. *Surf. Coat. Technol.* **2020**, *385*, 125433. [CrossRef]
78. Li, Y.; Wang, X.-F.; Yin, S.; Xu, S.-L. Influence of Particle Initial Temperature on High Velocity Impact Process in Cold Spraying. *Procedia Environ. Sci.* **2012**, *12*, 298–304. [CrossRef]
79. Morris, J.P.; Fox, P.J.; Zhu, Y. Modeling Low Reynolds Number Incompressible Flows Using SPH. *J. Comput. Phys.* **1997**, *136*, 214–226. [CrossRef]
80. Liu, M.; Liu, G.; Lam, K. Constructing smoothing functions in smoothed particle hydrodynamics with applications. *J. Comput. Appl. Math.* **2003**, *155*, 263–284. [CrossRef]
81. Lucy, L.B. A numerical approach to the testing of the fission hypothesis. *Astron. J.* **1977**, *82*, 1013–1024. [CrossRef]
82. Chun, D.-M.; Ahn, S.-H. Deposition mechanism of dry sprayed ceramic particles at room temperature using a nano-particle deposition system. *Acta Mater.* **2011**, *59*, 2693–2703. [CrossRef]
83. Park, H.; Kwon, J.; Lee, I.; Lee, C. Shock-induced plasticity and fragmentation phenomena during alumina deposition in the vacuum kinetic spraying process. *Scr. Mater.* **2015**, *100*, 44–47. [CrossRef]
84. Manap, A.; Nooririnah, O.; Misran, H.; Okabe, T.; Ogawa, K. Experimental and SPH study of cold spray impact between similar and dissimilar metals. *Surf. Eng.* **2014**, *30*, 335–341. [CrossRef]
85. Vural, M.; Ravichandran, G.; Rittel, D. Large strain mechanical behavior of 1018 cold-rolled steel over a wide range of strain rates. *Met. Mater. Trans. A* **2003**, *34*, 2873–2885. [CrossRef]
86. Johnson, G.R.; Cook, W.H. Fracture characteristics of three metals subjected to various strains, strain rates, temperatures and pressures. *Eng. Fract. Mech.* **1985**, *21*, 31–48. [CrossRef]
87. Preston, D.L.; Tonks, D.L.; Wallace, D.C. Model of plastic deformation for extreme loading conditions. *J. Appl. Phys.* **2003**, *93*, 211–220. [CrossRef]
88. Grujicic, M.; Zhao, C.; DeRosset, W.; Helfritch, D. Adiabatic shear instability based mechanism for particles/substrate bonding in the cold-gas dynamic-spray process. *Mater. Des.* **2004**, *25*, 681–688. [CrossRef]
89. Rahmati, S.; Ghaei, A. The Use of Particle/Substrate Material Models in Simulation of Cold-Gas Dynamic-Spray Process. *J. Therm. Spray Technol.* **2014**, *23*, 530–540. [CrossRef]
90. Bae, G.; Xiong, Y.; Kumar, S.; Kang, K.; Lee, C. General aspects of interface bonding in kinetic sprayed coatings. *Acta Mater.* **2008**, *56*, 4858–4868. [CrossRef]
91. Guetta, D.; Berger, M.-H.; Borit, F.; Guipont, V.; Jeandin, M.; Boustie, M.; Ichikawa, Y.; Sakaguchi, K.; Ogawa, K. Influence of Particle Velocity on Adhesion of Cold-Sprayed Splats. *J. Therm. Spray Technol.* **2009**, *18*, 331–342. [CrossRef]
92. Hassani-Gangaraj, M.; Veysset, D.; Champagne, V.K.; Nelson, K.A.; Schuh, C.A. Adiabatic shear instability is not necessary for adhesion in cold spray. *Acta Mater.* **2018**, *158*, 430–439. [CrossRef]
93. Ahmed, R.A.; Rahneshin, V.; Bond, T.; Vandadi, M.; Oghenevweta, J.E.; Navabi, A.; Oyewole, O.K.; Obayemi, J.D.; Rahbar, N.; Soboyejo, W.O. On the Role of Deformation and Cracking in the Cold Spray Processing of Refractory Ta Powders onto Ta or 4340 Steel Substrates: Effects of Topical Oxide Layers and Spray Velocity. *Met. Mater. Trans. A* **2022**, *53*, 3381–3391. [CrossRef]
94. Navabi, A.; Vandadi, M.; Bond, T.; Rahneshin, V.; Obayemi, J.; Ahmed, R.; Oghenevweta, J.; Champagne, V.; Rahbar, N.; Soboyejo, W. Deformation and cracking phenomena in cold sprayed 6061 Al alloy powders with nanoscale aluminum oxide films. *Mater. Sci. Eng. A* **2022**, *841*, 143036. [CrossRef]
95. Bansal, P.; Shipway, P.; Leen, S. A hybrid implicit—Explicit finite element methodology for coating formation in the high-velocity oxy-fuel spraying process. *Proc. Inst. Mech. Eng. L J. Mater. Des. Appl.* **2007**, *221*, 285–297. [CrossRef]
96. Micunovic, M.; Albertini, C.; Montagnani, M. High Strain Rate Thermo-Inelasticity of Damaged AISI 316H. *Int. J. Damage Mech.* **2003**, *12*, 267–303. [CrossRef]

97. Ghelichi, R.; Bagherifard, S.; Guagliano, M.; Verani, M. Numerical simulation of cold spray coating. *Surf. Coat. Technol.* **2011**, *205*, 5294–5301. [CrossRef]
98. Zhang, D.-N.; Shangguan, Q.-Q.; Xie, C.-J.; Liu, F. A modified Johnson–Cook model of dynamic tensile behaviors for 7075-T6 aluminum alloy. *J. Alloys Compd.* **2015**, *619*, 186–194. [CrossRef]
99. Lin, Y.; Chen, X.-M.; Liu, G. A modified Johnson–Cook model for tensile behaviors of typical high-strength alloy steel. *Mater. Sci. Eng. A* **2010**, *527*, 6980–6986. [CrossRef]
100. Chakrabarty, R.; Song, J. A modified Johnson-Cook material model with strain gradient plasticity consideration for numerical simulation of cold spray process. *Surf. Coat. Technol.* **2020**, *397*, 125981. [CrossRef]
101. Zhao, Y.; Sun, J.; Li, J.; Yan, Y.; Wang, P. A comparative study on Johnson-Cook and modified Johnson-Cook constitutive material model to predict the dynamic behavior laser additive manufacturing FeCr alloy. *J. Alloys Compd.* **2017**, *723*, 179–187. [CrossRef]
102. Rahmati, S.; Jodoin, B. Physically Based Finite Element Modeling Method to Predict Metallic Bonding in Cold Spray. *J. Therm. Spray Technol.* **2020**, *29*, 611–629. [CrossRef]
103. Su, J.; Kang, J.-J.; Yue, W.; Ma, G.-Z.; Fu, Z.-Q.; Zhu, L.-N.; She, D.-S.; Wang, H.-D.; Wang, C.-B. Review of cold spraying and its use for metallic glass coatings. *Mater. Sci. Technol.* **2019**, *35*, 1908–1923. [CrossRef]
104. Jočbalis, G.; Kačianauskas, R.; Borodinas, S.; Rojek, J. Comparative numerical study of rate-dependent continuum-based plasticity models for high-velocity impacts of copper particles against a substrate. *Int. J. Impact Eng.* **2023**, *172*, 104394. [CrossRef]
105. Henao, J.; Bolelli, G.; Concustell, A.; Lusvarghi, L.; Dosta, S.; Cano, I.; Guilemany, J. Deposition behavior of cold-sprayed metallic glass particles onto different substrates. *Surf. Coat. Technol.* **2018**, *349*, 13–23. [CrossRef]
106. Grujicic, M.; Pandurangan, B.; Yen, C.-F.; Cheeseman, B.A. Modifications in the AA5083 Johnson-Cook Material Model for Use in Friction Stir Welding Computational Analyses. *J. Mater. Eng. Perform.* **2012**, *21*, 2207–2217. [CrossRef]
107. Chen, Q.; Alizadeh, A.; Xie, W.; Wang, X.; Champagne, V.; Gouldstone, A.; Lee, J.-H.; Müftü, S. High-Strain-Rate Material Behavior and Adiabatic Material Instability in Impact of Micron-Scale Al-6061 Particles. *J. Therm. Spray Technol.* **2018**, *27*, 641–653. [CrossRef]
108. Schreiber, J.; Smid, I.; Eden, T.; Koudela, K.; Cote, D.; Champagne, V. Cold spray particle impact simulation using the Preston-Tonks-Wallace plasticity model. *Finite Elem. Anal. Des.* **2021**, *191*, 103557. [CrossRef]
109. Banerjee, B. An evaluation of plastic flow stress models for the simulation of high-temperature and high-strain-rate deformation of metals. *arXiv* **2005**, arXiv:cond-mat/0512466.
110. Fraser, K.; Kiss, L.I.; St-Georges, L.; Drolet, D. Optimization of Friction Stir Weld Joint Quality Using a Meshfree Fully-Coupled Thermo-Mechanics Approach. *Metals* **2018**, *8*, 101. [CrossRef]
111. Weiller, S.; Delloro, F. A numerical study of pore formation mechanisms in aluminium cold spray coatings. *Addit. Manuf.* **2022**, *60*, 103193. [CrossRef]
112. Henao, J.; Concustell, A.; Dosta, S.; Cinca, N.; Cano, I.G.; Guilemany, J.M. Influence of the Substrate on the Formation of Metallic Glass Coatings by Cold Gas Spraying. *J. Therm. Spray Technol.* **2016**, *25*, 992–1008. [CrossRef]
113. Voyiadjis, G.Z.; Abed, F.H. Microstructural based models for bcc and fcc metals with temperature and strain rate dependency. *Mech. Mater.* **2005**, *37*, 355–378. [CrossRef]
114. Abed, F.H.; Voyiadjis, G.Z. A consistent modified Zerilli-Armstrong flow stress model for BCC and FCC metals for elevated temperatures. *Acta Mech.* **2005**, *175*, 1–18. [CrossRef]
115. Khan, A.S.; Liang, R. Behaviors of three BCC metal over a wide range of strain rates and temperatures: Experiments and modeling. *Int. J. Plast.* **1999**, *15*, 1089–1109. [CrossRef]
116. Khan, A.S.; Liang, R. Behaviors of three BCC metals during non-proportional multi-axial loadings: Experiments and modeling. *Int. J. Plast.* **2000**, *16*, 1443–1458. [CrossRef]
117. Gao, C.; Zhang, L. Constitutive modelling of plasticity of fcc metals under extremely high strain rates. *Int. J. Plast.* **2012**, *32–33*, 121–133. [CrossRef]
118. Telford, M. The base for bulk metallic glass. *Mater. Today* **2003**, *7*, 36–43. [CrossRef]
119. Suryanarayana, C.; Inoue, A. Iron-based bulk metallic glasses. *Int. Mater. Rev.* **2013**, *58*, 131–166. [CrossRef]
120. Wang, Q.; Han, P.; Yin, S.; Niu, W.-J.; Zhai, L.; Li, X.; Mao, X.; Han, Y. Current Research Status on Cold Sprayed Amorphous Alloy Coatings: A Review. *Coatings* **2021**, *11*, 206. [CrossRef]
121. Miracle, D.B. A structural model for metallic glasses. *Nat. Mater.* **2004**, *3*, 697–702. [CrossRef] [PubMed]
122. Miracle, D.B. A Structural Model for Metallic Glasses. *Microsc. Microanal.* **2004**, *10* (Suppl. 2), 786–787. [CrossRef]
123. Inoue, A.; Takeuchi, A. Recent development and application products of bulk glassy alloys. *Acta Mater.* **2011**, *59*, 2243–2267. [CrossRef]
124. Das, J.; Tang, M.B.; Kim, K.B.; Theissmann, R.; Baier, F.; Wang, W.H.; Eckert, J. "Work-Hardenable" Ductile Bulk Metallic Glass. *Phys. Rev. Lett.* **2005**, *94*, 205501. [CrossRef]
125. Greer, J.R.; De Hosson, J.T. Plasticity in small-sized metallic systems: Intrinsic versus extrinsic size effect. *Prog. Mater. Sci.* **2011**, *56*, 654–724. [CrossRef]
126. Greer, A.; Cheng, Y.; Ma, E. Shear bands in metallic glasses. *Mater. Sci. Eng. R Rep.* **2013**, *74*, 71–132. [CrossRef]
127. Gao, M.; Lu, W.; Yang, B.; Zhang, S.; Wang, J. High corrosion and wear resistance of Al-based amorphous metallic coating synthesized by HVAF spraying. *J. Alloys Compd.* **2018**, *735*, 1363–1373. [CrossRef]
128. Shen, Y.; Perepezko, J. Al-based amorphous alloys: Glass-forming ability, crystallization behavior and effects of minor alloying additions. *J. Alloys Compd.* **2017**, *707*, 3–11. [CrossRef]

129. Goldman, M.E.; Ünlü, N.; Shiflet, G.J.; Scully, J.R. Selected Corrosion Properties of a Novel Amorphous Al-Co-Ce Alloy System. *Electrochem. Solid-State Lett.* **2005**, *8*, B1. [CrossRef]
130. Wang, D.; Li, P. Thermodynamic and mechanical properties of Cu–Zr–Al–Ti bulk metallic glasses. *AIP Adv.* **2018**, *8*, 125003. [CrossRef]
131. Wang, Y.; Li, M.; Sun, L.; Zhang, X.; Shen, J. Environmentally assisted fracture behavior of Fe-based amorphous coatings in chloride-containing solutions. *J. Alloys Compd.* **2018**, *738*, 37–48. [CrossRef]
132. Lin, J.; Wang, Z.; Cheng, J.; Kang, M.; Fu, X.; Hong, S. Effect of Initial Surface Roughness on Cavitation Erosion Resistance of Arc-Sprayed Fe-Based Amorphous/Nanocrystalline Coatings. *Coatings* **2017**, *7*, 200. [CrossRef]
133. Yasir, M.; Zhang, C.; Wang, W.; Xu, P.; Liu, L. Wear behaviors of Fe-based amorphous composite coatings reinforced by Al2O3 particles in air and in NaCl solution. *Mater. Des.* **2015**, *88*, 207–213. [CrossRef]
134. Qiao, J.-H.; Jin, X.; Qin, J.-H.; Liu, H.-T.; Luo, Y.; Zhang, D.-K. A super-hard superhydrophobic Fe-based amorphous alloy coating. *Surf. Coat. Technol.* **2018**, *334*, 286–291. [CrossRef]
135. Zhou, H.; Zhang, C.; Wang, W.; Yasir, M.; Liu, L. Microstructure and Mechanical Properties of Fe-based Amorphous Composite Coatings Reinforced by Stainless Steel Powders. *J. Mater. Sci. Technol.* **2015**, *31*, 43–47. [CrossRef]
136. Bahrami, F.; Amini, R.; Taghvaei, A.H. Microstructure and corrosion behavior of electrodeposited Ni-based nanocomposite coatings reinforced with Ni 60 Cr 10 Ta 10 P 16 B 4 metallic glass particles. *J. Alloys Compd.* **2017**, *714*, 530–536. [CrossRef]
137. Suresh, K.; Yugeswaran, S.; Rao, K.; Kobayashi, A.; Shum, P. Sliding wear behavior of gas tunnel type plasma sprayed Ni-based metallic glass composite coatings. *Vacuum* **2013**, *88*, 114–117. [CrossRef]
138. Wang, B.; Xu, K.; Shi, X.; Zhang, M.; Qiao, J.; Gao, C.; Wu, Y. Electrochemical and chemical corrosion behaviors of the in-situ Zr-based metallic glass matrix composites in chloride-containing solutions. *J. Alloys Compd.* **2019**, *770*, 679–685. [CrossRef]
139. Zhang, Y.; Yan, L.; Zhao, X.; Ma, L. Enhanced chloride ion corrosion resistance of Zr-based bulk metallic glasses with cobalt substitution. *J. Non-Cryst. Solids* **2018**, *496*, 18–23. [CrossRef]
140. Astarita, A.; Coticelli, F.; Prisco, U. Repairing of an Engine Block Through the Cold Gas Dynamic Spray Technology. *Mater. Res.* **2016**, *19*, 1226–1231. [CrossRef]
141. Concustell, A.; Henao, J.; Dosta, S.; Cinca, N.; Cano, I.; Guilemany, J. On the formation of metallic glass coatings by means of Cold Gas Spray technology. *J. Alloys Compd.* **2015**, *651*, 764–772. [CrossRef]
142. Moridi, A.; Hassani-Gangaraj, S.M.; Guagliano, M.; Dao, M. Cold spray coating: Review of material systems and future perspectives. *Surf. Eng.* **2014**, *30*, 369–395. [CrossRef]
143. Su, J.; Kang, J.-J.; Yue, W.; Ma, G.-Z.; Fu, Z.-Q.; Zhu, L.-N.; She, D.-S.; Wang, H.-D.; Wang, C.-B. Comparison of tribological behavior of Fe-based metallic glass coatings fabricated by cold spraying and high velocity air fuel spraying. *J. Non-Cryst. Solids* **2019**, *522*, 119582. [CrossRef]
144. Henao, J.; Concustell, A.; Cano, I.G.; Dosta, S.; Cinca, N.; Guilemany, J.M.; Suhonen, T. Novel Al-based metallic glass coatings by Cold Gas Spray. *Mater. Des.* **2016**, *94*, 253–261. [CrossRef]
145. Lahiri, D.; Gill, P.K.; Scudino, S.; Zhang, C.; Singh, V.; Karthikeyan, J.; Munroe, N.; Seal, S.; Agarwal, A. Cold sprayed aluminum based glassy coating: Synthesis, wear and corrosion properties. *Surf. Coat. Technol.* **2013**, *232*, 33–40. [CrossRef]
146. List, A.; Gärtner, F.; Mori, T.; Schulze, M.; Assadi, H.; Kuroda, S.; Klassen, T. Cold Spraying of Amorphous Cu50Zr50 Alloys. *J. Therm. Spray Technol.* **2014**, *24*, 108–118. [CrossRef]
147. Yoon, S.; Bae, G.; Xiong, Y.; Kumar, S.; Kang, K.; Kim, J.-J.; Lee, C. Strain-enhanced nanocrystallization of a CuNiTiZr bulk metallic glass coating by a kinetic spraying process. *Acta Mater.* **2009**, *57*, 6191–6199. [CrossRef]
148. Ajdelsztajn, L.; Jodoin, B.; Richer, P.; Sansoucy, E.; Lavernia, E.J. Cold Gas Dynamic Spraying of Iron-Base Amorphous Alloy. *J. Therm. Spray Technol.* **2006**, *15*, 495–500. [CrossRef]
149. Yoon, S.; Kim, J.; Bae, G.; Kim, B.; Lee, C. Formation of coating and tribological behavior of kinetic sprayed Fe-based bulk metallic glass. *J. Alloys Compd.* **2011**, *509*, 347–353. [CrossRef]
150. List, A.; Gärtner, F.; Schmidt, T.; Klassen, T. Impact Conditions for Cold Spraying of Hard Metallic Glasses. *J. Therm. Spray Technol.* **2012**, *21*, 531–540. [CrossRef]
151. Choi, H.; Yoon, S.; Kim, G.; Jo, H.; Lee, C. Phase evolutions of bulk amorphous NiTiZrSiSn feedstock during thermal and kinetic spraying processes. *Scr. Mater.* **2005**, *53*, 125–130. [CrossRef]
152. Yoon, S.; Lee, C.; Choi, H.; Jo, H. Kinetic spraying deposition behavior of bulk amorphous NiTiZrSiSn feedstock. *Mater. Sci. Eng. A* **2006**, *415*, 45–52. [CrossRef]
153. Kang, N.; Coddet, P.; Liao, H.; Coddet, C. The effect of heat treatment on microstructure and tensile properties of cold spray Zr base metal glass/Cu composite. *Surf. Coat. Technol.* **2015**, *280*, 64–71. [CrossRef]
154. Zhang, S.; Wang, Z.; Chang, X.; Hou, W.; Wang, J. Identifying the role of nanoscale heterogeneities in pitting behaviour of Al-based metallic glass. *Corros. Sci.* **2011**, *53*, 3007–3015. [CrossRef]
155. Jeong, J.I.; Lee, S.H.; Jeon, J.-B.; Kim, S.J. Excessively High Vapor Pressure of Al-Based Amorphous Alloys. *Metals* **2015**, *5*, 1878–1886. [CrossRef]
156. Sansoucy, E.; Kim, G.; Moran, A.; Jodoin, B. Mechanical Characteristics of Al-Co-Ce Coatings Produced by the Cold Spray Process. *J. Therm. Spray Technol.* **2007**, *16*, 651–660. [CrossRef]
157. Xueqing, W.; Mo, M.; Chaogui, T.; Xiufeng, W.; Jianguo, L. Comparative Study on Thermodynamical and Electrochemical Behavior of Al88Ni6La6 and Al86Ni6La6Cu2 Amorphous Alloys. *J. Rare Earths* **2007**, *25*, 381–384. [CrossRef]

158. Wang, X.; Wu, X.; Lin, J.; Ma, M. The influence of heat treatment on the corrosion behaviour of as-spun amorphous Al88Ni6La6 alloy in 0.01 M NaCl solution. *Mater. Lett.* **2007**, *61*, 1715–1717. [CrossRef]
159. Wu, J.; Peng, Z. Effects of microadditions on glass transition and hardness of Cu-based bulk metallic glasses. *Appl. Phys. A* **2018**, *124*, 632. [CrossRef]
160. Kim, J.; Kang, K.; Yoon, S.; Lee, C. Enhancement of metallic glass properties of Cu-based BMG coating by shroud plasma spraying. *Surf. Coat. Technol.* **2011**, *205*, 3020–3026. [CrossRef]
161. Lee, K.-A.; Jung, D.J.; Park, D.Y.; Kang, W.G.; Lee, J.K.; Kim, H.J. Study on the fabrication and physical properties of cold-sprayed, Cu-based amorphous coating. *J. Phys. Conf. Ser.* **2009**, *144*, 012113. [CrossRef]
162. Kim, K.-H.; Lee, S.-W.; Ahn, J.-P.; Fleury, E.; Kim, Y.-C.; Lee, J.-C. A Cu-based amorphous alloy with a simultaneous improvement in its glass forming ability and plasticity. *Met. Mater. Int.* **2007**, *13*, 21–24. [CrossRef]
163. Aldhameer, A.; El-Eskandarany, M.S.; Kishk, M.; Alajmi, F.; Banyan, M. Mechanical Alloying Integrated with Cold Spray Coating for Fabrication $Cu_{50}(Ti_{50-x}Ni_x)$, x; 10, 20, 30, and 40 at.% Antibiofilm Metallic Glass Coated/SUS304 Sheets. *Nanomaterials* **2022**, *12*, 1681. [CrossRef]
164. Wang, W.; Zhang, C.; Zhang, Z.-W.; Li, Y.-C.; Yasir, M.; Wang, H.-T.; Liu, L. Toughening Fe-based Amorphous Coatings by Reinforcement of Amorphous Carbon. *Sci. Rep.* **2017**, *7*, 4084. [CrossRef]
165. Tian, W.-P.; Yang, H.-W.; Zhang, S.-D. Synergistic Effect of Mo, W, Mn and Cr on the Passivation Behavior of a Fe-Based Amorphous Alloy Coating. *Acta Met. Sin. (Engl. Lett.)* **2018**, *31*, 308–320. [CrossRef]
166. Jiao, J.; Luo, Q.; Wei, X.; Wang, Y.; Shen, J. Influence of sealing treatment on the corrosion resistance of Fe-based amorphous coatings in HCl solution. *J. Alloys Compd.* **2017**, *714*, 356–362. [CrossRef]
167. Wu, J.; Zhang, S.; Sun, W.; Gao, Y.; Wang, J. Enhanced corrosion resistance in Fe-based amorphous coatings through eliminating Cr-depleted zones. *Corros. Sci.* **2018**, *136*, 161–173. [CrossRef]
168. Cinca, N.; Drehmann, R.; Dietrich, D.; Gaertner, F.; Klassen, T.; Lampke, T.; Guilemany, J.M. Mechanically induced grain refinement, recovery and recrystallization of cold-sprayed iron aluminide coatings. *Surf. Coat. Technol.* **2019**, *380*, 125069. [CrossRef]
169. Rojas, D.F.; Li, H.; Orhan, O.K.; Shao, C.; Hogan, J.D.; Ponga, M. Mechanical and microstructural properties of a CoCrFe0.75-NiMo0.3Nb0.125 high-entropy alloy additively manufactured via cold-spray. *J. Alloys Compd.* **2022**, *893*, 162309. [CrossRef]
170. Han, P.; Wang, W.; Liu, Z.; Zhang, T.; Liu, Q.; Guan, X.; Qiao, K.; Ye, D.; Cai, J.; Xie, Y.; et al. Modification of cold-sprayed high-entropy alloy particles reinforced aluminum matrix composites via friction stir processing. *J. Alloys Compd.* **2022**, *907*, 164426. [CrossRef]
171. Kwon, J.; Park, H.; Lee, I.; Lee, C. Effect of gas flow rate on deposition behavior of Fe-based amorphous alloys in vacuum kinetic spray process. *Surf. Coat. Technol.* **2014**, *259*, 585–593. [CrossRef]
172. White, B.; Story, W.A.; Brewer, L.; Jordon, J. Fracture mechanics methods for evaluating the adhesion of cold spray deposits. *Eng. Fract. Mech.* **2019**, *205*, 57–69. [CrossRef]
173. Cavaliere, P.; Perrone, A.; Silvello, A. Crystallization Evolution of Cold-Sprayed Pure Ni Coatings. *J. Therm. Spray Technol.* **2016**, *25*, 1158–1167. [CrossRef]
174. Sample, C.M.; Champagne, V.K.; Nardi, A.T.; Lados, D.A. Factors governing static properties and fatigue, fatigue crack growth, and fracture mechanisms in cold spray alloys and coatings/repairs: A review. *Addit. Manuf.* **2020**, *36*, 101371. [CrossRef]
175. Singh, R.; Schruefer, S.; Wilson, S.; Gibmeier, J.; Vassen, R. Influence of coating thickness on residual stress and adhesion-strength of cold-sprayed Inconel 718 coatings. *Surf. Coat. Technol.* **2018**, *350*, 64–73. [CrossRef]
176. Shi, H.; Liu, M.; Cong, L.; Wang, L. A study on preparation and mechanism of Ni based ternary alloy. *Mater. Express* **2019**, *9*, 681–685. [CrossRef]
177. Wang, A.P.; Zhang, T.; Wang, J.Q. Ni-based fully amorphous metallic coating with high corrosion resistance. *Philos. Mag. Lett.* **2006**, *86*, 5–11. [CrossRef]
178. Yoon, S.; Kim, H.J.; Lee, C. Deposition behavior of bulk amorphous NiTiZrSiSn according to the kinetic and thermal energy levels in the kinetic spraying process. *Surf. Coat. Technol.* **2006**, *200*, 6022–6029. [CrossRef]
179. Wang, A.; Chang, X.; Hou, W.; Wang, J. Preparation and corrosion behaviour of amorphous Ni-based alloy coatings. *Mater. Sci. Eng. A* **2007**, *449–451*, 277–280. [CrossRef]
180. Yoon, S.; Lee, C.; Choi, H. Evaluation of the effects of the crystallinity of kinetically sprayed Ni–Ti–Zr–Si–Sn bulk metallic glass on the scratch response. *Mater. Sci. Eng. A* **2007**, *449–451*, 285–289. [CrossRef]
181. Sugita, K.; Matsumoto, M.; Mizuno, M.; Araki, H.; Shirai, Y. Electron irradiation damage and the recovery in a Zr-based bulk amorphous alloy Zr55Cu30Al10Ni5. *J. Phys. Conf. Ser.* **2008**, *106*, 012024. [CrossRef]
182. Sun, Y.-S.; Zhang, W.; Kai, W.; Liaw, P.K.; Huang, H.-H. Evaluation of Ni-free Zr–Cu–Fe–Al bulk metallic glass for biomedical implant applications. *J. Alloys Compd.* **2014**, *586*, S539–S543. [CrossRef]
183. Liu, L.; Qiu, C.; Huang, C.; Yu, Y.; Huang, H.; Zhang, S. Biocompatibility of Ni-free Zr-based bulk metallic glasses. *Intermetallics* **2009**, *17*, 235–240. [CrossRef]
184. Yeh, J.-W.; Chen, S.K.; Lin, S.-J.; Gan, J.-Y.; Chin, T.-S.; Shun, T.-T.; Tsau, C.-H.; Chang, S.-Y. Nanostructured High-Entropy Alloys with Multiple Principal Elements: Novel Alloy Design Concepts and Outcomes. *Adv. Eng. Mater.* **2004**, *6*, 299–303. [CrossRef]
185. Akinbami, O.; Mohlala, L.M.; Klenam, D.; van der Merwe, J.; Bodunrin, M. The Status of High Entropy Alloys Studies in Africa: An Overview. *Key Eng. Mater.* **2022**, *917*, 41–53. [CrossRef]
186. Owen, L.; Jones, N. Quantifying local lattice distortions in alloys. *Scr. Mater.* **2020**, *187*, 428–433. [CrossRef]

187. Chen, H.; Kauffmann, A.; Laube, S.; Choi, I.-C.; Schwaiger, R.; Huang, Y.; Lichtenberg, K.; Müller, F.; Gorr, B.; Christ, H.-J.; et al. Contribution of Lattice Distortion to Solid Solution Strengthening in a Series of Refractory High Entropy Alloys. *Met. Mater. Trans. A* **2018**, *49*, 772–781. [CrossRef]
188. Owen, L.R.; Jones, N.G. Lattice distortions in high-entropy alloys. *J. Mater. Res.* **2018**, *33*, 2954–2969. [CrossRef]
189. Owen, L.; Pickering, E.; Playford, H.; Stone, H.; Tucker, M.; Jones, N. An assessment of the lattice strain in the CrMnFeCoNi high-entropy alloy. *Acta Mater.* **2017**, *122*, 11–18. [CrossRef]
190. Diao, H.; Santodonato, L.J.; Tang, Z.; Egami, T.; Liaw, P.K. Local Structures of High-Entropy Alloys (HEAs) on Atomic Scales: An Overview. *Jom* **2015**, *67*, 2321–2325. [CrossRef]
191. Guo, W.; Dmowski, W.; Noh, J.-Y.; Rack, P.; Liaw, P.K.; Egami, T. Local Atomic Structure of a High-Entropy Alloy: An X-Ray and Neutron Scattering Study. *Met. Mater. Trans. A* **2013**, *44*, 1994–1997. [CrossRef]
192. Santodonato, L.J.; Zhang, Y.; Feygenson, M.; Parish, C.M.; Gao, M.C.; Weber, R.J.; Neuefeind, J.C.; Tang, Z.; Liaw, P.K. Deviation from high-entropy configurations in the atomic distributions of a multi-principal-element alloy. *Nat. Commun.* **2015**, *6*, 5964. [CrossRef]
193. Abbasi, E.; Luo, Q.; Owens, D. A comparison of microstructure and mechanical properties of low-alloy-medium-carbon steels after quench-hardening. *Mater. Sci. Eng. A* **2018**, *725*, 65–75. [CrossRef]
194. Ahmady, A.R.; Ekhlasi, A.; Nouri, A.; Nazarpak, M.H.; Gong, P.; Solouk, A. High entropy alloy coatings for biomedical applications: A review. *Smart Mater. Manuf.* **2023**, *1*, 100009. [CrossRef]
195. Assadi, H.; Kreye, H.; Gärtner, F.; Klassen, T. Cold spraying—A materials perspective. *Acta Mater.* **2016**, *116*, 382–407. [CrossRef]
196. Ren, Y.; King, P.; Yang, Y.; Xiao, T.; Chu, C.; Gulizia, S.; Murphy, A. Characterization of heat treatment-induced pore structure changes in cold-sprayed titanium. *Mater. Charact.* **2017**, *132*, 69–75. [CrossRef]
197. Kiplangat, R.S.; Lin, T.-T.; Kipkirui, N.G.; Chen, S.-H. Microstructure and Mechanical Properties of the Plasma-Sprayed and Cold-Sprayed Al0.5CoCrFeNi2Ti0.5 High-Entropy Alloy Coatings. *J. Therm. Spray Technol.* **2022**, *31*, 1207–1221. [CrossRef]
198. Nikbakht, R.; Assadi, H.; Jodoin, B. Intermetallic Phase Evolution of Cold-Sprayed Ni-Ti Composite Coatings: Influence of As-Sprayed Chemical Composition. *J. Therm. Spray Technol.* **2021**, *30*, 119–130. [CrossRef]
199. Dai, C.-D.; Fu, Y.; Guo, J.-X.; Du, C.-W. Effects of substrate temperature and deposition time on the morphology and corrosion resistance of FeCoCrNiMo0.3 high-entropy alloy coating fabricated by magnetron sputtering. *Int. J. Miner. Met. Mater.* **2020**, *27*, 1388–1397. [CrossRef]
200. Yin, S.; Li, W.; Song, B.; Yan, X.; Kuang, M.; Xu, Y.; Wen, K.; Lupoi, R. Deposition of FeCoNiCrMn high entropy alloy (HEA) coating via cold spraying. *J. Mater. Sci. Technol.* **2019**, *35*, 1003–1007. [CrossRef]
201. Cavaliere, P.; Perrone, A.; Silvello, A.; Laska, A.; Blasi, G.; Cano, I.G. Fatigue Bending of V-Notched Cold-Sprayed FeCoCrNiMn Coatings. *Metals* **2022**, *12*, 780. [CrossRef]
202. Nair, R.B.; Perumal, G.; McDonald, A. Effect of Microstructure on Wear and Corrosion Performance of Thermally Sprayed AlCoCrFeMo High-Entropy Alloy Coatings. *Adv. Eng. Mater.* **2022**, *24*, 2101713. [CrossRef]
203. Rokni, M.R.; Widener, C.; Champagne, V.R. Microstructural Evolution of 6061 Aluminum Gas-Atomized Powder and High-Pressure Cold-Sprayed Deposition. *J. Therm. Spray Technol.* **2014**, *23*, 514–524. [CrossRef]
204. Hsu, W.-L.; Yang, Y.-C.; Chen, C.-Y.; Yeh, J.-W. Thermal sprayed high-entropy NiCo 0.6 Fe 0.2 Cr 1.5 SiAlTi 0.2 coating with improved mechanical properties and oxidation resistance. *Intermetallics* **2017**, *89*, 105–110. [CrossRef]
205. Ma, X.; Ruggiero, P.; Bhattacharya, R.; Senkov, O.N.; Rai, A.K. Evaluation of New High Entropy Alloy as Thermal Sprayed Bondcoat in Thermal Barrier Coatings. *J. Therm. Spray Technol.* **2022**, *31*, 1011–1020. [CrossRef]
206. Feng, S.; Guan, S.; Story, W.A.; Ren, J.; Zhang, S.; Te, A.; Gleason, M.A.; Heelan, J.; Walde, C.; Birt, A.; et al. Cold Spray Additive Manufacturing of CoCrFeNiMn High-Entropy Alloy: Process Development, Microstructure, and Mechanical Properties. *J. Therm. Spray Technol.* **2022**, *31*, 1222–1231. [CrossRef]
207. Lehtonen, J.; Koivuluoto, H.; Ge, Y.; Juselius, A.; Hannula, S.-P. Cold Gas Spraying of a High-Entropy CrFeNiMn Equiatomic Alloy. *Coatings* **2020**, *10*, 53. [CrossRef]
208. Cheng, J.; Liang, X.; Xu, B. Effect of Nb addition on the structure and mechanical behaviors of CoCrCuFeNi high-entropy alloy coatings. *Surf. Coat. Technol.* **2014**, *240*, 184–190. [CrossRef]
209. Cheng, J.; Liu, D.; Liang, X.; Chen, Y. Evolution of microstructure and mechanical properties of in situ synthesized TiC–TiB2/CoCrCuFeNi high entropy alloy coatings. *Surf. Coat. Technol.* **2015**, *281*, 109–116. [CrossRef]
210. Cheng, J.B.; Liang, X.B.; Wang, Z.H.; Xu, B.S. Formation and Mechanical Properties of CoNiCuFeCr High-Entropy Alloys Coatings Prepared by Plasma Transferred Arc Cladding Process. *Plasma Chem. Plasma Process.* **2013**, *33*, 979–992. [CrossRef]
211. Lu, J.; Wang, B.; Qiu, X.; Peng, Z.; Ma, M. Microstructure evolution and properties of CrCuFe x NiTi high-entropy alloy coating by plasma cladding on Q235. *Surf. Coat. Technol.* **2017**, *328*, 313–318. [CrossRef]
212. Cai, Z.; Wang, Y.; Cui, X.; Jin, G.; Li, Y.; Liu, Z.; Dong, M. Design and microstructure characterization of FeCoNiAlCu high-entropy alloy coating by plasma cladding: In comparison with thermodynamic calculation. *Surf. Coat. Technol.* **2017**, *330*, 163–169. [CrossRef]
213. Fang, Q.; Chen, Y.; Li, J.; Liu, Y.; Liu, Y. Microstructure and mechanical properties of FeCoCrNiNb high-entropy alloy coatings. *Phys. B Condens. Matter* **2018**, *550*, 112–116. [CrossRef]
214. Xiang, K.; Chen, L.-Y.; Chai, L.; Guo, N.; Wang, H. Microstructural characteristics and properties of CoCrFeNiNbx high-entropy alloy coatings on pure titanium substrate by pulsed laser cladding. *Appl. Surf. Sci.* **2020**, *517*, 146214. [CrossRef]

215. Chen, L.; Wang, Y.; Hao, X.; Zhang, X.; Liu, H. Lightweight refractory high entropy alloy coating by laser cladding on Ti–6Al–4V surface. *Vacuum* **2021**, *183*, 109823. [CrossRef]
216. Li, Y.; Liang, H.; Nie, Q.; Qi, Z.; Deng, D.; Jiang, H.; Cao, Z. Microstructures and Wear Resistance of CoCrFeNi2V0.5Tix High-Entropy Alloy Coatings Prepared by Laser Cladding. *Crystals* **2020**, *10*, 352. [CrossRef]
217. Wu, W.; Jiang, L.; Jiang, H.; Pan, X.; Cao, Z.; Deng, D.; Wang, T.; Li, T. Phase Evolution and Properties of Al2CrFeNiMo x High-Entropy Alloys Coatings by Laser Cladding. *J. Therm. Spray Technol.* **2015**, *24*, 1333–1340. [CrossRef]
218. Zhang, H.; Pan, Y.; He, Y.; Jiao, H. Microstructure and properties of 6FeNiCoSiCrAlTi high-entropy alloy coating prepared by laser cladding. *Appl. Surf. Sci.* **2011**, *257*, 2259–2263. [CrossRef]
219. Gu, Z.; Mao, P.; Gou, Y.; Chao, Y.; Xi, S. Microstructure and properties of MgMoNbFeTi2Yx high entropy alloy coatings by laser cladding. *Surf. Coat. Technol.* **2020**, *402*, 126303. [CrossRef]
220. Qiu, X.; Zhang, Y.; Liu, C. Effect of Ti content on structure and properties of Al2CrFeNiCoCuTix high-entropy alloy coatings. *J. Alloys Compd.* **2014**, *585*, 282–286. [CrossRef]
221. Li, X.; Feng, Y.; Liu, B.; Yi, D.; Yang, X.; Zhang, W.; Chen, G.; Liu, Y.; Bai, P. Influence of NbC particles on microstructure and mechanical properties of AlCoCrFeNi high-entropy alloy coatings prepared by laser cladding. *J. Alloys Compd.* **2019**, *788*, 485–494. [CrossRef]
222. Qiu, X. Microstructure, hardness and corrosion resistance of Al2CoCrCuFeNiTix high-entropy alloy coatings prepared by rapid solidification. *J. Alloys Compd.* **2018**, *735*, 359–364. [CrossRef]
223. Zhang, H.; Pan, Y.; He, Y.-Z. Synthesis and characterization of FeCoNiCrCu high-entropy alloy coating by laser cladding. *Mater. Des.* **2011**, *32*, 1910–1915. [CrossRef]
224. Ni, C.; Shi, Y.; Liu, J.; Huang, G. Characterization of Al0.5FeCu0.7NiCoCr high-entropy alloy coating on aluminum alloy by laser cladding. *Opt. Laser Technol.* **2018**, *105*, 257–263. [CrossRef]
225. Shu, F.; Wu, L.; Zhao, H.; Sui, S.; Zhou, L.; Zhang, J.; He, W.; He, P.; Xu, B. Microstructure and high-temperature wear mechanism of laser cladded CoCrBFeNiSi high-entropy alloy amorphous coating. *Mater. Lett.* **2018**, *211*, 235–238. [CrossRef]
226. Shu, F.; Zhang, B.; Liu, T.; Sui, S.; Liu, Y.; He, P.; Liu, B.; Xu, B. Effects of laser power on microstructure and properties of laser cladded CoCrBFeNiSi high-entropy alloy amorphous coatings. *Surf. Coat. Technol.* **2019**, *358*, 667–675. [CrossRef]
227. Jiang, Y.; Li, J.; Juan, Y.; Lu, Z.; Jia, W. Evolution in microstructure and corrosion behavior of AlCoCrxFeNi high-entropy alloy coatings fabricated by laser cladding. *J. Alloys Compd.* **2019**, *775*, 1–14. [CrossRef]
228. Zhang, H.; Wu, W.; He, Y.; Li, M.; Guo, S. Formation of core–shell structure in high entropy alloy coating by laser cladding. *Appl. Surf. Sci.* **2016**, *363*, 543–547. [CrossRef]
229. Guo, Y.; Shang, X.; Liu, Q. Microstructure and properties of in-situ TiN reinforced laser cladding CoCr2FeNiTi high-entropy alloy composite coatings. *Surf. Coat. Technol.* **2018**, *344*, 353–358. [CrossRef]
230. Guo, Y.; Liu, Q. MoFeCrTiWAlNb refractory high-entropy alloy coating fabricated by rectangular-spot laser cladding. *Intermetallics* **2018**, *102*, 78–87. [CrossRef]
231. Chao, Q.; Guo, T.; Jarvis, T.; Wu, X.; Hodgson, P.; Fabijanic, D. Direct laser deposition cladding of Al CoCrFeNi high entropy alloys on a high-temperature stainless steel. *Surf. Coat. Technol.* **2017**, *332*, 440–451. [CrossRef]
232. Juan, Y.; Li, J.; Jiang, Y.; Jia, W.; Lu, Z. Modified criterions for phase prediction in the multi-component laser-clad coatings and investigations into microstructural evolution/wear resistance of FeCrCoNiAlMox laser-clad coatings. *Appl. Surf. Sci.* **2019**, *465*, 700–714. [CrossRef]
233. Shu, F.; Yang, B.; Dong, S.; Zhao, H.; Xu, B.; Xu, F.; Liu, B.; He, P.; Feng, J. Effects of Fe-to-Co ratio on microstructure and mechanical properties of laser cladded FeCoCrBNiSi high-entropy alloy coatings. *Appl. Surf. Sci.* **2018**, *450*, 538–544. [CrossRef]
234. Cai, Z.; Cui, X.; Jin, G.; Liu, Z.; Zheng, W.; Li, Y.; Wang, L. Microstructure and thermal stability of a Ni-Cr-Co-Ti-V-Al high-entropy alloy coating by laser surface alloying. *Met. Mater. Int.* **2017**, *23*, 1012–1018. [CrossRef]
235. Cai, Z.; Jin, G.; Cui, X.; Liu, Z.; Zheng, W.; Li, Y.; Wang, L. Synthesis and microstructure characterization of Ni-Cr-Co-Ti-V-Al high entropy alloy coating on Ti-6Al-4V substrate by laser surface alloying. *Mater. Charact.* **2016**, *120*, 229–233. [CrossRef]
236. Zhang, S.; Wu, C.; Zhang, C.; Guan, M.; Tan, J. Laser surface alloying of FeCoCrAlNi high-entropy alloy on 304 stainless steel to enhance corrosion and cavitation erosion resistance. *Opt. Laser Technol.* **2016**, *84*, 23–31. [CrossRef]
237. Zhang, S.; Wu, C.; Yi, J.; Zhang, C. Synthesis and characterization of FeCoCrAlCu high-entropy alloy coating by laser surface alloying. *Surf. Coat. Technol.* **2015**, *262*, 64–69. [CrossRef]
238. Ye, Q.; Feng, K.; Li, Z.; Lu, F.; Li, R.; Huang, J.; Wu, Y. Microstructure and corrosion properties of CrMnFeCoNi high entropy alloy coating. *Appl. Surf. Sci.* **2017**, *396*, 1420–1426. [CrossRef]
239. Zhang, S.; Wu, C.; Zhang, C. Phase evolution characteristics of FeCoCrAlCuVxNi high entropy alloy coatings by laser high-entropy alloying. *Mater. Lett.* **2015**, *141*, 7–9. [CrossRef]
240. Wu, C.; Zhang, S.; Zhang, C.; Zhang, H.; Dong, S. Phase evolution and properties in laser surface alloying of FeCoCrAlCuNi high-entropy alloy on copper substrate. *Surf. Coat. Technol.* **2017**, *315*, 368–376. [CrossRef]
241. Smyrnova, K.V.; Pogrebnjak, A.D.; Beresnev, V.M.; Litovchenko, S.V.; Borba-Pogrebnjak, S.O.; Manokhin, A.S.; Klimenko, S.A.; Zhollybekov, B.; Kupchishin, A.I.; Kravchenko, Y.O.; et al. Microstructure and Physical–Mechanical Properties of (TiAlSiY)N Nanostructured Coatings Under Different Energy Conditions. *Met. Mater. Int.* **2018**, *24*, 1024–1035. [CrossRef]

242. Pogrebnjak, A.; Yakushchenko, I.V.; Bondar, O.; Beresnev, V.M.; Oyoshi, K.; Ivasishin, O.M.; Amekura, H.; Takeda, Y.; Opielak, M.; Kozak, C. Irradiation resistance, microstructure and mechanical properties of nanostructured (TiZrHfVNbTa)N coatings. *J. Alloys Compd.* **2016**, *679*, 155–163. [CrossRef]
243. Yu, X.; Wang, J.; Wang, L.; Huang, W. Fabrication and characterization of CrNbSiTiZr high-entropy alloy films by radio-frequency magnetron sputtering via tuning substrate bias. *Surf. Coat. Technol.* **2021**, *412*, 127074. [CrossRef]
244. Wang, J.; Kuang, S.; Yu, X.; Wang, L.; Huang, W. Tribo-mechanical properties of CrNbTiMoZr high-entropy alloy film synthesized by direct current magnetron sputtering. *Surf. Coat. Technol.* **2020**, *403*, 126374. [CrossRef]
245. Alvi, S.; Jarzabek, D.M.; Kohan, M.G.; Hedman, D.; Jenczyk, P.; Natile, M.M.; Vomiero, A.; Akhtar, F. Synthesis and Mechanical Characterization of a CuMoTaWV High-Entropy Film by Magnetron Sputtering. *ACS Appl. Mater. Interfaces* **2020**, *12*, 21070–21079. [CrossRef]
246. Li, X.; Zheng, Z.; Dou, D.; Li, J. Microstructure and Properties of Coating of FeAlCuCrCoMn High Entropy Alloy Deposited by Direct Current Magnetron Sputtering. *Mater. Res.* **2016**, *19*, 802–806. [CrossRef]
247. Cao, F.; Munroe, P.; Zhou, Z.; Xie, Z. Microstructure and mechanical properties of a multilayered CoCrNi/Ti coating with varying crystal structure. *Surf. Coat. Technol.* **2018**, *350*, 596–602. [CrossRef]
248. Braic, V.; Vladescu, A.; Balaceanu, M.; Luculescu, C.; Braic, M. Nanostructured multi-element (TiZrNbHfTa)N and (TiZrNbHfTa)C hard coatings. *Surf. Coat. Technol.* **2012**, *211*, 117–121. [CrossRef]
249. Zhang, W.; Tang, R.; Yang, Z.; Liu, C.; Chang, H.; Yang, J.; Liao, J.; Yang, Y.; Liu, N. Preparation, structure, and properties of an AlCrMoNbZr high-entropy alloy coating for accident-tolerant fuel cladding. *Surf. Coat. Technol.* **2018**, *347*, 13–19. [CrossRef]
250. Lin, C.; Duh, J. Corrosion behavior of (Ti–Al–Cr–Si–V)xNy coatings on mild steels derived from RF magnetron sputtering. *Surf. Coat. Technol.* **2008**, *203*, 558–561. [CrossRef]
251. Huang, P.-K.; Yeh, J.-W. Effects of nitrogen content on structure and mechanical properties of multi-element (AlCrNbSiTiV)N coating. *Surf. Coat. Technol.* **2009**, *203*, 1891–1896. [CrossRef]
252. Ren, B.; Shen, Z.; Liu, Z. Structure and mechanical properties of multi-element (AlCrMnMoNiZr)Nx coatings by reactive magnetron sputtering. *J. Alloys Compd.* **2013**, *560*, 171–176. [CrossRef]
253. Tsai, D.-C.; Deng, M.-J.; Chang, Z.-C.; Kuo, B.-H.; Chen, E.-C.; Chang, S.-Y.; Shieu, F.-S. Oxidation resistance and characterization of (AlCrMoTaTi)-Six-N coating deposited via magnetron sputtering. *J. Alloys Compd.* **2015**, *647*, 179–188. [CrossRef]
254. Johansson, K.; Riekehr, L.; Fritze, S.; Lewin, E. Multicomponent Hf-Nb-Ti-V-Zr nitride coatings by reactive magnetron sputter deposition. *Surf. Coat. Technol.* **2018**, *349*, 529–539. [CrossRef]
255. Tüten, N.; Canadinc, D.; Motallebzadeh, A.; Bal, B. Microstructure and tribological properties of TiTaHfNbZr high entropy alloy coatings deposited on Ti 6Al 4V substrates. *Intermetallics* **2019**, *105*, 99–106. [CrossRef]
256. Alamdari, A.A.; Unal, U.; Motallebzadeh, A. Investigation of microstructure, mechanical properties, and biocorrosion behavior of Ti1.5ZrTa0.5Nb0.5W0.5 refractory high-entropy alloy film doped with Ag nanoparticles. *Surf. Interfaces* **2022**, *28*, 101617. [CrossRef]
257. Chen, L.; Bobzin, K.; Zhou, Z.; Zhao, L.; Öte, M.; Königstein, T.; Tan, Z.; He, D. Wear behavior of HVOF-sprayed Al0.6TiCrFeCoNi high entropy alloy coatings at different temperatures. *Surf. Coat. Technol.* **2019**, *358*, 215–222. [CrossRef]
258. Löbel, M.; Lindner, T.; Lampke, T. High-temperature wear behaviour of AlCoCrFeNiTi0.5 coatings produced by HVOF. *Surf. Coat. Technol.* **2020**, *403*, 126379. [CrossRef]
259. Abhijith, N.V.; Kumar, D.; Kalyansundaram, D. Development of Single-Stage TiNbMoMnFe High-Entropy Alloy Coating on 304L Stainless Steel Using HVOF Thermal Spray. *J. Therm. Spray Technol.* **2022**, *31*, 1032–1044. [CrossRef]
260. Hsu, W.-L.; Murakami, H.; Yeh, J.-W.; Yeh, A.-C.; Shimoda, K. On the study of thermal-sprayed Ni 0.2 Co 0.6 Fe 0.2 CrSi 0.2 AlTi 0.2 HEA overlay coating. *Surf. Coat. Technol.* **2017**, *316*, 71–74. [CrossRef]
261. Tian, L.; Feng, Z.; Xiong, W. Microstructure, Microhardness, and Wear Resistance of AlCoCrFeNiTi/Ni60 Coating by Plasma Spraying. *Coatings* **2018**, *8*, 112. [CrossRef]
262. Wang, W.; Qi, W.; Xie, L.; Yang, X.; Li, J.; Zhang, Y. Microstructure and Corrosion Behavior of (CoCrFeNi)95Nb5 High-Entropy Alloy Coating Fabricated by Plasma Spraying. *Materials* **2019**, *12*, 694. [CrossRef]
263. Ang, A.S.M.; Berndt, C.C.; Sesso, M.L.; Anupam, A.; Praveen, S.; Kottada, R.S.; Murty, B.S. Plasma-Sprayed High Entropy Alloys: Microstructure and Properties of AlCoCrFeNi and MnCoCrFeNi. *Metall. Mater. Trans. A* **2015**, *46*, 791–800. [CrossRef]
264. Xiao, J.-K.; Tan, H.; Wu, Y.-Q.; Chen, J.; Zhang, C. Microstructure and wear behavior of FeCoNiCrMn high entropy alloy coating deposited by plasma spraying. *Surf. Coat. Technol.* **2020**, *385*, 125430. [CrossRef]
265. Xiao, J.-K.; Wu, Y.-Q.; Chen, J.; Zhang, C. Microstructure and tribological properties of plasma sprayed FeCoNiCrSiAlx high entropy alloy coatings. *Wear* **2020**, *448–449*, 203209. [CrossRef]
266. Anupam, A.; Kottada, R.S.; Kashyap, S.; Meghwal, A.; Murty, B.; Berndt, C.; Ang, A. Understanding the microstructural evolution of high entropy alloy coatings manufactured by atmospheric plasma spray processing. *Appl. Surf. Sci.* **2020**, *505*, 144117. [CrossRef]
267. Wang, L.; Chen, C.; Yeh, J.; Ke, S. The microstructure and strengthening mechanism of thermal spray coating NixCo0.6Fe0.2CrySizAlTi0.2 high-entropy alloys. *Mater. Chem. Phys.* **2011**, *126*, 880–885. [CrossRef]
268. Tian, L.-H.; Xiong, W.; Liu, C.; Lu, S.; Fu, M. Microstructure and Wear Behavior of Atmospheric Plasma-Sprayed AlCoCrFeNiTi High-Entropy Alloy Coating. *J. Mater. Eng. Perform.* **2016**, *25*, 5513–5521. [CrossRef]

269. Anupam, A.; Kumar, S.; Chavan, N.M.; Murty, B.S.; Kottada, R.S. First report on cold-sprayed AlCoCrFeNi high-entropy alloy and its isothermal oxidation. *J. Mater. Res.* **2019**, *34*, 796–806. [CrossRef]
270. Hushchyk, D.V.; Yurkova, A.I.; Cherniavsky, V.V.; Bilyk, I.I.; Nakonechnyy, S.O. Nanostructured AlNiCoFeCrTi high-entropy coating performed by cold spray. *Appl. Nanosci.* **2020**, *10*, 4879–4890. [CrossRef]
271. Zou, Y. Cold Spray Additive Manufacturing: Microstructure Evolution and Bonding Features. *Acc. Mater. Res.* **2021**, *2*, 1071–1081. [CrossRef]
272. Nikbakht, R.; Saadati, M.; Kim, T.-S.; Jahazi, M.; Kim, H.S.; Jodoin, B. Cold spray deposition characteristic and bonding of CrMnCoFeNi high entropy alloy. *Surf. Coat. Technol.* **2021**, *425*, 127748. [CrossRef]
273. Xu, Y.; Li, W.; Qu, L.; Yang, X.; Song, B.; Lupoi, R.; Yin, S. Solid-state cold spraying of FeCoCrNiMn high-entropy alloy: An insight into microstructure evolution and oxidation behavior at 700–900 °C. *J. Mater. Sci. Technol.* **2021**, *68*, 172–183. [CrossRef]
274. Yurkova, A.I.; Hushchyk, D.V.; Minitsky, A.V. Synthesis of High-Entropy AlNiCoFeCrTi Coating by Cold Spraying. *Powder Met. Met. Ceram.* **2021**, *59*, 681–694. [CrossRef]
275. Ahn, J.-E.; Kim, Y.-K.; Yoon, S.-H.; Lee, K.-A. Tuning the Microstructure and Mechanical Properties of Cold Sprayed Equiatomic CoCrFeMnNi High-Entropy Alloy Coating Layer. *Met. Mater. Int.* **2021**, *27*, 2406–2415. [CrossRef]
276. Lordejani, A.A.; Colzani, D.; Guagliano, M.; Bagherifard, S. An inclusive numerical framework to assess the role of feedstock features on the quality of cold spray deposits. *Mater. Des.* **2022**, *224*, 111374. [CrossRef]
277. Nikbakht, R.; Cojocaru, C.V.; Aghasibeig, M.; Irissou, É.; Kim, T.-S.; Kim, H.S.; Jodoin, B. Cold Spray and Laser-Assisted Cold Spray of CrMnCoFeNi High Entropy Alloy Using Nitrogen as the Propelling Gas. *J. Therm. Spray Technol.* **2022**, *31*, 1129–1142. [CrossRef]
278. Sova, A.; Doubenskaia, M.; Trofimov, E.; Samodurova, M. Deposition of High-Entropy Alloy Coating by Cold Spray Combined with Laser Melting: Feasibility Tests. *J. Therm. Spray Technol.* **2022**, *31*, 1112–1128. [CrossRef]
279. Han, P.; Lin, J.; Wang, W.; Liu, Z.; Xiang, Y.; Zhang, T.; Liu, Q.; Guan, X.; Qiao, K.; Xie, Y.; et al. Friction Stir Processing of Cold-Sprayed High-Entropy Alloy Particles Reinforced Aluminum Matrix Composites: Corrosion and Wear Properties. *Met. Mater. Int.* **2022**, *29*, 845–860. [CrossRef]
280. Silvello, A.; Cavaliere, P.; Yin, S.; Lupoi, R.; Cano, I.G.; Dosta, S. Microstructural, Mechanical and Wear Behavior of HVOF and Cold-Sprayed High-Entropy Alloys (HEAs) Coatings. *J. Therm. Spray Technol.* **2022**, *31*, 1184–1206. [CrossRef]
281. Feng, L.; Yang, W.-J.; Ma, K.; Yuan, Y.-D.; An, G.-S.; Li, W.-S. Microstructure and Properties of Cold Spraying AlCoCrCuFeNix HEA Coatings Synthesized by Induction Remelting. *Mater. Technol.* **2022**, *37*, 2567–2579. [CrossRef]
282. Zou, Y.; Qiu, Z.; Huang, C.; Zeng, D.; Lupoi, R.; Zhang, N.; Yin, S. Microstructure and tribological properties of Al2O3 reinforced FeCoNiCrMn high entropy alloy composite coatings by cold spray. *Surf. Coat. Technol.* **2022**, *434*, 128205. [CrossRef]
283. Yu, P.; Fan, N.; Zhang, Y.; Wang, Z.; Li, W.; Lupoi, R.; Yin, S. Microstructure evolution and composition redistribution of FeCoNiCrMn high entropy alloy under extreme plastic deformation. *Mater. Res. Lett.* **2022**, *10*, 124–132. [CrossRef]
284. Zhu, J.; Cheng, X.; Zhang, L.; Hui, X.; Wu, Y.; Zheng, H.; Ren, Z.; Zhao, Y.; Wang, W.; Zhu, S.; et al. Microstructures, wear resistance and corrosion resistance of CoCrFeNi high entropy alloys coating on AZ91 Mg alloy prepared by cold spray. *J. Alloys Compd.* **2022**, *925*, 166698. [CrossRef]
285. Akisin, C.J.; Bennett, C.J.; Venturi, F.; Assadi, H.; Hussain, T. Numerical and Experimental Analysis of the Deformation Behavior of CoCrFeNiMn High Entropy Alloy Particles onto Various Substrates During Cold Spraying. *J. Therm. Spray Technol.* **2022**, *31*, 1085–1111. [CrossRef]
286. Zehtabi, N.P.; Lordejani, A.A.; Guagliano, M.; Bagherifard, S. Numerical Simulation of Cold Spray Bonding for CrFeNi Medium-Entropy Alloy. *Adv. Eng. Mater.* **2022**, *24*, 2200603. [CrossRef]
287. Mahaffey, J.; Vackel, A.; Whetten, S.; Melia, M.; Kustas, A.B. Structure Evolution and Corrosion Performance of CoCrFeMnNi High Entropy Alloy Coatings Produced Via Plasma Spray and Cold Spray. *J. Therm. Spray Technol.* **2022**, *31*, 1143–1154. [CrossRef]
288. Supekar, R.; Nair, R.B.; McDonald, A.; Stoyanov, P. Sliding wear behavior of high entropy alloy coatings deposited through cold spraying and flame spraying: A comparative assessment. *Wear* **2023**, *516–517*, 204596. [CrossRef]
289. Yuan, Z.; Tian, W.; Li, F.; Fu, Q.; Hu, Y.; Wang, X. Microstructure and properties of high-entropy alloy reinforced aluminum matrix composites by spark plasma sintering. *J. Alloys Compd.* **2019**, *806*, 901–908. [CrossRef]
290. Lu, F.-F.; Ma, K.; Li, C.-X.; Yasir, M.; Luo, X.-T.; Li, C.-J. Enhanced corrosion resistance of cold-sprayed and shot-peened aluminum coatings on LA43M magnesium alloy. *Surf. Coat. Technol.* **2020**, *394*, 125865. [CrossRef]
291. Marzbanrad, B.; Toyserkani, E.; Jahed, H. Characterization of single- and multilayer cold-spray coating of Zn on AZ31B. *Surf. Coat. Technol.* **2021**, *416*, 127155. [CrossRef]
292. Yao, H.-L.; Yi, Z.-H.; Yao, C.; Zhang, M.-X.; Wang, H.-T.; Li, S.-B.; Bai, X.-B.; Chen, Q.-Y.; Ji, G.-C. Improved corrosion resistance of AZ91D magnesium alloy coated by novel cold-sprayed Zn-HA/Zn double-layer coatings. *Ceram. Int.* **2020**, *46*, 7687–7693. [CrossRef]
293. Siddique, S.; Bernussi, A.A.; Husain, S.W.; Yasir, M. Enhancing structural integrity, corrosion resistance and wear properties of Mg alloy by heat treated cold sprayed Al coating. *Surf. Coat. Technol.* **2020**, *394*, 125882. [CrossRef]
294. Xiong, Y.; Zhang, M.-X. The effect of cold sprayed coatings on the mechanical properties of AZ91D magnesium alloys. *Surf. Coat. Technol.* **2014**, *253*, 89–95. [CrossRef]
295. Dayani, S.; Shaha, S.; Ghelichi, R.; Wang, J.; Jahed, H. The impact of AA7075 cold spray coating on the fatigue life of AZ31B cast alloy. *Surf. Coat. Technol.* **2018**, *337*, 150–158. [CrossRef]

296. Tao, Y.; Xiong, T.; Sun, C.; Kong, L.; Cui, X.; Li, T.; Song, G.-L. Microstructure and corrosion performance of a cold sprayed aluminium coating on AZ91D magnesium alloy. *Corros. Sci.* **2010**, *52*, 3191–3197. [CrossRef]
297. Mušálek, R.; Kovářík, O.; Matějíček, J. In-situ observation of crack propagation in thermally sprayed coatings. *Surf. Coat. Technol.* **2010**, *205*, 1807–1811. [CrossRef]
298. Klenam, D.E.P.; Bodunrin, M.O.; Akromah, S.; Gikunoo, E.; Andrews, A.; McBagonluri, F. Ferrous materials degradation: Characterisation of rust by colour—An overview. *Corros. Rev.* **2021**, *39*, 297–311. [CrossRef]
299. Bodunrin, M.O.; Chown, L.H.; van der Merwe, J.W.; Alaneme, K.K.; Oganbule, C.; Klenam, D.E.P.; Mphasha, N.P. Corrosion behavior of titanium alloys in acidic and saline media: Role of alloy design, passivation integrity, and electrolyte modification. *Corros. Rev.* **2020**, *38*, 25–47. [CrossRef]
300. Klenam, D.E.P.; Chown, L.H.; Papo, J.M.; Smith, M.; Cornish, L.A. Corrosion and Mechanical Behaviour of Typical Railway Axle Steels in Water. *Afr. Corros. J.* **2016**, *2*, 1–10.
301. Thurn, G.; Schneider, G.A.; Aldinger, F. High-temperature deformation of plasma-sprayed ZrO2 thermal barrier coatings. *Mater. Sci. Eng. A* **1997**, *233*, 176–182. [CrossRef]

coatings

MDPI

Article

Effective Evaluation of Elastic Properties of a Graphene and Ceramics Reinforced Epoxy Composite under a Thermal Environment Using the Impact Hammer Vibration Technique

Nitesh Kumar [1,2], Ananda Babu [1], Alok Kumar Das [2,*] and Ashish Kumar Srivastava [3]

[1] Mechanical Engineering Department, SET, Sharda University, Greater Noida 201306, Uttar Pradesh, India
[2] Mechanical Engineering Department, Indian Institute of Technology, (ISM), Dhanbad 826004, Jharkhand, India
[3] Mechanical Engineering Department, G.L. Bajaj Institute of Technology and Management, Greater Noida 201306, Uttar Pradesh, India
* Correspondence: eralok@yahoo.co.in

Abstract: This paper presents an evaluation of the mechanical properties of nanocomposites when a lower concentration of nanoparticles graphene and ceramics are mixed with epoxy to determine the damping and stability characteristics of hybrid epoxy, using vibration techniques to extract accurate results. The effectiveness of the Impact hammer vibration technique is validated with mechanical testing such as three-point bending in terms of Young's modulus of the nanocomposite. The graphene nanocomposite carries nanoparticle 1 wt.% of epoxy, while the ceramic nanocomposite carries 3 wt.% of epoxy. It is observed that the reduction in frequency under a thermal environment is significantly less for graphene and ceramic reinforced hybrid nanocomposites, whereas the reduction in pure epoxy under a thermal environment is high. Thus, the results show that the addition of nanoparticles to composites shows improvement in the mechanical and thermal stability of elastic properties. The elastic properties obtained from the vibrational analysis are more consistent and economical than the three-point bending test for the evaluation of hybrid nanocomposites.

Keywords: graphene; ceramics; epoxy resin; elastic properties; vibration technique

Citation: Kumar, N.; Babu, A.; Das, A.K.; Srivastava, A.K. Effective Evaluation of Elastic Properties of a Graphene and Ceramics Reinforced Epoxy Composite under a Thermal Environment Using the Impact Hammer Vibration Technique. *Coatings* **2022**, *12*, 1325. https://doi.org/10.3390/coatings12091325

Academic Editor: Jiri Militky

Received: 12 July 2022
Accepted: 5 September 2022
Published: 12 September 2022

1. Introduction

Composites are widely used in the field of aerospace, automotive and other high-performance structural applications due to their high stiffness and strength-to-weight ratios. They are a cheaper lightweight option than conventional materials such as metals. Despite the several advantages of using composites, they have several drawbacks, including high stress and strain development under load conditions. However, research has shown that the addition of nanoparticles in the polymer matrix is considered a highly effective technique to improve the mechanical properties of composites. Amendola et al. [1] investigated that the addition of nanoparticles in the polymer matrix results in nanocomposites with enhanced thermal and mechanical properties. It was shown that there is a good agreement with the matrix and high surface-to-volume ratio of the fine nanoparticles, which is the main reason behind the enhancement of the mechanical properties of the nanocomposites [2–4]. Firsov et al. [5] used filler in nanocomposites due to its improved physical properties such as high aspect ratio, low electrical resistivity, high thermal conductivity, high strength and elastic modulus. K B Kanchrela et al. [6] observed that the use of Yttria-stabilised zirconia (YSZ) nanoparticles improved some mechanical properties of glass fabric composites. Kaushal Kumar et al. [7] found that the use of TiO_2 nanoparticles in an epoxy composite increased its tensile strength. T S Muthu Kumar et al. [8] found an increase in the thermal stability and tensile strength of the polymer matrix composites due to the presence of small coffee bean powder. Taqui ur Rehman et al. [9] observed that the use of fillers SiO_2, TiO_2

and TiO_2@ SiO_2 as fillers in Zepoxy have minimal value LC (leakage current) and PD (partial discharge) for the best insulation performance. P Venkateshwar Reddy et al. [10] investigated the mechanical properties of a Prosopis juliflora fibre reinforced hybrid composite, which increased when using Al_2O_3 as filler material. Wei et al. [11] investigated that the addition of graphene nanoparticles at lower concentrations (0.3%) showed increased tensile strength (12.6%) and increased flexural strength (10%). Srivastava et al. [12] investigated composites with graphene at lower weight ratios and with high aspect ratios, which improved the tensile strength by almost 30%. It was concluded that the mechanical properties of composite material can be increased with the addition of fillers such as graphene. Nanocomposites with lower concentrations of ceramic nanoparticles have high thermal conductivity and lower electrical conductivity, which is useful for industrial insulation and electrical packaging. Unnikrishnan [13] investigated the low concentrated epoxy-based nanocomposites with thermoplastic and particulate fillers. The toughening process increased fracture toughness and impact resistance.

1.1. Composite Made of Natural Fibre/Filler

Natural fillers may be preferred when bio-composites are required, according to P K Jagadeesh et al. [14]. These composites are referred to as renewable and eco-friendly composites. Up to a certain weight percentage, natural fillers perform well, but if you add more, the qualities of composite materials may suffer. When combined with hydrophilic fibres and hydrophobic matrices, fillers improve adhesion behaviour. The fillers can be added following the demands of the material's qualities, but they are typically added following the type of composite application.

As a more environmentally friendly, biodegradable, and renewable resource than petroleum-based synthetic polymers, biopolymers were suggested by A. Vinod et al. [15]. However, compared to synthetic polymers, the mechanical properties of materials are unsatisfactory and need additional exploitation. These days, adding plasticisers, nanofillers, and coupling agents to biopolymers and biopolymer blends is one of several approaches for improving the properties and structural integrity. Commercially available biopolymers include TPS, PVA, PLA, PHBV, Chitosan, epoxidized plant oils, and polysaccharides. However, these materials have significant drawbacks, including gas permeability, moisture sensitivity, short shelf lives, low mechanical strength, and susceptibility to bacteria and fungi. This is because the structural and physical characteristics of biopolymers can be specifically tailored by using nanoparticles as fillers.

According to MR Sanjay et al. [16], natural fibre composites have similar tensile strength, impact strength, interlaminar shear strength, thermal, water absorption, and tribological properties to synthetic fibre composites. However, several factors affect the properties of composites, including the type of resin used, the origin of the fibre (fruit, stem, leaf, etc.), the type of reinforcement used (powder form, short fibre, continuous fibre), the fibre orientation (unidirectional or multi-directional), the manufacturing method used (hand layup, compression moulding, injection moulding, etc.), the crystallinity index and crystallite size of the fibre, the chemical functional groups present in the fibre, and volume and weight (raw or surface treated).

1.2. Significance of Nano Filler

Ganapathy et al. [17] filled the fibres made from the aerial roots of banyans with graphene. To create better epoxy composites, he described the appropriate ratio of graphene powder to banyan fibres. He noted that the unfilled epoxy composite had a flexural strength of 155.51 MPa and tensile strength of 27.93 MPa, while the strongest hybrid composites in terms of tensile strength (40.6 MPa) and flexural strength were those that contain 4% graphene (163.23 MPa).

The impact of Al_2O_3 nanofillers on the mechanical, wear, and hardness properties of basalt/epoxy laminate composites were discovered by Vinay et al. [18]. By using the hand layup process, composite laminates of basalt/epoxy with varying amounts of Al_2O_3

nanofillers were created. According to ASTM standards, mechanical properties such as tensile strength, interlaminar shear strength (ILSS), flexural strength, impact strength, and hardness were examined. Flexural strength and ILSS were shown to increase for small percentages of nanofillers, whereas tensile strength declined for larger percentages of fillers, and hardness increased for larger percentages of fillers. As the content of nanofillers increased, the wear rate gradually decreased.

Cissus quadrangularis stem fibre (CQSF)/epoxy resin particulate with and without coconut shell ash (CSA) powder underwent mechanical characterisation by Jenish et al. [19]. The hand lay-up method was used to build the base material from epoxy and 30 wt.% CQSF with 40 mm fibre length, and CSA was added separately at 2.5, 5, 7.5, and 10 wt.%. The tensile test SEM image of the CQSF/epoxy with 5 wt.% CSA filler composite showed less matrix breakage and fibre/matrix bonding, which boosted the tensile strength of the composite material. At 10 wt.% CSA, the impact strength (20.03 J/cm^2) and hardness (98 HRRW) values were greater in the CQSF/epoxy resin composite, indicating that impact and hardness steadily rise as CSA filler content rises.

In this paper, a lower concentration of the nanoparticles was maintained with 1 wt.% of epoxy in the case of graphene nanocomposites and 3 wt.% of epoxy in the case of ceramic nanocomposites. To evaluate the properties of the nanocomposites, vibration techniques (ASTM E1876-15) were conducted. The validation of the elastic properties such as Young's modulus, Shear modulus and Poisson's ratio was carried out by comparing the results obtained from the above two methods.

2. Materials and Methods

In this study, a thermoset type of polymer matrix material epoxy LY556 was used. Araldite hardener HY 917 was used as a curing agent. Graphene nanoparticles and stoichiometric spinel ($MgAl_2O_4$) precursor prepared by solid-state synthesis (0.4 wt.%) were used as reinforcement. Pure Isopropanol (2-Propanol), C_3H_8O, M.W 60.10 and Acetone extra pure AR grade, C_3H_8O and M.W 58.08 were used to ease the sonication process by the addition of a volatile liquid. The lower concentration of nanoparticles was maintained with 1 wt.% of epoxy in the case of graphene nanocomposites and 3 wt.% of epoxy in the case of ceramic nanocomposites. The flow chart for preparation of Epoxy/Graphene Composite is shown in Figure 1.

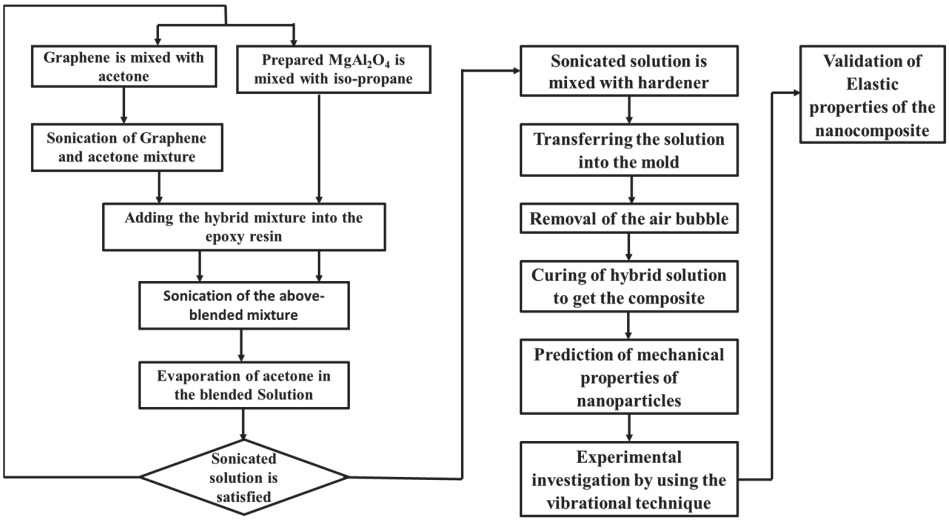

Figure 1. Flow Chart for preparation of Epoxy/Graphene Composite.

2.1. Sample Preparation of Graphene/Epoxy Nanocomposites

The epoxy composite samples mixed with epoxy resin LY556 were combined with hardener Araldite HY917 in a 10:1 ratio. The solution was manually stirred for 5 min and then poured into dies. To cure the samples, they were kept at 75 degrees for 1 h. The samples were machined according to the requirement of the testing apparatus. The graphene nanocomposites were prepared by a powder process. The sonication process was carried out while the samples were prepared to properly disperse the nanoparticles in the resin system. Failure to carry out the sonication process can severely affect the mechanical properties. The Sonication process was conducted in a sonicator with a titanium probe running at 1 Amp, 0.1 mV for 1 h. Sonicated solution was mixed with graphene nanoparticles manually. For preparing the sonicated solution, epoxy was heated and then mixed with a solution of acetone and graphene. Sonication was carried out in 3 intervals of 1 h. The solution was then kept in the oven to evaporate acetone from the solution. To prepare solid samples, the solution was mixed with hardener Araldite HY917 in a 10:1 ratio and then poured into the die for the curing process. The solidified samples were machined according to the requirement of the testing apparatus.

2.2. Sample Preparation of Ceramics/Epoxy Nanocomposites

The ceramic nanocomposites were prepared by the powder process. Sonicated solution was mixed with ceramic nanoparticles manually. For preparing the sonicated solution, epoxy was heated and then mixed with a solution of isopropanol and ceramic powder. Sonication was carried out for 30 min; the solution was then kept in the oven to evaporate isopropanol from the solution. To prepare solid samples, the solution was mixed with hardener Araldite HY917 in a 10:1 ratio and then poured into the die for the curing process. The solidified samples were machined according to the requirement of the testing apparatus. Figure 2 shows three different developed samples of pure Epoxy, Epoxy/Graphene and Epoxy/ceramic.

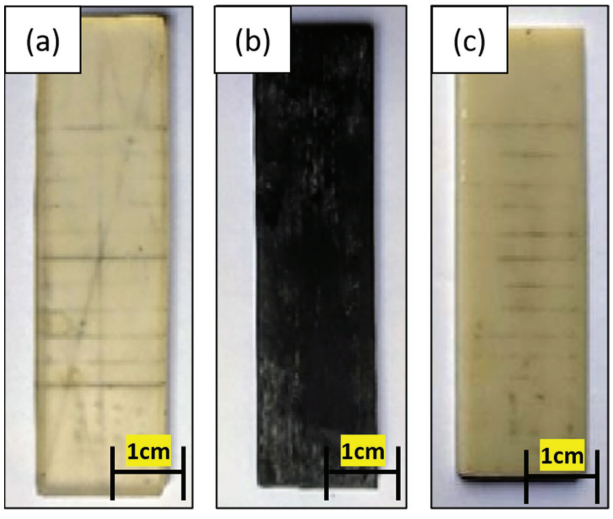

Figure 2. (**a**) Pure Epoxy sample (**b**) Epoxy/Graphene sample (**c**) Epoxy/ceramic sample.

3. Material Characterisation

Characterisation of materials was carried out to identify the mechanical properties of the nanocomposites. It helps in the proper evaluation of its capabilities. The three-point bending test and the Impact hammer test were conducted to evaluate the elastic properties.

3.1. Three-Point Bending Test-ASTM D7264

The three-point bending test (based on ASTM D7264) was conducted [20] using an Universal Testing Machine (Manufacturer INSTRON, Model 8801, Indian Institute of Technology, Dhanbad, India). The specimens were tested at room temperature under a uniform strain rate of 1 mm/min and the span to depth ratio was maintained to be greater than 16:1. The maximum flexure stress, maximum flexure extension and elastic modulus were obtained from the test as tabulated in Tables 1–3.

Table 1. Young's Modulus Values of Epoxy and Nanocomposites.

Sample	Epoxy (Mpa)	Graphene/Epoxy (Mpa)	Ceramic/Epoxy (Mpa)
1	4315.7	4470.9	4724.08
2	4685.9	5185.1	4866.4
3	4086.4	4361.5	-
Mean	4362.7	4672.5	4795.2

Table 2. Elastic properties of epoxy and Nanocomposites.

Elastic Properties	Epoxy	Graphene/Epoxy	Ceramic/Epoxy
Young's modulus (GPa)	3.99	4.156	4.34
Shear modulus (GPa)	1.511	1.6	1.72
Poisson's Ratio	0.320	0.298	0.261

Table 3. Epoxy sample readings at varying temperatures.

Elastic Properties	45 Degrees	60 Degrees	75 Degrees
Poisson ratio	0.205	0.166	0.161
Shear modulus (GPa)	1.41	1.2	1.073
Young's modulus (GPa)	3.4	2.8	2.492

3.2. Impact Hammer Test-ASTM E1876-15

To validate the improvements, we conducted impact hammer testing as used in [21] to explore the changes in elastic modulus along with damping characteristics. By measuring the resonant frequencies in a different configuration, Young's modulus, Shear modulus and Poisson's ratio were calculated using the ASTM E1876-15 [11]. The test samples were created according to the ASTM E1876-15, where B/t > 5 and L/t > 20 (B = breadth, L = Length & t = Thickness). The samples were placed on the specific fixtures and a contact accelerometer was placed to read the vibrations. The electrical signals were then transferred to software DeweSoft, (Version 2020, creator, Dewesoft, Indian Institute of Technology, Dhanbad, India) which converted them into vibrational signals to highlight the resonant frequency. Figure 3 shows the different positions of the testing fixture for evaluating elastic constants Young's and Shear moduli in bending and torsion modes of vibrations.

The Dynamic Young's modulus using standards.

$$E = 0.9465\left(\frac{mf_f^2}{b}\right)\left(\frac{L^3}{t^3}\right)T_1 \quad (1)$$

$$T_1 = \left[1.000 + 6.585\left(\frac{t}{L}\right)^2\right] \quad (2)$$

where: E = Dynamic Young's modulus, Pa; m = mass of the bar, g; b = width of the bar, mm; L = length of the bar, mm; t = thickness of the bar, mm; f_f = fundamental resonant frequency of bar in flexure, Hz; T_1 = correction factor for the fundamental flexural mode to account for the finite thickness of the bar.

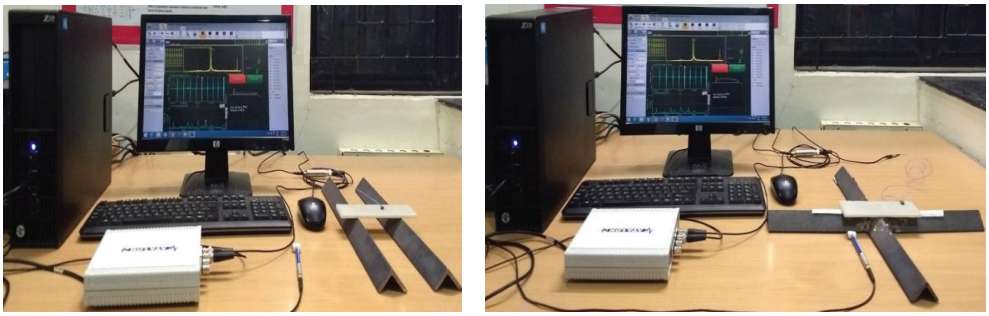

(**a**) (**b**)

Figure 3. (**a**) Out of Plane frequency. (**b**) Torsional frequency setup.

Dynamic shear modulus used formulas provided under ASTM standards.

$$G = \frac{4\,Lmf_t^2}{bt} R \tag{3}$$

$$R = \left[\frac{1+\left(\frac{b}{t}\right)^2}{4-2.521\frac{t}{b}\left(1-\frac{1.991}{e^{\pi\frac{b}{t}}+1}\right)}\right]\left[1+\frac{0.00851n^2b^2}{L^2}\right]-0.060\left(\frac{nb}{L}\right)^{\frac{3}{2}}\left(\frac{b}{t}-1\right)^2 \tag{4}$$

where G = Dynamic shear modulus, Pa; f_t = fundamental torsional resonant frequency of bar, Hz; n = the order of the resonance, here n = 1.

Poisson's ratio used formulas provided under ASTM standards.

$$\mu = \left(\frac{E}{2G}\right) - 1 \tag{5}$$

where μ = Poisson's ratio; E = Dynamic Young's Modulus. Pa; G = Dynamic Shear Modulus, Pa.

4. Results and Conclusions

The Young's modulus, Shear modulus and Poisson's ratios were calculated and tabulated after obtaining the resonant frequencies. The effect of the nanoparticles on the elastic properties has been discussed. There was an increase in Young's modulus due to the inclusion of nanoparticles in the matrix, as shown in Table 1 measured from UTM for Young's modulus, and Table 2 measured from vibration techniques for all the elastic constants. The inclusion of graphene nanoparticles showed an increase of 7.1%, while the inclusion of ceramic caused an increase of 10.4%.

Similar results to that of the three-point bending test were produced from the impact hammer test, with an error of about 8%. However, the values from this test are much more dependable as the number of iterations is more. The ceramic nanocomposites showed the highest improvement in Young's modulus (8%) and shear modulus (13%), while Graphene nanocomposites showed less of a decrease in Poisson's ratio due to lower brittleness.

4.1. Elastic Properties of Nanocomposites under Thermal Environment

To evaluate the thermal stability of the elastic properties, the entire set-up was transferred to an industrial oven. The temperature was increased slowly and the resonant frequencies were recorded. The elastic properties were then evaluated from the formulas provided in the ASTM standard. The trends of Young's modulus, Shear modulus and Poisson's Ratio is shown in Figure 4 and their corresponding values are given in Tables 4 and 5.

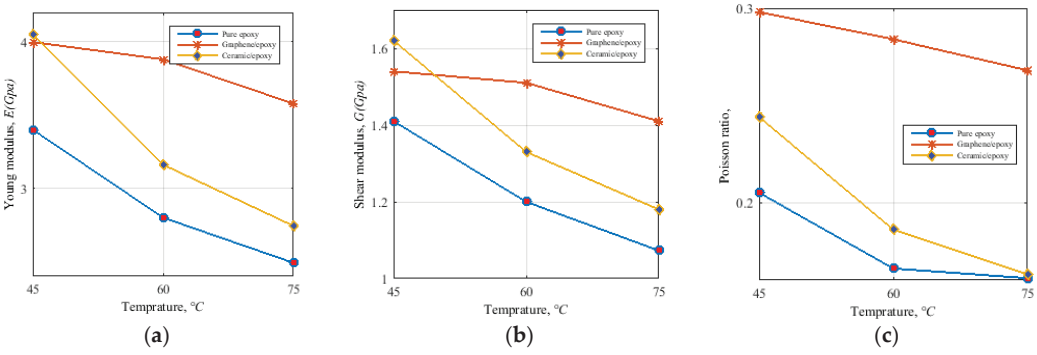

Figure 4. (**a**) Trends of Young's modulus (**b**) Trends of Shear modulus (**c**) Trends of Poisson's Ratio.

Table 4. Graphene/Epoxy sample reading at temperatures.

Elastic Properties	45 Degrees	60 Degrees	75 Degrees
Poisson ratio	0.298	0.284	0.268
Shear modulus (GPa)	1.54	1.51	1.41
Young's modulus (GPa)	3.998	3.880	3.578

Table 5. Ceramic/Epoxy sample reading at varying temperatures.

Elastic Properties	45 Degrees	60 Degrees	75 Degrees
Poisson ratio	0.244	0.186	0.163
Shear modulus (GPa)	1.62	1.33	1.18
Young's modulus (GPa)	4.053	3.161	2.744

The selected nanocomposites were tested up to 75 degrees, as the flash point for epoxy LY556 is 80 degrees. The inclusion of nanoparticles showed constantly better properties, even at elevated temperatures. The graphene nanoparticles showed the best performance under thermal conditions and, on average, lost 5% of their Young's modulus and a 4% decrease in Shear modulus. This is because graphene tends to disperse easily under high temperatures in a low viscosity system. Even though the ceramic lost up to 20% of its properties, its values were higher than that of pure epoxy composites.

4.2. Validation Conclusions

The investigation of elastic properties was carried out by performing a three-point bending test and an Impact hammer test. The results from the three-point bending test were investigated. There was an increase in Young's modulus with the addition of graphene nanoparticles (an increase of 7.1%), while the addition of ceramic nanoparticles showed an increase of 10.4%. Nanocomposites showed lower maximum flexural loads (7% decrease) as the addition of nanoparticles increases the brittleness of the composites. The graphene nanocomposites showed the lowest stress values (6% decreases) compared to that of pure epoxy composites. This is due to the dispersion of graphene in the epoxy matrix, forming a perfect continuous structure. The results from the Impact hammer test were investigated. The ceramic nanocomposites showed the highest improvement in Young's modulus (8%) and shear modulus (13%), while graphene nanocomposites showed less of a decrease in Poisson's ratio. This is because nanoparticles tend to disperse easily and form a continuous system in a low viscosity medium. The results from the three-point bending test and Impact hammer test were compared and given in Table 6.

Table 6. Comparison between Three-point bending and Vibrational hammer test.

Testing Method	Epoxy (GPa)	Graphene/Epoxy (GPa)	Ceramic/Epoxy (Gpa)
Three-point Bending test	4.36	4.67	4.79
Vibrational hammer test	3.99	4.15	4.34
Percentage difference (%)	9.2	12.5	10.4

There was a difference of 10%–12% between the final results but the impact hammer test was considered to be a more dependable test, as Young's modulus values after several iterations were found to be more consistent when compared to the three-point bending test results. As the Impact hammer test is non-destructive, a detailed analysis of elastic properties under varied thermal conditions was also possible. At elevated temperatures the graphene nanocomposites showed only a 5% decrease in Young's modulus and a 4% decrease in Shear modulus. Even though the ceramic lost up to 20% of its properties, its values were higher than that of pure epoxy composites. This is because graphene and ceramic nanoparticles tend to disperse easily under high temperatures in a low viscous system. Thus, the results show that the addition of nanoparticles to composites shows improvement in the mechanical and thermal stability of elastic properties. The Impact hammer vibration test can be carried out to efficiently investigate the elastic properties of the composites under varied thermal conditions.

5. Conclusions

Two different samples of nanocomposites have been developed with graphene/1 wt.% epoxy and ceramic/3 wt.% epoxy. The mechanical properties of the developed nanocomposites are compared in terms of young's modulus, shear modulus and Poisson's ratio at a temperature of 45 degrees, 60 degrees and 75 degrees. Further three-point bending tests and Impact hammer tests were carried out to compare the elastic properties of both the developed nanocomposites. The inclusion of graphene nanoparticles showed an increase of 7.1%, while the inclusion of ceramic caused an increase of 10.4%. At an increased temperature, the graphene nanoparticles showed the best performance under thermal conditions and, on average, lost 5% of their Young's modulus and there was a 4% decrease in Shear modulus, even though the ceramic lost up to 20% of its properties. The results from the three-point bending test shows lower maximum flexural loads (7% decrease), as the addition of nanoparticles increases the brittleness of the composites. The graphene nanocomposites showed the lowest stress values (6% decreases) compared to that of pure epoxy composites. The results from the Impact hammer test showed the highest improvement in Young's modulus (8%) and shear modulus (13%), while graphene nanocomposites showed less of a decrease in Poisson's ratio. There was a difference of 10%–12% between the final results of the three-point bending test and impact hammer test. However, the impact hammer test was considered to be a more dependable test, as Young's modulus values after several iterations were found to be more consistent when compared to the three-point bending test results.

Author Contributions: N.K., writing, investigation, conceptualization and software; A.B., data validation, formal analysis; A.K.D., supervision; A.K.S., review and editing. All authors have read and agreed to the published version of the manuscript.

Funding: This research received no external funding.

Institutional Review Board Statement: Not applicable.

Informed Consent Statement: Not applicable.

Data Availability Statement: Not applicable.

Conflicts of Interest: The authors declare no conflict of interest.

References

1. Amendola, E.; Scamardella, A.M.; Petrarca, C.; Acierno, D. Epoxy–Nanocomposites with Ceramic Reinforcement for Electrical Insulation. *J. Appl. Polym. Sci.* **2011**, *122*, 3686–3693. [CrossRef]
2. Srivastava, A.K.; Dixit, A.R.; Tiwari, S. A review on the intensification of metal matrix composites and its nonconventional machining. *Sci. Eng. Compos. Mater.* **2016**, *25*, 213–228. [CrossRef]
3. Srivastava, A.K.; Dixit, A.R.; Tiwari, S. Investigation of microstructural and mechanical properties of metal matrix composite A359/B4C through electromagnetic stir casting. *Indian J. Eng. Mater. Sci.* **2016**, *23*, 171–180.
4. Avila, A.F.; Duarte, H.V.; Donadon, L.V. Mechanical properties of nanocomposite laminated structure and its sensibility to modal analysis procedure. *Lat. Am. J. Solids Struct.* **2014**, *11*, 245–259.
5. Firsov, A.; Zhang, Y.; Novoselov, K.S.; Grigorieva, I.V.; Geim, A.K.; Jiang, D.; Morzov, S.V.; Jiang, D.; Zhang, Y.; Dubonos, S.V. Electric field effect in atomically thin carbon films. *Science* **2004**, *306*, 1095–9203.
6. Kanchrela, K.B.; Subbappa, D.B. Enhancing mechanical properties of glass fabric composite with surfactant treated Zirconia nanoparticle. *Compos. Part A* **2019**, *118*, 131–141. [CrossRef]
7. Kumar, K.; Ghosh, P.K.; Kumar, A. Improving mechanical and thermal properties of Tio_2 epoxy nanocomposite. *Compos. Part B Eng.* **2016**, *97*, 353–360. [CrossRef]
8. Kumar, T.S.M.; Rajini, N.; Huafeng, T.; Rajulu, A.V.; Ayrilmis, N.; Siengchin, S. Improved mechanical and thermal properties of spent coffee bean particulate reinforced poly composites. *Part. Sci. Technol.* **2019**, *37*, 643–650. [CrossRef]
9. Rahman, T.; Amin, S.; Shaukat, H.; Haroon, S.S.; Sajjad, I.A.; Awais, M. Effect of nano filler concentration on leakage current and partial discharge of zepoxy nano composite. *SN Appl. Sci.* **2019**, *1*, 1218. [CrossRef]
10. Reddy, P.V.; Prasad, P.R.; Krishnudu, D.M.; Hussain, P. Influence of fillers on mechanical properties of prosopis juliflora fiber reinforced hybrid composites. *Mater. Today Proc.* **2019**, *19*, 384–387. [CrossRef]
11. Wei, J.; Atif, R.; Inam, F. Graphene Nanoplatelets in Epoxy System: Dispersion, Reaggregation, and Mechanical Properties of Nanocomposites. *J. Nanomater.* **2015**, *16*, 374. [CrossRef]
12. Srivastava, A.K.; Sharma, B.; Saju, B.R.; Shukla, A.; Saxena, A.; Maurya, N.K. Effect of Graphene nanoparticles on microstructural and mechanical properties of aluminum based nanocomposites fabricated by stir casting. *World J. Eng.* **2020**, *17*, 859–866. [CrossRef]
13. Unnikrishnan, K.P.; Thachil, E.T. Toughening of epoxy resins. *J. Des. Monomers Polym.* **2012**, *9*, 129–152. [CrossRef]
14. Jagadeesh, P.; Girijappa, Y.G.T.; Puttegowda, M.; Sanjay, M.R.; Siengchin, S. Effect of natural filler materials on fiber reinforced hybrid polymer composites: An overview. *J. Nat. Fibers* **2020**. [CrossRef]
15. Vinod, A.; Sanjay, M.R.; Suchart, S.; Jyotishkumar, P. Renewable and sustainable biobased materials: An assessment on biofibers, biofilms, biopolymers and bio composites. *J. Clean. Prod.* **2020**, *258*, 120978. [CrossRef]
16. Sanjay, M.R.; Madhu, P.; Jawaid, M.; Senthamaraikannan, P.; Senthil, S.; Pradeep, S. Characterisation and Properties of Natural Fiber Polymer Composites: A comprehensive Review. *J. Clean. Prod.* **2018**, *172*, 566–581. [CrossRef]
17. Ganapathy, T.; Sathiskumar, R.; Sanjay, M.R.; Senthamaralikannan, P.; Sarvanakumar, S.S.; Parmeswaranpillai, J.; Siengchin, S. Effect of Graphene Powder on Banyan Aerial Root Fibers Reinforced Epoxy Composites. *J. Nat. Fibers* **2021**, *18*, 1029–1036. [CrossRef]
18. Vinay, S.S.; Sanjay, M.R.; Siengchin, S.; Venkatesh, C.V. Effect of Al2O3 nanofillers in basalt/epoxy composites: Mechanical and tribological properties. *Polym. Compos.* **2020**, *42*, 1727–1740. [CrossRef]
19. Jenish, I.; Chinnasamy, S.G.V.; Basavarajappa, S.; Indran, S.; Divya, D.; Liu, Y.; Sanjay, M.R.; Siengchin, S. Tribo-Mechanical characterisation of carbonised coconut shell micro particle reinforced with Cissus quadrangularis stem fiber/epoxy novel composite for structural application. *J. Nat. Fibers* **2022**, *19*, 2963–2979. [CrossRef]
20. *ASTM D7264/D7264M-15*; Standard Test Method for Flexural Properties of Polymer Matrix Composite Materials. ASTM International: West Conshohocken, PA, USA, 2015.
21. *ASTM E1876-15*; Standard Test Method for Dynamic Young's Modulus, Shear Modulus, and Poisson's Ratio by Impulse Excitation of Vibration. ASTM International: West Conshohocken, PA, USA, 2022.

coatings

MDPI

Article

Tribological Characteristics of Al359/Si3N4/Eggshell Surface Composite Produced by Friction Stir Processing

Ashish Kumar Srivastava [1], Suryank Dwivedi [2], Ambuj Saxena [1], Deepak Kumar [2], Amit Rai Dixit [2,*], Gyanendra Kumar Singh [3], Javed Khan Bhutto [4] and Rajesh Verma [4]

[1] Department of Mechanical Engineering, G.L. Bajaj Institute of Technology and Management, Greater Noida 201306, Uttar Pradesh, India
[2] Department of Mechanical Engineering, Indian Institute of Technology (ISM), Dhanbad 826004, Jharkhand, India
[3] Department of Mechanical Engineering, School of Mechanical, Chemical and Materials Engineering, Adama Science and Technology University, Adama P.O. Box 1888, Ethiopia
[4] Department of Electrical Engineering, College of Engineering, King Khalid University, Abha 61421, Saudi Arabia
* Correspondence: amitraidixit@iitism.ac.in

Abstract: In the present study, the surface composite Al359/Si3N4/Eggshell is prepared by friction stir processing (FSP). The effect of reinforced particle volume fraction on the microstructural and tribological properties of the Al359/Si3N4/Eggshell surface composites was investigated and compared with the friction stir processed (FSPed) Al359 alloy. The microstructural properties were further investigated by light microscopy, FESEM, and EDS mapping. The tribological properties of the developed composite and FSPed Al359 were investigated using a reciprocating ball-on-plate universal tribometer. The microstructural results showed that defect-free composite surfaces are produced due to improved physical properties, severe plastic deformation, and better grain refinement. Moreover, the mean value of the friction coefficient (μ) for the developed composite and FSPed alloy are 0.36 μ and 0.47 μ, respectively. The obtained results indicated that Si_3N_4/Eggshell is a promising reinforced particle for improving microstructural and tribological performance in journal bearing, rotors, and machinery applications.

Keywords: Al359 alloy; friction stir processing; friction and wear; Si_3N_4; eggshell waste; composite structure

Citation: Srivastava, A.K.; Dwivedi, S.; Saxena, A.; Kumar, D.; Dixit, A.R.; Singh, G.K.; Bhutto, J.K.; Verma, R. Tribological Characteristics of Al359/Si3N4/Eggshell Surface Composite Produced by Friction Stir Processing. *Coatings* **2022**, *12*, 1362. https://doi.org/10.3390/coatings12091362

Academic Editor: Jinyang Xu

Received: 11 August 2022
Accepted: 14 September 2022
Published: 18 September 2022

1. Introduction

In the past decade, researchers and modern industries have been continuously finding new quality materials that are lightweight, dimensionally accurate, have a high-quality surface finish, a high production rate, are cost-effective to produce, and are environment friendly [1–4]. For these reasons, aluminium alloys and their composites are the primary preference for the aerospace and automotive industries due to their lightweight, good mechanical, and tribological properties [5]. However, the need for specific engineering materials for specific engineering applications is still open to investigation. Aluminium metal matrix composites (AMMCs) have been developed as advanced engineering materials for weight-saving applications in both industries. AMMCs exhibit an excellent combination of high specific strength, hardness, and better wear resistance for various applications. Moreover, the enhancement of all desired properties, such as physical and mechanical, depends on reinforcement/particulates and microstructure [6]. Several researchers have experimented with using different reinforcement particles (SiC, Al_2O_3, B_4C, Gr, TiC, Si_3N_4, and TiB_2, etc.). Si_3N_4 is considered a standout reinforcement and one of the most promising ceramics because of its high levels of hardness. It also has other extraordinary characteristics, such as low density, high melting point, high thermal stability, and good chemical

stability [7]. Si_3N_4 also has excellent ballistic and mechanical properties, making it a desirable material for several defence applications [8]. Waste eggshell is a new engineering reinforcement, containing around 95% calcium carbonate ($CaCO_3$), 3% phosphorus, and signs of magnesium, zinc, sodium, potassium, iron, and copper [9,10]. It can be used as a bio-waste material to meet the different requirements of modern products, and also to create new value. It is an inexpensive reinforcement material with excellent properties, such as low density, hardness, compressive strength, high thermal stability, and it is renewable [11]. These mechanical properties qualify it as an excellent candidate to reinforce aluminium and its alloys, usually used in the automobile industry [12]. Kumar et al. examined the effect of different reinforcement microparticles (SiC, Al_2O_3, and Ti) with the addition of waste carbonized eggshell powder. Ti/eggshell base reinforcement in AMMCs obtained an excellent hardness compared to the other reinforcement particles [13]. However, other reinforced composites possess good hardness compared with the base material. The addition of commonly used reinforced particles, such as SiC, Al_2O_3, and B_4C, in the metal matrix improves tensile strength, yield strength, and hardness, but reduces ductility.

Both phase fabrication methods, such as liquid and solid phases, have been successfully used to make the desired composite. Several studies presented the enhancement of the specific mechanical properties and modified the microstructure of the matrix material. However, liquid state processing presents major drawbacks, such as porosity, solute redistribution, and solidification cracking [12–14]. High temperature is required for solid-to-liquid and vapour phase changing processes, but the reverse process (liquid-to-solid phase) reduces some of the special properties of the composites. Several research studies have found that friction stir processing (FSP) is a suitable process for fabricating composites that work in the solid-to-solid state phase, thus eliminating these drawbacks [15,16].

FSP is a technique that has become very popular in recent decades. FSP is a versatile method of solid-state processing, and it is an energy efficient technique that results in no residual stresses that refine the microstructure, densification, and homogeneity of the structure [17,18]. Figure 1a shows the schematic arrangement of FSP. In this process, the matrix material is processed by a non-consumable tool with a shoulder-pin arrangement that rotates at high speed. The friction between the tool and matrix material generates sufficient heat. The tool traverses to cover up the desired area and is stirred by the tool shoulder-pin arrangement in the coverage area. Due to the stirring of the material, severe plastic deformation occurs, which causes refined microstructure, densification, and homogeneity in the formed composites [19,20]. The process parameters can directly control the advantage of FSP on mechanical and microstructural properties. Thus, FSP has manifested a similar or better tribological performance than other conventional processes [21,22].

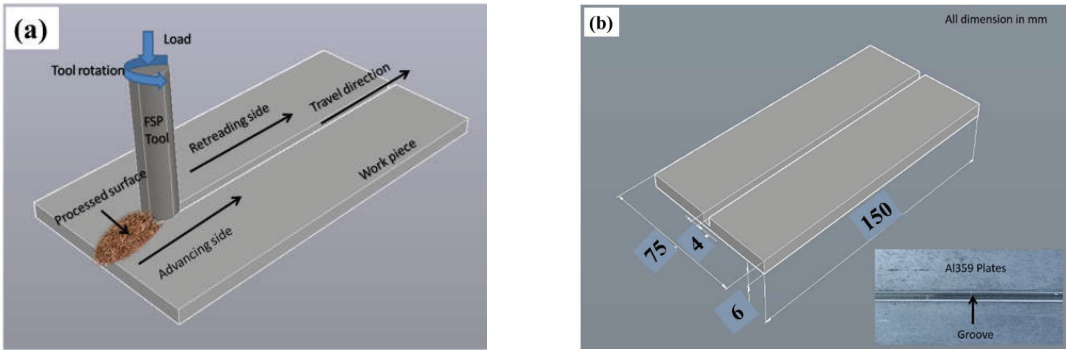

Figure 1. Schematic arrangement of the (**a**) friction stir processing and (**b**) aluminium alloy AL359 plate.

The focus of the present research is placed on tribological characteristics. Generally, composites demonstrate a high friction coefficient in the range of 0.5–0.8, except for those that slide in water or under other lubricants. In the present work, a vertical milling machine

is used to produce the surface composites. Al359 aluminium alloy was used as a matrix material, while Si_3N_4 and waste eggshell powder was used as reinforcement materials (6% by volume). The tribological tests are carried out to test the frictional properties of Al-6% Si_3N_4/Eggshell composites. The microstructural study was done with the help of light microscopy, FE-SEM equipped with EDS mapping.

2. Experimental Procedure

Commercially available Al359 aluminium alloy was used as a matrix material. It is a suitable material in applications including aerospace, automotive, and for highly stressed parts (gears, fuse parts, and structural components). Al359 plates were purchased with a dimension of 75 mm× 150 mm× 6 mm, as shown in Figure 1b. Before FSP, a square groove was cut transversely from the middle according to the 6% reinforcement volume. Si_3N_4 and ball-milled carbonized eggshell powder, each of 3% volume, were selected as the primary and secondary reinforcement. Figure 2a shows the Si_3N_4 particle size varying between 5 μm to 80 μm with an average diameter of 18 μm.

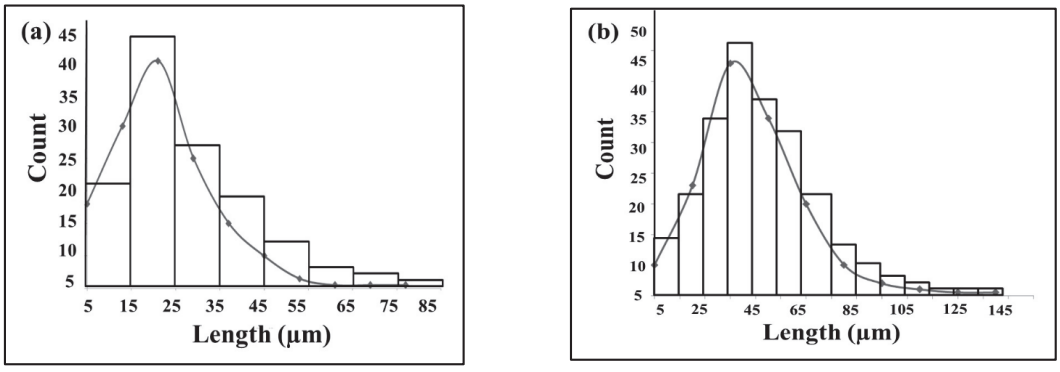

Figure 2. The particle size distribution of (**a**) Si3N4 particles and (**b**) eggshell particles.

Waste eggshells were collected from local shops to prepare the carbonized eggshell. They were cleaned to remove any dust and egg liquid. Next, they were solar-dried for 48 h to remove the moisture. Dry eggshells were preheated to a temperature of 1000 °C for 1 h. Carbonized eggshells were ball milled to obtain a fine powder. The obtained powder was passed through multiple sieves of the required size to ensure that particles in the correct range were obtained [23]. Figure 2b showed the eggshell particle size varying between 5 μm to 140 μm with an average diameter of 33 μm. Previous research and lab experimentations have found that the process parameters of FSP affect the mechanical and physical properties of the developed composites. Parameters, such as rotational tool speed, traverse speed, tilt angle, and axial force, can improve the properties of the composites. The preferred process parameters for fabricating Al359/Si_3N_4/Eggshell surface composites are given in Table 1, and are based on the pilot experiments and the authors' own previous published literature.

Table 1. Process parameters used in the fabrication of Al359/Si_3N_4/Eggshell surface composites.

Process Parameters	Values
Rotational speed (rpm)	2250
Transverse speed (mm/min)	25
Tool Tilt angle (°)	2
Shoulder diameter (mm)	18
Axial Pressure (kN)	8
Pin profile of the tool	Triangular
Pin length (mm)	4
Pin edges (mm)	4

A non-consumable HSS tool with a shoulder diameter of shoulder 18 mm, shoulder length of 70 mm, and a triangular profile pin with 4 mm edges were prepared as shown in Figure 3. To make the homogeneous mixture, 3% of both types of reinforcements were chosen and mixed manually after preheating to 350 °C. The homogeneous preheated mixture of Si_3N_4/Eggshell powder (6% by volume) was filled into the square groove (dimensions are decided based on the 6% volume of reinforcement material) made on the top surface of the base plate. A pin-less HSS tool was used to cover the reinforcement powder to prevent it from spurting out of the track during the FSP processing. Then the primary FSP process was carried out using a vertical milling machine at room temperature, and within the process parameters described in Table 1, and with 6% volume of the reinforcement material. Figure 4 shows Al359/Si_3N_4/Eggshell surface composite after the FSP.

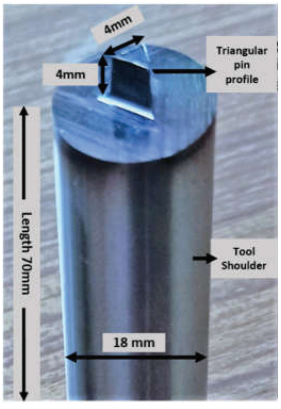

Figure 3. Photographic view of the HSS tool used in the experiment.

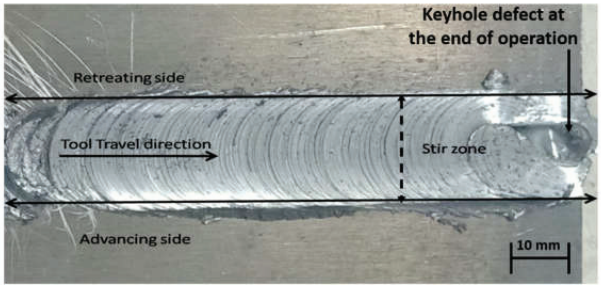

Figure 4. Photographic view of Al359/Si_3N_4/Eggshell surface composite after FSP.

The friction stir processed (FSPed) samples were cut using the Wire-EDM (CNC wire-cut electric discharge machine manufactured by Electronica Machine Tool Ltd, IIT ISM

Dhanbad, India) and polished in the YZ plane using SiC paper of grit size 600 grade (230 × 280 mm) to remove uneven surfaces.

For the microstructural study, rectangular cross-section of the specimens was obtained as per the ASTM-E3 standard. Further, it was polished with diamond paste and etched in a solution of Keller's reagent (15 mL HCL + 25 mL HNO_3 + 10 mL HF + 50 mL H_2O). The microstructure of the specimens was studied through inverted light microscope (manufacturer Leica- model- DMI3000 M, IIT ISM Dhnabad, India) and FE-SEM (Jeol jsm-7800 prime field emission scanning electron microscopy) coupled with an EDS detector (LN_2 Free SDD X-max 80 energy dispersive detector). The sliding wear behaviour of the FSPed Al359/Si_3N_4/Eggshell sample and FSPed Al359 without any reinforcement were studied using a reciprocating-type ball-on-plate universal tribometer (MFT 5000, Rtec instruments, USA). The 2D schematic of the used tribometer setup is depicted in Figure 5. Before the tribological analysis, specimens were prepared as per the ASTM G99 standard procedures. The samples were cut and cleaned in isopropyl alcohol solution for 10 min, followed by deionized water. The ultrasonically cleaned samples were dried in a furnace at 100 °C to remove the moisture from the samples' surface. The reciprocating-type ball-on-plate wear mode was set to perform the tribological analysis, and a stainless steel ball (6 mm diameter) was used as a counter body. Thus, a sliding pair of Al359/Si_3N_4/Eggshell and a stainless steel 316 ball worked as a working pair. During the sliding wear tests, a 2 Hz frequency was set to achieve the sliding velocity of 10 mm/s. A 15 N load and 5 mm stroke length were applied for the test duration of 10 min. The average coefficient of friction (COF) and frictional force (F_x) for the Al359/Si_3N_4/Eggshell composite sample was obtained as per the ASTM standard G115 for the sliding wear test. Thereafter, to remove worn-out debris, the samples were ultrasonically cleaned and dried in the furnace (Stericox, India) at 100 °C temperature for 30 min. Further, the 3D images of the worn samples were captured and studied in detail to study the wear mechanism.

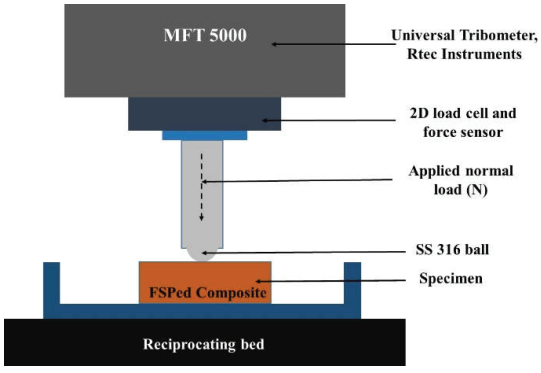

Figure 5. 2D Schematic arrangement of the ball-on-plate tribometer for the friction and wear test of Al359/Si_3N_4/Eggshell sample against the SS316 steel ball.

3. Results and Discussion

The microstructures of the FSPed specimen were observed using light microscopy, as shown in Figure 6a,b taken at two different locations (a) stir zone (SZ) (b) thermomechanical affected zone (TMAZ). The matrix phase of the alloy is shown by the brighter regions, and the reinforcement phase is shown by the darker regions in the micrograph. From Figure 6, it can be seen that reinforced particles are dispersed homogeneously with a minor porosity due to the high tool rotation. Moreover, the distribution of the reinforced particles is more homogeneous with the reduced density, which decreases the porosity in the sample. When compared to the base alloy, the larger grains break into smaller sized grains with the increased number of the grain boundary. The result shows that the FSPed zone produces a

defect-free composite that can offer excellent mechanical, physical, and plastic deformation and better grain refinement.

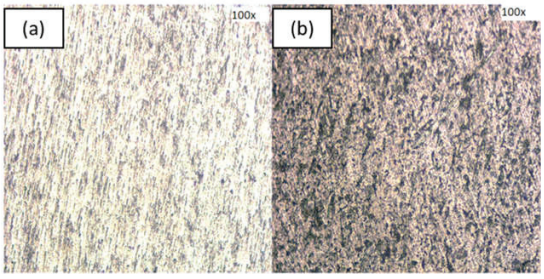

Figure 6. Optical photomicrograph of Al359/Si3N4/Eggshell surface composites. (**a**) stir zone (SZ) (**b**) thermomechanical affected zone (TMAZ).

Morphological studies of the FSPed sample were done using FESEM, which was coupled with EDS mapping. This was used to produce a detailed study of the microstructure, plastic deformation, grain refinement, and chemical composition of the composite. The SEM micrograph of the FSPed composite at different magnifications and different locations of stir zone at 10 μm, TMAZ location at 1 μm and 10 μm) is presented in Figure 7a–d, respectively. The obtained micrograph depicted the severe plastic deformation of the base alloy and the presence of a reinforcement phase in the stir zone region and TMAZ. A fine-grained structure with a large number of grain boundaries was formed, which is attributed to the dynamic recrystallization during the FSP process. The optimized parameters were used to produce the equiaxed and refined grain structure, which highlights the capability of FSP processing. It is revealed from the FESEM images that a uniform distribution of the Si_3N_4/Eggshell reinforced particles was obtained. The desired composites, consisting of matrix material and reinforced particles, have fine and smooth surfaces caused by the FSP with proper shoulder design. However, few defects, such as clustering of the reinforcement phase and micro-pores, can be seen in the micrographs. These defects can be considered negligible due to the enhanced microstructural features. The chemical composition of the Al359/Si_3N_4/Eggshell developed surface composites is presented in Figure 8a,b.

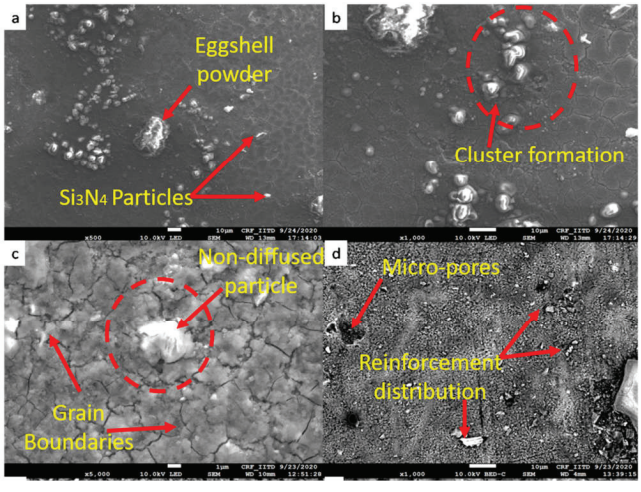

Figure 7. FE-SEM micrograph of Al359/Si_3N_4/Eggshell surface composites. (**a**) stir zone location 1 at 10 μm; (**b**) stir zone location 2 at 10 μm (**c**) TMAZ location 1 μm (**d**) TMAZ location 10 μm.

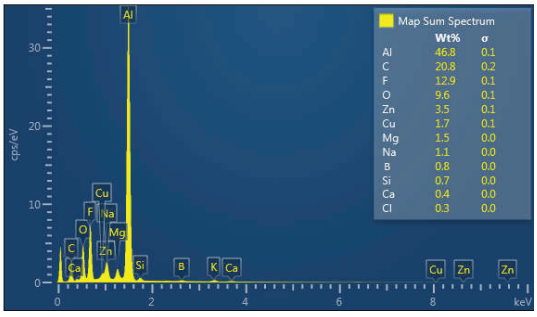

(**a**)

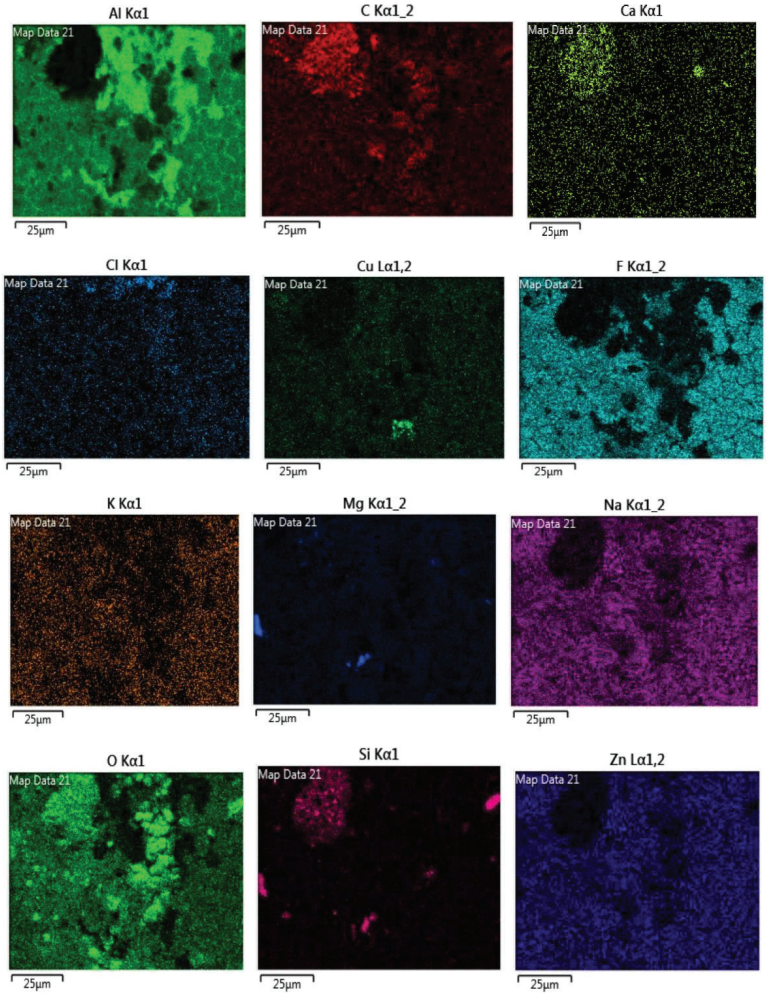

(**b**)

Figure 8. (**a**) EDS spectrum of Al359/Si_3N_4/Eggshell surface composites. (**b**) EDS phase mapping of Al359/Si_3N_4/Eggshell surface composites.

Figure 8a shows the EDS spectrum and Figure 8b shows the element mapping of the composition of surface composite Al359/Si_3N_4/Eggshell. The EDS spectrum of all the major constituents of the developed composite, such as Al, Si, and Ca, can be seen in the elemental list along with their significant weight percentage. The small contribution of other constituents of base alloy Al359, such as Zn, Cu, and Mg, are also present in the selected phase of the EDS mapping. It is evident from Figure 8b that the major elements of Al359/Si_3N_4/Eggshell surface composite, such as Zn, Cu, Mg, and Ca, are completely diffused with the Al matrix material. This is because, during the FSP, the frictional heat plastically deformed the aluminium matrix material below its melting temperature, resulting in a softening of the matrix. In this region, it can be concluded that proper wettability formed between the reinforced particles and matrix material. However, the Si phase is seen in low density. This is attributed to the fact that the Si_3N_4 particles are not completely diffused into the matrix material due to their low density and high melting temperature. Some other elements, i.e., carbon, oxygen, and fluorine, also showed they can exist in the matrix material due to chemical and metallurgical reactions during the preparation of the composites by FSP.

Further, the sliding wear test was carried out using the ball-on-plate reciprocating-type universal tribometer. During the test, a constant normal load of 15 N and sliding speed of 10 mm/s were used to evaluate the friction and wear performance of the developed surface composites. A frictional force (F_x) and normal force (F_z) were measured during the test run. The 2D load cell was used to maintain the normal force (F_z) of 15 N $\pm$ 1 N during the test, which can be seen in Figure 9. Furthermore, a coefficient of friction (COF) value was calculated as a function of time from the force data set and presented in Figure 10.

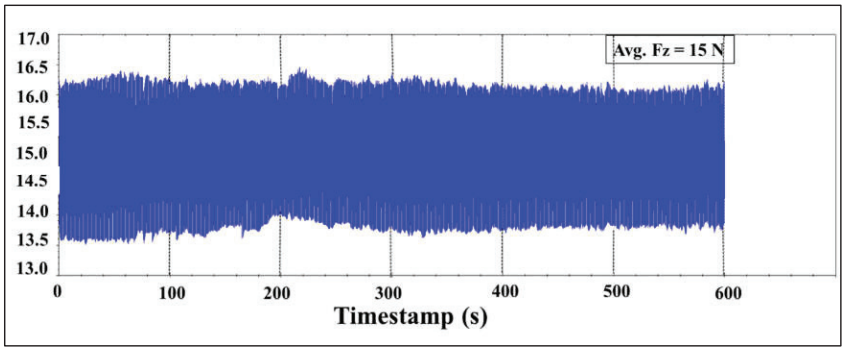

Figure 9. Generation of normal force (F_z) graph for Al359/Si_3N_4/Eggshell surface composites.

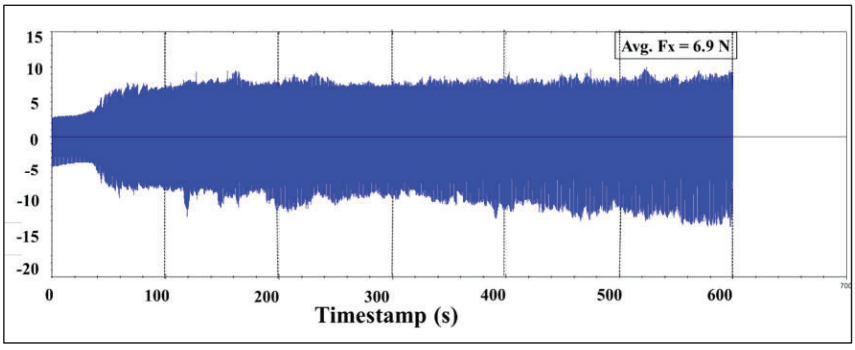

Figure 10. Generation of the friction force (F_x) graph for Al359/Si_3N_4/Eggshell surface composites.

Figure 9 highlights the generation of the frictional force (F_x) value for the composite surface. At the beginning of the process, the generation of the frictional force value is low, but later on it increases and stabilizes (Figure 10). The average F_x value for the composite surface is 6.9 N. Further, Figure 11 depicts the COF (μ) values for both the FSPed Al359 without reinforcement and Al359/Si_3N_4/Eggshell surface composite. During the test, the COF value for the surface composite steadily increased during the first 80 s, and then continued to rise until approximately 170 s, where it reached roughly 0.42 μ. Afterwards, the COF value was reduced and stabilized at 0.39 μ. The mean value of the COF for the produced composite was 0.37. Furthermore, for the FSPed Al359 without reinforcement, the COF increases at a higher rate than the composite surface, and attains an average COF value of 0.48 μ (Figure 11), which dictates the poor tribological performance of the FSPed material. The tribological results show that the COF value for the surface composite is 23% lower than the FSPed Al359 without reinforcement. Moreover, the variation in friction coefficient with time was observed for the FSPed sample, with greater variation during the first 80 s, influenced by the "stick-slip" phenomena. This effect can occur when objects are analysed while in the dynamic contact between two surfaces, resulting in a spontaneous jerking motion and unstable movement along the sliding track. However, during the dynamic contact, a significant increase in the friction force and friction coefficient was observed due to the unevenness that comes from the developed surface material and the counter body (SS316L ball). This unevenness causes a specific roughness value, piloting to an insignificant contact surface between the ball and the plate, which leads to the separation of the soft particle from the mating surface. However, it should also be noted that the decrease in friction coefficient is mainly caused by a growth of an adhesion layer of the reinforced particles, and due to the formation of the uniform fine grain structure in the stir zone.

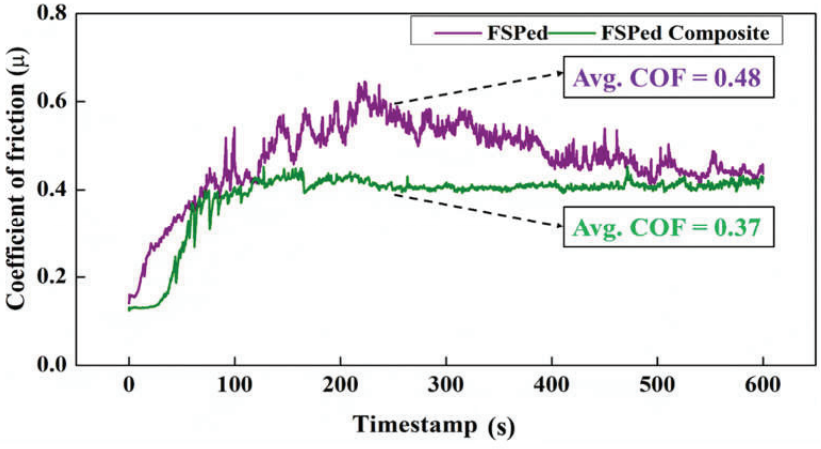

Figure 11. Generation of COF with sliding time for FSPed and Al359/Si_3N_4/Eggshell surface composites.

The EDX (Figure 8a) and elemental mapping (Figure 8b) results show the presence of oxygen and carbon elements that dictate the presence of oxides and carbides over the composite surfaces. The modified elemental composition helps to increase the hardness of the prepared surface composite [24]. However, according to the Pascal Law, it is known that the wear resistance property is directly proportional to the hardness value of that sample [25]. The increased surface hardness leads to improved tribological performance, as can be seen in Figure 11. Therefore, the obtained results help to understand the tribological performance of the composite surfaces and presents the relationship between the mechanical, microstructural, and tribological performance of the Al359/Si_3N_4/Eggshell composite and FSPed Al359 alloy.

Figure 12a–d shows the 3D images of the tribological wear track on Al359/Si_3N_4/Eggshell surface composites during the reciprocating ball-on-plate test. The worn-out depth profile was captured, as per the given ASTM standard G133-05. The 3D profiles were captured at five different locations to study the generation of the wear depth. During the wear test, the applied normal force (15 N) ensured continuous contact between the mating surfaces, thus producing friction and leading to the generation of the wear-out profiles. Figure 12a shows the lack of uniformity of the wear track due to increased amplitude values, which refers to an increase in volatility during the initial timestamp. A tribolayer is formed with a discontinuous layer, with a small amount of debris and material ruptures because these particles have mechanically adhered to the surface. Figure 12b shows the formation of a continuous layer due to the rapid growth of the temperature in the contact area. Both friction forces and temperature conditions favour the Al alloy's adhesive phenomena to reinforcement material. Figure 12c shows the adhered layered became unstable and possibly detached due to the reaction of friction forces on the wear surface. Figure 12d reveals the continuous layer and the dynamic behaviours of the adhesion wear mechanism.

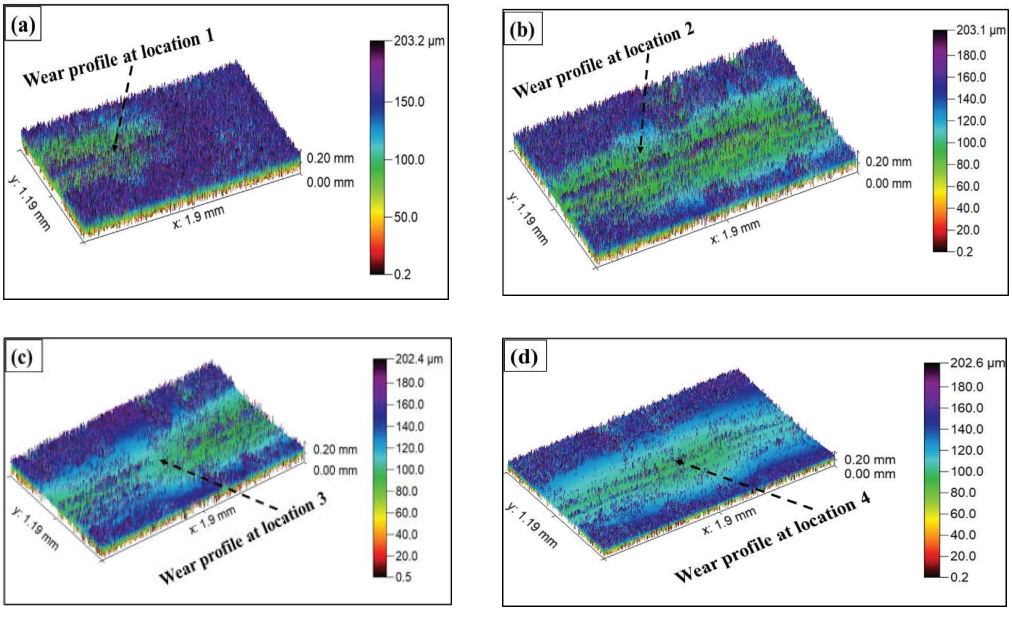

Figure 12. 3D image of the tribological wear track on FSPed composites during the ball-on-plate wear test as per the ASTM standard G133-05 at five different locations. (**a**) location 1; (**b**) Location 2 (**c**) Location 3 (**d**) Location 4.

The red colours in Figure 13 shows the formed valley in the wear track. The reinforced (Si_3N_4/Eggshell) particles are adhered by the Al alloy layer's wear, which accelerates the worn particles over the surface. Due to this impact, debris from Al alloy and reinforced particles (hard particles) is again deposited on the wear track and produces improved frictional properties. In recent years, individually customized products have gained favour, and the design of suitable composite materials has become more flexible for various applications, such as aerospace and automobiles. The results show that friction stir processing can be a promising approach for producing such components using Al359/Si_3N_4/Eggshell composites with improved physical properties.

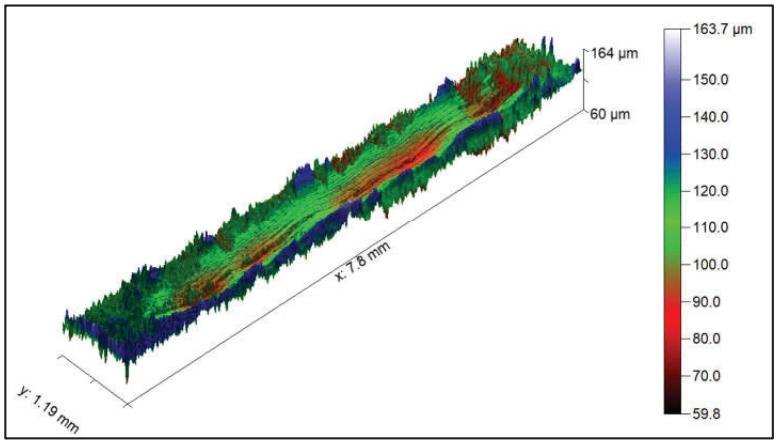

Figure 13. 3D image of the tribological wear track on FSPed composites during the reciprocation ball-on-plate wear test.

4. Conclusions

In this study, an Al359/Si_3N_4/Eggshell surface composite was fabricated by friction stir processing at room temperature. The microstructural results confirm the uniform and homogeneous distribution of Si_3N_4/Eggshell throughout the stir zone. The FESEM images show that the FSPed region has refined grains and a large number of grain boundaries due to severe plastic deformation, leading to better tribological properties. The tribological study reveals that the mean friction coefficient values for the FSPed Al359 without reinforcement and Al359/Si_3N_4/Eggshell surface composite specimens are 0.48 µ and 0.37 µ, respectively, which proves the improved frictional properties of the composite surface. The tribological results show that the COF value for the surface composite is 23% lower than that of FSPed Al359 without reinforcement. In addition to being a replacement for surface modification, the surface composite may be used to improve friction performance above and beyond traditional surface modification techniques. The obtained results indicate that Si_3N_4/Eggshell is a promising reinforced particle for the improvement of microstructural and tribological performance in journal bearing, rotors, and machinery applications.

Author Contributions: Conceptualization, A.K.S., and S.D.; methodology, S.D., A.S.; software, A.S., D.K.; validation, A.R.D., A.K.S., and G.K.S.; formal analysis, A.K.S., and S.D.; writing—A.K.S., and S.D., supervision, A.R.D.; funding acquisition, J.K.B. and R.V. All authors have read and agreed to the published version of the manuscript.

Funding: This research was funded by Javed Khan Bhutto and Rajesh Verma, grant number RGP 2/91/43. The APC was funded by [King Khalid University, Saudi Arabia].

Institutional Review Board Statement: Not applicable.

Informed Consent Statement: Not applicable.

Data Availability Statement: Not applicable.

Acknowledgments: The authors extend their appreciation to the Deanship of Scientific Research at King Khalid University, Saudi Arabia, for funding this work through the Research Group Program under Grant No: RGP 2/91/43.

Conflicts of Interest: The authors declare no conflict of interest.

References

1. Srivastava, A.K.; Dixit, A.R.; Maurya, M.; Saxena, A.; Maurya, N.K.; Dwivedi, S.P.; Bajaj, R. 20th century uninterrupted growth in friction stir processing of lightweight composites and alloys. *Mater. Chem. Phys.* **2021**, *266*, 124572. [CrossRef]
2. Dwivedi, R.; Srivastava, A.K.; Singh, R.K. Effect of eggshell waste and B4C particles on the mechanical and tribological properties of Al7075 alloy developed by friction stir processing. *Metall. Res. Technol.* **2022**, *119*, 508. [CrossRef]
3. Dwivedi, R.; Singh, R.K.; Kumar, S.; Srivastva, A.K. Parametric optimization of process parameters during the friction stir processing of Al7075/SiC/waste eggshell surface composite. *Mater. Today Proc.* **2021**, *47*, 3884–3890. [CrossRef]
4. Srivastava, A.K.; Kumar, N.; Dixit, A.R. Friction stir additive manufacturing–An innovative tool to enhance mechanical and microstructural properties. *Mater. Sci. Eng. B* **2021**, *263*, 114832. [CrossRef]
5. Rajawat, M.S.; Pagrut, S.; Dwivedi, S.; Raj, R.; Dixit, A.R. Microstructural characterization of Friction stir assisted laminated lap welding of AA6063 sheets. *Mater. Today Proc.* **2022**, *56*, 949–953. [CrossRef]
6. Kurt, A.; Uygur, I.; Cete, E. Surface modification of aluminium by fraction stir processing. *J. Mater. Process. Technol.* **2011**, *211*, 313–317. [CrossRef]
7. Srivastava, A.K.; Maura, N.K. Experimental investigation of A359/Si_3N_4 surface composite produced by multi-pass friction stir processing. *Mater. Chem. Phys.* **2021**, *257*, 123717. [CrossRef]
8. Srivastava, A.K.; Maurya, M.; Saxena, A.; Maurya, N.K.; Dwivedi, S.P.; Dixit, A.R. Microstructural and fractographic analysis of A359/Si3N4 surface composite produced by friction stir processing. *Int. J. Mater. Res.* **2021**, *112*, 68–77. [CrossRef]
9. Srivastava, A.K.; Saxena, A.; Dixit, A.R. Investigation on the thermal behaviour of AZ31B/waste eggshell surface composites produced by friction stir processing. *Compos. Commun.* **2021**, *28*, 100912. [CrossRef]
10. Srivastava, A.K.; Kumar, N.; Saxena, A.; Tiwari, S. Effect of friction stir processing on microstructural and mechanical properties of lightweight composites and cast metal alloys—A review. *Int. J. Cast Met. Res.* **2021**, *34*, 169–195. [CrossRef]
11. Bahrami, A.; Soltani, N.; Pech-Canul, M.I.; Gutiérrez, C.A. Development of metal matrix composites from industrial/agricultural waste materials and their derivatives. *Crit. Rev. Environ. Sci. Technol.* **2016**, *46*, 143–208. [CrossRef]
12. Dwivedi, R.; Kumar Singh, R.; Kumar Srivastava, A.; Anand, A.; Kumar, S.; Pal, A. Statistical optimization of process parameters during the friction stir processing of Al7075/Al2O3/waste eggshell surface composite. In *Recent Trends in Industrial and Production Engineering*; Springer: Singapore, 2021; pp. 107–118. [CrossRef]
13. Kumar, S.; Srivastava, A.K.; Singh, R.K. Fabrication of AA7075 Hybrid Green Metal Matrix Composites by Friction Stir Processing Technique. *Ann. Chim. Sci. Matériaux* **2020**, *44*, 295–300. [CrossRef]
14. Yuvaraj, N.; Aravindan, S. Fabrication of Al5083/B_4C surface composite by friction stir processing and its tribological characterization. *J. Mater. Res. Technol.* **2015**, *4*, 398–410. [CrossRef]
15. Karpasand, F.; Abbasi, A.; Ardestani, M. Effect of amount of TiB_2 and B_4C particles on tribological behaviour of Al7077/TiB_2/B_4C mono and hybrid surface composites produced by friction stir processing. *Surf. Coat. Technol.* **2020**, *390*, 125680. [CrossRef]
16. Kumar, S.; Srivastava, A.K.; Singh, R.K.; Dwivedi, S.P. Experimental study on hardness and fatigue behavior in joining of AA5083 and AA6063 by friction stir welding. *Mater. Today Proc.* **2020**, *25*, 646–648. [CrossRef]
17. Thankachan, T.; Prakash, K.S. Micro structural mechanical and tribological behaviour of aluminium nitride reinforced copper surface composites fabricated through friction stir processing route. *Mater. Sci. Eng. A* **2017**, *688*, 301–308. [CrossRef]
18. Ma, Z.Y. Friction stir processing technology: A review. *Metall. Mater. Trans. A* **2008**, *39*, 642–658. [CrossRef]
19. Mishra, R.S.; Ma, Z.Y.; Charit, I. Friction stir processing; a novel technique for fabrication of surface composite. *Mater. Sci. Eng. A* **2003**, *341*, 307–310. [CrossRef]
20. Sharma, V.; Gupta, Y.; Kumar, V.M.; Prakash, U. Friction stir processing strategies for uniform distribution of reinforcement in a surface composite. *Mater. Manuf. Process.* **2015**, *31*, 1384–1392. [CrossRef]
21. Mostafapour, A.; Khandani, S.T. Role of hybrid ratio in microstructural, mechanical and sliding wear properties of the Al5083/Graphite/Al_2O_3 a surface hybrid nanocomposite fabricated via friction stir processing method. *Mater. Sci. Eng. A* **2013**, *559*, 549–557. [CrossRef]
22. Sahu, P.S.; Banchhor, R. Effect of silicon carbide reinforcement on wear and tribological properties of aluminium matrix composites. *Int. J. Innov. Sci. Eng. Technol.* **2015**, *3*, 293–299.
23. Singh, R.K.; Srivastava, A.K.; Singh, D.K. Microstructural and X-ray Diffraction Analysis of Surface Composite AZ31b/MgO/B_4C Produced by Friction Stir Processing. In *Recent Trends in Industrial and Production Engineering*; Lecture Notes in Mechanical Engineering; Dvivedi, A., Sachdeva, A., Sindhwani, R., Sahu, R., Eds.; Springer: Singapore, 2022. [CrossRef]
24. Prakash, O.; Dwivedi, S.; Pagrut, S.; Rajawat, M.S.; Raj, R.; Srivastava, A.K.; Dixit, A.R. Investigation on the friction stir assisted lap joining of pure copper and aluminium 6063 alloy. *Mater. Today Proc.* **2022**, *62*, 398–403. [CrossRef]
25. Dwivedi, S.; Dixit, A.R.; Das, A.K.; Adamczuk, K. Additive texturing of metallic implant surfaces for improved wetting and biotribological performance. *J. Mater. Res. Technol.* **2022**, *20*, 2650–2667. [CrossRef]

coatings

MDPI

Article

Control of Static and Dynamic Parameters by Fuzzy Controller to Optimize Friction Stir Spot Welding Strength

Maha M. A. Lashin [1], Ali M. Al Samhan [2], Ahmed Badwelan [2] and Muhammad Ijaz Khan [3,4,*]

[1] College of Engineering, Princess Nourah bint Abdulrahaman University, Riyadh 11564, Saudi Arabia
[2] Industrial Engineering Department, College of Engineering, King Saud University, Riyadh 11421, Saudi Arabia
[3] Mathematical Modelling and Applied Computation Research Group (MMAC), Department of Mathematics, King Abdulaziz University, Jeddah 21589, Saudi Arabia
[4] Department of Mathematics and Statistics, Riphah International University, Islamabad 44000, Pakistan
* Correspondence: mikhan@math.qau.edu.pk

Abstract: Solid-state welding is a derivative of the friction stir spot welding (FSSW) technique, which has been developed as a new method for joining aluminum alloys. FSSW is a variant of linear friction stir welding intended to deal with lightweight alloy resistance spot welding (RSW) and riveting. Tensile strength refers to a material's ability to withstand excessive stress when being stretched or pulled before necking; it is expressed in terms of force per unit area. The tensile strength in stir spot welding is affected by dynamic and static parameters. The control of dynamic parameters and static parameters is studied in this paper to optimize the friction stir spot welding strength. A fuzzy logic control system is used to optimize the process as a new approach that can be used in this field. The obtained results prove that the fuzzy logic control system is an easy and inexpensive technology that can be used in prediction and optimization for the strength of FSSW. Furthermore, the results show the efficacy and adequacy of the proposed fuzzy logic control system.

Keywords: friction stir spot welding; dynamic parameters; static parameters; fuzzy logic control system

Citation: Lashin, M.M.A.; Al Samhan, A.M.; Badwelan, A.; Khan, M.I. Control of Static and Dynamic Parameters by Fuzzy Controller to Optimize Friction Stir Spot Welding Strength. *Coatings* **2022**, *12*, 1442. https://doi.org/10.3390/coatings12101442

Academic Editor: Ashish Kumar Srivastava

Received: 5 September 2022
Accepted: 27 September 2022
Published: 30 September 2022

Publisher's Note: MDPI stays neutral with regard to jurisdictional claims in published maps and institutional affiliations.

1. Introduction

Friction stir spot welding (FSSW) is a pressure welding method that operates below the workpieces' melting temperature [1]. FSSW is implemented on the welded sheet through steps such as plunging, stirring, and retracting, as shown in Figure 1. A welding tool, rotating with a high angular speed, enters the workpiece to form a weld spot (tool shoulder contacts the upper workpiece surface). Expelling of the material occurs during the plunging step; then, the tool reaches a predetermined depth in the stirring step. The frictional heat that is generated during the plunging and stirring steps causes heating, softening, and mixing in materials adjacent to the tool. Retraction of the tool from the workpiece occurs when acceptable bonding is obtained [2].

The main speeds that must be taken into consideration during the friction stir spot welding process are the speed of tool rotation and the speed of the tool traversing along the interface. An increasing tool rotating speed and decreasing tool traversing speed have a good effect on the quality of the welding process and the welded surface. The friction that is implemented by the tool and traversal speeds produces heat around the tool to minimize the forces acting on the tool [3].

The rotational speed of the tools and the welding speed are the parameters that are controlled to achieve the correction of heat and pressure when forming the weld. They are adjusted to heat the interface to the temperature of the plastic state. Vickers hardness tests showed a strong relation between the weld strength and tool and welding speeds [4].

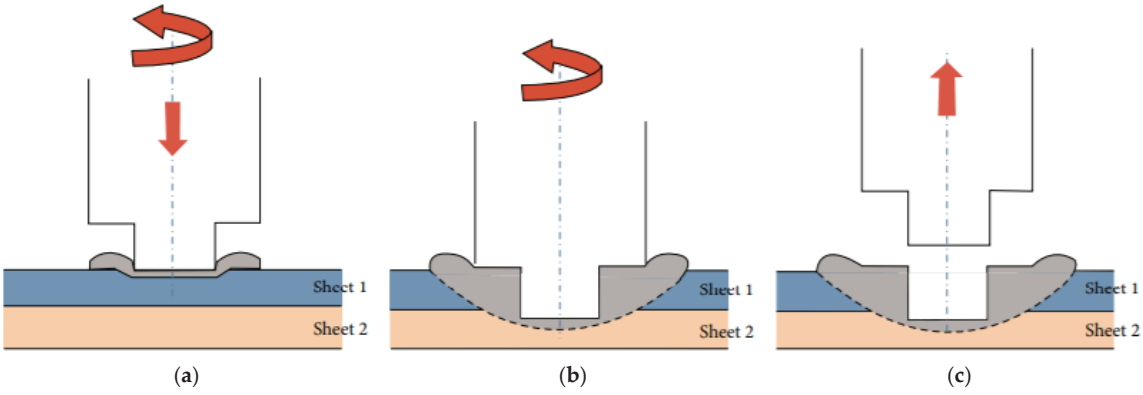

Figure 1. FSSW process: (**a**) plunging, (**b**) stirring, and (**c**) retracting [5].

Increasing the feed rate leads to a reduction in friction heating, grain, ductility, and the strain hardening exponent of the joint. Increasing the feed rate also causes increases in fragmentation and homogenization [6].

The tool rotation speed and feed rate are affected by the surface appearance, microstructure, and microhardness of the weld. In the friction stir spot welding process, the high rotational speed and feed rate cause the more uniform distribution of the steel particles in the stir zone [7].

Plunge depth is defined as the depth of the lowest point of the shoulder below the surface of the welded plate [8], or the contact between the tool shoulder and the workpiece [9]. Plunge depth affects the heat generation and the proper consolidation of the material without defects. It affects the force required during the plunging operation. Defect-free welds can be obtained with a zero plunge depth. An increase in plunge depth increases excessive flash and voids. The tensile properties of welds with zero plunge depth match with the properties of the base material. An increase in plunge depth decreases the hardness value and tensile properties [10].

Several factors can influence the FSSW process, including the tool material, tool rotation speed, tool head angle, pin length, pin profile, workpiece material and thickness, temperature input, and welding speed. These parameters are distinct, yet they each have an impact on the others [11]. To obtain products with the best mechanical performance while keeping costs to a minimum, the most appropriate process conditions should be chosen while considering the intervention requirements among these factors [12]. Considering new advances in artificial intelligence (AI) technology, its applications have grown significantly in numerous industrial domains [13–17]. Some other techniques used in the field of material engineering provide precise formulations for strength prediction; however, the accuracy is compromised [18–22]. The accuracy of the developed model depends on the optimization parameters, the number of input variables, and the number of entries being used while modeling [23,24].

Artificial intelligence (AI) approaches are increasingly being employed in FSSW investigations due to their remarkable performance, ease of implementation, as well as flexibility in any discipline [25–28]. Numerous factors in the FSSW technique are optimized and estimated using AI techniques [29]. The fuzzy logic meta-heuristic technique, artificial neural networks (ANN), heuristic fuzzy, wavelet, and heuristic-ANN are among the most prominent AI techniques being used for FSSW [30]. These techniques are employed interchangeably, although they are also recommended for distinct reasons due to their benefits and drawbacks over one another.

Fuzzy logic (FL) is an extremely viable approach for regulating systems that are quasi, complicated, challenging to describe, and have questionable or precise data reliability. It functions in the same way as human logic does, with intermediate variables such as

extremely long, short, and so on. There is currently no work published in the literature that predicts FSSW properties by employing only a fuzzy logic control system (FLCS). Furthermore, fuzzy control is divided into the Mamdani and Sugano categories, and it is employed in a variety of applications, including control and prediction [31,32].

Mohanty et al. [33] studied the impact of tool probe diameter, tool type, and shoulder interaction area on the strength of welds. They developed an ANN architecture and Mamdani FLCS to produce seven distinct triangular fuzzy memberships. The authors found that the fuzzy logic outperformed the ANN structure in modeling the connections of each FSSW characteristic with the output results.

A Mamdani fuzzy system was used for predicting and exploring the influence of friction stir spot process parameters on the tensile strength of AA1100 joints. The fuzzy model showed the increasing tensile strength of friction stir spot-welded joints with increasing pin diameter, tool rotating speed, welding speed, and feed rate. This methodology is a useful tool to assess the tensile strength of friction stir-welded AA1100 [34].

Mamdani fuzzy models implemented at forward and rotational speed as inputs and mechanical properties as outputs based on experimental data have been proposed. The results indicate the appropriate of the fuzzy method [35].

In this ongoing study, Mamdani FLCS was employed to build a model for the estimation and evaluation of the impact of FSSW workflow conditions on the tensile strength of Al 1050 joints, considering dynamic welding parameters (DWP) as a novel approach to achieve increasing weld strength. With the welding stroke, FSSW variables including tool feed rate and spindle speed fluctuate. The tensile strength improves substantially when DWPs are applied in the FSSW technique, in comparison with static welding parameters.

2. Material Specifications (Friction Stir Spot Welding of Al 1050)

Al 1050 exhibits outstanding corrosion resistance, higher electrical conductivity, higher ductility, and strength and can be produced with highly reflective finishing. Due to its lower weight and non-toxic nature, it is most suitable to be used for architectural flashings, industrial containers, lamp reflectors, and cable sheathings. Furthermore, it can also be used effectively in chemical processing plants. Strips of Al 1050 with the dimensions, chemical composition, and mechanical properties shown in Figure 2 and Tables 1 and 2, respectively, were used to study the strength of friction stir spot welding [36].

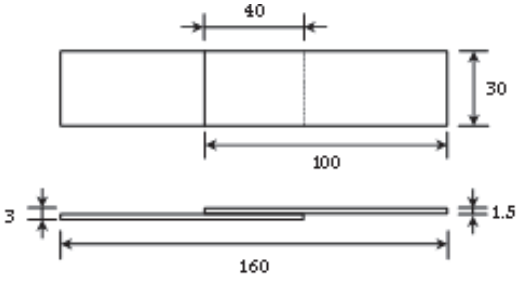

Figure 2. Dimensions of Al 1050 strips.

Table 1. Chemical composition of Al 1050.

Material	Aluminum (Al)	Zirconium (Zr)	Strontium (Sr)	Vanadium (V)	Lithium (Li)	Others
Percent	99.60	0.0015	0.00013	0.0080	0.00010	0.39027

Table 2. Mechanical properties of Al 1050.

Property	Yield Strength	Ultimate Tensile Strength	Elongation at Break	Young's Modulus
Value	128 MPa	137.5 MPa	8.45 mm	67,648 MPa

Overlapping Al 1050 strips were welded at the German Computer Numerical Control (CNC) Vertical Machining Center with a developed welding fixture for maintaining the welding spot in the middle of the overlapping region, as shown in Figure 3. The fixture's holding tray was subsequently placed on top of the load cell. A circular cylinder-shaped temperature sensor was installed in the middle of the grip plate, with a 1.5 mm gap between the Al 1050 welding strip and the temperature sensor. A welding strip, holding bracket, grip plate assembly, and holding screws comprised the holding tray. The designed welding fixture's primary goal was to keep the welding point in the central overlapped area of the Al 1050 strip. The NI-USB-6341 data capture device was employed to gather temperature and welding force measurements corresponding to the welding stroke.

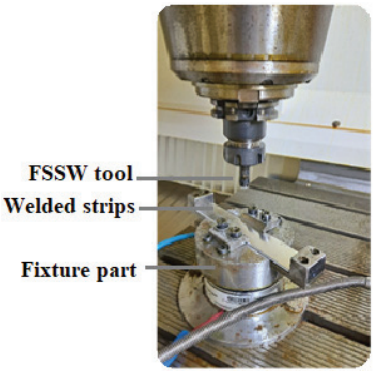

Figure 3. Friction stir spot welding machine setup.

Spindle speed (SS), tool feed rate (FR), and plunging depth (PD) were the static friction stir spot welding parameters, while the fixed values of feed rate (FR) and spindle speed (SS) throughout the welding stroke were considered as dynamic parameters, as shown in Figure 4.

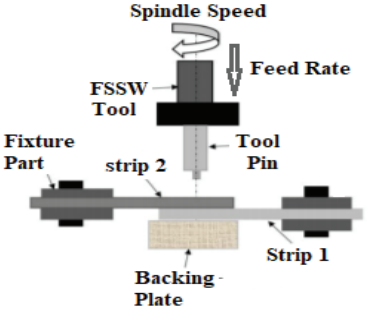

Figure 4. Schematic representation of friction sir spot welding process.

Ninety experiments were performed with different values of SS, FR, and PD to study the influence of welding parameters on FSSW strength. Values of FR, SS, and PD during experiments on friction stir spot welding are shown in Table 3. The complete experimental procedure included two different phases. In the first phase, during the welding process, the

welding parameters were kept constant, while in the second phase, the welding parameters such as SS and FR were varied for the period of welding stroke, which were then labeled as dynamic welding parameters (DWP). In the DWP method, the SS or FR was varied (decreased or increased) for the period of welding stroke, in comparison with the original (initial) value.

Table 3. FSSW parameters for experimental study.

Parameters	Values
Plunging depth PD (mm)	2.3, 2.5, 2.7
Feed rate FR (mm/min)	5, 10, 15, 20, 25, 30
Spindle speed SS (rev./min)	1000, 1500, 2000, 2500, 3000

All the weld strength tests were carried out via the Instron-3300 mechanical testing setup, having a tension rate equal to 5 mm per minute, while the microhardness was checked via a DuraScan-10 computer. The ISO standard 6507-1:2018 was followed by applying a 100 (g) load for the duration equal to 15 s, with a space between the consecutive grooves. Following the same ISO standard, for the chosen FSSW samples, the microhardness was measured twice [37], i.e., vertically with the starting point as the tool pin area (bottom to top of welded sheets) and horizontally across the welded samples' seam line.

Changes in FSSW strength with changing welding parameters during the welding process are summarized in Table 4. From the table, it can be noticed that the FSSW strength increased with an increase in plunging depth. Increasing spindle speed causes a decrease in welding strength at the same values of feed rate and plunging depth. Moreover, a decreasing feed rate causes an increase in welding strength.

Table 4. Strength of FSSW with FR, SS, and PD.

PD (mm)																														
	2.30																													
FR (mm/min)	5.00					10.00					15.00					20.00					25.00					30.00				
SS (rev./min)	1000	1500	2000	2500	3000	1000	1500	2000	2500	3000	1000	1500	2000	2500	3000	1000	1500	2000	2500	3000	1000	1500	2000	2500	3000	1000	1500	2000	2500	3000
FSSW Strength (N)	2100	2100	1600	1550	1900	1600	1650	1710	1750	1750	1500	1100	1510	1750	1900	500	1530	1500	1490	2000	750	1250	1500	1490	2000	750	760	1250	1500	1750
PD (mm)	**2.50**																													
FR (mm/min)	5.00					10.00					15.00					20.00					25.00					30.00				
SS (rev./min)	1000	1500	2000	2500	3000	1000	1500	2000	2500	3000	1000	1500	2000	2500	3000	1000	1500	2000	2500	3000	1000	1500	2000	2500	3000	1000	1500	2000	2500	3000
FSSW Strength (N)	2900	2600	2500	2500	2450	2500	2550	2490	2850	2750	2500	2250	2500	2500	2490	2370	2470	2480	2480	2500	2490	2500	2550	2600	2480	2460	2250	2100	2450	2500
PD (mm)	**2.70**																													
FR (mm/min)	5.00					10.00					15.00					20.00					25.00					30.00				
SS (rev./min)	1000	1500	2000	2500	3000	1000	1500	2000	2500	3000	1000	1500	2000	2500	3000	1000	1500	2000	2500	3000	1000	1500	2000	2500	3000	1000	1500	2000	2500	3000
FSSW Strength (N)	3092	2650	2650	2500	2450	3000	2900	2600	2600	2490	2900	2850	2650	2650	2580	2910	2700	2700	2760	2490	2950	2850	2650	2600	2490	2920	2600	2610	2615	2500

The desirability approach is a common method for assigning a "score" to a group of responses and selecting factor settings to optimize this score. One of the most used approaches in industry for optimizing multiple response processes is the desirability feature approach [38].

An individual desirability function was used as an optimizing technique to optimize the friction stir spot welding process parameters. The maximum value of strength throughout the 90 experiments shown in Table 5, with optimized values of static parameters.

Table 5. Optimum values of FSSW parameters.

Parameters	Values
FR (mm/min)	5
SS (rev./min)	1000
PD (mm)	2.7
Weld strength (N)	3092.7

3. Fuzzy Logic Control System (Optimization, Results and Discussion)

A fuzzy logic control system (FLCS) was used to optimize the strength of FSSW by controlling the static parameters of the welding process. The results of the fuzzy system

were compared with individual desirability function results to determine the feasibility of using the FLCS technique to optimize the welding strength by controlling the dynamic parameters' values for the same welding material (Al 1050). A flow chart of the FLCS used is shown in Figure 5.

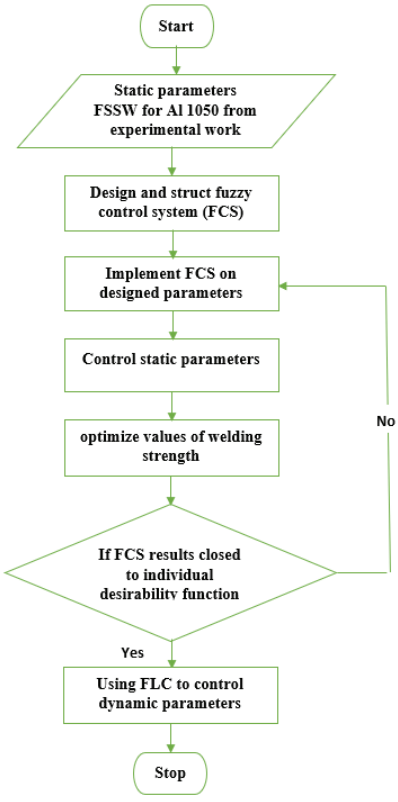

Figure 5. Flow chart of FLCS to optimize FSSW strength.

3.1. Fuzzy Logic Control System

The fuzzy logic control framework breaks down parameters into simple values regarding either 1 (true) or 0 (false) qualities. Fuzzy sets classify objects easily by relying upon enrollment, making them useful for estimation models [39]. Fuzzy logic control systems rely upon the guidelines of appointing the yield and are contingent upon the likelihood of the condition of the information. If–Then rules are utilized due to their great benefits in planning FLCS [40]. The fuzzy logic control system in the presented paper is used as an artificial intelligence tool, to optimize the strength of friction stir spot welding by controlling the welding parameters (static and dynamic parameters).

3.1.1. Architecture of Fuzzy Logic Controller

The fuzzifier (fuzzification step), information base, fuzzy principal base (fuzzy knowledge base), and defuzzifier (defuzzification step) are the fundamental components in the construction of a fuzzy system regulator for any controlled framework, as shown in Figure 6.

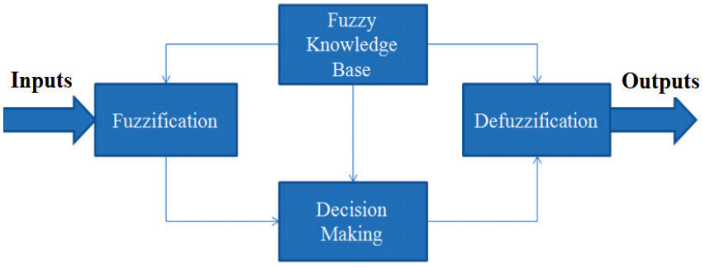

Figure 6. Structure of fuzzy logic controller.

Changing estimations of the contribution of fuzzy qualities are obtained through the fuzzification step in a fuzzy logic control system. Data sources and yield familiarities of fuzzy connections result in different participation capacities for every one of them [41]. The If–Then rule is the basic rule used in fuzzy systems to join the membership functions of inputs and outputs. The inference engine is the center of any FLCS since it performs inexact thinking [42]. The defuzzification process or step performed through the defuzzifier serves to transform the fuzzy values of the fuzzy inference engine into new values [43]. The design and implementation of the fuzzy logic control system is achieved by using the fuzzy logic toolbox of MATLAB.

3.1.2. Fuzzy System for Static Parameters

A three-input–one-output fuzzy logic control system is designed and implemented to optimize the friction stir spot welding strength of Al 1050 samples by controlling the values of static parameters (SS, FR, PD) of the welding process. Spindle speed (SS), feed rate (FR), and plunging depth (PD) were the inputs and welding strength was the output of the fuzzy system. The structure of the FSSW strength fuzzy system is shown in Figure 7.

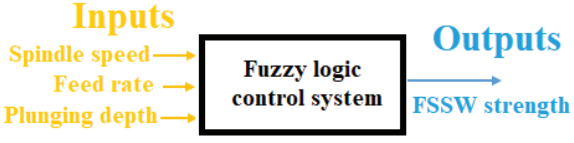

(**a**)

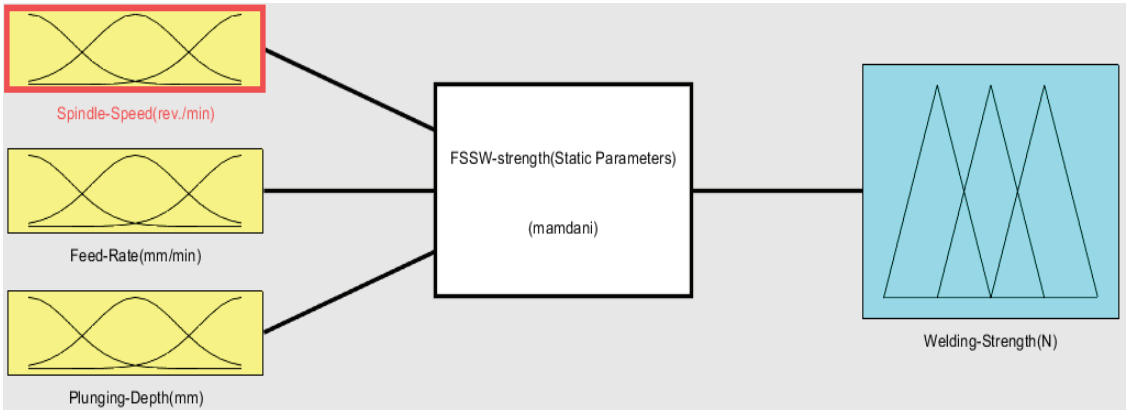

(**b**)

Figure 7. FSSW strength (static parameter) fuzzy logic control system (**a**) inputs and outputs (**b**) Mamdani FLCS.

3.1.3. Inputs and Outputs of Membership Function

The fuzzy set's function is to reflect the pointer work for old-style sets. It produces a a graphical fuzzy set representation (A) for debate (X) as μA:X → [0, 1], and this means that the value between 0 and 1 is mapped to (X). The (x) axis is the universe of debate, while the (y) axis is the degree of membership in the [0, 1] set. The mathematical form for a triangular membership function is shown in Figure 8, where a and b are the lower and upper limits, respectively [44].

$$\mu_A(X) = \begin{cases} 0 & x \le a \\ \dfrac{x-a}{m-a} & a < x \le m \\ \dfrac{b-x}{b-m} & m < x < b \\ 0 & x \ge b \end{cases}$$

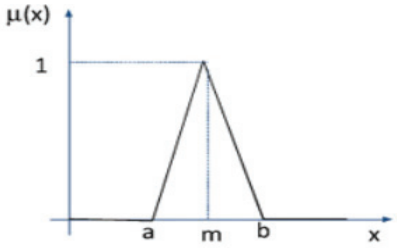

Figure 8. Triangular membership function for fuzzy system inputs and outputs.

Through the fuzzification step in the fuzzy system, the quantity of inputs is converted to a fuzzy quantity through identifying the deterministic quantities as completely nondeterministic. The triangular membership function used to fuzzify inputs to three levels (low, medium, and high) of fuzzy input values, as shown in Figure 9. The range of fuzzy system inputs (SS, FR, PD) with three levels, low, medium, and high, is shown in Figure 10 and Table 6, respectively.

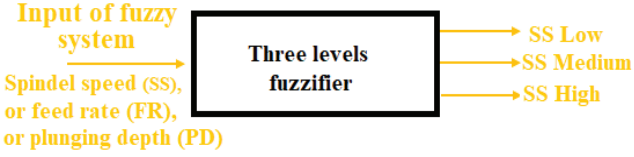

Figure 9. Fuzzification of FSSW strength fuzzy system inputs.

Table 6. Membership functions of FSSW strength fuzzy system inputs.

Fuzzy System Input Variable	Unit	Membership Function	Range of Inputs		
			Low	Medium	High
SS	rev./min	Triangular MF	998–1510	1511–2490	2491–3001
FR	mm/min	Triangular MF	4.5–11	11.5–21	21.5–31
PD	mm	Triangular MF	2.2–2.4	2.48–2.6	2.63–2.8

The defuzzification step in a fuzzy system is performed through a number of rules that transform several variables into fuzzy results to define fuzzy sets and membership function degrees, as shown in Figure 11.

To defuzzify the fuzzy output into low, medium, and high levels through defuzzification, the triangular membership function is used, as shown in Figure 12. Levels of fuzzy system output are detailed in Table 7.

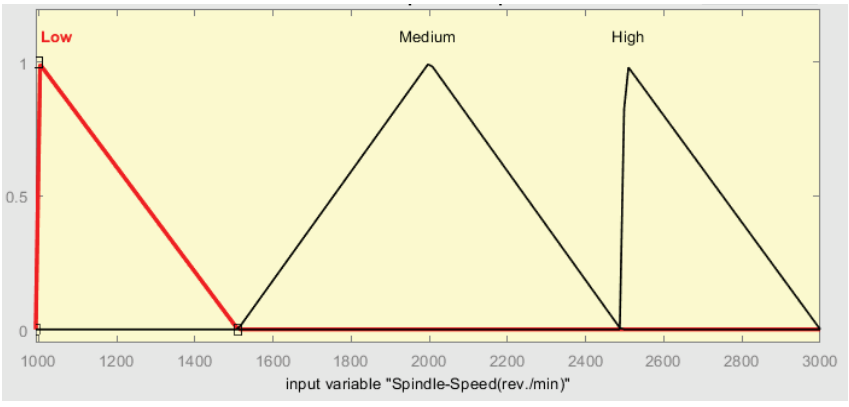

(**a**)

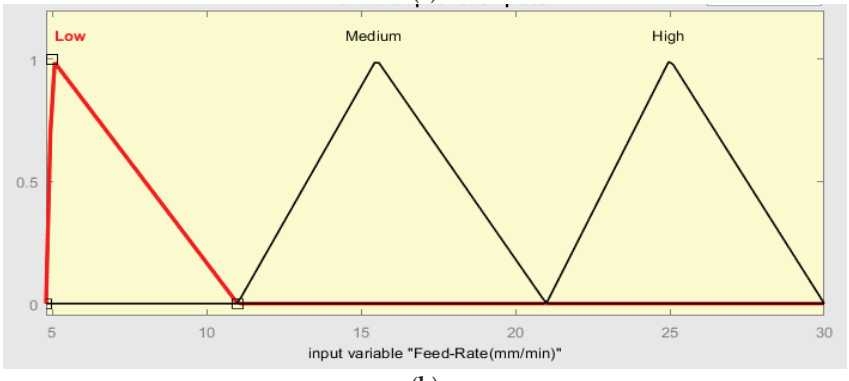

(**b**)

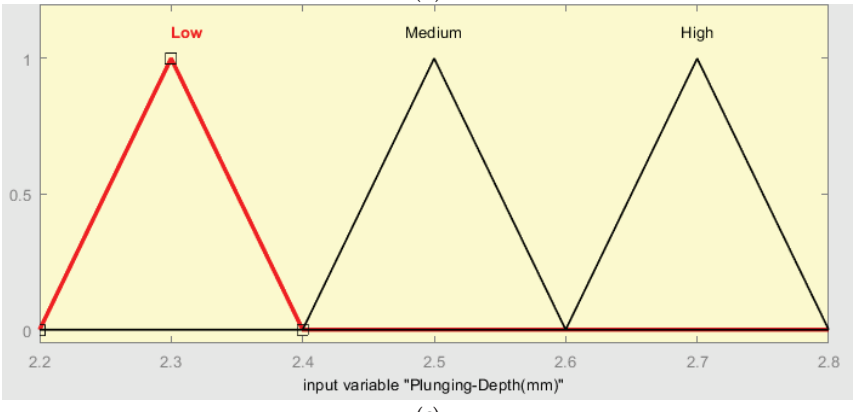

(**c**)

Figure 10. Triangular membership functions for fuzzy system inputs (**a**) SS, (**b**) FR, (**c**) PD.

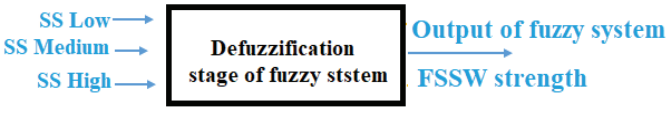

Figure 11. Defuzzification process in FSSW strength fuzzy system.

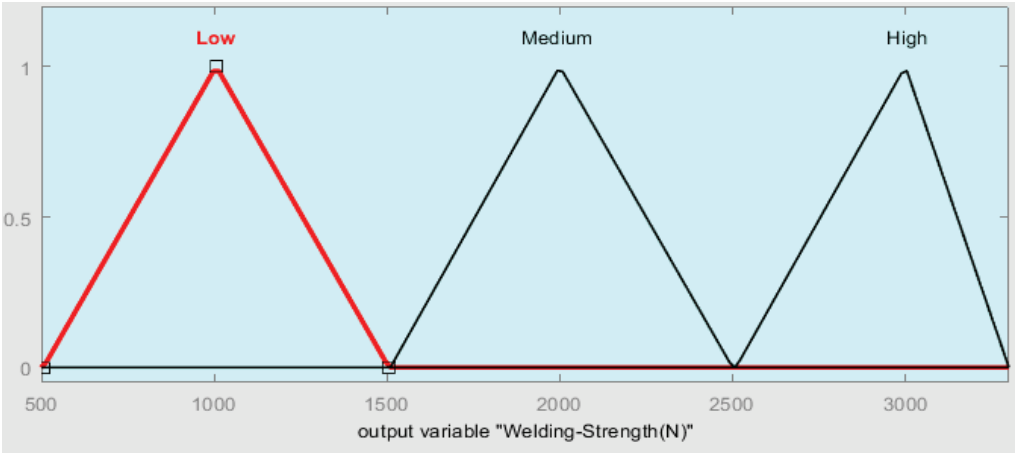

Figure 12. Outputs of FSSW strength fuzzy system.

Table 7. Membership functions of FSSW strength fuzzy system outputs.

Fuzzy System Output Variable	Membership Function	Range of Outputs		
		Low	Medium	High
FSSW Strength	Triangular MF	500–1500	1510–2500	2510–3100

3.1.4. FLCS Base Rules

The If–Then rule is a fuzzy system-based rule used to join fuzzy system inputs and outputs. Some of the rules that are used in the friction stir spot welding strength fuzzy logic control system are shown in Table 8.

Table 8. FSSW strength fuzzy system's If–Then rules.

Fuzzy Rules (If–Then Rules)
If (Spindle-Speed(rev./min) is Low) and (Feed-Rate(mm/min) is Low) and (Plunging-Depth(mm) is Low) then (Welding-Strength(N) is Low)
If (Spindle-Speed(rev./min) is Low) and (Feed-Rate(mm/min) is Low) and (Plunging-Depth(mm) is High) then (Welding-Strength(N) is High)
If (Spindle-Speed(rev./min) is Low) and (Feed-Rate(mm/min) is Low) and (Plunging-Depth(mm) is High) then (Welding-Strength(N) is High)
If (Spindle-Speed(rev./min) is Low) and (Feed-Rate(mm/min) is Low) and (Plunging-Depth(mm) is High) then (Welding-Strength(N) is High)
If (Spindle-Speed(rev./min) is Low) and (Feed-Rate(mm/min) is Medium) and (Plunging-Depth(mm) is Low) then (Welding-Strength(N) is Medium)
If (Spindle-Speed(rev./min) is Low) and (Feed-Rate(mm/min) is Medium) and (Plunging-Depth(mm) is High) then (Welding-Strength(N) is High)
If (Spindle-Speed(rev./min) is Low) and (Feed-Rate(mm/min) is Medium) and (Plunging-Depth(mm) is Medium) then (Welding-Strength(N) is Medium)
If (Spindle-Speed(rev./min) is Low) and (Feed-Rate(mm/min) is High) and (Plunging-Depth(mm) is Medium) then (Welding-Strength(N) is Medium)
If (Spindle-Speed(rev./min) is Low) and (Feed-Rate(mm/min) is High) and (Plunging-Depth(mm) is Low) then (Welding-Strength(N) is Low)
If (Spindle-Speed(rev./min) is Low) and (Feed-Rate(mm/min) is High) and (Plunging-Depth(mm) is High) then (Welding-Strength(N) is High)
If (Spindle-Speed(rev./min) is Medium) and (Feed-Rate(mm/min) is Low) and (Plunging-Depth(mm) is Medium) then (Welding-Strength(N) is High)

Table 8. *Cont.*

Fuzzy Rules (If–Then Rules)
If (Spindle-Speed(rev./min) is Medium) and (Feed-Rate(mm/min) is Medium) and (Plunging-Depth(mm) is Low) then (Welding-Strength(N) is Low)
If (Spindle-Speed(rev./min) is Medium) and (Feed-Rate(mm/min) is Medium) and (Plunging-Depth(mm) is High) then (Welding-Strength(N) is High)

Figure 13 and Table 9 present the optimum values of friction stir spot welding strength that result from using the designed FSSW fuzzy system. Figure 13 presents the effects of changes in SS and PD values on the strength of welding.

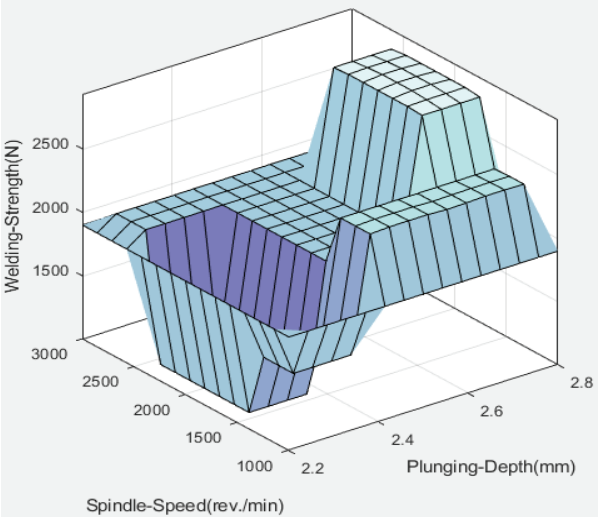

Figure 13. Three-dimensional surface result of FSSW fuzzy system.

Table 9. Output results of FSSW fuzzy system.

	Inputs			Outputs
	SS (rev./min)	**FR (mm/min)**	**PD (mm)**	**FSSW Strength (N)**
Values	1000	5	2.7	2940

A comparison was performed between the individual desirability function results and the results of the FSSW fuzzy system, as shown in Table 10, to verify the effectiveness of the designed FLCS in optimizing the welding strength value. The deviation between the two techniques used is 7%, and this means that we can use the fuzzy logic control system to control the static welding parameters to obtain the optimum value of FSSW strength.

Table 10. The optimum values of static welding parameters of desirability function and fuzzy system.

Parameters	SS		FR		PD		FSSW Strength	
	Desirability Function	**Fuzzy System**	**Desirability Function**	**Fuzzy System**	**Desirability Function**	**Fuzzy System**	**Desirability Function**	**Fuzzy System**
Values	1000	1000	5	5	2.7	2.7	3092.7	2940

After using the fuzzy controller to optimize the strength of stir welding through controlling the static parameters of the welding process, another fuzzy model was designed to

optimize the welding strength but this time through the control of the dynamic parameters of the welding process.

3.2. Fuzzy System for Dynamic Parameters

A two-input–one-output fuzzy system was designed to be implemented on the dynamic parameters (spindle speed and feed rate) to optimize the strength of friction stir spot welding for Al 1050 alloy samples. The model of the FSSW strength (dynamic parameters) fuzzy system is shown in Figure 14.

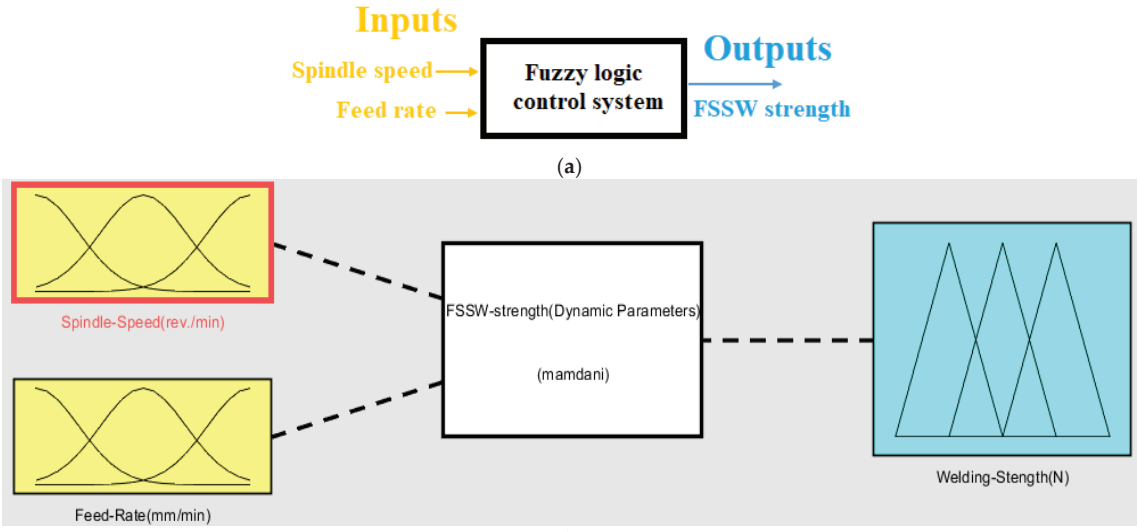

Figure 14. FSSW strength (dynamic parameters) fuzzy logic control system (**a**) inputs and outputs (**b**) Mamdani FLCS.

The triangular membership function used to fuzzify the inputs to five levels (very low, low, medium, high, and very high) of fuzzy input values is shown in Figure 15, with ranges given in Figure 16 and Table 11, respectively.

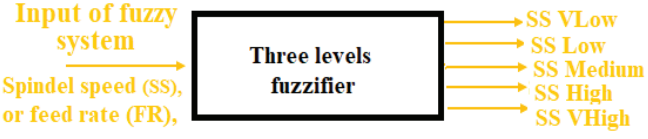

Figure 15. Fuzzification of FSSW strength fuzzy system inputs.

Table 11. Membership functions of FSSW strength fuzzy system inputs.

Fuzzy System Input Variable	Membership Function	Range of Inputs				
		Very Low	Low	Medium	High	Very High
SS	Triangular MF	375–625	625–875	875–1125	1125–1375	1375–1625
FR	Triangular MF	1.875–3.125	3.125–4.375	4.375–5.625	5.625–6.875	6.875–8

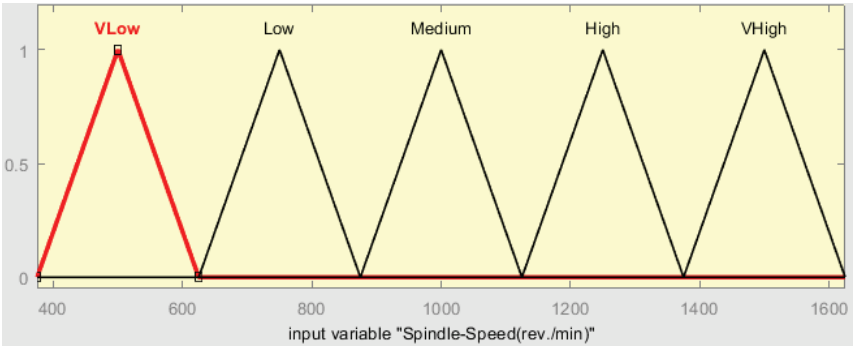

(**a**)

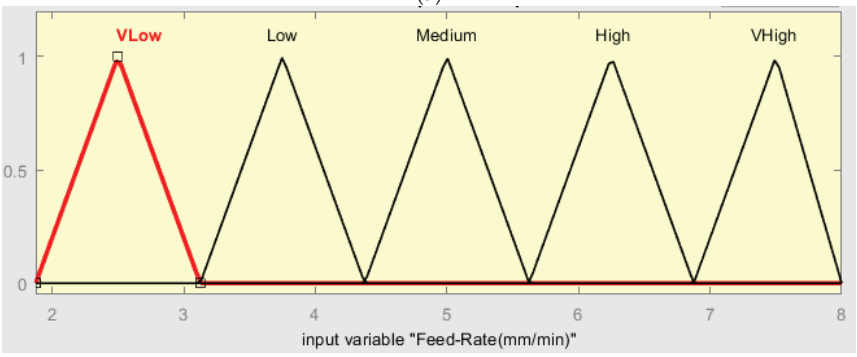

(**b**)

Figure 16. Triangular membership functions for fuzzy system inputs (**a**) SS, (**b**) FR.

The final decision or fuzzy model result obtained from defuzzification by the number of rules to defined fuzzy sets and membership function degrees is as shown in Figure 17. The range of triangle membership functions that are used to defuzzify the fuzzy output into very low, low, medium, high, and very high levels is shown in Figure 18 and Table 12, respectively.

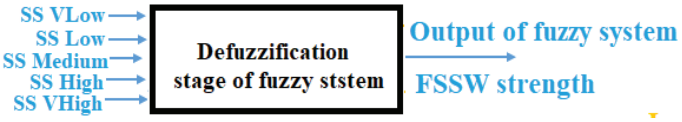

Figure 17. Defuzzification step in FSSW strength (dynamic parameters) fuzzy system.

Table 12. Membership functions of FSSW strength fuzzy system output.

Fuzzy System Input Variable	Membership Function	Range of Inputs				
		Very Low	Low	Medium	High	Very High
FSSW Strength	Triangular MF	2800–2960	2960–3120	3120–3280	3280–3440	3440–3600

Table 13 shows the If–Then rules that are used in the FSSW strength (dynamic parameters) fuzzy system to join the fuzzy system inputs and output.

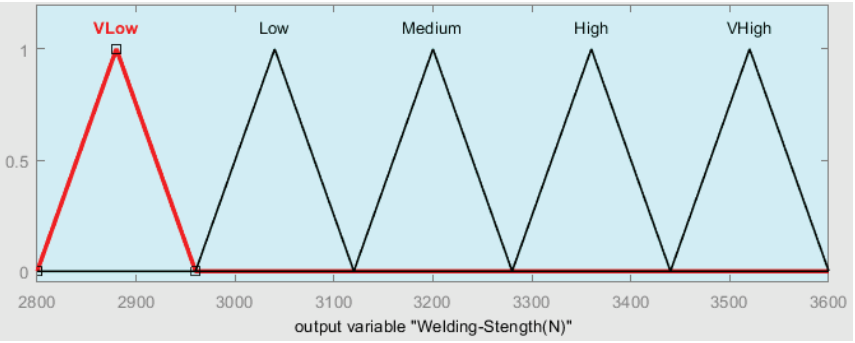

Figure 18. Outputs of FSSW strength (dynamic parameters) fuzzy system.

Table 13. If–Then rules of FSSW strength fuzzy systems.

Fuzzy Rules (If–Then Rules)
If (Spindle-Speed(rev./min) is V Low) and (Feed-Rate(mm/min) is Medium) then (Welding-Strength (N) is V High)
If (Spindle-Speed(rev./min) is Medium) and (Feed-Rate(mm/min) is V Low) then (Welding-Strength (N) is Medium)
If (Spindle-Speed(rev./min) is Medium) and (Feed-Rate(mm/min) is High) then (Welding-Strength (N) is Low)
If (Spindle-Speed(rev./min) is High) and (Feed-Rate(mm/min) is Medium) then (Welding-Strength (N) is Medium)

The optimum value of friction stir spot welding related to the controlled dynamic parameters (SS, FR), explained in terms of the surface view for this fuzzy system, is as shown in Figure 19.

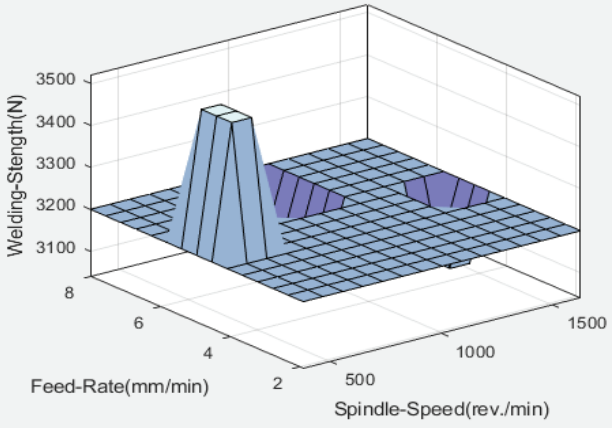

Figure 19. Welding strength variation with spindle speed and feed rate.

Table 14 shows the output result of the designed fuzzy model of the dynamic parameters of friction stir spot welding.

Table 14. Results of FSSW strength fuzzy system (dynamic parameters).

	Output		
	SS (rev./min)	**FR (mm/min)**	**FSSW Strength (N)**
Values	1000	5.66	3040.5

A comparison was performed between the results of experiments and the designed FSSW fuzzy system's results, as shown in Table 15. The deviation between the two results was around 7%, and this mean that using the fuzzy logic control system as a technique to control the dynamic welding parameters will optimize the strength of friction stir spot welding.

Table 15. The optimum values for dynamic welding parameters of experiment and fuzzy system.

Parameter	SS		FR		FSSW Strength	
	Experiment	Fuzzy System	Experiment	Fuzzy System	Experiment	Fuzzy System
Value	1000	1000	5	5.66	3092.7	3040.5

4. Conclusions

A fuzzy logic controller was designed and used to optimize the strength of friction stir spot welding by controlling the welding parameters. Two fuzzy models, one for controlling the static welding parameters and another for the dynamic welding parameters, were designed to optimize the strength of the friction stir spot welding of Al 1050 alloy samples. The results obtained from fuzzy logic, which is considered a type of artificial intelligence, proved that the fuzzy logic control system is an easy and inexpensive technology that can be used in the prediction and optimization of the strength of friction stir spot welding (FSSW). The results obtained show the efficacy and adequacy of the proposed fuzzy logic control system.

Author Contributions: M.M.A.L. wrote the paper and completed the experimental design; A.M.A.S. supervised and provided project funding; A.B. revised the manuscript, performed validation and visualization, and helped with results; M.I.K. performed supervision, writing—review and editing, and software implementation. All authors have read and agreed to the published version of the manuscript.

Funding: The authors express their gratitude to the Princess Nourah bint Abdulrahman University Researchers Supporting Project (Grant No. PNURSP2022R152), Princess Nourah bint Abdulrahman University, Riyadh, Saudi Arabia.

Institutional Review Board Statement: Not applicable.

Informed Consent Statement: Not applicable.

Data Availability Statement: All the data are clearly presented in the manuscript.

Conflicts of Interest: The authors declare no conflict of interest.

References

1. Yang, X.; Fu, T.; Li, W. Friction stir spot welding: A review on joint macro-and microstructure, property, and process modelling. *Adv. Mater. Sci. Eng.* **2014**, *2014*, 697170. [CrossRef]
2. Nguyen, N.; Kim, D.; Kim, H. Assessment of the failure load for an AA6061-T6 friction stir spot welding joint. *Proc. Inst. Mech. Eng. Part B J. Eng. Manuf.* **2011**, *225*, 1746–1756. [CrossRef]
3. Ugla, A.A.; Al Roubaiy, A.O.; Alazawi, F.H. Effect of Dwell Time and Tool Rotational Speed of Friction Stir Spot Welding on the characteristics of AA3105 joints. *Thi-Qar Univ. J. Eng. Sci.* **2018**, *9*, 51–58. [CrossRef]
4. Karthikeyan, P.; Thiagarajan, D.; Mahadevan, K. Study of relation between welding and hardening parameters of friction stir welded Aluminium 2024 alloy. *Procedia Eng.* **2014**, *97*, 505–512. [CrossRef]
5. Iwashita, T. Method and Apparatus for Joining. U.S. Patent 6,601,751, 2003.
6. El Rayes, M.M.; Soliman, M.S.; Abbas, A.T.; Pimenov, D.Y.; Erdakov, I.N.; Abdel-mawla, M.M. Effect of feed rate in FSW on the mechanical and microstructural properties of AA5754 joints. *Adv. Mater. Sci. Eng.* **2019**, *2019*, 4156176. [CrossRef]
7. Habibnia, M.; Shakeri, M.; Nourouzi, S.; Karimi, N. Effect of tool rotation speed and feed rate on friction stir welding of 1100 aluminum alloy to carbon steel. In *Advanced Materials Research*; Trans Tech Publications Ltd.: Wollerau, Switzerland, 2012; pp. 741–746.
8. Devanathan, C.; Babu, A.S. Effect of plunge depth on friction stir welding of Al 6063. In Proceedings of the International Conference on Advanced Manufacturing and Automation (INCAMA-2013), Tamilnadu, India, 28–30 March 2013.

9. Leonard, A. Microstructure and aging behaviour of FSW in Al alloys 2014A-T651 and 7075-T651. In Proceedings of the 2nd International Symposium on FSW (CD Rom), Gothenburg, Sweden, 27–29 June 2000.
10. Soundararajan, V.; Yarrapareddy, E.; Kovacevic, R. Investigation of the friction stir lap welding of aluminum alloys AA 5182 and AA 6022. *J. Mater. Eng. Perform.* **2007**, *16*, 477–484. [CrossRef]
11. Threadgill, P.; Leonard, A.; Shercliff, H.; Withers, P. Friction stir welding of aluminium alloys. *Int. Mater. Rev.* **2009**, *54*, 49–93. [CrossRef]
12. Salvati, E.; Everaerts, J.; Kageyama, K.; Korsunsky, A.M. Transverse fatigue behaviour and residual stress analyses of double sided FSW aluminium alloy joints. *Fatigue Fract. Eng. Mater. Struct.* **2019**, *42*, 1980–1990. [CrossRef]
13. Yavuz, H. Function-oriented design of a friction stir welding robot. *J. Intell. Manuf.* **2004**, *15*, 761–775. [CrossRef]
14. Mohammadi, M.-R.; Hadavimoghaddam, F.; Pourmahdi, M.; Atashrouz, S.; Munir, M.T.; Hemmati-Sarapardeh, A.; Mosavi, A.H.; Mohaddespour, A. Modeling hydrogen solubility in hydrocarbons using extreme gradient boosting and equations of state. *Sci. Rep.* **2021**, *11*, 17911. [CrossRef]
15. Haji-Savameri, M.; Norouzi-Apourvari, S.; Irannejad, A.; Hemmati-Sarapardeh, A.; Schaffie, M.; Mosavi, A. Experimental study and modelling of asphaltene deposition on metal surfaces with superhydrophobic and low sliding angle inner coatings. *Sci. Rep.* **2021**, *11*, 16812. [CrossRef] [PubMed]
16. Meiabadi, M.S.; Moradi, M.; Karamimoghadam, M.; Ardabili, S.; Bodaghi, M.; Shokri, M.; Mosavi, A.H. Modeling the producibility of 3D printing in polylactic acid using artificial neural networks and fused filament fabrication. *Polymers* **2021**, *13*, 3219. [CrossRef] [PubMed]
17. Dehghan Manshadi, M.; Ghassemi, M.; Mousavi, S.M.; Mosavi, A.H.; Kovacs, L. Predicting the Parameters of Vortex Bladeless Wind Turbine Using Deep Learning Method of Long Short-Term Memory. *Energies* **2021**, *14*, 4867. [CrossRef]
18. Aldrees, A.; Khan, M.A.; Tariq, M.A.U.R.; Mustafa Mohamed, A.; Ng, A.W.M.; Bakheit Taha, A.T. Multi-Expression Programming (MEP): Water Quality Assessment Using Water Quality Indices. *Water* **2022**, *14*, 947. [CrossRef]
19. Khan, M.A.; Aslam, F.; Javed, M.F.; Alabduljabbar, H.; Deifalla, A.F. New prediction models for the compressive strength and dry-thermal conductivity of bio-composites using novel machine learning algorithms. *J. Clean. Prod.* **2022**, *350*, 131364. [CrossRef]
20. Li, P.; Khan, M.A.; El-Zahar, E.R.; Awan, H.H.; Zafar, A.; Javed, M.F.; Khan, M.I.; Qayyum, S.; Malik, M.; Wang, F. Sustainable use of chemically modified tyre rubber in concrete: Machine learning based novel predictive model. *Chem. Phys. Lett.* **2022**, *793*, 139478. [CrossRef]
21. Khan, M.A.; Memon, S.A.; Farooq, F.; Javed, M.F.; Aslam, F.; Alyousef, R. Compressive strength of fly-ash-based geopolymer concrete by gene expression programming and random forest. *Adv. Civ. Eng.* **2021**, *2021*, 6618407. [CrossRef]
22. Mohammadzadeh, S.D.; Kazemi, S.-F.; Mosavi, A.; Nasseralshariati, E.; Tah, J.H. Prediction of compression index of fine-grained soils using a gene expression programming model. *Infrastructures* **2019**, *4*, 26. [CrossRef]
23. Ayub, S.; Guan, B.H.; Ahmad, F.; Javed, M.F.; Mosavi, A.; Felde, I. Preparation Methods for Graphene Metal and Polymer Based Composites for EMI Shielding Materials: State of the Art Review of the Conventional and Machine Learning Methods. *Metals* **2021**, *11*, 1164. [CrossRef]
24. Peng, Y.; Ghahnaviyeh, M.B.; Ahmad, M.N.; Abdollahi, A.; Bagherzadeh, S.A.; Azimy, H.; Mosavi, A.; Karimipour, A. Analysis of the effect of roughness and concentration of Fe3O4/water nanofluid on the boiling heat transfer using the artificial neural network: An experimental and numerical study. *Int. J. Therm. Sci.* **2021**, *163*, 106863. [CrossRef]
25. Tavoosi, J.; Zhang, C.; Mohammadzadeh, A.; Mobayen, S.; Mosavi, A.H. Medical image interpolation using recurrent type-2 fuzzy neural network. *Front. Neuroinform.* **2021**, *15*, 667375. [CrossRef] [PubMed]
26. Tavoosi, J.; Suratgar, A.A.; Menhaj, M.B.; Mosavi, A.; Mohammadzadeh, A.; Ranjbar, E. Modeling renewable energy systems by a self-evolving nonlinear consequent part recurrent type-2 fuzzy system for power prediction. *Sustainability* **2021**, *13*, 3301. [CrossRef]
27. Sadeghiravesh, M.H.; Khosravi, H.; Abolhasani, A.; Ghodsi, M.; Mosavi, A. Fuzzy Logic Model to Assess Desertification Intensity Based on Vulnerability Indices. *Acta Polytech. Hung* **2021**, *18*, 7–24. [CrossRef]
28. Claywell, R.; Nadai, L.; Felde, I.; Ardabili, S.; Mosavi, A. Adaptive neuro-fuzzy inference system and a multilayer perceptron model trained with grey wolf optimizer for predicting solar diffuse fraction. *Entropy* **2020**, *22*, 1192. [CrossRef] [PubMed]
29. Dinaharan, I.; Murugan, N. Optimization of friction stir welding process to maximize tensile strength of AA6061/ZrB2 in-situ composite butt joints. *Met. Mater. Int.* **2012**, *18*, 135–142. [CrossRef]
30. Bilgiç, H.H.; Sen, M.A.; Kalyoncu, M. Tuning of LQR controller for an experimental inverted pendulum system based on The Bees Algorithm. *J. Vibroeng.* **2016**, *18*, 3684–3694. [CrossRef]
31. Farajdadian, S.; Hosseini, S.H. Design of an optimal fuzzy controller to obtain maximum power in solar power generation system. *Sol. Energy* **2019**, *182*, 161–178. [CrossRef]
32. Azizi, M.; Mousavi Ghasemi, S.A.; Ejlali, R.G.; Talatahari, S. Optimum design of fuzzy controller using hybrid ant lion optimizer and Jaya algorithm. *Artif. Intell. Rev.* **2020**, *53*, 1553–1584. [CrossRef]
33. Mohanty, H.; Mahapatra, M.; Kumar, P.; Biswas, P.; Mandal, N.R. Predicting the effects of tool geometries on friction stirred aluminium welds using artificial neural networks and fuzzy logic techniques. *Int. J. Manuf. Res.* **2013**, *8*, 296–312. [CrossRef]
34. Vignesh, R.V.; Padmanaban, R. Modelling tensile strength of friction stir welded aluminium alloy 1100 using fuzzy logic. In Proceedings of the 2017 11th International Conference on Intelligent Systems and Control (ISCO), Coimbatore, India, 5–6 January 2017; pp. 449–456.

35. Khansari, N.M.; Karimi, N.; Sabour, M.H. Optimization of friction stir welding by fuzzy logic. In Proceedings of the 2013 13th Iranian Conference on Fuzzy Systems (IFSC), Qazvin, Iran, 27–29 August 2013; pp. 1–6.
36. Badwelan, A.; Al-Samhan, A.M.; Anwar, S.; Hidri, L. Novel Technique for Enhancing the Strength of Friction Stir Spot Welds through Dynamic Welding Parameters. *Metals* **2021**, *11*, 280. [CrossRef]
37. Mekri, H.; Bouchouicha, B.; Miloudi, A.; Christophe, H.; Imad, A. Influence of the coupling between the mechanical characteristics and the welding conditions by the FSSW process: Case of the bi-material aluminum-steel. *Frat. Integrità Strutt.* **2018**, *46*, 62–72.
38. Kruse, R.; Borgelt, C.; Braune, C.; Mostaghim, S.; Steinbrecher, M.; Klawonn, F.; Moewes, C. *Computational Intelligence*; Springer: Berlin/Heidelberg, Germany, 2011.
39. Jantzen, J. *Foundations of Fuzzy Control*; John Wiley & Sons, Inc.: Hoboken, NJ, USA, 2007.
40. Khuntia, S.R.; Mohanty, K.; Panda, S.; Ardil, C. *A Comparative Study of PI, IP, Fuzzy and Neuro-Fuzzy Controllers for Speed Control of DC Motor Drive*; World Academy of Science and Technology: Paris, France, 2009; Volume 68.
41. Thaker, S.; Nagori, V. Analysis of fuzzification process in fuzzy expert system. *Procedia Comput. Sci.* **2018**, *132*, 1308–1316. [CrossRef]
42. Silva, J.F.; Pinto, S.F. Linear and nonlinear control of switching power converters. In *Power Electronics Handbook*; Elsevier: Amsterdam, The Netherlands, 2018; pp. 1141–1220.
43. Gomes, H.M. Fuzzy logic for structural system control. *Lat. Am. J. Solids Struct.* **2012**, *9*, 111–129. [CrossRef]
44. Lee, D.H.; Jeong, I.J.; Kim, K.J. A desirability function method for optimizing mean and variability of multiple responses using a posterior preference articulation approach. *Qual. Reliab. Eng. Int.* **2018**, *34*, 360–376. [CrossRef]

coatings

MDPI

Article

Microstructural Evaluation of Graphene-Reinforced Nickel Matrix Ni-P-Gr Coating on Ti-6Al-4V Alloy by the Electroless Coating Method

Hatice Gunduz [1], Ramazan Karslioglu [2,3] and Fahrettin Ozturk [1,4,*]

[1] Department of Mechanical Engineering, Ankara Yildirim Beyazit University, Ankara 06760, Turkey
[2] Department of Industrial Design, Ankara Yildirim Beyazit University, Ankara 06760, Turkey
[3] AYBU Central Research Laboratory Research and Application Center, Ankara Yildirim Beyazit University, Ankara 06760, Turkey
[4] Turkish Aerospace Industries, Inc., Ankara 06980, Turkey
* Correspondence: fahrettin71@gmail.com or fahrettinozturk@aybu.edu.tr

Abstract: Titanium alloys are widely used in many industrial applications, from aerospace to automotive, and from defense to medical, as they combine superior properties such as high strength and low density. Still, titanium and its alloys are insufficient in environments with friction and wear because of their weak tribological properties. In the literature, numerous research works on improving the surface quality of titanium alloys have been conducted. Electroless coatings, on the other hand, are one of the most widely used surface improvement methods due to its homogeneous thickness achievement, high hardness, and good corrosion resistance. The autocatalytic reduction in the coating process enhances the surface quality of the material or alloy considerably. In addition, many studies in the literature aim to carry the properties of electroless coatings to a higher point by creating a composite coating with the addition of extra particles. In this study, graphene-reinforced nickel matrix Ni-P-Gr coating was applied to the surface of Ti-6Al-4V alloy, in order to enhance weak tribological behaviors, by the electroless coating method. Moreover, the coated and uncoated, heat-treated, and non-heat-treated specimens were subjected to abrasion in linear reciprocating ball-on-plate configuration to observe tribological properties. Microstructure examination of the samples was performed using a scanning Electron Microscope (SEM), X-ray Diffractometer (XRD), X-ray Photon Spectrometry (XPS), and Raman Spectroscopy. Specific wear rates of specimens were calculated using microstructural analysis and the hardness of the produced samples was measured using the Vickers hardness test. Results indicate that both the coating and the heat treatment improved the microstructure and tribological properties significantly. With the graphene-reinforced Ni-P coating via electroless coating process, the hardness of the substrate increased by about 34%, while it increased by approximately 73% using subjected heat treatment. Furthermore, the wear rate of the Ti-6Al-4V substrate was approximately 98% higher than that of the heat-treated nanocomposite coating. The highest wear resistance was obtained at the heat-treated nanocomposite coating.

Keywords: graphene; nanocomposite; nickel matrix coatings; titanium coating; electroless nickel coating; Ni-P electroless coating

Citation: Gunduz, H.; Karslioglu, R.; Ozturk, F. Microstructural Evaluation of Graphene-Reinforced Nickel Matrix Ni-P-Gr Coating on Ti-6Al-4V Alloy by the Electroless Coating Method. *Coatings* **2022**, *12*, 1827. https://doi.org/10.3390/coatings12121827

Academic Editor: Alicia de Andrés

Received: 10 October 2022
Accepted: 19 November 2022
Published: 25 November 2022

1. Introduction

The surface properties of engineering materials directly affect the performance of applications because most of the failures such as corrosion, fatigue, wear, and friction occur on the material surface. Electroless Ni-P coating is widely used in many areas from the automotive to the computer industry since they have properties such as good corrosion resistance, high hardness, thickness uniformity, and good wear resistance [1,2]. Electroless Ni-P coating is an important surface improvement method to improve the

physical and chemical properties of materials due to the autocatalytic reduction process. Many researchers [3–7] have focused on the subject.

It has been stated in many studies in the literature that metal matrix composites are ahead of monolithic metals in terms of properties such as high strength, high electrical conductivity, high toughness, and low density [8–10]. In addition, it has been reported that metal matrix composite coatings can be produced by adding third-phase reinforcements to increase the properties of the coatings such as corrosion-wear resistance and strength, provided that they have biological and chemical compatibility [11–13].

It is common practice to obtain composite electroless nickel plating by adding various particles to electroless nickel plating [14–17]. These particles are completely and evenly distributed in the electroless nickel matrix and are firmly attached to the substrate, making electroless coatings more durable and long lasting than other lubrication and wear resistant alternatives [18]. It is widely accepted in the industry. In this application, it has been demonstrated that microhardness and tribological properties can be significantly improved by particle refining mechanism and charge transfer [19].

Carbon-based materials are the most common reinforcing materials used when creating electroless composite coatings. There have been several studies [20–30] in the literature characterizing their performance. Graphene nanoparticles, on the other hand, are one of the most advantageous carbon-based materials due to their ability to provide fracture strength up to 125 GPa and Young's modulus up to 1 TPa [31]. Thanks to its honeycomb-shaped hexagonal structure, graphene is endowed with numerous strengths such as being atomically thin, inert, wear-resistant, impermeable, and mechanically durable [23,32,33]. The addition of graphene-based materials to electroless nickel coatings has been a recent development and the properties of coatings has great attention. For example, Ni-P coatings prepared by Huihui et al. [20] with graphene oxide reinforcement showed excellent mechanical properties and hardness. Similarly, Tamilarasan et al. [21] synthesized Ni-P-GO with an electroless coating technique, and declared that graphene entering the Ni-P matrix could improve the wear properties of the coating alloy due to the lubricating effect of the graphene. Other researchers produced reduced graphene oxide (rGO) doped electroless Ni-P coating and revealed that the composite coating exhibits a rougher structure [22–24]. On the other hand, in other studies that produced metal matrix composite coatings using rGO, it was emphasized that the optimum amount of reinforcement should be adjusted, and it was revealed that adding a very high amount of rGO particles would adversely affect the hardness [25–27]. Hu et al. [28] used the electroless coating method for the first time for the synthesis of Ni/Graphene sheets and reported that no aggregates were formed despite obtaining a high nickel accumulation rate. Yu et al. [29] produced graphene-doped electroless Ni-P coatings on stainless steel specimens and reported that the graphene reinforcement gave higher Young's modulus and higher hardness.

On the other hand, in some studies in the literature, Ni-P coating and Ni-P-Gr coatings were studied together. The effects of graphene on Ni-P coating were investigated. Mindivan et al. [32] used St-37 substrate in their studies where they produced Ni-P and graphene nano-plate-reinforced Ni-P coating by electrolytic coating method. They found that the lowest wear rate and the highest hardness would be obtained in the composite coating. As a result of microstructural investigations, they stated that this improvement was due to the more compact structure of the composite coating. Uysal [26] produced Ni-P coatings using electroless coating method in his study using mild steel as a substrate. They investigated the effects of graphene oxide and TiO_2 particles on morphology, corrosion and tribological properties, and as a result, they revealed that the presence of graphene oxide and TiO_2 particles improved the hardness of the coating. Yu et al. [29] prepared pure Ni-P coating and graphene-reinforced Ni-P coatings by ultrasonic-assisted electroless plating on mold material (06Cr25Ni20) substrates. In this study, which aims to improve the mechanical properties, the hardness value of the Ni-P coating increased from 1096.4 to 1184.6 HV, while the Young's modulus of the composite coating increased by 8.2%. In other studies using different substrates, it was reported that graphene reinforcement improves

the properties of the Ni-P coating, and the composite coating is particularly tribologically advanced compared to the pure Ni-P coating [23,25,28].

Titanium and its alloys have excellent mechanical and physical properties such as high strength, low weight, and remarkable corrosion resistance, so it is used in many industries, especially in aerospace. Especially, Ti-6Al-4V is a light but strong alloy and saves weight in highly loaded structures, so it is extremely suitable for jet engines, gas turbines, and many airframe components [34–37]. Although titanium and its alloys have been widely used in many areas due to its advanced physical and mechanical properties, unfortunately, it is insufficient in areas which require wear and friction resistance due to electron arrangements and crystalline structures. Many surface improvement methods have been tested to improve the tribological properties of titanium and its alloys [38–41].

The purpose of this study was to investigate the effects of electroless Ni-P coating with graphene nanoparticle reinforcement on the microstructure and weak tribological properties of Ti-6Al-4V. Ni-P-Gr coatings have been produced on different types of substrates by an electroless-deposition method in many studies in the literature. However, to the best of our knowledge, there have been no studies on the production of Ni-P-Gr film, which is associated with the tribological properties of Ti-6Al-4V by electroless deposition method. In addition, the effect of heat treatment on microstructure and tribological properties of the uncoated and coated titanium alloys was investigated. It was found that graphene-reinforced Ni-P matrix nanocomposite coating could be successfully applied on Ti-6Al-4V substrate. Microstructural properties of heat-treated and non-heat-treated, non-coated, and nanocomposite layers were investigated by Scanning Electron Microscopy (SEM), X-ray Diffractometer (XRD), X-ray Photon Spectrometry (XPS), and Raman Spectroscopy. In addition, tribological and mechanical properties were analyzed by a reciprocating the ball-on-plate and the Vickers microhardness test devices. It was concluded that graphene addition and heat treatment remarkably improved the microstructure and tribological properties.

2. Materials and Methods

In this study, Ti-6Al-4V titanium substrates were used. All the substrates have 50 mm × 50 mm × 2 mm dimensions at the beginning of the processes. Surface preparation processes were applied to the Ti-6Al-4V substrates before the coating process. Due to their thermodynamic behavior, titanium alloys tend to form a passive and persistent oxide layer, making it difficult to coat. In addition, if electroless nickel coatings are applied to dirty or oxidized surfaces, desired coating quality cannot be achieved. In order to prevent the oxidation of the titanium surface, the zincating process was carried out. The surface preparation, activation, and oxide layer avoidance processes applied for the Ti-6Al-4V substrates in order. The substrates were degreased with acetone and then air-dried. Afterward, the chemical etching process of the substrates immersed in a 6% hydrogen fluoride (HF) acid solution was completed and rinsed in deionized water. Afterward, the samples, which were zincate for 90 s and then dipped directly into the nanocomposite coating solution. Commercial electroless Ni-P coating solution was used for the coating process. A total of 2 g/L graphene nanoparticle was added to the solution. The average radius of the graphene nanoparticle is 1.5 μm. Electroless nickel phosphate graphene coating bath was mixed with an ultrasonic homogenizer for 1 h in order to prevent the nano powders from clumping and collapsing during the coating process. The coating process took 60 min, the temperature was kept at 90–92 °C during the process and a magnetic stirrer was used to ensure homogeneous mixing. It is a well-known fact that the superiority of the Ni-P-Gr composite coating over the Ni-P coating has already been proven. Therefore, pure Ni-P coating was not applied and eventually a comparison was not made.

In order to observe the effect of the heat treatment after the coating process, a group of samples were exposed to heat treatment. After the electroless coating process was performed, samples were separated into two groups and one was heat-treated for 1 h at 450 °C in an argon atmosphere heat treatment furnace and then the samples were left to

cool down for all night long. The other group was left as non-heat-treated. The wear and friction tests of the samples were carried out in the linear (reciprocating) module of the UTS Tribometer T30M-HT (UTS Scientific Instruments, Trabzon, Turkey) wear test device. The wear tests are based on the ball-on-plate tribo-testing configuration technique and the schematic view of reciprocating wear mechanism is shown in Figure 1. The experiments were carried out at room temperature (RT), in an oil-free environment, under a normal load of 1 N. A ball made of Al_2O_3 with a diameter of 10 mm was used to wear samples with a constant sliding speed of 100 mm/s for the total sliding distance of 100 m.

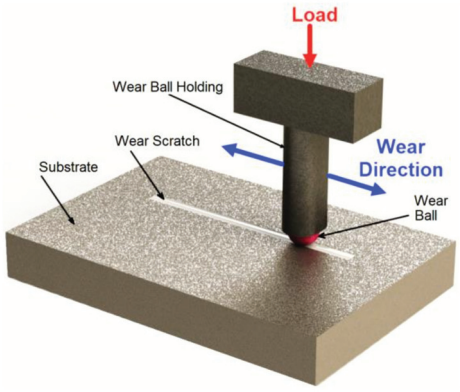

Figure 1. Schematic view of reciprocating wear mechanism.

Surface morphologies were analyzed by Scanning Electron Microscope (Hitachi SU5000, Tokyo, Japan) and Raman analyses were performed with Jasco NRS-4500 Raman spectrometer (Easton, MD, USA) in Ankara Yıldırım Beyazıt University (AYBU) Central Laboratory. The elemental analysis was performed using a PANalytica X'pert Pro MDP Brand XRD scanning device (Great Neck, NY, USA) with Cu K alpha monochromator at a speed of 2°/min. The wavelength of the beam is 1.54059 Å. The analysis of the peaks from the XRD analysis was conducted with the help of computer software. The crystal structure characterization of the Ni-P-Gr coating layer produced in the study, the region where 2θ is between 10° and 110°, was investigated. The chemical composition was investigated by XPS analysis. In addition, XPS measurements were performed on the PHI 5000 Thermo Scientific K-Alpha instrument (Waltham, MA, USA) with a 50 W X-ray anode sourced from monochromatic Al-K (1486.6 eV) beams at a vacuum of 10^{-10} Torr. X-ray Photoelectron Spectroscopy (XPS) analyzes were taken on both the normal sample surface and wear marks. Before starting the analysis, ion beam etching was conducted. This process was performed in order to clean the surface, in case there was 10 nm of pollution, oxidation, etc. on this surface. While looking for nickel, carbon, phosphate, and oxygen in the analysis of normal surfaces, aluminum was also added to the analysis of the wear marks, being the material of the ball. Vickers microhardness studies were carried out for the nano composite coatings, and a load of 200 gr was applied for 15 s in the measurements made using the Matsuzawa HWMMT-X3 brand microhardness test device (Tokyo, Japan). In this study, the microstructural examination of the composite coating was carried out using SEM images, while the presence of graphene was investigated using the XPS and the Raman spectrum analyses. For this reason, the measurement of the coating thickness of the samples was measured using a Leica CTR6000 microscope (Wetzlar, Germany).

3. Results and Discussion

The sectional images taken using a microscope are displayed in Figure 2a,b for the titanium alloy substrate and the nanocomposite coating, respectively. In Figure 2b, the substrate, the substrate-coating interface, and the coating are clearly visible. The interface

lies homogeneously on the substrate. Different studies have stated that, since the electroless coating process takes place in the bath solution, the homogeneous coating thickness was obtained regardless of the substrate shape, and Figure 2b supports this information [42–45]. Also, with the use of the microscope's own scale, ten different measurements were taken on the coating. These measurements yielded a mean coating thickness of 12.47 μm. In a study by Meshram et al. [46], Ni-P and Ni-P-Gr coatings were successfully deposited on the substrate via the electrodeposition method for 1 h. As a result, the coating thickness for Ni-P coating was approximately 3.30 μm, while the coating thickness was found to be approximately 7 μm for each ratio with graphene reinforcement at different ratios. Graphene added to the Ni-P matrix provides more surface area for the reduction in nickel-phosphorus, which may increase the deposition rate leading to the observed increase in the thickness of the graphene-reinforced coatings [46]. Although the coating time of this study is the same, the reason for obtaining a higher coating thickness than that in the Meshram's study can be explained by the addition of graphene at a higher rate. As a matter of fact, the volume of graphene entering the structure increases due to the increase in the graphene added to the bath composition by weight [47]. Likewise, Yasin et al. [47] aimed to produce graphene-reinforced Ni-P coating at different rates using the electrochemical coating technique in their study and obtained the maximum coating thickness at the maximum graphene ratio (0.4 g/L).

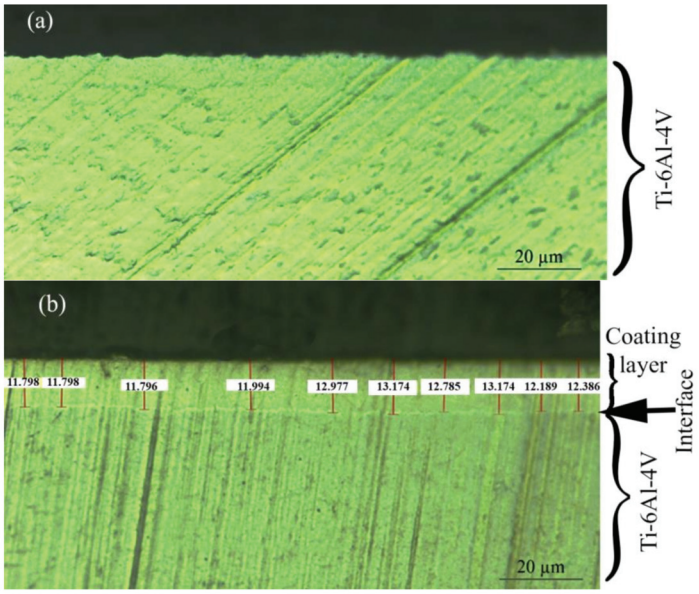

Figure 2. Section from (**a**) Ti-6Al-4V, (**b**) coated sample.

After the successful coating operations, the surfaces were investigated. Figure 3 shows SEM and EDS images of the graphene-doped nickel matrix nanocomposite of Ti6-Al-4V alloys. When the surface morphology of the Ti-6Al-4V alloy was examined, it was clearly seen that there were surface segregations. These segregations were caused by the coaxial α phase and the intergranular β phase in the Ti-6Al-4V alloy microstructure [48]. In the EDS elemental analysis, the elements on the surface of the Ti-6Al-4V alloy are as shown in Figure 3b; after the coating process was applied to the substrate, both the surface morphology and the elemental composition were completely changed and this change is shown in Figure 3c,d, respectively. A homogeneous, crack-free, non-porous, and spherical microstructure was obtained with the coating process. In many studies in the literature, it was pointed out that this nodular microstructure is the characteristic feature of nickel

phosphate coating [49]. On the other hand, when the elemental analysis of the coating is examined, as shown in Figure 3d, it can be understood that the elements belong to the coating on the surface instead of the Ti-6Al-4V alloy. These results prove that the composite coating layers were successfully deposited on the substrate.

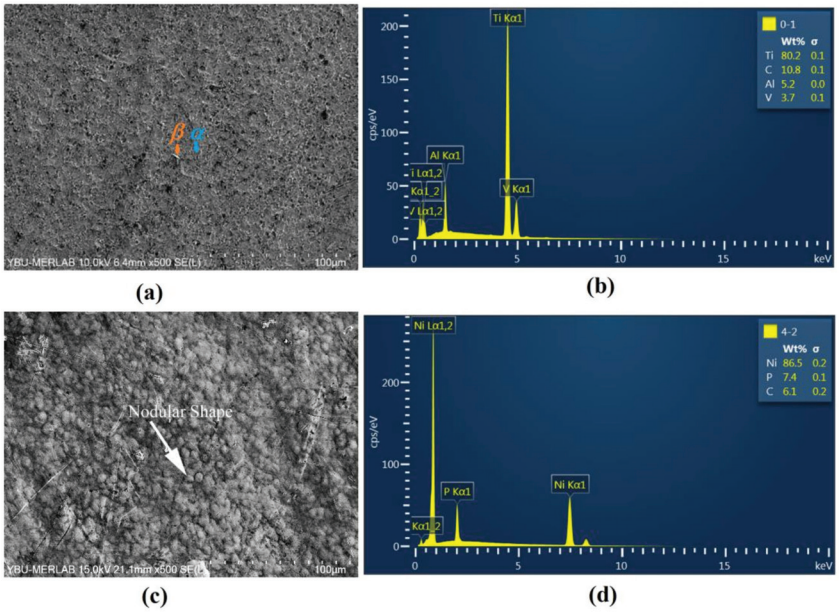

Figure 3. Surface morphologies and SEM, EDS images of the substrates (**a**) SEM image of Ti-6Al-4V; (**b**) EDS image of Ti-6Al-4V; (**c**) SEM image of Ni-P-Gr; (**d**) EDS image of Ni-P-Gr.

As shown in Figure 4, the effects of both the coating and heat treatment on the crystal structure of the samples were investigated by the XRD. Figure 4a shows the crystal structure of Ti-6Al-4V, while Figure 4b belongs to the Ni-P-Gr composite coating. The blue lines in the figures are for the samples that are not heat-treated and the orange lines are for the samples that are heat-treated. Evans et al. [50] stated that crystallinity decreased at the XRD profiles where wide, low, and smooth domes replaced with sharp peaks. The crystalline structure shown with the blue line in Figure 4a undergoes a change and an amorphous structure occurs due to the coating process. This transformation is an expected change since it is known from the research in the literature that the micro structure of the Ni-P coating is also amorphous [51–53]. On the other hand, the blue line indicates the amorphous structure in Figure 4b which is transformed a crystalline structure by heat treatment indicated by the orange line. Amorphous materials are metastable and become stable by heat treatment [18]. A careful examination of the XRD of the Ni-P-Gr coating shows that there is a large peak of face-centered cubic (FCC) Ni (111) at the point where the amorphous and crystalline structures coexist and 2θ equals 45°.

Figure 5 demonstrates the average Vickers hardness values. The highest hardness value was measured at the heat-treated nanocomposite coating. An increase in the microhardness value was observed due to the coating process. It is based on the grain size reduction which generates the crystalline strengthening mechanism and also graphene can avoid dislocation movement in the nickel matrix [32,54–58]. The heat treatment significantly changes the hardness of the Ni-P coating [3,43,59]. As a matter of fact, while the average hardness of the nanocomposite coating was 438.52 HV, it increased by approximately 29% during the heat treatment and became 566.9 HV.

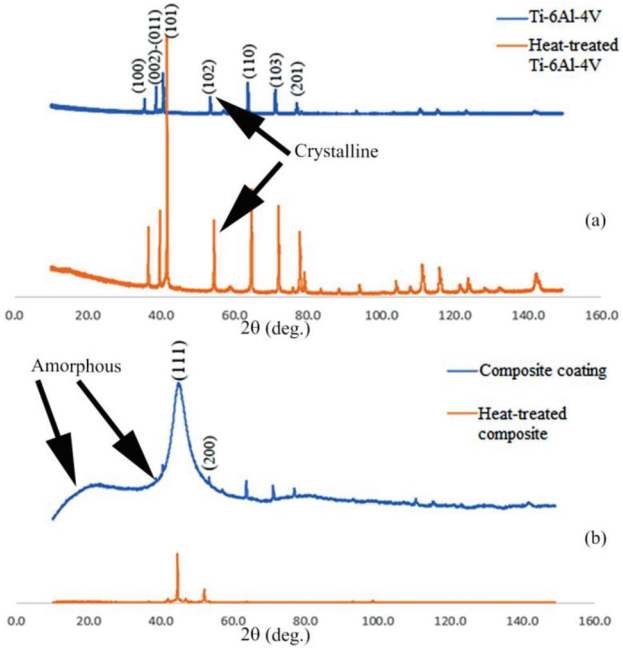

Figure 4. XRD patterns of (**a**) Ti-6Al-4V and (**b**) the coated sample, the blue lines show the non-heat-treated samples, while the oranges are for the heat-treated samples.

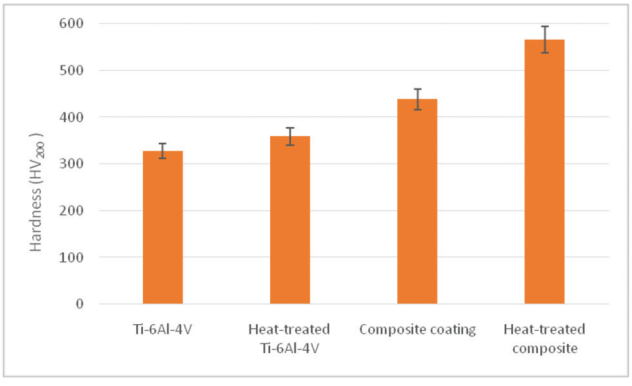

Figure 5. Average micro hardness values.

After the linear reciprocating wear process, wear traces were formed, and the high magnification of SEM photographs of these wear traces are shown in Figure 6. The red arrow in the figure indicates the sliding direction of the abrasive ball. Figure 6a, b are images of untreated and heat-treated Ti-6Al-4V substrates, respectively. During the linear reciprocating motion of the abrasive ball, slip lines parallel to the ball movement were formed due to the plastic deformation on both surfaces. Based on the studies in the literature, this can be interpreted as the occurrence of abrasive wear [58,60,61]. In Figure 6a, partial eruptions are also visible on the worn surface of the samples that are non-heat-treated. Since Xu et al. [59] stated that the adhesive wear mechanism could be seen as eruptions in SEM images. These eruptions are associated with the predominant wear

mechanism being the adhesive wear mechanism. In Figure 6b, however, the dominant wear mechanism underwent abrasive wear, as the debris resulting from this adhesive wear decreased.

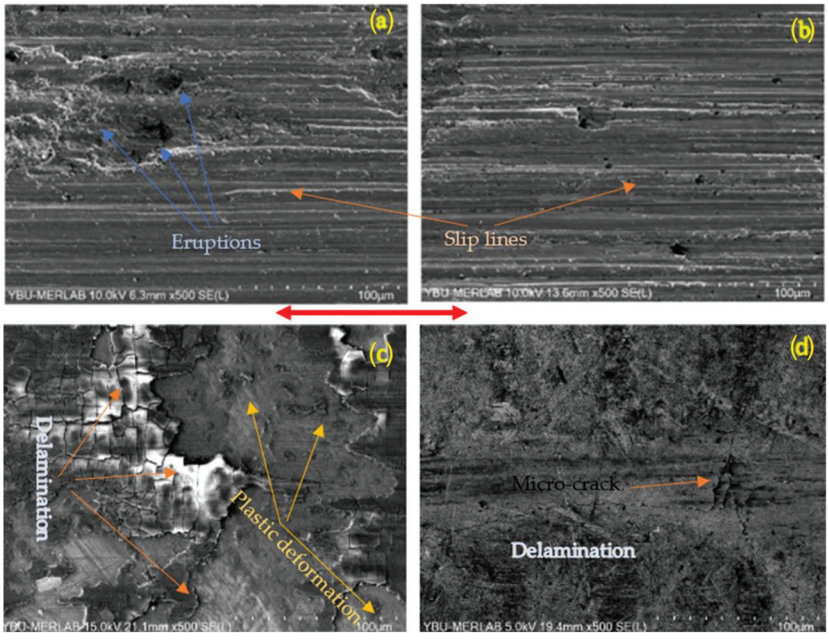

Figure 6. Wear traces of substrates: (**a**) non-heat-treated and (**b**) heat-treated Ti-6Al-4V; (**c**) non-heat-treated and (**d**) heat-treated Ni-P-Gr.

Figure 6c,d shows SEM images of non-heat-treated and heat-treated Ni-P-Gr nanocomposite coatings, respectively. As can be seen from the microstructure in Figure 6c, plastic deformation occurred because of the abrasive forces acting on the substrate, and microcracks turned into debris. Similar wear mechanism has been observed in studies in the literature and this wear mechanism has been associated with delamination. [26,32,60,62]. In addition to this, the presence of abrasive wear traces is also seen in the samples that are non-heat-treated. On the other hand, when the microstructure of the heat-treated coating was examined, it was observed that microcracks formed due to the loads on the substrate during the wear tests, but these cracks did not progress enough to cause delamination. When considered together with the hardness results presented above, the failure of the cracks to progress and the minimum amount of wear can be associated with the highest hardness in this sample. As a matter of fact, it is the subject of many studies that hardness and wear resistance are directly proportional [63–65]. When the figures are examined, it can be seen that the most wear traces are observed in Ti-6Al-4V samples, and as a result of the heat treating and coating, partial spills occur in the Ti-6Al-4V heat- treated sample, while only micro-cracks occur in the heat-treated coating. Abrasive wear resistance decreases with increasing hardness, which proves the change in the dominant wear mechanism in the composite coating. When the hardness increases, abrasive wear resistance decreases; therefore, regarding the change of the dominant wear mechanism, it can be proven that the hardness increases regarding both the heat treatment and coating [61].

On the other hand, the wear scar widths formed after the wear tests are shown in Figure 7. Trace widths were measured using the ImageJ software program and found to be 1.226 mm for Ti-6Al-4V (Figure 7a). The effect of heat treatment on the wear scar width is seen in Figure 7b and the scar width with heat treatment decreased slightly to

1.127 mm. Moreover, the wear scar width was measured as 0.367 mm for the Ni-P-Gr nano composite coating and 0.342 mm for the heat-treated coating. This reduction in track width can be interpreted as the composite coating, significantly increasing the wear resistance of the surface. As a matter of fact, it has been mentioned in many studies in the literature that the Ni-P-Gr coating improves the tribological properties of different surfaces. Mindivan et al. [32] and Algul et al. [58] produced graphene-reinforced Ni-P coatings by electroplating and found that the wear marks on the composite coated surface were reduced. The main reason is the fact that the composite coating increases the hardness and graphene has solid lubricating properties [66].

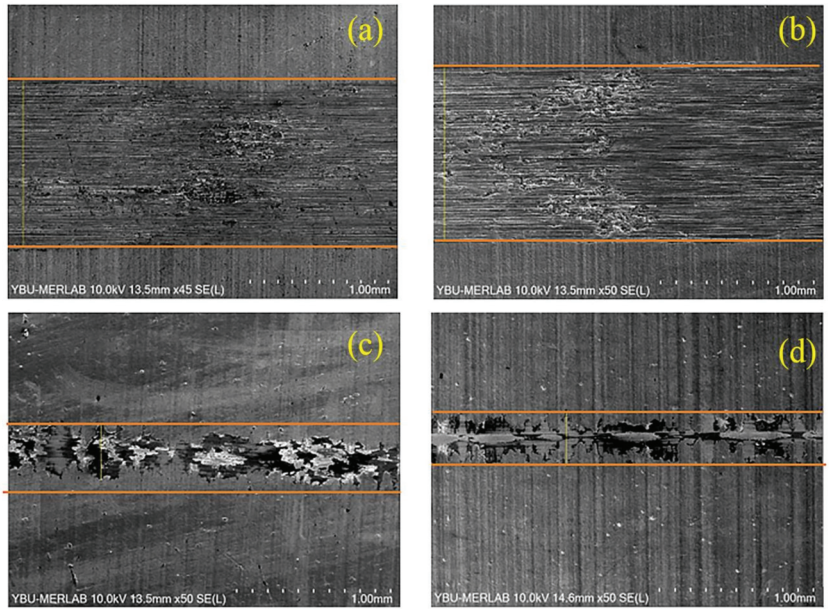

Figure 7. SEM morphologies of the wear tracks of substrates: (**a**) Ti-6Al-4V (**b**) Heat-treated Ti-6Al-4V (**c**) Composite coating (**d**) Heat-treated composite coating. The orange lines show the wear mark width and the yellow lines are the parallel lengths calculated by the ImageJ program.

The volume of wear loss was calculated geometrically using the wear scar width data measured with ImageJ V 1.8.0 software in Figure 7a–d. The calculated wear scar geometry is presented in Figure 8. Then, the specific wear rate was calculated using Equation (1) [67],

$$Wr = W/NL \quad (1)$$

where Wr is the specific wear rate [$mm^3/(Nm)$], N is the normal load, L is the sliding distance, and W is the calculated wear volume [67]. Specific wear rates were calculated as shown in Figure 9. The wear rate decreased significantly with the electroless coating process, this rate increased even more with the effect of the heat treatment, the lowest specific wear rate was obtained in the heat-treated coating. The calculated wear rates were 8.22, 6.38, 0.24 and 0.19 ($\times 10^{-9}$) mm^3/Nm, respectively. The specific wear rate for Ti-6A-4V reduced by approximately 22% due to the effect of heat treatment. The wear rate was reduced by approximately 98% by the graphene enhanced nickel-phosphorus coating of Ti-6Al-4V. In addition, the heat treatment negatively affected the wear rate of the coated sample, and a 21% reduction was achieved in the wear rate. As a result, it has been observed that both the heat treatment and the composite coating increase the wear resistance of the Ti-6Al-4V material. The highest wear resistance was observed in the

heat-treated Ni-P-Gr nanocomposite coating. In other studies in the literature, it has been emphasized that the wear resistance increases, especially with graphene reinforcement [62]. During the tribological test, the temperature rises at the contact surface due to frictions. Graphene is not stable at high temperatures; therefore, graphene converts to graphite on nanocomposite surfaces. The converted graphites significantly reduce the coefficient of friction due to the high temperature generated on the friction surfaces, another factor that reduces wear loss [68].

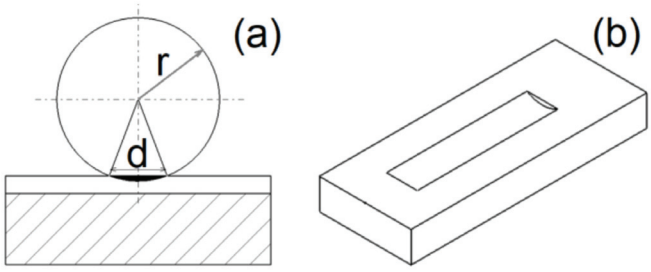

Figure 8. The wear scar generated by reciprocating sliding motion of the ball on a flat specimen; (**a**) 2D view of the wear scar [67] (**b**) 3D view of the wear scar [62].

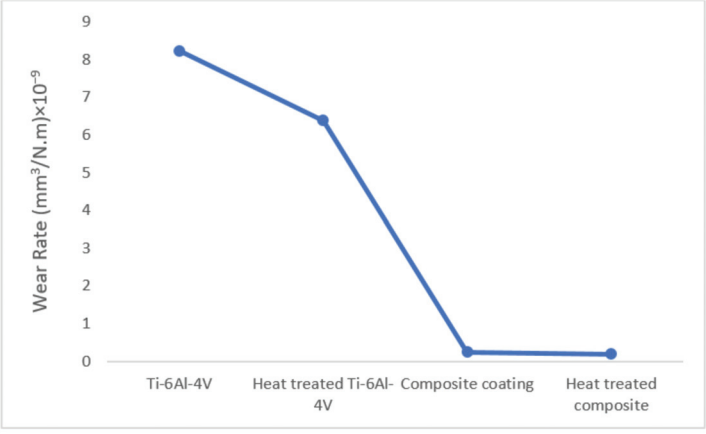

Figure 9. Specific wear rates.

The chemical composition of the Ni-P-Gr composite coating was investigated using the XPS analysis and the spectra obtained from the coating surface are given in Figure 10a–d. The Ni2P spectrum of the Ni-P-Gr composite coating was characterized by a highly intensity peak at 853.3 eV. This spectrum could be related to the nickel element [69,70]. Moreover, graphene's chemical state is sp2 and the binding energy for this state is approximately 284 eV [71]. A C1s peak was observed on approximately 284 eV in Figure 10a,b. In Figure 10c,d, an Ni2P spectrum was observed about 854 eV. These peaks indicate the presence of nickel and graphene in chemical composition.

Raman spectroscopy plays an important role in the structural characterization of graphene-based materials, and Figure 11a–d show the Raman spectroscopy of the non-heat-treated and heat-treated composite coatings. Raman spectroscopy provides important information about graphene defects and stacking. Graphene can be clearly distinguished from graphite by the Raman spectrometry [72]. The main features in the graphite/graphene Raman spectrum are represented by the D, G, and 2D peaks. A G peak at approximately 1580 cm^{-1} and a 2D peak at approximately 2700 cm^{-1} is observed on graphite samples.

It was seen that the 2D graphite tape always has a shoulder of about 2650 cm^{-1} and this shoulder represents graphite. The D band was found at about 1330 cm^{-1} and is indicative of defects in the sample [1,73,74]. As seen in the figure, each sample has a D peak at approximately 1370 cm^{-1}, a G peak at 1590 cm^{-1}, and a 2D peak at 2790 cm^{-1}, and there was no shoulder on the 2D peak in any of the samples. The Raman spectra obtained from composite coatings confirm that graphene was successfully reinforced into nickel-phosphorus obtained by the electroless coating method. In Figure 11a,b, the peak densities decreased a little bit with the effect of heat treatment, and in Figure 11c, it underwent a great change with the effects of wear and heat treatment. In Figure 11d, the peak intensities have approached zero. After searching the literature, we found that it has been concluded that structural defects occur in graphene structures due to the mechanical loads occurring during wear and the high-temperature effect caused by friction, and due to these defects, the graphene structure deteriorates and transforms into a graphite-like structure [61]. Graphite is known to be one of the most widely used lubricants. In this case, when the wear and the Raman analysis results were examined together, it was determined that these graphite-like structures reduce the wear loss at the interface.

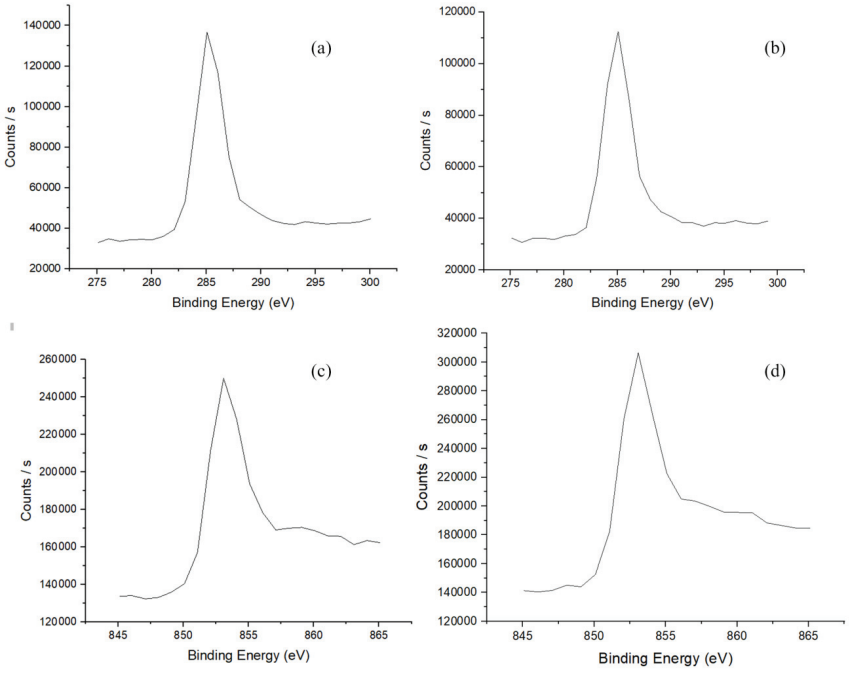

Figure 10. C1s and Ni 2p3/2 regions of high-resolution XPS spectra obtained with carbon and Ni in the Ni-graphene nanocomposite coating: (**a**) C1s on surface; (**b**) C1s on scratch; (**c**) Ni2P on surface; (**d**) Ni2P on scratch.

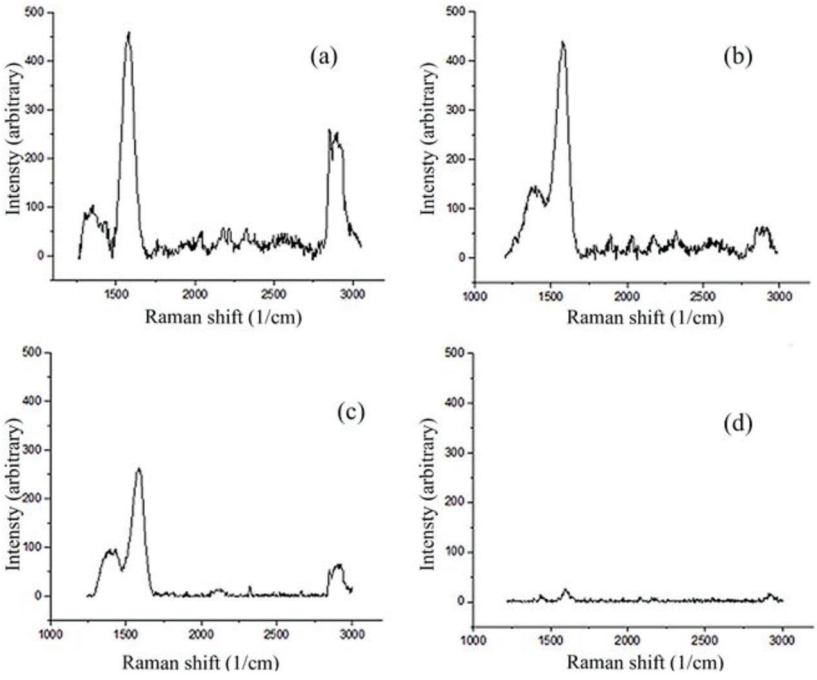

Figure 11. Raman spectroscopy of composite coating: (**a**) coated surface; (**b**) coated scratch; (**c**) coated heat-treated surface; (**d**) coated heat-treated scratch.

4. Conclusions

In this study, graphene-reinforced nickel matrix Ni-P-Gr coating was applied to the surface of Ti-6Al-4V alloy using the electroless coating method. The effects of composite coating and heat treatment on microstructure and tribological properties were investigated. Following conclusions were drawn:

- The Gr-Ni-P coating was successful. The microstructure of titanium alloy turned into a nodular structure. In addition, a 12.47 μm coating thickness was achieved on titanium alloy substrates.
- The crystal structure of the Ti-6Al-4V material turned into an amorphous structure with the composite coating process.
- The heat treatment applied to the composite coating caused the phase transformation and made the crystal structure more stable.
- The heat treatment had a positive effect on the wear resistance in both coated and uncoated structures.
- Both coating and heat treatment had a positive effect on the microhardness values. The highest hardness value of 566.9 HV was achieved at the heat-treated Ni-P-Gr coating.
- It was observed that the wear was higher in uncoated samples. The lowest wear scar width was obtained in the heat-treated graphene-reinforced nanocomposite coating.
- The highest wear resistance was obtained in the heat-treated nanocomposite coating.
- In the XPS analysis, binding energies of approximately 284 and 853 eV were obtained, revealing the presence of Gr and Ni in the coating structure, respectively.
- Raman spectrometry analysis revealed that the lubrication property was increased with the heat treatment.
- The wear rate of the Ti-6Al-4V substrate is approximately 98% higher than that of the heat-treated nanocomposite coating. The highest wear resistance was observed on the heat-treated nanocomposite coating.

Author Contributions: Conceptualization, R.K.; Methodology, R.K. and H.G.; Validation, experimental study and characterization, H.G., Supervision, R.K. and F.O.; Writing—original draft, H.G.; Writing—review & editing, F.O. All authors have read and agreed to the published version of the manuscript.

Funding: This study was supported by Ankara Yildirim Beyazit University (AYBU), Scientific Research Projects Unit (FYL-2021-2229).

Institutional Review Board Statement: Not applicable.

Informed Consent Statement: Not applicable.

Data Availability Statement: Not applicable.

Acknowledgments: AYBU support is greatly appreciated.

Conflicts of Interest: The authors declare no conflict of interest.

References

1. Su, F.; Liu, C.; Guo, J.; Huang, P. Characterizations of nanocrystalline Co and Co/MWCNT coatings produced by different electrodeposition techniques. *Surf. Coat. Technol.* **2013**, *217*, 94–104. [CrossRef]
2. Mina, M.; Bastwros, H.; Esawi AM, K.; Wifi, A. Friction and wear behavior of Al-CNT composites. *Wear* **2013**, *307*, 164–173.
3. Mallory, G.O.; Hadju, J.B. *Electroless Plating: Fundamentals and Applications*; American Electroplaters and Surface Finishers Society: New York, NY, USA, 1990.
4. Zhang, Q.; Wu, M.; Zhao, W. Electroless nickel plating on hollow glass microspheres. *Surf. Coat. Technol.* **2005**, *192*, 213–219. [CrossRef]
5. Martyak, N.; McCaskie, J. Speciation in electroless nickel solutions. *Plat. Surf. Finish.* **1996**, *83*, 62–66.
6. Wang, X.C.; Cai, W.B.; Wang, W.J.; Liu, H.T.; Yu, Z.Z. Effects of ligands on electroless Ni–P alloy plating from alkaline citrate–ammonia solution. *Surf. Coat. Technol.* **2003**, *168*, 300–306. [CrossRef]
7. Pei, S.; Li, S.; Zhong, L.; Cui, K.; Yang, J.; Yang, Z. Analysis of the causes of differences between the upper and lower surfaces of electroless Ni-P Coating on LZ91 Magnesium-Lithium Alloy. *Coatings* **2022**, *12*, 1157. [CrossRef]
8. Mazumdar, S.K. *Composites Manufacturing: Materials, Product and Process Engineering*; CRC Press LLC: Boca Raton, FL, USA, 2002.
9. Akbulut, H. Alümina Fiber Takviyeli Al-Si Metal Matriksli Kompozit Üretimi ve Mikroyapı Özellik Ilişkilerinin Incelenmesi. Ph.D. Thesis, İstanbul Teknik Üniversitesi, Istanbul, Turkey, 1995.
10. Evans, A.; SanMarchi, C.; Mortensen, A. *Metal Matrix Composites in Industry: An Introduction and a Survey*; Chawla, N., Chawla, K.K., Eds.; Metal Matrix Composites; Springer: New York, NY, USA, 2003.
11. Bakhita, B.; Akbaria, A.; Nasirpouria, F.; Hosseini, M.G. Corrosion resistance of Ni–Co alloy and Ni–Co/SiC nanocomposite coatings electrodeposited by sediment codeposition technique. *Appl. Surf. Sci.* **2014**, *307*, 351–359. [CrossRef]
12. Gül, H.; Kılıç, F.; Uysal, M.; Aslan, S.; Alp, A.; Akbulut, H. Effect of Particle Concentration On the Structure and Tribological Properties of Submicron Particle Sic Reinforced Ni Metal Matrix Composite (MMC) Coatings Produced by Electrodeposition. *Appl. Surf. Sci.* **2012**, *258*, 4260–4267. [CrossRef]
13. Gül, H.; Akbulut, H.; Aslan, S.; Alp, A. Effect of Reciprocating Sliding Speed on the Tribological Performance of Nano SiCp Reinforced Ni-Metal Matrix Composites Produced by Electrocodeposition. *J. Nanosci. Nanotechnol.* **2012**, *12*, 9076–9087. [CrossRef]
14. Ding, X.; Wang, W.; Zhang, A.; Zhang, L.; Yu, D. Efficient Visible Light Degradation of Dyes in Wastewater by Nickel–phosphorus Plating–titanium Dioxide Complex Electroless Plating Fabric. *J. Mater. Res.* **2019**, *34*, 999–1010. [CrossRef]
15. Hsu, C.-I.; Hou, K.-H.; Ger, M.-D.; Wang, G.-L. The Effect of Incorporated SelfLubricated BN(h) Particles on the Tribological Properties of Ni–P/BN(h) Composite Coatings. *Appl. Surf. Sci.* **2015**, *357*, 1727–1735. [CrossRef]
16. Huang, Z.; Zhou, Y.; Nguyen, T. Study of nickel matrix composite coatings deposited from electroless plating bath loaded with TiB2, ZrB2 and TiC particles for improved wear and corrosion resistance. *Surf. Coat. Technol.* **2019**, *364*, 323–329. [CrossRef]
17. Arulvel, S.; Elayaperumal, A.; Jagatheeshwaran, M.S.; Satheesh, K.A. Comparative Study on the Friction-Wear Property of As-Plated, Nd-YAG Laser Treated, and Heat-Treated Electroless Nickel-Phosphorus/Crab Shell Particle Composite Coatings on Mild Steel. *Surf. Coat. Technol.* **2019**, *357*, 543–558. [CrossRef]
18. Delaunois, F.; Vitry, V.; Bonin, L. (Eds.) *Electroless Nickel Plating Fundamentals to Applications*; CRC Press: Boca Raton, FL, USA, 2020.
19. Shi, L.; Sun, C.; Gao, P.; Zhou, F.; Liu, W. Mechanical properties and wear and corrosion resistance of electrodeposited Ni–Co/SiC nanocomposite coating. *Appl. Surf. Sci.* **2006**, *252*, 3591–3599. [CrossRef]
20. Jibo, J.; Haotian, C.; Liying, Z.; Qian, W.; Han, S.; Lin, H.; Huihui, W. Effect of heat treatment on structures and mechanical properties of electroless Ni-P-GO composite coatings. *RSC Adv.* **2016**, *6*, 10900.
21. Tamilarasan, T.R.; Sanjith, U.; Rajendran, R.; Rajagopal, G.; Sudagar, J. Effect of Reduced Graphene Oxide Reinforcement on the Wear Characteristics of Electroless Ni-P Coatings. *J. Mater. Eng. Perform.* **2018**, *27*, 3044–3053. [CrossRef]
22. Lee, C.K.; Teng, C.L.; Tan, A.H.; Yang, C.Y.; Lee, S.L. Electroless Ni-P/Diamond/Graphene Composite Coatings and Characterization of Their Wear and Corrosion Resistance in Sodium Chloride Solution. *Key Eng. Mater.* **2015**, *656*, 51–56. [CrossRef]

23. Sadhir, M.H.; Saranya, M.; Aravind, M.; Srinivasan, A.; Siddharthan, A.; Rajendran, N. Comparison of in Situ and Ex Situ Reduced Graphene Oxide Reinforced Electroless Nickel Phosphorus Nanocomposite Coating. *Appl. Surf. Sci.* **2014**, *320*, 171–176. [CrossRef]
24. Jiang, N.; Fu, C.Q.; Wang, Z. Research on the Microstructure and Tribological Properties of the Electroless Ni–P-PTFE Composite Repairing Coating on Gears. *Appl. Mech. Mater.* **2013**, *327*, 136–139. [CrossRef]
25. Wu, H.; Liu, F.; Gong, W.; Ye, F.; Hao, L.; Jiang, J.; Han, S. Preparation of Ni–P–GO Composite Coatings and Its Mechanicals. *Surf. Coat. Technol.* **2015**, *272*, 25–32. [CrossRef]
26. Uysal, M. Electroless Codeposition of Ni–P Composite Coatings: Effects of Graphene and TiO2 on the Morphology, Corrosion, and Tribological Properties. *Metall. Mater. Trans. A* **2019**, *50*, 2331–2341. [CrossRef]
27. Kumari, S.; Panigrahi, A.; Singh, S.K.; Pradhan, S.K. Corrosion-Resistant Hydrophobic Nanostructured Ni-Reduced Graphene Oxide Composite Coating with Improved Mechanical Properties. *J. Mater. Eng. Perform.* **2018**, *27*, 5889–5897. [CrossRef]
28. Hu, Q.-H.; Wang, X.-T.; Chen, H.; Wang, Z.-F. Synthesis of Ni/Graphene Sheets by an Electroless Ni-plating Method. *New Carbon Mater.* **2012**, *27*, 35–41. [CrossRef]
29. Yu, Q.; Zhou t Jiang, Y.; Yan, X.; An, Z.; Wang, X.; Zhang, D.; Ono, T. Preparation of Graphene-Enhanced Nickel-Phosphorus Composite Films by Ultrasonic-Assisted Electroless Plating. *Aplied Surf. Sci.* **2018**, *435*, 617–625. [CrossRef]
30. Srivatswa, A.; Sarkar, S.; De, J.; Majumdar, G. Parametric optimization of electroless Ni-P-CNT coating using genetic algorithm to maximie the rate of deposition. *Mater. Today Proc.* **2022**, *66*, 3769–3774.
31. Rashad, M.; Pan, F.; Tang, A.; Asif, M. Effect of Graphene Nanoplatelets addition on mechanical properties of pure aluminum using a semi-powder method. *Prog. Nat. Sci. Mater. Int.* **2014**, *24*, 101–108. [CrossRef]
32. Mindivan, F.; Aydın, K.; Mindivan, H. Production and Characterization of Electrodeposited Nickel/Graphene Composite Coatings. *Nevşehir Bilim Ve Teknol. Derg.* **2019**, *8*, 29–36. [CrossRef]
33. Gao, X.; Yue, H.; Guo, E. Mechanical properties and thermal conductivity of graphene reinforced copper matrix composites. *Powder Technol.* **2016**, *301*, 601. [CrossRef]
34. Bardes, B.P. *Metals Handbook, Volume 3 Properties and Selection: Stainless Steels, Tool Materials and Species-Purpose Metals Titanium and Titanium Alloys*, 9th ed.; ASM: Almere, The Netherlands, 1980.
35. Tanrıöver, K.; Taşçı, A. Titanyum Alaşımlarının Isıl İşlemi. *Makine Mag.* **1997**, *1*, 58.
36. Brunette, D.M.; Tengwall, B.; Textor, M.; Thomsen, P. *Titanium in Medicine*; Springer: Heidelberg, Germany, 2001.
37. Long, M.; Rack, H.J. Titanium alloys in total joint replacement- a materials science perspective. *Biomaterials* **1998**, *19*, 1621–1639. [CrossRef]
38. Gupta, M.K.; Etri, H.E.; Korkmaz, M.E.; Ross, N.S.; Krolczyk, G.M.; Gawlik, J.; Pimenov, D.Y. Tribological and surface morphological characteristics of titanium alloys: A review. *Arch. Civ. Mech. Eng.* **2022**, *22*, 72. [CrossRef]
39. Shum, P.W.; Zhou, Z.F.; Li, K.Y. Investigation of the tribological properties of the different textured DLC coatings under reciprocating lubricated conditions. *Tribol. Int.* **2013**, *65*, 259–264. [CrossRef]
40. Kaur, S.; Ghadirinejad, K.; Reza, H.O. An Overview on the Tribological Performance of Titanium Alloys with Surface Modifications for Biomedical Applications. *Lubricants* **2019**, *7*, 65. [CrossRef]
41. Yilbaş, B.S.; Şahin, A.Z.; Al-Garni, A.Z.; Said, S.A.; Ahmed, Z.; Abdulaleem, B.J.; Sami, M. Plasma nitriding of Ti 6Al 4V alloy to improve some tribological properties. *Surf. Coat. Technol.* **1996**, *80*, 287–292. [CrossRef]
42. Schlesinger, M. *Modern Electroplating*, 5th ed.; John Wiley & Sons Inc: Toronto, ON, Canada, 2010.
43. Riedel, W. *Electroless Nickel Plating, Metals Park*; ASM International: Novelty, OH, USA, 1991.
44. Çakır, A.F. Akımsız Nikel Kaplamalar ve Uygulamaları. *Yüzey İşlemler* **2001**, *98*, 76–83.
45. Shahin, G.E. Comparison of Electroless Nickel & Functional Chromium. In Proceedings of the SUR/FIN 2009 Technical Conference, Louisville, KY, USA, 16–17 June 2009.
46. Meshram, A.P.; Kumar, M.K.P.; Srivastava, C. Enhancement in the corrosion resistance behaviour of amorphous Ni-P coatings by incorporation of graphene. *Diam. Relat. Mater.* **2020**, *105*, 107795. [CrossRef]
47. Yasin, G.; Khan, M.A.; Arif, M.; Shakeel, M.; Hassan, T.M.; Khan, W.Q.; Korai, R.M.; Abbas, Z.; Zuo, Y. Synthesis of spheres-like Ni/graphene nanocomposite as an efficient anti-corrosive coating; effect of graphene content on its morphology and mechanical properties. *J. Alloys Compd.* **2018**, *755*, 79–88. [CrossRef]
48. Brunelli, K.; Dabala, M.; Magrini, M. Diffusion treatment of Ni–B coatings by induction heating to harden the surface of Ti–6Al–4V alloy. *Mater. Chem. Phys.* **2009**, *115*, 467–472. [CrossRef]
49. Balaraju, J.N.; Saroary, J.; Anjana, J.; Rajam, K.S. Structure and phase transformation behavior of electroless Ni–P alloys containing tin and tungsten. *J. Alloys Compd.* **2007**, *436*, 319–327. [CrossRef]
50. Thomas, E.W.; Schlesinger, M. The Effect of Solution PH and Heat-Treatment on the Properties of Electroless Nickel-boron Films. *J. Electrochem. Soc.* **1994**, *141*, 78–82. [CrossRef]
51. Du, S.; Li, Z.; He, Z.; Ding, H.; Wang, X.; Zhang, Y. Effect of Temperature on the Friction and Wear Behavior of Electroless Ni–P–MoS2–CaF2 Self-Lubricating Composite Coatings. *Tribol. Int.* **2018**, *128*, 197–203. [CrossRef]
52. Wu, Y.T.; Lei, L.; Shen, B.; Hu, W.B. Investigation in Electroless NiP- Cg(Graphite)-SiC Composite Coating. *Surf. Coat. Technol.* **2006**, *201*, 441–445. [CrossRef]
53. Apachitei, I.; Duszczyk, J.; Katgerman, L.; Overkamp, P.J.B. Electroless Ni–P Composite Coatings: The Effect of Heat Treatment on The Microhardness of Substrate and Coating. *Scr. Mater.* **1998**, *38*, 1347–1353. [CrossRef]

54. Zhecheva, A.; Sha, W.; Malinov, S.; Long, A. Enhancing the microstructure and properties of titanium alloys through nitriding and other surface engineering methods. *Surf. Coat. Technol.* **2015**, *200*, 2192–2207. [CrossRef]
55. Praveen, B.M.; Venkatesha, T.V. Electrodeposition and properties of Zn–Ni–CNT composite coatings. *J. Alloys Compd.* **2009**, *482*, 53–57. [CrossRef]
56. Baudrand, D.W. *Electroless Nickel Plating*; ASM International: Materials Park, OH, USA, 1994.
57. Kumar, C.M.P.; Venkatesha, T.V.; Shabadi, R. Preparation and corrosion behavior of Ni and Ni–graphene composite coatings. *Mater. Res. Bull.* **2013**, *48*, 1477–1483. [CrossRef]
58. Algul, H.; Tokur, M.; Ozcan, S.; Uysal, M.; Cetinkaya, T.; Akbulut, H.; Alp, A. The effect of graphene content and sliding speed on the wear mechanism of nickel–graphene nanocomposites. *Appl. Surf. Sci.* **2015**, *359*, 340–348. [CrossRef]
59. Xu, Z.Q.; Zhang, X.; Shi, W.; Zhai, K.Y. Tribological Properties of TiAl Matrix Self-Lubricating Composites Containing Multilayer Graphene and Ti3SiC2 at High Temperatures. *Tribol. Trans.* **2015**, *58*, 1131–1141. [CrossRef]
60. Karslıoğlu, R. Karbon Nanotüp Takviyeli Nikel-Kobalt Kaplamaların Geliştirilmesi. Ph.D. Thesis, Sakarya University, Serdivan, Turkey, 2014.
61. Karslioglu, R.; Akbulut, H. Comparison microstructure and sliding wear properties of nickel–cobalt/CNT composite coatings by DC, PC and PRC current electrodeposition. *Appl. Surf. Sci.* **2015**, *353*, 615–627. [CrossRef]
62. Sharma, S.; Sangal, S.; Monda, K. On the optical microscopic method for the determination of ball-on-flatsurface linearly reciprocating sliding wear volume. *Wear* **2013**, *300*, 82–89. [CrossRef]
63. Bai, H.; Zhong, L.; Kang, L.; Zhuang, W.; Lv, Z.; Xu, Y. A review on wear-resistant coating with high hardness and high toughness on the surface of titanium alloy. *J. Alloys Compd.* **2021**, *882*, 160645. [CrossRef]
64. Uygunoğlu, T.; Brostow, W.; Gunes, I. Wear and friction of composites of an epoxy with boron containing wastes. *Polimeros* **2015**, *25*, 271–276. [CrossRef]
65. Khruschov, M. Resistance of metal to wear by abrasion as related to hardness. In Proceedings of the Conference Lubrication and Wear, London, UK, 1–3 October 1957; Institution of Mechanical Engineers: London, UK; pp. 655–659.
66. Tiwari, S.K.; Kumar, V.; Huczko, A.; Oraon, R.; Adhikari, A.D.; Nayak, G.C. Magical Allotropes of Carbon: Prospects and Applications. Crit. Rev. *Solid State Mater. Sci.* **2016**, *41*, 257–317. [CrossRef]
67. Zeng, Q.; Erdemir, A.; Eryılmaz, O. Ultralow Friction of ZrO_2 Ball Sliding against DLC Films under Various Environments. *Appl. Sci.* **2017**, *7*, 938. [CrossRef]
68. Penkov, O.V. *Tribology of Graphene: Simulation Methods, Preparation Methods, and Their Applications*; Elsevier Inc.: Zhejiang, China, 2020.
69. Zhang, W.; Li, Y.; Zeng, X.; Peng, S. Synergetic effect of metal nickel and graphene as a cocatalyst for enhanced photocatalytic hydrogen evolution via dye sensitization. *Sci. Rep.* **2015**, *5*, 10589. [CrossRef]
70. Johra, F.T.; Lee, J.W.; Jung, W.G. Facile and Safe Graphene Preparation on Solution-based platform. *J. Ind. Eng. Chem.* **2014**, *20*, 2883–2887. [CrossRef]
71. Binding Energy of Graphene (n.d). Available online: https://www.jp.xpssimplified.com/elements/carbon.php (accessed on 25 February 2022).
72. Malard, L.M.; Pimenta, M.A.; Dresselhaus, G.; Dresselhaus, M.S. Raman spectroscopy in graphene. *Phys. Rep.* **2009**, *473*, 51–87. [CrossRef]
73. Ferrari, A.C. Raman spectroscopy of graphene and graphite: Disorder, electron-phonon coupling, doping and nonadiabatic effects. *Solid State Commun.* **2007**, *143*, 47–57. [CrossRef]
74. Vidano, R.P.; Fischbach, D.B.; Willis, L.J.; Loehr, T.M. Observation of Raman Band Shifting with Excitation Wavelength for Carbons and Graphites. *Solid State Commun.* **1981**, *39*, 341–344. [CrossRef]

coatings

MDPI

Article

Microwave-Assisted Synthesis, Characterization and Tribological Properties of a g-C_3N_4/MoS_2 Nanocomposite for Low Friction Coatings

Mukul Saxena [1], Anuj Kumar Sharma [1,*], Ashish Kumar Srivastava [2], Rabesh Kumar Singh [1], Amit Rai Dixit [3], Akash Nag [4] and Sergej Hloch [5]

[1] Centre for Advanced Studies, Lucknow 226031, Uttar Pradesh, India
[2] Department of Mechanical Engineering, G.L. Bajaj Institute of Technology and Management, Greater Noida 201306, Uttar Pradesh, India
[3] Department of Mechanical Engineering, Indian Institute of Technology (ISM), Dhanbad 826004, Jharkhand, India
[4] Faculty of Mechanical Engineering, VŠB—Technical University of Ostrava, 70800 Ostrava, Czech Republic
[5] Faculty of Manufacturing Technologies, TUKE with a Seat in Prešov, 080 01 Prešov, Slovakia
* Correspondence: anujksharma@cas.res.in

Abstract: This study explores the tribological performance of microwave-assisted synthesized *g*-C_3N_4/MoS_2 coatings. The two-dimensional transition metal dichalcogenide (TMD) nanosheet is getting prominence in the study of tribology due to its layered structure. The graphitic carbon nitride (g-C_3N_4) nanosheet was made using the calcination method and its nanocomposite with molybdenum disulfide (MoS_2) was produced using a microwave-assisted method. The structure and morphology of the samples were characterized by some well-known methods, and tribological properties were studied by a pin-on-disc (POD) apparatus. Morphological analysis revealed that graphitic carbon nitride and molybdenum disulfide coexisted, and the layer structured MoS_2 was well dispersed on graphitic carbon nitride nanosheets. BET analysis was used to determine the pore volume and specific surface area of the synthesized materials. The inclusion of MoS_2 nanoparticles caused the composite's pore volume and specific surface area to decrease. The reduction in g-C_3N_4 pore volume and specific surface area confirmed that the pores of calcinated graphitic carbon nitride were filled with MoS_2 nanoparticles. The tribological property of g-C_3N_4/MoS_2 nanocomposite was systematically investigated under different factors such as applied loads (5N to 15N), sliding speed (500 to 1000 mm/s) and material composition (uncoated, MoS_2-coated, 9 wt.% of g-C_3N_4 and 20 wt.% of g-C_3N_4 in the composite). The optimal composite material ratio was taken 9%, by weight of g-C_3N_4 in the g-C_3N_4/MoS_2 composite for a variety of levels of loads and sliding speeds. The results indicates that the incorporation of g-C_3N_4 in nanocomposites could reduce friction and improve wear life, which were better than the results with single MoS_2. This study demonstrates a solution to broaden the possible uses of g-C_3N_4 and MoS_2-based materials in the field of tribology.

Keywords: microwave synthesis; transition metal dichalcogenide; graphitic carbon nitride; coatings; characterization; tribology; wear; steel substrate

Citation: Saxena, M.; Sharma, A.K.; Srivastava, A.K.; Singh, R.K.; Dixit, A.R.; Nag, A.; Hloch, S. Microwave-Assisted Synthesis, Characterization and Tribological Properties of a g-C_3N_4/MoS_2 Nanocomposite for Low Friction Coatings. *Coatings* **2022**, *12*, 1840. https://doi.org/10.3390/coatings12121840

Academic Editors: Cecilia Bartuli and Ajay Vikram Singh

Received: 27 October 2022
Accepted: 25 November 2022
Published: 28 November 2022

1. Introduction

Friction and wear are the primary causes of failure in many mechanical engineering components used in design. Much energy is used to overcome the resistance to motion caused by friction. Friction causes heat and wear, which in turn can cause material fatigue, noise emissions, surface deterioration, mechanical energy losses, and shortened service life of the components [1]. The cost of fitting, machinery and maintenance because of wear and tear and frictional faults affects the economy of a company. In passenger vehicles, around one third of the gasoline is utilized to overcome friction and wear [2].

One major way to reduce energy consumption is by improving the tribological characteristics of the mating surfaces. The requirements for enhanced lubricants are becoming more and more demanding as a result of their qualities, which include the ability to be used across a wider temperature range, larger loads, faster speeds, and increased endurance and service life [3]. To satisfy the needs of heavy machinery in severe working environments, it is essential to create novel and efficient friction-resistant plus high-bearing lubricant additives. Producing novel lubricants that meet changing requirements in many key domains, including as transportation, industry, and defense, is one of the major scientific problems of the twenty-first century [4].

Rosentsveig et al. [5] suggested that the use of nanoparticles in lubricants might improve their tribological characteristics, significantly lowering the coefficient of kinetic friction in working equipment. Numerous nanoparticle classes have been experimentally explored as potential lubricants [6]. Several nanoparticles are made up of two-dimensional structures that are adjacent to one another and are held together by weak Van der Waal forces. These structures are responsible for lowering the shear strength of the system as well as generating lubricating or sliding effects on the adjoining layer structure [7,8].

When compared to other nanomaterials, 2D nanomaterials have a greater specific surface area for absorbing onto the surface of a substrate, hence reducing, or eliminating, the amount of friction that occurs between the contact surfaces [9]. Because of its chemical and physical stability in a coating, molybdenum-disulfide is currently found as a promising two dimensional transition metal chalcogenide. The materials are resistant to most acids, chemically balanced and irradiation-resistant. The rate at which the lubricant works is regulated by the crystalline lamella structure of the lubricant, in which the sulfur lamella is connected by a weak Van der Waals affinity, resulting in lower fiction [10]. The layers of molybdenum disulfide efficiently slide against each other and align parallel to the relative motion during sliding, resulting in the lubricating effect. The strong ionic connection between sulfur and molybdenum atoms, on the other hand, makes the lamellar very resistant to asperity penetration [11]. However, pure molybdenum disulfide quickly absorbs the moisture in any surrounding environment that is humid and can be oxidized in an environment that contains either atomic or molecular oxygen [12]. This results in a rapid increase in the coefficient of friction and a reduction in the lifespan of the frictional surface. Most of the time, the coefficient of friction increases to a value greater than 0.2 because of the oxidation of molybdenum disulfide [13,14]. Because of these factors, its practical application is restricted and limited. The super-lubricity of molybdenum disulfide can be enhanced at the molecular or atomic scale under appropriate ordering of structure or orientations in a humid free dry setting, or can be used in vacuum environment [15].

MoS_2 is often mixed with other materials, such as polyurethane and graphene, as well as metals such as titanium [16], aluminum [17], copper [18], and chromium [19,20] to circumvent these restrictions and acquire its superior frictional resistance, mechanical, and thermal qualities. It is presently recognized as a major issue to improve the wear life and coefficient of friction of molybdenum sulfide for its use as a solid lubricant in different fields of application. It is now recognized as a substantial problem to extend the wear life of MoS_2 for its application as a solid lubricant in different field while keeping the coefficient of friction at a low level [21]. However, the expensive cost of the metal additions in MoS_2 coatings restricts their utilization. Theoretically, materials that are not metals, such as layered graphitic carbon nitride, which has the characteristics of being affordable, easily accessible, adequately stable, and environmentally acceptable, can replace metal components [22,23].

Currently, a variety of disciplines make use of polymer semiconductor graphitic carbon nitride (CN), which exhibits weak Van Der Waals forces between its layers and tris-triazine units [22,24]. CN is frequently added to lubricating oil to improve friction performance. For example, the bonding of CN with octadecylamine resulted in the creation of an efficient boundary coating on the friction surface, which increased the material's resistance to wear [25]. Duan et al. [26] adopted CN as a base oil additive because it

considerably improves the wear resistance of thermoset polyimide. Zhu et al., created g-C_3N_4/poly vinylidene difluoride (PVDF) composites and discovered that the g-C_3N_4 filler was advantageous in reducing composite wear loss [27].

Several preliminary approaches for the synthesis of MoS_2 nanoparticles have been devised, including, high-temperature sulfurization [28], CVD (chemical vapor deposition) [29], laser ablation, hydrothermal process [30], and sometimes even thermal reduction [31]. MoS_2 nanoparticles were synthesized with higher yields using hydrothermal and microwave (MW) synthesis processes. The hydrothermal approach is widely employed because to the ease of access to processing equipment, although it suffers from insufficient uniform heating. However, during MW-assisted synthesis, the compounds can be rapidly heated, which results in a more consistent temperature ramp in comparison to the conventional oven based hydrothermal process. Aside from that, the Teflon lined vessel that is used for the reaction is translucent to microwaves, which ensures that the heating is continuous and sustained throughout the reaction vessels. Furthermore, the microwave has advantages over traditional approaches in terms of speedy and accelerated heating, high-temperature uniformity, and selective heating compared to traditional methods [32]. The reactions are essentially dependent on the capacity of their precursors, particularly solvents, to effectively use microwave energy. Because of its homogeneous heating, low energy consumption, greater yield, and quicker synthesis time, the microwave synthesis process outperforms the hydrothermal technique.

In certain articles [33–35], the MoS_2 nanosheets are synthesized using microwave technology, which takes less than 30 min, as opposed to conventional heating in the oven, which takes around 24 h. Both MoS_2 and CN can be used as lubricants, however little research has examined the use of graphitic carbon nitride as an additive in MoS_2 to create solid nanocomposite lubricants. Because MoS_2 and CN have atomic layers, they may readily move from one to the next when combined, enhancing the friction capabilities. Even though sophisticated microwave-assisted synthesis of MoS_2 and its composite with g-C_3N_4 haven't been reported in the literature much, and their composites made via microwave heating for the field of tribology haven't been published yet, this study shows that it is possible to make these materials.

In this study, a one-step microwave-assisted (MW) process was used to synthesize the g-C_3N_4/MoS_2 nanocomposite, and its tribological properties as an anti-friction coating were examined. The details of synthesis, characterization, and tribological property of the g-C_3N_4/MoS_2 nanocomposite are described. For tribological analysis, it is important to find the endurance of the coating, and for this purpose three factors at different levels were considered. These factors include the applied load, sliding speed, and composition. Due to the three factors, with three levels of sliding speed, applied load and four levels of composition, the design contained 36 different possible combinations to perform experimental work.

2. Materials and Methods

For the synthesis of the material, a microwave reactor (Model Monowave450, Anton-Paar, CAS-Lucknow, India) was used, and a sample drying oven (Model HTF-T-1600, Tempsens, CAS-Lucknow, India) was used for the drying process. XRD (Ultima IV with Copper K_α radiation, current 150 mA, and potential 40 kV (wavelength = 1.5418 Å), Rigaku, IIT ISM, Dhanbad, India) was used in examine the phase composition of the developed samples in the range 10–70 °C at 4 °C steps. A FTIR spectrometer (Alpha II, BRUKER, CAS-Lucknow, India) was used to analyse the FTIR spectra of the sample materials. The microstructures were observed using a FESEM (Gemini500, Zeiss equipped with EDS, CAS-Lucknow, India). BET analysis was performed on Belsorp (mini X) to determine the pore volume, mean pore diameter, and specific surface area of synthesized materials in the relative pressure range (P to P_0) of 0 to 1. The friction pairs and worn surface of the coated steel substrate were characterized using Stereo microscope (Olympus, SZX10, CAS-Lucknow, India).

The analytical grade reagents used in this investigation were sodium molybdate dihydrate ($Na_2MoO_4{\cdot}H_2O$), thioacetamide (CH_3CSNH_2), absolute ethanol, and urea ($NH_2{\cdot}CO{\cdot}NH_2$). All of the reagents employed were of analytical quality and did not require further purification. First, graphitic carbon nitride powder was prepared by a solid reaction. Urea (20 g) taken into a 50 mL crucible and dried at about 80 °C. After the crucible had been allowed to dry, it was covered with a lid, then coated in several layers of aluminum foil, and finally put in a muffle furnace. After that, it underwent calcination at 550 °C for four hours at a rate of 3 °C per minute. Following the lowering of the temperature to room temperature, the g-C_3N_4 powder was prepared using the grinding technique. After being cooled to room temperature (~22 °C), the g-C_3N_4 powder was produced by grinding. The conversion of urea ($NH_2{\cdot}CO{\cdot}NH_2$) into g-C_3N_4 in the process was around 4.5 percent, as calculated from Equation (1) and presented in Table 1.

$$\textbf{Yield percent} = \left(\frac{m_t - m_c}{m_u}\right) \textbf{XX 100} \quad (1)$$

where, m_t = mass of obtained catalyst, m_c = mass of crucible, m_u = initial urea mass.

Table 1. Yield percent calculation.

Variable	Sample Weight (g)
m_t	134.4628
m_c	133.5627
m_u	20
Yield percent	4.5005%

g-C_3N_4, sodium molybdate dehydrate and thioacetamide were mixed to a 100 mL beaker containing 70 mL deionized (DI) water in a molar ratio 1:0.89:1.91 and 1:2.33:5.01. This mixture was then subjected to a sonication treatment for three hours, during which time the reagents were mixed thoroughly in the distilled water, and then magnetic stirring for 1 h at room temperature. A schematic of the process is shown in Figure 1.

The solution was transferred into a 30 mL vial and put into microwave reactor for the synthesis. The heat ramp for the microwave-assisted synthesis is shown in Figure 2.

Following the completion of the reaction, the mixture was allowed to reach room temperature by means of a flow of compressed air. Next, filtration was carried out, and g-C_3N_4/MoS_2 powder was collected. After that, the powder was dried in a hot air oven at a temperature of 80 degrees Celsius for two hours. For comparison, the same process was used to create MoS_2 without the inclusion of g-C_3N_4. In order to prepare the surface of steel substrate for coating, acetone was used to clean it, and then it was ultrasonically stirred for one hour. Composition of the substrate was calculated from EDX analysis and listed in Table 2.

Table 2. Composition of steel substrate analyzed by EDX spectroscopy.

Element	Weight %
C	9.43
Fe	54.9
Ni	0.12
Cu	0.71
Si	2.55
W	9.72
P	0.14
Mo	9.06
V	5.73
Cr	7.1
Mn	0.53

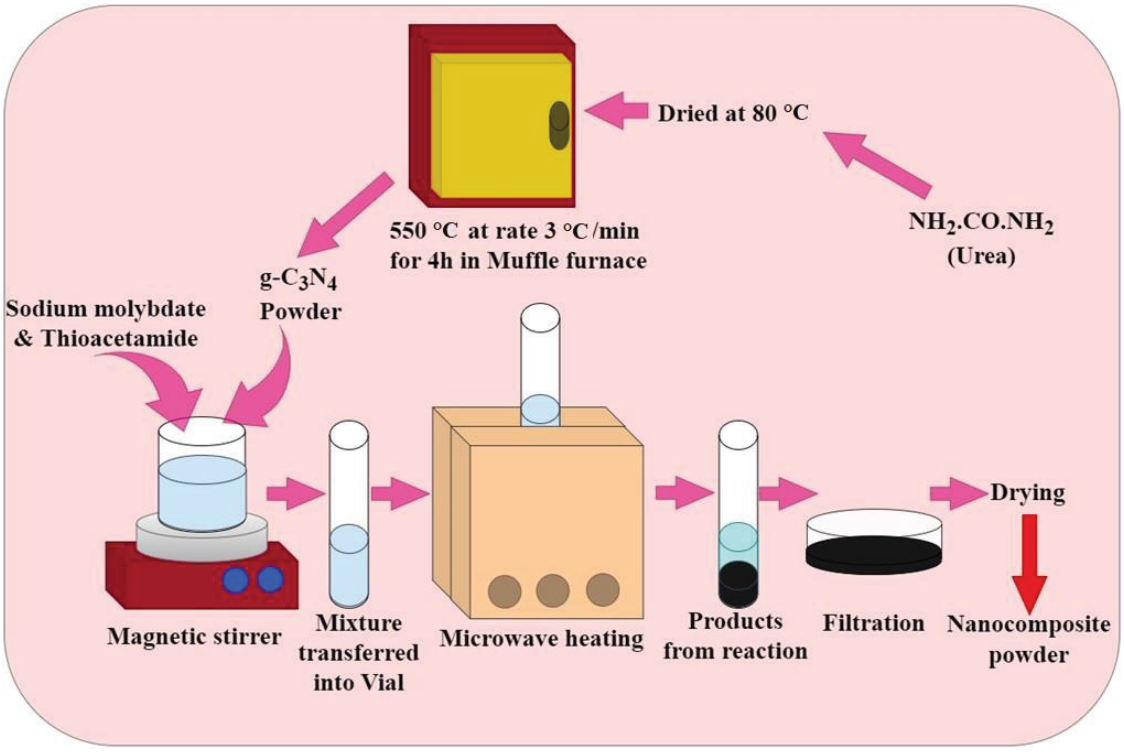

Figure 1. Synthesis of material.

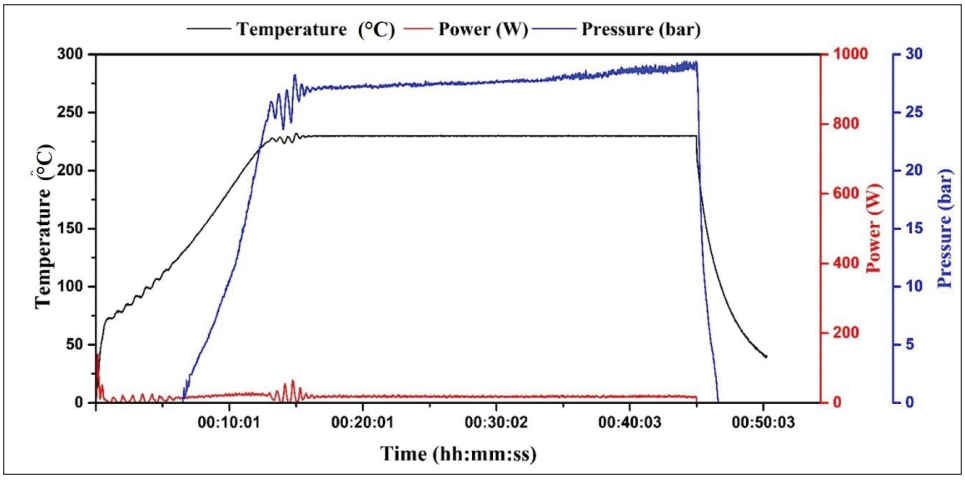

Figure 2. Heat ramp for microwave synthesis.

The MoS_2 powder and g-C_3N_4/MoS_2 nanocomposite were dissolved separately and dispersed into a medium size beaker that contained 50 mL of ethanol. The solution was coated on the substrate by a spin coater after 30 min of ultra-sonication. Spin coating is an easy and efficient technique for coating nanomaterial on a flat surface. The coating solution spreads out over the substrate at low rotational speeds, and coated films are created at high

rotational speeds. The substrate was first mounted on the spin chuck. The substrate was held in place by turning on the vacuum line. To coat the sample material, a predetermined volume of substrate was dispensed onto it with a disposable pipette. The substrate was spun after the coating solution was applied, and the lid was then put on the spin coated. After the solution was entirely suspended, the MoS_2 and g-C_3N_4/MoS_2 nanomaterial suspension were deposited on the substrate.

A pin-on-disc (POD) Tester (Model: TR-20LE PHM-400, DUCOM Instruments) was employed for the friction studies on the coating. Figure 3 is a schematic illustration of this POD tester. The counterpart pin of diameter 8 mm was made out of AISI304 stainless steel pin. All of the studies were conducted in an environment that had a relative humidity (RH) of around 30% ± 2, and the surrounding temperature was approximately 24 degrees Celsius.

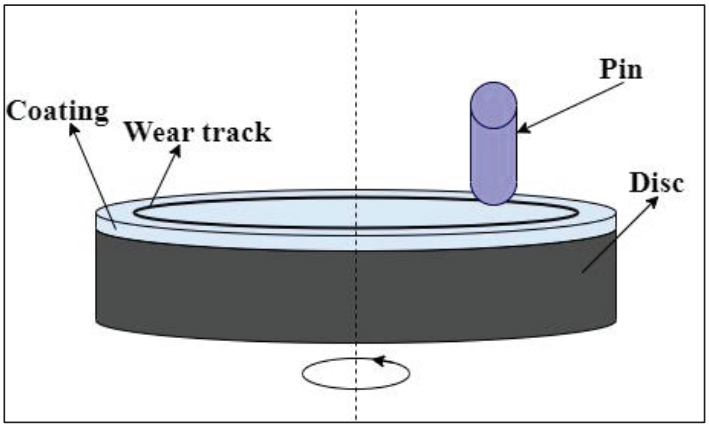

Figure 3. Schematic illustration of the POD tester.

The design of experiment (DOE) was created with the help of MINITAB-19, and for the purpose of conducting an analysis, three factors at their different levels were considered. These factors include the applied load, sliding speed, and composition. Table 3 presents the parameters used as inputs in the investigation.

Table 3. Parameters utilized as inputs for the investigation.

Factors & Levels	L-[1]	L-[2]	L-[3]	L-[4]
Applied Load (N)	5	10	15	-
Sliding Speed (mm/s)	500	750	1000	-
Composition	Uncoated	MoS_2	wt.% 9 of g-C_3N_4 in composite	wt.% 20 of g-C_3N_4 in composite

Due to three factors with three levels of sliding speed, applied load and four levels of composition, the design contained 36 different possible combinations to perform experimental work. The real time data of the coefficient of friction were continually recorded in software. To rule out the possibility of inadvertent mistakes, every experiment was carried out three times, and the average of the results was then determined.

3. Results and Discussion

X-ray diffraction and Fourier transform infrared spectroscopy were used, respectively, to investigate the crystal structures and functional groups of synthesized materials (pure MoS_2, graphitic carbon nitride, wt.% 9 and 20 g-C_3N_4/MoS_2 composite). Diffraction peaks for g-C_3N_4 were found at 2θ = 13.0° and 27.5°, as shown in Figure 4 (JCPDS#87-1526).

These values correspond to (100) and (002) crystallographic planes, respectively. These two peaks are indicative of conjugated aromatic systems with interlayer stacking [27]. The peaks at 2θ = 14°, 32.7°, 35.871°, and 58.3°, respectively, are attributable to the (002), (100), (102), and (110) planes of the hexagonal MoS_2 (JCPDS#37-1492) [36,37].

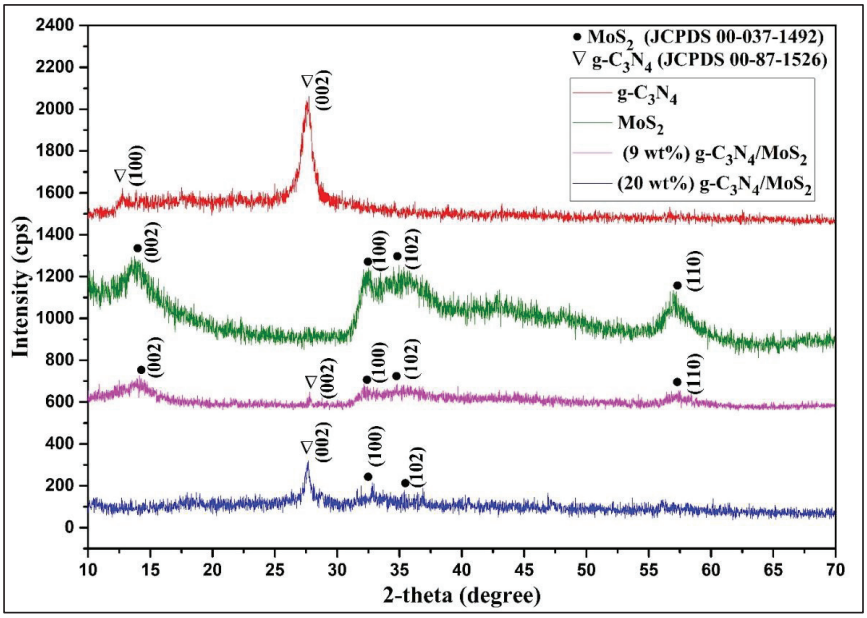

Figure 4. XRD pattern of MoS_2, g-C_3N_4 and their composites.

FTIR results of synthesized materials are shown in Figure 5. The peaks at 1237.4 and 808 cm^{-1} in the FTIR spectrum are responsible for the aromatic ring structure and the breathing mode of a triazine ring of g-C_3N_4, respectively [22]. The extension and respiration of C=N and C-C heterocyclic structure in g-C_3N_4 results in the peaks at 1407.1 and 1638.9 cm^{-1} [26,38]. Furthermore, the peak at wavenumber 3432 cm^{-1} is attributable to stretching vibration due to -NH residual in the C-N ring as well as -OH vibration in the H_2O that was absorbed on the surface [22,26,38].

The characteristic peaks of graphitic carbon nitride and molybdenum disulfide present in the FTIR pattern of g-C_3N_4/MoS_2 suggests that MoS_2 has no effect on the functional group for g-C_3N_4 in nanocomposite while microwave-assisted synthesis. The results of all of the characterizations point to the conclusion that the nano-composite of g-C_3N_4/MoS_2 that was successfully synthesized by the microwave-assisted method consisted of two distinct structures of g-C_3N_4 and MoS_2. FESEM was used to examine the surface morphology and microstructures of the samples. Figure 6 depicts FESEM images of the samples.

It can be seen from Figure 6 that the flower-like structure of molybdenum disulfide assembled in several nanosheets, while a smooth and layered structure of graphitic carbon nitride is seen in Figure 7.

Figure 8 shows that MoS_2 and g-C_3N_4 in the developed composite are bundled together, showing that the components of composite were mixed successfully and may provide the lubrication property of the coating.

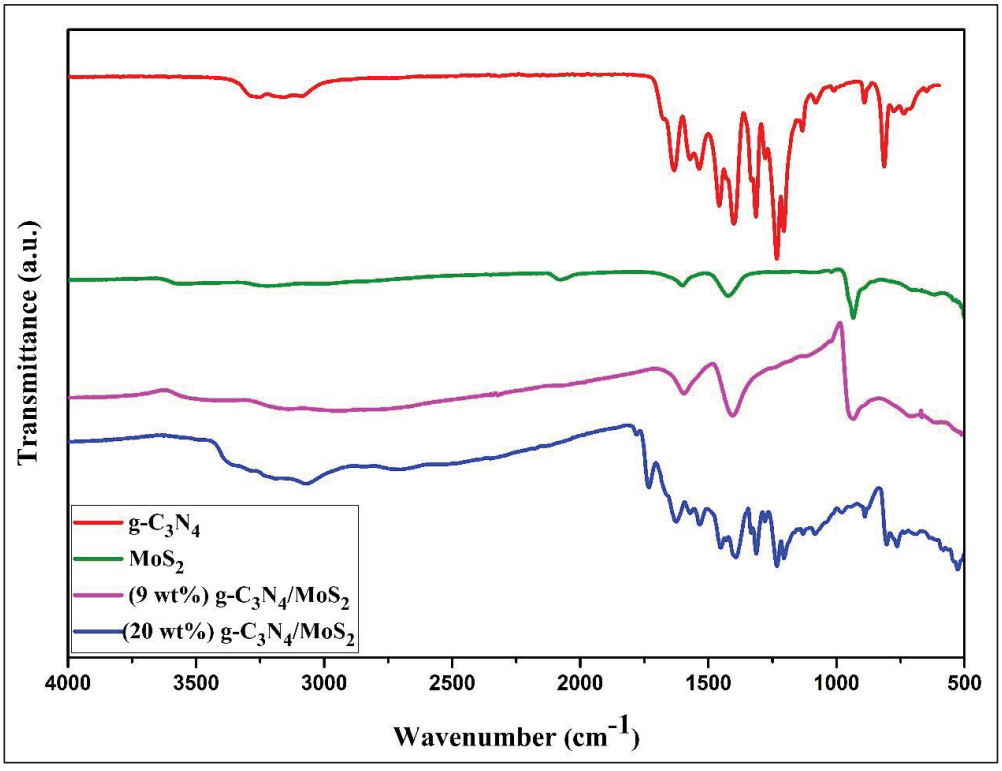

Figure 5. FTIR pattern of MoS_2, g-C_3N_4 and their composites.

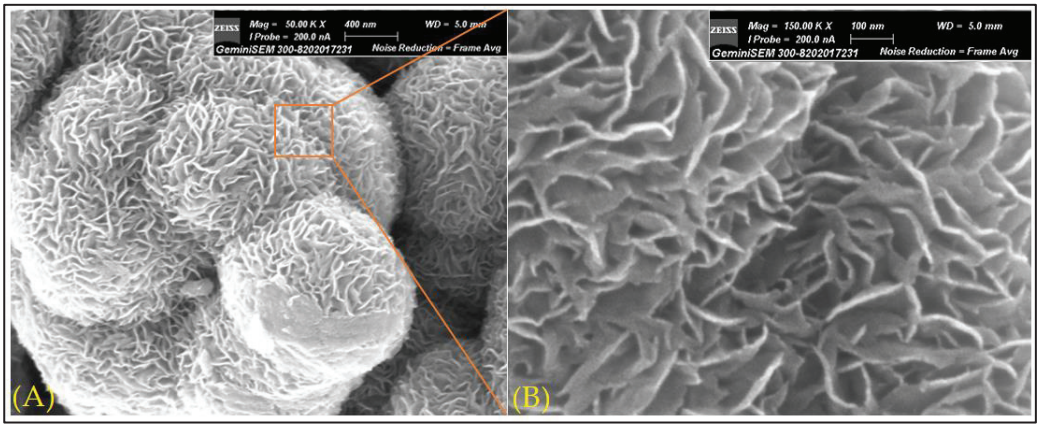

Figure 6. FESEM images of MoS_2 at magnifications of 400 nm (**A**) and 100 (**B**).

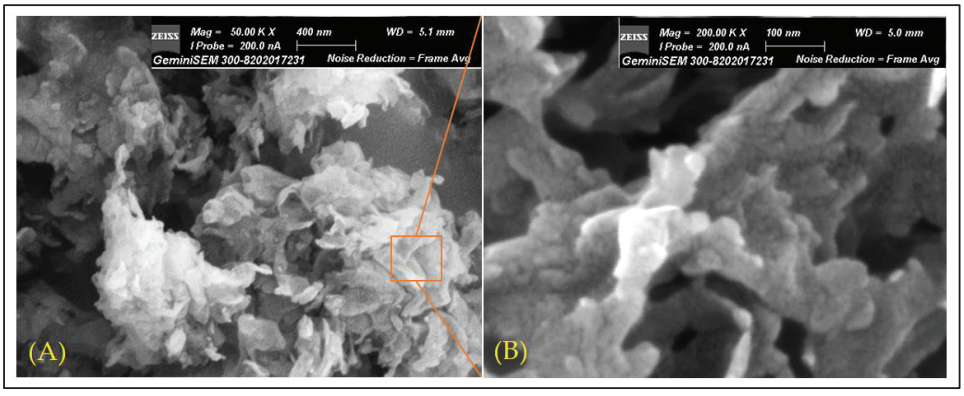

Figure 7. FESEM image for g-C_3N_4 at magnifications of 400 nm (**A**) and 100 (**B**).

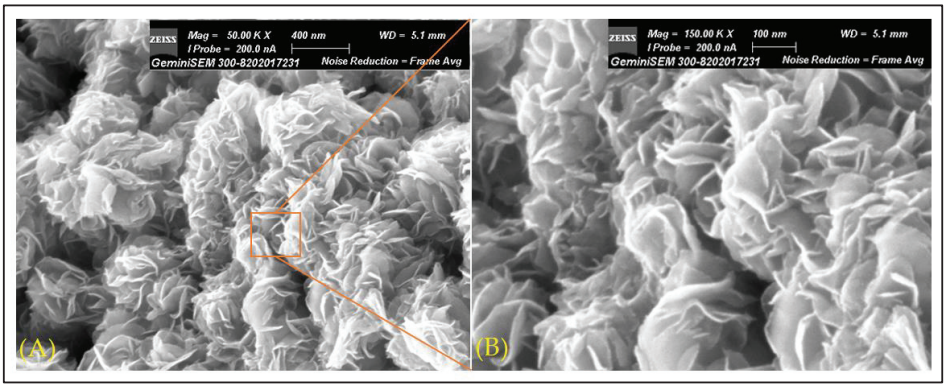

Figure 8. FESEM images 9 wt.% g-C_3N_4/MoS_2 at magnifications of 400 nm (**A**) and 100 (**B**).

It can be seen from Figure 9 that on increasing the weight percentage of graphitic carbon nitride in the composite, MoS_2 predominates.

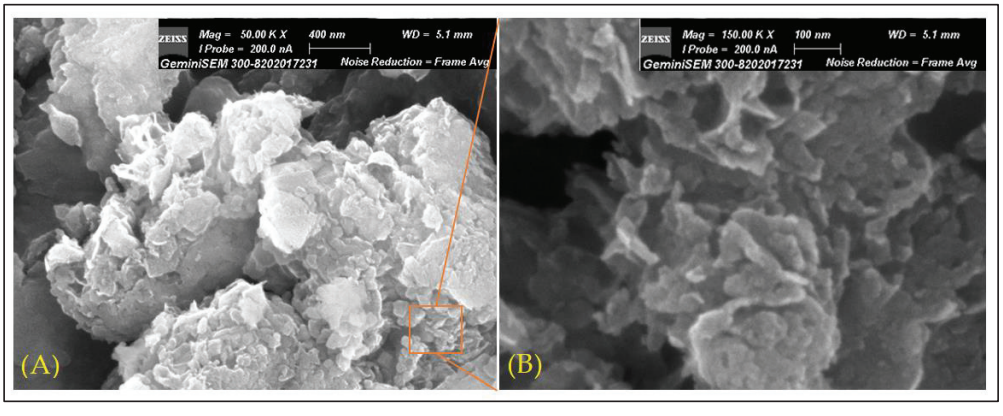

Figure 9. FESEM images 20 wt.% g-C_3N_4/MoS_2 at magnifications of 400 nm (**A**) and 100 (**B**).

An EDX detector was used to identify distributed elements in the composite. Carbon, nitrogen, molybdenum, and sulfur are among of the components that make up the composite, as seen in Figure 10.

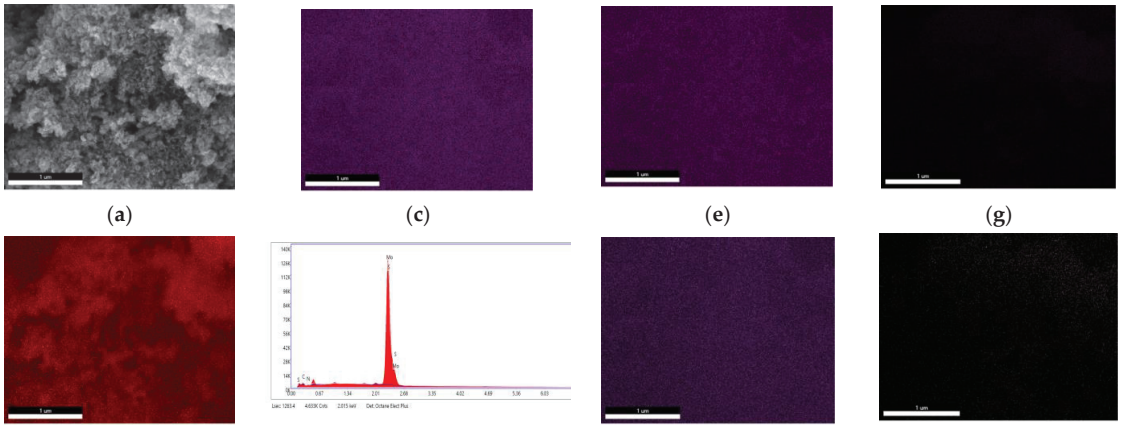

Figure 10. (**a**) SEM image; (**b**) live map; (**c**) element overlay; (**d**) elemental analysis; element (**e**) molybdenum, Mo; (**f**) sulfur, S; (**g**) carbon, C and (**h**) nitrogen, N of the g-C_3N_4/MoS_2 composite.

EDX elemental analysis results for graphitic carbon nitride, molybdenum disulfide and their composites are summarized in Table 4.

Table 4. Elemental composition of synthesized materials from EDX elemental analysis.

	g-C_3N_4		**MoS_2**		*g-C_3N_4/MoS_2 (wt.% 9)*				*g-C_3N_4/MoS_2 (wt.% 20)*			
Element	**C**	**N**	**Mo**	**S**	**C**	**N**	**Mo**	S	C	N	Mo	S
Atomic%	42.79	57.21	37.82	62.18	11	1.5	31.49	55.07	59.82	21.15	7.83	11.2

The nitrogen adsorption/desorption analysis determines the specific area of surface (a_s) of each sample (MoS_2, g-C_3N_4, and their composite), as shown in Figure 11. The hysteresis curve loops of the samples were recorded and found to be the H3-IV type.

The specific surface areas of g-C_3N_4, MoS_2 and g-C_3N_4/MoS_2 were approximately 78.94, 1.46, and 25.71 m^2g^{-1}. The addition of stacked MoS_2 nanoparticles may result in a reduction in the BET specific surface areas of g-C_3N_4/MoS_2. The pore volumes of g-C_3N_4, MoS_2 and g-C_3N_4/MoS_2 were approximately 0.142, 0.072 and 0.021 cm^3g^{-1}. In this instance, the inclusion of MoS_2 nanoparticles caused the composite's pore volume to decrease. The reduction in g-C_3N_4 pore volume confirms that the pores of calcinated graphitic carbon nitride were filled with MoS_2 nanoparticles [39], so a range up to 15 wt.% was employed for the friction studies on the coating.

A pin-on-disc (POD) wear test was employed for the tribological investigation of the coating. The testing parameters for tribological investigations were selected as per the specifications of the machine available, and three loads of 5, 10 and 15 N with sliding speeds as 1000, 750 and 500 mm/s were used. The revolutions per minute required for the analysis were calculated from the equation $S = \frac{\pi.d.\ N}{60}$, where S = sliding speed, d = track diameter and N = required revolutions per minute. The total track length covered by the pin that slid against disc was calculated from the equation $L = (\pi.d).N.T$, where L = sliding speed, d = track diameter, N = required revolutions per minute and T = test duration. Sliding speeds of 1000, 750 and 500 mm/s covered track lengths 600,000 mm, 450,000 mm and 300,000 mm, respectively which were required for effectively analyzing the effect of the coating and its tribological aspects for ultra-long wear life.

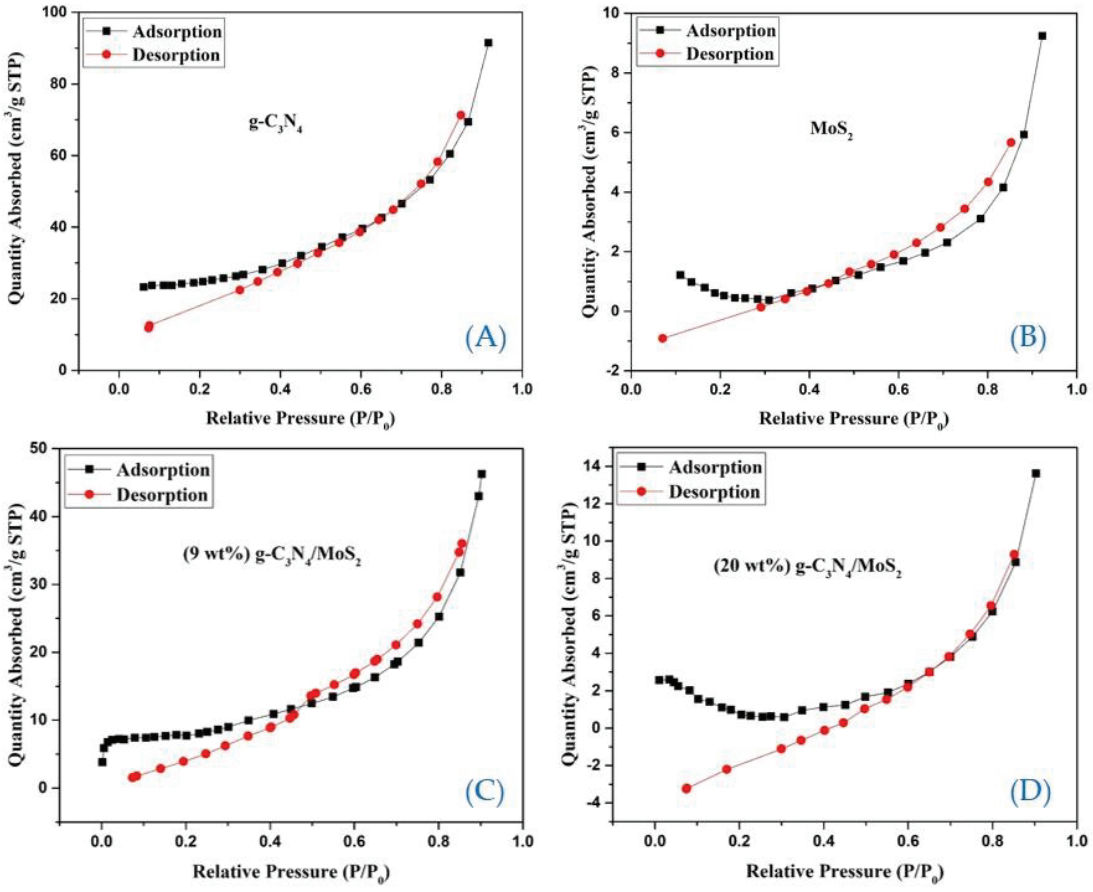

Figure 11. Nitrogen adsorption-desorption isotherm curves of (**A**) g-C_3N_4, (**B**) MoS_2, (**C**) g-C_3N_4/MoS_2 (9 wt.%) and (**D**) g-C_3N_4/MoS_2 (20 wt.%).

Figure 12 depicts the wear of substrates coated with g-C_3N_4, MoS_2, and g-C_3N_4/MoS_2 coatings in various ratios under loads ranging from 5N to 15N and sliding speeds ranging from 500 to 1000 mm/s as per the design of experiment done with the help of MINITAB-19, as depicted in Table 3. Maximum wear depth was recorded approximately 900 μm for uncoated steel substrate disc for a test duration of 10 min, but was reduced to approximately 500 μm for the MoS_2-coated disc (Figure 12B). The MoS_2-coated disc restrict the friction and sliding forces for a short duration as compared to the g-C_3N_4/MoS_2 coatings. The wear depth for coated disc dropped to approximately 66% and 50%, respectively at 9 wt.% (Figure 12C) and 20 wt.% (Figure 12D) of graphitic carbon nitride compared to the uncoated steel disc. Figure 12 shows that the optimal composite material ratio was proven to be weight percent 9 of g-C_3N_4 in the g-C_3N_4/MoS_2 composite for a variety of levels of loads and sliding speeds. The figure also indicates that the friction lifetime might be increased while minimizing wear. Figure 12 also reveals a higher rate of wear for pure steel substrates, which may be due to the direct contact that occurs in between the respective pins and the steel substrates. Substrate coated with only MoS_2 had lower wear than uncoated steel substrates but a shorter wear-life since MoS_2 is heavily impacted by the environment. Due to the reciprocating type shear stress, the materials with g-C_3N_4 (9 wt.% and 20 wt.%) in MoS_2 were compacted during the running-in phase, generating a dense layer on the coated surface, as shown in Figure 12c,d.

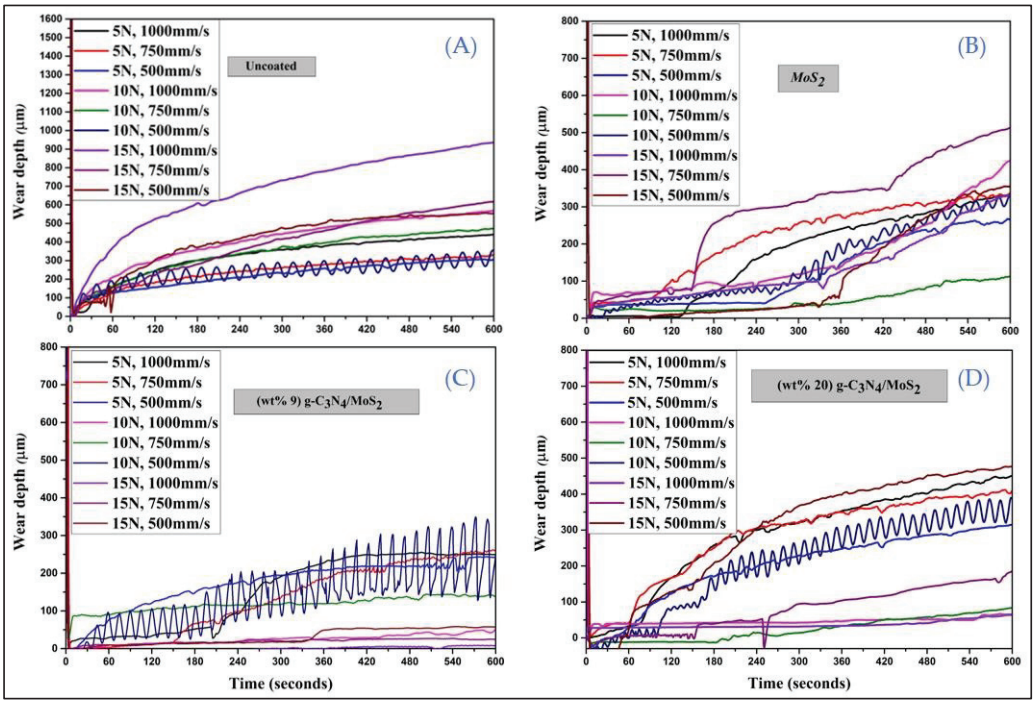

Figure 12. Wear depth vs. Time (**A**) for uncoated substrate; (**B**) for pure MoS_2-coated substrate; (**C**) for 9 wt.% g-C_3N_4/MoS_2 (**D**) 20 wt.% g-C_3N_4/MoS_2, at different sliding speeds and loadings.

Furthermore, the friction process could exfoliate MoS_2 nanosheets into lamella due to the reciprocating type shear stress that arises as a result of the sliding friction between the coating and counterpart pin. Instrument software recorded the mean coefficient of friction (COF) for different combinations of factors and levels as summarized in Table 5.

Table 5. Mean coefficient of friction for different combinations of factors.

S No	Applied Load (N)	Sliding Speed (mm/s)	*g-C_3N_4* Weight%	*COF*, Mean
1	5	500	uncoated	0.993
2	5	500	0	0.994
3	5	500	9	1.604
4	5	500	20	4.222
5	5	750	uncoated	2.456
6	5	750	0	1.167
7	5	750	9	0.403
8	5	750	20	1.542
9	5	1000	uncoated	0.288
10	5	1000	0	0.403
11	5	1000	9	1.278
12	5	1000	20	0.748
13	10	500	uncoated	0.915
14	10	500	0	1.285
15	10	500	9	0.11
16	10	500	20	2.89
17	10	750	uncoated	0.344
18	10	750	0	0.389
19	10	750	9	0.228

Table 5. *Cont.*

S No	Applied Load (N)	Sliding Speed (mm/s)	*g-C_3N_4* Weight%	*COF*, Mean
20	10	750	20	0.181
21	10	1000	uncoated	1.515
22	10	1000	0	1.108
23	10	1000	9	0.138
24	10	1000	20	0.597
25	15	500	uncoated	0.357
26	15	500	0	0.38
27	15	500	9	0.222
28	15	500	20	0.086
29	15	750	uncoated	0.595
30	15	750	0	0.19
31	15	750	9	0.226
32	15	750	20	0.384
33	15	1000	uncoated	0.357
34	15	1000	0	0.624
35	15	1000	9	0.145
36	15	1000	20	0.452

The coating material doesn't peel off instantly, preventing substrate from exposure to the pin directly. Despite the fact that the mean coefficient of friction of g-C_3N_4/MoS_2 is somewhat lower than that of pure MoS_2, g-C_3N_4 exhibits outstanding resistance to wear and may greatly extend the wear life of MoS_2. The coefficient of friction was determined to be at its lowest when the load being applied was approximately 15 Newton, which demonstrates that the greater the load, the lower the coefficient of friction. This is due to the fact that the rate of increases in load is higher than that for increase in contact area.

Figure 13 shows a microscopic view of the material wear loss for a nanocomposite-coated steel substrate disc. It shows that the amount of wear loss leading to a small ploughing action. With different material composition in the coating, the chance of pin-to-disc contact increased. While analyzing the worn surface, some small micro cracks and grooves could be seen in the MoS_2-coated substrate (Figure 13a) which may be due to oxidation of molybdenum disulfide at high-speed sliding between pin and substrate disc. The increase in wear loss of the 20 wt.% g-C_3N_4/MoS_2 composite at the applied load caused ploughing on the surface, and deep grooves with large amount of wear debris were found (Figure 13c). It can be seen from Figure 13b that the nanocomposite coating with 9 wt.% g-C_3N_4/MoS_2 shows a lower value of wear loss when compared with MoS_2, as well as 20 wt.% of g-C_3N_4 in the composite. An amount of coating remained on the substrate disc even after long-duration sliding, as can clearly be seen in Figure 13b. A few traces of g-C_3N_4/MoS_2 material within the valleys would continue to provide lubrication, and affirms good adhesion of coating to substrate. Uncoated bare substrate was strongly affected by sliding with the pin due to shear fracture and a comparatively rough surface was found after the wear test. Some wear debris, deep groves, abrasive and ploughing lines can be clearly seen in Figure 13d. Worn surface analysis confirms the addition of g-C_3N_4 would reduce the wear loss of the MoS_2 nanocomposite-coated substrate and increase the wear resistance.

The notable features of g-C_3N_4/MoS_2 coating were excellent wear protection and lifetime of the composite coating. The aforementioned phenomena suggest that MoS_2 (solid lubricant) and an additive of g-C_3N_4 have effective characteristics when used together. g-C_3N_4/MoS_2 composites have a lower coefficient of friction (COF) and a longer wear-life because the proper quantity of addition of MoS_2 can greatly reduce the coefficient of friction for g-C_3N_4, while g-C_3N_4 can enhance the wear-life of MoS_2.

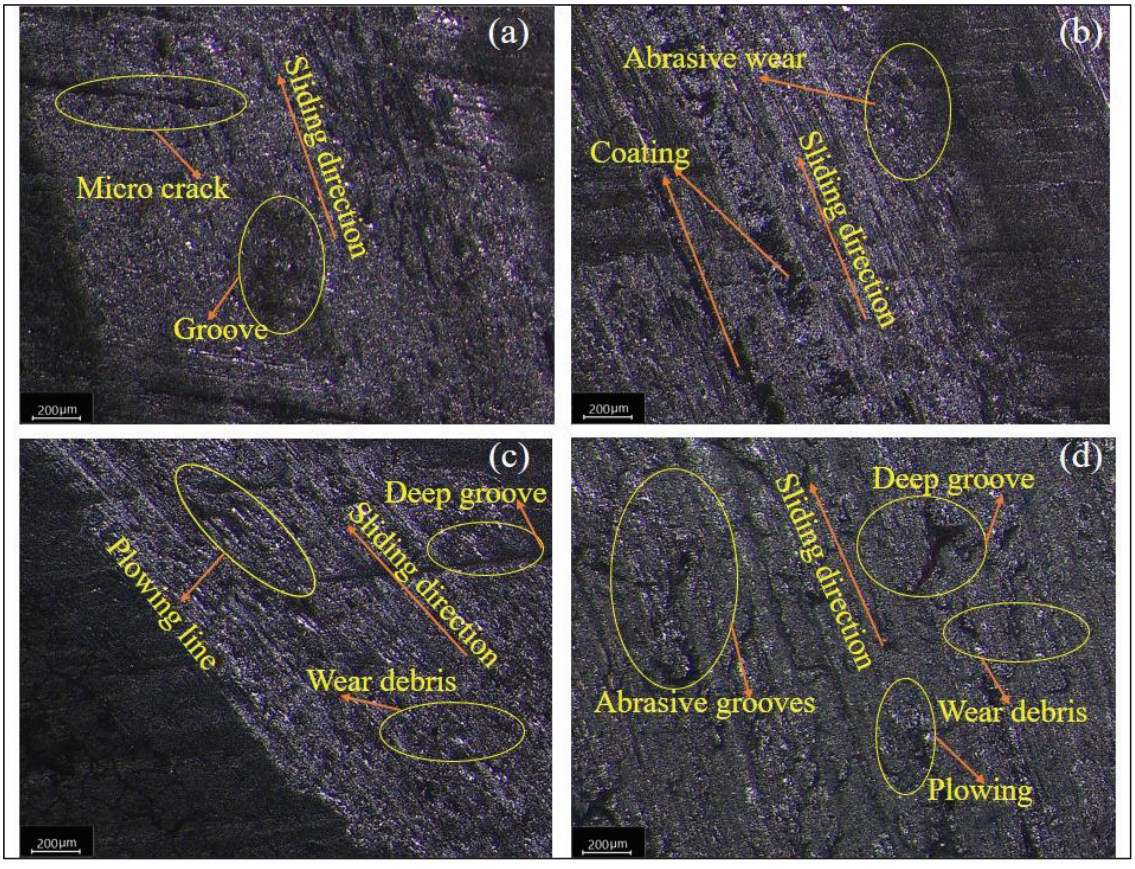

Figure 13. Micro-graphs of wear surfaces: (**a**) MoS_2; (**b**) 9 wt.% g-C_3N_4/MoS_2; (**c**) 20 wt.% g-C_3N_4/MoS_2; (**d**) uncoated steel substrate.

4. Conclusions

Calcination of urea was used to make graphitic carbon nitride nanosheets, and a novel microwave-assisted synthesis process was used to make a g-C_3N_4/MoS_2 nanocomposite. Physical and morphological characterizations were performed by XRD, FTIR, FESEM and EDX spectroscopy and showed the well-controlled morphology of MoS_2 nanosheets and the structural features of nanocomposites. The tribological characteristics of coated steel substrate were studied using a pin-on-disc (POD) test for different loads and sliding speeds between AISI304 steel pin and substrate.

After analyzing and comparing the results, the following conclusions can be made:

- In comparison to the MoS_2-coated substrate, addition of g-C_3N_4 to nanocomposite minimized friction and improved wear life.
- The remarkable tribological properties of the prepared nanocomposite may be attributed to the excellent adhesion and support effects of g-C_3N_4, as well as the synergistic friction reduction and wear-resistant effects of g-C_3N_4 and MoS_2 nanosheets.
- Pure MoS_2 has a low wear as compared to uncoated steel substrate but shorter wear-life, as MoS_2 is highly affected by the environment.
- It was determined that the ideal composite material ratio was 99 wt.% of g-C_3N_4 in the nanocomposite g-C_3N_4/MoS_2 for a variety of levels of loads and sliding speeds. This ratio exhibited the least amount of wear and the longest friction lifespan.

- It was established that the coefficient of friction was at its lowest when the applied load was approximately 15 N, indicating that the higher the load, the lower the coefficient of friction. This is because the rate of increase in the applied load exceeded the rate of increase in contact area.

This study provides a solution to broaden the potential application of graphitic carbon nitride and molybdenum disulfide-based materials in the domain of tribology.

Author Contributions: M.S.: Conceptualization, Writing; A.K.S. (Anuj Kumar Sharma): Review and editing; A.K.S. (Ashish Kumar Srivastava): methodology, validation, Visualization, Writing—Review & Editing; R.K.S.: resources; A.R.D.: Supervison; Writing—Review & Editing, A.N.: software, data curation; S.H.: project administration, Writing—Review & Editing, Visualization. All authors have read and agreed to the published version of the manuscript.

Funding: This study was supported by the Slovak Research and Development Agency under Contract No. APVV-17-0490.

Institutional Review Board Statement: Not applicable.

Informed Consent Statement: Not applicable.

Data Availability Statement: Data sharing is not applicable to this article.

Conflicts of Interest: The authors declare no conflict of interest.

References

1. Srivastava, A.K.; Kumar, N.; Dixit, A.R. Friction stir additive manufacturing—An innovative tool to enhance mechanical and microstructural properties. *Mater. Sci. Eng. B* **2021**, *263*, 114832. [CrossRef]
2. Holmberg, K.; Andersson, P.; Erdemir, A. Global energy consumption due to friction in passenger cars. *Tribol. Int.* **2012**, *47*, 221–234. [CrossRef]
3. Srivastava, A.K.; Dwivedi, S.; Saxena, A.; Kumar, D.; Dixit, A.R.; Singh, G.K.; Bhutto, J.K.; Verma, R. Tribological Characteristics of Al359/Si_3N_4/Eggshell Surface Composite Produced by Friction Stir Processing. *Coatings* **2022**, *12*, 1362. [CrossRef]
4. Srivastava, A.K.; Dixit, A.R.; Maurya, M.; Saxena, A.; Maurya, N.K.; Dwivedi, S.P.; Bajaj, R. 20th century uninterrupted growth in friction stir processing of lightweight composites and alloys. *Mater. Chem. Phys.* **2021**, *266*, 124572. [CrossRef]
5. Rosentsveig, R.; Gorodnev, A.; Feuerstein, N.; Friedman, H.; Zak, A.; Fleischer, N.; Tannous, J.; Dassenoy, F.; Tenne, R. Fullerene-like MoS_2 nanoparticles and their tribological behavior. *Tribol. Lett.* **2009**, *36*, 175–182. [CrossRef]
6. Kalin, M.; Kogovšek, J.; Remškar, M. Mechanisms and improvements in the friction and wear behavior using MoS_2 nanotubes as potential oil additives. *Wear* **2012**, *280*, 36–45. [CrossRef]
7. Hilton, M.R.; Bauer, R.; Didziulis, S.V.; Dugger, M.T.; Keem, J.M.; Scholhamer, J. Structural and tribological studies of MoS_2 solid lubricant films having tailored metal-multilayer nanostructures. *Surf. Coat. Technol.* **1992**, *53*, 13–23. [CrossRef]
8. He, X.; Xiao, H.; Choi, H.; Díaz, A.; Mosby, B.; Clearfield, A.; Liang, H. α-Zirconium phosphate nanoplatelets as lubricant additives. *Colloids Surf. A Physicochem. Eng. Asp.* **2014**, *452*, 32–38. [CrossRef]
9. Vattikuti, S.V.; Byon, C. Synthesis and characterization of molybdenum disulfide nanoflowers and nanosheets: Nanotribology. *J. Nanomater.* **2015**, *2015*, 9. [CrossRef]
10. Berman, D.; Erdemir, A.; Sumant, A.V. Graphene: A new emerging lubricant. *Mater. Today* **2014**, *17*, 31–42. [CrossRef]
11. Dallavalle, M.; Saändig, N.; Zerbetto, F. Stability, dynamics, and lubrication of MoS_2 platelets and nanotubes. *Langmuir* **2012**, *28*, 7393–7400. [PubMed]
12. Cizaire, L.; Vacher, B.; le Mogne, T.; Martin, J.M.; Rapoport, L.; Margolin, A.; Tenne, R. Mechanisms of ultra-low friction by hollow inorganic fullerene-like MoS_2 nanoparticles. *Surf. Coat. Technol.* **2002**, *160*, 282–287. [CrossRef]
13. Curry, J.F.; Wilson, M.A.; Luftman, H.S.; Strandwitz, N.C.; Argibay, N.; Chandross, M.; Sidebottom, M.A.; Krick, B.A. Impact of microstructure on MoS_2 oxidation and friction. *ACS Appl. Mater. Interfaces* **2017**, *9*, 28019–28026. [CrossRef] [PubMed]
14. Donnet, C.; Martin, J.M.; Le Mogne, T.; Belin, M. Super-low friction of MoS_2 coatings in various environments. *Tribol. Int.* **1996**, *29*, 123–128. [CrossRef]
15. Berman, D.; Erdemir, A.; Sumant, A.V. Approaches for achieving superlubricity in two-dimensional materials. *ACS Nano* **2018**, *12*, 2122–2137. [PubMed]
16. Bülbül, F.; Efeoğlu, İ.; Arslan, E. The effect of bias voltage and working pressure on S/Mo ratio at MoS_2–Ti composite films. *Appl. Surf. Sci.* **2007**, *253*, 4415–4419. [CrossRef]
17. Yao, S.-H.; Kao, W.-H.; Su, Y.-L.; Liu, T.-H. On the tribology and micro-drilling performance of TiN/AlN nanolayer coatings. *Mater. Sci. Eng. A* **2004**, *386*, 149–155. [CrossRef]
18. Peng, W.; Yue, W.; Lu, Z.; Zhang, G.; Zhu, L. Friction and wear properties of MoS_2-based coatings sliding against Cu and Al under electric current. *Tribol. Int.* **2018**, *127*, 379–388.

19. Elianov, O.; Garusi, S.; Rosentsveig, R.; Cohen, S.R.; Feldman, Y.; Pinkas, I.; Bendikov, T.; Kaplan-Ashiri, I.; Moshkovich, A.; Perfilyev, V.; et al. Deposition of metal coatings containing fullerene-like MoS_2 nanoparticles with reduced friction and wear. *Surf. Coat. Technol.* **2018**, *353*, 116–125. [CrossRef]
20. Lee, D.B.; Kim, S.K. High temperature oxidation of a (Cr_2N−Mo_2S_3)/Cr double-layered coating deposited on steel by DC magnetron sputtering. *Met. Mater. Int.* **2005**, *11*, 227–232. [CrossRef]
21. Li, H.; Wang, J.; Gao, S.; Chen, Q.; Peng, L.; Liu, K.; Wei, X. Superlubricity between MoS_2 monolayers. *Adv. Mater.* **2017**, *29*, 1701474. [CrossRef] [PubMed]
22. Zhang, Y.; Jin, Z.; Su, Y.; Wang, G. Charge separation and electron transfer routes modulated with Co-Mo-P over g-C3N4 photocatalyst. *Mol. Catal.* **2019**, *462*, 46–55. [CrossRef]
23. Flores-Ruiz, F.J.; Enriquez-Flores, C.I.; Chiñas-Castillo, F.; Espinoza-Beltrán, F.J. Nanotribological performance of fullerene-like carbon nitride films. *Appl. Surf. Sci.* **2014**, *314*, 193–198. [CrossRef]
24. Xu, Z.D.; Xin, J.B.; Fan, R.X.; Wang, K.; Yang, J. A simple approach to fabricate CN/MoS_2 nanocomposite and its application as a lubricant additive. *Dig. J. Nanomater. Biostruct.* **2018**, *13*, 731–741.
25. Kumar, A.; Thakre, G.D.; Arya, P.K.; Jain, A.K. 2D Structured Nano-Sheets of Octadecylamine Grafted Graphitic-Carbon Nitride (g-C3N4) as Lubricant Additives. *Macromol. Symp.* **2017**, *376*, 1700009. [CrossRef]
26. Duan, C.; Yuan, D.; Yang, Z.; Li, S.; Tao, L.; Wang, Q.; Wang, T. High wear-resistant performance of thermosetting polyimide reinforced by graphitic carbon nitride (g-C_3N_4) under high temperature. *Compos. Part A Appl. Sci. Manuf.* **2018**, *113*, 200–208. [CrossRef]
27. Zhu, L.; Wang, Y.; Hu, F.; Song, H. Structural and friction characteristics of g-C_3N_4/PVDF composites. *Appl. Surf. Sci.* **2015**, *345*, 349–354. [CrossRef]
28. Li, X.L.; Li, Y.D. Formation of MoS_2 inorganic fullerenes (IFs) by the reaction of MoO_3 nanobelts and S. *Chem. A Eur. J.* **2003**, *12*, 2726–2731. [CrossRef]
29. Rapoport, L.; Fleischer, N.; Tenne, R. Applications of WS 2 (MoS_2) inorganic nanotubes and fullerene-like nanoparticles for solid lubrication and for structural nanocomposites. *J. Mater. Chem.* **2005**, *15*, 1782–1788. [CrossRef]
30. Tang, G.; Wang, Y.; Chen, W.; Tang, H.; Li, C. Hydrothermal synthesis and characterization of novel flowerlike MoS_2 hollow microspheres. *Mater. Lett.* **2013**, *100*, 15–18. [CrossRef]
31. Gawande, M.B.; Shelke, S.N.; Zboril, R.; Varma, R.S. Microwave-assisted chemistry: Synthetic applications for rapid assembly of nanomaterials and organics. *Acc. Chem. Res.* **2014**, *47*, 1338–1348. [CrossRef]
32. Li, W.-J.; Shi, E.-W.; Ko, J.; Chen, Z.-Z.; Ogino, H.; Fukuda, T. Hydrothermal synthesis of MoS_2 nanowires. *J. Cryst. Growth* **2003**, *250*, 418–422. [CrossRef]
33. Lin, H.; Chen, X.; Li, H.; Yang, M.; Qi, Y. Hydrothermal synthesis and characterization of MoS_2 nanorods. *Mater. Lett.* **2010**, *64*, 1748–1750. [CrossRef]
34. Peng, Y.; Meng, Z.; Zhong, C.; Lu, J.; Yu, W.; Yang, Z.; Qian, Y. Hydrothermal synthesis of MoS_2 and its pressure-related crystallization. *J. Solid State Chem.* **2001**, *159*, 170–173. [CrossRef]
35. Muralikrishna, S.; Manjunath, K.; Samrat, D.; Reddy, V.; Ramakrishnappa, T.; Nagaraju, D.H. Hydrothermal synthesis of 2D MoS_2 nanosheets for electrocatalytic hydrogen evolution reaction. *RSC Adv.* **2015**, *5*, 89389–89396. [CrossRef]
36. Yi, M.; Zhang, C. The synthesis of MoS_2 particles with different morphologies for tribological applications. *Tribol. Int.* **2017**, *116*, 285–294. [CrossRef]
37. Li, H.; Zhang, G.; Wang, L. Low humidity-sensitivity of MoS_2/Pb nanocomposite coatings. *Wear* **2016**, *350*, 1–9. [CrossRef]
38. Wu, L.; Zhang, Z.; Yang, M.; Yuan, J.; Li, P.; Guo, F.; Men, X. One-step synthesis of g-C3N4 nanosheets to improve tribological properties of phenolic coating. *Tribol. Int.* **2019**, *132*, 221–227. [CrossRef]
39. Yang, X.; Ma, F.; Li, K.; Guo, Y.; Hu, J.; Li, W.; Huo, M.; Guo, Y. Mixed phase titania nanocomposite codoped with metallic silver and vanadium oxide: New efficient photocatalyst for dye degradation. *J. Hazard. Mater.* **2010**, *175*, 429–438. [CrossRef]

coatings

MDPI

Article

Surface Modification and Parametric Optimization of Tensile Strength of Al6082/SiC/Waste Material Surface Composite Produced by Friction Stir Processing

Nitesh Kumar [1], Rakesh Kumar Singh [1,*], Ashish Kumar Srivastava [2], Akash Nag [3], Jana Petru [3] and Sergej Hloch [4]

[1] Department of Mechanical Engineering, Noida Institute of Engineering and Technology, Greater Noida 201306, India
[2] Department of Mechanical Engineering, G.L. Bajaj Institute of Technology and Management, Greater Noida 201306, India
[3] Faculty of Mechanical Engineering, VŠB–Technical University of Ostrava, 70800 Ostrava, Czech Republic
[4] Faculty of Manufacturing Technologies, TUKE with a Seat in Prešov, 080 01 Prešov, Slovakia
* Correspondence: rakesh310miet@gmail.com

Abstract: Friction stir processing (FSP) is one of the promising tools to enhance the mechanical and microstructural features of any engineering material due to its excellence in grain refinement. Further, the successful utilization of waste material into a useful product instigates the use of chicken bone powder (CBP), walnut shell powder (WSP), and rice husk powder (RHP) as secondary reinforcement to develop surface composites and metal matrix composites to enhance the mechanical properties. In the present work, a surface composite of base alloy Al6082 is developed through the utilization of SiC as primary reinforcement and CBP, WSP, and RHP as secondary reinforcement. The experiments were performed as per Taguchi's L9 orthogonal array and the analysis of variance (ANOVA) response is discussed in detail. The process parameters taken for the study are the type of tool pin profile such as hexagonal, square, and cylindrical threaded along with rotational speed and tool tilt angle. The result revealed the microstructural characterization through field emission scanning electron microscopy (FESEM) images equipped with energy-dispersive X-ray spectroscopy (EDS) phase mapping and elemental spectrum. The tensile strength of each specimen was tested through a horizontal tensometer and further studied to get the optimized value of the process parameter to achieve a larger value. The use of a hexagonal pin profile with the optimized value of the rotational speed of 1500 rpm and 3° tilt angle gives the higher tensile strength of 250.64 MPa.

Keywords: Al6082; friction stir processing; chicken bone powder; walnut shell powder; rice husk powder; Taguchi's L9 orthogonal array

Citation: Kumar, N.; Singh, R.K.; Srivastava, A.K.; Nag, A.; Petru, J.; Hloch, S. Surface Modification and Parametric Optimization of Tensile Strength of Al6082/SiC/Waste Material Surface Composite Produced by Friction Stir Processing. *Coatings* **2022**, *12*, 1909. https://doi.org/10.3390/coatings12121909

Academic Editor: Chang-Hwan Choi

Received: 8 November 2022
Accepted: 2 December 2022
Published: 6 December 2022

1. Introduction

Friction stir processing (FSP) is the trending technique for grain refinement as well as modification of the microstructure of the material. Modification happened due to severe plastic deformation. It was developed in 1991 by "The welding Institute" (TWI) [1]. Every day, the need for sophisticated engineered materials with specialized qualities grows. As a substitute for ferrous alloys, composites are growing because of their lightweightedness, low density, high strength, and corrosion resistance, and aluminum has proven to be an excellent alternative [2]. During FSP, the composite made is named a surface composite due to the processing of the top surface of the base material [3]. The properties of the top surface of the base material are altered with processing due to severe plastic deformation and grain refinement [4]. Ceramics such as silicon carbide (SiC), titanium carbide (TiC), zirconium dioxide (ZrO_2), boron carbide (B_4C) etc., were used to reinforce alloys, resulting in surface composites [5]. When compared to base alloys, surface composites offer better mechanical and wear properties [6].

SiC is a mixture of silicon as well as carbon. It has many properties due to which it is the best choice for many researchers and different composite material-related industries. Low thermal expansion coefficient, high hardness and rigidity are some of its common properties [7]. Hybrid composite materials are becoming more popular in many engineering applications due to their improved features and benefits over non-hybrid with using only one reinforcement [8]. Hybrid composites consist of two or more reinforcements. It has great potential to improve differential mechanical properties such as tensile, hardness, wear resistance, and many more [9]. Nowadays some biowaste materials are also proven as a reinforcement to upgrade the properties of existing materials such as chicken bone powder (CBP), which is a waste material and is generally produced from the poultry farm. Storing this waste is a big problem because it produces unwanted gases which are harmful to the environment; however, utilizing the waste before it produces harmful gases is an eco-friendly alternative [10,11]. The chicken bone powder has a good amount of carbon as well as calcium which is a very useful for reinforcing elements. It also has good potential to provide strength as a calcium source. Walnut shell powder (WSP) is a green waste which is produced by walnut farm industries. Its soft abrasive nature has unique physical and chemical properties. It contains cellulose and lignin in high amounts which is structured as large and medium fiber. The covalent bond of lignin enhances the bonding strength which leads to improved mechanical properties while using as a reinforcement. It has also the potential to improve strength as well as wear properties. Rice husk powder (RHP) is an agricultural waste which is produced from farming. Its storage is a big problem for many farmers; hence, they destroy them by burning which produces unwanted gases which when comes in contact with the environment also changes the climate of the surrounding area. Rice husk has also good strength, good wear resistance, low coefficient of friction, and excellent machinability which makes it superior if used as a reinforcement [12].

In view of the mechanical properties, tensile test will provide the various results such as tensile modulus, yield and ultimate strength, percentage elongation, and other elastic coefficients. The general solution for the tensile properties of the material is given by generalized hook's law. The elastic constants can also be obtained by the simulated results and can be useful to predict the elastic constants and other mechanical properties prior to the experimental run [13]. These properties also depend on the optimized values of process parameters. The process parameters of FSP play a significant role in the microstructural and mechanical properties of the surface composites. Process parameters such as tool rotational speed, traverse speed (feed rate), tool tilt angle, tool pin geometry (shape and size) etc., need to be optimized to complete the processing. Various optimization techniques such as Taguchi's orthogonal array, response surface methodology (RSM) are reported by authors to find the optimum solution of the experimental problem. Taguchi's design is considered as one of the standard designs of experiment (DOE) method to solve the experimental problems where approximated results are to be predicted with the help of analysis of variance (ANOVA) response in terms of significance. It is a robust design by eliminating and minimizing noise factors. The method is capable to predict both "larger is better", as well as "smaller is better" approach in terms of signal to noise ratio. L9 (3^4) orthogonal array includes nine different experiments covering the range of the selected process parameter and used for approximation of the factors that influence the performance standards [14].

Several researchers have worked to optimize the different process parameters of the FSP operation. Awasthi et al. [15] optimized the process parameters i.e., tool rotation speed, tool tilt angle, and weight percentage on ZK60A/SiC/B_4C using FSP. Results revealed that optimized values are 1000 rpm (rotation speed), 2° (tilt angle), and 75/25 (wt.%). They also concluded that with increased wt.% of reinforcement particles of B_4C with scroll shoulder there is increased hardness. Taghiabadi and Moharami [16] optimized the effect of process parameters i.e., traverse speed and tool rotational speed on Mg_4Si using FSP. Results revealed that the optimized value of the traverse speed is 12.5 mm/min and the rotation speed is achieved at 1250 rpm. Tensile strength is increased up to 150 MPa whereas

hardness is also increased up to 65 HV which is 140 and 20 times the multiple of base material, respectively. Moharami and Razaghian [17] investigated the effect of process parameters i.e., number of passes and tool rotation speed also examine corrosion behavior on Al-Mg_2Si using FSP. Results revealed that by increasing the number of passes from one to three, the corrosion resistance is reduced to $(6.92 - 4.11) \times 10^{-7}$ A·cm^{-2} which will also help to wear resistance. There is also grain refinement that occurs from 112 μm to $(10.5 - 2.3)$ μm in the first and third pass of FSP.

In the present work, SiC (2% by wt.) is used as a primary reinforcement and waste materials such as CBP, WSP, and RHP (vary from 2% to 6%) are used as secondary reinforcement. The study revealed the microstructural characteristics and effect of process parameters (rotational speed and tool tilt angle) along with the type of tool pin profile (Hexagonal, Square, Threaded) on the tensile strength of the developed specimens. Taguchi's L9 orthogonal array is applied to examine the effect of process parameters and the analysis of variance (ANOVA) response is discussed in terms of the significance of the process parameters.

2. Experimental Procedure

Al6082 is chosen as a base material, which is available in the form of a plate of dimension $(100 \times 65 \times 10)$ mm^3. The chemical composition and mechanical properties of Al6082 are given in Tables 1 and 2.

Table 1. Chemical composition of Al6082 alloy.

Elements	Aluminum (Al)	Silicon (Si)	Magnesium (Mg)	Manganese (Mn)	Iron (Fe)	Chromium (Cr)	Zinc (Zn)	Titanium (Ti)	Copper (Cu)
wt. %	95.2	1.3	1.2	1.0	0.5	0.25	0.2	0.1	0.1

Table 2. Mechanical properties of Al6082 alloy.

Mechanical Properties	Values
Tensile Strength	180 MPa
Hardness Value (BHN)	49 BHN

A groove of (3×3) mm is prepared at the center of the Al6082 plate with the help of a shaper machine to accommodate the mixture of reinforcement. As a reinforcement, SiC (2% by wt.) is used as a primary reinforcement and waste materials such as CBP, WSP, and RHP (vary from 2% to 6%) are used as secondary reinforcement. The waste material reinforcements were prepared by ball milling operation with a planetary mono mill (Pulverisette 6 classic, made by Fritsch). The BPR and rpm kept for the operation were 12:1 and 300 rpm respectively with the Tungsten carbide ball of 20 mm diameter. The field emission scanning electron microscopy (FESEM) image and their corresponding energy-dispersive X-ray spectroscopy (EDS) spectrum for the presence of elements of CBP, WSP and RHP are shown in Figure 1a–c.

For the fabrication of the composite, there are three different pin profile tools chosen i.e., hexagonal (HEX), square (SQR), and threaded (THRD) as shown in Figure 2.

In the present work, the Taguchi method is used for the optimization of different process parameters. For this research L_9, the orthogonal array is used for the selection of process parameters of FSP operation such as type of tool, tool rotational speed, tool tilt angle, and type of secondary reinforcement with their wt. % (vary from 2% to 6%). The level of design of process parameters and L_9 orthogonal is illustrated in Tables 3 and 4.

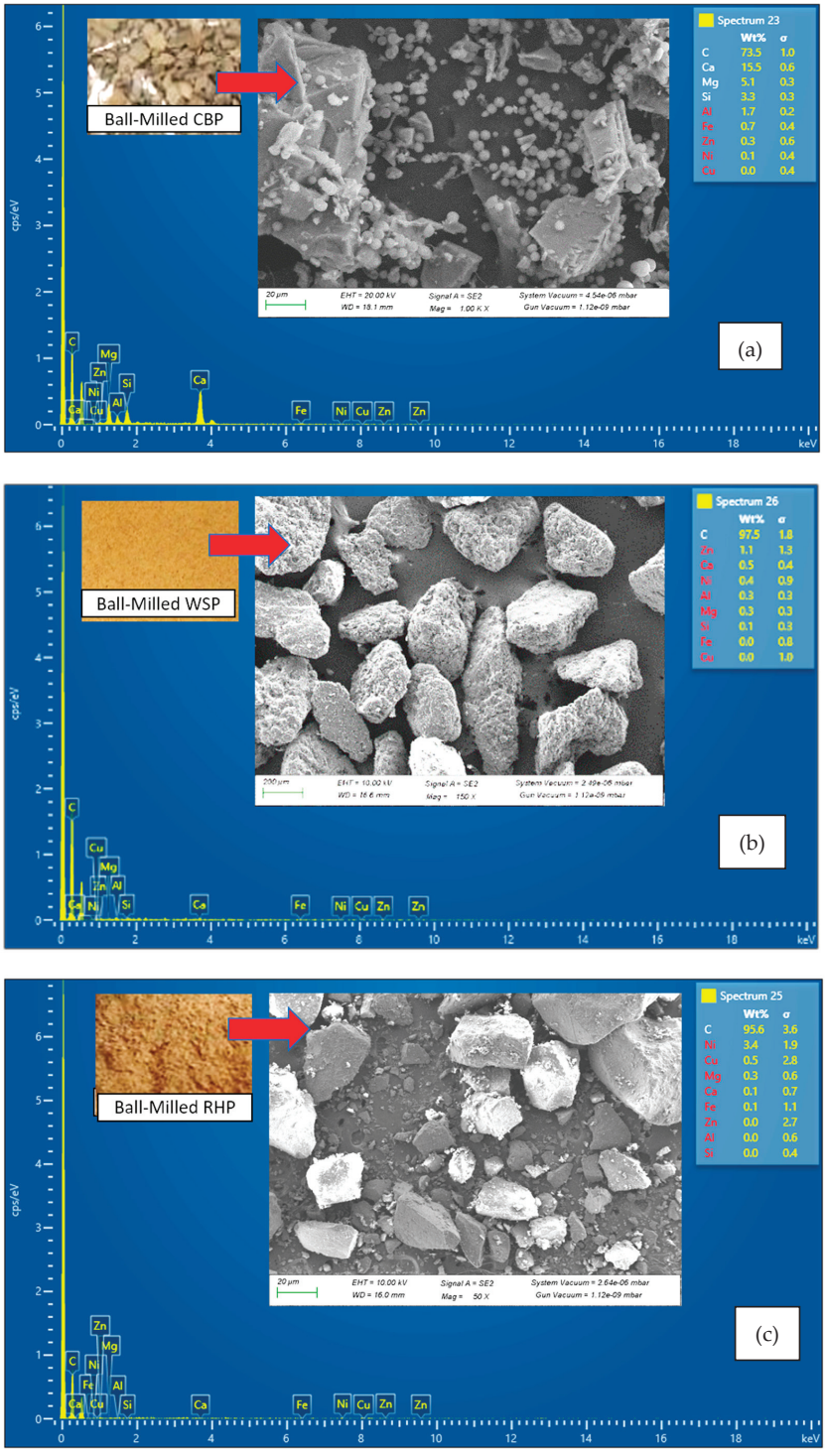

Figure 1. FESEM image and their corresponding EDS spectrum for (**a**) CBP (**b**) WSP (**c**) RHP.

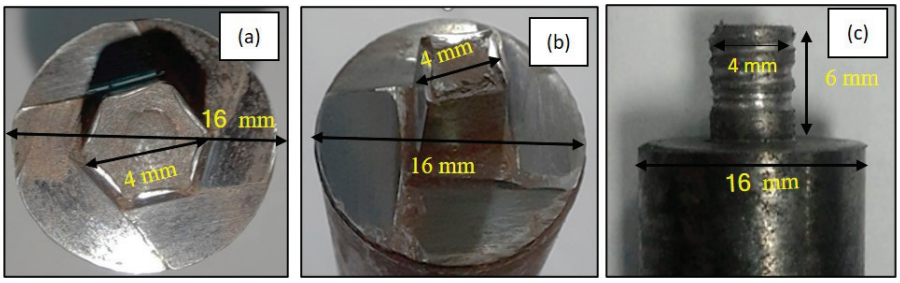

Figure 2. Different tool pin profile; (**a**) hexagonal, (**b**) square, (**c**) threaded.

Table 3. Level of design of process parameters.

Factors \ Levels	1	2	3
Tool	SQR	HEX	THRD
Tool Rotation Speed (RPM)	1000	1500	2000
Tilt Angle (°)	1	2	3
Secondary Reinforcement	CBP	WSP	RHP
% of Secondary Reinforcement (%)	2	4	6

Table 4. L_9 orthogonal array.

Experimental Run	Tool Pin Profile	Tool Rotation Speed (RPM)	Tool Tilt Angle (°)	Hybrid Reinforcement (By Wt.%) SiC (2%) +
1	SQR	1000	1	CBP (2%)
2	SQR	1500	2	CBP (4%)
3	SQR	2000	3	CBP (6%)
4	HEX	1000	2	WSP (2%)
5	HEX	1500	3	WSP (4%)
6	HEX	2000	1	WSP (6%)
7	THRD	1000	3	RHP (2%)
8	THRD	1500	1	RHP (4%)
9	THRD	2000	2	RHP (6%)

The FSP operation is performed on a vertical milling machine (make of "Rainu machine tools") with the help of a special design fixture to hold the workpiece. A total of 9 experiments were conducted as per the process parameters given in Table 4 and made 9 specimens of FSP were for study purposes.

Each specimen was tested for morphological characterization through FESEM images, EDS study, and mechanical properties such as tensile strength and hardness (BHN). The microstructural specimens were prepared for 2% SiC/2% of each type of reinforcement (CBP/WSP/RHP). ASTM E3 standard was used to prepare the specimen for microstructural study followed by etching through Keller's reagent (15 mL HCL + 25 mL HNO_3 + 10 mL HF + 50 mL H_2O). The FESEM images were taken by Joel jsm-7800 Prime field emission scanning electron microscope coupled with an EDS detector (LN_2 Free SDD X-max 80 Energy dispersive detector) at an acceleration voltage of 20 Kv and acquisition time of 60.4. The EDS spectrum is further discussed to confirm the presence of elemental percentage of composition of the type of primary reinforcement (SiC) and secondary reinforcement (CBP, WSP and RHP). As an outcome of the study, tensile strength is studied for all nine specimens to get the optimized value of process parameters of FSP. A tensile test was conducted on a horizontal Tensometer, made of KIPL, Model PC-2000. Specimens for the tensile study were developed as per ASTM E8 standard.

3. Result and Discussion

A total of nine specimens were developed through FSP operation as shown in Figure 3. An addition experiment with adding 2% SiC (primary reinforcement) without any secondary reinforcement is performed to evaluate the effect of secondary reinforcements in terms of tensile strength. The traverse speed for FSP operation was fixed to 25 mm/min while other process parameters taken for nine specimens are as per Taguchi's L9 array given in Table 4. All the physical specimens were seeming adequate because of no major defects such as misrun or tunnelling. Tool traces and cutting marks are seen on the top of the FSPed region. However, it was removed by polishing it with grit paper before making specimens for testing purposes.

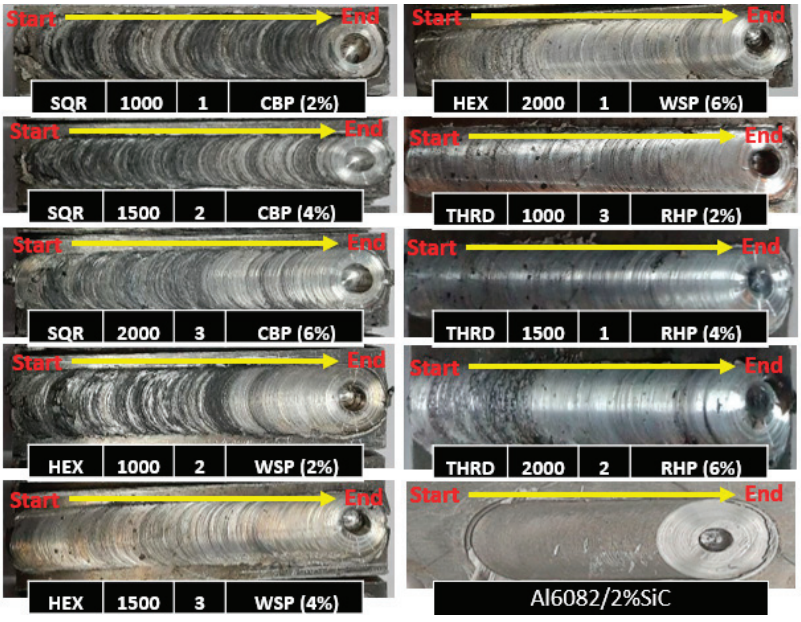

Figure 3. FSP operation at different process parameters based on L_9 Orthogonal Array.

Figures 4–6 show the FESEM images, phase mapping, and EDS spectrum for Al6082/2%SiC/2%(CBP/WSP/RHP) surface composites, respectively. FESEM images show the uniform distribution of both SiC and waste material (CBP/WSP/RHP) in the stirring zone. The FSP operation improves the microstructural features by refining the grains. A large number of equiaxed grains and grain boundaries can be seen in the FESEM images. The average grain size of the developed specimens varies in the range of 20 to 35 μm for all three types of composites. The minimum grain size of 6 μm is observed for Al6082/2%SiC/2%WSP. Clustering of the secondary reinforcements (CBP/WSP/RHP) can also be seen in the FESEM images. It is because adding CBP/WSP/RHP will utilize the frictional heat and create a hindrance to the movement of free electrons into the matrix material. Therefore, an energy gap is created which tends to accumulate the clustering of these particles. However, the clustering occurs in negligible amount. Similar observations were also recorded in other similar published work [18,19].

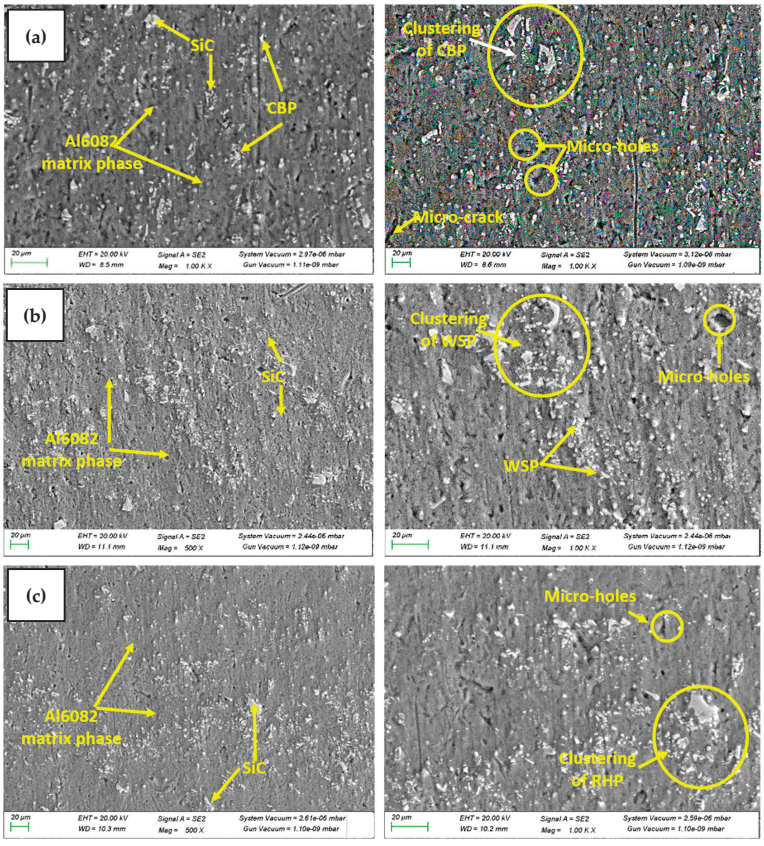

Figure 4. FESEM images of (**a**) Al6082/2% SiC/2%CBP, (**b**) Al6082/2% SiC/2%WSP, (**c**) Al6082/2% SiC/2%RHP.

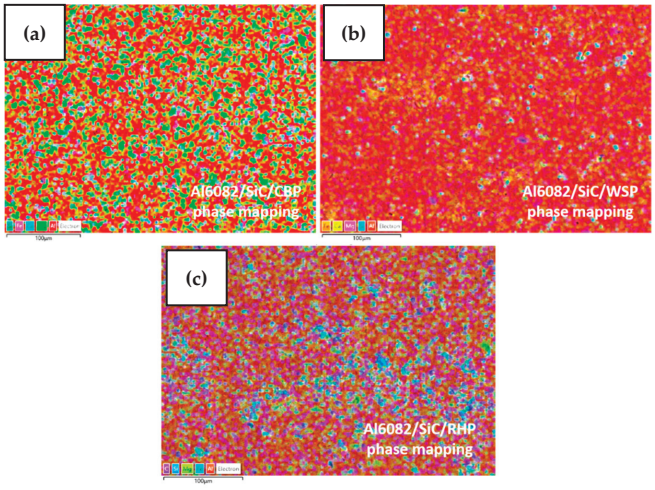

Figure 5. EDS phase mapping; (**a**) Al6082/2% SiC/2%CBP, (**b**) Al6082/2% SiC/2%WSP, (**c**) Al6082/2% SiC/2%RHP.

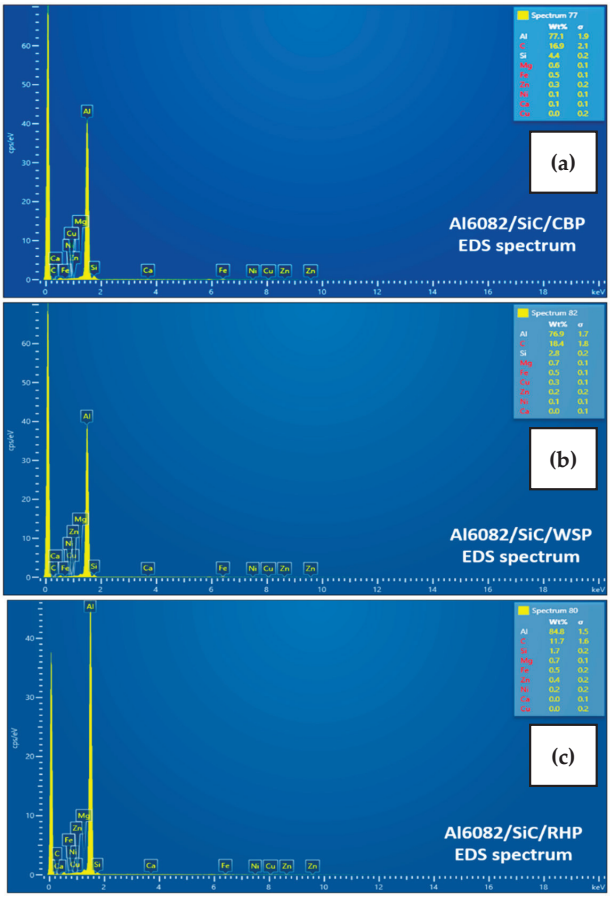

Figure 6. EDS spectrum of (**a**) Al6082/2% SiC/2%CBP, (**b**) Al6082/2% SiC/2%WSP, (**c**) Al6082/2% SiC/2%RHP.

Phase mapping and EDS spectrum of the developed Al6082/2%SiC/2% (CBP/WSP/RHP) show the presence of major constituents of the matrix and alloy phase. The major elements such as Al and Si, of the matrix and primary reinforcement phase, can be seen more largely. However, the major constituents of secondary reinforcement such as Ca, Mg, Zn, and Fe are also seen in the significant amount. It is evident from the study that the reinforcement phase is completely diffused into the matrix material. Some other constituents of the reinforcement phase which have lower atomic numbers are not completely diffused and hence not seen in the EDS spectrum. Some other elements such as Ni, Cr, and F are present in specimens due to the chemical, metallurgical reactions, and etching operation. Carbon is available due to the presence of SiC and oxygen due to aluminum alloy, which naturally forms the native oxide layer and oxygen.

Further, a tensile test was carried out on each specimen as per standards. The graph of load vs elongation of tensile testing of all nine specimens is shown in Figure 7 and their corresponding values of tensile strength are presented in Table 5. The tensile testing of Al6082/2%SiC specimen is also conducted through the same standards and the average value was found to be 197.4 MPa. It is indicated that the addition of secondary and primary reinforcement increases the tensile strength compared to the 180 MPa of base alloy Al6082 tested with the same standards. The result also revealed that adding of primary reinforce-

ment improves the tensile strength. However, the increment in numerical values of tensile strength observed are comparatively low by adding both primary and secondary reinforcement. It indicates that the addition of secondary reinforcement significantly affected the tensile strength and overall mechanical properties of the specimens. The load vs elongation curve revealed the mixed nature of the ductile and brittle failure. It is because the presence of hard reinforcement particles SiC and secondary reinforcement (CBP/WSP/RHP) has strong bonding strength capability, which improves the mechanical properties.

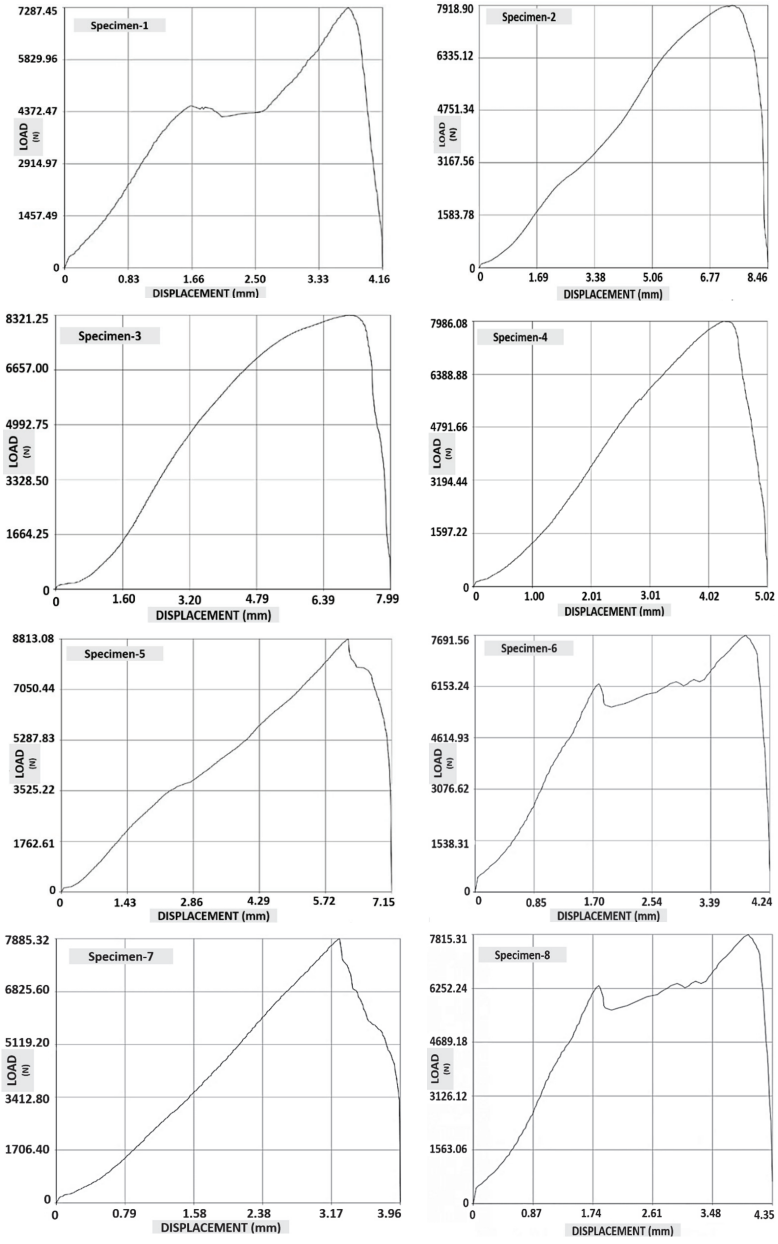

Figure 7. *Cont.*

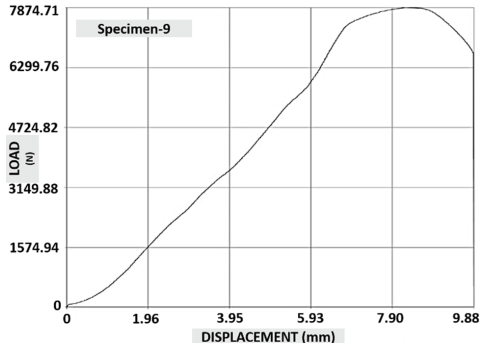

Figure 7. Load vs elongation curve for each specimen of Al6082/2% SiC/2% (CBP/WSP/RHP).

Table 5. Experimental value of fabricated composite Al6082/2% SiC/2% (CBP/WSP/RHP).

Experimental Run	Tool Pin Profile	Rotation Speed (RPM)	Tilt Angle (°)	Tensile Strength (Avg. of 3 Readings) (MPa)
1	SQR	1000	1	206.55 ± 2
2	SQR	1500	2	223.34 ± 7
3	SQR	2000	3	236.62 ± 5
4	HEX	1000	2	224.98 ± 4
5	HEX	1500	3	249.91 ± 3
6	HEX	2000	1	217.07 ± 6
7	THRD	1000	3	240.09 ± 5
8	THRD	1500	1	220.81 ± 4
9	THRD	2000	2	222.09 ± 10
			Mean	226.83 ± 5

Further, the study is carried out to optimize the process parameters such as tool pin profile, tool rotation speed, and tilt angle through S/N ratio (Larger is better) and ANOVA. Taguchi's design is analyzed with the help of Minitab 17 software. The estimated model coefficient for S/N ratios and mean are shown in Tables 6 and 7. ANOVA response for the S/N ratio and mean are given in Tables 8 and 9. It is observed from the ANOVA responses that the p value is less than 0.05 which confirms the statistical significance and rejects the null hypothesis. Similarly, the response table for the S/N ratio and mean is shown in Tables 10 and 11. Response table describes the rank which is based on Delta value. The largest Delta value is 1.04 and 27.4 of tilt angle for S/N ratio and mean, which confirms the first rank as a result of greater impact on the response. However, the lower Delta value is 0.29 and 7.5 of tool rotational speed for S/N ratio and mean which is the lowest value than other parameters which shows the lesser impact on the response. While analyzing larger the better is chosen to get the best-optimized value with the goal of achieving maximum response. The main effect describes how much variation has taken place compared to the mean of the response at a lower value of the process parameter and the mean of the response at a higher value of the process parameter which is illustrated in Figures 8 and 9. The optimized values are hexagonal (HEX) tool pin profile at 1500 rpm tool rotation speed with tilt angle 3° which is shown on the 5th experimental run of the design table.

Table 6. Estimated model coefficients for SN ratios.

Term	Coef	SE Coef	T	*p*
Constant	47.1028	0.01954	2410.254	0.000
Tool SQR	−0.1825	0.02764	−6.603	0.022
Tool HEX	0.1407	0.02764	5.092	0.036
RPM 1000	−0.1192	0.02764	−4.312	0.050
RPM 1500	0.1690	0.02764	6.115	0.026
Tilt Ang 1	−0.4652	0.02764	−16.831	0.004
Tilt Ang 2	−0.1134	0.02764	−4.105	0.055
S = 0.5863	R-Sq = 99.7%	R-Sq(adj) = 98.6%		

Table 7. Estimated model coefficients for mean.

Term	Coef	SE Coef	T	*p*
Constant	226.872	0.3345	678.311	0.000
Tool SQR	−4.702	0.4730	−9.941	0.010
Tool HEX	3.781	0.4730	7.944	0.015
RPM 1000	−2.999	0.4730	−6.340	0.024
RPM 1500	4.481	0.4730	9.474	0.011
Tilt Ang 1	−12.062	0.4730	−25.501	0.002
Tilt Ang 2	−3.272	0.4730	−6.918	0.020
S = 1.003	R-Sq = 99.9%	R-Sq(adj) = 99.4%		

Table 8. Analysis of variance for SN ratios.

Source	DF	Seq SS	Adj SS	Adj MS	F	*p*	PC (%)
Tool	2	0.16457	0.16457	0.082283	23.94	0.040	8.23
RPM	2	0.13574	0.13574	0.067871	19.75	0.048	6.79
Tilt Angle	2	1.69210	1.69210	0.846048	246.14	0.004	84.64
Residual Error	2	0.00687	0.00687	0.003437			
Total	8	1.99928					

Table 9. Analysis of variance for means.

Source	DF	Seq SS	Adj SS	Adj MS	F	*p*	PC (%)
Tool	2	111.77	111.77	55.884	55.51	0.018	8.09
RPM	2	93.81	93.81	46.906	46.59	0.021	6.79
Tilt Angle	2	1174.05	1174.05	587.025	583.05	0.002	84.97
Residual Error	2	2.01	2.01	1.007			
Total	8	1381.64					

Table 10. Response table for signal-to-noise ratios.

Level	Tool	RPM	Tilt Angle
1	46.92	46.98	46.64
2	47.24	47.27	46.98
3	47.14	47.05	47.68
Delta	0.32	0.29	1.04
Rank	2	3	1
Larger is better			

Table 11. Response table for means.

Level	Tool	RPM	Tilt Angle
1	222.2	223.9	214.8
2	230.7	231.4	223.5
3	227.7	225.3	242.2
Delta	8.5	7.5	27.4
Rank	2	3	1
Larger is better			

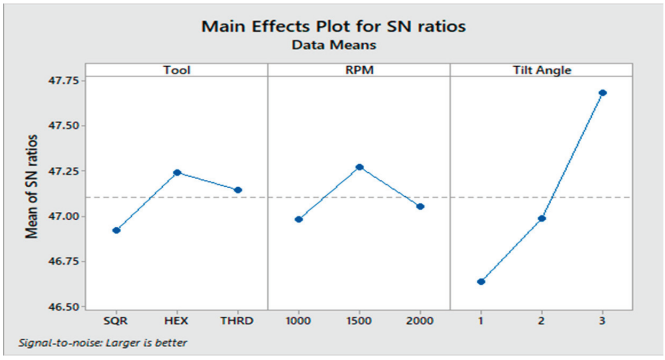

Figure 8. Main effects between the mean of SN ratio and process parameters.

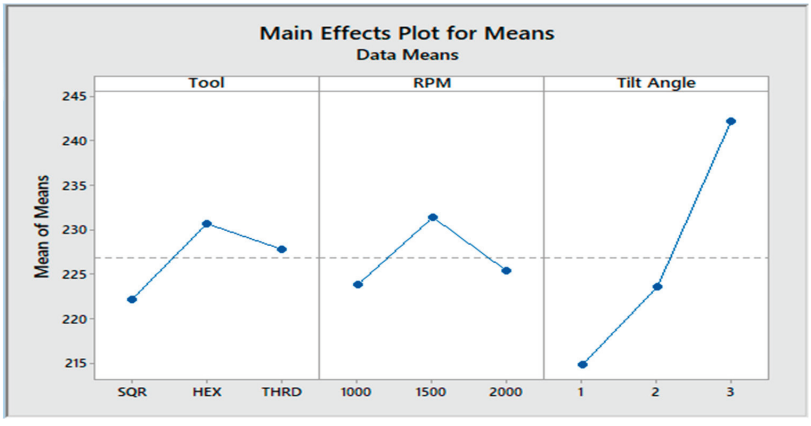

Figure 9. Main effects between the mean of means and process parameters.

The confirmation experiment has been conducted based on the optimized value of process parameters and found the maximum ultimate tensile strength of 250.64 MPa which is approximately closer to the experimental value. While discussing the effect of process parameters, each parameter has a significant effect on FSP operation and mechanical properties. In the present study, there are three pin profile tools are used. However, the hexagonal pin profile showed the optimum value of process parameters to achieve higher tensile strength. It is attributed to the fact that the hexagonal pin has sharp edges to remove the extra material from the front and mixed the reinforcement with it and deposit it at the back with the proper distribution. However, due to lower edges in the square, it does not show optimum value, whereas the threaded pin profile shows the better than square due to having better material flow. Rotational speed shows a vital role while the development

of Al6082/2% SiC/2% (CBP/WSP/RHP). In the present study, three different tool rotation speeds are selected i.e., lower (1000 rpm), medium (1500 rpm), and higher (2000 rpm). At lower rpm, the result shows that insufficient friction takes place which causes lower heat generation, whereas sufficient heat generation takes place using a rotational speed of 1500 rpm. However, at 2000 rpm excessive heat was generated due to which improper material flow occurred compared to processing at a lower feed rate. At a tilt angle from 1° to 3° the tensile strength significantly increases. This happened due to good consolidation of the material under the tool shoulder while increasing the tilt angle from 1° to 3°. At a lower tilt angle, there is more contact between the tool shoulder and the workpiece, as a result, more friction takes place due to which no proper stirring action takes place; however, at a higher tilt angle defect-free optimized result is obtained.

4. Conclusions

The waste material CBP, WSP, and RHP are successfully utilized as secondary reinforcement to develop surface composites from FSP operation. Microstructural and mechanical characterization of the developed specimens evidences the improvement in overall properties. The followings are the conclusive results based on the study:

1. FESEM images show the uniform distribution of both SiC and secondary reinforcement CBP, WSP, and RHP into the stir zone of the matrix material. The average grain size of the developed specimens varies in the range of 20 to 35 μm for all three types of composites. The minimum grain size of 6 μm is observed for Al6082/2%SiC/2%WSP.
2. Phase mapping and EDS spectrum of the developed Al6082/2% SiC/2% (CBP/WSP/RHP) show the presence of major constituents of the matrix and alloy phase. It is evident from the study that the reinforcement phase is completely diffused into the matrix material.
3. As an outcome, the tensile strength of each specimen has been evaluated and found significant increment of around 20% to 35% of tensile strength compared to base alloy Al6082.
4. Taguchi's L9 optimization approach and ANOVA response show the significance of the rotational speed and tool tilt angle and selected tool pin profile. It is concluded from the study that the tensile strength of processed samples is increased with using the hexagonal pin profile tool due to better stirring action as a result proper material flow takes place.
5. Tool tilt angle also plays a vital role in increasing tensile strength. These values are increased after increasing the tilt angle. It is attributed to the thrusting effect and also due to contact between the shoulder and workpiece.
6. The optimized value for tensile strength is in the range of (247.32–253.96) MPa with a hexagonal (HEX) tool pin profile, 1500 rpm, and 3° tilt angle.

Author Contributions: N.K.: Writing, methodology; R.K.S.: Supervision, conceptualization; A.K.S.: review and editing; A.N.: review and editing, software; J.P.: project administration; funding acquisition; S.H.: Visualization, Supervision. All authors have read and agreed to the published version of the manuscript.

Funding: The study was undertaken in connection with the project Innovative and Additive Manufacturing Technology—New Technological Solutions for 3D Printing of Metals and Composite Materials, reg. No. CZ.02.1.01/0.0/0.0/17_049/0008407 financed by the Structural and Investment Funds of the European Union.

Institutional Review Board Statement: Not applicable.

Informed Consent Statement: Not applicable.

Data Availability Statement: No data included.

Conflicts of Interest: The authors declare no conflict of interest.

References

1. Srivastava, A.K.; Dixit, A.R.; Maurya, M.; Saxena, A.; Maurya, N.K.; Dwivedi, S.P.; Bajaj, R. 20th century uninterrupted growth in friction stir processing of lightweight composites and alloys. *Mater. Chem. Phys.* **2021**, *266*, 124572. [CrossRef]
2. Dwivedi, R.; Singh, R.K.; Kumar, S.; Srivastva, A.K. Parametric optimization of process parameters during the friction stir processing of Al7075/SiC/waste eggshell composite. *Mater. Today Proc.* **2021**, *47*, 3884–3890. [CrossRef]
3. Kumar, S.; Srivastava, A.K.; Singh, R.K. Fabrication of AA7075 hybrid green metal matrix composites by friction stir processing technique. *Ann. Chim.-Sci. MatÉRiaux* **2020**, *44*, 295–300. [CrossRef]
4. Ma, Z.Y. Friction stir processing technology: A review. *Metall. Mater. Trans. A* **2008**, *39*, 642–658. [CrossRef]
5. Srivastava, A.K.; Maurya, N.K.; Dixit, A.R.; Dwivedi, S.P.; Saxena, A.; Maurya, M. Experimental investigation of A359/Si_3N_4 composite produced by multi-pass friction stir processing. *Mater. Chem. Phys.* **2021**, *257*, 123717. [CrossRef]
6. Kumar, S.; Srivastava, A.K.; Singh, R.K.; Dwivedi, S.P. Experimental study on hardness and fatigue behavior in joining of AA5083 and AA6063 by friction stir welding. *Mater. Today Proc.* **2020**, *25*, 646–648. [CrossRef]
7. Rathee, S.; Maheshwari, S.; Siddiquee, A.N.; Srivastava, M. Investigating the effects of SiC particle sizes on the microstructural and mechanical properties of AA5059/SiC composites during multi pass FSP. *Silicon* **2019**, *11*, 797–805. [CrossRef]
8. Dwivedi, R.; Kumar Singh, R.; Kumar Srivastava, A.; Anand, A.; Kumar, S.; Pal, A. Statistical optimization of process parameters during the friction stir processing of Al7075/Al_2O_3/waste eggshell surface composite. In *Recent Trends in Industrial and Production Engineering*; Lecture Notes in Mechanical Engineering, Dvivedi, A., Sachdeva, A., Sindhwani, R., Sahu, R., Eds.; Springer: Singapore, Singapore, 2022. [CrossRef]
9. Srivastava, A.K.; Saxena, A.; Dixit, A.R. Investigation on the thermal behaviour of AZ31B/waste eggshell composites produced by friction stir processing. *Compos. Commun.* **2021**, *28*, 100912. [CrossRef]
10. Srivastava, A.K.; Kumar, N.; Dixit, A.R. Friction stir additive manufacturing—An innovative tool to enhance mechanical and microstructural properties. *Mater. Sci. Eng. B* **2021**, *263*, 114832. [CrossRef]
11. Srivastava, A.K.; Kumar, N.; Saxena, A.; Tiwari, S. Effect of friction stir processing on microstructural and mechanical properties of lightweight composites and cast metal alloys—A review. *Int. J. Cast Met. Res.* **2021**, *34*, 169–195. [CrossRef]
12. Srivastava, A.K.; Maurya, M.; Saxena, A.; Maurya, N.K.; Dwivedi, S.P.; Dixit, A.R. Microstructural and fractographic analysis of A359/Si3N4 composite produced by friction stir processing. *Int. J. Mater. Res.* **2021**, *112*, 68–77. [CrossRef]
13. Pei, J.; Wu, Z.; Hu, Y.; Fu, X.; Wang, J.; Song, X.; Sun, Z.; Wang, M. Molecular dynamic simulations and experimental study on pBAMO-b-GAP copolymer/energetic plasticizer mixed systems. *FirePhysChem* **2022**, *2*, 67–71. [CrossRef]
14. Rathee, S.; Maheshwari, S.; Siddiquee, A.N.; Srivastava, M.; Sharma, S.K. Process parameters optimization for enhanced microhardness of AA 6061/ SiC surface composites fabricated via Friction Stir Processing (FSP). *Mater. Today: Proc.* **2016**, *3*, 4151–4156. [CrossRef]
15. Awasthi, S.; Gupta, P.; Pachuri, P.; Tyagi, M. Optimization of magnesium ZK60A/SiC/B4C hybrid composite fabricated by friction stir processing. *Mater. Today Proc.* **2022**, *62*, 191–197. [CrossRef]
16. Taghiabadi, R.; Moharami, A. Mechanical properties enhancement of Mg–4Si in-situ composites by friction stir processing. *Mater. Sci. Technol.* **2021**, *37*, 66–77. [CrossRef]
17. Moharami, A.; Razaghian, A. Corrosion behaviour of friction stir processed Al–Mg_2Si composites. *Mater. Sci. Technol.* **2020**, *36*, 1922–1929. [CrossRef]
18. Srivastava, A.K.; Dwivedi, S.; Saxena, A.; Kumar, D.; Dixit, A.R.; Singh, G.K.; Bhutto, J.K.; Verma, R. Tribological characteristics of Al359/Si3N4/eggshell surface composite produced by friction stir processing. *Coatings* **2022**, *12*, 1362. [CrossRef]
19. Dwivedi, R.; Srivastava, A.K.; Singh, R.K. Effect of eggshell waste and B_4C particles on the mechanical and tribological properties of Al7075 alloy developed by friction stir processing. *Metall. Res. Technol.* **2022**, *119*, 508. [CrossRef]

coatings

MDPI

Article

An Investigation for Minimizing the Wear Loss of Microwave-Assisted Synthesized g-C_3N_4/MoS_2 Nanocomposite Coated Substrate

Mukul Saxena [1], Anuj Kumar Sharma [1,*], Ashish Kumar Srivastava [2,*], Narendra Singh [3] and Amit Rai Dixit [4]

[1] Centre for Advanced Studies, Lucknow 226031, Uttar Pradesh, India
[2] Department of Mechanical Engineering, G.L. Bajaj Institute of Technology and Management, Greater Noida 201306, Uttar Pradesh, India
[3] Department of Chemical Engineering, Indian Institute of Technology, Tirupati 517619, Andhra Pradesh, India
[4] Department of Mechanical Engineering, Indian Institute of Technology (ISM), Dhanbad 826004, Jharkhand, India
* Correspondence: anujksharma@cas.res.in (A.K.S.); ashish7185@gmail.com (A.K.S.)

Abstract: Mechanical components frequently come into contact against one another causing friction that produces heat at the contact area and wear of the components that shortens part life and increases energy consumption. In the current study, an attempt was made to optimize the parameters for the pin-on-disc wear tester. The experiments were carried out in ambient thermal conditions with varying sliding speeds (0.5 m/s, 0.75 m/s, and 1.0 m/s) and applied loads (5 N, 10 N, and 15 N) for pure molybdenum disulfide with 9% and 20% weight percentage of graphitic carbon nitride (g-C_3N_4) in molybdenum-disulfide (MoS_2)-nanocomposite-coated steel substrate. Analysis of variance (ANOVA) was used to determine the outcome of interaction between various constraints. To identify the minimum wearing conditions, the objective was defined as the criterion 'smaller is better'. The maximum impact of the applied load on the coefficient of friction and wear depth was estimated to be 59.6% and 41.4%, respectively, followed by sliding speed. The optimal condition for the minimum coefficient of friction and wear was determined to be 15 N for applied load, 0.75 m/s for sliding speed, and weight percentage of 9 for g-C_3N_4 in MoS_2 nanocomposite. At the 95% confidence level, applied load was assessed to have the most significant effect on the coefficient of friction, followed by sliding speed and material composition, whereas material composition considerably impacts wear, followed by loading and sliding speed. These parameters show the effect of mutual interactions. Results from the Taguchi method and response surface methodology are in good agreement with the experimental results.

Keywords: optimization; tribology; ANOVA; transition metal dichalcogenide; graphitic carbon nitride; nanocomposites

Citation: Saxena, M.; Sharma, A.K.; Srivastava, A.K.; Singh, N.; Dixit, A.R. An Investigation for Minimizing the Wear Loss of Microwave-Assisted Synthesized g-C_3N_4/MoS_2 Nanocomposite Coated Substrate. *Coatings* **2023**, *13*, 118. https://doi.org/10.3390/coatings13010118

Academic Editor: Manuel António Peralta Evaristo

Received: 14 December 2022
Revised: 3 January 2023
Accepted: 5 January 2023
Published: 8 January 2023

1. Introduction

The fundamental reasons for breakdown in many moving parts employed in mechanical work are friction and wear. A significant amount of energy is expended to eliminate frictional resistance. A result of friction is wear and heat, which can lead to noise emissions, material fatigue, mechanical losses, surface deterioration, and shorter component service life [1]. The cost of maintenance, machinery, and fitting due to wear and tear with frictional problems has an impact on a company's economy [2]. Enhancing the tribological characteristics of the contacted surfaces is a primary technique to reduce energy usage. Enhancing the tribological characteristics of the mating surfaces is a primary technique to reduce energy usage. The need for improved lubricants is increasing due to its properties including the capacity for use throughout a wider temperature range, higher loads and speeds, and durability with operational life [3]. For fulfilling the demands of machinery in

harsh situations, unique and efficient friction-resistant lubricants with high-load-bearing additives must be developed [4].

Two-dimensional nanoparticles have a larger specific surface area than other nanomaterials for absorbing onto a substrate's surface, which reduces or eliminates friction between the contacted surfaces [5]. Molybdenum disulfide (MoS_2) was discovered as a potential 2D transition-metal chalcogenide (TMD) due to its chemical stability and can be used as a coating material. Lower fiction is caused by a weakened Van der Waals attraction connecting the sulfur lamella [6]. The lubrication effect is produced by the molybdenum disulfide's layers, which effectively slide across each other and align parallel to the relative movement while sliding. The lamella, on the other hand, is particularly resistant to asperity penetration due to the strong ionic interaction between molybdenum and sulfur atoms [7]. Molybdenum disulfide in pure form, on the other hand, easily absorbs moisture and could be oxidized in any environment containing either molecular or atomic oxygen [8]. This produces a rapid growth in the frictional coefficient and deterioration in the durability of the frictional surface [9,10]. As a result of these limitations, its practicality is constrained and limited. Improving the coefficient of friction and wear life of molybdenum sulfide used as a lubricant (solid) in various domains of areas is becoming a serious problem. Increasing the wear behavior of MoS_2 for practical usage as a lubricant in various industries while retaining a low frictional coefficient is currently recognized as a significant concern [11].

Using a four-ball tribometer, the tribological characteristics of the nanoparticle mixture consisting of lubricating oil and MoS_2 under different friction conditions were examined and modeled. The MoS_2 particles' influence on the coefficient of friction and severe load of the lubricating mixture was due to the easier adsorption of MoS_2 particles on the sliding surfaces of the ball and the creation of MoO_3, which was a protective and lubricating coating. This was made feasible by the relatively simple oxidation of MoS_2 during the sliding process, which occurred after its release and passage through the valley onto the contact metal surfaces and their separation at the interface [12]. Nanoparticles developed on the highly-oriented pyrolytic (HOP) MoS_2 and graphite were utilized for a model to examine the dependency of frictional forces on the contact area. The power dissipation required for nanoparticle translation was linearly dependent on the contacting area in between the substrate and MoS_2 nanoparticles [13].

Graphitic carbon nitride (g-C_3N_4), which has weakened forces (Van Der Waals) in between the layer and tri-s-triazine unit, is now used in a range of disciplines [14,15]. For improving frictional performance, graphitic carbon nitride is often added to the lubricating medium. The bonding of graphitic carbon nitride with the octadecylamine, for example, led into the creation of boundary layers on surfaces, which improved the resistance to wear of material [16]. Duan et al. [17] selected g-C_3N_4 as a basic oil additive since it significantly increases thermoset polyimide wear resistance. Zhu et al. [18] developed g-C_3N_4/PVDF composites and observed that the g-C_3N_4 filler improved composite wearing.

Austenitic steel, which has a strong corrosion resistance, is the most commonly utilized substrate material. However, when analyzed in a tribological investigation, performance suffers due to various types of wear. Surface modification is probably the most often utilized strategy for mitigating these issues. Carbonitriding, nitriding, carburizing, coating or cladding, and other methods are commonly employed to improve the surface qualities of steel substrate [19]. Microwave radiation heats the substance at the molecular scale, resulting in uniform volume heating. Because the heating begins at the molecule across the bulk, the process is far faster than conventional methods of heating in which heating of the material is dependent on the traditional modes of transmission of heat [20]. However, microwave energy's adaptability in processing metal components is difficult due to the coefficient of absorption for metallic substance radiation at 2.45 Ghz being substantially lower at ambient temperature [21]. Cladding is often defined by partial substrate dilution and the formation of metallurgical adhesion between the deposit and substrate. Gupta et al. [22] developed a novel technique in surface improvement techniques via microwave cladding. Microwave hybrid heating (MHH) was used to create clads using tungsten-carbide-based

powder (WC10Co2Ni) over steel substrate [22]. The homogeneous distribution of the clad element across the substrate eliminates interfacial flaws and fractures. This contributes to improving the material's microstructure [23].

To analyze the tribological characteristics of friction set, a scientific method is required due to the intricacy of the wearing process. Design of the experiment (DOE) is among the most essential statistical analyses for investigating various process parameters by minimizing the number of multiple trials. The Taguchi method provides the most cost-effective technique for the design of experiments since it is possible to construct a strong design by using expensive parts with high quality materials or even adjusting process factors, but these solutions are rarely effective [24]. Dr. Genichi Taguchi created a range of unique statistical tools, concepts, and methodologies for increasing product quality, most of which are subjected to the statistical theory of DOE [25]. Taguchi describes how he developed his methodology by using a design of experiment to develop a system that can endure a wide range of conditions and fluctuations as well as lowering the target value to limit fluctuation [26]. The Taguchi method was chosen because it is a cost-effective method [27]. Optimization is the process of determining the effective or most efficient use of any condition or resource [28]. The Taguchi design method removes superfluous experimentation from the process. ANOVA analysis is then performed. As a result, the critical characteristics that determine the wear rate are identified. ANOVA is also required to identify how much of any wear process parameter contributes to material wear loss [29,30]. As a consequence, when combined with analysis of variance (ANOVA), Taguchi's testing method provides a robust instrument for analyzing the effect of various process parameters [31–34].

The aim of this study is to achieve the optimal results in terms of establishing a minimum coefficient of friction and wear depth by analyzing the impact of various process parameters, such as applied load and sliding speed, on different coating material compositions under dry sliding conditions for g-C_3N_4/MoS_2-nanocomposite-coated substrate with different weight percentages of g-C_3N_4 in the nanocomposite, which has never been performed before. The findings of this study give insight on the selection of a combination of parameters to achieve the minimum wear and the coefficient of friction.

2. Materials and Methods

For the tribological investigations on coating, a pin-on-disc POD testing apparatus (TR20LEPHM400, DUCOM Instruments, Bangalore, India) was used. Figure 1 depicts the experimental setup for the testing. The counterpart pin is made of AISI304 grade stainless steel and listed in Table 1 together with the substrate's composition, which was determined by energy dispersive X-ray analysis.

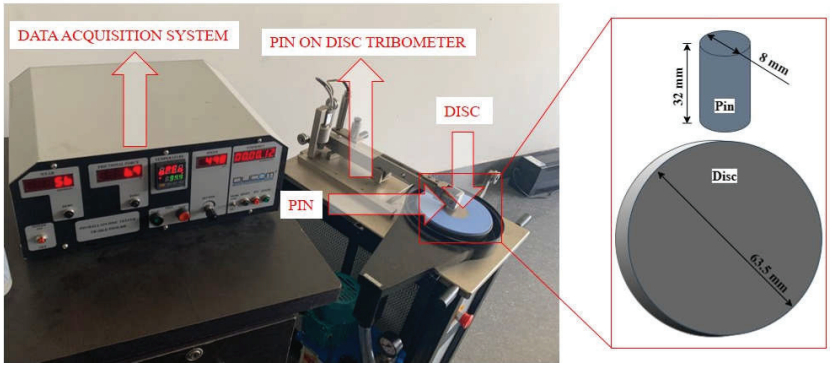

Figure 1. The experimental setup for tribological investigation.

Table 1. Composition of disc and pin material [35].

Disc	Elements	C	Fe	Ni	Cu	Si	W	P	Mo	V	Cr	Mn
	Weight %	9.43	54.9	0.12	0.71	2.55	9.72	0.14	9.06	5.73	7.1	0.53
Pin	Elements	S	P	C	Mo	Cu	Si	Mn	Ni	Cr	Fe	
	Weight %	0.02	0.027	0.065	0.13	0.14	0.3	1.78	8.1	18.2	71.2	

The ambient temperature was nearly 24 degrees Celsius, and the relative humidity (RH) was around 30%. This environment was used for all of the studies. Microwave-assisted synthesized pure molybdenum disulfide (MoS_2) with 9% and 20% weight percentage of graphitic carbon nitride (g-C_3N_4) in MoS_2 nanocomposite was taken as coating material for the analysis. Separately, synthesized MoS_2 powder and g-C_3N_4/MoS_2 nanocomposite were dissolved and dispersed in absolute ethanol (99.9%). After 30 min of ultrasonication, the solution was then deposited on the substrate with a spin coater (Holmarc, CAS, Lucknow, India).

At low rotating speed, the coating solution spreads across the substrates, and at high rotating speed, coated films were formed. First, the substrate was placed on the spin chuck. Turning on the vacuum liner kept the substrate in place. A preset volume of coating material was dispensed onto the substrate disc with a disposable pipette to coat it. After applying the coating solution, the substrate was spun, and the lid was fixed on the spin-coating. The MoS_2 and g-C_3N_4/MoS_2 nanomaterial suspensions were coated on the substrate once the solution was completely suspended. The thickness of the coating on substrate was then calculated from SEM analysis of the cross section of the coated substrate and found to be approximately 4.5 µm as shown in Figure 2.

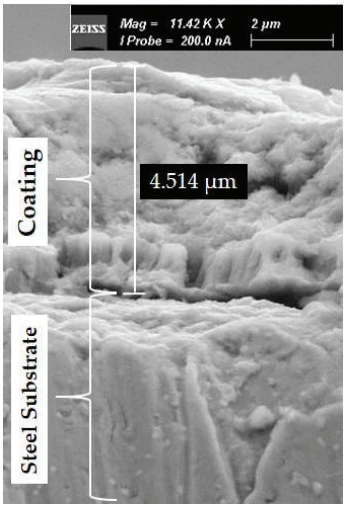

Figure 2. Coating thickness measurement from scanning electron microscopy.

Tribological experiments were carried out on POD tester with varying sliding speeds (0.5 m/s, 0.75 m/s, and 1.0 m/s) and applied loads (5 N, 10 N, and 15 N). The radius of the disc and pin utilized in the test were 31.75 mm and 4 mm, respectively.

After studying past research on the effect of input parameters on output parameters and the prediction of responses, the Taguchi method and response surface method was chosen for the prediction of response parameters. The objective of this analysis was to determine the correlation between the operating and the response parameters of the nanocomposite-coated disc and counterpart pin. As shown in Table 2, the signal-to-noise

(SN) ratio was selected as a performance metric. This ratio evaluates the output's convergence to such an objective under various noise situations. The following was the formula:

$$SN = -10 \log \frac{1}{n}\left(\sum {y_i}^2\right) \quad (1)$$

where 'n' represents the observation number and 'y_i' represents the data. The noise is denoted by the variable 'N.' The letter 'S', on the other hand, represents the signal. SN ratios were determined with the experiment purpose of 'smaller is better' in order to reduce frictional coefficient and depth of wear between the surfaces. The response was calculated using the results of adjusting a process parameter. The optimal wear conditions of a microwave-aided synthesized nanocomposite-coated steel disc were identified. The noise was decreased by altering the dependent variables. It was challenging to adjust the external variables to alter noise. These consist of applied load, sliding speed, and material composition. The procedure determines the optimal process variables for decreasing the wear depth and coefficient of friction. The interactions between the factors were also taken into account.

Table 2. Signal-to-noise (SN) ratios with the objectives and their meanings [36].

SN Ratio	Objective	Meaning
$-10 \log \frac{1}{n}\left(\sum \frac{1}{y_i^2}\right)$	'Larger was better'	Maximization of response
$-10 \log\left(\frac{\mu}{\sigma}\right)^2$	'Nominal was the best'	Shifts to a target parameter
$-10 \log \frac{1}{n}\left(\sum {y_i}^2\right)$	'Smaller was better'	Minimization of response

The orthogonal arrays were utilized to build the experiment design and engineering optimization. The detected input factors and related levels are listed in Table 3. The levels were chosen as per the specification of the instrument available at the center.

Table 3. Control factors with respective levels for analyzing wear behavior of the coating material.

Level	Factors		
	Load Applied (N)	**Sliding Speed (m/s)**	**Weight Percentage of gC_3N_4 in Nanocomposite (%)**
1	5	0.5	0
2	10	0.75	9
3	15	1.0	20

3. Results and Discussion

3.1. Design of Experiment (DOE)

The most fundamental strategy for simultaneous examination of the numerous components affecting the process is the design of experiment. It not only limits the number of trials that must be conducted, but it also specifies the research projects required to reach the objective. Effective factor identification was required to evaluate the methodological approach [32–34]. Employing a Taguchi L-9 array, the combination of parameters used in the process for each experiment in the present investigation was obtained. Wear depth was estimated using the pin-on-disc tribometer, which was equipped with a linear-variable differential transformer (LVDT) sensor with a range of up to 2000 μm with least count of 0.1 micron and accuracy of 1 ± 1% of calculated wear. Table 4 contains the parameters of all 27 trials as well as the experimental results for coefficient of friction and wear in a previous investigation [35].

Table 4. Design of experiment (DOE) with experimental results.

	Factor-1	Factor-2	Factor-3	Response-1	Response-2
S.N.	**Applied Load (N)**	**Sliding Speed (m/s)**	**g-C_3N_4 wt.% (%)**	**COF**	**Wear Depth (micrometers)**
1	5	0.5	0	0.994	267.64
2	5	0.5	9	1.604	243.85
3	5	0.5	20	4.222	315.67
4	5	0.75	0	1.167	336.72
5	5	0.75	9	0.403	262.86
6	5	0.75	20	1.542	413.73
7	5	1.0	0	0.403	333.47
8	5	1.0	9	1.278	255.67
9	5	1.0	20	0.748	450.20
10	10	0.5	0	1.285	333.79
11	10	0.5	9	0.110	349.34
12	10	0.5	20	2.890	389.67
13	10	0.75	0	0.389	112.41
14	10	0.75	9	0.228	144.49
15	10	0.75	20	0.181	105.20
16	10	1.0	0	1.108	425.73
17	10	1.0	9	0.138	100.10
18	10	1.0	20	0.597	135.70
19	15	0.5	0	0.380	355.60
20	15	0.5	9	0.222	128.30
21	15	0.5	20	0.086	479.12
22	15	0.75	0	0.190	513.40
23	15	0.75	9	0.226	98.2
24	15	0.75	20	0.384	184.60
25	15	1.0	0	0.624	331.35
26	15	1.0	9	0.145	112.1
27	15	1.0	20	0.452	123.30

3.2. Signal-to-Noise (SN) Analysis of Wear Depth and Coefficient of Friction

The purpose of the study was to determine the critical parameters impacting the wear mechanism as well as the related conditions for minimum wear depth and coefficient of friction. Figure 3 depicts the normal probability plot of the experiment. Because there was no indication of skew in the probability line, the line indicates the normality of the data distribution. Aside from the factors of interest, the graph shows no slope. This means that there was no influence of any unknown variables or other substantial variables influencing the response.

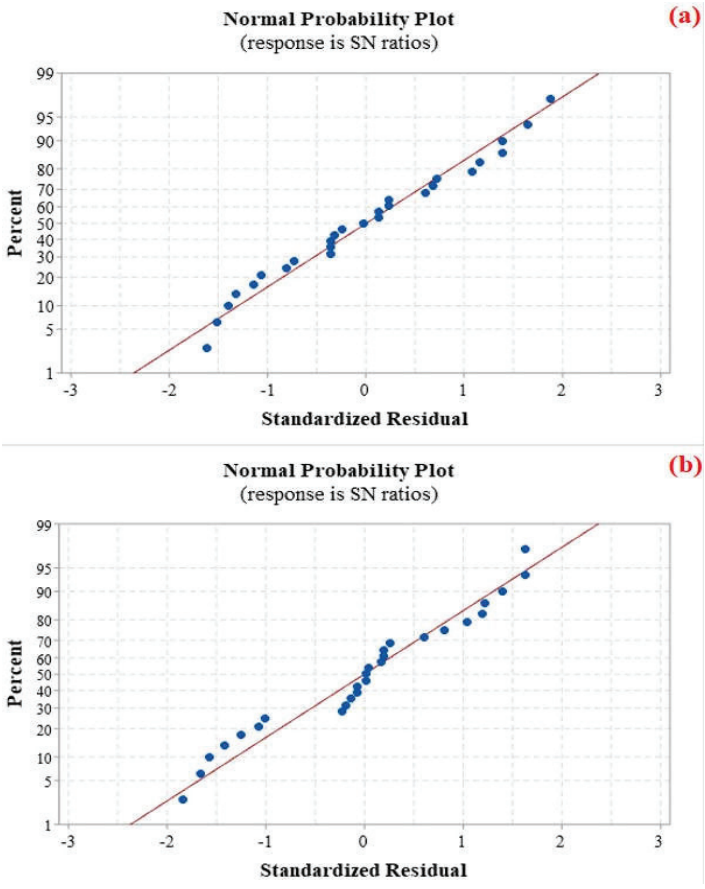

Figure 3. Normal probability plot of residuals when response is SN ratio (**a**) COF and (**b**) wear depth.

Figure 4 shows the main effects plot for the experiment. The slope of the plots showed that the applied load and weight percentage of g-C_3N_4 in the composite have the significant impact on the COF and wear, respectively, for the current experimentation state. As a result, any small variation in these parameters results in a significant difference in the COF and wear of the substrate.Therefore, substantial changes to this parameter are restricted. It can be seen from Figure 4 that the sliding speed was the least impacting parameter. With the associated optimum environment and wear mechanism, the effect of wear on control limits was investigated. Based on the SN ratios and data means, as reported in Table 5, the impact of input conditions was examined. The levels for every factor were established with the concept that they would indicate the range needed for the analysis, from low loading conditions to high. The 'data means' were the factor means for every factor and level combination, as presented in Table 5. The quantity of effects or the delta was calculated by subtracting the highest to lowest averages for any factor. When examining rank in the response table, it is simpler to understand which factor has the greatest impact.

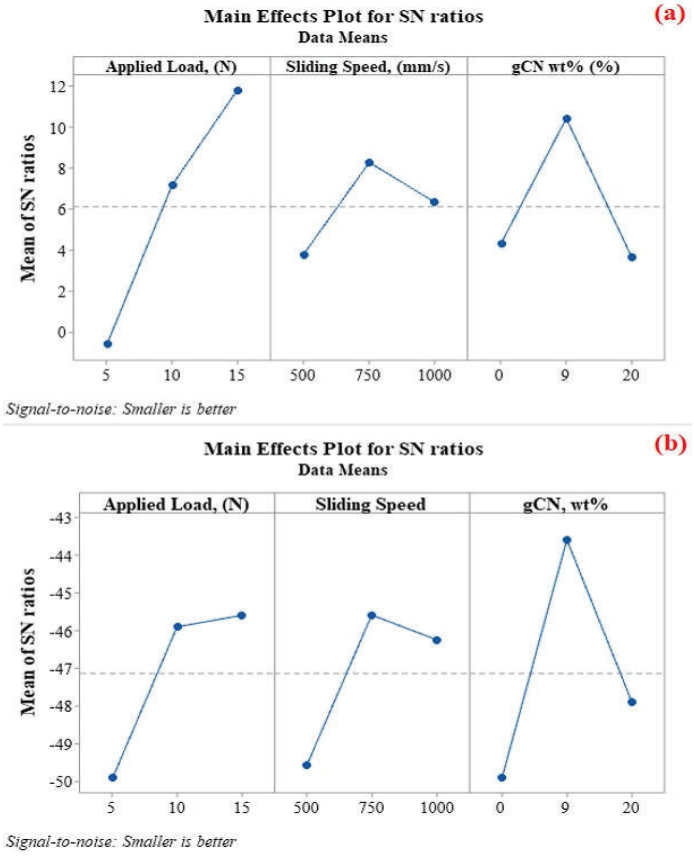

Figure 4. The main effect plots for SN ratios (**a**) COF and (**b**) wear depth at different parameters, such as applied load, sliding speed, and g-C_3N_4 weight percentage in nanocomposite.

Table 5. Response table for SN ratio for COF, wear depth, and the corresponding rank of process parameters.

	For Coefficient of Friction			For Wear Depth		
Level	**Applied Load**	**Sliding Speed**	**g-C_3N_4 wt.%**	**Applied Load**	**Sliding Speed**	**g-C_3N_4 wt.%**
1	1.3734	1.3103	0.7267	320.0	318.1	334.5
2	0.7696	0.5233	0.4838	232.9	236.5	178.9
3	0.3010	0.6103	1.2336	249.0	247.4	288.6
Delta	1.0724	0.7870	0.7498	87.0	81.6	155.6
Rank	1	2	3	2	3	1
Combination	15	750	9	15	750	9
Mean		0.256556			92.4630 µm	

The factor with the largest delta value has been assigned rank 1, followed by the factor with the second largest delta and so on. The SN ratio for input parameter behavior was statistically significant. In Table 5, each delta, rank, and factor level's signal-to-noise ratio is given in each row. The table has a column for each factor. The same method as before was used to calculate delta and rank. In the experiment, the applied load had the

greatest influence on the coefficient of friction, followed by sliding speed and g-C_3N_4 weight percentage. Figure 4a,b and Figure 5 depict the principal design of control for the SN ratio, data means, and the interaction effects with controlling inputs. The main impression curves' bends indicate how each parameter has an impact. The most important factor was the one with the highest elevation of the line. The applied load for COF and g-C_3N_4 weight percentage for wear depth were shown to be the most important factors in Figure 4a,b.

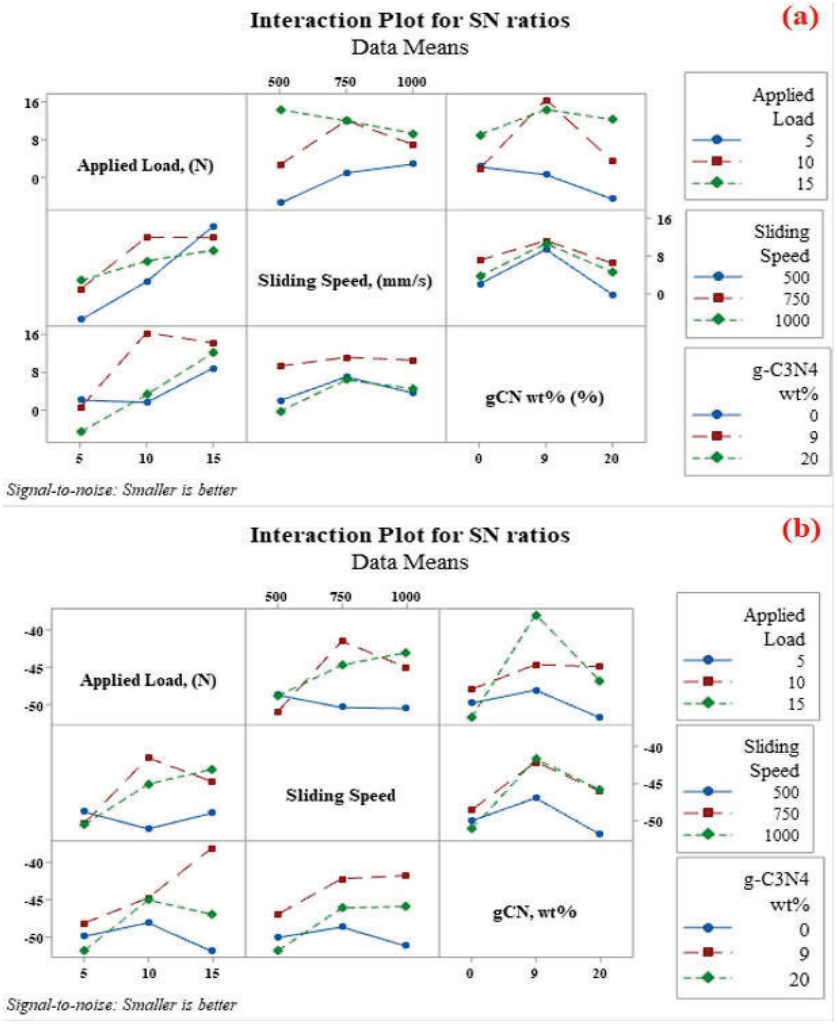

Figure 5. Interaction effect of load, sliding distance, and sliding speed on the wear rate of friction material at different operating conditions (**a**) COF and (**b**) wear depth.

The interaction plots of the present investigation are shown in Figure 5. All of the input variables have an interaction effect on the output variable. Because of this, the variations in the results generated is not due to one of the input parameters alone but rather to the combined effects of all input parameters that are taken into account. Any interaction plot can be used to determine the existence of effects from any non-parallel factor. A non-parallel interaction indicates weak interaction; complimentary interaction indicates a strong relationship. According to the findings of this investigation, the applied load for

coefficient of friction and wt.% of g-C_3N_4 in nanocomposite had the most significant effects on response. Figure 5 and the contour plots in Figure 6a–c show how the various inputs interact and have an impact on wear depth and coefficient of friction, respectively. Figure 5 illustrates how the applied load surpassed the variance in other inputs. Examining how each factor's deviation affects the COF and wear depth is simple and intuitive when using the contour map.

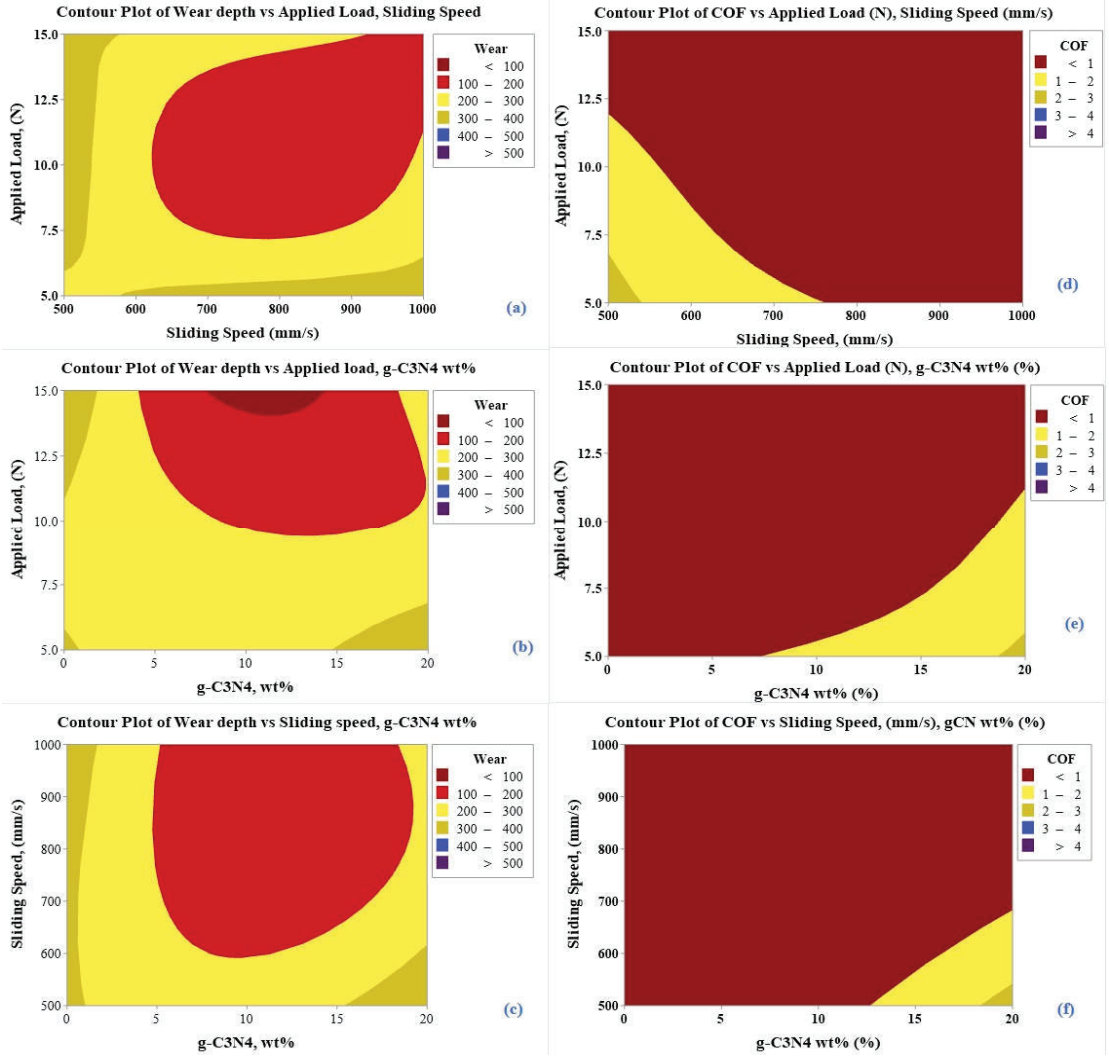

Figure 6. Contour plot for wear depth and coefficient of friction for (**a**,**d**) applied load vs. sliding speed; (**b**,**e**) applied load vs. weight percent of g-C_3N_4 in composite; (**c**,**f**) applied load vs. weight percent of g-C_3N_4 in composite.

3.3. Analysis of Variance (ANOVA) for Wear Depth and Coefficient of Friction

ANOVA is a statistical method used to estimate processes and examine mean differences. It is used to determine the test's statistical significance. It is used to investigate the effect of applied load, sliding velocity, and graphitic carbon nitride weight percentage in

nanocomposite on output COF and wear depth in a controlled manner. The difference between averages divided by the difference across yields was used to calculate the F-value (factor value). A significant difference among specimen average with the variation of the parameters confirms the higher F-value. The related probability value was lower if the factor value was higher. The *p*-value reflects the probability of any error. Table 6 shows the correlations between the data after they were corrected at three levels. Sources from Table 6 were utilized to figure out which parameter regulates the other parameter and how significantly each single factor contributed. A confidence level of 95% was employed in this study. The source that contributed to this performance metric was statistically significant, with *p*-values < 0.05. The following equations were utilized in the analysis of variance [36–38]:

$$PQ_T = PS_L + PS_{SS} + PS_{wt} \tag{2}$$

$$PQ_T = \sum_1^n d_i^2 - \frac{d^2}{n} \tag{3}$$

$$PS_v = \sum_{k=1}^t \left(\frac{Sd_i^2}{t} \right) - \frac{d^2}{n} \tag{4}$$

where n is the number of repititions, $Sd_i{}^2$ is the addition of the experimental trials involving constants v at a level k, d is the resultant data for all the test trails, PQ_T is the total addition of squares, PS_L is the applied load addition on squares, PS_{SS} is the sliding speed addition on squares, and PS_{wt} is the weight percentage of g-C_3N_4-addition of squares.

Table 6. Analysis of variance (ANOVA) for signal-to-noise (SN) ratios.

	For Coefficient of Friction					For Wear Depth				
Source	**Sum of Squares**	**Degree of Freedom**	**Mean of Square**	**F-Value**	***p*-Value**	**Sum of Squares**	**Degree of Freedom**	**Mean of Square**	**F-Value**	***p*-Value**
Applied Load	707.82	2	353.912	5.60	0.030	104.93	2	52.47	4.99	0.039
Sliding Speed	90.91	2	45.456	0.72	0.516	82.79	2	41.40	3.94	0.065
g-C_3N_4 wt.%	249.91	2	124.953	1.98	0.201	188.24	2	94.12	8.95	0.009
Applied Load × Sliding Speed,	192.26	4	48.064	0.76	0.579	116.13	4	29.03	2.76	0.103
Applied Load × g-C_3N_4 wt.%	256.27	4	64.068	1.01	0.455	150.87	4	37.72	3.59	0.059
Sliding Speed × g-C_3N_4 wt.%	23.25	4	5.812	0.09	0.982	46.26	4	11.56	1.10	0.419

The analysis of variance (ANOVA) table can be seen in Table 6, and it is evident from table that each of the parameters taken into consideration has a significant effect on wear behavior. The much more significant parameters for COF and wear depth were applied load and graphitic carbon nitride in nanocomposite, respectively. This could be attributed to the reason that as the applied load rises, the pressure at the contact between the pin and disc rises, resulting in a lubricating characteristic of g-C_3N_4/MoS_2. Additionally, the wt.% of g-C_3N_4 enhances to the wear preservation of the coating as the MoS_2 could be quickly oxidized due to theheat generated between the surfaces. Because the material of the coating (i.e., nanocomposite) was removed in powder form, the eliminated material adhered to the disc surface, reducing the raw surface contact and reducing wear. Finally, due to the support of molybdenum disulfide and its nanocomposite with graphitic carbon nitride in the lubricating mechanism, the sliding speed has the lowest impact on wear.The wear of the coating material was most significantly impacted by the applied load. As a consequence, during the wear, the applied load, followed by the other parameters, were critical control components to consider. The COF and wear depth were only slightly impacted by the interaction between the different inputs, i.e., applied load, sliding speed, and nanocomposite composition.

3.4. Modeling through Response Surface Methodology (RSM)

RSM is a multipurpose technique that can be used to construct mathematical models to predict responses, analyze surface responses using response surface curves to help explain how an input parameter affects a response parameter, analyze variance in process parameter values, and determine the optimal parameter. In order to analyze the data, determine the significance of parameters for the model, calculate the mean response, and find the optimal operating condition for the control variables which assist in achieving a minimum or maximum response over a particular interested region, a linear and second-degree model was used in this paper.

As a result, the model was created for analyzing variance to assess the significance and stability of response as well as the process parameters. This was performed after obtaining the response parameters (Table 4).

The equations below address the mathematical model which was developed by using the MINITAB-19 to analyze the response parameters:

$$\text{COF} = 462 - (7.10 \times \text{Load\_Applied, (N)}) - (0.142 \times \text{Sliding\_Speed (m/s)}) - (1.85 \times \text{g-}C_3N_4 \text{ wt.\% (\%)}) \quad (5)$$

$$\text{Wear} = 1069 - 48.3\ \text{Load\_Applied, (N)} - 1.25\ \text{Sliding\_Speed (m/s)} - 29.6\ \text{g}C_3N_4 \text{ wt.\% (\%)} + 2.06\ \text{Load\_Applied, (N)} \times \text{Load\_Applied, (N)} + 0.000740\ \text{Sliding\_Speed, (m/s)} \times \text{Sliding\_Speed, (m/s)} + 1.363\ \text{g-}C_3N_4 \text{ wt.\% (\%)} \times \text{g-}C_3N_4 \text{ wt.\% (\%)} \quad (6)$$

The aforementioned regression model aids in the prediction of the response parameters, i.e., wear depth and coefficient of friction. The influence and significance of the parameters and related factors on the parameters for response must now be examined using the variance analysis (ANOVA) for response surface methodology. The probability value (*p*-value) for the factors must be below 0.05 to fulfill the criterion of a factor that was significant criteria as the ANOVA was performed at 95% confidence level. Table 7 provides the ANOVA analysis for response surface methodology, which summarizes the degree of freedom, sum of squares, *p*-value, and F-value of response parameters in MoS_2 and g-C_3N_4/MoS_2 nanocomposite.

Table 7. ANOVA analysis of pin-on-disc wear test on g-C_3N_4/MoS_2-nanocomposite-coated steel substrate.

	For Coefficient of Friction					For Wear Depth				
Source	**Sum of Squares**	**Degree of Freedom**	**Mean of Square**	**F-Value**	***p*-Value**	**Sum of Squares**	**Degree of Freedom**	**Mean of Square**	**F-Value**	***p*-Value**
Model	8.688	6	1.86470	3.26	0.021	1,92,321	6	31,500	2.19	0.088
Linear	8.688	3	2.84561	4.97	0.010	54,669	3	18,223	1.27	0.313
Applied Load	5.1756	1	5.17562	9.05	0.007	22,667	1	22,667	1.57	0.224
Sliding Speed	2.2050	1	2.20500	3.85	0.064	22,530	1	22,530	1.56	0.225
g-C_3N_4 wt.%	1.1562	1	1.15621	2.02	0.171	9472	1	9472	0.66	0.427
Square	2.4998	3	0.83328	1.46	0.256	137,653	3	45,884	3.19	0.046
Applied Load × Applied Load	0.0275	1	0.02747	0.05	0.829	15,948	1	15,948	1.11	0.305
Sliding Speed × Sliding Speed	1.1458	1	1.14581	2.00	0.172	12,844	1	12,844	0.89	0.356
g-C_3N_4 wt.% (%) × g-C_3N_4 wt%	1.3266	1	1.32656	2.32	0.143	108,860	1	108,860	7.56	0.012

The ANOVA analysis for the coefficient of friction and wear depth is shown in Table 7 to examine the significance of the process factors and their influence on response parameters, namely frictional coefficient and wear depth. Load applied on coated substrate has

a significant effect on COF, roughly 59.6%, which was the greatest between all parameters with their factors. Additionally, in Table 7, the ANOVA analysis for wear depth is shown for analyzing the significance of process parameters with the impact on the response parameter, i.e., wear depth. It can be seen from Table 7 that the applied load and sliding speed makes a significant impact on wear depth, approximately 41.4 % and 41.2%, which was the greatest among the other process parameters with their factors.

As analysis of variance studied the effect of parameters used for process on the parameters for response, similarly, variation in the parameters for response by changing inputs can be studied by response surface plots. Figure 7 depicts the response surface curve at applied load, sliding speed, and g-C_3N_4 weight percentage in nanocomposite. Figure 7a–c shows variation in wear depth with applied load, sliding speed, and weight percentage of g-C_3N_4 in g-C_3N_4/MoS_2 nanocomposite, and it can be analyzed that at applied load 15N, sliding speed 0.75 m/s, and 9 wt.% of g-C_3N_4, minimum wear depth was found. Figure 7d–f show variation in coefficient of friction with the factors and as the same combination for that of wear depth, and it was found minimized at 15 N applied load, 0.75 m/s sliding speed, and 9% of weight percentage in g-C_3N_4/MoS_2 nanocomposite due to the combined effects of response parameters and their interactions as the study was to optimize the wear depth with COF generated in the wear process.

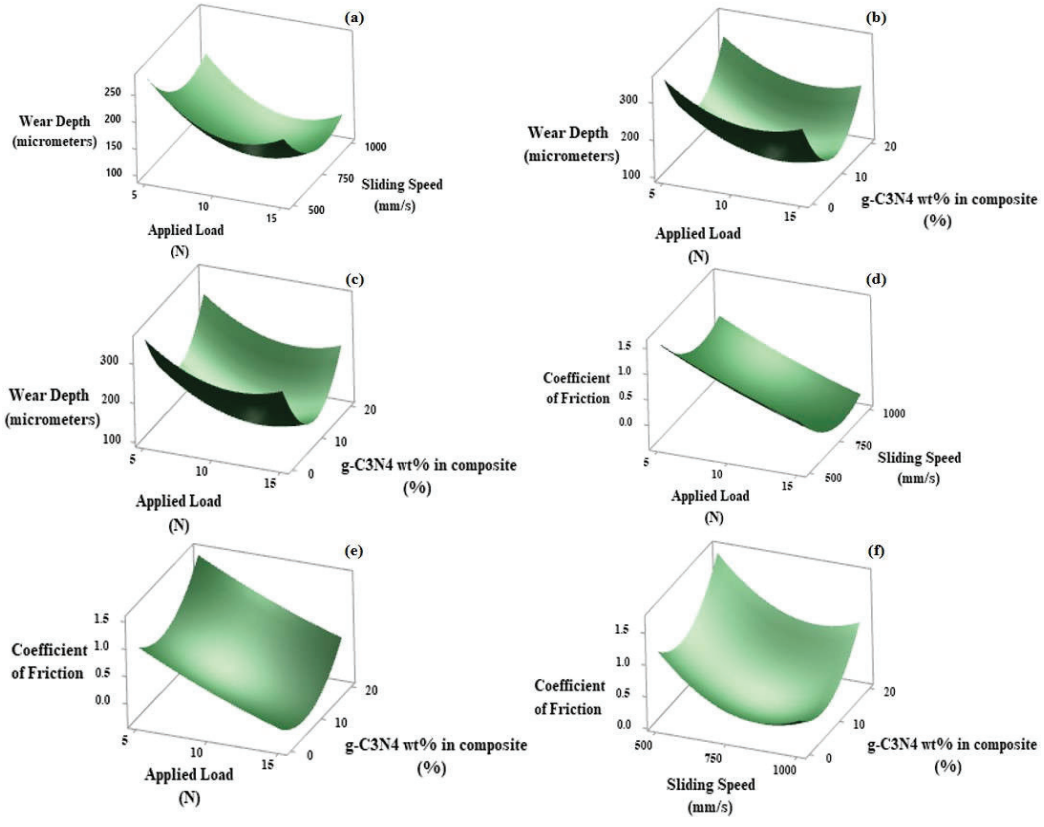

Figure 7. Response surface for wear depth and coefficient of friction for (**a,d**) applied load vs. sliding speed; (**b,e**) applied load vs. weight percent of g-C_3N_4 in composite; (**c,f**) applied load vs. weight percent of g-C_3N_4 in composite.

Attributed to the reason that molybdenum disulfide can quickly oxidize at high temperatures between the pin and disc surfaces while used in pure form, and MoS_2 predominates

when the wt.% of g-C_3N_4 in the composite increases, the reduction in wear depth and coefficient of friction were higher in the case of g-C_3N_4 at a wt.% of 9 in nanocomposite.

A response optimizer for experimentation was developed by response surface method and is depicted in Figure 8. The optimization of the process parameters to achieve the lower COF and wear depth is illustrated by the red-colored line, which was approximately same as obtained by the Taguchi method.

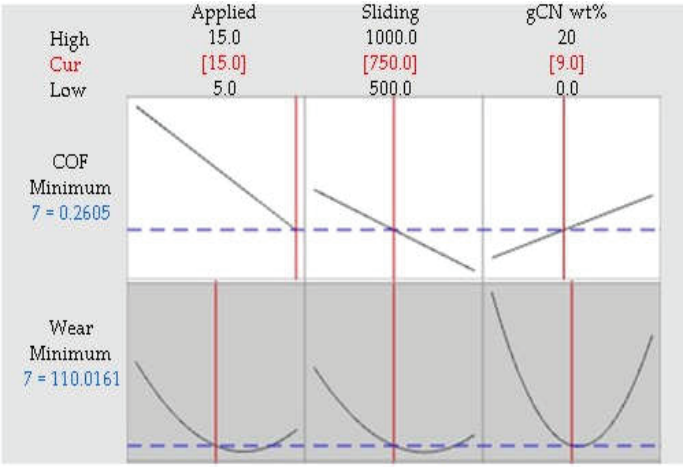

Figure 8. Plot for optimization for wear COF and wear.

The optimum results for response factors (i.e., coefficient of friction and wear depth) obtained from the Taguchi method and response surface methodology (RSM) with experimental results are summarized in Table 8. In all methods, the results are very comparable with each other. A minor difference was found while predicting the responses through Taguchi and RSM. The coefficient of friction varies by approx. 13% and 15% and wear depth by approx. 5% and 12% from the experimental findings while predicting the COF and wear depth through Taguchi and response surface methods, respectively.

Table 8. Calculated coefficient of friction and wear depth from different methods.

Coefficient of Friction				
Parameters/Method	**Applied Load, (N)**	**Sliding Speed, (m/s)**	**g-C_3N_4 wt.% (%)**	**Output Response**
Experimental [28]	15	0.75	9	0.226
Taguchi	15	0.75	9	0.256
RSM	15	0.75	9	0.2605
Wear Depth				
Experimental [28]	15	0.75	9	98.2 μm
Taguchi	15	0.75	9	92.46 μm
RSM	15	0.75	9	110.01 μm

3.5. Wear Mechanism

Figure 9 shows FESEM images of the worn surfaces of an uncoated steel substrate disc and a g-C_3N_4/MoS_2 (9 wt.%)-nanocomposite-coated steel substrate disc, after a wear test at 0.75 m/s sliding speed and 15 N applied stress. Figure 9 depicts the amount of wear loss caused by plastic deformation and ploughing. The wearing was heavily influenced

by abrasive wear. Several deep scratches and craters, as well as small micro cracks with sheared off asperities of pin material, were detected while inspecting the worn surface. Figure 9a also shows some sheets that indicate the creation of an oxide layer during wear.

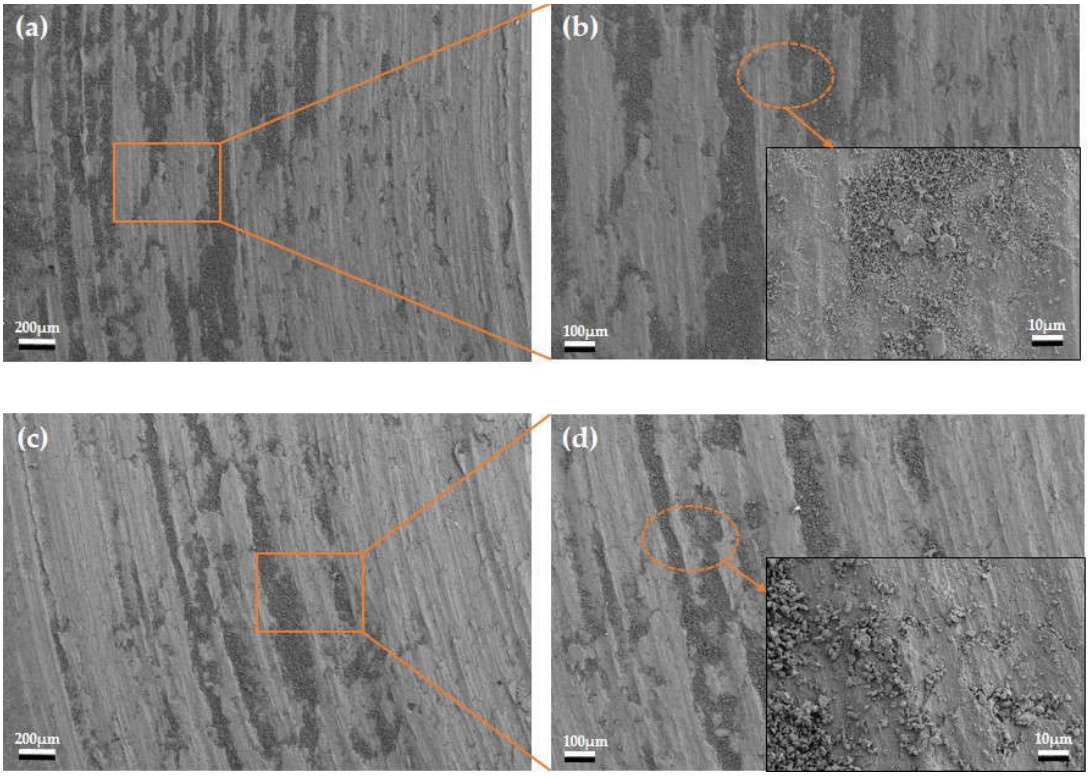

Figure 9. FESEM images of worn disc surface for (**a**,**b**) pure MoS_2 disc and (**c**,**d**) g-C_3N_4/MoS_2 (9 wt.%) nanocomposite coated disc.

Figures 10 and 11 show the EDX elemental analysis results of a worn disc coated with pure MoS_2 and g-C_3N_4/MoS_2 (9 wt.%) nanocomposite, respectively. The results of EDX in Figure 11 corroborate the conclusion that the groove included g-C_3N_4/MoS_2 and that the elements were carbon, nitrogen, molybdenum, and sulfur.

Some oxygen elements were also detected in the EDX mapping in Figure 10 as a result of the oxidation of molybdenum disulfide into molybdenum oxide owing to excessive heating while wearing, however it can be seen from Figure 11 that oxidation was decreased to some extent when g-C_3N_4 was added in the nanocomposite.

Figure 12 shows the FESEM image of worn out of corresponding pin. Worn surfaces of the counterpart pin used for the tribo test against the g-C_3N_4/MoS_2 (9 wt.%)-nanocomposite-coated disc (Figure 12a) and FESEM images of the counterpart pin used for the pure MoS_2-coated disc (Figure 12b) are depicted. The images indicate that rubbing a pin against a pure MoS_2-coated disc causes it to wear off unevenly and roughly. This is because the MoS_2 was highly oxidized by the heat created by the rubbing of the pin against the disc and the creation of its oxide. The depiction also illustrates ploughing and abrasive wear grooves on the pin. However, when g-C_3N_4 was included in the nanocomposite, the wear of the pin was found to be less than when the pin was rubbed against the disc coated with pure MoS_2, and a comparably smaller quantity of coating was transferred from disc to pin, ensuring adequate adhesion. The worn area on the pin used for the wear test against

the g-C_3N_4/MoS_2 (9 wt.%)-nanocomposite-coated disc was about 7.671 mm^2, which was 23% less than the worn area on the pin used for the pure MoS_2-coated substrate. This demonstrated that the inclusion of g-C_3N_4 has a considerable impact on wear reduction.

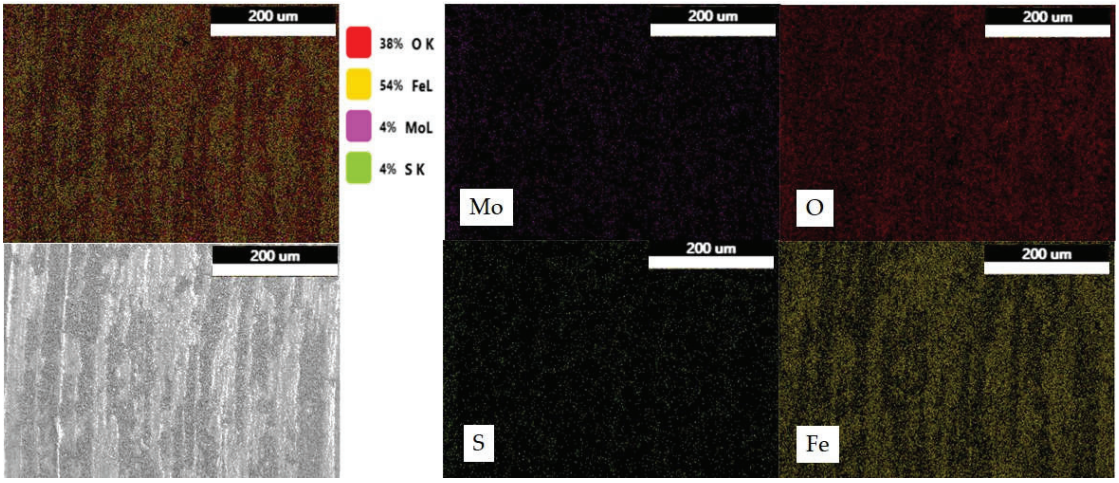

Figure 10. EDX elemental mapping of MoS_2-coated disc after wear test at 15 N applied load and 0.75 m/s sliding speed.

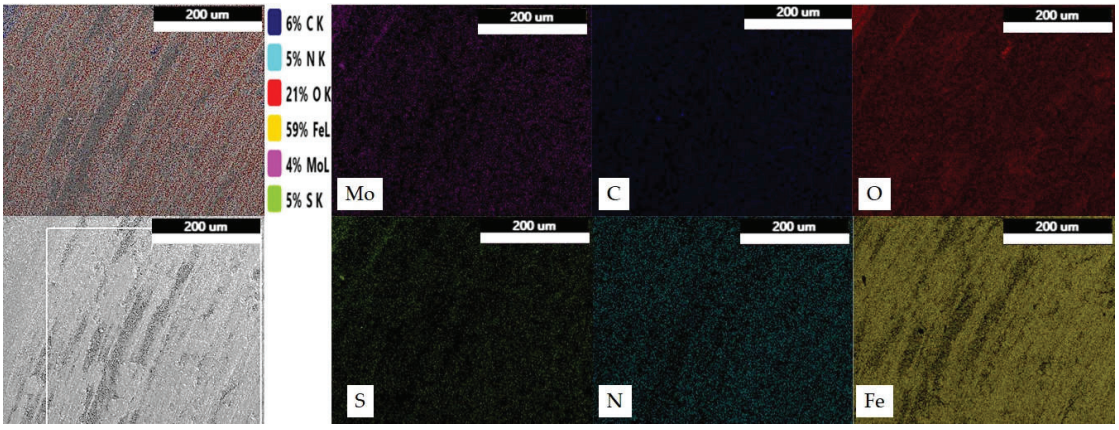

Figure 11. EDX elemental mapping of g-C_3N_4/MoS_2 (9 wt.%) nanocomposite coated disc after wear test at 15 N applied load and 0.75 m/s sliding speed.

The results of an energy-dispersive X-ray spectroscopy examination of the pin surface that was rubbed against the g-C_3N_4/MoS_2 (9 wt.%)-nanocomposite-coated disc are depicted in Figure 13, confirming that the material transferred from the disc to the pin surface after the wear test was the g-C_3N4/MoS_2 nanocomposite.

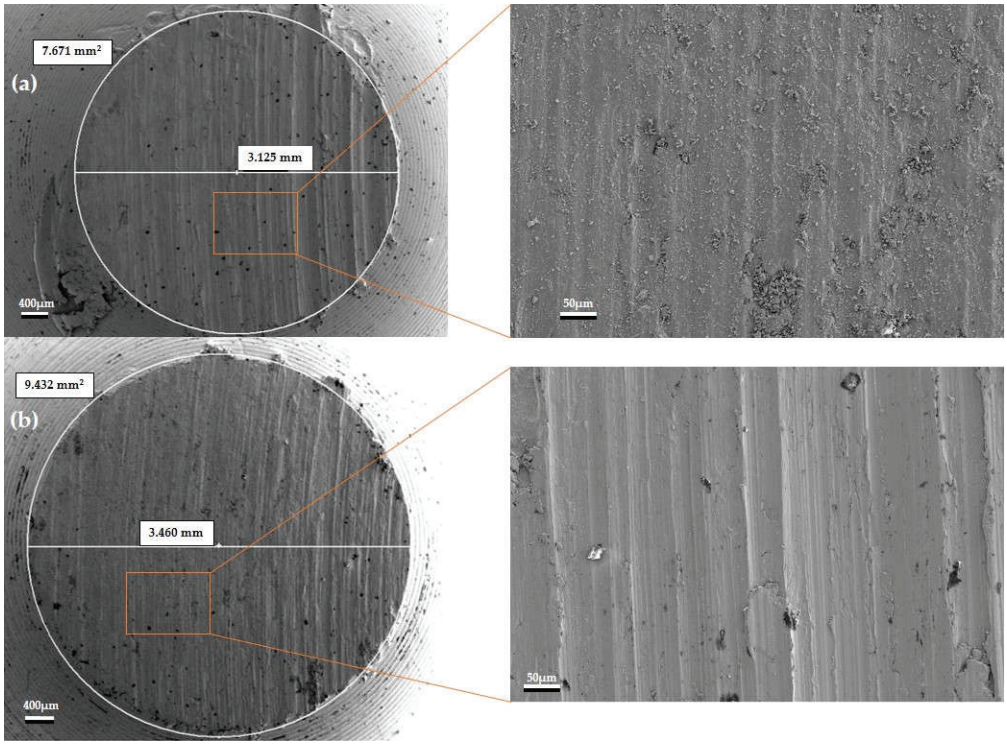

Figure 12. FESEM images of worn pin surface (**a**) of counterpart pin for g-C_3N_4/MoS_2 (9 wt.%) nanocomposite-coated disc and (**b**) of counterpart pin for MoS_2 coated disc.

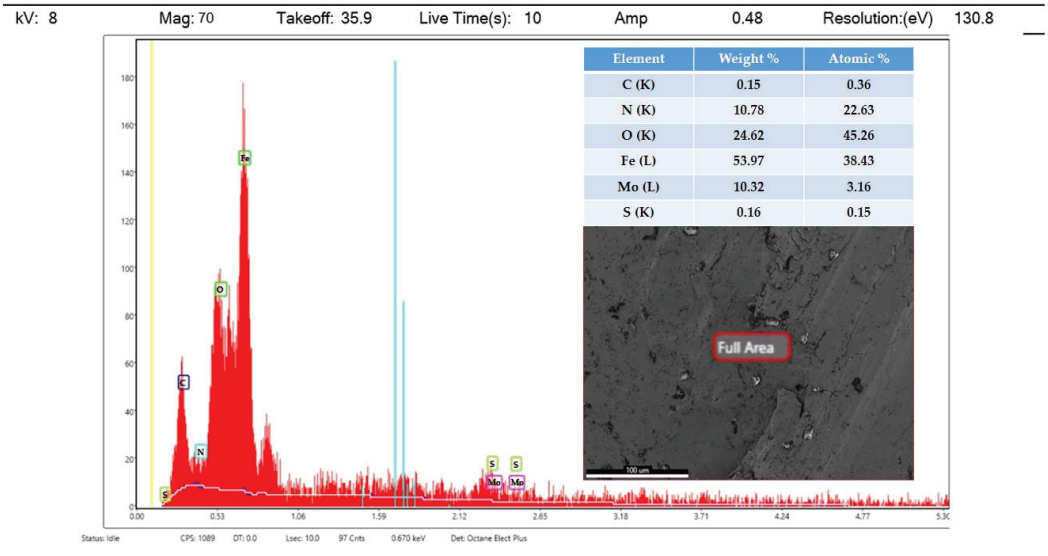

Figure 13. EDX elemental analysis of selected full area of pin surface used against g-C_3N_4/MoS_2 (9 wt.%) nanocomposite coated disc tested at 0.75 m/s sliding speed and 15 N applied load.

4. Conclusions

The current effort was aimed at the determination of appropriate process parameters for a pin-on-disc (POD) wear tester to analyze the coating material that may result in a low frictional coefficient between the mating surfaces of pin and disc and minimum wear of the substrate disc. For this, discs were coated at different weight percentages of g-C_3N_4 in molybdenum disulphide (MoS_2), and coated discs were tested using a pin-on-disc machine wear testing machine under different operating parameters, such as applied load ranges from 5 to 15 N and sliding speed from 0.5 to 1.0 m/s. The Taguchi method was used to develop a design of experiment and the ANOVA method was employed to find the significance of the process parameters. The results obtained from the RSM method were used to build the mathematical model. After a prolonged wear test, worn surfaces showed evidence of abrasive wear with ploughing, and there was a transfer of coating from the substrate disc to the counterpart pin. The following are the major findings of this study:

1. The created model was significant since it has a high R squared value and a *p* value that is less than 0.05 for various parameter combinations.
2. The coefficient of friction and wear depth for any alternative values of the parameters being evaluated can be predicted using the optimization plot that was created using RSM.
3. According to the ANOVA table, applied load had significant effects on coefficient of friction, followed by sliding speed and material composition, whereas wear was significantly influenced by material composition, then by applied load and sliding speed. Other parameters demonstrate the impact of their interactions. As a result, changing one parameter changes how another parameter responds.
4. According to the optimal condition and response table, the loading of 15 N, speed of 0.75 m/s, and the weight percentage of 9 were found to be the values that caused the least amount of wear loss in the present investigation.
5. Attributed to the reason that molybdenum disulfide can quickly oxidize at high temperatures between the pin and disc surfaces while used in pure form, and MoS_2 predominates when the wt.% of graphitic carbon nitride in the composite increases, the reduction in depth of wear and frictional coefficient were higher in the case of g-C_3N_4 at a wt.% of 9 in nanocomposite.
6. The applied load had the largest impact on the frictional coefficient and wear depth, that is 59.6% and 41.4%, respectively, followed by sliding speed.
7. In comparison to pure MoS_2 (wt.% 0 of g-C_3N_4) with weight percentages 9 and 20 of graphitic carbon nitride in the synthesized nanocomposite, the wt.% 9 of graphitic carbon nitride exhibits the least wear owing to its composition itself. The superior coating material for reduced friction and wear was determined to be the graphitic carbon nitride (wt.% 9) in the synthesized nanocomposite with MoS_2.
8. Results from the Taguchi method and response surface methodology were in good agreement with experimentation findings, which confirms its industrial application for predicting the output responses which save more time and effort. A confirmatory test can also be performed if the input parameter combinations were different than the available inputs.
9. Availability of the variety in process parameters (input data) and the experimental results (responses) makes the methodology limited, as without the previous results one cannot apply any prediction method.
10. In future work, this g-C_3N_4/MoS_2 nanocomposite shall be tested for higher loads and sliding speeds.

Author Contributions: M.S.—Conceptualization, Writing; A.K.S. (Anuj Kumar Sharma)—Review and editing; A.K.S. (Ashish Kumar Srivastava)—methodology, validation, N.S.—Review and editing; A.R.D.—supervison; All authors have read and agreed to the published version of the manuscript.

Funding: This research received no external funding.

Institutional Review Board Statement: Not applicable.

Informed Consent Statement: Not applicable.

Data Availability Statement: Not applicable.

Conflicts of Interest: The authors declare no conflict of interest.

References

1. Tung, S.C.; McMillan, M.L. Automotive tribology overview of current advances and challenges for the future. *Tribol. Int.* **2004**, *37*, 517–536. [CrossRef]
2. Holmberg, K.; Andersson, P.; Erdemir, A. Global energy consumption due to friction in passenger cars. *Tribol. Int.* **2012**, *47*, 221–234. [CrossRef]
3. Srivastava, A.K.; Dwivedi, S.; Saxena, A.; Kumar, D.; Dixit, A.R.; Singh, G.K.; Bhutto, J.K.; Verma, R. Tribological Characteristics of Al359/Si_3N_4/Eggshell Surface Composite Produced by Friction Stir Processing. *Coatings* **2022**, *12*, 1362. [CrossRef]
4. Wu, Y.Y.; Tsui, W.C.; Liu, T.C. Experimental analysis of tribological properties of lubricating oils with nanoparticle additives. *Wear* **2007**, *262*, 819–825. [CrossRef]
5. Srivastava, A.K.; Sharma, B.; Saju, B.R.; Shukla, A.; Saxena, A.; Maurya, N.K. Effect of Graphene nanoparticles on microstructural and mechanical properties of aluminum based nanocomposites fabricated by stir casting. *World J. Eng.* **2020**, *17*, 859–866. [CrossRef]
6. Berman, D.; Erdemir, A.; Sumant, A.V. Graphene: A new emerging lubricant. *Mater. Today* **2014**, *17*, 31–42. [CrossRef]
7. Dallavalle, M.; Sändig, N.; Zerbetto, F. Stability, dynamics, and lubrication of MoS_2 platelets and nanotubes. *Langmuir* **2012**, *28*, 7393–7400. [CrossRef] [PubMed]
8. Cizaire, L.; Vacher, B.; Le Mogne, T.; Martin, J.; Rapoport, L.; Margolin, A.; Tenne, R. Mechanisms of ultra-low friction by hollow inorganic fullerene-like MoS_2 nanoparticles. *Surf. Coat. Technol.* **2002**, *160*, 282–287. [CrossRef]
9. Curry, J.F.; Wilson, M.A.; Luftman, H.S.; Strandwitz, N.C.; Argibay, N.; Chandross, M.; Sidebottom, M.A.; Krick, B.A. Impact of microstructure on MoS_2 oxidation and friction. *ACS Appl. Mater. Interfaces* **2017**, *9*, 28019–28026. [CrossRef]
10. Donnet, C.; Martin, J.; Le Mogne, T.; Belin, M. Super-low friction of MoS_2 coatings in various environments. *Tribol. Int.* **1996**, *29*, 123–128. [CrossRef]
11. Li, H.; Wang, J.; Gao, S.; Chen, Q.; Peng, L.; Liu, K.; Wei, X. Superlubricity between MoS_2 monolayers. *Adv. Mater.* **2017**, *29*, 1701474. [CrossRef]
12. Ilie, F.; Cristescu, A.-C. A Study on the Tribological Behavior of Molybdenum Disulfide Particles as Additives. *Coatings* **2022**, *12*, 1244. [CrossRef]
13. Ilie, F. Energy Dissipation during Adhesion and Friction at the Atomic Scale of MoS_2 Nanoparticles on the Surface of MoS_2. *J. Adv. Microsc. Res.* **2013**, *8*, 270–275. [CrossRef]
14. Zhang, Y.; Jin, Z.; Su, Y.; Wang, G. Charge separation and electron transfer routes modulated with Co-Mo-P over g-C_3N_4 photocatalyst. *Mol. Catal.* **2019**, *462*, 46–55. [CrossRef]
15. Xu, Z.D.; Xin, J.B.; Fan, R.X.; Wang, K.; Yang, J. A simple approach to fabricate CN/MoS_2 nanocomposite and its application as a lubricant additive. *Dig. J. Nanomater. Biostruct.* **2018**, *13*, 731–741.
16. Ajay, K.; Thakre, G.D.; Arya, P.K.; Jain, A.K. 2D Structured Nano-Sheets of Octadecylamine Grafted Graphitic-Carbon Nitride (g-C_3N_4) as Lubricant Additives. *Macromol. Symp.* **2017**, *376*, 1700009.
17. Duan, C.; Yuan, D.; Yang, Z.; Li, S.; Tao, L.; Wang, Q.; Wang, T. High wear-resistant performance of thermosetting polyimide reinforced by graphitic carbon nitride (g-C_3N_4) under high temperature. *Compos. Part A Appl. Sci. Manuf.* **2018**, *113*, 200–208. [CrossRef]
18. Zhu, L.; Wang, Y.; Hu, F.; Song, H. Structural and friction characteristics of g-C_3N_4/PVDF composites. *Appl. Surf. Sci.* **2015**, *345*, 349–354. [CrossRef]
19. Gupta, D.; Bhovi, P.M.; Sharma, A.K.; Dutta, S. Development and characterization of microwave composite cladding. *J. Manuf. Process.* **2012**, *14*, 243–249. [CrossRef]
20. Sharma, A.; Aravindhan, S.; Krishnamurthy, R. Microwave glazing of alumina–titania ceramic composite coatings. *Mater. Lett.* **2001**, *50*, 295–301. [CrossRef]
21. Leonelli, C.; Veronesi, P.; Denti, L.; Gatto, A.; Iuliano, L. Microwave assisted sintering of green metal parts. *J. Mater. Process. Technol.* **2008**, *205*, 489–496. [CrossRef]
22. Gupta, D.; Sharma, A.K. Microwave cladding: A new approach in surface engineering. *J. Manuf. Process.* **2014**, *16*, 176–182. [CrossRef]
23. Somani, N.; Kumar, K.; Gupta, N. Review on microwave cladding: A new approach. In *Advances in Materials Processing*; Springer: Singapore, 2020; pp. 77–90.
24. Kumar, N.; Singh, R.K.; Srivastava, A.K.; Nag, A.; Petru, J.; Hloch, S. Surface Modification and Parametric Optimization of Tensile Strength of Al6082/SiC/Waste Material Surface Composite Produced by Friction Stir Processing. *Coatings* **2022**, *12*, 1909. [CrossRef]

25. Taguchi, G.; Phadke, M.S. Quality engineering through design optimization. In *Quality Control, Robust Design, and the Taguchi Method*; Springer: Boston, MA, USA, 1989; pp. 77–96.
26. Montgomery, D.C.; Woodall, W.H. A discussion on statistically-based process monitoring and control. *J. Qual. Technol.* **1997**, *29*, 121. [CrossRef]
27. Joshua, J.J.; Andrews, A.A.E. Design of experiments to optimize casting process of aluminum alloy 7075 in addition of TiO_2 using Taguchi method. *Mater. Today Proc.* **2020**, *33*, 3353–3358. [CrossRef]
28. Chiang, K.-T.; Liu, N.-M.; Tsai, T.-C. Modeling and analysis of the effects of processing parameters on the performance characteristics in the high pressure die casting process of Al–SI alloys. *Int. J. Adv. Manuf. Technol.* **2009**, *41*, 1076–1084. [CrossRef]
29. Liati, A.; Schreiber, D.; Lugovyy, D.; Gramstat, S.; Eggenschwiler, P.D. Airborne particulate matter emissions from vehicle brakes in micro-and nano-scales: Morphology and chemistry by electron microscopy. *Atmos. Environ.* **2019**, *212*, 281–289. [CrossRef]
30. Kumar, S.; Ghosh, S.K. Statistical and computational analysis of an environment-friendly MWCNT/$NiSO_4$ composite materials. *J. Manuf. Process.* **2021**, *66*, 11–26. [CrossRef]
31. Dwivedi, R.; Singh, R.K.; Kumar, S.; Srivastava, A.K. Parametric optimization of process parameters during the friction stir processing of Al7075/SiC/waste eggshell surface composite. *Mater. Today Proc.* **2021**, *47 Pt 13*, 3884–3890. [CrossRef]
32. Veličković, S.; Stojanović, B.; Babić, M.; Bobic, I. Optimization of tribological properties of aluminum hybrid composites using Taguchi design. *J. Compos. Mater.* **2017**, *51*, 2505–2515. [CrossRef]
33. Pattanaik, A.; Satpathy, M.P.; Mishra, S.C. Dry sliding wear behavior of epoxy fly ash composite with Taguchi optimization. *Eng. Sci. Technol. Int. J.* **2016**, *19*, 710–716. [CrossRef]
34. Li, G.; Hao, S.; Gao, W.; Lu, Z. The Effect of Applied Load and Rotation Speed on Wear Characteristics of Al-Cu-Li Alloy. *J. Mater. Eng. Perform.* **2022**, *31*, 5875–5885. [CrossRef]
35. Saxena, M.; Sharma, A.K.; Srivastava, A.K.; Singh, R.K.; Dixit, A.R.; Nag, A.; Hloch, S. Microwave-Assisted Synthesis, Characterization and Tribological Properties of a g-C_3N_4/MoS_2 Nanocomposite for Low Friction Coatings. *Coatings* **2022**, *12*, 1840. [CrossRef]
36. Mustapha, A.N.; Zhang, Y.; Zhang, Z.; Ding, Y.; Yuan, Q.; Li, Y. Taguchi and ANOVA analysis for the optimization of the microencapsulation of a volatile phase change material. *J. Mater. Res. Technol.* **2021**, *11*, 667–680. [CrossRef]
37. Reddy, V.V.; Mandava, R.K.; Rao, V.R.; Mandava, S. Optimization of dry sliding wear parameters of Al 7075 MMC's using Taguchi method. *Mater. Today Proc.* **2022**, *62*, 6684–6688. [CrossRef]
38. Taguchi, G.; Rafanelli, A.J. Taguchi on robust technology development: Bringing quality engineering upstream. *J. Electron. Packag.* **1994**, *116*, 161. [CrossRef]

coatings

MDPI

Article

Effect of Mesogenic Phase and Structure of Liquid Crystals on Tribological Properties as Lubricant Additives

Han Wu [1,2], Ying Jiang [1], Wenjing Hu [1,*], Sijing Feng [3,*] and Jiusheng Li [1,*]

[1] Laboratory for Advanced Lubricating Materials, Shanghai Advanced Research Institute, Chinese Academy of Sciences, Shanghai 201210, China
[2] School of Environmental Science and Engineering, Liaoning University of Engineering and Technology, Fuxin 123032, China
[3] Business School, Shanghai Jian Qiao University, Shanghai 201306, China
* Correspondence: huwj@sari.ac.cn (W.H.); fengsijing2003@126.com (S.F.); lijs@sari.ac.cn (J.L.)

Abstract: To develop a high-performance additive that can meet different operating conditions, three liquid crystals (LCs) were developed as additives for a base oil. The structures and thermal stabilities of the obtained LCs were characterized by nuclear magnetic resonance (NMR), Fourier transform infrared (FT-IR) spectroscopy, mass spectroscopy (MS), and thermogravimetric analysis (TGA). The effects of mesogenic-phase temperature ranges on tribological properties were analyzed using differential scanning calorimetry (DSC) and polarized optical microscopy (POM). UMT-TriboLab friction and wear tester was used to study the friction-reducing properties of LCs. The width of wear marks was observed by a Contour GT-K 3D profiler to illustrate the anti-wear performance of LCs. The friction surface was characterized by scanning electron microscopy (SEM) and Raman spectroscopy. It was demonstrated that, in comparison with the base oil, the addition of LCs caused a remarkable reduction in the coefficient of friction (21.57%) and wear width (31.82%). In addition, LCs show better tribological abilities in the mesogenic-phase temperature ranges. According to the results, we demonstrated that LCs can be used as lubricant additives, especially for several operating conditions under specific temperatures.

Keywords: liquid crystals; mesogenic-phase temperature ranges; lubricant additives; tribological property

Citation: Wu, H.; Jiang, Y.; Hu, W.; Feng, S.; Li, J. Effect of Mesogenic Phase and Structure of Liquid Crystals on Tribological Properties as Lubricant Additives. *Coatings* **2023**, *13*, 168. https://doi.org/10.3390/coatings13010168

Academic Editor: Ashish Kumar Srivastava

Received: 9 December 2022
Revised: 9 January 2023
Accepted: 10 January 2023
Published: 12 January 2023

1. Introduction

With the increased mechanization of modern society, energy loss caused by friction and wear has been constantly increased [1–3]. Friction can be greatly reduced by using lubricants, thus lowering the energy waste [4–6]. Lubricants can form a stabilized film of lubrication on the surface of the mechanical part and prevent direct contact with the micro-convexity of the metal surface [7]. Additives, which can tune the tribological behavior of the oil-based lubricant, are a type of important materials that help develop different lubricants for different working scenarios [8,9]. Therefore, there is a need to explore high-performance lubricant additives for meeting the growing lubrication requirements resulting from the development of mechanical society.

Liquid crystals (LCs) are special materials with rheological properties, having the fluidity of a liquid-crystal (LC) and the anisotropy of a single crystal, which can be a long-range ordered arrangement at the molecular level [10–12]. Moreover, due to the low viscosities of LCs, they can effectively fill the contact surface during the sliding process, resulting in reduced friction [13]. Because of these properties, LCs are considered new tribological materials with applications in the field of lubrication. LCs are characterized by excellent heat resistance and chemical stability, as well as an orderly transformation of molecular orientation and arrangement order when stimulated by an external electric or magnetic field or temperature [14]. Due to LCs' controllable nature, they can serve as

potential materials for tribological properties in a specific temperature range. Existing research reported that the use of LCs can significantly improve the tribological properties of a base oil when used as lubricant additives. Yang's team [15] reported that 1,3-diketone EPND (1-(4-ethyl phenyl) nonane-1,3-dione), a nematic LC lubricant additive with excellent tribological properties, is particularly suitable for the severe operating conditions of low load and friction. Additionally, Mokshin [16] reported that cholesteryl stearate and fatty acid cholesterol esters LCs were used as lubricant additives. The tribological properties of LCs were evaluated, and the addition of LCs was found to significantly reduce the coefficient of friction (COF). Ghosh and colleagues [17] blended three different series of LCs with polydecyl acrylate as lubricant additives. The study indicated that the addition of very small amounts of LCs could significantly improve the additive properties of polydecyl acrylate. Among the various types of LCs, cyanobiphenyl-type LCs were focused on due to their ability to form ordered molecular films on the friction surface [18].

The rigid structure in the molecule of a cyanobiphenyl-type LC provides orderliness, and the alkyl chains in the molecule offer the mobility of mesocrystals [19]. Related experiments have demonstrated that cyanobiphenyl-type LCs subjected to an applied electric field can increase their viscosity in the direction perpendicular to the wear surface, which facilitates the formation of a boundary lubrication state [18]. In addition to the electric field, the tribological properties of LCs have been affected by their structure. Polar molecules such as benzene rings, ester groups with longer alkyl chains, or ether groups in the structure usually exhibit better tribological properties, and the addition of flexible groups also improves the solubility of the compounds in base oil [20,21]. Additionally, the fluorinated substituent can be placed in a terminal position and within a terminal chain in the LC structure, and the addition of a fluorinated substituent can cause a remarkably steric effect by improving the melting point and mesogenic-phase temperature ranges [22]. On this basis, we designed and synthesized cyanobiphenyl-type LCs to evaluate their effects on tribological properties.

In this research, the objective was to investigate the effect of the structure of cyanobiphenyl-type LC molecules and mesogenic-phase temperature ranges on their tribological properties. Three cyanobiphenyl-type LCs were designed and synthesized. The structures of the LCs were verified with Fourier transform infrared (FT-IR) spectroscopy, nuclear magnetic resonance (NMR) spectra, and mass spectroscopy (MS). The thermal stability was analyzed using a thermogravimetric analyzer (TGA). The characteristics of LCs were obtained using differential scanning calorimetry (DSC) and polarized optical microscopy (POM) to investigate the influence of the mesogenic-phase temperature range on the tribological properties. The influence of the structures and mesogenic-phase temperature ranges of LCs were evaluated on their tribological properties and the related lubrication mechanism was analyzed. This work provides a novel idea for developing new LC friction materials.

2. Experimental

2.1. Chemicals

Ethyl 6-bromohexanoate, 4′-hydroxy-4-biphenylcarbonitrile, 4′-hydroxy-4-biphenylcarboxylic acid, ethanol, dichloromethane (DCM), N, N-dimethylformamide (DMF), 4-Dimethylaminopyridine (DMAP), (S)-2-Octanol, hydrogen peroxide, potassium sulfate, magnesium Sulfate, ethyl acetate (EA), petroleum ether (PE) triethylamine (TEA), tetrahydrofuran (THF), and 1-(3-Dimethylaminopropyl)-3-ethylcarbodiimide Hydrochloride (EDCI) were obtained from Titan Scientific Co., Ltd., Shanghai, China. The 4-(Trifluoromethyl) phenol, methyl chloroformate, triphenyl phosphite, sodium hydroxide, potassium carbonate, ammonia water, and potassium iodide (KI), were purchased from Sinopharm Chemical Reagent Co., Ltd., Shanghai, China. The 4-(2-Methoxyethyl) phenol was purchased from Shanghai Aladdin Bio-Chem Technology Co., Ltd., Shanghai, China. Zinc dialkyl dithiophosphates (ZDDP) were obtained from Huihua Chemical Co., Ltd., Dongguan, China. The base oil used in the experiment was palmester 3970 (TTO) from Taiko Palm-Oleo Co. Ltd., Shanghai, China. All the above reagents can be used directly without further purification treatment.

2.2. Measurements

FT-IR was achieved using a Paragon 1000 (PerkinElmer, Waltham, MA, USA) with a measurement range from 4000 to 1000 cm^{-1}. Bruker Avance III HD (400 MHz) spectrometer (Bruker, Billerica, MA, USA) for the analysis of ^{1}H and ^{13}C NMR spectrometer. Mass spectroscopy analysis was characterized using a MALDI TOF 7090 mass spectrometer (Bruker, Billerica, MA, USA). The SDT-Q600 Simultaneous TGA/DSC (TA instrument, New Castle, DE, USA) was used to characterize the thermal properties in a nitrogen atmosphere. The temperature was increased from 30 °C to 800 °C at a speed of 10 °C/min. The mesogenic-phase temperature range of the LCs was achieved with a TA DSC 25 (TA instrument, New Castle, DE, USA), and the textures were obtained with a XP-330C POM (Shanghai Caikon, Shanghai, China). The width of the wear marks on the steel plates surface after the test were measured with a Contour GT-K 3D profiler (Bruker, Billerica, MA, USA). The analysis of deposits on the wear surface following experimentation was performed using a LabRAM HR800 Raman spectrometer (Horiba Jobin Yvon, Pairs, France). The scanning electron microscope (SEM) was obtained from SU8010 (Hitachi, Tokyo, Japan).

2.3. Synthesis of ethyl 6-(4-cyanobiphenyl-4-yloxy) Hexanoate (Intermediate 1)

Anhydrous potassium carbonate (15 g, 108.5 mmol) was powdered and dissolved in 50 mL DMF. It was then poured into glassware and stirred under nitrogen protection to 50 °C. KI was added and stirred at 50 °C for 48 h. Next, 4-hydroxy-4-biphenylcarbonitrile (20 g, 102.5 mmol), ethyl 6-bromohexanoate (27.3 g, 123 mmol), and KI (0.5 g, 3 mmol) were added and stirred at 50 °C with 48 h. At the end of the reaction, the DMF was removed by spinning. The resultant residue was washed three times with water and finally recrystallized using 100 mL of ethanol to obtain a white powder.

2.4. Synthesis of 6-(4-cyanobiphenyl-4-yloxy) Hexanoate Acid (Intermediate 2)

Intermediate 1 (31.9 g, 94.54 mmol) was dissolved in ethanol in glassware and stirred at room temperature. Sodium hydroxide (6 g, 150 mmol) was then added, stirred for 10 min, and raised to reflux. This reaction lasted for 6 h. After finishing, the pH was adjusted to 2–4, and a large number of solids were precipitated. After extraction, the result was washed with 500 mL of water and extracted again to achieve the crude product. A white powder was obtained by recrystallizing it with 200 mL of ethanol.

2.5. Synthesis of (R)-octan-2-yl 4′-((methoxycarbonyl) oxy-[1,1-biphenyl]-4-carboxylate (Intermediate 3)

4′-hydroxy-4-biphenylcarboxylic acid (30.4 g, 141 mmol) was dissolved in 250 mL of water in glassware and stirred under an ice bath. The aqueous sodium hydroxide solution was poured into a dropping funnel and slowly dripped into the glassware. Subsequently, 30 mL of methyl chloroformate was added on a dropwise basis over 30 min and stirred overnight at room temperature. This reaction was followed by filtration to obtain the residue, which was recrystallized with 500 mL of EA to give a white powder (4′-(methoxycarbonyl) biphenyl-4-carboxylic acid).

4′-(methoxycarbonyl) biphenyl-4-carboxylic acid (16.32 g, 63.75 mmol), (s)-2-octanol (7.1 g, 54.52 mmol), and triphenyl phosphite (21 g, 67.68 mmol) were added to 120 mL of THF and stirred at −10 °C under nitrogen. DIAD was dissolved in 60 mL of THF and slowly dropped into glassware. After 5 h, the reaction gradually rose to room temperature and lasted for 36 h. The product was dissolved with 250 mL of DCM, extracted using 200 mL of 15% hydrogen peroxide, 200 mL of potassium sulfate solution, and 200 mL of water, in turn. After drying with anhydrous magnesium sulfate and removing the solvent, the purified product ((R)-octyl-2-yl 4′-((methoxycarbonyl) oxy)-[1,1′-biphenyl]-4-carboxylic acid ester) was obtained using column chromatography.

(R)-octyl-2-yl 4′-((methoxycarbonyl) oxy)-[1,1′-biphenyl]-4-carboxylic acid ester was dissolved in ethanol in glassware. The reaction was monitored by thin-layer chromatography with the addition of 100 mL of ammonia water. After the reaction, the solvent was

removed, and 200 mL water was added for extraction. The residue was then recrystallized using EA and PE. It was then placed in a refrigerator and filtered to obtain a white powder ((R)-octyl-2-yl 4′-((methoxycarbonyl)oxy)-[1,1′-biphenyl]-4-carboxylate, intermediate 3).

2.6. Synthesis of LCs

2.6.1. Synthesis of LC-A

Intermediate 2 (2.27 g, 7.35 mmol) and EDCI (2.38 g, 12.26 mmol) were added to 100 mL of DCM with stirring. The reaction solution was white and turbid. TEA was added dropwise and warmed up to 30 °C to improve solubility; it stopped heating to room temperature after dissolution. Intermediate 3 (2 g, 6.13 mmol) and DMAP (0.22 g, 1.84 mmol) were dissolved in 50 mL of DCM, heated, stirred until completely dissolved, and poured into a dropping funnel. The above solution was slowly dropped into glassware to maintain the reaction for 24 h. Next, 5 mL of water was added and stirred for 30 min, and 300 mL of water was added to adjust the pH to 2 after removing the solvent. Finally, the LC-A (3.28 g, 72.36%) was obtained by column chromatography. ^{1}H NMR and ^{13}C NMR spectra are shown in Figure 1a,b and FT-IR is shown in Figure 2. ^{1}H NMR ($CDCl_3$, 500 MHz) δ 8.13–8.08 (m, 2H, 30, 32), 7.68 (d, J = 8.4 Hz, 2H, 4, 6), 7.66–7.59 (m, 6H, 1, 3, 8, 12, 29, 33), 7.56–7.51 (m, 2H, 24, 26), 7.21–7.16 (m, 2H, 9, 11), 7.03–6.97 (m, 2H, 23, 27), 5.17 (h, J = 7.0, 6.3 Hz, 1H, 36), 4.05 (t, J = 6.3 Hz, 2H, 14), 2.65 (t, J = 7.4 Hz, 2H, 18), 1.95–1.83 (m, 4H, 15, 17), 1.81–1.71 (m, 1H, 46′), 1.70–1.58 (m, 4H, 16, 45), 1.35 (d, J = 6.3 Hz, 3H, 37), 1.50–1.20 (m, 7H, 46″, 44, 43, 42). ^{13}C NMR ($CDCl_3$,125 MHz) δ 172.04 (19), 166.03 (34), 159.67 (10), 150.72 (22), 145.23 (5), 144.49 (28), 137.82 (25), 132.58 (1, 3), 131.42 (7), 130.08 (29, 33), 129.82 (31), 128.37 (4, 6), 128.34 (30, 32), 127.09 (8, 12), 126.93 (24, 26), 122.06 (23, 27), 119.11 (2), 115.09 (9, 11), 110.09 (40), 71.85 (36), 67.76 (14), 36.11 (43), 34.29 (18), 31.77 (46), 29.19 (15), 28.92 (44), 25.67 (17), 25.45 (45), 24.66 (16), 22.61 (42), 20.13 (37), 14.09 (41). MS(ESI): calcd $C_{40}H_{43}NO_5$ $[M + H]^+$ 618.31, found 618.32. FT-IR (ATR): 2928, 2866, 2226, 1754, 1718, 1604, 1496, 1380, 1282, 1181, and 1116 cm^{-1}.

2.6.2. Synthesis of LC-D

LC-D was obtained in a method analogous to LC-A using intermediate 2 (5.5 g, 17.78 mmol) and 4-(Trifluoromethyl) phenol (3.46 g, 21.33 mmol) as reactants with a white powder product (8.06 g, 73.28%). ^{1}H NMR and ^{13}C NMR spectra are shown in Figure 1c,d and FT-IR is shown in Figure 2. ^{1}H NMR ($CDCl_3$, 500 MHz) δ 7.69 (d, J = 8.4 Hz, 2H, 4, 6), 7.67–7.61 (m, 4H, 1, 3, 8, 12), 7.56–7.50 (m, 2H, 25, 27), 7.21 (d, J = 8.4 Hz, 2H, 9, 11), 7.03–6.97 (m, 2H, 24, 28), 4.05 (t, J = 6.3 Hz, 2H, 14), 2.64 (t, J = 7.4 Hz, 2H, 19), 1.94–1.80 (m, 4H, 15, 18), 1.70–1.57 (m, 2H, 16). ^{13}C NMR ($CDCl_3$, 125 MHz) δ 171.51 (20), 159.63 (10), 153.17 (23), 145.22 (5), 132.58 (1, 3), 131.46 (7), 128.37 (4, 6), 128.07 (q, J = 32.8 Hz, 26), 127.09 (8, 12), 126.79 (q, J = 3.7 Hz, 25, 27), 123.85 (q, J = 273.1 Hz, 31), 122.06 (24, 28), 119.11 (2), 115.07 (9, 11), 110.11 (30), 67.70 (14), 34.21 (19), 28.90 (15), 25.64 (18), 24.55 (16). MS(ESI): calculated $C_{26}H_{22}F_3NO_3$ $[M + Na]^+$ 476.16, found 476.14. FT-IR (ATR): 2948, 2866, 2226, 1752, 1604, 1494, 1328, 1174, 1126, and 1062 cm^{-1}.

2.6.3. Synthesis of LC-Z

LC-Z was obtained in a method analogous to LC-A using intermediate 2 (2.03 g, 6.56 mmol) and 4-(2-Methoxyethyl) phenol (1.2 g, 7.87 mmol) as reactants with a white powder product (2.08 g, 71.5%). ^{1}H NMR and ^{13}C NMR spectra are shown in Figure 1e,f and FT-IR is shown in Figure 2. ^{1}H NMR ($CDCl_3$, 500 MHz) δ 7.70–7.67 (m, 2H, 4, 6), 7.65–7.61 (m, 2H, 1, 3), 7.55–7.50 (m, 2H, 8, 12), 7.24–7.20 (m, 2H, 24, 26), 7.04–6.97 (m, 4H, 9, 11, 23, 27), 4.04 (t, J = 6.3 Hz, 2H, 14), 3.58 (t, J = 7.0 Hz, 2H, 29), 3.35 (s, 3H, 31), 2.87 (t, J = 7.0 Hz, 2H, 28), 2.60 (t, J = 7.4 Hz, 2H, 18), 1.93–1.78 (m, 5H, 15, 17), 1.69–1.56 (m, 3H, 16). ^{13}C NMR ($CDCl_3$, 125 MHz) δ 172.17 (19), 159.68 (10), 149.09 (22), 145.25 (5), 136.58 (25), 132.57 (1, 3), 131.39 (7), 129.79 (24, 26), 128.36 (4, 6), 127.09 (8, 12), 121.37 (23, 27), 119.12 (2), 115.09 (9, 11), 110.07 (33), 73.47 (29), 67.77 (14), 58.69 (28), 35.60 (31), 34.27 (18), 28.91 (15),

25.65 (17), 24.68 (16). MS(ESI): calculated $C_{28}H_{29}NO_4$ $[M + NH_4]^+$ 461.21, found 461.24. FT-IR (ATR): 2932, 2864, 2224, 1754, 1604, 1494, 1386, 1294, 1250, 1204, 1144, and 1108 cm^{-1}.

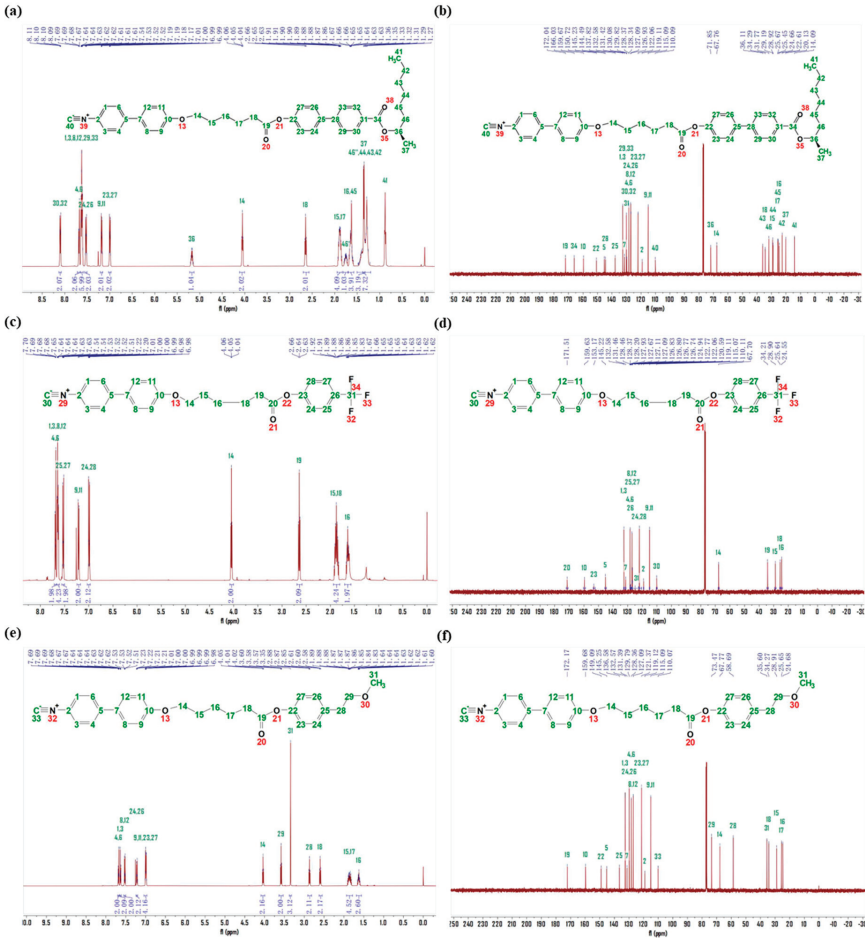

Figure 1. (**a**) ^1H NMR of LC-A; (**b**) ^{13}C NMR of LC-A; (**c**) ^1H NMR of LC-D; (**d**) ^{13}C NMR of LC-D; (**e**) ^1H NMR of LC-Z; and (**f**) ^{13}C NMR of LC-Z.

2.7. Tribological Test and Characterization of Worn Surface

To verify the effect of the mesogenic-phase temperature ranges on the tribological properties of LCs, LCs were evaluated in a point-to-point contact mode with a UMT-TriboLab friction and wear tester (Bruker, Billerica, MA, USA). The steel ball and steel plate used in the experiment were made of 304 stainless steel, and the diameter of the steel ball was 8 mm. The experimental parameters are shown in Table 1 and the model schematic is shown in Figure 3. Tests were conducted at 25 °C, 50 °C, 75 °C, 100 °C, 125 °C, 150 °C, 175 °C, and 200 °C. Before each test, the steel ball and steel plate were sonicated using a mixture of ethanol and petroleum ether; the procedure lasted for 30 min. A computer was used to record the curve of the coefficient of friction and the sliding time. During the test, the friction-pair was completely immersed in the base oil with or without additives. Each experiment was repeated at least twice to make the experimental results accurate.

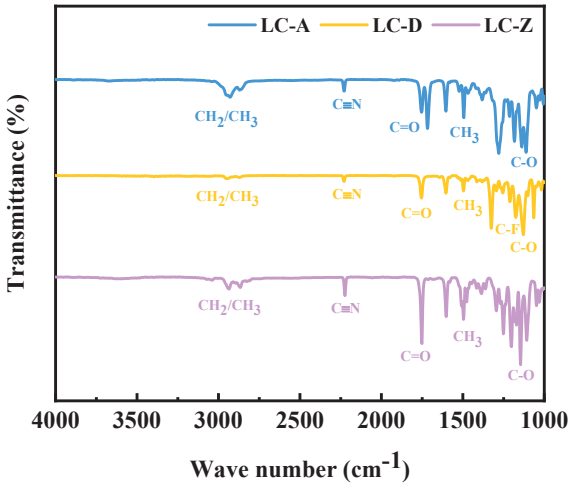

Figure 2. Fourier transform infrared of LC-A, LC-D, and LC-Z.

Table 1. Experimental parameters of the UMT-TriboLab friction and wear tester.

Load (N)	Frequency (Hz)	Time (min)	Stroke Length (mm)
3	4	10	10

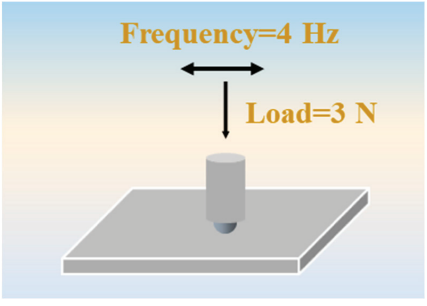

Figure 3. Model schematic of UMT-TriboLab friction and wear tester.

After the test, the steel plates were cleaned using petroleum ether. The width of the wear surface was characterized by a Contour GT-K 3D profiler. Finally, the wear surfaces were characterized using Raman and SEM spectrometers to illustrate the mechanism of action of LCs as lubricant additives.

3. Results and Discussion

3.1. Mesogenic-Phase Behaviors of the Synthesized LCs

DSC and POM were used to characterize the LCs properties. DSC thermograms of the three LCs, from which the three LCs exhibit characteristics, are shown in Figure 4. LC-D exhibits the corresponding LC properties only in the heating cycle, and the mesogenic-phase temperature range is narrow. LC-A and LC-Z display mesophases as well as wide mesogenic-phase temperature ranges in both heating and cooling cycles. Therefore, compared to LC-D, LC-A and LC-Z have almost symmetrical mesophases and wider mesogenic-phase temperature ranges. From Figure 4a, LC-A shows three heat absorption peaks during the heating process. The first peak corresponds to the melting temperature (T_m), which refers to the temperature at which LC-A was melted by heat into the

LC phase; the second peak indicates that the phase transition occurred in the smectic C phase of LC-A; and the third peak shows the disappearance of the LC phase while entering the isotropic liquid phase, which is indicated using the clearing point (T_d). LC-D and LC-Z have two heat absorption peaks, corresponding to T_m and T_d, respectively. The phase-transition temperature and the mesogenic-phase temperature range of the three LCs during the heating process are shown in Table 2. The T_m of LC-A, LC-D, and LC-Z are 33.7 °C, 100.5 °C, and 37.8 °C, respectively. Depending on the mesophase temperature range, the order of the LCs is LC-A > LC-Z > LC-D, which is closely related to the molecular structure of the LCs. When compared with LC-D, LC-A and LC-Z show superior LC properties due to their longer chain lengths. Moreover, the two ester groups in the LC-A structure make it easier to form a smectic phase with a wider mesogenic-phase temperature range. Figure 5 shows the optical textures of the LCs, which were observed using POM. From Figure 5a, LC-A shows a schlieren texture at 65.9 °C. From Figure 5b, LC-D exhibits a fan-shaped focal conic texture at 100.6 °C, while Figure 5c shows the focal conic texture of LC-Z at 56.5 °C. The three synthetic LCs exhibit a colorful LC texture.

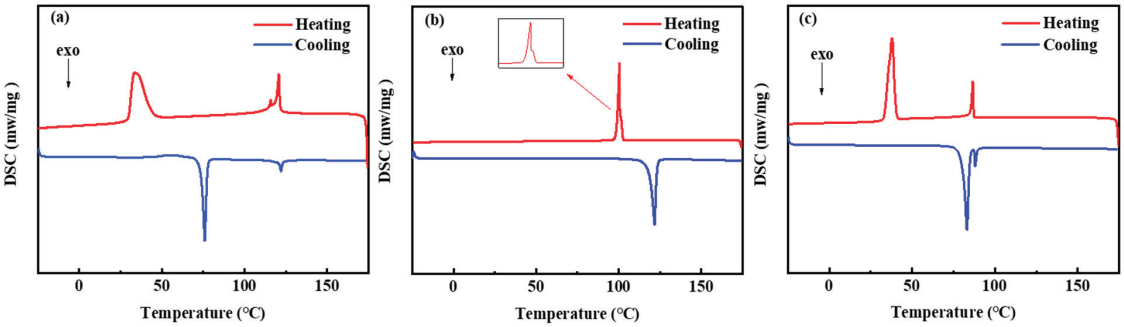

Figure 4. DSC thermograms of LCs: (**a**) LC-A; (**b**) LC-D; and (**c**) LC-Z.

Table 2. Phase-transition temperature of LCs.

Samples	T_m (°C)	T_d (°C)	ΔT [1] (°C)
LC-A	33.7	120.8	87.1
LC-D	100.5	100.9	0.4
LC-Z	37.8	86.6	48.8

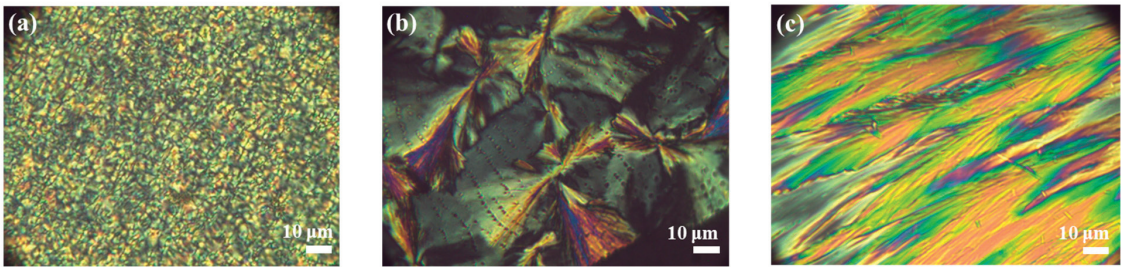

Figure 5. (**a**) Schlieren texture of LC-A at 65.9 °C; (**b**) fan-shaped focal conic texture of LC-D at 100.6 °C; and (**c**) focal conic texture of LC-Z at 56.5 °C.

3.2. Analysis of Thermal Stability

Thermal stability is an index used to evaluate the anti-decomposition and anti-aging qualities of a lubricant, and good thermal stability is necessary for lubricant additives. The thermogravimetric analysis curve of TGA is shown in Figure 6. The initial decomposition

temperatures of LC-A, LC-D, and LC-Z were 309.3 °C, 271.9 °C, and 340.7 °C, respectively, mainly due to the decomposition of ether bonds and ester groups in the structure of LCs. When compared with LC-D and LC-Z, LC-A contains two ester groups in its structure, which may be the reason for its second decomposition starting at 400 °C. LC-D starts its second decomposition around 340 °C, probably due to the presence of trifluoromethyl in its molecular structure. In addition, the final decomposition temperatures of the three LCs were 431.5 °C, 354.1 °C, and 409.9 °C, respectively. The analytical results show that LCs have excellent thermal stability due to their molecular structure, having the potential to be used as lubricant additives.

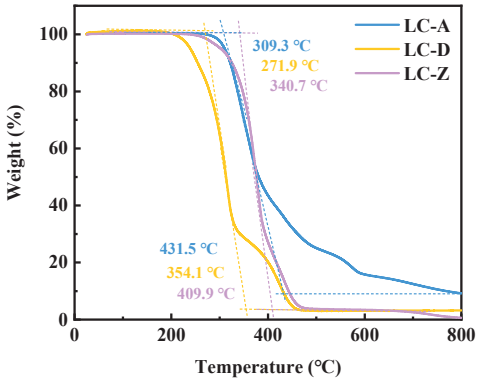

Figure 6. Thermogravimetric analysis curve of LC-A, LC-D, and LC-Z.

3.3. Anti-friction Analysis

The feasibility of LCs as lubricant additives was investigated using a UMT friction and wear tester. TTO was selected as the base oil, and 2 wt% of LCs were added as an additive. A comparison was made with the commercial lubricant additive ZDDP, thus illustrating the anti-friction effect. Figures 7 and 8 display the friction coefficient curves and average friction coefficient over a temperature range for pure TTO and TTO containing 2 wt% ZDDP, LC-A, LC-D, and LC-Z, respectively. The tested temperature points were 25 °C, 50 °C, 75 °C, 100 °C, 125 °C, 150 °C, 175 °C, and 200 °C. From Figures 7 and 8, pure TTO exhibited bad friction-reduction performance in the tested temperature range and its performance was less affected by an increasing temperature. When compared to the samples of TTO with LCs added, the friction coefficient curves show an increasing trend in general with large fluctuations. In contrast, the oil containing LCs had a lower average friction coefficient in a specific temperature range, and the friction coefficient curves showed less fluctuation and an overall decreasing trend, especially in the range of 75–150 °C. It is noteworthy that there are differences in the mesogenic-phase temperature ranges in which the three LCs have friction-reducing effects. As can be seen from Figure 8, LC-A can reduce the average friction coefficient of TTO at 25–175 °C; LC-D has the ability to reduce friction from 75–200 °C, and LC-Z can achieve a certain friction reduction effect across the whole temperature range of the test. Additionally, LC-A and LC-D have the best friction-reduction effects at 100 °C, with reductions of 19.25% and 21.57% when compared to the base oil, respectively. LC-Z showed the best performance in anti-friction at 75 °C, with a reduction of 19.59%. When combined with the DSC, the anti-friction properties of the LCs were very closely connected with the mesogenic-phase temperature ranges, and the optimum temperatures for their tribological properties were close to or within this range. Among them, LC-D has a mesophase temperature range of 100.5 °C to 100.9 °C. The narrower intermediate-phase temperature range may limit the range in which it can exert its friction-reducing effect. Compared with LC-D, LC-A and LC-Z have a wider intermediate-phase temperature range and can be used as additives to reduce the average friction coefficient over a wider temperature range. According to the analysis, it can be speculated that the

phase-change temperature range of LCs is an influential factor on their friction-reduction performance, and the temperature range which exerts the friction-reduction effect will be wider than the phase-change temperature range in general. In addition, ZDDP is the most widely used and effective lubricant additive. As can be seen from Figures 7 and 8, the trend of tribological performance with temperature remains insignificant when ZDDP is added to the base oil. The LC additives displayed superior friction-reduction performances compared to ZDDP, and the effect of friction-reduction was influenced by temperature. Even at 175 °C, the LCs' average friction coefficients remained superior when compared with ZDDP, which demonstrates that LCs can be used in lubricant applications. It is worth noting that each LC has its corresponding optimal temperature interval, within which the LC additives can improve the friction-reduction performance of the oil and yet can be applied to several operating conditions under specific temperatures, thus enabling the controllability of the oil temperature.

3.4. Anti-Wear Analysis

The width of the wear scar was characterized by a Contour GT-K 3D profiler to illustrate the anti-wear performance of LCs as lubricant additives. The average of the three measurements was calculated to illustrate the width of the wear scars. The results are shown in Figure 9. All LC additives exhibited superior anti-wear performance at different temperatures when compared with TTO. Even at 50–175 °C, the anti-wear performance of the three LC additives was significantly better than that of the commercially available additive ZDDP. It is noteworthy that, compared with LC-D, the addition of LC-Z resulted in a smaller width of wear marks on the steel plate over a wide temperature range of 25 to 75 °C. Among them, the width of wear marks at 75 °C was reduced by 31.82%. The addition of LC-A can also significantly improved the anti-wear performance of the oil, with a 25.78% reduction in the width of wear marks at 75 °C, which may be caused by the longer chain length of LC-A and LC-Z, resulting in wide-mesophase temperature ranges. It can be seen from Figure 9 that LC-D has good anti-friction properties throughout the temperature range, especially at 125 °C, with a 30.07% reduction in width of the wear scars, which is probably due to the presence of trifluoromethyl in its structure. In addition, the three LC additives can dramatically enhance the anti-wear performance of TTO in a wide temperature range of 25 to 175 °C, which is consistent with the following conclusion: the temperature interval in which the LC additives have tribological performance effects is wider than their mesophase temperature ranges. Therefore, the chemical structure and mesophase temperature ranges of LC additives are critical factors affecting their anti-wear performance.

3.5. Surface Analysis

3.5.1. SEM Analysis

The morphology of the wear surface was further observed with SEM. Figure 10 shows the SEM images and the width of wear scars at 100 °C. As can be seen from Figure 10, the wear scars were deeper with pure TTO lubrication and an obvious furrow appeared, indicating that no stable lubrication film was formed on the wear surface. The addition of LC additives can reduce the degree of wear on the wear surface and form a stable lubricating film, so as to improve the anti-wear properties of the base oil. The width of the wear marks of pure TTO is 381.2 μm, and the width of the wear marks of the three LC additives are 305.4 μm, 297.7 μm, and 308.3 μm, respectively. Compared to pure TTO, the anti-wear effects of LCs are 19.89%, 21.88%, and 19.11%, respectively. The anti-wear effect of LC-A is better than LC-Z, which was in line with the mesophase temperature ranges. The anti-wear effect of LC-D was significantly better than the other two LC additives, which was probably due to the presence of trifluoromethyl in its structure, which forms a stable lubricating film and leads to the improvement of the anti-wear properties of the oil. It can be seen from Figure 10c,c', that there was a slight corrosive wear on the wear surface of LC-D, which may be due to the chemical reaction between the free fluorine atoms and iron elements on the wear surface.

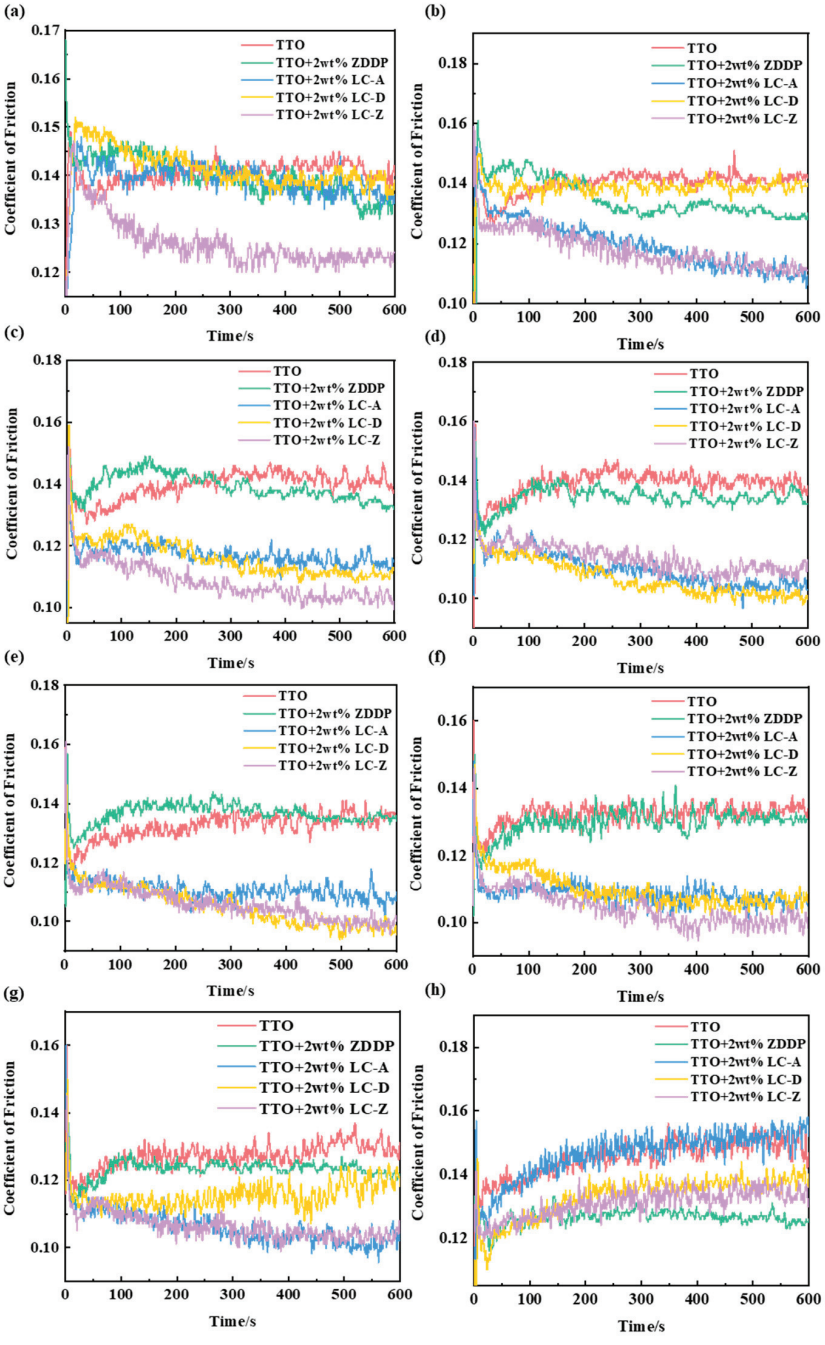

Figure 7. The friction coefficients of TTO and TTO containing 2 wt% ZDDP, LC-A, LC-D, and LC-Z at different temperature points: (**a**) at 25 °C; (**b**) at 50 °C; (**c**) at 75 °C; (**d**) at 100 °C; (**e**) at 125 °C; (**f**) at 150 °C; (**g**) at 175 °C; and (**h**) at 200 °C.

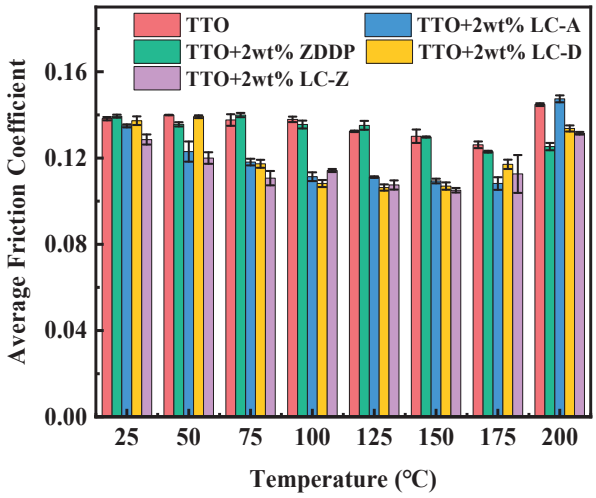

Figure 8. Average friction coefficient of pure TTO and TTO with 2 wt% ZDDP, LC-A, LC-D, and LC-Z under different temperature points.

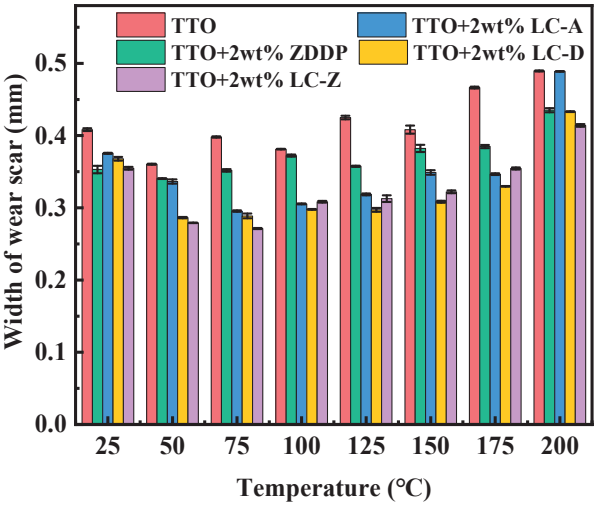

Figure 9. Width of wear scars of pure TTO and TTO with 2 wt% ZDDP, LC-A, LC-D, and LC-Z under different temperature points.

3.5.2. Raman Spectroscopy Analysis

The lubrication mechanism of the worn surface was analyzed using Raman spectroscopy. After the test, we cleaned the steel plates with petroleum ether. The wear marks on the surfaces of the steel plates were characterized with Raman spectroscopy to illustrate the mechanism of action of LCs as lubricant additives. Figure 11 shows the Raman spectra after the UMT-TriboLab friction and wear tester, excited by the 532 nm laser. We can see that the strong peak at 663 cm^{-1} is Fe_3O_4, the peaks at 1357 cm^{-1} and 1573 cm^{-1} belong to the D and G peaks, respectively, and the strong peak at 2890 cm^{-1} is associated is with the 2D peak. From Figure 11a, the surface lubricated by base oil mainly contains Fe_3O_4, and the signals of the D peak and G peak are weak, which indicates that the carbon content in the base oil is relatively low. The surface of the friction marks after adding LCs is dominated

by Fe_3O_4, D peak and G peak, and has an obvious 2D peak. It can be confirmed that a carbon film and iron oxide film were formed on the friction surface, which played a role in reducing friction and increasing anti-wear properties. Significantly, the characteristic group with LC additives can be observed on the wear surface lubricated with 2 wt% LC-A, which indicates that the LCs has a strong adsorption ability on the metal surface and can generate a lubricant film with the chemical reaction on it. Figure 12 shows the schematic representation of the lubrication mechanism. It can be hypothesized that LC additives can form a lubricant film on the surface, preventing the direct contact of the rough surfaces and thus achieving the effect of friction-reduction and anti-wear.

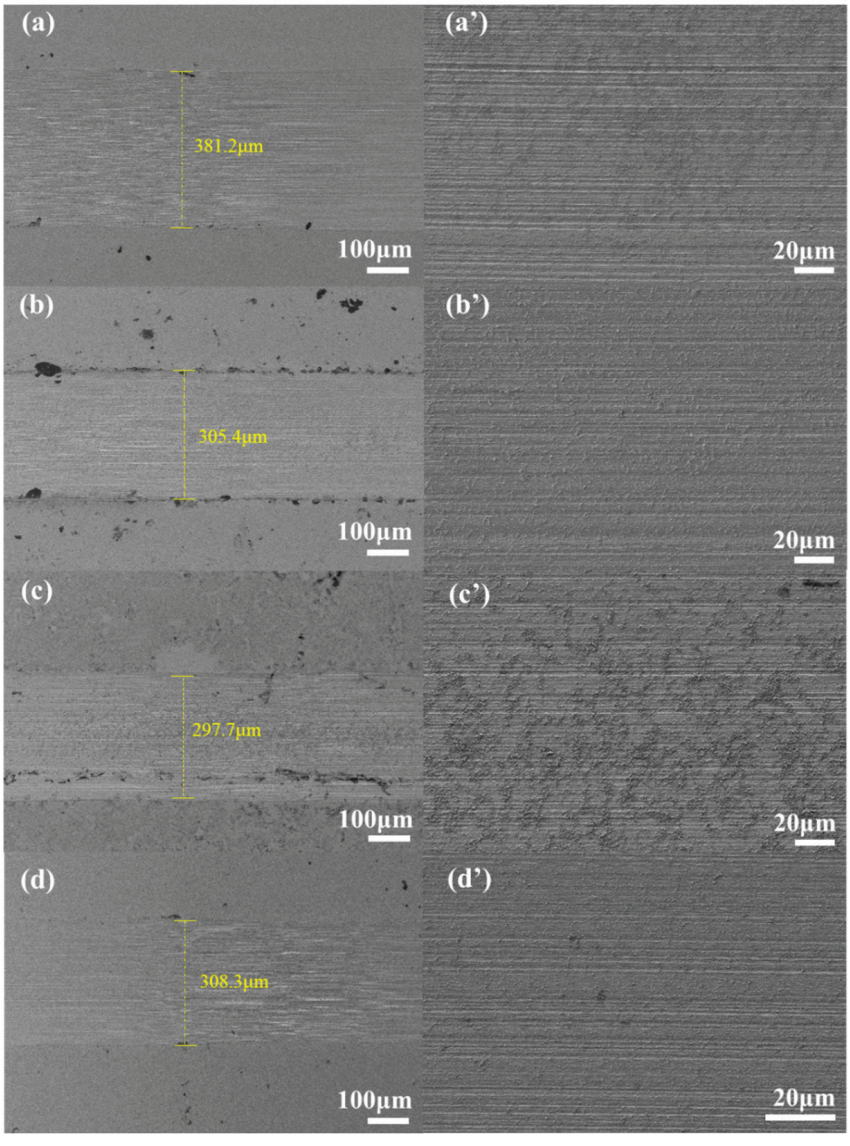

Figure 10. SEM images of the wear surface after UMT tests at 100 °C: (**a**,**a′**) are TTO; (**b**,**b′**) are 2 wt% LC-A added to TTO; (**c**,**c′**) are 2 wt% LC-D added to TTO; and (**d**,**d′**) are 2 wt% LC-Z added to TTO.

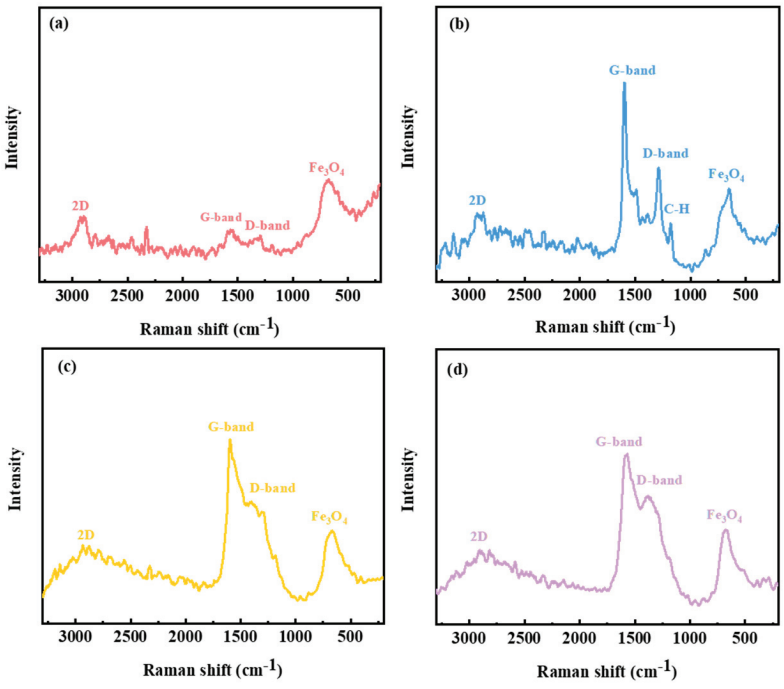

Figure 11. Raman spectra at wear marks after UMT: (**a**) TTO; (**b**)TTO + 2 wt% LC-A; (**c**) TTO + 2 wt% LC-D; and (**d**)TTO + 2 wt% LC-Z.

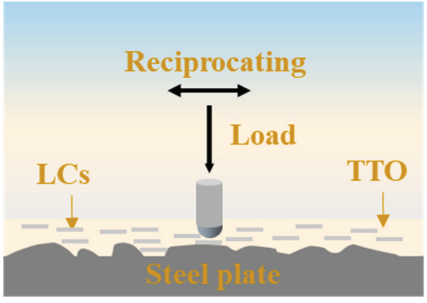

Figure 12. The schematic representation of the lubrication mechanism.

4. Conclusions

1. Three LCs were synthesized and characterized for their structures and thermal stability. The results indicate that they have excellent thermal stability. The LCs' properties were examined, and it was found that three LCs exhibited good mesogenic-phase behavior and that the chain length was an essential factor affecting the width of the mesogenic-phase temperature ranges. Among the LCs, LC-A showed the longest chain length and the widest mesogenic-phase temperature range.
2. The synthesized LCs were used as lubricant additives to investigate tribological behavior. The three LCs showed excellent friction-reduction and anti-wear properties when compared to the base oil. Furthermore, the tribological properties of the LCs were very closely connected with their mesogenic-phase temperature ranges, and the best tribological properties of LCs are found in or close to the temperature range.

3. To analyze the lubrication mechanism of LCs, it is found that the addition of LCs additive can reduce the width of wear marks and the surface furrow, which can form a lubricant film on the wear surface and prevent the direct contact of frictional pairs on the sliding surface, leading to the improvement of tribological properties of the base oil.

Author Contributions: Conceptualization, W.H. and J.L.; methodology, W.H. and S.F.; validation, H.W.; formal analysis, H.W. and Y.J.; investigation, H.W.; data curation, H.W.; writing—original draft preparation, H.W. and W.H.; writing—review and editing, W.H. and J.L. All authors have read and agreed to the published version of the manuscript.

Funding: This research was funded by the Youth Innovation Promotion Association (2019288), the Shanghai Pudong New Area Science and Technology Development Fund (PKJ2019-C01), and the Strategic Priority Research Program of the Chinese Academy of Sciences (XDA21021202).

Institutional Review Board Statement: Not applicable.

Informed Consent Statement: Not applicable.

Data Availability Statement: Data is contained within the article.

Conflicts of Interest: The authors declare no conflict of interest.

References

1. Guo, H.; Adukure, A.R.; Iglesias, P. Effect of Ionicity of Three Protic Ionic Liquids as Neat Lubricants and Lubricant Additives to a Biolubricant. *Coatings* **2019**, *9*, 713. [CrossRef]
2. Liao, M.; Nicolini, P.; Du, L.; Yuan, J.; Wang, S.; Yu, H.; Tang, J.; Cheng, P.; Watanabe, K.; Taniguchi, T.; et al. UItra-low friction and edge-pinning effect in large-lattice-mismatch van der Waals heterostructures. *Nat. Mater.* **2022**, *21*, 47–53. Available online: https://www.nature.com/articles/s41563-021-01058-4 (accessed on 6 January 2023). [CrossRef]
3. Wang, J.; Li, Z.; Xu, Y.; Hu, W.; Zheng, G.; Zheng, L.; Ren, T. Synthesis and Tribological Behavior of Bridged Bicyclic Polymers as Lubricants. *Ind. Eng. Chem. Res.* **2022**, *169*, 107458. [CrossRef]
4. Uzoma, P.C.; Hu, H.; Khadem, M.; Penkov, O.V. Tribology of 2D Nanomaterials: A Review. *Coatings* **2020**, *10*, 897. [CrossRef]
5. Wang, Y.; Zhang, T.; Qiu, Y.; Guo, R.; Xu, F.; Liu, S.; Ye, Q.; Zhou, F. Nitrogen-doped porous carbon nanospheres derived from hyper-crosslinked polystyrene as lubricant additives for friction and wear reduction. *Tribol. Int.* **2022**, *169*, 107458. [CrossRef]
6. Yaqoob, H.; Teoh, Y.H.; Sher, F.; Jamil, M.A.; Nuhanovi, M.; Razmkhah, O.; Erten, B. Tribological behaviour and lubricating mechanism of tire pyrolysis oil. *Coatings* **2021**, *11*, 386. [CrossRef]
7. Pandey, P.; Somers, A.; Hait, S.; Ramakumar, S. Synthesis of oil miscible novel silane functionalised imidazoline-based ILs as lubricant additives: Characterization and tribological evaluations. *Tribol. Int.* **2022**, *70*, 25. Available online: https://link.springer.com/article/10.1007/s11249-022-01567-6 (accessed on 6 January 2023). [CrossRef]
8. Zhang, X.J.; Liu, X.X.; Zhang, X.H.; Tian, Y.; Meng, Y.G. Ordering of the 7CB liquid crystal induced by nanoscale confinement and boundary lubrication. *Liq. Cryst.* **2012**, *39*, 1305–1313. [CrossRef]
9. Peng, J.F.; Shen, M.X.; Cai, Z.B. Nano Diesel Soot Particles Reduce Wear and Friction Performance Using an Oil Additive on a Laser Textured Surface. *Coatings* **2018**, *8*, 89. [CrossRef]
10. Zhang, Z.; Demir, K.G.; Gu, G.X. Developments in 4D-printing: A review on current smart materials, technologies, and applications. *Int. J. Smart. Nano. Mat.* **2019**, *10*, 205–224. [CrossRef]
11. Jeong, U.; Yin, Y. Smart and responsive micro and nanostructured materials. *Adv. Funct. Mater.* **2020**, *30*, 1907059. [CrossRef]
12. Huang, C.Y. Effect of Thicknesses of Liquid Crystal Layers on Shift of Resonance Frequencies of Metamaterials. *Coatings* **2021**, *11*, 578. [CrossRef]
13. Guo, Y.M.; Li, J.S.; Zhou, X.J.; Tang, Y.Z.; Zeng, X.Q. Formulation of lyotropic liquid crystal emulsion based on natural sucrose ester and its tribological behavior as novel lubricant. *Friction* **2022**, *10*, 1879–1892. Available online: https://link.springer.com/article/10.1007/s40544-021-0565-6 (accessed on 6 January 2023). [CrossRef]
14. Chiang, W.F.; Lu, Y.Y.; Chen, Y.P.; Lin, X.Y.; Huang, C.Y. Passively Tunable Terahertz Filters Using Liquid Crystal Cells Coated with Metamaterials. *Coatings* **2021**, *11*, 381. [CrossRef]
15. Yang, J.; Yuan, Y.; Li, K.; Amann, C.W.; Yuan, C.Q.; Neville, A. Ultralow friction of 5CB liquid crystal on steel surfaces using a 1,3-diketone additive. *Wear* **2021**, *480–481*, 203934. [CrossRef]
16. Mokshin, V. Tribological capabilities of chiral nematic liquid crystal additives in mineral motor oil. *Adv. Mech. Eng.* **2020**, *12*, 1–9. [CrossRef]
17. Ghosh, P.; Upadhyay, M.; Das, M.K. Studies on the additive performance of liquid crystal blended polyacrylate in lubricating oil. *Liq. Cryst.* **2013**, *41*, 30–35. [CrossRef]
18. Nakano, K. Scaling Law on Molecular Orientation and Effective Viscosity of Liquid-Crystalline Boundary Films. *Tribol. Lett.* **2003**, *14*, 17–24. [CrossRef]

19. Novotná, V.; Hamplová, V.; Kapar, M.; Glogarová, M. New chlorine-substituted ferroelectric liquid crystals with four aromatic rings in the mesogenic core. *Liq. Cryst.* **2002**, *29*, 1435–1439. [CrossRef]
20. Gao, M.; Ma, L.; Luo, J.B. Effect of alkyl chain length on the orientational behavior of liquid crystals nano-film. *Tribol. Lett.* **2016**, *62*, 24. [CrossRef]
21. Qiao, X.X.; Zhang, X.J.; Guo, Y.B.; Yang, S.K.; Tian, Y.; Meng, Y.G. Boundary layer viscosity of CNT-doped liquid crystals: Effects of phase behavior. *Rheol. Acta.* **2013**, *52*, 939–947. [CrossRef]
22. Hird, M. Fluorinated liquid crystals—Properties and applications. *Chem. Soc. Rev.* **2007**, *36*, 2070. [CrossRef] [PubMed]

coatings

MDPI

Article

Effect of Ni Coating on Microstructure and Property of Al Alloy/Steel CMT Welding-Brazing Joints

Chao Zhang [1,2], Mingfang Wu [1], Juan Pu [1,*], Jiawei Rao [1], Weimin Long [3] and Yuanxun Shen [3]

[1] School of Materials Science and Engineering, Jiangsu University of Science and Technology, Zhenjiang 212003, China
[2] School of Public Utilities, Jiangsu Urban and Rural Construction Vocational College, Changzhou 213003, China
[3] Zhengzhou Research Institute of Mechanical Engineering, Zhengzhou 450001, China
* Correspondence: pu_juan84@163.com; Tel.: +86-15952815816

Abstract: The cold metal transfer (CMT) welding-brazing process was chosen to join Al alloy and Ni-coated steel using AlSi12 as the filler wire. The macrostructure and microstructure of the joints were tested by using an optical microscope (OM), scanning electron microscope (SEM), energy dispersive spectrometry (EDS), and X-ray diffraction (XRD). The tensile properties and corrosion properties of the joints were also tested. The results showed that Ni coating could improve the wettability and spreadability of molten AlSi12 filler metal on the steel surface, resulting in a good appearance for the Al alloy/steel joint. Ni coating could hinder the chemical metallurgical reaction between Al atom and Fe atoms to inhibit the formation of brittle Fe-Al intermetallic compounds (IMCs) and reduce the thickness of the IMCs layer. Meanwhile, the Ni atom reacted with the Fe and Al atoms to form Al_3Ni_2, (Fe, Ni) Al_3 and (Fe, Ni)$_2Al_3$, which improved the tensile strength of the joints. All joints with Ni coating cracked near the Al alloy. When the Ni-coating thickness was 5 μm, the tensile strength of the joint reached a maximum of 202.5 MPa. The addition of Ni could also improve the corrosion resistance of the joints. Significantly, when the Ni-coating thickness was 10 μm, most of the Ni coating was still solid, and the interface reaction layer was mainly composed of α-Ni solid solution and some (Fe, Ni)$_2Al_3$.

Keywords: interface reaction mechanism; Ni coating; microstructure; property; CMT

Citation: Zhang, C.; Wu, M.; Pu, J.; Rao, J.; Long, W.; Shen, Y. Effect of Ni Coating on Microstructure and Property of Al Alloy/Steel CMT Welding-Brazing Joints. *Coatings* **2023**, *13*, 418. https://doi.org/10.3390/coatings13020418

Academic Editors: Ashish Kumar Srivastava and Amit Rai Dixit

Received: 6 January 2023
Revised: 2 February 2023
Accepted: 6 February 2023
Published: 12 February 2023

1. Introduction

The "Made in China 2025" development strategy proposes that the manufacturing industry changes from a traditional to an intelligent and green industry. Realizing weight reduction is considered a vital way to achieve this change [1,2]. Al alloys, which have the advantages of light weight, high specific strength, corrosion resistance, and good comprehensive performance, are widely used in aerospace, railway transportation, automobiles, and refrigeration [3–5]. They partially replace steel to form Al alloy/steel structures for achieving lightweight structures. Al alloy/steel parts have the characteristics of the lightweight of Al alloy together with the advantages of high strength and low cost of steel. They are widely used in the covering parts and chassis parts of automobiles. Undoubtedly, the Al alloy/steel hybrid body has become the trend of future development in the industry. Therefore, the connection of Al alloy/steel parts has high requirements.

For the joining of Al alloy and steel, some of the difficulties are as followings [6]: Firstly, the thermal expansion coefficients are different, which results in the severe deformation of the joints and thus produce considerable residual stress in the welding process. Secondly, due to their poor metallurgical compatibility, a series of brittle IMCs (i.e., $FeAl_3$, Fe_2Al_5, $FeAl_2$, FeAl) form, which deteriorates the mechanical properties of the joints. Thirdly, the potential of Al alloy is different from that of steel, and the localized electrochemical

corrosion near the steel occurred in a humid atmosphere. At the same time, porosity and defects in the joints would accelerate the process of electrochemical corrosion [7].

In order to prepare composite materials with excellent performance, many studies have been carried out. Farhad Ostovan et al. [8–10] believed that Gas Tungsten Arc Welding (GTAW) had the unique advantages due to its easy control of heat input. Qin et al. [11] compared and analyzed the advantages of several welding methods to join Al alloy and steel, such as mechanical connection, solid phase connection, liquid-solid diffusion, brazing, GTAW brazing and so on. They found that laser welding brazing, electron beam welding brazing and arc+laser hybrid welding could achieve high-quality Al alloy/steel joints by controlling the welding heat input. Maryam Roudbari et al. [12] reinforced the Al plates with steel wires by using the method of explosive welding. They determined the optimal parameters through the numerical simulation. The simulation results agreed very well with the experimental data. Then they studied the mechanical properties of aluminum base composite materials [13]. The results showed that the tensile strength of the reinforced composite was 8% higher than that of the unreinforced material. However, the explosive welding was limited by the weather and gave rise to the air pollution.

Our research team studied the joining of Al alloy and steel by using welding-brazing technology. Shao et al. [14] used different Al-Si filler metals to join Al alloy and steel by CMT welding brazing, respectively. They reported that Si element could inhibit the formation of brittle IMCs at the interface reaction layer. Shi et al. [15] showed that TIG welding brazing could control welding heat input precisely. The addition of Zn element could improve the wettability of AlSi5 filler metal and also enhance the corrosion resistance of the joint. Chao et al. [16] studied the effect of Cu coating on the microstructure and properties of the joints by CMT welding brazing. They found that with the increase in Cu-coating thickness, the thickness of the IMCs layer decreased and the corrosion resistance of the Al alloy/steel joint increased. When the Cu-coating thickness was 10 μm, the tensile strength and corrosion resistance of the joints were up to the optimum. Other researchers [17] have reported that Ni coating on the steel surface could change the IMCs composition of joints by laser welding brazing. However, they did not discuss the formation mechanism of IMCs compounds in detail, nor did they study the corrosion resistance of the Al/steel joints.

Therefore, in this paper, different thicknesses of Ni layer were designed to be coated on steel surfaces. The CMT welding-brazing process of Al alloy/steel was conducted using AlSi12 as the filler wire. The effects of different Ni-coating on the macrostructure, microstructure, tensile strength, and corrosion resistance of the joints were studied. We focused on exploring the action mechanism of Ni coating on the interface reaction layer of joints.

2. Experimental Materials and Methods

2.1. Experimental Materials

The purchased 6082 Al alloy and Q235B steel with dimensions of 150 mm × 100 mm × 2 mm were used as the base metals. AlSi12 flux-cored wire with a diameter of 1.6 mm was used as the filler material, and it was composed of AlSi12 wire and NOCLOCK flux. The chemical composition and tensile properties of the above materials are listed in Table 1.

Table 1. Chemical compositions and tensile properties of base metal and flux-cored wire.

Materials	Elements (wt.%)							Tensile Strength R_m/MPa
6082 Al alloy	Mg 0.6–1.2	Zn 0.20	Mn 0.4–1.0	Cu 0.10	Si 0.7–1.3	Fe 0.50	Al Bal.	240
Q235B Steel	C 0.2	Si 0.2	Mn 0.2	S 0.03	P 0.03	Cr 0.70	Fe Bal.	375

Table 1. *Cont.*

Materials	Elements (wt.%)							Tensile Strength R_m/MPa
AlSi12	Si 12.15	Cu 0.0057	Zn 0.0048	Mg 0.0002	Mn 0.075	Fe 0.209	Al Bal.	
NOCLOCK flux		KAlF4 97			CsAlF4 3			

2.2. Coating Process of Ni on the Steel Surface

Ni layers that ranged from 0 μm and 10 μm were coated on the surface of Q235B steel by the electroplating process. At least five samples were prepared and tested for each Ni-coating thickness. Before electroplating, all steel plates were polished with sandpaper to remove burrs. Subsequently, the steel plates were immersed into an alkaline solution at 80 °C for 20 min to remove oil stains. The composition of the alkaline solution was 30 g/L NaOH, 35 g/L $NaCO_3$, 20 g/L $NaPO_4$, and 7.5 g/L OP-10. Then, they were immersed in the acid solution for 2 minutes, which was composed of 5% H_2SO_4, 15% HCl, and 80% distilled water. After chemical cleaning, the steel plates were washed in the acetone solution with an ultrasonic cleaner to be electroplated. The electroplating solution containing 200 g/L $NiSO_4$, 30 g/L $NiCl_2$, 30 g/L H_3BO_3, 0.1 g/L $C_{12}H_{25}NaSO_3$ and 0.5 g/L saccharin was prepared and stirred for 30 min. Finally, the treated steel plates were placed into the electroplating solution. During the electroplating process, the nickel plate was used as the anode, while the steel plate was used as the cathode. The process parameters of electroplating were a pH of 4, a temperature of 50 °C, and a current density of 1.5 A/min. The schematic diagram of the electroplating process is shown in Figure 1.

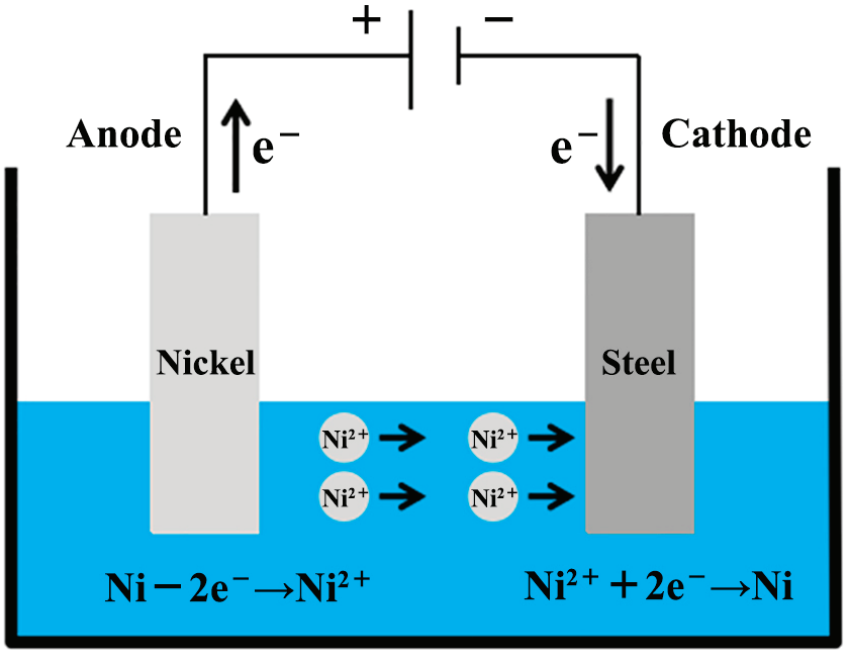

Figure 1. Schematic diagram of the electroplating process for Ni coating on the steel surface.

2.3. CMT Welding-Brazing Process to Join Al Alloy/Steel

A CMT5000i welding machine (Fronius company) was used to join Al alloy and Ni-coated steel with the AlSi12 filler wire. Before CMT welding brazing, we cleaned the base metals with the acetone. The Al alloy plates had no groove while the steel plates were equipped with a single V-shaped groove of 30°. The root gap was 0.1 mm for assembly, and we used the copper backing to solidify the welding joint. The inclination angle of the torch was set to 70° and the distance from the tip of the welding wire to the workpiece was 2 mm. The welding process was protected by Argon gas with 99.99% purity. The schematic diagram of the CMT welding-brazing process is illustrated in Figure 2. Its detailed parameters are listed in Table 2.

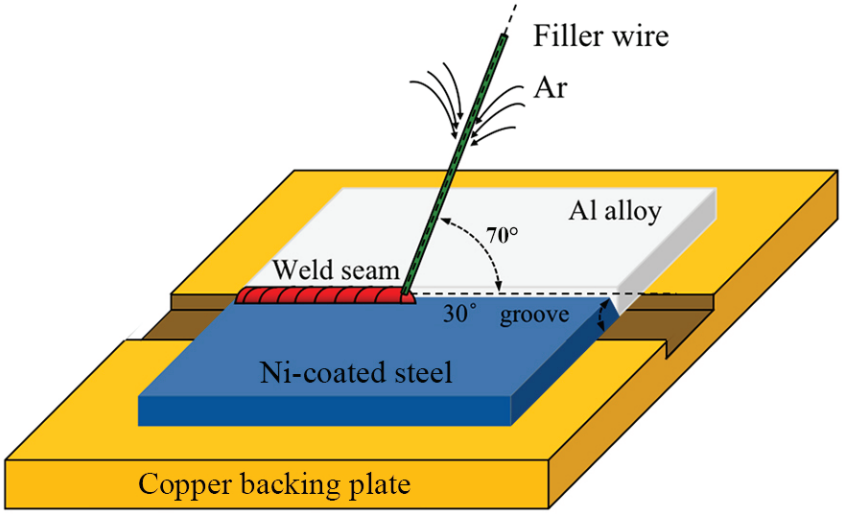

Figure 2. Schematic diagram of CMT welding-brazing process.

Table 2. Process parameters of CMT welding brazing.

Parameters	Value
Welding voltage, V	12.0
Welding current, A	105
Welding speed, mm/min	300
Shielding gas flow, L/min	18
Wire feeding speed, m/min	5.5

2.4. Analysis of Microstructure and Tensile Properties of Al Alloy/Steel Joints

After CMT welding brazing, samples for the investigation of microstructure and tensile properties were prepared. All the microstructure analysis samples were mechanically ground with sandpaper and polished with diamond suspension, and then etched by Keller's reagent for 10–15 s. The macrostructure was observed by a ZEISS optical microscope (OM, Oberkochen, Germany). The microstructure was analyzed by a JSM-6480 scanning electron microscope (SEM, JEOL, Tokyo, Japan), and the element distribution was identified by energy dispersive spectroscopy (EDS). We stripped the Al alloy/steel joint along the side of the steel, and the phase composition of the interface reaction layer and fusion zone were confirmed by an XRD-6000 X-ray diffractometer instrument (XRD, Shimadzu, Kyoto, Japan) with a scanning angle (2θ) ranging from 10° to 90° and a scanning speed of 3 °/min.

According to GB/T 2651-2008 standard, the tensile properties of the joints were tested on an ETM605D mechanical tester at a constant rate of 1 mm/min. The fracture surfaces were observed by SEM.

2.5. Electrochemical Corrosion Measurements of Al Alloy/Steel Joints

An Electrochemical Workstation (No. EGM283) was used to carry out the electrochemical experiments in a 3.5 wt. % NaCl solution. We used a saturated calomel electrode (SCE) as a reference electrode, a platinum plate as an auxiliary electrode, and the Al alloy/steel joint as the working electrode. The specimens including Al alloy, steel, and the Al alloy/steel joint with dimensions of 10 mm × 10 mm × 2 mm were prepared. The potentiodynamic polarization curves were recorded with a scanning rate of 2 mV/s and a scanning range starting at −1 V up to 1.5 V.

3. Results and Discussions

3.1. Effect of Ni Coating on Macrostructure of Al Alloy/Steel Joints

Figure 3 shows the weld seam appearance and cross-section appearance of Al alloy/steel joints with different thicknesses of Ni coating. For Al alloy/steel joints without a Ni coating, the top weld seam shape (see Figure 3a) and the bottom weld seam shape (see Figure 3b) were not continuous and not smooth. When the Ni-coating thickness was 5 μm and 10 μm, the shape of the top weld seam (see Figure 3d,g, respectively) and the bottom weld seam (see Figure 3e,h, respectively) appeared better and smoother.

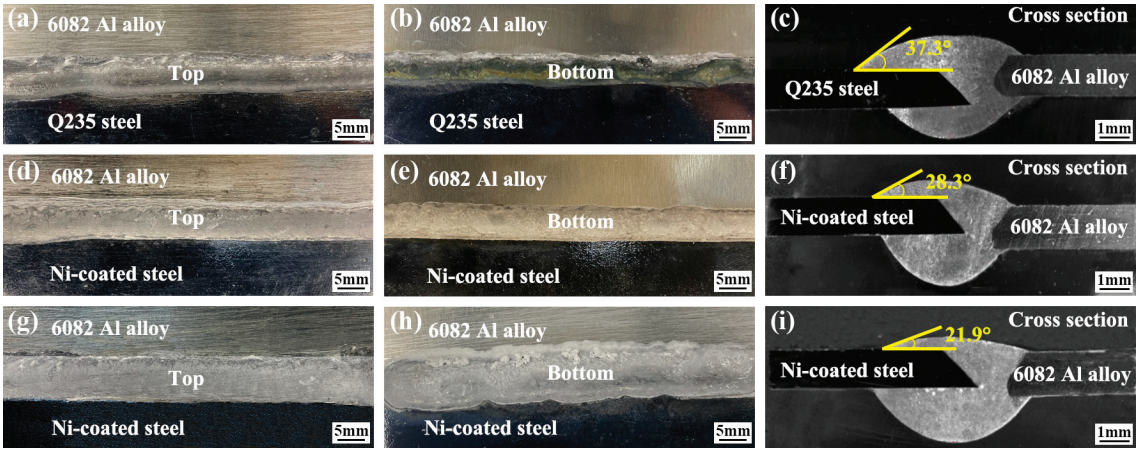

Figure 3. Macrostructure of joints under different thicknesses of Ni coatings: (**a**–**c**) without Ni coating; (**d**–**f**) with 5 μm Ni coating; (**g**–**i**) with 10 μm Ni coating.

Seen from the cross-section appearance of the joints, Ni coating has a significant influence on the wettability and spreading of AlSi12 filler metal on the steel surface. For Figure 3c,f,i, the wetting angle of molten AlSi12 filler metal on the steel surface decreased from 37.3° to 28.3° and then 21.9°. Generally, the smaller the wetting angle, the better the wettability. Thus, the results implied that the addition of Ni could improve the wettability and spreadability of molten Al-Si metal on the steel surface. Yang et al. [18] had reported that Ni could reduce the melting point of Ag-based filler metal and improve its wettability. Sun et al. [19] found Ni coating on the surface of Al_2O_3 particles could improve the wettability of Al_2O_3/Al-10Si composites. These results are consistent with our research results.

3.2. *Influence of Ni Coating on Microstructure of Al Alloy/Steel Joints*

In the process of CMT welding brazing, part of the Al alloy base metal together with AlSi12 filler metal preferred to melt under the action of arc heat due to their low melting point (below 660°C), and the fusion zone formed at the side of Al alloy base metal. Then, the molten Al alloy metal wet and spread on the steel surface, which was still solid because of its high melting point (above 1500°C), so the brazing interface reaction zone formed at the side of the steel base metal [20,21]. The fusion zone and brazing interface reaction zone were analyzed by SEM with EDS point and line scanning. The results are shown in Figure 4 and Table 3.

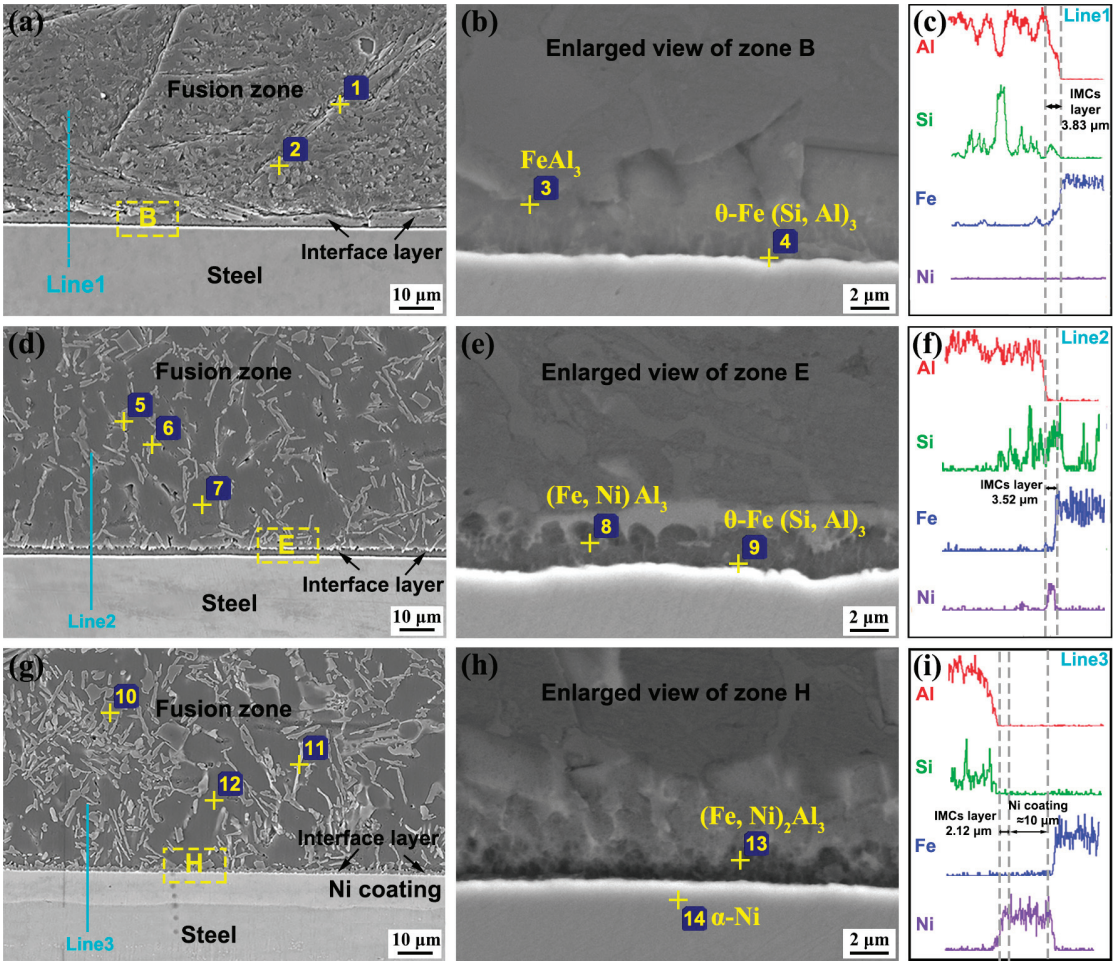

Figure 4. The microstructure and corresponding EDS line scanning results of joints: (**a**–**c**) without Ni coating; (**d**–**f**) with 5 μm Ni coating; (**g**–**i**) with 10 μm Ni coating.

Table 3. The EDS points scanning results and possible phase of corresponding characteristic points in Figure 4.

Points	Atomic Percentage (at. %)				Possible Phase
	Al	Si	Fe	Ni	
1	77.5	4.9	17.6	—	τ_5-$Al_{7.2}Fe_{1.8}Si$
2	97.5	1.2	1.3	—	α-Al
3	69.5	4.0	26.5	—	$FeAl_3$
4	76.6	11.1	12.3	—	θ-Fe (Si, Al)$_3$
5	61.3	0.5	0.2	38.0	Al_3Ni_2
6	80.6	6.0	13.4	1.07	τ_5-$Al_{7.2}$(Fe, Ni)$_{1.8}$Si
7	98.2	1.1	0.7	—	α-Al
8	69.4	3.4	15.7	11.5	(Fe, Ni) Al_3
9	70.8	8.7	20.5	—	θ-Fe (Si, Al)$_3$
10	61.6	0.8	0.2	37.4	Al_3Ni_2
11	78.3	7.1	7.5	7.1	τ_5-$Al_{7.2}$(Fe, Ni)$_{1.8}$Si
12	97.4	0.9	0.9	0.8	α-Al
13	69.3	2.4	18.1	10.2	(Fe, Ni)$_2Al_3$
14	1.7	—	0.3	98.0	α-Ni

Figure 4a exhibits SEM images of the Al alloy/steel joint without Ni coating. The fusion zone near the Al alloy is composed of needle-like compounds and granular-shaped compounds. Figure 4b shows the enlarged view of zone B in Figure 4a. The brazing interface reaction layer at the steel side is composed of dark gray compounds. Points 1-4 were analyzed by EDS point scanning and the results were listed in Table 2. The interface reaction layer was analyzed by EDS line scanning as shown in Figure 4c. From Figure 4c, the thickness of the IMCs layer was about 3.83 μm. The content of Al element decreased, whereas the content of Fe element increased along the path from the fusion zone to the brazing interface reaction zone. According to the EDS points analysis results and Al-Fe-Si ternary alloy phase diagram, in the fusion zone, the thin needle-like phase (point 1) was a τ_5-$Al_{7.2}Fe_{1.8}Si$ and the dark gray phase (point 2) was an α-Al solid solution. Correspondingly, the interface reaction layer consisted of $FeAl_3$ (point 3) formed near the fusion zone and θ-Fe (Si, Al)$_3$ (point 4) formed at the steel side.

Figure 4d shows the microstructure of the joint with 5 μm Ni coating. Figure 4e shows the enlarged view of zone E in Figure 4d. As can be observed, a large number of thin needle-like phases are distributed uniformly in the fusion zone, and the thickness of the IMCs layer decreased to 3.52 μm. Figure 4f shows that the Ni content increases at the interface reaction layer, and Ni element diffuses into the fusion zone. Therefore, in the fusion zone, Al atoms react with the Ni atoms to form Al_3Ni_2 (point 5) and the thin needle-like phase changed from τ_5-$Al_{7.2}Fe_{1.8}Si$ into τ_5-$Al_{7.2}$(Fe, Ni)$_{1.8}$Si (point 6). The α-Al solid solution (point 7) also contained Ni element. Meanwhile, Ni atoms replace some Fe atoms and then react with Al atoms to form (Fe, Ni) Al_3 (point 8) at the interface reaction layer. The gray compound (point 9) was still θ-Fe (Si, Al)$_3$.

When the Ni-coating thickness was 10 μm, the fusion zone contained some small block-shaped tissue, some white dendritical tissue, and a dark-grey matrix. Significantly, the thickness of the interface reaction layer was 12.12 μm, comsisting of about 10 μm Ni coating and 2.12 μm IMCs layer, as shown in Figure 4g,h. Based on the results listed in Table 2, the small block-shaped tissue (point 10) was determined to be Al_3Ni_2, the white dendritical tissue (point 11) was τ_5-$Al_{7.2}$(Fe, Ni)$_{1.8}$Si, and the dark-grey matrix (point 12) was α-Al solid solution. The interface reaction layer was composed of (Fe, Ni)$_2Al_3$ (point 13) near the fusion zone and α-Ni solid solution (point 14). Figure 4i exhibits the elements distribution of A, Si, Fe, and Ni between the Al alloy and steel. Ni element was mainly concentrated in the interface layer. Meanwhile, a small amount of Al and Si elements in the fusion zone passed through the Ni coating to the steel side, and a few Fe elements arrived at the side of the fusion zone. Most of the Ni coating was still solid, so it hindered the diffusion between

Al element and Fe element. Hence, the interface reaction layer was mainly composed of α-Ni solid solution, and some $(Fe, Ni)_2Al_3$ compound formed.

To confirm the phase composition, the Al alloy/steel joint was stripped along the side of the steel, and then the XRD analysis of the fusion zone and the interface reaction zone were performed. The results are shown in Figure 5. For the joint without Ni coating, compounds of α-Al solid solution and τ_5-$Al_{7.2}Fe_{1.8}Si$ appeared. When the thickness of the Ni coating was 10 μm, the Al_3Ni_2 compound and the α-Ni solid solution formed in the joints. Some other phases were hard to be determined.

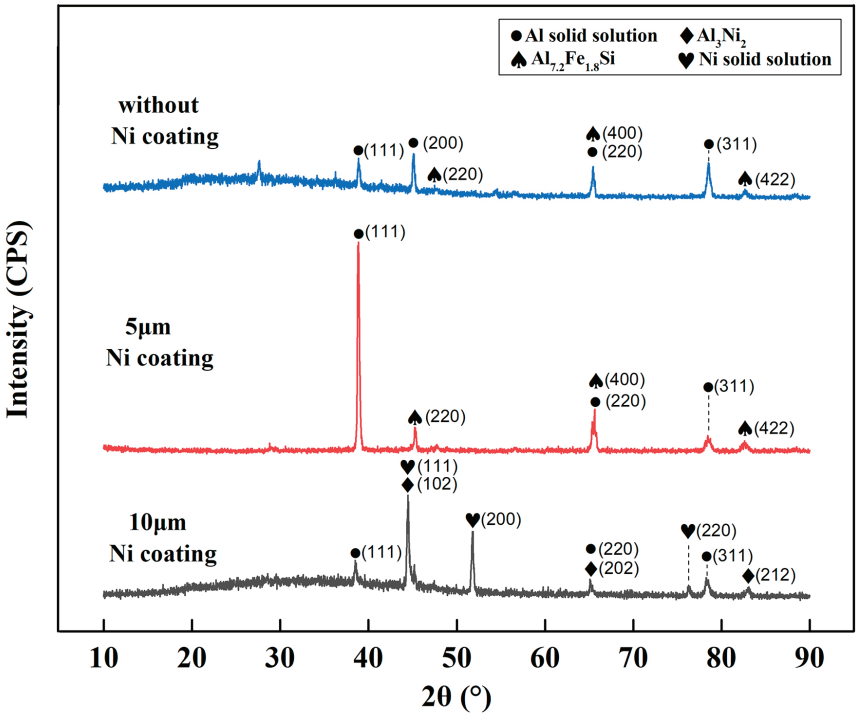

Figure 5. XRD results of Al alloy/steel joints.

Based on the above investigations, using AlSi12 filler metal to join Al alloy and steel by CMT technology, the joint was mainly composed of α-Al solid solution and τ_5-$Al_{7.2}Fe_{1.8}Si$ in the fusion zone, and $FeAl_3$ together with θ-Fe $(Si, Al)_3$ in the interface reaction zone. After coating 5 μm Ni on the steel surface, Ni participated in the metallurgical reaction, and reacted with Al, Fe, and Si elements to form some new phases of τ_5-$Al_{7.2}(Fe, Ni)_{1.8}Si$ and Al_3Ni_2 in the fusion zone. Meanwhile, (Fe, Ni) Al_3 replaced $FeAl_3$ in the interface reaction zone. It can be predicted that the change in microstructure composition will improve the mechanical properties of the joints. When the Ni-coating thickness increased to 10 μm, most of the Ni coating did not melt, so the diffusion between Al element and Fe element was blocked. Interestingly, the $FeAl_3$ phase disappeared, and a new phase of $(Fe, Ni)_2Al_3$ appeared in the IMCs layer near the Al alloy. The interface reaction zone was mainly composed of α-Ni solid solution. Hence, the mechanical properties of the joint will not be poor.

3.3. Action Mechanism of Ni Coating in Interface Reaction Layer

Generally, ΔG^0 is a criterion to predict the spontaneity of a chemical reaction. When the value of ΔG^0 is negative, the chemical reaction occurs easily. Moreover, compounds with the lowest ΔG^0 are most likely to be formed.

Based on thermodynamic data of Al-Fe compounds [22,23], the functions of several compounds are calculated as followings:

$$\Delta G^0_{FeAl^3} = -142770 + 50.58T \quad (1)$$

$$\Delta G^0_{Al^{7.2}Fe_{1.8}Si} = -295355 + 94.59T \quad (2)$$

$$\Delta G^0_{Fe(Al,Si)} = -142770.0 + 50.8T \quad (3)$$

where T represents temperature. During CMT welding brazing, the temperature ranges from 900 K to 1300 K, and the result is $\Delta G^0_{Al^{7.2}Fe_{1.8}Si} < \Delta G_{0\ FeAl_3}$, which indicates that τ_5-$Al_{7.2}Fe_{1.8}Si$ preferentially forms when Al, Fe and Si atoms interact at the interface of the Al alloy and steel.

Figure 6 shows the schematic diagram of the interface reaction layer growth mechanism of an Al alloy/Steel joint with Ni coating by CMT technology. At the initial stage, as shown in Figure 6a, under the action of a pulsed arc, AlSi12 filler metal and a small amount of Al alloy base metal start to melt, while Ni coating remains semi-solid. At this time, Fe and Al atoms cannot form compounds because the Ni coating acts as a barrier layer. However, with the melting of the Ni coating under the action of arc heat, Fe atoms in the steel passed through Ni coating to react with Al and Si atoms, which come from the AlSi12 filler metal and Al alloy base metal, and then τ_5-$Al_{7.2}Fe_{1.8}Si$ formed preferentially. Subsequently, $FeAl_3$ also formed as shown in Figure 6b.

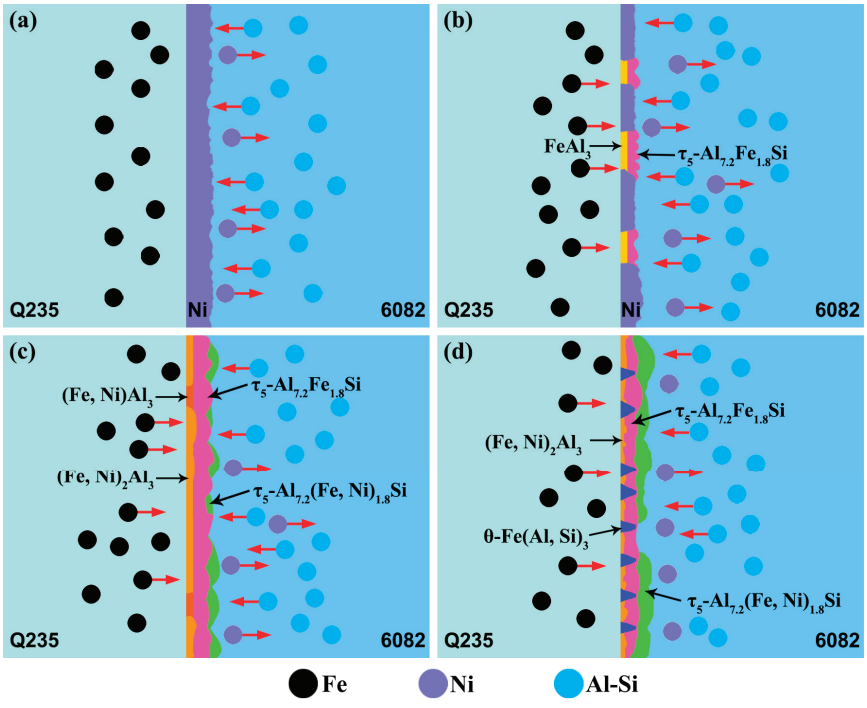

Figure 6. Interface reaction layer growth mechanism of Al alloy/steel joint with Ni coating: (**a**) stage I; (**b**) stage II; (**c**) stage III; (**d**) stage IV.

Generally, the possible compounds between Al and Ni can be calculated by the following formulas:

$$\Delta G^0_{Al_3Ni_2} = -71545.2 + 13.7T \quad (4)$$

$$\Delta G^0_{Al_3Ni} = -48483.8 + 12.7T \quad (5)$$

Based on formulas (4) and (5), Al_3Ni_2 is easier to generate. When the Ni coating starts to melt, Al_3Ni_2 had already appeared in the weld seam zone according to the above microstructure analysis. Fe element is a relative of Ni, so Fe atoms can occupy the positions of Ni atoms to form $(Fe, Ni)_2Al_3$, (Fe, Ni) Al_3 and τ_5-$Al_{7.2}(Fe, Ni)_{1.8}Si$ as a result of their similar electronic structures [24]. Therefore, $(Fe, Ni)_2Al_3$, (Fe, Ni) Al_3, τ_5-$Al_{7.2}Fe_{1.8}Si$, and τ_5-$Al_{7.2}(Fe, Ni)_{1.8}Si$ formed in the interface reaction layer, as shown in Figure 6c.

With the wetting and spreading of molten liquid filler metal on the steel surface, Fe atoms reacts with τ_5-$Al_{7.2}Fe_{1.8}Si$ as follows:

$$Fe + \tau_5\text{-}Al_{7.2}Fe_{1.8}Si = \theta\text{-}Fe\ (Al,Si)_3 \quad (6)$$

Finally, the interface reaction layer consists of τ_5-$Al_{7.2}Fe_{1.8}Si$ and τ_5-$Al_{7.2}(Fe, Ni)_{1.8}Si$ in the weld seam zone together with θ-Fe (Al, $Si)_3$ and $(Fe, Ni)_2Al_3$ at the steel side, as shown in Figure 6d.

3.4. Effect of Ni Coating on Tensile Properties of Al Alloy/Steel Joints

Figure 7 shows the fracture location and tensile strength of joints. For the joint without Ni, it cracked at the brazing interface reaction layer, as shown in Figure 7a. When the Ni-coating thickness was 5 μm and 10 μm, the fracture mode was located in the fusion zone at the Al alloy side, as shown in Figure 7b,c, respectively. With the increase in Ni-coating thickness from 0 μm to 10 μm, the tensile strength first increased and then decreased, and the tensile fracture displacement gradually increased. When the Ni-coating thickness was 5 μm, the tensile strength value reached the maximum of 202.5 Mpa, as shown in Figure 7d. Figure 7e indicates that the addition of Ni coating improves the plastic toughness of the joints.

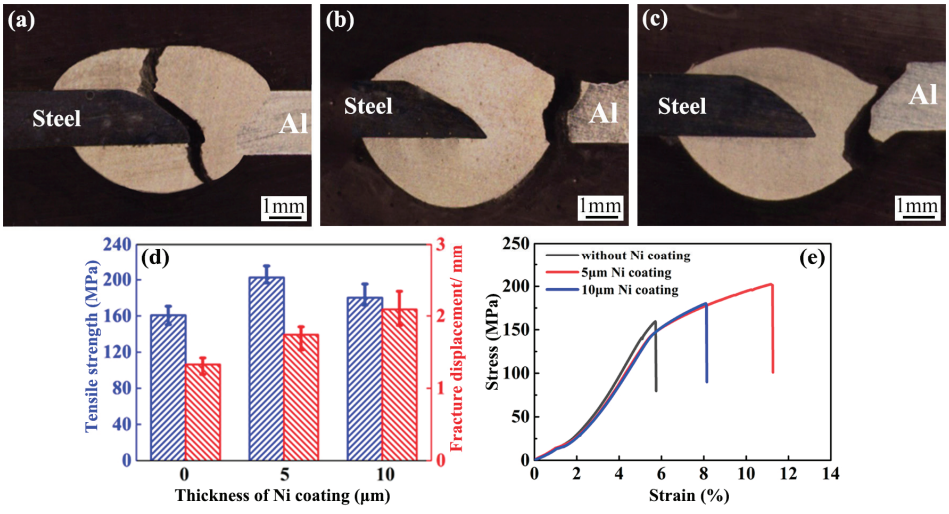

Figure 7. Tensile properties and fracture section morphology of joints: (**a**) fracture location without Ni coating; (**b**) fracture location with 5 μm Ni coating; (**c**) fracture location with 10 μm Ni coating; (**d**) tensile strength and fracture displacement; (**e**) stress-strain curves.

For the joint without Ni coating, $FeAl_3$ formed in the interface reaction layer. The brittle $FeAl_3$ tended to become the source of crack propagation, which resulted in the weakness of the joint during the tensile process. Therefore, the joint cracked at the interface reaction layer. For the joint with Ni coating, the Ni coating melted to occupy the position of the Fe atoms and then generated (Fe, Ni) Al_3, $(Fe, Ni)_2Al_3$ and τ_5-$Al_{7.2}(Fe, Ni)_{1.8}Si$ under the heat action of the arc. The tensile strength of the interface reaction layer was improved as a result of adding Ni into Fe-Al-Si compounds [25,26]. Moreover, when the thickness of the Ni coating was 10 μm, it was too heavy to melt and hindered the diffusion of Fe atoms and Al atoms to avoid the generation of the brittle Fe-Al IMCs and prompt the formation of Ni solid solution. Thus, the tensile strength of the interface reaction layer was high, and the joint cracked at the Al alloy side.

The fracture morphologies of the joints were observed by SEM and are shown in Figure 8. In Figure 8a, tearing ridges and cleavage steps were observed in the fracture surface, which exhibited the brittle fracture mode. Based on the EDS result for point 15, the brittle IMC in the fracture surface was $FeAl_3$, which easily became a source of crack propagation and promoted the crack growth, so the corresponding tensile strength of the joint was the lowest. In Figure 8b,c, a large number of dimples were found in the fracture surface, and they showed a typical ductile fracture mode. In addition, the dimples in the fracture with 5 μm Ni coating were more uniform and finer than that with 10 μm Ni coating. The tensile strength of the former joint reached up to the maximum.

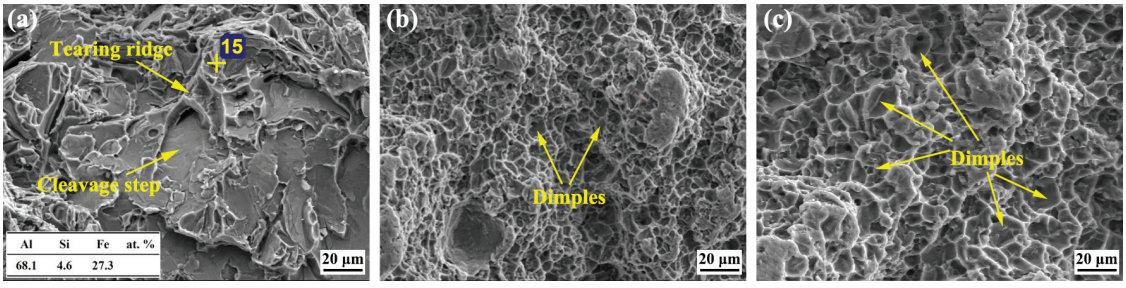

Figure 8. Tensile fracture morphology of Al alloy/steel joints under different thicknesses of Ni coating: (**a**) without Ni coating; (**b**) with 5 μm Ni coating; (**c**) with 10 μm Ni coating.

3.5. Effect of Ni Coating on Corrosion Resistance of Al Alloy/Steel Joints

The potentiodynamic polarization curves of joints were measured to investigate the corrosion resistance and the results are shown in Figure 9. Figure 9a shows the variation curve of open-circuit potential with time. When the open circuit potential stabilized, the polarization curves were recorded. As can be seen in Figure 9b, all the curves of joints showed an obvious passivation area, and this indicated the passive film on the surface of joints formed spontaneously to delay their corrosion, but their potential range of the passivation area was different. In order to obtain the related data about the corrosion potential (E_{corr}) and the self-corrosion current density (I_{corr}), CView software was used to fit the curves, and the fitting results are listed in Table 4.

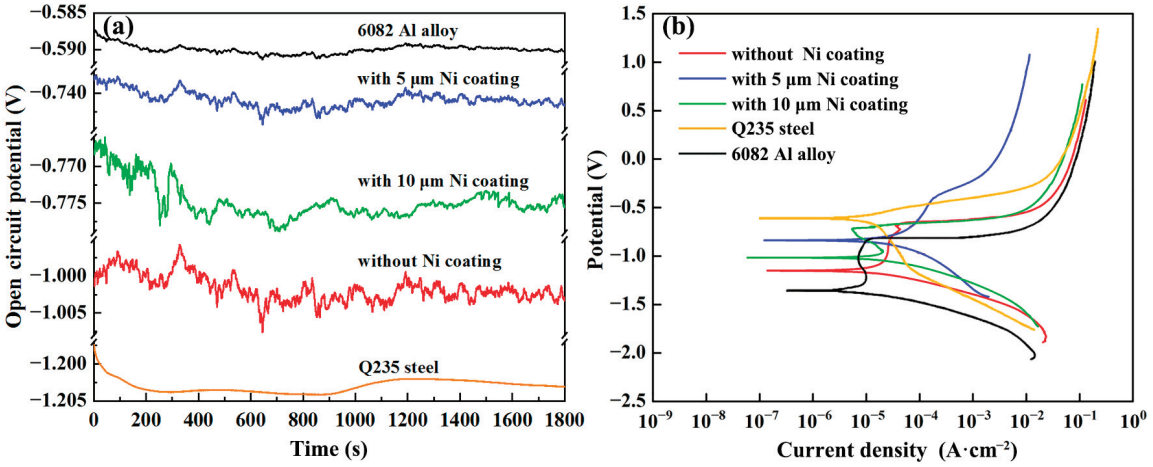

Figure 9. Polarization curves of Al alloy/steel joints with different thicknesses of Ni coating: (**a**) open circuit potential–time curves; (**b**) polarization curves.

Table 4. E_{corr} and I_{corr} fitted for the curves in Figure 9.

Samples	E_{corr}/V	I_{corr}/(A·cm^{-2})
Al alloy	−0.592	3.35×10^{-6}
Steel	−1.200	5.20×10^{-5}
Without Ni coating	−1.003	8.60×10^{-6}
5 μm Ni coating	−0.742	5.65×10^{-6}
10 μm Ni coating	−0.775	4.94×10^{-6}

As seen from Figure 9 and Table 4, the E_{corr} of the Al alloy plate was the highest, that of the steel plate was the lowest, and that of the joint was between them. Nevertheless, their corrosion current was in reverse order. Meanwhile, compared with the joints without Ni coating and with Ni coating, the E_{corr} of the joint with Ni coating was higher while the I_{corr} of the joint with Ni coating was smaller. Some studies [27] have shown that E_{corr} reflects the corrosion tendency of materials, and I_{corr} reflects the corrosion rate of materials. The greater E_{corr} and the smaller I_{corr}, the better the corrosion resistance of materials.

For the Al alloy/steel joints, galvanic corrosion occurred between the weld seam zone and the steel. The steel with a low corrosion potential can protect the weld seam from corrosion. It was also found that the IMCs layer can accelerate the corrosion of the joint. After adding Ni into the joint, the corrosion resistance of the joint was improved. One reason was that Ni coating hindered the diffusion reaction between Al and Fe, which resulted in a reduction in IMCs thickness. The other reason was that Ni atoms reacted with Al to form Ni_2Al_3 and replaced Fe atoms to form $(Fe, Ni)_2Al_3$, and these compounds improve the corrosion resistance of the joints [28–30].

4. Conclusions

In this paper, a CMT welding-brazing process was conducted to join Al alloy and the steel under different Ni coatings by using AlSi12 as a filler wire. The effects of Ni coating on macrostructure, microstructure, tensile properties, and corrosion resistance of the joints were investigated. The main conclusions can be summarized as follows:

(1) Ni coating can improve the wettability and spreadability of molten AlSi12 filler metal on the steel surface to obtain a good appearance of Al alloy/Steel joints.

(2) For the joint without Ni coating, the weld seam zone of the joint was mainly composed of α-Al solid solution and τ_5-$Al_{7.2}Fe_{1.8}Si$. For the joint with Ni coatings of 5 μm and

10 μm thicknesses, the weld seam zone of joints consisted of α-Al solid solution, τ_5-$Al_{7.2}(Fe,Ni)_{1.8}Si$, and newly formed Al_3Ni_2.

(3) Ni coating can change the phase composition, and the brittle IMCs were from $FeAl_3$ to (Fe, Ni) Al_3 and (Fe, Ni)$_2Al_3$ at the interface reaction layer.

(4) Ni coating can improve the tensile strength of Al alloy/Steel joints such that these joints cracked at the weld seam zone near the Al alloy. When the thickness of the Ni coating was 5 μm, the tensile strength of the joint reached a maximum of 202.5 Mpa. Additionally, Ni coating on the steel surface can improve the corrosion resistance of the joints.

Author Contributions: Conceptualization, C.Z., J.P. and M.W.; methodology, C.Z., Y.S. and J.R.; validation, C.Z. and M.W.; writing—original draft preparation, C.Z. and J.P.; writing—review and editing, W.L. and Y.S. All authors have read and agreed to the published version of the manuscript.

Funding: This work is sponsored by the National Natural Science Foundation of China (No. 51675249), Natural Science Research General Project of Jiangsu Province (No. 19KJB46001), the Excellent Scientific and Technological Innovation Team of Universities in Jiangsu Province and Engineering Research Center Program of Development & Reform Commission of Jiangsu Province (Grant No. [2021] 1368) and Changzhou Science and Technology Plan Project (No. CJ20190028).

Institutional Review Board Statement: Not applicable.

Informed Consent Statement: Not applicable.

Data Availability Statement: The data used to support the findings of this study are available from the corresponding authors upon request.

Conflicts of Interest: The authors declare no conflict of interest.

References

1. Liu, Z.; Li, Y.; Zhao, J.; Fu, L.; Li, L.; Yu, K.; Mao, X.; Zhao, P. Research on Aluminum Alloy Materials and Application Technology for Automobile Lightweigh. *Mater. China* **2022**, *41*, 786–795.
2. Kang, Y. Lightweight Vehicle Advanced High Strength Steel and Energy-Saving and Emission Reduction. *Iron Steel.* **2008**, *6*, 1–7.
3. Singh, J.; Arora, K.; Shukla, D. Dissimilar MIG-CMT weld-brazing of aluminium to steel: A review. *J. Alloys Compd.* **2019**, *783*, 753–764. [CrossRef]
4. Chen, Y.; Xue, S.; Wang, B.; Han, Y. Development Status and Future Direction of Welding Technology in the Automotive Lightweight. *Mater Rep.* **2019**, *33*, 431–440.
5. Li, L.; Xia, C.; Song, Y.B.; Zhou, D.J. Application status and outlook of aluminum alloys in new energy vehicles. *Light Alloy Fabr. Technol.* **2017**, *45*, 18–25.
6. Wu, J.; Xue, S.; Fei, W.P.; Han, Y.; Zhang, P. Present Status and Development Trend for Brazing Aluminum to Steel. *Mater Rep.* **2019**, *33*, 3533–3540.
7. Gao, C.; Yang, J.; Li, Z.; Zhao, Y.; Liu, H.; Zhang, L. Research progress on advanced dissimilar joining methods of aluminum/steel. *Weld. Join.* **2021**, *29*, 7–20.
8. Farhad, O.; Ehsan, S.; Meysam, T.; Fadhlina, M.; Masoud, S. On the role of molybdenum on the microstructural, mechanical and corrosion properties of the GTAW AISI 316 stainless steel welds. *Journal of Materials Research and Technology* **2021**, *13*, 2115–2125.
9. Farhad, O.; Ehsan, H.; Meysam, T.; Ehsan, S.; Khairur, J.; Astuty, A. Microstructure, Hardness and Corrosion Be-havior of Gas Tungsten Arc Welding Clad Inconel 625 Super Alloy over A517 Carbon Steel Using ERNiCrMo3 Filler Metal. *J. Mater. Eng. Perform.* **2020**, *29*, 6919–6930.
10. Amiri, E.; Farhad, O.; Meysam, T.; Ehsan, S.; Fadhlina, M.I. Study and selection of most appropriate filler rod for GTAW of S32750 super duplex steel joints: A comprehensive study on microstructural, mechanical and corrosion properties. *Mater. Chem. Phys.* **2021**, *270*, 124839. [CrossRef]
11. Qin, G.L.; Wu, C.S. State-of-art of Brazing-fusion Welding Processes of Dissimilar Metals between Aluminum Alloy and Steel. *J. Mech. Eng.* **2016**, *52*, 24–35. [CrossRef]
12. Maryam, R.; Nima, R.; Ali, M. Improvement of mechanical properties of aluminum base composite reinforced by steel Ck75 wire through explosive welding. *Rev. Metal. Madrid.* **2021**, *57*, 196.
13. Maryam, R.; Nima, R.; Mehdipour, O. Production of steel 1006 wire reinforced aluminum base composite by explo-sive welding. *Rev. Metal. Madrid.* **2020**, *56*, 165.
14. Shao, Z.Y.; Zhang, C.; Lin, Y.M.; Tan, Z.Y. Effect of Different Wire Composition on Microstructure and Properties of CMT Welding-brazing of Aluminum/Steel. *H. Work. Technol.* **2022**, *51*, 114–119.

15. Shi, Z.; Li, R.; Yu, Z.; Ge, Q.; Wu, M. Effect of wettability and spreadability of AlSi5 filler and interfacial behavior of AlSi5 filler and galvanized steel with TIG welding-brazing. *Weld. Technol.* **2014**, *43*, 7–9+5.
16. Zhang, C.; Wu, M.; Pu, J.; Shan, Q.; Sun, Y.; Wang, S.Q.; Hermann, S.K.U.G. Effect of Cu Coating on Microstructure and Properties of Al/Steel Welding-Brazing Joints Obtained by Cold Metal Transfer (CMT). *Coatings* **2022**, *12*, 1123. [CrossRef]
17. Huang, J.-K.; Wang, Z.-Y.; Liu, N.; Yu, S.R.; Fan, D. Effect of Metal Coating on Microstructure and Properties of Aluminum/Steel Laser Welding-Brazing Joint. *J. Mater. Eng.* **2018**, *46*, 99–105.
18. Yang, G.J.; Liu, J.W.; Han, L. Effect of Cu,Sn,Ni on property of Al-Si based solder. *Weld Join.* **2015**, *5*, 50–55+70–71.
19. Sun, P.; Dong, Z.; Chen, Y.; Yan, H.; Luo, C.; Song, H.; Hu, Z. Characterization of Ni coating layer of Al_2O_3 particles and their wettability behavior in Al_2O_3@Ni/Al-10Si composites. *Appl. Surf. Sci.* **2020**, *526*, 146660. [CrossRef]
20. Yang, J.; Hu, A.M.; Li, Y.L.; Zhang, P.; Chandra, S.; Yu, Z. Heat input, intermetallic compounds and mechanical properties of Al/steel cold metal transfer joints. *J. Mater. Process. Technol.* **2018**, *272*, 40–46. [CrossRef]
21. Singh, J.; Arora, K.S.; Shukla, D.K. Lap weld-brazing of aluminium to steel using novel cold metal transfer process. *J. Mater. Process. Technol.* **2020**, *283*, 116728. [CrossRef]
22. Hultgren, R.; Desai, P.D.; Hawkins, D.T.; Gleiser, M.; Kelley, K.K. *Selected values of the thermodynamic properties of binary alloys*; American Society for Metals: Metals Park, OH, USA, 1973; p. 536.
23. Richards, R.W.; Jones, R.D.; Clements, P.D.; Clarke, H. Metallurgy of continuous hot dip aluminizing. *Int. Mater. Rev.* **1994**, *39*, 191–212. [CrossRef]
24. Qi, J.; Song, Y.Q. Experimental studies on the diffusion reaction of Al /Ni /Fe interface. *Met. Mater. Metall. Eng* **2007**, 8–10+14.
25. Liu, C.T.; Jemian, W.; Inouye, H.; Cathcart, J.V.; David, S.A.; Horton, J.A.; Santella, M.L. *Initial Development of Nickel and Nickel-Iron Aluminides for Structural Uses*; No. ORNL-6067; Oak Ridge Natl. Lab.: Oak Ridge, TN, USA, 1984.
26. Bertoncello, J.C.; Manhabosco, S.M.; Dick, L.F. Corrosion study of the friction stir lap joint of AA7050-T76511 on AA2024-T3 using the scanning vibrating electrode technique. *Corros. Sci.* **2015**, *94*, 359–367. [CrossRef]
27. Pu, J.; Xie, P.; Long, W.; Wu, M.; Sheng, Y.; Sheng, J. Effect of current on corrosion resistance of duplex stainless steel layer obtained by plasma arc cladding. *Crystals* **2022**, *12*, 341. [CrossRef]
28. Wu, J.; Liu, Y.; Li, C.; Wu, Y.; Xia, X.; Li, H. Recent Progress of Microstructure Evolution and Performance of Multiphase Ni_3Al-Based Intermetallic Alloy with High Fe and Cr Conten. *Acta Metall. Sin.* **2020**, *56*, 21–35.
29. Popov, A. Effect of electronic nature and substitution behavior of ternary microadditions on the ductility of polycrystalline nickel aluminides. *Acta Mater.* **1997**, *45*, 1613. [CrossRef]
30. David, S.; Jemian, W.; Liu, C.; Horton, J. Welding and weldability of nickel-iron aluminides. *Weld J.* **1985**, *64*, 22.

coatings

MDPI

Article

The Effect of Various Contaminants on the Surface Tribological Properties of Rail and Wheel Materials: An Experimental Approach

Rabesh Kumar Singh [1], Mahesh Shindhe [2,*], Prashant Rawat [3,*], Ashish Kumar Srivastava [4], Gyanendra Kumar Singh [5], Rajesh Verma [6], Javed Khan Bhutto [6] and Hany S. Hussein [6,7]

[1] Centre for Advanced Studies, Lucknow 226031, Uttar Pradesh, India
[2] Department of Mechanical Engineering, Indian Institute of Technology (ISM), Dhanbad 826004, Jharkhand, India
[3] Department of Aerospace Engineering, Indian Institute of Technology Madras, Chennai 600036, Tamil Nadu, India
[4] Department of Mechanical Engineering, G.L. Bajaj Institute of Technology and Management, Greater Noida 201306, Uttar Pradesh, India
[5] Department of Mechanical Engineering, School of Mechanical, Chemical and Materials Engineering, Adama Science and Technology University, Adama P.O. Box 1888, Ethiopia
[6] Department of Electrical Engineering, College of Engineering, King Khalid University, Abha 61411, Saudi Arabia
[7] Department of Electrical Engineering, Faculty of Engineering, Aswan University, Aswan 81528, Egypt
* Correspondence: itsshindhe@gmail.com (M.S.); prashant.rawat@iitm.ac.in (P.R.)

Abstract: This study reports on the tribological behavior of Indian rail track and wheel materials under different contaminants. A pin-on-disc tribometer was selected for the experimental analysis in ambient conditions (temperature of 24.9 °C and relative humidity of 66%). Sand, mist, leaves, and grease were the contaminants used in this investigation. The railway track was used to make the pin, and the wheel was used to make the disc. The acquired results were analyzed using frictional force and wear depth as a function of time as the variables. These pollutant effects were compared to no-contaminant conditions. It was observed that the sand increased the friction force and wear depth, whereas oil decreased friction and wear. Mist and leaves also reduced friction and wear. The effect of leaves was higher than the mist. The effect of load on various contaminants was also investigated. The results showed that as the load increased, the friction force and wear also increased for all contaminants. The results of this study can help in understanding the wear phenomenon of wheels and rail tracks in different parts of India.

Keywords: wear; rail track; rail wheels; pin-on-disc; friction; contamination

Citation: Singh, R.K.; Shindhe, M.; Rawat, P.; Srivastava, A.K.; Singh, G.K.; Verma, R.; Bhutto, J.K.; Hussein, H.S. The Effect of Various Contaminants on the Surface Tribological Properties of Rail and Wheel Materials: An Experimental Approach. *Coatings* **2023**, *13*, 560. https://doi.org/10.3390/coatings13030560

Academic Editor: Esteban Broitman

Received: 3 February 2023
Revised: 24 February 2023
Accepted: 1 March 2023
Published: 5 March 2023

1. Introduction

Goods and public transportations are critical for the growth of any nation. Because of its low cost, the railway is one of India's most vital modes of transportation. The maintenance of railway tracks and wheels is difficult and necessary because both are directly exposed to different environmental conditions. As the rail moves from one region to another, the environmental conditions may change gradually or drastically. This change in environmental conditions profoundly influences the wear and friction behavior of the wheel and track. Further, the railway tracks are also surrounded by unwanted objects or pollutants, which may get engaged between the railway wheels and tracks. These pollutants also affect the wear and friction between the railway track and the wheel. These pollutants include small plants around the rail track or left-out grease after the maintenance of the railway tracks also affect the wear and friction behavior between the railway track and wheel.

Under these environmental conditions, it is critical to monitor the wear of rail tracks and wheels [1]. If the wear on the rail track and wheels is not noticed and resolved promptly, it can lead to fatal accidents. Hence, it is essential to properly investigate the tribological characteristics of rail tracks and wheels and their performance under varied pollutants, similar to real-life situations. Wheel and rail tracks perform motion in two ways, i.e., rolling and sliding (Figure 1). The wheel flange and rail head undergo slipping motion, whereas the rail head and wheel tread accomplish rolling motion [2]. Extreme sliding motion occurs when the wheel flange and rail head make contact. Wear and friction are high at this point of contact, and the contact area is about 1 cm^2 [3]. It is also known that friction is a desired property for the rail wheel pair, but it should not be too high or too low [4]. A desirable coefficient of friction between the rail track and wheel is 0.25 to 0.4. This range of coefficient of friction is considered to be desirable, which provides sufficient traction between the rail track and wheel to maintain control and prevent sliding. Within this range, the wear and tear between the rail track and wheel are minimal.

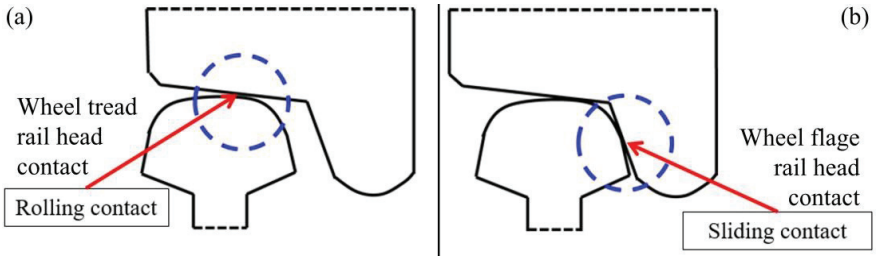

Figure 1. Rail track and wheel contact.

1.1. Effect of Temperature

Diverse external environments and pollutants affect the contact conditions and alter the tribology between the rail track and wheel. Some researchers investigated the influence of temperature variation, which takes place due to changes in bulk material characteristics [5]. As the temperature at the rail track and wheel contact increases, the oxidation process at the contact point also increases. Furthermore, the oxidation at the point the rail track and wheel meet causes wear and friction [6]. The increase in temperature contributes to the formation of oxide debris, which contributes to the formation of a wear-resistant layer, which reduces the wear [7]. Furthermore, a few studies have also shown a reduction in wear and friction levels with an increase in temperature [8,9]. However, the wear rate on contact surfaces increases significantly with the reduction in external temperature [10].

1.2. Effect of Humidity

The relative humidity reduces the coefficient of friction until saturation, at which time the coefficient of friction becomes independent of relative humidity [11]. Above 70% relative humidity, the friction levels are low, whereas the friction levels at 40% relative humidity (approximately) are comparable to dry circumstances [12]. Corrosive wear in train wheels is more prevalent when relative humidity exceeds 80%. If the relative humidity is greater than 10% but less than 70%, adhesive wear occurs [13]. An increase in humidity causes an oxide layer to grow on the worn surface. As a result, it reduces the adhesion phenomena, lowering the coefficient of friction [14]. Along with the presence of water, the parameters between the points of contact change. Water is known to diminish the adhesion of the rail to the wheel. For flat surfaces, the adhesion coefficient attained is low due to the presence of water. Surface oxidation is responsible for this phenomenon. This decrease in adhesion is influenced by surface topography, water temperature, and surface oxidation [15]. The water temperature also has a significant effect on adhesion. Adhesion increases if the temperature is kept high under wet environmental conditions [16]. If snow particles are present in the contact, they melt in layers responding to pressure. This results

in the formation of haematite (Fe_2O_3) flakes. This phenomenon reduces both friction and wear. The principal mechanism of wear is oxidative wear due to the presence of snow [17]. The hardness of hematite flakes is greater than the rail track and wheel. These flakes are also brittle and can be crushed easily into particles of small sizes during sliding. This hard particle debris between the rail track and wheel then acts as third-body wear debris [18]. These oxide flakes undergo minimal elastic and/or plastic deformation during contact. Furthermore, as the hardness of these particles is greater than the rail track and wheel, they embed themselves into the clean area of the rail track and wheel. These embedded flakes now act as a barrier between the rail track and wheel, which avoids direct contact between the rail track and wheel [19]. Moreover, the embedded flake particles help in holding the applied lubricants more firmly for a longer time. As a result, the wear rate between the rail track and wheel reduces.

1.3. Effect of Lubricant

Lubricants are designed to reduce friction wherever they are employed [20,21]. When a lubricant is applied between the rail wheel pair, the coefficient of friction decreases. Grease, as a lubricant, performs a similar function and prevents subsurface degradation [22]. In dry contact conditions (without lubricant), surface damage occurs [23]. Furthermore, when oil and water are added simultaneously, they generate a boundary or mixed film that reduces adhesion between the rail and the wheel [24]. Compared to dry circumstances, the presence of leaves effectively lowers the coefficient of friction by a factor of four. The leaves cause a slick coating to grow on the tracks [25]. Leaves also have a chemically reactive surface. This chemically reactive surface of phosphate and calcium is easily sheared away [26]. If the glycol water combination is present and leaves are added, the coefficient of friction does not reduce. In this scenario, the glycol water combination hinders the activity of leaves [27].

1.4. Effect of Parameters

Several other impurities, such as cement and iron oxides, affect the friction and wear between the rail track and wheel. Silica granules in cement penetrate rail wheel contact and cause three-body abrasion, in the same way as sand. Cement also reduces the energy wear coefficient [28]. Oxide flakes lower the amount of wear. When oxide layers are thin, they protect against wear and smooth topography. However, thicker layers or rough topography increase the wear [9,28]. The iron oxide can assist in the preservation of friction values. There is a relationship between increasing wear volume and acting pressure [27,29]. The wear rate depends on contact pressure; as the contact area increases, the wear rate decreases because the contact pressure decreases. As a result, independent of load, the wear rate increases as contact pressure increases [30]. High adhesive force is related to high frictional force [31]. The frictional force defines the grip between the rail track and the wheel. This is defined as the degree of traction or traction level. It is referred to as the amount of grip or friction between two surfaces in contact with each other. The degree of traction is also affected by these various parameters. If the degree of traction is high, then there is better control and stability, whereas lower levels of traction can increase the risk of sliding, slipping, or losing control. The traction level increases in the presence of leaves or water, which is equivalent to the absence of leaves [32].

The above review proved that various environmental variables substantially impact the wear phenomena of rail wheels and tracks. The rail tracks are open environments surrounded by dirt and contaminants. A train might encounter these multiple adversaries in a single run. The current investigation addressed the effect of contaminants found around the rail track on the wear rate of the rail track and wheel. The experiment was conducted using a universal pin-on-disc tribometer. The rail track was used to make the pin, and the rail wheel was used to make the disc. The contaminants considered for the study were sand particles, leaves, mist, and grease. All the contaminants were collected from the nearest railway track. The effect of these contaminants on the wear rate between the rail track and wheel was examined and compared with the pure dry (no contamination)

situation. This investigation was conducted at room temperature and relative humidity for three different loading conditions 5 N, 10 N, and 15 N.

2. Materials and Experiment

2.1. Experimental Setup

A pin-on-disc tribometer (DUCOM) was used in the experiment (Figure 2). The setup consisted of three components: a tester with a pin and disc configuration, a controller for managing rpm, temperature, and time, and a computer system for data storage and analysis. The load capability of the machine used as a tribometer was 5–100 N. The disc had a rotational speed minimum of 200 and a maximum of 2000. The machine had several environments to perform different tests. The pin was static in a pin holder, and the disc rotated according to the input value within the machine's capacity. The track diameter was adjustable. Figure 2c depicts the configuration for forming mist using a minimum quantity lubricant (MQL) unit and compressor, as well as a nozzle at the pin and disc arrangement. The temperature sensor in Figure 2c displays the room temperature and humidity.

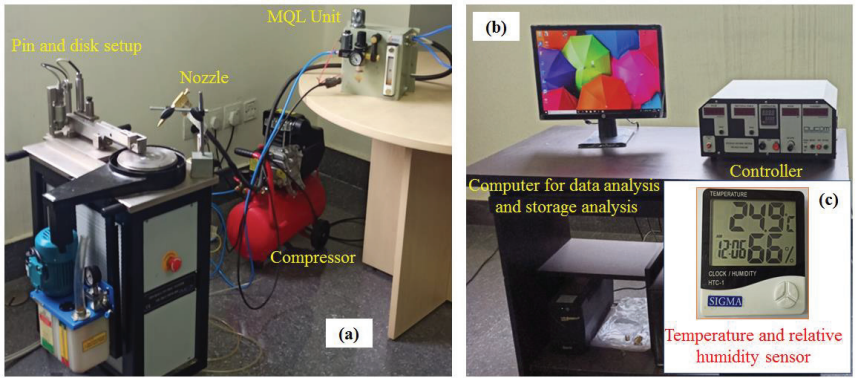

Figure 2. (**a**) Pin-on-disc tribometer setup, (**b**) Control and data analysis system, and (**c**) Temperature and relative humidity sensor showing the ambient conditions.

2.2. Materials

The Research Design and Standards Organisation (RDSO), Lucknow, India, provided the experimental materials, i.e., both railway track and wheel. The chemical composition and mechanical properties of the materials are shown in Tables 1–4. Figure 3 shows the preparation of a test specimen of a pin made of rail material and a disc built of wheel material. Both were prepared as per the ASTM G99 testing standard. The peak diameter of the disc (rail wheel) was 155 mm with 8 mm disc thickness. The surface roughness of the disc before the experiment was 0.2 µm.

Table 1. Chemical components in the wheel [33].

Specification	C %	Mn %	P %	S %	Si %
IRS: R19/93	0.52	0.60–0.85	0.03	0.03	0.15–0.4

Table 2. Mechanical properties of wheel [33].

Specification	Yield Strength (MPa)	Ultimate Tensile Strength (MPa)
IRS: R19/93	50% of Ultmiate tensile strength	820–940

Table 3. Chemical components in rail [33].

Specification	C %	Mn %	P %	S %	Si %	Al %
Rail (grade 880)	0.60–0.80	0.80–1.35	0.03	0.03	0.10–0.50	0.015

Table 4. Mechanical properties of rail [33].

Specification	Yield Strength (MPa)	Ultimate Tensile Strength (MPa)
Rail (grade 880)	460	880

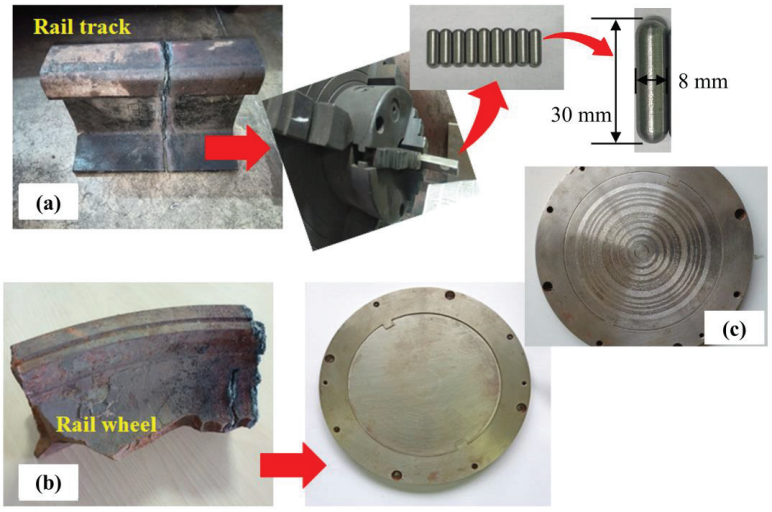

Figure 3. Fabrication of (**a**) pin and (**b**) disc from rail track and wheel material, (**c**) Disc after testing.

2.3. Experimental Details

The experiment was carried out under five distinct conditions. There were three experiments for each condition with three distinct loads, namely 5 N, 10 N, and 15 N. Table 5 displays the experimental details. The initial contact Hertzian pressure was calculated using the Hertzian contact theory equation (Equation (1)). The theory makes the following assumptions: (i) Contacting bodies are elastic, (ii) Material properties of both contacting bodies are Homogeneous and isotropic, and (iii) Deformation is small.

$$Intial\ Contact\ Hertzian\ Pressure\ (P_O) = F \times \left[\frac{1-\vartheta^2}{E_{eff}}\right] \times \left[\left(R_{pin}^{-1.5} + R_{disc}^{-1.5}\right)^2\right] \quad (1)$$

where,

P_O is the initial contact Hertzian pressure in Mpa,
F is the applied normal load in N (5 N, 10 N, and 15 N for this investigation),
ν is the Poisson's ratio of the pin and disc,
E_{eff} is the effective elastic modulus of the contacting bodies in Pa^{-1},
R_{pin} is the radius of curvature of the hemispherical nose of the cylindrical pin in mm,
R_{disc} is the radius of the curvature of the flat disc in mm.

Here, the E_{eff} can be calculated using Equation (2).

$$\frac{1}{E_{eff}} = \frac{1-\vartheta_{pin}^2}{E_{pin}} + \frac{1-\vartheta_2^2}{E_{disc}} \quad (2)$$

where,

ϑ_{pin} is the Poisson's ratio of pin (0.3 for this investigation),
ϑ_{disc} is the Poisson's ratio of the disc (0.3 for this investigation),
E_{pin} is Young's modulus of the pin in GPa (190 GPa for this investigation),
E_{disc} is Young's modulus of the disc in GPa (200 GPa for this investigation).

Here, the radius of curvature of the pin can be calculated using Equation (3).

$$R_{pin} = \frac{(h - r_{nose})^2}{2 \times r_{nose}} \tag{3}$$

where,

h is the total height of the pin in mm (30 mm for this investigation),
r is the radius of the hemispherical nose in mm (4 mm for this investigation).

Here, the radius of curvature of the flat disc can be estimated using Equation (4).

$$R_{disc} = \frac{D^2}{8t} \tag{4}$$

where,

D is the diameter of the disc in mm (155 mm for this investigation),
t is the thickness of the disc in mm (8 mm for this investigation).

The initial contact Hertzian pressure for loading conditions 5 N, 10 N, and 15 N can be estimated using Equations (1)–(4). The estimated initial contact Hertzian pressure for loading conditions 5 N, 10 N, and 15 N were 3.62 MPa, 7.25 MPa, and 10.88 MPa, respectively.

According to the Track Design Handbook for Broad Gauge, published by the Research Designs and Standards Organization (RDsO), the maximum permissible contact pressure between the wheel and the track is 10–12 MPa for passenger trains and 14–16 MPa for heavy freight trains. The experimental initial contact Hertzian pressure values approximately reached the maximum standard values provided by the RDSO at higher loads only.

Table 5. Experimental details.

Parameters	Dry
Temperature (°C)	24.9
Relative Humidity (%)	66
Load (N)	5, 10, 15
Sliding Distance (m)	100
Time (s)	100
sliding velocity (m/s)	1

The experiment was carried out over a 100 m continuous sliding distance. The sliding speed was also maintained at 1 m/s. The temperature was 24.9°C, and the relative humidity was 66%, which remained constant throughout the experiment. There were five conditions dry, using water as MQL, sand, leaf, and grease. The wear track diameter and the rpm are shown in Table 6. The variation of wear track diameter was done by keeping the sliding velocity constant.

Table 6. Wear track diameter, RPM variation as per the different loads.

Conditions	Variables	5 N	10 N	15 N
Dry	Track diameter (mm)	15	22	40
	RPM	1273	868	477
Leaves	Track diameter (mm)	48	54	60
	RPM	398	354	318
Sand	Track diameter (mm)	72	76	82
	RPM	265	251	239
MQL	Track diameter (mm)	94	90	88
	RPM	.212	212	217
Grease	Track diameter (mm)	96	104	108
	RPM	199	184	174

The MQL represented the mist conditions of the Western Ghats or during rainfall. The mist would probably affect the tribology of the rail and wheel. The water in MQL was supplied at a rate of 200 mL/hr to create a mist condition for the pin-on-disc test. Babool (Acacia Nilotica) leaves were used. These leaves are widely available in India. Furthermore, these plants are frequently seen near railway lines. As a result, these leaves will get in between the rail and wheel contacts, influencing the tribology between the rail and wheel. The effect of these leaves on the contact state of the rail wheel was measured using the leaves in a pin-on-disc tribometer configuration. The leaves and sand used for the experiments can be seen in Figure 4a,b. The sand was fairly common in the Rajasthan state since there is a desert area (Thar Desert), and several rivers across the Indian continent carry the sand. Sand might become entrapped between the rail and the wheel of a railway operating in these places. The sand was applied between the rail and the wheel to achieve the necessary amount of adhesion when adhesion declined. As a result, it became vital to investigate the influence of sand on rail and wheel tribology. The sand used in the study was river sand obtained from the riverbanks. Another condition in the current investigation was the influence of lubrication or grease. Grease and lubricants were placed on the railway lines when appropriate. As a result, grease might have easily gotten between the rail and wheel contact. As a result, the current work considered the effect of grease by inserting grease between the pin and disc. Figure 4c depicts the grease utilized. Table 7 displays the grease specifications.

All four conditions, namely, leaves, sand, MQL, and grease, were compared with the fifth condition, which was the pure dry condition. The dry condition had ambient humidity and ambient temperature, and no contaminants. Here, all experiments were carried out at 24.9°C and 66% relative humidity.

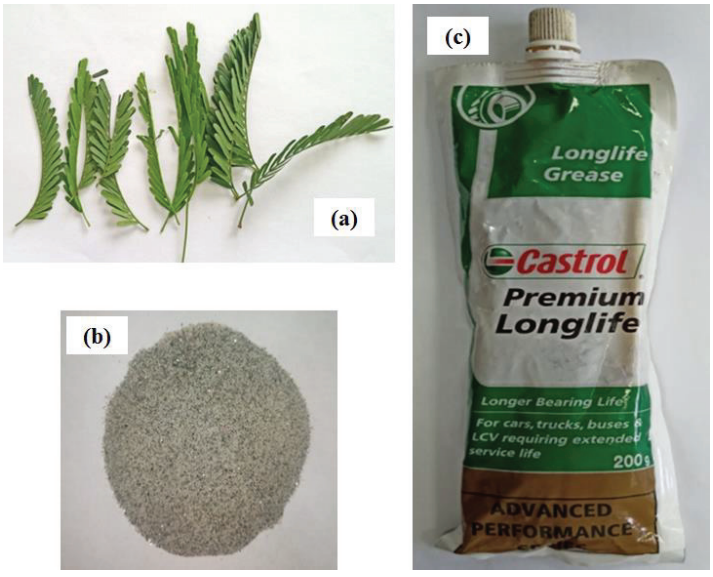

Figure 4. The contaminating materials considered for the experimental work (**a**) Babool Leaves (Acacia Nilotica), (**b**) Sand, and (**c**) Grease.

Table 7. Grease Specification [34].

Name	Method	Units	Grease Specification
Thickener	-	-	Lithium
Base Oil	-	-	Mineral Oil
Appearance	BAM 300	-	Bright and shiny
Structure	-	-	Smooth and buttery
NLGI Grade	ASTM D 217	-	3
Dropping Point	IP 132	°C	192
Cone Penetration (60 strokes)	IP 50	10 ths/mm	231
Base Oil Viscosity (at 100 °C)	IP 71	cSt	15.4
4 Ball Weld Point	IP 239	kg	200

3. Results and Discussion

The friction force vs. time and wear depth vs. time graph were obtained from experiments performed on a pin-on-disc tribometer in five distinct situations. Each condition was subjected to three experiments with three distinct loads (5 N, 10 N, and 15 N).

3.1. Friction Force

Figure 5 shows the fluctuation of friction force vs. time at three weights. The graph clearly shows that the sand had the greatest friction levels. The grease condition offered the lowest values of friction force. Compared to the dry conditions, oil reduced friction by a factor of 8. Only the sand had a higher friction level compared to the dry conditions. The friction levels were relatively lower in the other conditions. When Acacia Nilotica leaves were present between the rail and the wheel, the friction levels were lower than in the dry state but higher than in the grease condition. The friction levels in the mist state, measured by MQL, were lower than in the dry condition but higher than in the Acacia Nilotica leaves.

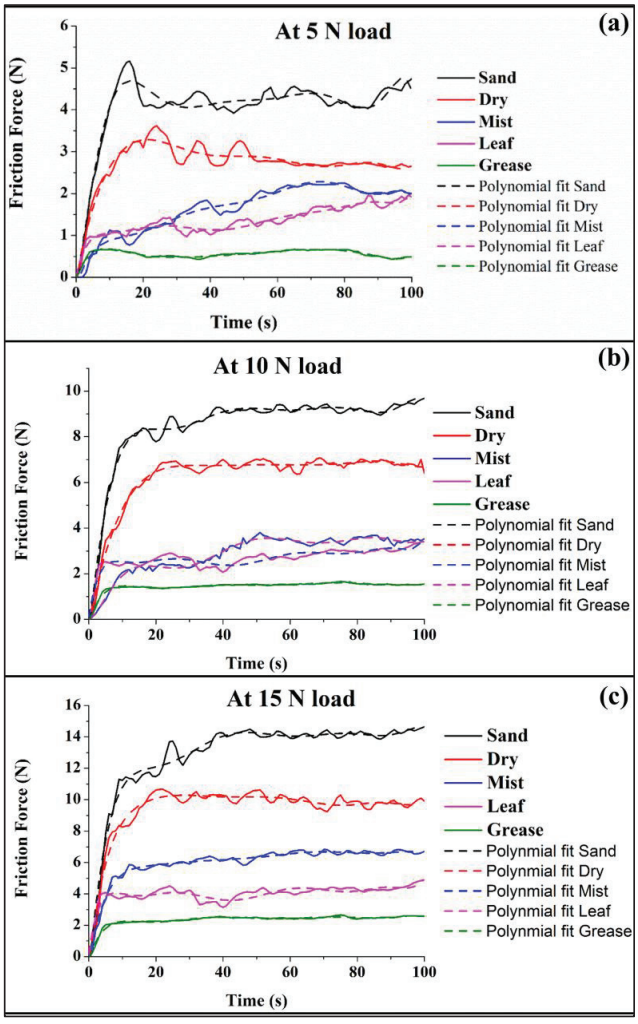

Figure 5. Variation of friction force versus time for normal loads (**a**) 5 N (**b**) 10 N (**c**) 15 N.

In each case, first, the friction force grew rapidly until a certain point, after which it stabilized but exhibited occasional variations with no net increase in friction force. Except for the grease condition, the curvature of each condition varied. The oil made the slide smooth, resulting in little to no fluctuations. The stick-slip phenomenon caused the variations [35].

3.2. Wear Depth

Figure 6 illustrates the wear depth vs. time at three loads for all five conditions at a fixed load of 5 N. The graph shows that the wear was growing across the graph under all conditions. Sand caused the highest wear compared to the other conditions. The grease resulted in the least amount of wear. Compared to the dry environment, the mist condition had much less wear. The Acacia Nilotica leaves have reduced wear even more than the mist condition.

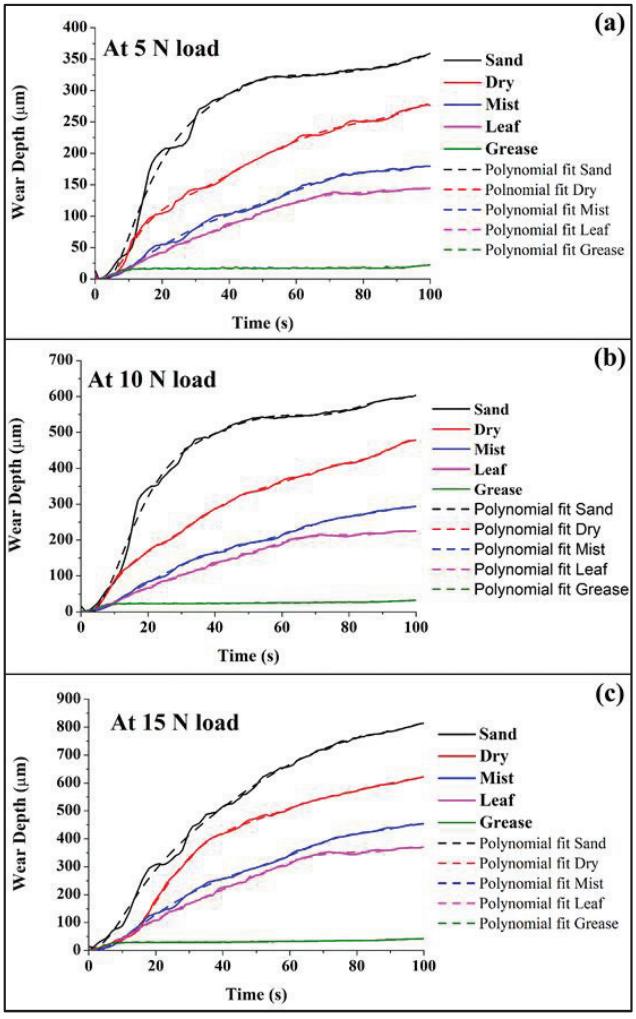

Figure 6. Variation of wear depth versus time for normal loads (**a**) 5 N (**b**) 10 N (**c**) 15 N.

The curves for all circumstances increased, but not significantly, except for the sand condition, where the rise was significant. For the first 10 s, the dry, leaf, mist, and grease behaviors overlapped. The slope was highest in the sand condition and reduced in the following order: dry, mist, Acacia Nilotica leaves, and grease. For all situations, the slope steadily diminished. The slope for the grease condition was insignificant. Wear increased as load increased. The slope was steeper at first but gradually decreased in each case. Initially, the dry and sand condition curves overlapped. Also, the curves for mist and leaf conditions overlapped for a few seconds before they separated. The grease had some slope initially, but the slope diminished as the curve progressed.

3.3. Effect of Load on Friction Force

Figure 7 illustrates the friction force as a function of time under all situations. The amount of friction force increased significantly with increasing loads in the sand condition, as shown in Figure 7a. In contrast, the behavior was similar at all three friction loads. The friction force curve fluctuated less at 5 N and more at 15 N. In the dry situation,

increasing the load caused high friction levels, as seen in Figure 7b. The curve's behavior was consistent for all loads. At smaller loads, the friction force fluctuated less. Figure 7c shows that for the mist conditions, larger loads resulted in increased wear and friction force. The friction force increased with increasing load (Figure 7d). The friction force curve was quite similar at all loads. Initially, there were three clear, distinct curves with little to no overlapping in the leaf state. Figure 7e for the grease condition shows that increasing the load caused a rise in the friction force. The curve at each load was different, and there was no overlapping at first. As a result, it was clear that the friction force increased due to the increase in load.

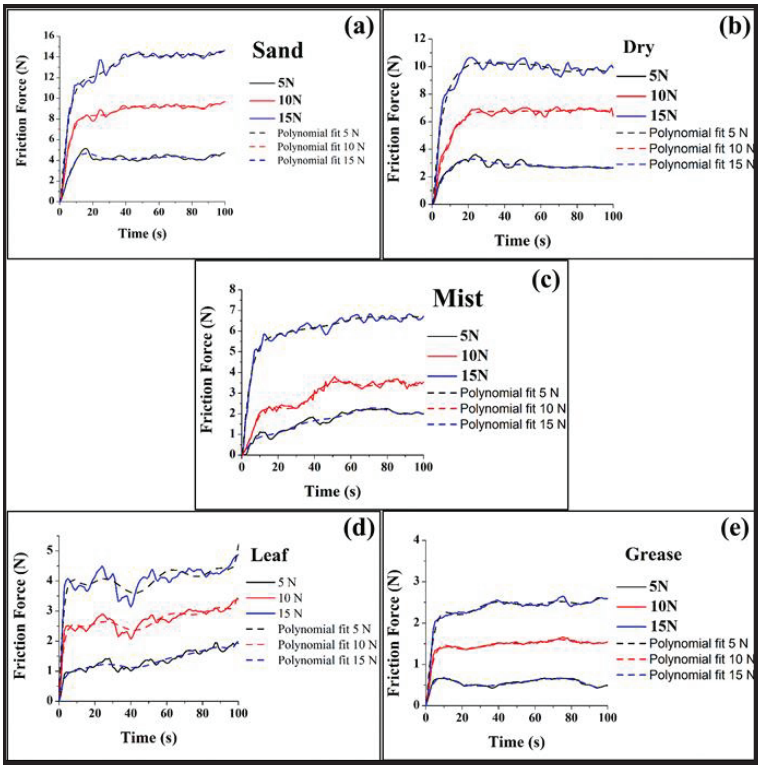

Figure 7. Effect of load on friction force for (**a**) sand, (**b**) dry, (**c**) mist, (**d**) leaf, and (**e**) grease.

3.4. Effect of Load on Wear Depth

Figure 8 represents the wear vs. friction force for all evaluated situations. Figure 8a shows that wear was high for larger loads in the sand condition. At first, there was significant overlap for the 10 N and 15 N loads, but the curves subsequently distinguished themselves. The wear behavior vs. time for the dry state at three different loads is given in Figure 8b. It was evident that under the dry state, an increase in load would result in excessive wear. The curve's behavior was more or less consistent for all wear loads. In dry conditions, the wear appeared to be proportional to the increase in load.

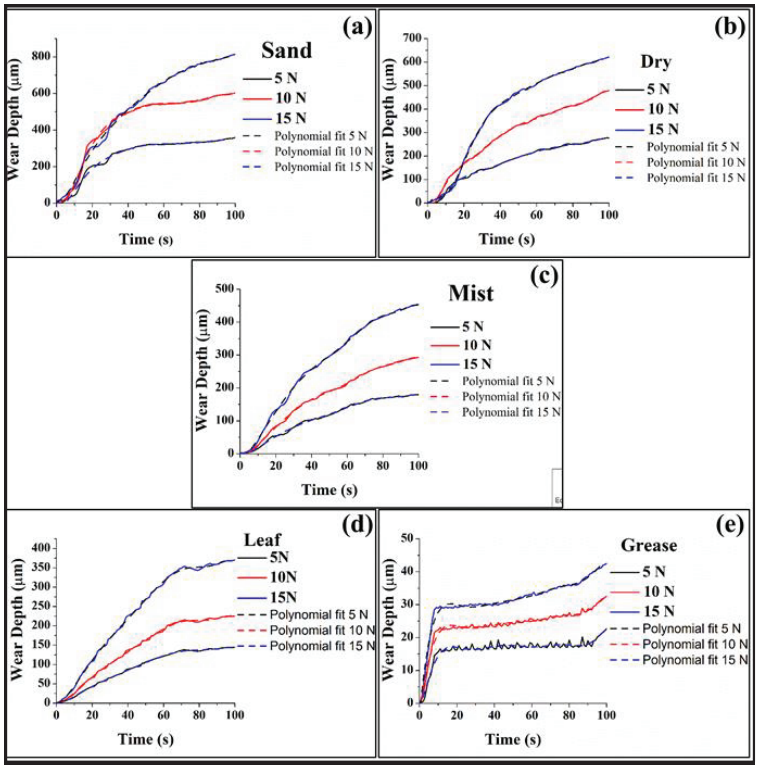

Figure 8. Effect of load on wear depth for (**a**) sand, (**b**) dry, (**c**) mist, (**d**) leaf, and (**e**) grease.

Figure 8c indicates that wear was higher in the mist conditions for larger loads. The 15 N load wore the most. The graph trend is consistent across all loads. For all three loads, the wear behavior was symmetrical. In this case, the increase in wear also appeared to be proportional to the increase in load for the leaf condition, as indicated in Figure 8d. Figure 8e shows that the wear depth increased with increasing load in the grease condition. The wear rose as the load increased. The wear behavior with variable load was comparable to that of other circumstances. Higher loads resulted in increased wear. The wear curve was quite similar at all loads. Initially, there was a clear distinction between the three curves with little to no overlapping for the leaf condition. In this situation, the increase in wear was proportional to the increase in load. As applied loads were increased, wear and friction were also improved. Except for the sand condition, the increase in wear was proportionate to the increase in load.

4. Conclusions

The major objective of this research was to investigate the tribological behavior of rails and wheels in a variety of situations. The investigation was done in sand, dry mist, leaf (Acacia Nilotica), and grease environments. For each condition, the studies were carried out at three distinct loads: 5 N, 10 N, and 15 N. The tests were carried out in a room with a temperature of 24.9°C and relative humidity of 66%. The following conclusions were obtained when compared to the dry condition:

- Both contaminants and load affected the wear rate, frictional levels, and wear depth of the rail track and wheel

- Among all the contaminants, the grease showed the least frictional levels, followed by leaves, mist, dry, and sand, irrespective of the load. However, these frictional levels increased as the load increased for all the contaminants.
- The wear depth increased with the increase in load for all the contaminants. Among all the contaminants, the highest wear depth was observed for sand contaminants, followed by dry, mist, leaves, and grease.
- The fluctuations in the frictional force increased with the increase in load for all the contaminants. The frictional forces were highest for sand conditions followed by dry, mist, leaves, and grease.
- It can be summarised that contaminants such as leaves and mist around the rail track are rather more desirable than leaving the rail track dry. However, the contaminant sand around the rail track is not desirable.

For future studies, it is advisable to apply lubricant or grease to prevent wear where excessive sliding takes place but not when rolling occurs, resulting in a loss of needed adhesion. Further study might be conducted to determine the function of particle emission from the occurring contact and the role of surface roughness in these varied rail wheel contact scenarios.

Author Contributions: Writing, R.K.S.; methodology, M.S.; conceptualization; P.R.; review and editing, software, A.K.S.; Supervision; G.K.S.; project administration, R.V.; funding acquisition, Visualization, J.K.B.; project administration, funding acquisition, H.S.H. All authors have read and agreed to the published version of the manuscript.

Funding: The authors extend their appreciation to the Deanship of Scientific Research at King Khalid University, Kingdom of Saudi Arabia, for funding this work through the Large Groups Project under Grant Number: RGP. 2/162/43.

Institutional Review Board Statement: Not applicable.

Informed Consent Statement: Not applicable.

Data Availability Statement: Not applicable.

Acknowledgments: The authors extend their appreciation to the Deanship of Scientific Research at King Khalid University, Kingdom of Saudi Arabia, for funding this work through the Large Groups Project under Grant Number: RGP. 2/162/43.

Conflicts of Interest: The authors declare no conflict of interest.

References

1. Gershon, R.R.M.; Qureshi, K.A.; Barrera, M.A.; Erwin, M.J.; Goldsmith, F. Health and Safety Hazards Associated with Subways: A Review. *J. Urban Health* **2005**, *82*, 10–20. [CrossRef]
2. Khalladi, A.; Elleuch, K. Tribological Behavior of Wheel-Rail Contact under Different Contaminants Using Pin-On-Disk Methodology. *J. Tribol.* **2017**, *139*, 011102. [CrossRef]
3. Olofsson, U.; Lewis, R.; Harmon, M. Tribology of the Wheel-Rail Contact. In *Handbook of Railway Vehicle Dynamics*; CRC Press: Boca Raton, FL, USA, 2019; pp. 281–305. ISBN 042946939X.
4. Olofsson, U.; Lyu, Y. Open System Tribology in the Wheel-Rail Contact-A Literature Review. *Appl. Mech. Rev.* **2017**, *69*, 060802. [CrossRef]
5. Bosomworth, C.; Spiryagin, M.; Alahakoon, S.; Cole, C.; Sneath, B.; Makin, B. Rail Temperature Variation under Heavy Haul Operations. *Railw. Eng. Sci.* **2022**, *30*, 148–161. [CrossRef]
6. Blau, P.J. Elevated-Temperature Tribology of Metallic Materials. *Tribol. Int.* **2010**, *43*, 1203–1208. [CrossRef]
7. Stott, F.H. High-Temperature Sliding Wear of Metals. *Tribol. Int.* **2002**, *35*, 489–495. [CrossRef]
8. Yadav, A.; Sachin; Dubey, V.; Singh, R.K.; Sharma, A.K. Effect of Temperature and Humidity on Tribological Properties of Rail and Wheel Using Pin-On-Disc. In *Recent Advances in Smart Manufacturing and Materials: Select Proceedings of ICEM 2020*; Lecture Notes in Mechanical Engineering; Springer: Cham, Switzerland, 2021; pp. 237–244.
9. Lyu, Y.; Zhu, Y.; Olofsson, U. Wear between Wheel and Rail: A Pin-on-Disc Study of Environmental Conditions and Iron Oxides. *Wear* **2015**, *328–329*, 277–285. [CrossRef]
10. Ma, L.; Shi, L.B.; Guo, J.; Liu, Q.Y.; Wang, W.J. On the Wear and Damage Characteristics of Rail Material under Low Temperature Environment Condition. *Wear* **2018**, *394–395*, 149–158. [CrossRef]

11. Zhu, Y.; Olofsson, U.; Chen, H. Friction between Wheel and Rail: A Pin-on-Disc Study of Environmental Conditions and Iron Oxides. *Tribol. Lett.* **2013**, *52*, 327–339. [CrossRef]
12. Lewis, S.R.; Lewis, R.; Olofsson, U.; Eadie, D.T.; Cotter, J.; Lu, X. Effect of Humidity, Temperature and Railhead Contamination on the Performance of Friction Modifiers: Pin-on-Disk Study. *Proc. Inst. Mech. Eng. Part F J. Rail Rapid Transit* **2013**, *227*, 115–127. [CrossRef]
13. Barthel, A.J.; Gregory, M.D.; Kim, S.H. Humidity Effects on Friction and Wear between Dissimilar Metals. *Tribol. Lett.* **2012**, *48*, 305–313. [CrossRef]
14. Chen, Z.; He, X.; Xiao, C.; Kim, S.H. Effect of Humidity on Friction and Wear-A Critical Review. *Lubricants* **2018**, *6*, 74. [CrossRef]
15. Zhu, Y. Adhesion in the Wheel-Rail Contact. Ph.D. Thesis, Royal Institute of Technology, Stockholm, Sweden, 2013.
16. Chen, H.; Ban, T.; Ishida, M.; Nakahara, T. Experimental Investigation of Influential Factors on Adhesion between Wheel and Rail under Wet Conditions. *Wear* **2008**, *265*, 1504–1511. [CrossRef]
17. Lyu, Y.; Bergseth, E.; Olofsson, U. Open System Tribology and Influence of Weather Condition. *Sci. Rep.* **2016**, *6*, 32455. [CrossRef] [PubMed]
18. Berthier, Y.; Descartes, S.; Busquet, M.; Niccolini, E.; Desrayaud, C.; Baillet, L.; Baietto-Dubourg, M.C. The Role and Effects of the Third Body in the Wheel–Rail Interaction. *Fatigue Fract. Eng. Mater. Struct.* **2004**, *27*, 423–436. [CrossRef]
19. Kaliyannan, G.V.; Kumar, P.S.; Kumar, S.M.; Deivasigamani, R.; Rajasekar, R. Mechanical and Tribological Behavior of SiC and Fly Ash Reinforced Al 7075 Composites Compared to SAE 65 Bronze. *Mater. Test.* **2018**, *60*, 1225–1231. [CrossRef]
20. Li, C.; Li, X.; Huang, S.; Li, L.; Zhang, F. Ultra-Precision Grinding of Gd3Ga5O12 Crystals with Graphene Oxide Coolant: Material Deformation Mechanism and Performance Evaluation. *J. Manuf. Process.* **2021**, *61*, 417–427. [CrossRef]
21. Li, C.; Piao, Y.; Meng, B.; Hu, Y.; Li, L.; Zhang, F. Phase Transition and Plastic Deformation Mechanisms Induced by Self-Rotating Grinding of GaN Single Crystals. *Int. J. Mach. Tools Manuf.* **2022**, *172*, 103827. [CrossRef]
22. Hardwick, C.; Lewis, R.; Eadie, D.T. Wheel and Rail Wear-Understanding the Effects of Water and Grease. *Wear* **2014**, *314*, 198–204. [CrossRef]
23. Vo, K.D.; Tieu, A.K.; Zhu, H.T.; Kosasih, P.B. A Tool to Estimate the Wheel/Rail Contact and Temperature Rising under Dry, Wet and Oily Conditions. In *Computers in Railways XIV: Railway Engineering Design and Optimization*; WIT Press: Billerica, MA, USA, 2014; Volume 135, pp. 191–201.
24. Olofsson, U.; Zhu, Y.; Abbasi, S.; Lewis, R.; Lewis, S. Tribology of the Wheel-Rail Contact-Aspects of Wear, Particle Emission and Adhesion. *Veh. Syst. Dyn.* **2013**, *51*, 1091–1120. [CrossRef]
25. Olofsson, U.; Sundvall, K. Influence of Leaf, Humidity and Applied Lubrication on Friction in the Wheel-Rail Contact: Pin-on-Disc Experiments. *Proc. Inst. Mech. Eng. Part F J. Rail Rapid Transit* **2004**, *218*, 235–242. [CrossRef]
26. Olofsson, U. A Multi-Layer Model of Low Adhesion between Railway Wheel and Rail. *Proc. Inst. Mech. Eng. Part F J. Rail Rapid Transit* **2007**, *221*, 385–389. [CrossRef]
27. Zhu, Y.; Lyu, Y.; Olofsson, U. Mapping the Friction between Railway Wheels and Rails Focusing on Environmental Conditions. *Wear* **2015**, *324–325*, 122–128. [CrossRef]
28. Zhu, Y.; Chen, X.; Wang, W.; Yang, H. A Study on Iron Oxides and Surface Roughness in Dry and Wet Wheel-Rail Contacts. *Wear* **2015**, *328–329*, 241–248. [CrossRef]
29. Deters, L.; Proksch, M. Friction and wear testing of rail and wheel material. *Wear* **2005**, *258*, 981–991. [CrossRef]
30. Ravikiran, A.; Jahanmir, S. Effect of Contact Pressure and Load on Wear of Alumina. *Wear* **2001**, *250–251*, 980–984. [CrossRef]
31. Mcfarlane, J.S.; Tabor, D. Relation between Friction and Adhesion. *Proc. R. Soc. Lond. Ser. A Math. Phys. Sci.* **1950**, *202*, 244–253. [CrossRef]
32. Gallardo-Hernandez, E.A.; Lewis, R. Twin Disc Assessment of Wheel/Rail Adhesion. *Wear* **2008**, *265*, 1309–1316. [CrossRef]
33. Report on rail, axle, wheel sets, Steel Authority of India Ltd. Available online: https://sail.co.in/sites/default/files/product-brochure/2020-04/Railway-Products.pdf (accessed on 31 December 2022).
34. Shah, R.; Tung, S.; Chen, R.; Miller, R. Grease Performance Requirements and Future Perspectives for Electric and Hybrid Vehicle Applications. *Lubricants* **2021**, *9*, 40. [CrossRef]
35. Yang, Z.; Zhang, P.; Moraal, J.; Li, Z. An Experimental Study on the Effects of Friction Modifiers on Wheel–Rail Dynamic Interactions with Various Angles of Attack. *Railw. Eng. Sci.* **2022**, *30*, 360–382. [CrossRef]

coatings

MDPI

Article

Firefly Algorithm and Neural Network Employment for Dilution Analysis of Super Duplex Stainless Steel Clads over AISI 1020 Steel Using Gas Tungsten Arc Process

Mohd. Majid [1], Love Goel [1], Abhinav Saxena [2,*], Ashish Kumar Srivastava [3,*], Gyanendra Kumar Singh [4], Rajesh Verma [5], Javed Khan Bhutto [5] and Hany S. Hussein [5,6]

[1] Sant Longowal Institute of Engineering and Technology, Longowal 148106, Punjab, India
[2] Department of Electrical Engineering, JSS Academy of Technical Education, Noida 201301, Uttar Pradesh, India
[3] Department of Mechanical Engineering, G.L. Bajaj Institute of Technology and Management, Greater Noida 201306, Uttar Pradesh, India
[4] Department of Mechanical Engineering, School of Mechanical, Chemical and Materials Engineering, Adama Science and Technology University, Adama P.O. Box 1888, Ethiopia
[5] Department of Electrical Engineering, College of Engineering, King Khalid University, Abha 61411, Saudi Arabia
[6] Department of Electrical Engineering, Faculty of Engineering, Aswan University, Aswan 81528, Egypt
* Correspondence: abhinaviitroorkee@gmail.com (A.S.); ashish7185@gmail.com (A.K.S.)

Abstract: Traditional low-carbon steels provide the strength needed to satisfy industrial demands. Low-carbon steel's poor corrosion resistance is one of its main drawbacks. Due to this restriction, corrosion-resistant materials such as super duplex stainless steels are frequently used for cladding onto the surface of low-carbon steel. The cladded surface possesses superior chloride stress corrosion cracking resistance, pitting and crevice corrosion resistance, yield strength, ductility, and impact toughness. Mild steel with measurements of 300 × 300 × 12 mm has been selected as the substrate material, and super duplex stainless steel (S32950) with an electrode diameter of 2.4 mm has been selected as the filler wire. Gas Tungsten Arc (GTA) cladding was performed onto the surface of low-carbon steel for experimentation. The clad was deposited in the flat position with four different currents, i.e., 120 A, 130 A, 140 A, and 150 A. Cladding was performed on different layers of each current level, i.e., single layer, double layers, and triple layers. After experimenting and overviewing the outcomes, it can be concluded that the optimum input parameters would be a 3-layered clad at a 140 A current level. Cladding of the super duplex stainless steel over mild steel improves the corrosive properties. The percentage ratio of reactivation current density to activation current density (I_r/I_a%) improves from 29% (mild steel) to 4.1% at the top layer and 11.9% at the intermediate layer. The microhardness of the clad decreases with an increase in both the current level and the number of layers. Microhardness varies between 191–248 at the clad, 170–189 at the HAZ, and 143–153 at the substrate for a 1 kgf load. Dilution refers to the change in the cladding alloy composition due to the mixing of the molten matrix. The composition of the clad changes under a high dilution, resulting in a decrease in the mechanical as well as corrosion properties of the clad. However, if the dilution is too small, the bond between the substrate and the clad is poor. Therefore, dilution is one of the most important process control parameters and the key to obtaining high-quality cladding. Thus, the dilution effect is also analyzed on all three clad layers deposited at various current levels using the firefly algorithm (FA) and artificial neural network (ANN). It is observed that dilution levels are found to be more approachable to the experimental setup data with FA in comparison to ANN for various current levels.

Keywords: GTAW; cladding; super duplex stainless steel; FA; ANN; dilution

Citation: Majid, M.; Goel, L.; Saxena, A.; Srivastava, A.K.; Singh, G.K.; Verma, R.; Bhutto, J.K.; Hussein, H.S. Firefly Algorithm and Neural Network Employment for Dilution Analysis of Super Duplex Stainless Steel Clads over AISI 1020 Steel Using Gas Tungsten Arc Process. *Coatings* **2023**, *13*, 841. https://doi.org/10.3390/coatings13050841

Academic Editors: Guangyi Ma and Rafael Comesaña

Received: 28 February 2023
Revised: 25 April 2023
Accepted: 26 April 2023
Published: 27 April 2023

1. Introduction

Cladding is the procedure of forming a protective coating in which a metal is coupled under higher pressure and higher temperature with another metal. It gives several desired properties which are not found in single metal. In cladding, the base material is chosen considering its cost or structural properties and filler material used for surface protection. It is necessary to provide an optimum number of clad layers to obtain the desired dilution for the proper bonding of the clad material to the substrate. Cladding can be performed using several welding processes either manually, semi-automatically, or automatically. As a result, the surface of the metals that are presently available is changed with bare welding rods, covered electrodes, coiled wire, paste, and powders [1]. Austenitic stainless steel and nickel-based amalgam are excellent non-corrosive and heat-resistant alloys that are better suited for the cladding of pressure vessels in petrochemical industries. It can be produced using a variety of settings for the welding variables, fluxes, and strips or electrodes. Traditional low-carbon steels provide the strength needed to satisfy industrial demands. Because low-carbon steels generally have low costs and are easily available, these steels are preferred for fabrication works. The low-carbon steel's poor corrosion resistance is one of its main drawbacks. Due to this restriction, corrosion-resistant materials, including stainless steel, have been developed. The microstructure of stainless steel has a direct impact on its properties. At about 300 °C, duplex stainless steels break down into the ferrite phase and form intermetallic phases that reduce their ability to resist corrosion and maintain their mechanical qualities. Due to its superior chloride stress corrosion cracking resistance, pitting and crevice corrosion resistance, yield strength, ductility, impact toughness, and weldability, super duplex stainless steel is frequently used in weld cladding [2]. Super duplex stainless steel could be deposited to enhance the surfaced layer's durability under a high-temperature corrosive environment [3,4]. The manufacturing sectors of India are crucial to the nation's economic development. Effective calculation, avoidance, and management of corrosion present difficult challenges for these sectors. It has become essential for Indian industries to improve production by reducing the loss from downtime as well as any accidents while also making the best use of human effort and resources in order to compete with rapidly expanding Asian nations such as China. A disturbing percentage of the overall expense of corrosion across all sectors is contributed by the cost of rust in the chemical, nature, manufacturing, shipping, oil and gas, and petrochemical industries. This essay provides a general summary of corrosion costs in India and their relationship to GDP [5–8]. Duplex stainless steel's joint durability may be negatively impacted by nitrogen loss from laser welding melt ponds. When laser welding, this impact can be reduced by using nitrogen as a shielding gas. Nitrogen usage causes the welded metal to contain more austenite, resulting in higher degrees of toughness [9–13]. Microstructures as well as the welding pool shape of 304 stainless steel during GTAW are being studied theoretically as well as experimentally. A research project looking at how changes in heat input affect the microstructure of less activated ferritic martensitic steel weld metal produced by the GTAW method of GTAW fusing inline phase characterization for ultra ferritic stainless-steel welding. Additionally, neural network analysis was conducted on a joint bead shape of austenitic stainless steel GTAW. Chloride Pitting Corrosion Resistance: Weldability of Nitrogen-Containing Austenitic Stainless Steel, Part I. [14] At room temperature, the impact of magnetite concentration on stress-induced cracking within duplex stainless steel weld alloys has been discussed in [14–19]. A grid-integrated wind-driven DFIG is optimized for invasive weeds for sensorless regulation. A solar MPPT with simplified propagation using a fusion firefly algorithm in partial shading situations and a flux-cored arc forging method using a multivariate stochastic optimization method have been discussed in [20–22].

The improvement in the dilution characteristic level for the various current levels with a hardware setup and its validation with the firefly algorithm and ANN is the novelty of the proposed scheme. Such novelty makes it different from the existing literature.

2. Design of Experiment

The analysis of experimental data, which leads to the optimization of process parameters, is frequently accomplished using the Design of Experiments (DOE) technique. It is a method of practical, experimental, and statistical modeling that is used to concurrently solve several equations utilizing quantitative results from well-designed experiments using multiple regression analyses. It is a systematic structured method for analyzing any scenario where the outcome depends on one or more independent factors. It is frequently applied to complicated issues where more than one variable may have an impact on the outcome and where two or more factors may interact. Using the ideal number of experimental observations, it can provide the answers to specific queries about a system's behavior. The impact of two separate parameters has been examined using a historical data design with twelve sample data. Important components for conducting the experiment and determining their impact on the dilution are the current and clad layer. The other factors were all constant. For the study of the data, one numeric factor—current—and one categorical factor—clad layers—have been chosen. Except for the ones being considered, both direct and indirect parameters have indeed been kept constant. A discrete type of numerical factor with four levels has been chosen for the current, and a nominal type of categorical factor with three levels has been chosen for clad layer. Input parameters with their level and units are shown in Table 1, and the design matrix developed to analyze the 12 responses of historical data is shown in Table 2.

Table 1. Parameters with their level and units.

Symbol	Name	Unit	Type	Levels	L_1	L_2	L_3	L_4
A (Numeric)	Current	A	Discrete	4	120	130	140	150
B (Categoric)	Layer		Nominal	3	Single	Double	Triple	

Table 2. Design matrix table.

S. No	Current	Layer
1	120	Single
2	120	Double
3	120	Triple
4	130	Single
5	130	Double
6	130	Triple
7	140	Single
8	140	Double
9	140	Triple
10	150	Single
11	150	Double
12	150	Triple

2.1. Base Metal and Filler Metal

With measurements of 300 × 300 × 12 mm, AISI 1020 (mild steel) had been chosen as the base material. Before cladding, the surface was thoroughly cleaned with acetone to get rid of any oxide scales and surface contaminants and then polished to a smooth finish to eliminate all dirt, oil, grease, and rust. Mild steel was chosen as it was the most affordable type of steel and also had outstanding mechanical qualities, such as strength and toughness. It was chosen as the substrate for the super duplex stainless steel cladding in order to make the active surface corrosion resistant. As a result, the clad mild steel might be made accessible as a highly affordable alternative to the super duplex stainless-steel substrate. The GTA method was used to clad super duplex stainless steel (S32950), as in this welding process, a non-consumable tungsten electrode is used, and shielding of weld

pool against the atmospheric gases is provided by inert gases such as orgon, helium, or a mixture of these two gases. Additionally, GTA clads are neat and free from spatters owing to better process control capabilities. Super duplex stainless steel (S32950) had been chosen as a filler wire with a diameter of 2.4 mm. Table 3 shows the chemical composition of the base metal used.

Table 3. Chemical composition (wt.%) of base material.

Material	Element (% wt)								
	C (%)	Si (%)	Mn (%)	P (%)	S (%)	Cr (%)	Ni (%)	Mo (%)	Cu (%)
Substrate (AISI 1020)	0.196	0.293	1.12	0.0041	0.011	0.128	0.034	0.027	
Filler Wire (S32950)	0.026	0.46	0.74	0.021	0.010	23.16	8.40	2.74	0.36

2.2. Cladding

GTA was used for laying claddings, as it is the most versatile process. Parameters selected for cladding after conducting trial runs are presented in Table 4. GTA setup used having the following specifications:

Table 4. GTA cladding parameters.

Shielding Gas	Pure (99.99%) Argon
Shielding gas flow rate	10 L·min^{-1}
Filler rod diameter	2.4 mm
Non-consumable tungsten electrode	AWS EWTH-2 (98% W + 2% Th)
Filler wire diameter	2.4 mm
Polarity	Electrode negative (EN)
Arc voltage (V)	15 V
Heat input	0.94 kJ·mm^{-1}
Material thickness	12 mm

- Manufacturer: Tech Pro, Pvt. Ltd., Delhi, India;
- Supply voltage: 380/415/440 V;
- Cladding current range: 5 A–350 A (DC);
- Open circuit voltage: 80 V.

The substrate surfaces were cleaned with acetone to eliminate any oxide scales and impurities before even being prepared for cladding. This process removed all dirt, oil, grease, and rust from the surfaces. The rolling orientation of the substrate plate was chosen as that of the orientation of the cladding. First, trial runs were conducted to find out the current range to be used. The GTA cladding was conducted in the flat position with four different currents: 120 A, 130 A, 140 A, and 150 A. Additionally, different layers for each current setting were laid: single layer, double layers, and triple layers. Various layers of cladding were deposited simultaneously without maintaining any interpass temperature. The cladding plate and its cross-section are shown in Figures 1 and 2.

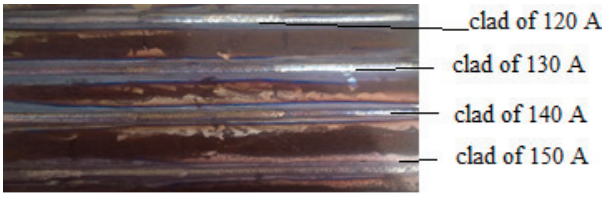

Figure 1. Cladded plate.

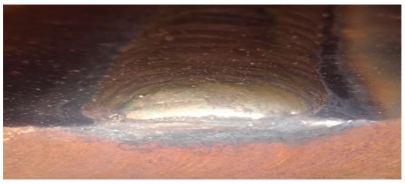

Figure 2. Cladded plate view.

2.3. Preparation of Microhardness, Optical Microscopy, Pitting Corrosion, and Ferrite Percentage Evaluation Specimens

After cladding the AISI 1020 steel plate with super duplex stainless steel via the GTA process, different specimens for metallurgical and pitting corrosion studies were extracted. The method adopted for sectioning and specimen preparation for performing different tests are discussed in the following subsection. Different specimens required for performing tests were machined out from the clad plate in the transverse direction to cladding. The sectioning was carried out using a wire-cut electric discharge machine (WEDM) with a 0.5 mm wire diameter. WEDM was used to reduce material wastage, achieve dimensional accuracy, and avoid overheating test specimens.

Microhardness, optical microscopy, and pitting corrosion studies of the clad specimens were carried out on their cross-sectional area, which includes layers, viz., single, double, and triple. The specimen for microhardness, metallographic, and pitting corrosion studies were prepared in accordance with ASTM E3-11 standards (ASTM, 2011a). The operation involved in preparing different test specimens, including cutting, grinding, polishing, and etching is discussed below.

Cutting: Cutting of welded samples could be performed by various operations such as power hacksaw, wire-cut electric discharge machining (WEDM), plasma-cutting torches, abrasive wheels, etc. In this present research work, wire-cut electric discharge machining (WEDM) was used for sectioning because it results in a superior surface finish, maintains dimensional accuracy, and retains material properties as less heat was generated and minimum wastage of material.

Grinding: Fully automatic surface grinder with a magnetic chuck and movable table was used for surface grinding/finishing. Grinding was performed to remove all the dents/marks and scales from the area to be polished. Coolant was pumped onto the grinding wheel as well as the specimen to protect it from excessive heat produced during grinding.

Polishing: Metallographic and pitting corrosion test specimens were polished to a mirror-like and less scratchy appearance. Proper polishing is necessary for qualitative and quantitative accurate interpretations of metallographic and pitting corrosion and determining ferrite content present in the substrate and clads. Specimens were ground manually using emery papers ranging in fineness from 100–3000 equivalent mesh and then polished using alumina suspensions and velvet cloth.

Etching: Etching was carried out to reveal the microstructure of the metal sample. An etchant usually breaks the grain boundaries, which enables us to distinguish them evidently, so that grain size, shape, and orientation can be studied. The specimen to be etched should be carefully cleaned and should be free from grease, oil, rust, oxides, and the remnants of polishing materials. Subsequently, after etching, the specimen was splashed properly with water, rinsed with ethanol, and dried by forced hot air to avoid the watermark formation. Since metallic etched surfaces are extremely reactive and can smear rapidly in the air, predominantly in humid atmospheres, etched specimens were thus stored in sealed desiccators.

3. Testing

3.1. Microstructure Characterization

From the clad plate, several cladded specimens of the proper sizes were sectioned off and processed for metallographic testing using normal polishing techniques, which entailed

grinding with various emery grades before polishing with diamond paste. Etching was conducted by immersing the specimens in the respective etchant containing $CuCl_2$ (5 gm) + Ethanol (100 mL) + HCl (100 mL), followed by cleaning the etched surface with acetone. The surfaces were then examined using an optical microscope to take micrographs of various areas of the various clad layers for the purpose of examining various microstructural phases.

3.2. Micrograph Hardness Test

Metallographically ready specimens were subjected to microhardness assessment using a microhardness tester of 1 kg to 10 kg capacity and applied testing condition of 1 kg load with a dwell time of 15 s. Different layers, i.e., single, double, and triple layers of the clads were observed along the clad center to study microhardness variation across different clad layers of SDSS and in AISI 1020 substrate.

3.3. Double Loop Electrochemical Potentio-Kinetic Reactivation Tests (DL-EPR)

Using the DL-EPR test, which involved interoperable kinetic scanning in an appropriate electrolyte from an active to a passive domain (activation or anodic scan), accompanied by a restoration to the initial potential, the corrosion resistance of SDSS claddings was assessed (reverse or reactivation scan). The counter, reference, and work electrodes were, successively, a platinum foil, a saturated calomel electrode (SCE), as well as a test specimen. The DLEPR tests were performed in a modified 2 M H_2SO_4 + 1 M HCl solution at 35 ± 10 °C. For the purpose of removing the dissolved oxygen prior to the test, the solutions were blasted with high-purity N2 at a flow rate of 0.3 L/min for 30 min. The tested samples have clad layers (exposed area: 0.196 cm^2). The specimen was progressively ground from 280 to 1500 grit with a succession of emery sheets and polished to a mirror finish with a 2.5 m diamond paste afterward in order to lessen the impact of surface condition on the test result. The sample was cathodically polarized at 750 mV/SCE for 3 min prior to the DLEPR test procedure in order to increase repeatability. The test was initiated in an anodic manner from −100 mV/SCE + E_{corr} (corrosion potential) at 1 mV/s until the potential hit 600 mV/SCE + E_{corro} in the passive area after the open-circuit potential (E_{ocp}) had stabilized for around 1 h. When the potential had once more approached E_{corro}, the scan was then reversed in the cathodic direction. In both the forward and reverse scans, the current of activation (I_a) and reactivation (I_r) were measured. The ratio (I_r/I_a) × 100% was calculated to rank the localized corrosion susceptibility.

3.4. Dilution

Dilution is usually taken to be the proportion of the cross-sectional area of melted base material to the entire cross-sectional area of the fusion zone and is described as the percentage of base material in the resulting clad layer deposit. To perform the test of dilution, samples were sectioned, polished, and etched in a solution of $CuCl_2$ (5 gm) + Ethanol (100 mL) + HCl (100 mL). Digital photographs were taken from the etched surface of the samples, and then dilution (D) was calculated via image analyzer software, i.e., ImageJ (Fiji) software.

3.5. Ferrite Number

The ferrite content in the specimen was measured with the help of a ferrite scope from Fischer. This handy equipment provides rapid and accurate data via highly mobile digital technology. Ferrite content measurement was used to measure the ferrite content in SDSS clads. Test results can be represented by ferrite number (FN) or by ferrite content (%).

4. Result and Discussion

4.1. Pitting Corrosion Test (DLEPR)

Figures 3 and 4 show the DL-EPR curves of the top clad layer and intermediate clad layer with pure argon as the shielding gas in 2 M H_2SO_4 + 1 M HCl solution at 35 °C. Figure 5 shows the DLEPR curve of the substrate AISI 1020 steel. The I_r/I_a values after

the DL-EPR measurements are listed in Table 5. It can be observed that the value of I_a was almost the same for the top clad and intermediate clad layers; however, a significant difference of 1.606 E-3 (A/cm^2) in I_r values of the top clad and intermediate clad layers has been observed. I_r/I_a% values showed a remarkable difference of 7.8% between the top clad layer and the intermediate clad layer. The lower the I_r/I_a% value, the better the pitting corrosion resistance/localized corrosion. Thus, the top clad layer demonstrated a lower I_r/I_a value (4.1%), indicating better resistance to pitting corrosion in acidified chloride environment. The I_r/I_a% of 11.9% observed in the case of the intermediate clad layer demonstrate that the intermediate clad layer possesses higher pitting corrosion/localized corrosion resistance in acidified chloride environment compared to AISI 1020 steel having I_r/I_a of 29.6%, but not as much compared to the top clad layer. So, it is clear from the above results that after cladding super duplex stainless steel over mild steel, the corrosive properties show significant improvement.

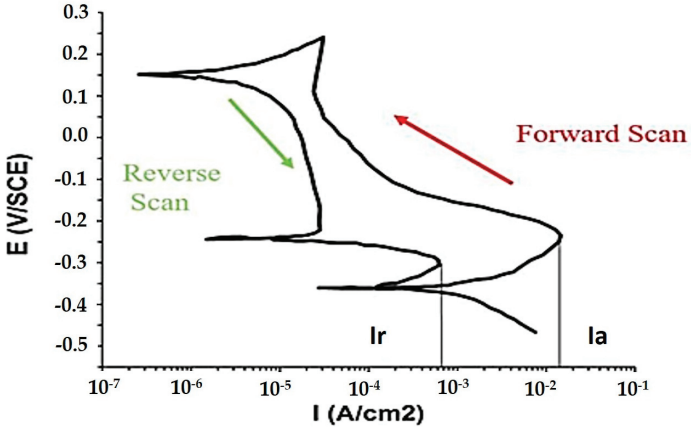

Figure 3. The DLEPR curve of clad layer.

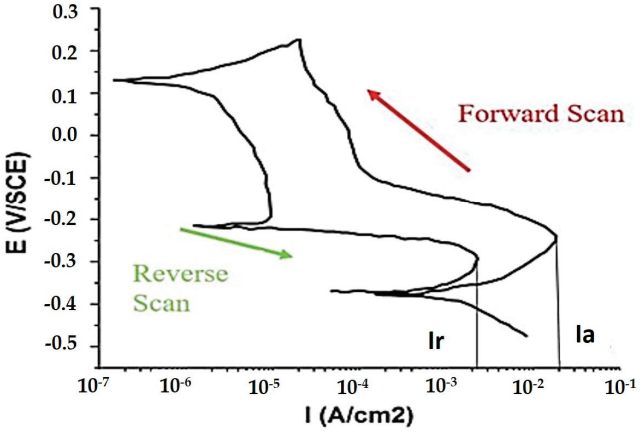

Figure 4. The DLEPR curve of intermediate clad layer.

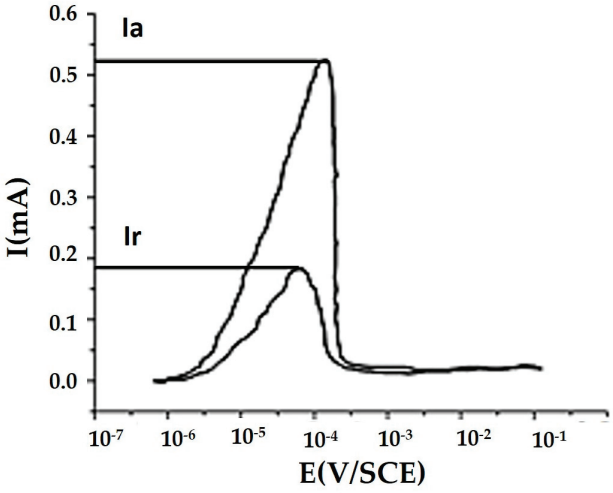

Figure 5. The DLEPR curve of base metal.

Table 5. I_r/I_a values of DLEPR pitting corrosion test.

S.No.	Testing Zone	I_a	I_r	I_r/I_a (%)
1	Top clad layer	1.56×10^{-2} (A/cm^2)	6.44×10^{-4} (A/cm^2)	4.1
2	Intermediate clad layer	1.89×10^{-2} (A/cm^2)	2.25×10^{-3} (A/cm^2)	11.9
3	Base metal (AISI 1020 steel)	0.54 mA	0.16 mA	29.6

4.2. Microhardness

Hardness plays an important role in the wear behavior of materials. Microhardness at the clad, heat-affected zone, and base metal have been determined using a Vickers hardness tester confirming ASTM-E384. Figure 6 shows the different zone at which the microhardness value has been taken and the graphical representation of the microhardness value at the different zone with variation in current and layers. It can be observed from Figure 7 that microhardness of the clad decreases with an increase in both the current level and the number of layers. Due to the high heat input, initially, the grains get softer, but after cooling down to ambient temperature, the grains become coarser, resulting in a noticeable decrement in the microhardness values of SDSS clads. Additionally, decreasing trends in microhardness amongst the top, intermediate, and bottom layers can be attributed to the fact that the re-melting retards the cooling rate of the previous layers of the clad surface because of whichever grain coarsening occurs in the previously cladded layers.

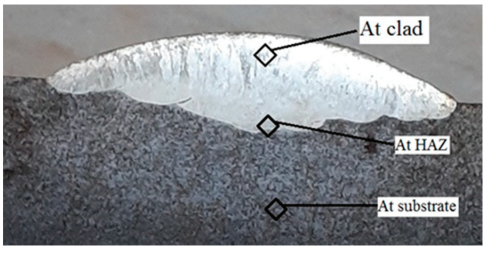

Figure 6. Hardness in different zones.

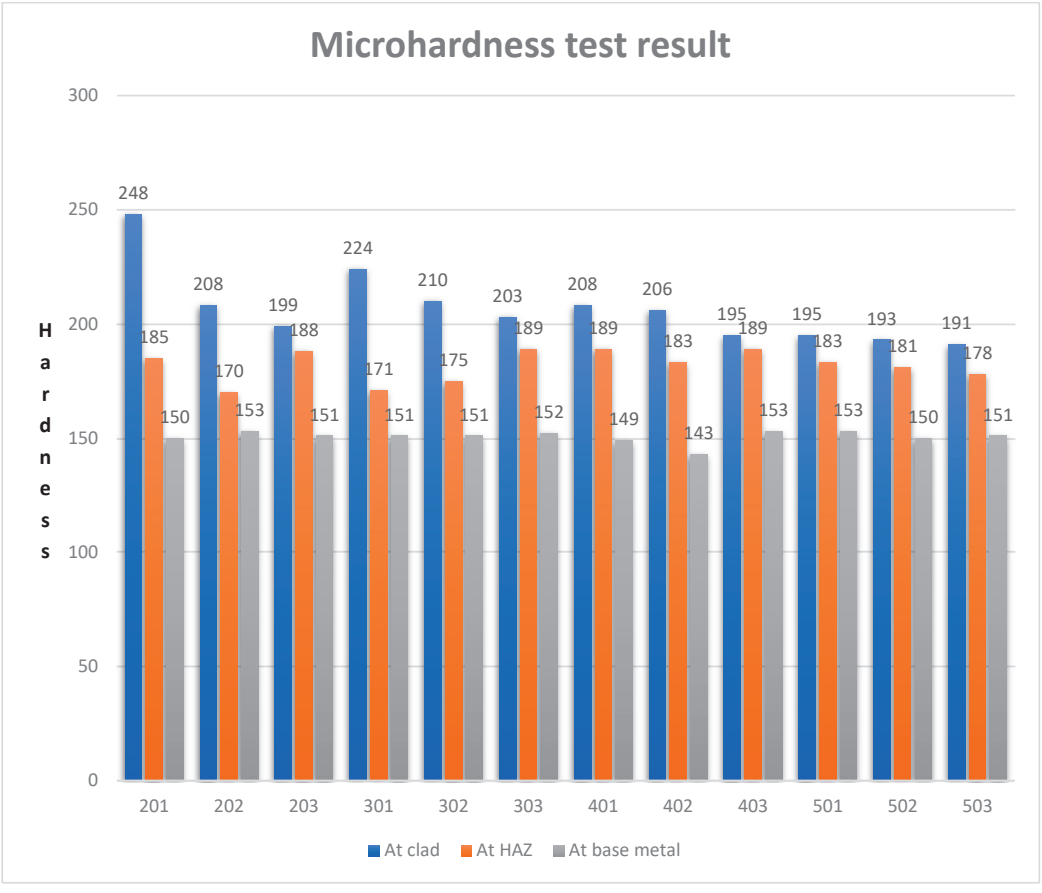

Figure 7. Microhardness test results at the clad, heat-affected zone, and base metal.

4.3. Microstructure Characterization

Generally, austenite contains two types: primary austenite and secondary austenite γ_2. The primary austenite is mainly formed from the subsequent solid-state phase transition of the ferrite after being solidified from molten metal. There are four different types of primary austenite in the WM and HAZ, including grain boundary austenite (GBA), Widmanstatten austenite (WA), intragranular austenite (IGA), and partially transformed austenite. The typical microstructures of clad layers at different current levels are shown in Figure 8. When a new layer is laid onto the previous layer, re-melting of the previously laid clad layer takes place. Hence, intragranular primary austenite and secondary austenite are formed at HAZ. The amount of austenite formed is higher in HAZ than that in clad, as observed in Figure 8j. The clad region comprises grain boundary austenite, intragranular, and Widmanstatten austenite formed in a ferrite matrix. Coarse ferrite grains are observed in the clad region. From Figure 8c,f,i,l, it can be concluded that on increasing the current level, the grains become coarser, which implies that microhardness is decreasing. When high heat input is employed, large grain sizes and higher contents of austenite are observed in Figure 8b,e,h,k.

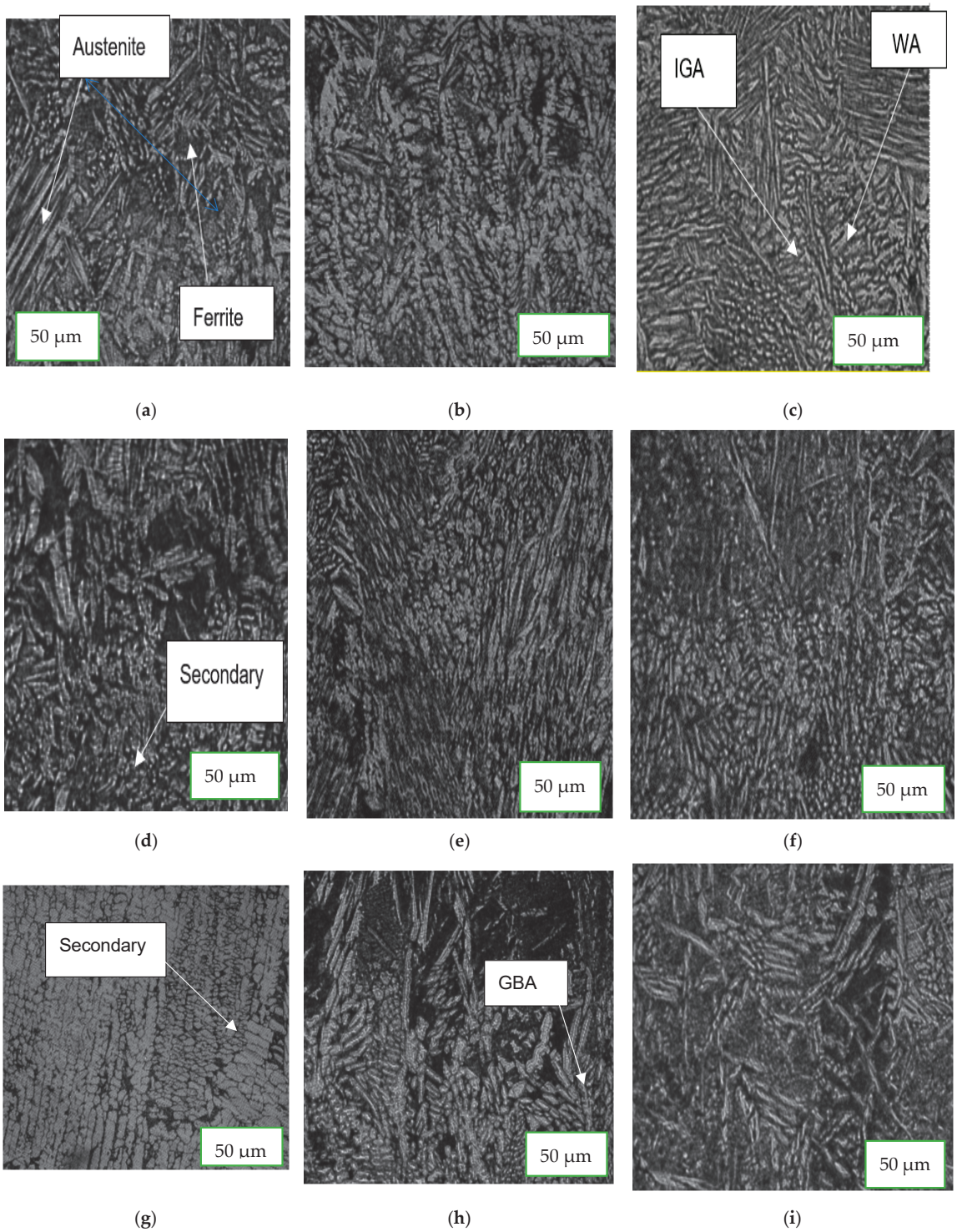

Figure 8. *Cont.*

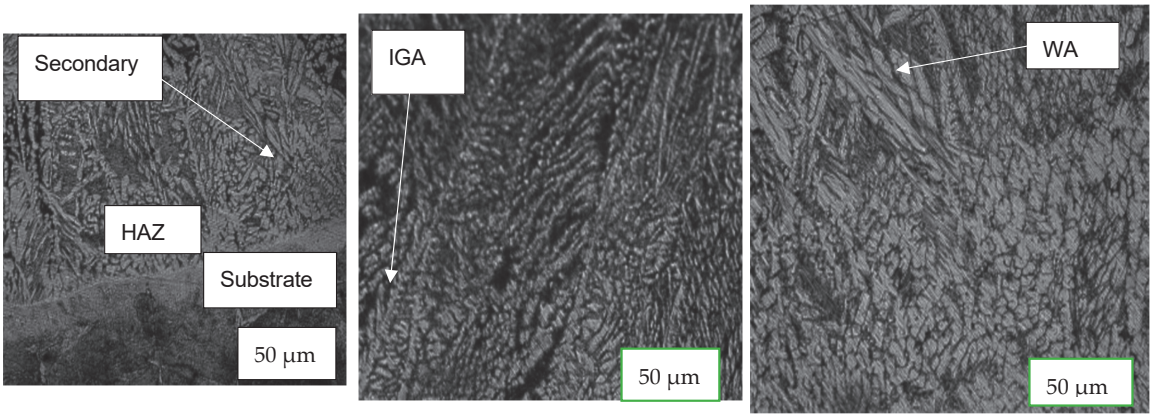

(**j**) (**k**) (**l**)

Figure 8. Microstructure of samples: (**a**) at 120 A, single layer; (**b**) at 120 A, double layers; (**c**) at 120 A, triple layers; (**d**) at 130 A, single layer; (**e**) at 130 A, double layers; (**f**) at 130 A, triple layers; (**g**) at 140 A, single layer; (**h**) at 140 A, double layers; (**i**) at 140 A, triple layers; (**j**) at 150 A, single layer; (**k**) at 150 A, double layers; (**l**) at 150 A, triple layers.

4.4. Ferrite Number

Ferrite content measurement was conducted using Fisher's ferrite scope, and the results are presented in Figure 9. The result shows that an increase in the number of clad layers increases the ferrite content. Generally, austenite contains two types: primary austenite and secondary austenite γ_2. Intragranular primary austenite and secondary austenite are formed at the root. The reheating of clad layers is the main reason for the formation of secondary austenite. Secondary austenite formation takes place near the HAZ, so ferrite content decreases near the HAZ, which is clearly shown in the result of ferrite content. So, in a single-layered clad, the value of the ferrite number increases from top to bottom due to the dilution effect. However, in a double-layered clad, higher ferrite content is noticed at the clad cap compared to the single-layer-clad cap; this shows that the composition retains itself more at the second-layer-clad cap. From top to bottom, the ferrite number first decreases and then increases. Ferrite number decreases due to the conversion of ferrite into austenite after re-melting and increases due to the dilution effect. In a triple-layered clad, at the top layers, SDSS retains its composition, i.e., the austenite/ferrite ratio approaches almost 1:1, as the effect of dilution is minimum at the top layers. Again, in the case of triple layers, from top to bottom, ferrite number first decreases and then increases due to the formation of a secondary austenite and the dilution effect of the substrate, respectively. So, it can be concluded that after evaluating the ferrite content, a greater number of layers is preferable to keep the dilution minimum, but it cannot be exceeded; otherwise, the cost of cladding will also get soot up. Additionally, an optimization solution would be helpful for the determination of the optimum number of layers required.

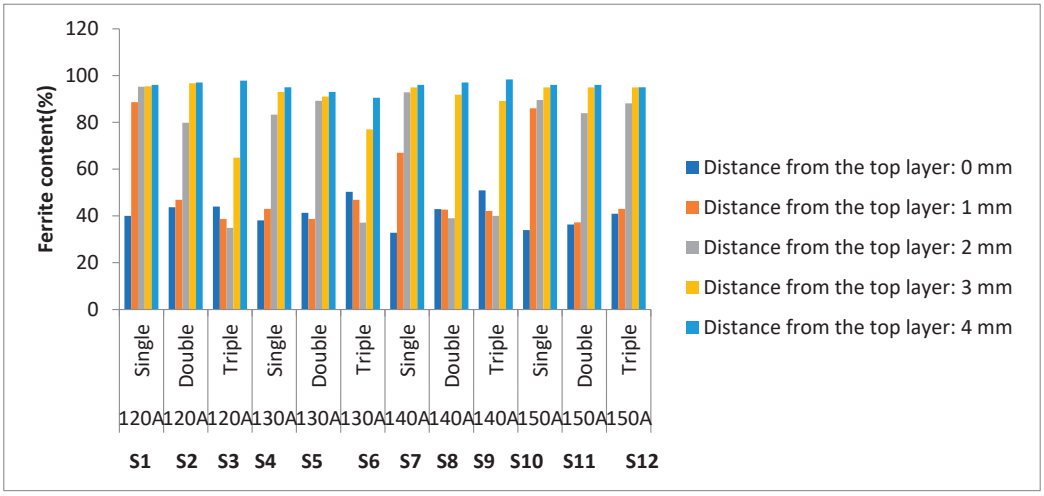

Figure 9. Ferrite content analysis for 12 samples of various current levels.

4.5. Dilution

Dilution can be defined as the proportion of base material in the resultant clad layer deposited, usually taken to be the ratio of the cross-sectional area of melted base material to the total cross-sectional area of the fusion zone. The dilution (D) was obtained using the following formula:

$$D = (\text{Area of the base material})/(\text{total molten area}). \quad (1)$$

Digital macrographs of the polished surface of different cladded specimens were taken via image analyzer software, i.e., ImageJ (Fiji) software, as shown in Figure 10, and complete clads profiles were obtained. Dilution (D) for each specimen was calculated using Equation (1). The graphical representation of variation in the dilution with change in the current level and number of clad layers is shown in Figure 11. Dilution depends upon the clad penetration, width, and reinforcement. If the penetration is high compared to the width and reinforcement, dilution increases, and if the penetration is low compared to the width and reinforcement, dilution decreases. For cladding purposes, low dilution is required because low dilution due to the reinforcement as well as the width of the clad increases, resulting in a larger coverage area onto the substrate surface. Additionally, the effective constituents required in the clad layers retain themselves. For a single-layered clad, on increasing the current level, the deposition rate of filler wire increases, resulting in an increase in the clad reinforcement compared to the penetration level, so the value of dilution decreases, which is also shown in Figure 11. In the case of double layers of clads on increasing current level, dilution decreases, as the increment in the clad width as well as reinforcement is more due to simultaneous re-melting of the previously laid clad layer in addition to the new layer. In the case of triple-layered clads, on increasing current level, no significant change in dilution is noticed. It can be observed from Figure 11 that the dilution is almost constant at ~35%. This is because on increasing the current level, clad width increases more compared to that of reinforcement.

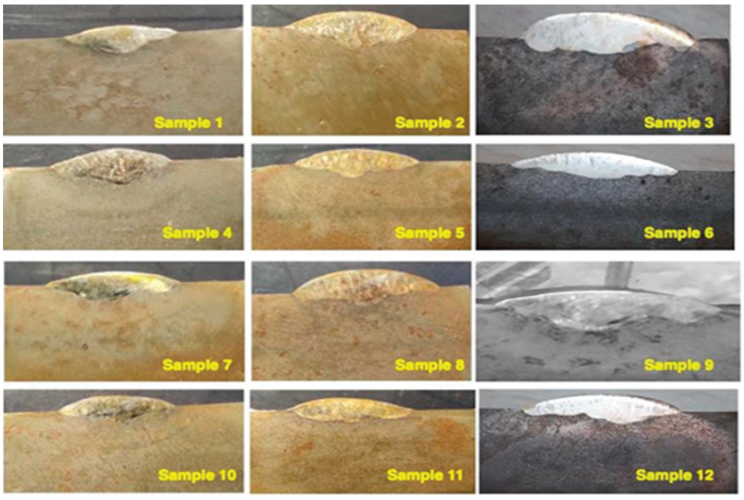

Figure 10. Macrographs of typical transverse clad sections.

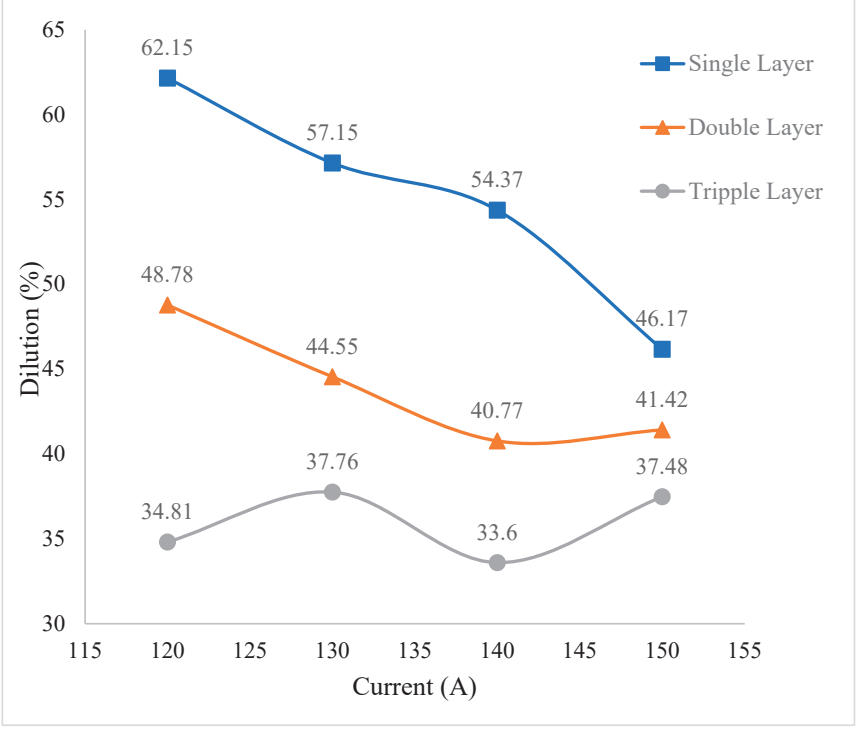

Figure 11. Variation in dilution with current for a single layer, double layers, and triple layers.

4.6. Optimization of the Dilution Result

Assuming a cubic relationship in the first instance and considering all the possible two-factor interactions and confounded interactions, it could be written as follows in Equation (2):

$$Y = b0 + b1A + b2B\,[1] + b3B\,[2] + b4AB\,[1] + b5AB\,[2] + b6A^2 + b7A^2B\,[1] + b8A^2B\,[2] + b9A. \quad (2)$$

The factorial design of twelve experimentations is implemented via the software, Design-for-expert (DX 11) version 11, as well as a model illustrating the relationships between both the response Y (dilution) and the processing parameters (welding current and the clad layers B) for coded values of each processing parameters is developed. The variance analysis has been used to assess the appropriateness of the derived models' validity and quality of fit (ANOVA). When all other factors are maintained constant, the coefficient estimate shows the expected change in reaction per unit change in factor value. The average response of all the runs is the interception in an orthogonal design. Depending on the factor values, the coefficients modify the average around it. When the factors are perpendicular, the VIFs are 1. Whenever the factors are multi-colinear, the VIFs are higher than 1. The greater the VIF, the more intense the correlation of the variables. VIFs under 10 are generally considered tolerable. The estimated coefficient is shown in Table 6.

Table 6. The estimated coefficient.

Term	Coefficient Estimate	DF	Standard Error	95% CI Low	95% CI High	VIF
Intercept	44.65	1	1.18	39.58	49.71	
A Current	−5.60	1	3.51	−20.72	9.52	12.67
B [1]	11.31	1	1.67	4.15	18.48	
B [2]	−2.29	1	1.67	−9.46	4.87	
AB [1]	−3.97	1	1.40	−9.98	2.03	
AB [2]	−0.2425	1	1.40	−6.25	5.76	
A^2	0.4894	1	1.66	−6.63	7.61	1.0000
A^2B [1]	−2.29	1	2.34	−12.36	7.78	
A^2B [2]	2.26	1	2.34	−7.82	12.33	
A^3	2.15	1	3.70	−13.77	18.08	12.67

4.6.1. Regression Equation of Dilution

It is possible to anticipate the reaction for specific levels of each element using the equation expressed in terms of coded factors. By definition, the factors' high levels are recorded as +1 and their low levels as −1. By evaluating the factor coefficients from Equations (3)–(6), the coded equation is helpful in determining the relative impact of the components.

$$D = +44.65 - 5.60*A + 11.31*B\,[1] - 2.29*B\,[2] - 3.97*AB\,[1] - 0.2425*AB\,[2] + 0.4894*A^2 - 2.29*A^2B\,[1] + 2.26*A^2B\,[2] + 2.15*A^3 \quad (3)$$

For a single layer, the relevant equation is expressed as follows:

$$D = -1574.24150 + 36.42282*Current - 0.266525*Current^2 + 0.000638*Current^3 \quad (4)$$

For double layers, the relevant equation is expressed as follows:

$$D = 1253.26250 + 31.21742*Current - 0.246325*Current^2 + 0.000638*Current^3 \quad (5)$$

For triple layers, the relevant equation is expressed as follows:

$$D = -1480.07600 + 34.18077*Current - 0.256200*Current^2 + 0.000638*Current^3 \quad (6)$$

4.6.2. Effect of Current on Dilution

Variation in dilution with currents for single, double, and triple layers is shown in Figure 12. Moreover, the optimized input value for dilution must be determined.

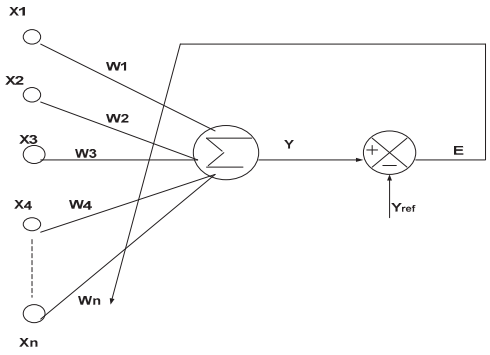

Figure 12. Structure of ANN view.

To determine the optimized value from the input parameters, first decide the criteria for each input and output parameter which are as follows:

- The current value should be in the range of 120 A–150 A;
- Clad layers should be single, double, or triple;
- The response, i.e., dilution, should be minimum.

After applying this condition in the software design-for-expert (DX11), the optimum results are shown in Table 7.

Table 7. Optimized results.

Number	Current	Layer	Dilution	Desirability	
1	140.830	Triple	35.289	0.941	Selected
2	140.935	Triple	35.289	0.941	
3	140.456	Triple	35.291	0.941	
4	120.000	Triple	35.376	0.938	
5	144.246	Double	40.302	0.765	
6	144.061	Double	40.303	0.765	
7	150.000	Single	46.743	0.540	

From the above solution, it is clear that, on 140.83 A current with 3 layers of the clad, the dilution is minimum, and it has maximum desirability.

4.7. Artificial Neural Network (ANN) for the Optimization of the Dilution

The dilution effect is now further analyzed with ANN. The design aspect of ANN is referred to in [20]. For the given system, the design of ANN has been considered via an extended Equation (2). This equation can be expressed as a general expression of ANN as shown in Equation (7).

$$Y = W_1X_1 + W_2X_2 + W_3X_3 + W_4X_4 \ldots\ldots\ldots \quad (7)$$

This output will be checked with its reference value, which gives an error that is given in Equation (8).

$$E = \frac{(Y - Y_{ref})^2}{2} \quad (8)$$

The error will update the new weight, as shown in Equation (9).

$$W_{new} = W_{old} - \eta \frac{E}{W_{old}} \quad (9)$$

The structure and deployment of ANN for the estimation of dilution are shown in Figure 12.

4.8. Design and Development of Firefly Algorithm (FA) for the Optimization of the Dilution

The process of the firefly algorithm [21] has been explained through a flowchart, as shown in Figure 13. In the beginning, fireflies are distributed uniformly from Y_1 to Y_n. Then, each firefly's matching power at its various positions is gauged and noted. It is observed that fireflies are attracted to the nearby neighborhood of the best firefly. The general expression of the propagation of firefly i towards the brighter firefly j is given as the following Equations (10) and (11).

$$Y_i^{t+1} = Y_i^t + \beta Y_{ij} + \alpha(\text{ran} - 0.5) \tag{10}$$

$$\beta = \beta_o e^{(-\gamma D_{ij})^2} \tag{11}$$

where Y_i^t and Y_i^{t+1} are the present and next position of firefly i. Y_{ij} is the distance between firefly i and firefly j. α and ran denotes the coefficient and a random number of adjusting movements. β is the degree of attraction, and β_o is the initial attractiveness. γ is the light absorption coefficient.

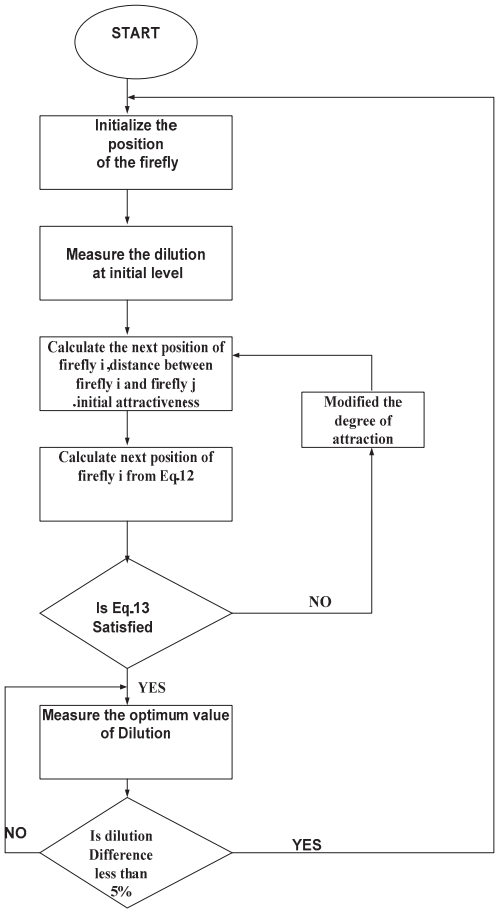

Figure 13. Flowchart illustrating the firefly algorithm.

β_o can also be expressed as follows:

$$\beta_o = \frac{2}{1 + e^{(-5(1-\frac{Y_i}{Y_j}))}} - 1,$$

where Y_i and Y_j show the power output of firefly i and firefly j. The movement of firefly i is attracted by brighter firefly j, which is given by Equation (12).

$$Y_i^{t+1} = Y_i^t + \beta Y_{ij} \tag{12}$$

β is set to 0.25, which increases unity after every iteration to enhance the searching speed. The following convergence must be satisfied for the given algorithm, as shown in Equation (13).

$$Y_{i,max}^t - Y_{i,min}^t < 5\% \tag{13}$$

The operating point with Y_i, max is regarded as the algorithm's estimated maximum practical precision as soon as convergence is verified, or the maximum number of iterations is reached.

The comparison of dilution of various current levels for the firefly algorithm and ANN for the first, double, and third layers is shown in Figure 14.

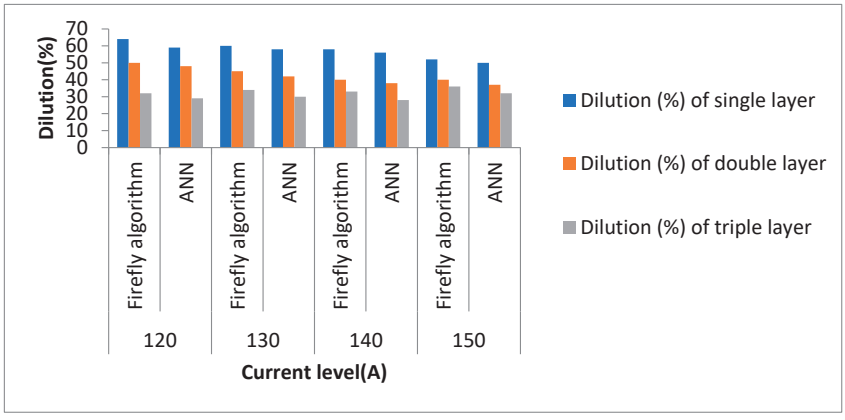

Figure 14. Comparison of the variation of dilution of single layer, double layers, and triple layers of various current levels via firefly algorithm and ANN.

In Figure 14, the best dilution level is achieved for the third layer in comparison to the first and second layers. It is observed that dilution (%) for single layer, double layers, and triple layers is found to be best with the firefly algorithm in comparison to ANN for various current levels.

5. Advanced Study and Analysis of Multivariable System

The three different studies are analyzed in the section which is explained in the following subsection.

5.1. Multivariable System Approach for Dilution Estimation

Let us discuss the four variables system which are represented in terms of voltage (V), current (I in Ampere), welding speed ($\omega_{welding}$ in mm/s), and thermal efficiency ($\eta_{thermal,efficiency}$).

Basically, dilution is dependent on the heat input (J/mm).

Dilution (D) is also directly proportional to heat input (H), and its representation in the form of proportionality constant (K) is mentioned in Equation (14) as follows:

$$D = KH. \tag{14}$$

The heat input can be represented as Equation (15).

$$H = \frac{\eta_{thermal,efficiency} VI}{\omega_{welding}} \tag{15}$$

Input the value of H from Equation (15) into Equation (14), then Equation (16) is obtained as follows:

$$D = \frac{K\eta_{thermal,efficiency} VI}{\omega_{welding}}. \tag{16}$$

As can be seen, dilution depends on four parameters.

Let us analyze dilution with the firefly algorithm and ANN.

The process and design of the firefly algorithm are already explained in Section 4.8.

The design of ANN is also explained in Section 4.7. However, for the four variables, the design is a little bit different as follows:

Take the log on both sides in Equation (16), then Equation (17) is attained.

$$\log D = \log K + \log \eta_{thermal,efficiency} + \log V + \log I - \log \omega_{welding} \tag{17}$$

Equation (17) can be written as the general equation of ANN, mentioned in Equation (18) as follows:

$$Y = W_1X_1 + W_2X_2 + W_3X_3 + W_4X_4 + c, \tag{18}$$

whereas

$$Y = \log D, W_1 = \log \eta_{thermal,efficiency}, W_2 = \log V, W_3 = \log I, W_4 = -\log \omega_{welding}, c = \log K$$

This output will be checked with its reference value, which gives an error given in Equation (19) as follows:

$$E' = \frac{(Y - Y_{ref})^2}{2}. \tag{19}$$

The error will update the new weight, as shown in Equation (20).

$$W_{new} = W_{old} - \eta \frac{E'}{W_{old}} \tag{20}$$

The old and modified values of weights are given in Table 8.

Table 8. Old and modified values of weights.

S.No	W_{old}	Value	W_{new}	Value
1	W_1	7.8	W_1	8.5
2	W_2	8.2	W_2	9.4
3	W_3	9.1	W_3	9.6
4	W_4	8.9	W_4	9.7

After upgrading the weights, the dilution level has been improved considerably for the various current levels.

The performance level of dilution under various current levels, voltage, thermal efficiency, and welding speed with the firefly algorithm and ANN is shown in Table 9, and its graphical analysis is shown in Figure 15.

Table 9. Dilution at various current levels, voltage, welding speed, and thermal efficiency with firefly algorithm and ANN.

Dilution (%)	120 A Current Level, Voltage, Welding Speed, Thermal Efficiency		130 A Current Level, Voltage, Welding Speed, Thermal Efficiency		140 A Current Level, Voltage, Welding Speed, Thermal Efficiency		150 A Current Level, Voltage, Welding Speed, Thermal Efficiency	
	Firefly Algorithm	ANN	Firefly Algorithm	ANN	Firefly Algorithm	ANN	Firefly Algorithm	ANN
Single layer	75.6	68.2	76.9	69.3	78.2	71.6	80.8	75.2
Double layer	76.2	69.3	77.5	70.4	78.8	72.7	81.4	76.3
Third layer	78.2	71.3	79.5	72.4	80.8	74.7	83.4	78.3

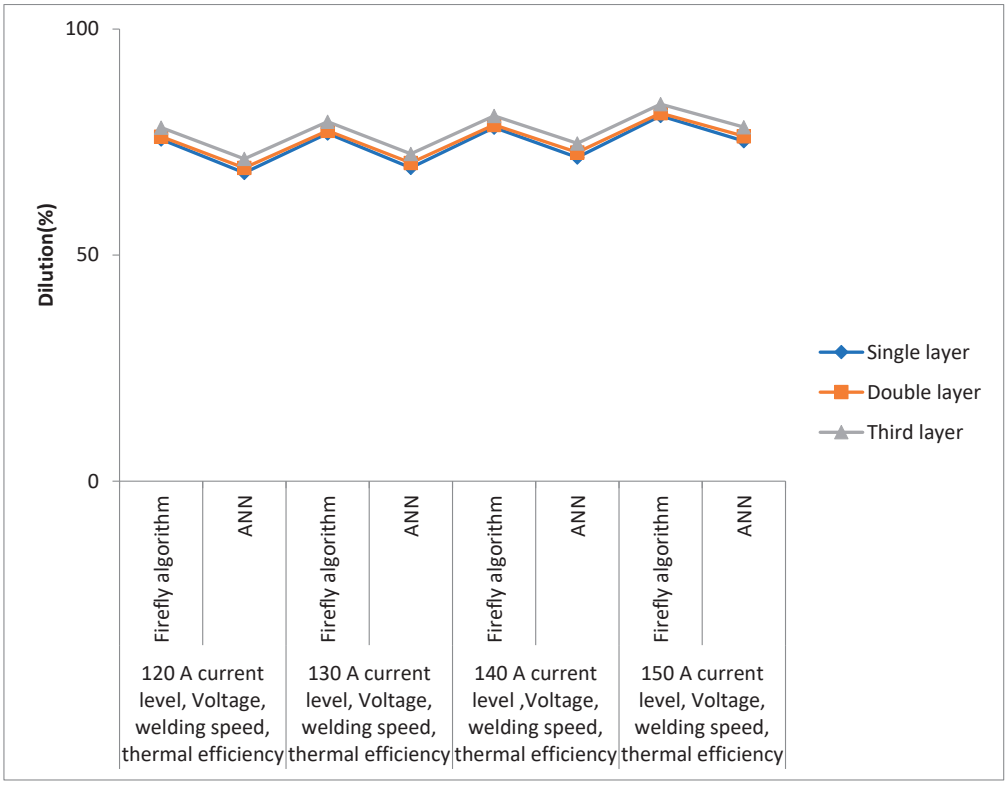

Figure 15. Comparison of dilution at various current levels, voltage, welding speed, and thermal efficiency with firefly algorithm and ANN.

It is observed that dilution level has been improved a lot with the firefly algorithm in comparison to ANN for various current levels, voltage, welding speed, and thermal efficiency.

The experimental set consists of the following data:

Heat input = 0.9 J/mm with a deviation of 5%;

Thermal efficiency = 0.6 with a deviation of 3%;

Welding speed = 10 mm/s with a deviation of 2%.

5.2. Three Principles of Experimental Setup

Let us understand the three basic principles of the experimental design: randomization, replication, and blocking. It is required to analyze and elaborate on these principles in our experimental setup one by one.

5.2.1. Randomization

It is a random process of assigning the task to various units of the experimental setup. Every potential treatment allocation has an equal probability under the stochastic process, i.e., it is implied. There were 12 samples taken for experimental setup, as shown in Figure 10 of the manuscript.

Twelve samples are distinguished and independent of each other; furthermore, their names are given in Table 10.

Table 10. Naming and labeling of 12 samples.

Samples	Labeling
Sample 1	A
Sample 2	B [1]
Sample 3	B [2]
Sample 4	AB [1]
Sample 5	AB [2]
Sample 6	A^2
Sample 7	A^2B [1]
Sample 8	A^2B [2]
Sample 9	A^3
Sample 10	A
Sample 11	B [1]
Sample 12	B [2]

It is observed from Table 10 that all the events or samples occur independently, but all 12 samples are tested 3 times in different possible ways, as shown in Table 11.

Table 11. A total of 36 possible combinations of occurrence of 12 samples.

Events	Test 1	Test 2	Test 3
1	Sample 1	Sample 4	Sample 10
2	Sample 2	Sample 5	Sample 11
3	Sample 3	Sample 6	Sample 9
4	Sample 4	Sample 7	Sample 1
5	Sample 5	Sample 1	Sample 2
6	Sample 6	Sample 2	Sample 3
7	Sample 7	Sample 11	Sample 4
8	Sample 8	Sample 12	Sample 8
9	Sample 9	Sample 10	Sample 12
10	Sample 10	Sample 9	Sample 6
11	Sample 11	Sample 3	Sample 7
12	Sample 12	Sample 8	Sample 5

It can be seen from Table 11 that each sample is occurring thrice in various tests as follows: Sample 1 is occurring in Events 1, 5, and 4; Sample 2 is occurring in Events 2, 6, and 5; Sample 3 is occurring in Events 3, 11, and 6; Sample 4 is occurring in Events 4, 1, and 7; Sample 5 is occurring in Events 5, 2, and 12; Sample 6 is occurring in Events 6, 3, and 10; Sample 7 is occurring in Events 7, 4, and 11; Sample 8 is occurring in Events 8, 12, and 8; Sample 9 is occurring in Events 9, 10, and 3; Sample 10 is occurring in Events 10, 9, and 1; Sample 11 is occurring in Events 11, 7, 2; Sample 12 is occurring in Events 12, 8, 9.

The total number of elements is $12 \times 3 = 36$.

The probability of occurrence of each sample is 3/36.

5.2.2. Replication

It is the number of repetitions applied to each experimental sample unit and further comparison occurred among various sample values. It increases the precision value by reducing the standard error, S_e.

The mathematical expression of standard error, S_e, is given as $s/\sqrt{r}$, where 'r' is the no. of replication (=3), and 's' is the standard deviation.

The value of standard error is already calculated for 12 samples, which are shown in Table 6 and further shown separately in Table 12.

Table 12. Value of standard error of 12 samples.

Samples	Standard Error (S_e)
Sample 1	1.18
Sample 2	3.51
Sample 3	1.67
Sample 4	1.67
Sample 5	1.40
Sample 6	1.40
Sample 7	1.66
Sample 8	2.34
Sample 9	2.34
Sample 10	3.70
Sample 11	1.67
Sample 12	1.67

5.2.3. Blocking

It is used to restrict or block the unavoidable source of variation from the sample units. The blocking is carried out with the primary goal of improving the experimental design efficiency by lowering the experimental error.

5.3. Estimation of Variance

Let us perform the diagnostic and adequacy checking by estimating the variance of samples.

It is seen from the previous section that standard deviation (s) is given by multiplication of standard error (S_e) and no. of replications (r), as shown in Equation (21).

$$s = S_e\sqrt{r} \tag{21}$$

The distribution of all the data points in an information set is taken into consideration by the variance, which is a measure of distribution. Along with the standard deviation, which is just the square root of the variance, it is the measure of spread that is most

frequently employed. The relationship between variance (Var) and standard deviation (s) is given in Equation (22).

$$\mathrm{Var} = s^2 \tag{22}$$

Input the value of Equation (21) in Equation (22), then the final expression of variance is shown in Equation (23).

$$\mathrm{Var} = \left(S_e\sqrt{r}\right)^2 \tag{23}$$

The value of variance for various samples is shown in Table 13, and its graphical analysis is shown in Figure 16.

Table 13. Value of standard error of 12 samples.

Samples	Variance (Var)
Sample 1	4.18
Sample 2	36.96
Sample 3	8.37
Sample 4	8.37
Sample 5	5.88
Sample 6	5.88
Sample 7	8.27
Sample 8	16.43
Sample 9	16.43
Sample 10	41.07
Sample 11	8.37
Sample 12	8.37

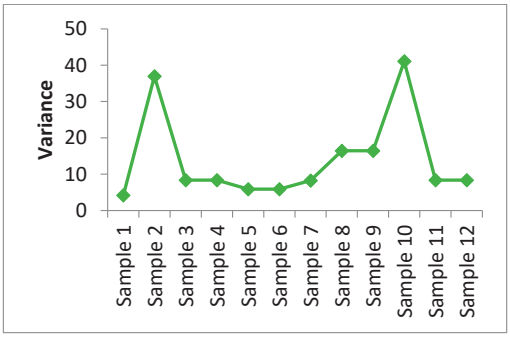

Figure 16. Pattern of variance for various samples.

6. Conclusions

The GTA cladding of super duplex stainless steel over AISI 1020 steel was successfully completed. The study portrays the effect of the current level and clad layers on the microstructure, dilution, ferrite content, microhardness, and pitting corrosion/localized corrosion. Based on the results of this present work, the following conclusions were drawn:

* The cladding of the super duplex stainless steel over mild steel improves the corrosive properties. The I_r/I_a% improves from 29% (mild steel) to 4.1% at the top and 11.9% at the intermediate layers;
* The microhardness of the clad decreases with an increase in both the current level and the number of layers;

- Microhardness varies between 191–248 at the clad, 170–189 at the HAZ, and 143–153 at the substrate for a 1 kgf load;
- For a single-layered clad, on increasing the current level, the deposition rate of filler wire increases, resulting in an increase in the clad reinforcement compared to the penetration level, so the value of dilution decreases;
- In the case of double layers of a clad, on increasing current level, dilution decreases due to the increment in clad width as well as reinforcement (simultaneous re-melting of the previously laid clad layer takes place in addition to the new layer deposit);
- All triple layers possess almost the same dilution at different levels of current, but compared to a single layer and double layers, it was found to be minimum. Dilution reduces due to the re-melting of two successive layers in addition to the new layer deposit, which further reduces dilution;
- Parametric optimization yields that a triple layer made at ~140 A shows minimum dilution (33.6%), optimum ferrite content (50.9%), optimum microhardness (195) maximum pitting corrosion/localized corrosion resistance, i.e., I_r/I_a% (4.1%).

Using the firefly algorithm (FA) and an artificial neural network, the dilution impact is also examined on three layers of different current levels (ANN). For different current levels, it is seen that dilution levels are more suitable to the experimental setup reading with FA than ANN.

Author Contributions: Conceptualization, M.M. and L.G.; methodology, A.S. and L.G.; software, A.K.S.; validation, A.S. and G.K.S.; formal analysis, M.M.; investigation, M.M. and L.G.; writing—original draft preparation, M.M. and L.G.; writing—review and editing, A.S., A.K.S. and H.S.H.; supervision, G.K.S. and J.K.B.; funding acquisition, R.V.; project administration, R.V. All authors have read and agreed to the published version of the manuscript.

Funding: The authors extend their appreciation to the Deanship of Scientific Research at King Khalid University for funding this work through a Large Group Research Project under grant number: RGP 2/177/44.

Institutional Review Board Statement: Not applicable.

Informed Consent Statement: Not applicable.

Data Availability Statement: Not applicable.

Conflicts of Interest: The authors declare no conflict of interest.

References

1. Kahar, S.D. Review on electro-slag strip cladded weld overlays. *Int. J. Adv. Eng. Res. Dev.* **2016**, *3*, 1–8.
2. Paschold, R.; Karlsson, L.; Gittos, M.F. Disbonding of austenitic weld overlays in hydroprocessing applications. *ESAB Svetsaren* **2007**, *62*, 10–15.
3. Bhatt, R.B.; Kamat, H.S.; Ghosal, S.K.; De, P.K. Influence of nitrogen in the shielding gas on corrosion resistance of duplex stainless steel welds. *ASM J. Mater. Eng. Perform.* **1999**, *8*, 591–597. [CrossRef]
4. Murugan, N.; Parmar, R.S. Mathematical models for bead geometry prediction in automatic stainless steel surfacing by MIG welding. *Int. J. Join. Mater.* **1995**, *7*, 71–80.
5. de Lima-Neto, P.; Farias, J.P.; Herculano, L.F.G.; de Miranda, H.C.; Araújo, W.S.; Jorcin, J.B.; Pébère, N. Determination of the sensitized zone extension in welded AISI 304 stainless steel using non-destructive electrochemical techniques. *Corros. Sci.* **2008**, *50*, 1149–1155. [CrossRef]
6. Paschold, R.; Karlsson, L. Electroslag strip cladding for corrosion resistance. *ESAB Svetsaren* **2001**, *56*, 62–67.
7. Koch, G.H.; Brongers, M.P.; Thompson, N.G.; Virmani, Y.P.; Payer, J.H. *Corrosion Cost and Preventive Strategies in the United States*; National Academy of Sciences, USA (No. FHWA-RD-01-156); Federal Highway Administration: Washington, DC, USA, 2002.
8. Singh, B.; Basak, M.; West, M.; Guha, I. Estimating the cost of corrosion in Indian industry. In Proceedings of the PETROTECH-2010, New Delhi, India, 31 October–3 November 2010. Available online: http://hdl.handle.net/20.500.11937/18048 (accessed on 4 January 2023).
9. Parmar, R.S. *Welding Process and Technology*; Khanna Publisher: New Delhi, India, 2003.
10. Srinath, K. Investigation on 410 L Stainless Steel Cladding of Mild Steel Valve Seat Rings by Plasma Transferred Arc Welding. Ph.D. Thesis, Anna University Chennai, Chennai, India, 2012.

11. Liu, Y.; Ding, Y.; Yang, L.; Sun, R.; Zhang, T.B.; Yang, X. Research and progress of laser cladding on engineering alloys: A review. *J. Manuf. Process.* **2021**, *66*, 341–363. [CrossRef]
12. Lucas, W. Arc surfacing and cladding processes to enhance performance in service and to repair worn components. *Weld. Metal Fabr.* **1994**, *62*, 55–61.
13. Keskitalo, M.; Mäntyjärvi, K.; Sundqvist, J.; Powell, J.; Kaplan, A.F.H. Laser welding of duplex stainless steel with nitrogen as shielding gas. *J. Mater. Process. Technol.* **2015**, *216*, 381–384. [CrossRef]
14. Aval, H.J.; Farzadi, A.; Serajzadeh, S.; Kokabi, A.H. Theoretical and experimental study of microstructures and weld pool geometry during GTAW of 304 stainless steel. *Int. J. Adv. Manuf. Technol.* **2009**, *42*, 1043–1051. [CrossRef]
15. Arivazhagan, B.; Srinivasan, G.; Albert, S.; Bhaduri, A. A study on influence of heat input variation on microstructure of reduced activation ferritic martensitic steel weld metal produced by GTAW process. *Fusion Eng. Des.* **2011**, *86*, 192–197. [CrossRef]
16. Elsawy, A.H. Characterization of the GTAW fusion line phases for super ferritic stainless steel weldments. *J. Mater. Process. Technol.* **2001**, *118*, 127–131. [CrossRef]
17. Ghanty, P.; Paul, S.; Mukherjee, D.P.; Vasudevan, M.; Pal, N.R.; Bhaduri, A.K. Modelling weld bead geometry using neural networks for GTAW of austenitic stainless steel. *Sci. Technol. Weld. Join.* **2007**, *12*, 649–658. [CrossRef]
18. Ogawa, T.; Aoki, S.; Sakamoto, T.; Zaizen, T. Weldability of Nitrogen-Containing Austenitic Stainless Steel: Part I. Chloride Pitting Corrosion Resistance. *WELDING J.* **1982**, *61*, 139–148.
19. Baeslack, W.A., III; Duquette, D.J.; Savage, W.F. The effect of ferrite content on stress corrosion cracking in duplex stainless steel weld metals at room temperature. *Corrosion* **1979**, *35*, 45–54. [CrossRef]
20. Saxena, A.; Kumar, R.; Singh, J.; Singh, G.K.; Kumar, V.S.; Pandey, J.P. An Invasive Weed Optimization for Sensor Less Control of Grid Integrated Wind Driven Doubly Fed Induction Generator. *IEEE Access* **2022**, *10*, 109082–109096. [CrossRef]
21. Huang, Y.P.; Huang, M.Y.; Ye, C.E. A Fusion Firefly Algorithm with Simplified Propagation for Photovoltaic MPPT Under Partial Shading Conditions. *IEEE Trans. Sustain. Energy* **2020**, *11*, 2641–2652. [CrossRef]
22. Torres, A.F.; Rocha, F.B.; Almeida, F.A.; Gomes, J.H.; Paiva, A.P.; Balestrassi, P.P. Multivariate Stochastic Optimization Approach Applied in a Flux-Cored Arc Welding Process. *IEEE Access* **2020**, *8*, 61267–61276. [CrossRef]

MDPI
St. Alban-Anlage 66
4052 Basel
Switzerland
www.mdpi.com

Coatings Editorial Office
E-mail: coatings@mdpi.com
www.mdpi.com/journal/coatings

Academic Open
Access Publishing

www.mdpi.com

ISBN 978-3-0365-7845-3